DTU Library

Characterization and modeling of bifacial photovoltaic modules and systems

Riedel-Lyngskær, Nicholas Christopher

Publication date:
2023

Document Version
Publisher's PDF, also known as Version of record

Characterization and modeling of bifacial photovoltaic modules and systems

Nicholas Riedel-Lyngskær

PhD Thesis January 2023

Submitted to
The Department of Electrical and Photonics Engineering,
Technical University of Denmark (DTU)

Main Supervisor: Associate Professor Sergiu V. Spătaru, DTU
Co-Supervisor: Senior Researcher Michael L. Jakobsen, DTU
Industrial Supervisor: Jan Vedde, European Energy A/S

Thesis submitted:	January 6, 2023
PhD supervisor:	Associate Prof. Sergiu Viorel Spătaru Technical University of Denmark
Assistant PhD supervisors:	Senior Researcher Michael Linde Jakobsen Technical University of Denmark Jan Vedde European Energy A/S
PhD committee:	Senior Researcher Kaushik Das Technical University of Denmark Prof. Wilfred van Sark Utrecht University Jonathan Leloux LuciSun

English Abstract

In the last decade, bifacial photovoltaic (PV) modules have burgeoned from niche to mainstream technology, encompassing nearly 40% of global PV module sales in 2021. The main drivers behind the increased bifacial PV adoption are twofold: First, the higher energy yields of bifacial systems (5–10% in most conditions) are attractive to project developers that try to maximize PV production within constricted land areas. Second, the industry has optimized the processing steps required to transform the opaque rear surface of a traditional monofacial PV cell and module into a fully transparent one with active PV area on the backside, which in turn has significantly reduced the price premium of bifacial PV modules.

Despite recent rapid adoption of bifacial PV modules, the capacity of bifacial systems represents less than 10% of global PV installations, most of which were deployed in the last three years. The lack of long-term field experience with bifacial systems means that the PV industry is still pressed with open questions, some of which have been addressed in this PhD project such as: i) What is the accuracy of bifacial PV energy yield simulation models and software; ii) what are the best-practices for operation and maintenance of utility scale bifacial PV plants, and iii) what is the optimal use of bifacial modules in utility-scale applications. This thesis addresses each of these issues in turn using a combination of simulations and extensive laboratory and field testing.

The higher energy yield of bifacial PV systems is only considered bankable by investors if it can be accurately predicted. Therefore, **Chapter 2** quantifies the principal uncertainties in bifacial modeling. The chapter begins with a study that benchmarked eight bifacial PV performance models against the high-quality operational PV data recorded at the Technical University of Denmark's (DTU) Risø Campus. The chapter then presents results from an international PV modeling intercomparison – the results of which highlight the substantial variability that even expert users can add to the PV modeling process. The chapter ends by quantifying the possible reduction in uncertainty that can be achieved if rear plane-of-array irradiance modeling is improved, and by providing practical recommendations for harmonizing interpretations of the IEC 61853-3 energy rating standard.

The spatial variation of rear plane-of-array irradiance and the spectral nature of albedo are nuanced effects that preclude accurate bifacial PV modeling, if they are not well understood. **Chapter 3** therefore presents investigations that use theory and experiments to characterize these mechanisms that are specific to bifacial PV systems. The first is an investigation of the electrical mismatch induced by non-uniform illumination on the back of tracked bifacial systems. The second study examines how shifts in the spectral distribution of ground reflected light (albedo) alter the photocurrent generated by different bifacial cell technologies. Although these two studies were initially intended to support the development of more accurate rear irradiance models, it was found that the experimental results could also be used to develop best practices for designing bifacial PV monitoring systems.

Chapter 4 focuses on laboratory PV characterizations and continuous outdoor monitoring strategies. In the first part of the chapter, the importance of interlaboratory measurement comparisons to decrease uncertainty in PV yield estimates is described. The results of two interlaboratory comparisons (or "round robins") are presented: One that assesses the comparability among European labs in performing I-V measurements of bifacial modules per IEC TS 60904-1-2 and a second effort where measurements of cell-level incident angle modifier (IAM) response per IEC 61853-2 were compared among labs in Europe

and the United States. The chapter ends by presenting a study that suggests improvements in the irradiance monitoring of bifacial systems via the reference module approach. It is found that calibrated reference modules can be used to reduce the variation in bifacial performance ratio calculations, while at the same time simplifying the monitoring system design and offering the ability to estimate cell temperature through the open-circuit voltage of the I-V curve.

Finally, the energy produced by bifacial systems can be improved by simply increasing the albedo of the ground below the arrays. However, the amortized value of the energy gain must be greater than the upfront and ongoing costs of the albedo enhancement for the solution to be commercially viable. **Chapter 5** therefore provides a technoeconomic analysis of an actual tarp-based albedo enhancement solution that was deployed on 12 kWp tracked and fixed tilt bifacial systems. Although the results of the case study show that the tarp-based albedo enhancement results in lower levelized cost of energy (LCOE) than bifacial systems without it, it is concluded that the uncertainty in upfront and ongoing costs of altering the ground in utility-scale PV parks makes such a solution unadvisable. However, directions for future work in albedo enhancements are offered as well as recommendations that could create more favorable economics for albedo enhancements in large-scale bifacial systems.

Dansk Sammenfatning

I løbet af det sidste årti har tosidede solcellemoduler udviklet sig fra at være en nicheteknologi til et attraktivt produkt, som efterhånden udgør næste 40 % af det samlede globale solcellesalg i 2021. To hovedaspekter har drevet udviklingen af dette marked frem: For det første giver det tosidede solpanel en højere energiproduktion (typisk 5–10 %) end et tilsvarende én-side solcellepanel af samme størrelse. Det er en attraktiv fordel for projektudviklere, der skal optimere energiproduktionen fra et begrænset landareal. For det andet har industrien videreudviklet processer, som kan transformere det oprindelige koncept med solceller på begge sider af et uigennemsigtigt substrat til et transparent koncept med solceller på begge sider. Det sidste koncept har væsentligt reduceret prisen på tosidede solcellemoduler.

På trods af den hastige adoptering af tosidede solcellemoduler, så udgør de kun knapt 10% af de samlede solcelleinstallationer, der globalt er blevet igangsat indenfor de sidste tre år. På grund af den manglende lang-tids erfaring med tosidede solcellemoduler i solcelleanlæg, så mangler solcelleindustrien stadig svar på en række tekniske spørgsmål, som kan have stor betydning for afkastet af investeringer i denne teknologi. Denne afhandling vil adressere en del af disse spørgsmål: i) Hvor præcist kan de gængse modeller og simuleringspakker forudsige energiproduktionen fra solcelleanlæg, der er baseret på tosidede solcellemoduler, ii) hvorledes udføres drift og vedligehold af tosidede moduler bedst muligt i stor-skala solanlæg, og hvorledes optimeres brugen af tosidede solcellemoduler i større anlæg. Denne afhandling adresserer hvert af disse spørgsmål ved at kombinere brugen af simuleringer samt eksperimenter udført i både laboratorier og på adskillige solcelleanlæg.

Det højere energiudbytte for tosidede solcellesystemer bliver kun inkluderet i potentielle investorers vurderinger, hvis det tilsvarende afkast kan beregnes med stor pålidelighed. **Kapitel 2** sætter derfor fokus på de væsentligste usikkerheder ved modellering af anlæg baseret på tosidede solcellemoduler. Kapitlet begynder med et studie, der sammenligner otte forskellige modeller for tosidede solcellemoduler op mod de høj-kvalitetsmålinger, som løbende er blevet foretaget i det solcelleanlæg, som European Energy har stillet til rådighed for Danmarks Tekniske Universitet (DTU) Risø Campus. Kapitel 2 præsenterer dernæst resultaterne fra en international sammenligning af forskellige solcellemodeller – resultaterne demonstrerer den konkrete variation, som selv eksperter kan tillægge modelleringen af de solcelleprocesser. Kapitel 2 afsluttes med en kvantificering af den mulige reducering af usikkerhederne, som kan opnås med en mere nøjagtig model for indstrålingen på bagsiden af solpanelet, samt ved at følge praktiske anbefalinger for at balancere fortolkningen af IEC 61853 standarden for energimærkning.

Den rumlige variation af belysningen af solpanelernes bagside, samt den spektrale variation af albedo er begge nuancerede effekter, der kan forhindre en pålidelig modellering af de tosidede solpaneler, hvis de ikke anvendes korrekt. Derfor præsenterer **Kapitel 3** både teoretiske og eksperimentelle undersøgelser af disse to effekter, som er helt karakteristiske for tosidede solcellesystemer. Den første undersøgelse studerer den elektriske ubalance, som forårsages af en ikke-ensartet indstråling på bagsiden af det tosidede solcellepanel. I det andet forsøg undersøges det, hvorledes et skifte i den spektrale fordeling af lys, der er reflekteret fra underlaget (albedo), ændrer den fotostrøm, som forskellige tosidede solcelleteknologier producerer. På trods af at disse studier oprindeligt var tiltænkt til at udvikle en mere præcis og pålidelig model, så konkluderes det, at de eksperimentelle resultater på tilsvarende måde kan bruges til at anbefale det bedst mulige design af systemer til monitorering af tosidede solcelle systemer.

Kapitel 4 fokuserer på en karakterisering af solceller i laboratorier samt kontinuerlige overvågningsstrategier af udendørssystemer. I første del af kapitlet beskrives vigtigheden af at sammenligne målemetoder for solcelleeffektiviteten på tværs af forskellige laboratorier. Resultatet af to sammenligninger foretaget på tværs af forskellige laboratorier præsenteres: En undersøgelse af I-V målinger for tosidede solceller (IEC TS 60904-1-2) foretaget af en række europæiske laboratorier samt en undersøgelse af effekten af indfaldsvinkel modifikation (IAM) (IEC 61853-2) foretaget af laboratorier i både Europa og USA. Kapitlet afsluttes med et studie, som foreslår forbedringer til at overvåge af indstråling på det tosidede solcellesystem via en metode, der er baseret på et referencemodul. Det konkluderes, at kalibrerede referencemoduler kan bruges til at reducere den usikkerhed, som optræder i effektivitetsberegningerne for de tosidede solceller. Samtidigt simplificeres designet af overvågningssystemet og muligheden for at estimere temperaturen i den enkelte celle via spændingen over det åbne solcellekredsløb (uden belastning).

Endelig, kan den energi, der produceres af det tosidede solcellesystem øges ved at optimere underlagets albedo. Dog skal prisen for både indkøb og vedligeholdelse af et albedo forbedrende underlag holdes op imod den tilsvarende energigevinst for, at forbedringen kan blive kommercielt levebar. **Kapitel 5** leverer derfor en teknologi-økonomisk analyse af en aktuel presenningbaseret albedo forbedrende løsning, som blev testet på 12 kWp tosidede solcellesystemer, som enten automatisk fulgte solen eller havde en fast vinkel i forhold til samme. Selvom resultatet af dette studie viste, at det presenningbaserede albedo forbedrende underlag resulterede i en effektiv lavere energipris (LCOE) end et tilsvarende system uden underlag, så konkluderes det, at usikkerheden ved at investere og løbende vedligeholde et ændret underlag i et stor-skala solcelleanlæg, gør sådan en løsning ikke-anbefalingsværdig. Til gengæld gives der retningslinjer til fremtidigt arbejde, samt anbefalinger som kan danne grundlag for mere attraktive albedoforbedringer i stor-skala tosidede solcellesystemer.

Acknowledgements

This project could not have been realized without contributions from several individuals. Peter Poulsen and Sune Thorsteinsson from the Applied Photovoltaics (APV) team have been generous with their time from the grant writing phase all the way to the finish line, providing critical resources and expertise throughout the project. I have also been privileged to work with skilled and dedicated master's students including Alexander Aguilar Protti, Daniel Alvarez Mira, Manon Petit, and Martynas Ribaconka – you all made meaningful contributions to some of the articles presented here.

I am grateful that my supervisors Sergiu Spataru, Michael Jakobsen, and Jan Vedde, all gave me freedom to pursue my own research ideas throughout the course of this project. Furthermore, I am grateful that I had the opportunity to design and build the measurement systems presented in publications 3, 5 and 8 – not every PhD student is bestowed with such confidence from their supervisors and with such financial resources. For the latter, I must also thank the funding from Innovation Fund Denmark (IFD) and the Danish Energy Development and Demonstration Program (EUDP).

This project was partially financed by the Danish PV project developer European Energy A/S, which added a useful commercial perspective to some of the work presented here. Thank you to Morgane Fleurance from the procurement department for engaging in many interesting discussions on PV module testing, and for providing information on the latest industry trends. Thanks also to Martin Kolkenbrock from the operations department for always answering my questions about PV operation and maintenance practices, and for providing me access to plenty of data from utility-scale PV assets.

My external research stay at Sandia National Laboratories (SNL) was the opportunity of a lifetime. A big thanks to Joshua Stein for integrating me into the SNL-PSEL team and for making me feel welcome. Thanks also to Marios Theristis of SNL for the exciting collaboration on the PVPMC blind modeling comparison, and to Bruce King of SNL for the interesting discussions on outdoor PV testing.

I am overall deeply thankful to have had the opportunity to directly participate in the scientific process. This includes the conferences, working groups, and numerous collaborations with external partners. All the coauthors listed in the Appended Articles section have contributed to this great pleasure.

Finally, I would like to thank my wife Anni and son Elliot for being the loving and supportive family that you are. You guys helped me to stay even keeled throughout these three challenging years.

Table of Contents

List of Figures

Nomenclature

List of Abbreviations:

1P	One module in portrait
2D/3D	Two dimensional/Three dimensional
2P	Two modules in portrait
Al-BSF	Aluminum Back Surface Field
AM	Air Mass
AOI	Angle of Incidence
ARC	Anti-reflective Coating
BFIR	Back-to-front Irradiance Ratio
bPV	Bifacial Photovoltaic
BSi RIE	Black Silicon with Reactive Ion Etching
CAPEX	Capital Expenditures
CDF	Cumulative Distribution Function
CI	Confidence Interval
CSER	Climate Specific Energy Rating
c-Si	Crystalline Silicon
DK2	Spot price in the Danish nordpool electricity market
DTU	Technical University of Denmark
DUT	Device Under Test
EE	European Energy A/S
EVA	Ethylene Vinyl Acetate
GWp	Gigawatt Peak
HIT	Heterojunction with Intrinsic Thin layer
HSAT	Horizontal Single-Axis Tracker
IAM	Incidence Angle Modifier
IBC	Interdigited Back Contact
IEC	International Electrotechnical Commission
IFD	Innovation's Fond Danmark
IRR	Internal Rate of Return
ITRPV	International Technology Roadmap for PV
LCOE	Levelized Cost of Energy
LDLS	Lased Driven Light Source
LeTID	Light and Elevated Temperature Degradation
LID	Light Induced Degradation
MAE	Mean Absolute Error
MBE	Mean Bias Error
MERLIN	Mini-modules for Estimating Rear Light Intensity Nonuniformity
MML	Mismatch Losses
MODIS	Moderate Resolution Imaging Spectroradiometer
MPPT	Maximum Power Point Tracking
mPV	Mono-facial Photovoltaic

NMOT	Nominal Module Operating Temperature
NOCT	Nominal Operating Cell Temperature
n-PERT	Passivated Emitter and Rear Totally Diffused
O&M	Operation and Maintenance
OPEX	Operational Expenditures
PERC	Passivated Emitter and Rear Cell
POA	Plane-of-array
POE	Polyolefin Elastomer
PR	Performance Ratio
PV	Photovoltaic
RMSE	Root Mean Squared Error
RT	Raytracing
RTR	Row-to-row
SDE	Single Diode Equation
SHJ	Silicon Heterojunctions
SMARTS	Simple Model for Atmospheric Radiative Transfer of Sunshine
SMM	Spectral Mismatch factor
SR	Spectral Responsivity
STC	Standard Test Conditions
TC	Technical Committee
TWp	Terawatt Peak
TS	Technical Specification
TT	Torque Tube
VF	View factor
WG	Working Group

List of Symbols:

BEG_λ	Spectrally weighted bifacial energy gain
DF	Diffuse Fraction
$DfHI$	Diffuse Horizontal Irradiance
DNI	Direct Normal Irradiance
$DrHI$	Direct Horizontal Irradiance
E_n	Metrological proficiency statistic
G_E	Total effective irradiance
GHI	Global Horizontal Irradiance
G_{Meas}	Measured irradiance
G_{POA}	Global irradiance in plane-of-array
G_{Ref}	Refence irradiance
GRI	Ground Reflected Irradiance
I_0	Dark saturation current
I_{MAX}	Current at maximum power
I_{SC}	Short-circuit current
I-V	Current-Voltage characteristic

K_t	Clear sky index
n	Diode quality factor
P_{MAX}	Maximum Power Point
RHI	Reflected irradiance measured in a horizontal plane
ρ	Albedo
R_{POA}	Global irradiance in the rear plane-of-array
R_S	Series resistance
R_{SH}	Shunt resistance
SR_{DUT}	Spectral responsivity of the device under test
SR_{Ref}	Spectral responsivity of the reference device
T_{MOD}	Module Temperature
V_{MAX}	Voltage at maximum power
V_{OC}	Open-circuit voltage
X_{ref}	Reference value

Chapter 1. Project Background

This work has been financed by the Innovation Fund Denmark's (IFD's) Industrial PhD Program. This funding mechanism aims to provide Danish companies a competitive edge by investing in industry-academic collaborations that can result in patents, licenses, new jobs, and other positive economic outcomes. The work presented here was developed in close collaboration with the Danish renewable energy project developer European Energy A/S (EE). Although no patents have been acquired during the project period, the knowledge collected has informed decisions within various EE departments including Innovation, Operations and Maintenance (O&M), Engineering, and Procurement. Specifically, the results accumulated in the last three years have provided EE with insights regarding the expected yield of different bifacial PV system designs in Denmark, optimal techniques for solar resource monitoring (including rear irradiance and albedo) and best practices for modeling PV systems.

The data analyzed in this thesis were collected primarily at a 420 kWp outdoor test site located within the Technical University of Denmark's (DTU) Risø campus [1]. This test site was constructed in summer 2018 by EE to measure bifacial energy gains on large-scale fixed tilt and single axis tracker systems. Several specialized testbeds were constructed at the facility during this PhD project (2019–2022) thanks to funding from the Danish Energy Development and Demonstration Program (EUDP) as well as IFD and EE. These well-instrumented testbeds were designed to study several nuanced characteristics of bifacial PV performance such as non-uniformity of rear irradiance and the spectral distribution of rear irradiance. Some of the experimental systems that formed a basis for the research articles produced during this PhD project are shown in Figure 1.1.

Figure 1.1: Test beds at DTU's outdoor PV test facility. Top left) Albedo enhancement under single-axis trackers. Top right) irradiance uniformity mapping set up on the back of single-axis tracker. Bottom left) rear plane-of-array irradiance monitoring plate including small-area sensors and large-area reference panels. Bottom right) spectral albedo test stand above gravel.

1.1 Bifacial photovoltaics: Technology and market outlook

Bifacial photovoltaic (bPV) cells generate charge carriers from photons impinging on the front and rear, thereby generating electricity from light shining on both sides. bPV technology is not a new idea. The first known bPV solar cell patent was submitted in 1961 by Hiroshi Mori while working at a company that later became the Sharp Corporation [2]. Notable bPV developments since then include deployment of bPV cells in multiple soviet satellites during the 1970s [3], bPV cell patents submitted by University of Madrid in the late 1970s [4], the first commercial production of bPV modules by the company Isofoton between 1984 and 1989 [5], the SunPower interdigitated back contact (IBC) bPV cell in 1997 [6], and Sanyo's inherently bifacial heterojunction intrinsic thin-layer (HIT) cells in 2011 [7]. Some of the first bPV systems were single modules above whitewashed ground in the 1980s [5], bPV noise barriers in 1998 [8] and bPV sun-shade elements in 2003 [9]. Although the bPV concept dates back nearly 60 years, the mass production and integration of bPV into utility-scale systems began in earnest roughly a decade ago. Chinese manufacturers currently dominate all stages of the solar supply chain by producing roughly 80% of the world's polysilicon, wafers, cells, and modules [10].

Starting in 2016, the annual International Technology Roadmap for Photovoltaics (ITRPV) reports have included ten-year forecasts for the share of bPV cells in the global PV market. The ITRPV reports, and the projections within them, are generated with survey responses from producers within the PV supply chain. The ten-year forecasts published between 2016 and 2022 [11] – [17] are shown in Figure 1.2 where a rapidly growing market share of bPV is seen. Figure 1.2 also shows how the bPV market projections have become increasingly ambitious, and how the ITRPV reports largely underestimate the actual market share of bPV. Note that the forecasts in Figure 1.2 are for bPV cells, not bPV modules. The market share of bPV modules is lower than that of bPV cells because it is possible to encapsulate a bPV cell within a monofacial laminate (i.e., a module with opaque backsheet).

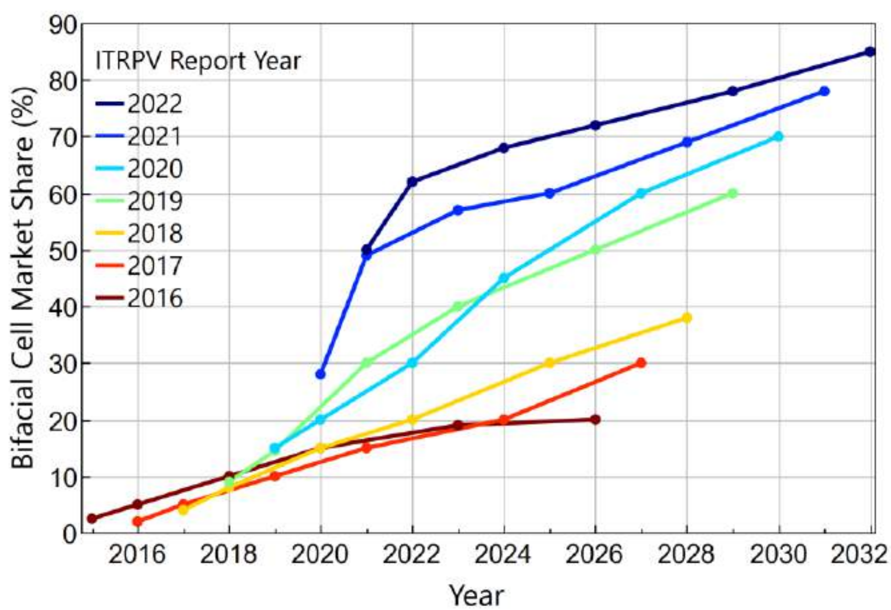

Figure 1.2: Forecasts of the bifacial PV cell market share. Data are collected from the ITRPV reports publish in 2016–2022.

The tipping point for widespread bPV adoption was arguably 2017–2018 when multi-megawatt scale bPV systems began appearing on a regular basis. For example, the largest known bPV system in 2013 was the 1.3 MWp Hokuto plant in Japan [18], but by 2018 the largest bPV plant size increased 75-fold with the 100 MWp Wuhai City plant in China [19]. At the time of writing, the largest bPV system that the we are aware of is the 1.3 gigawatt peak (GWp) Kalyon Karapinar plant in Türkiye [20], which is roughly half the size of the current world's largest monofacial PV system – the 2.7 GWp Bhadla Solar Park in India [21].

The principal reason for the recent widespread bPV adoption is that system-level bifacial energy gains, typically 6–10%, are achievable at reduced costs. The exact price premium of a bPV module over its monofacial equivalent is a difficult figure to pinpoint because it is often sensitive information that varies with producer as well as a buyer's relationship with that producer. Published price premiums for bPV modules vary from +0.015 USD/W (~4%) [22], to some producers stating no price premium on bPV modules [23], and some cell producers claiming that bPV cells are cheaper than monofacial [23].

Durable and high performance bPV modules require a bill of materials (BoM) that is likely to come with some added costs. Firstly, an extra sheet of glass is often used in bPV modules to replace the traditional opaque backsheet. Whether a sheet of 2–3 mm thick structured or float glass is more expensive than a backsheet is not a clarified matter. Stein and Jordan asked this question to several manufacturers, wherein one Chinese manufacturer stated that glass is cheaper, but the survey found the majority opinion to be that glass is more expensive than backsheet material [24]. Further complicating the matter is that the cost of PV-grade glass is not stable with time: the IEA reported a 50% price surge on PV-grade glass in the second half of 2020 due to the increased bPV demand [25]. The price premium on glass versus backsheet also depends on how the glass is processed. For example, an added cost of many glass/glass bPV modules is a back glass with a white lattice patterned ceramic coating between the cell gaps, which boosts frontside power by 2–5% due to internal scattering effects [24], [26], [27]. Bypass diodes may be another source of added cost to bPV as they must be rated to pass the higher currents produced from the rear irradiance that is absorbed by bPV modules [28]. Finally, ethylene vinyl acetate (EVA) has been shown to have high degradation rates when used in a glass/glass package [29] – [31], therefore, polyolefin elastomer (POE) is becoming the popular alternative to conventional low-cost EVA [17].

Nevertheless, the low bPV premiums are an undeniable byproduct of the passivated emitter and rear cell (PERC) concept transitioning from laboratory to mass production [32], [33]. The PERC concept was proposed in 1989[1] to overcome two prevalent loss mechanisms found in conventional aluminum back surface field (Al-BSF) cells: 1) the recombination of charge carriers near the highly doped rear wafer surface, and 2) the absorption of near infrared light by the fully covered rear Al layer [34]. The rear Al layer of a PERC cell contacts the p-type bulk *locally* in areas where the rear passivation has been removed (Figure 1.3). This "point" contacting reduces recombination at the metal-semiconductor interface, while a high-quality oxide (e.g., SiNx or AlO_2) between the semiconductor and Al increases reflectivity of infrared light and saturates dangling bonds. The result is that PERC cells have a notably

[1] It took 25 years for PERC, an adaptation of conventional Al-BSF cells, to go from a laboratory concept to an industrially scaled commercial product. This time horizon is good to consider when reading about the commercial promise of next generation high efficiency devices such as Perovskites.

higher quantum efficiency in the near infrared (1000–1100 nm) and a higher overall efficiency than Al-BSF cells.

To convert a monofacial PERC to a bifacial PERC cell, or so-called PERC+, the Al screen-print must be changed from full-area backside coverage (Figure 1.3a) to an H-pattern (Figure 1.3b). This process does not require PERC cell producers to invest in additional equipment [35], which is why PERC cells have become the workhorse of the present bifacial era. Additional steps can be made to optimize the performance of bifacial PERC (e.g., changing the thickness of the rear passivation), but the most critical process is the selective screen-printing of Al to permit collection of rear side photogenerated current. An H-patterned rear grid has an added economic benefit of significantly reducing Al paste consumption [33].

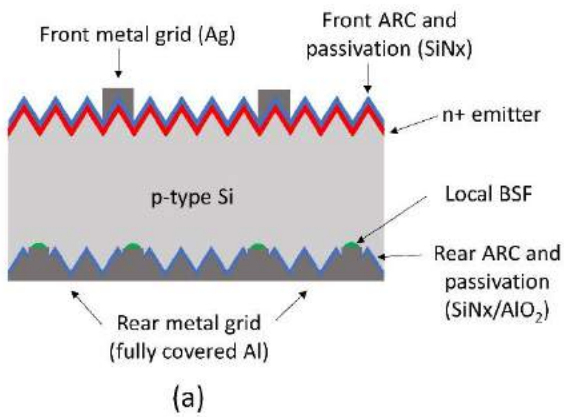

Figure 1.3: Cross-sectional diagrams that highlight the difference between monofacial PERC (a) and bifacial PERC (b). The figure is redrawn from [35].

It is likely that many bPV module manufacturers will soon switch from PERC cells to higher efficiency cell concepts based on n-type substrates such as tunnel oxide passivation (TOPcon), interdigitated back contact (IBC), or silicon heterojunction with intrinsic amorphous layer (SHJ). The 2022 ITRPV report predicts that the PERC's current 85% market share will decrease to 45% by 2032 and will be replaced largely by n-type cell concepts. This transition will occur primarily because PERC cells with p-type bulk are reaching their efficiency limits [36], but other reasons to switch to n-type cell concepts include PERC's low rear side efficiency and PERC's susceptibility to light induced degradation (LID) when doped with Boron. Presently, the highest frontside efficiencies of PERC modules in mass production are 20.9–21.6%, while the top efficiencies of mass-produced modules with n-type cells (incl. TOPcon, IBC and SHJ) are 21.7–22.8% [37]. Cells with n-type substrates have higher efficiencies than those with p-type because the Phosphorous doping in n-type bulk creates positively charged minority carriers that have higher carrier lifetimes and less susceptibility to metallic impurities (e.g., Iron) than the negatively charged minority carriers in p-type substrates [38].

Recent years have demonstrated that the economics of bPV, and consequently any individual PV technology, can be subject to country-specific trade policies. An example of this is the United States (US) Section 201 trade tariffs, which imposed import duties on foreign-made solar cells and modules for a four-year period starting in 2018. The tariffs were initially set at 30%, but there was an exemption for bPV modules [39], which made bPV the clear technology choice for developers of large-scale PV projects. The Trump administration vacillated on the bPV exemption by revoking it [40], reinstating it

[41], and revoking it again [42]. The US Solar Energy Industries Association (SEIA) estimated that the tariffs on bPV modules resulted in 4 GW fewer utility-scale PV deployments between 2019 and 2021 [43]. The Biden administration extended the Section 201 tariffs before they expired in 2022, but reestablished the bPV exemption when doing so – a decision that was not ideal, but still to the satisfaction of downstream PV installers in the US [44].

The annual growth rate of global PV installations in the last three decades is about 30% per year [45], wherein a landmark of 1 terawatt peak (TWp) total capacity was surpassed in 2022 [46]. It is difficult to precisely isolate the capacity of bPV installations from this total. The 2021 review paper by Kopecek and Libal [36] is helpful in this regard because it includes estimates for how much bPV was installed between 2016 and 2020. The estimated global bPV capacity from Kopecek and Libal [36] and the total PV capacity published by the International Renewable Energy Agency (IRENA) [47] is overlayed in Figure 1.4. An exponential curve fit to the Kopecek and Libal data gives 55 GWp of bPV installed in 2021, which is 6.5% of the 850 GWp total PV stated by IRENA [47]. A similar estimate of 6.8% bPV share is obtained with data from the 2022 ITRPV report that stated 28% of module shipments in 2021 were bPV [17]. Indeed, most PV modules and PV systems are still monofacial, yet because bPV is a rapidly growing and mainstream technology, comes the likelihood that bPV will be the predominant PV system type within a decade.

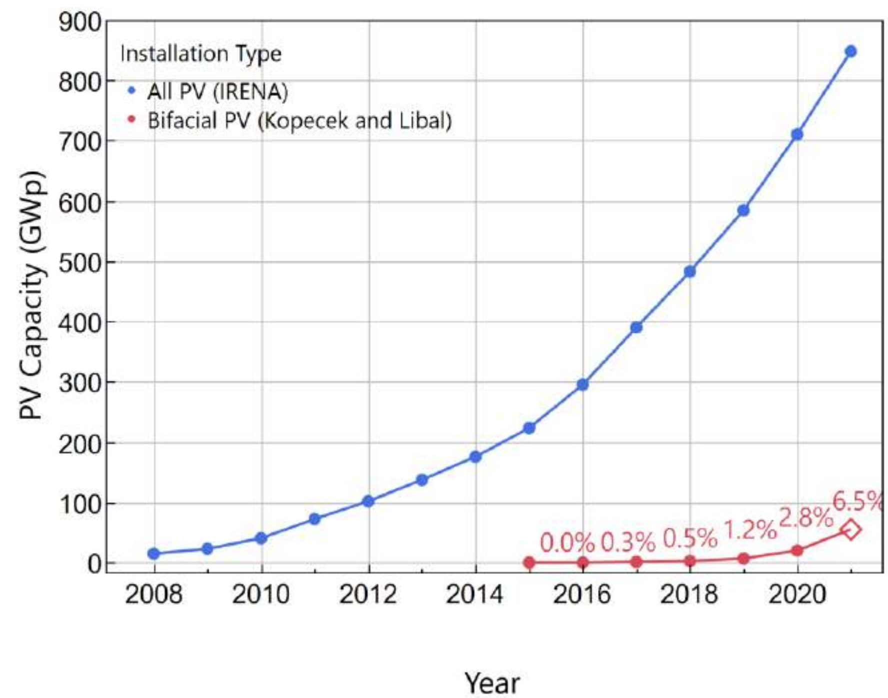

Figure 1.4: Global Installed capacity of all PV systems with data from [47] (blue curve) and installed capacity of bifacial PV systems from [36] (red curve). The red diamond in 2021 is exponentially fit to the data reported in [36] and the percentage values above the red points show the ratio of bifacial to monofacial PV system capacity.

Figure 1.4 shows that the first 1 GW of bPV was installed around 2017. This reveals that there is less than a decade of large-scale bPV experience from which the industry can assemble best-practices for essential tasks such as laboratory measurement, energy modeling and condition monitoring. Indeed, as bPV became mainstream in the last five years came a flurry of research work to update international standards [28] [48] [49], update yield prediction tools [50] [51], investigate new failure modes [52] [53], document the variation of terrestrial albedo [54] – [56], and understand the factors that influence rear plane of array irradiance (R_{POA}) and bPV performance [57], [58].

1.2 Project Formulation

1.2.1 Photovoltaic simulation models and software

The process of predicting power output of a PV system first requires location-specific meteorological data, which will typically include solar irradiance, ambient temperature, windspeed, and relative humidity. From this so-called 'meteo file', a PV modeler must then quantify all the dynamic energy losses as photons originating from the sun are converted into electrical energy. This process is commonly referred to as the 'PV model chain' and is summarized in Figure 1.5 for grid-connect systems. Figure 1.5 illustrates how PV performance modeling is comprised of several algorithms linked together. The PV model chain is often partitioned into optical, thermal, and electrical modeling stages, which are highlighted in blue, red, and green, respectively.

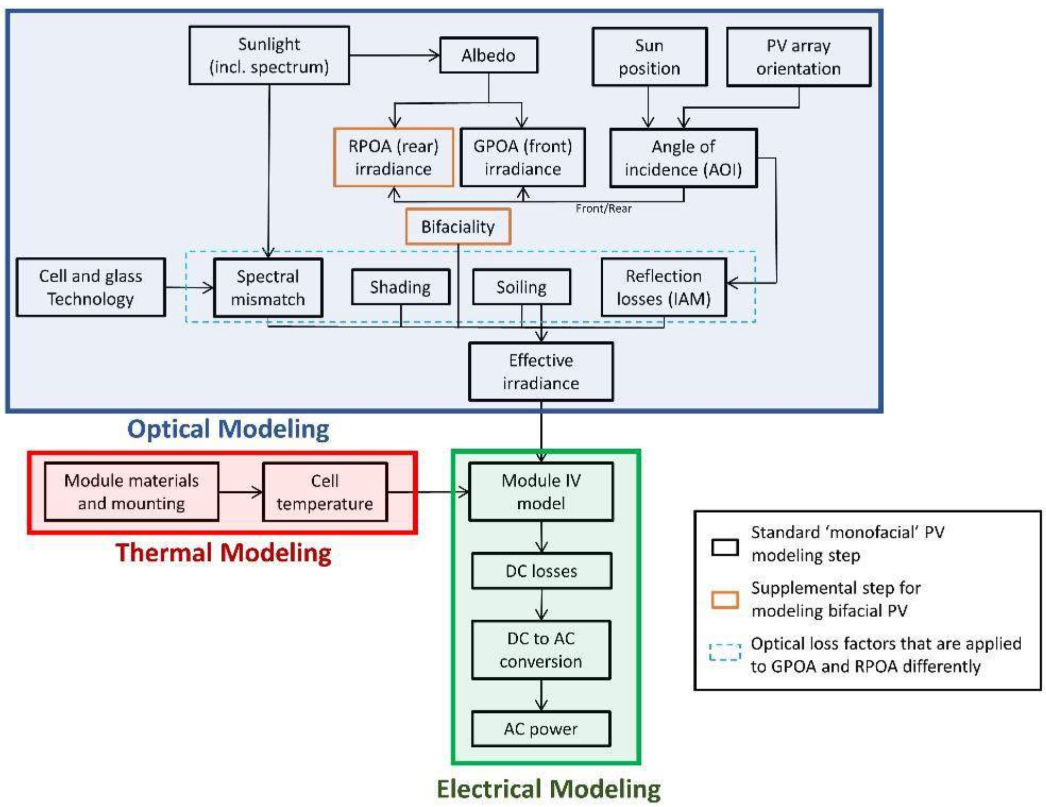

Figure 1.5: Flow diagram showing the steps involved to model PV energy yield, also known as the PV model chain. The added steps for simulating bifacial PV energy yield are highlighted in orange, and the optical loss factors that may be different for front and back sides of PV module are highlighted in dashed blue. The figure is adapted from [59].

Each block in Figure 1.5 represents an algorithm wherein a PV modeler has a variety of choices as to which model should be applied. For example, the literature contains over a dozen models for elevating horizontal irradiance to a tilted surface (i.e., the so-called transposition to POA step) [60] [61]. Similarly, the literature contains over a dozen cell temperature models [62] [63], nearly all of which assume steady-state weather conditions, but transient thermal models have been developed recently [64] and integrated into PV modeling software [65].

Note that Figure 1.5 describes the conventional PV model chain, which primarily consists of parametric, empirical, and some first-principles models. It does not pertain to artificial intelligence (AI) algorithms such as artificial neural networks (ANN) that have been applied to PV energy yield and solar forecasting problems in the last decades [66] – [68].

PV simulation software packages such as PVsyst [51], PlantPredict [69], SolarFarmer [70], or SAM [65] simplify a PV modeler's task to some extent because the user interfaces offer limited choices for how each sub-step can be modeled. For example, PVsyst users are restricted to either the Perez [71] or Hay [72] models for the transposition step. Similarly, PVsyst users' choices for module temperature models are restricted to an adapted form of the Faiman model [73] and the NOCT model [74]. A PV software developer's decision to include certain algorithms and exclude others is not entirely arbitrary – it ideally originates from independent validation of the model against field data. For example, the Hay Davies and anisotropic Perez models are widely used in PV modeling because several reports have shown low errors when these transposition models are compared to measurements at various tilts under all sky conditions [75] – [78].

Optical Modeling

In Figure 1.5, the blocks highlighted in black show the steps required by both monofacial PV (mPV) and bPV modeling pipelines, while the blocks highlighted in orange show the additional steps required to model bPV systems. The key addition to the bPV modeling pipeline is the R_{POA} estimation step, but ultimately, R_{POA} is adjusted for the bPV module's backside conversion efficiency, or 'bifaciality' factor. The measurement of bifaciality will be explained in **Section 1.2.3**.

The most common approach to R_{POA} simulations is the view factor method. View factors (VF), sometimes called configuration factors or shape factors, have their origin in radiative heat transfer modeling [79]. A VF is a geometric quantity, from zero to one, that describes the fraction of radiation emitted by surface 1 received by surface 2 (Figure 1.6a). The VF from surface 1 to surface 2 ($VF_{1\rightarrow2}$) can also be interpreted as the fraction of space that is visible from surface 1 and occupied by surface 2. This interpretation leads to the summation rule of VFs, which states that the sum of all VFs from a given surface equals one. Another important property of VFs is the reciprocity theorem, which allows one to calculate $VF_{2\rightarrow1}$ if one already knows $VF_{1\rightarrow2}$ and the areas of surfaces 1 and 2 [80].

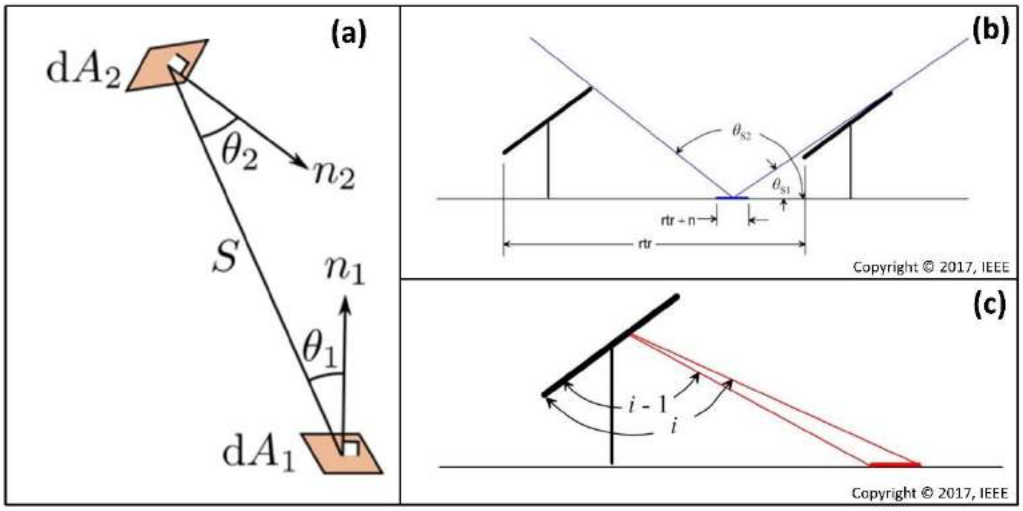

Figure 1.6: (a) view factors of two differential areas [81]. (b) field of view angles for determining VFs for the sky diffuse radiation incident on a ground segment [82]. (c) field of view of the ground for a one-degree segment depicted by the angles *I* and i–1 [82]. Figures (b) and (c) are from [82] with permissions from publisher.

Marion et al. presented one of the first systematic applications of VFs to estimate R_{POA} in bPV systems [82]. Marion et al. did not present the first use of VFs in bPV modeling – credit for the first application of VFs in bPV modeling goes to Krenzinger and Lorenzo's 1986 paper [83] – but the two-dimensional (2D) VF model of Marion et al. implements VFs in a relatively straightforward manner, which is why it is used here to demonstrate the VF concept. Figure 1.6b shows how the row-to-row (RTR) distance is first divided into *n* segments, typically 100 (Figure 1.6b). Then, the VF of each segment *n* to the sky dome ($VF_{n\rightarrow sky}$) is calculated using Equation 1.1, which accounts for masking of sky diffuse irradiance by neighboring PV rows.

$$VF_{n\rightarrow sky} = 0.5 \cdot (\cos\theta_{S1} - \cos\theta_{S2}) \tag{1.1}$$

Each segment *n* is determined to be either shaded by preceding PV rows, or not. Then, the direct horizontal irradiance (DrHI) at each segment is calculated according to Equation 1.2.

$$DrHI = \begin{cases} DNI \cdot \cos(\theta_z) & if\ n\ is\ unshaded \\ 0 & if\ n\ is\ shaded \end{cases} \tag{1.2}$$

Where DNI is the direct normal irradiance, and θ_Z is the solar zenith angle. Once DrHI is determined, the ground reflected irradiance (GRI) at each segment *n* is calculated with Equation 1.3.

$$GRI_n = \rho \cdot [DrHI + VF_{n\rightarrow sky} \cdot DfHI] \tag{1.3}$$

Where ρ is the albedo and DfHI is the diffuse horizontal irradiance. Note that a deep explanation of albedo will be provided in **Section 1.2.4**. Figure 1.6c shows how the view from the back of the bPV array is then divided into 180 segments. The figure shows segmentation performed at roughly 65% of the full array height, but in practice the calculation could be done at multiple array heights and doing so would illustrate the vertical non-uniformity of R_{POA}. The VF of each 180 segments on the back of the array is calculated with Equation 1.4.

$$VF_i = 0.5 * [\cos(\mathrm{i}-1) - \cos(\mathrm{i})] \tag{1.4}$$

VFs near the top and bottom array edges (e.g., where *i* = 0° or *i* = 180°) will have smaller values than VFs where *i* equals 90°. This means that irradiance sources originating from oblique angles will contribute less to R_{POA} than light sources normal to the rear module plane. R_{POA} is finally calculated with Equation 1.5.

$$R_{POA} = \mathrm{b} \cdot \mathrm{IAM(AOI)} + \sum_{i=1°}^{180°} VF_i \cdot IAM_i \cdot I_i \qquad 1.5$$

The I_i parameter in Equation 1.5 represents the irradiance source that each VF_i is viewing, which could be the ground (GRI), the sky (DfHI), or the module row behind (I_{refl}). The irradiance reflected from the front surface of PV modules (I_{refl}) only considers the diffuse radiation because specular reflection of beam irradiance is assumed not to contribute to R_{POA} in most circumstances. The IAM and AOI are the incident angle modifier and angle of incidence, respectively. The IAM describes reflection losses at the glass-air interface and will be explained in greater detail in **Section 1.2.3**. In Equation 1.5, *b* is a factor that has a non-zero value only when the sun is behind the bPV rack and is calculated with Equation 1.6. In south-facing fixed-tilt systems, this condition would occur when the solar azimuth is north-east or north-west. Such a condition should not occur, in principle, for horizontal single-axis tracking (HSAT) systems

$$b = \begin{cases} DNI \cdot \cos(AOI) & if\ sun\ is\ behind\ PV \\ 0 & if\ sun\ is\ infront \end{cases} \qquad 1.6$$

The VF method remains the most common approach to calculate R_{POA} because it is relatively simple to implement, and it requires minimal computational power when the meshing is 2D, and the resolution is comparable to that shown in the previous example. It is well-known that the disadvantages of the VF method include the inability to simulate the complex geometries that are ubiquitous in real PV systems (e.g., structural support members), and the assumption that all surfaces are Lambertian (i.e., 100% diffuse scatterers). For these reasons, the VF method cannot inherently account for shading induced by structural support members, nor can it simulate specular reflections from mirror-like surfaces. 2D VF models are also incapable of simulating edge brightening effects, and therefore, can only simulate bPV systems with regularly spaced rows that are assumed to be infinitely long. bPV performance software that use a VF model for R_{POA} calculations must apply adjustment factors, or R_{POA} derates, to account for backside structural shading. Ray tracing (RT) simulations are often used to overcome the shortcomings of the VF approach [84] – [86], and to estimate the structural shade adjustment factors [87], but drawbacks to RT include the significantly increased computational requirements, and the specialized expertise that is often required to implement the model.

In 2019, when this PhD project began, there was already an abundance of bifacial irradiance models published in the literature. An incomplete list of models from that period includes the following: Sandia National Laboratory's 3D VF model [88], SunPower's 2D VF model pvfactors [89], NREL's SAM that implements the Marion 2D VF model [50], ECN's bigeye software with 3D VF model [90], ISC Konstanz's MoBiDiG software with 2D VF model [91], IMEC's Energy Yield Simulation Framework with RT model [92], PV Lighthouse's Sunsolve software with RT model [93], EDF's PVNOV software with reverse RT model [94], NREL's bifacial_radiance software [95] that interfaces with the backwards RT software Radiance [96], CEA-INES's 3D VF model Trifactors, DNVGL's SolarFarmer software with 2D VF model from Mikofski et al. [70], PVsyst's infinite sheds 2D VF model [51], the 2D VF model of Yusufoglu et al [97], Applebaum's detailed VF formulations [98], and Kreinin's RT simulations [84].

Of course, bifacial performance models continued to be published post 2019 [e.g., [5], [99] – [106]. This abundance of R_{POA} simulation tools and methodologies indicated that our research efforts were better used validating bifacial irradiance models, rather than developing a new bPV model or software. Therefore, **Chapter 2** of this thesis describes the results of a study that benchmarked the accuracy of state-of-the-art RPOA modeling practices against operational data from large-scale bPV systems (**Publication I** and **Publication II**). This study investigated the accuracy of various bPV modeling software to estimate R_{POA}, and the electrical performance of the PV system, providing an indication for how accurate R_{POA} simulations can be.

Within the PV model chain (Figure 1.5), there are several steps (or 'submodels') wherein appropriate coefficient values must be determined. If reliable measurement data are available, then the coefficient values can be extracted by fitting the model equation to the data. This process generates a significant amount of inter-user variability because the data filtering practices and fitting algorithm influence the model parameter values and results that are achieved [107] – [109]. There is also potential for inter-user variability when measured data are not available, because in this case, a PV modeler must consider coefficient values from various sources, which may include the software provider, external databases [e.g., PV-USA] or literature (e.g., [110], [111]).

Thermal Modeling

The following example will demonstrate the effect of parameter values at a single modeling step – the calculation of cell temperature. Consider the Faiman steady-state temperature model, which is used in the IEC 61853-3 energy rating standard (Equation 1.7).

$$T_{MOD} = T_{AMB} + \frac{G_{POA}}{U_0 + U_1 \cdot WS} \tag{1.7}$$

Where T_{MOD} (°C) is the module temperature[2], T_{AMB} (°C) is the ambient temperature, G_{POA} (W/m^2) is the in-plane irradiance (adjusted for reflection losses) and WS (m/s) is the windspeed. The two free model parameters U_0 and U_1 represent the effect of shortwave solar radiation and convection, respectively. Thermal conduction is ignored because the heat transfer between the module frame and mounting structure is negligible, and the model does not consider longwave radiation (i.e., Planck radiation), which is a weakness because effects like sky temperature can significantly alter the thermal balance of PV systems [112].

The values of U_0 and U_1 depend on the module BoM and the mounting design of the PV array. Faiman monitored seven c-Si modules mounted on an open rack in Negev, Israel and found U_0 values between 24.0–26.4 W·m^{-}2·K^{-1} and U_1 values between 6.3–7.7 W·m^{-}3·s·K^{-1}. Koehl et al. monitored seven c-Si modules in the Alps and reported U_0 values of 22.4–32.0 W·m^{-}2·K^{-1} and U_1 values of 6.0–9.2 W·m^{-}3·s·K^{-1}. Bourne and Chaudhari estimated coefficient values for the PVsyst thermal model – a model based on Equation 1.7 that modifies the G_{POA} term by a factor of α·(1–η) and exchanges the name U_0 for U_C, and the name U_1 for U_V.

[2] It is generally accepted that module temperature (i.e., back-of-module temperature) and cell temperature (i.e., p-n junction temperature) are not equivalent. For modules mounted on open-air racks, it is common to add an offset of 3°C·(G_{POA}/1000 W·m^{-2}) to module temperature to arrive at a modeled cell temperature. The specific offset is dependent on the system design (e.g., open-air versus insulated back surface).

$$T_{MOD} = T_{AMB} + \frac{G_{POA} \cdot \alpha \cdot (1 - \eta)}{U_C + U_V \cdot WS} \qquad 1.8$$

In Equation 1.8, α is the PV module absorbance and η is the electrical efficiency. A common assumption for α is 0.9. With the α·(1–η) factor in the numerator of Equation 1.8, it is expected that U_C values would be lower than U_0 values extracted from the same dataset.

Bourne and Chaudhari [113] used operational PV data from various PV system types across the United States to obtain U_C and U_V values with onsite meteorological data and with satellite weather data. The authors found that ground mounted systems had U_C values between 25–45 $W\cdot m^{-2}\cdot K^{-1}$ (median of 32.5 $W\cdot m^{-2}\cdot K^{-1}$) and U_V values between 1.9–9.2 $W\cdot m^{-3}\cdot s\cdot K^{-1}$ (median of 5.9 $W\cdot m^{-3}\cdot s\cdot K^{-1}$) when onsite meteorological data was used. Figure 1.7 shows how annual energy yield calculations differ when the two thermal coefficients are swept within the range of values found in the literature and recommended by PVsyst [114]. The calculations used to arrive at Figure 1.7 followed the IEC 61853-3 procedures and were done for a c-Si module mounted at 20° in a temperate coastal climate (56° N, 4° W) where the average annual WS is 3.2 m/s and T_{AMB} is 8.4°.

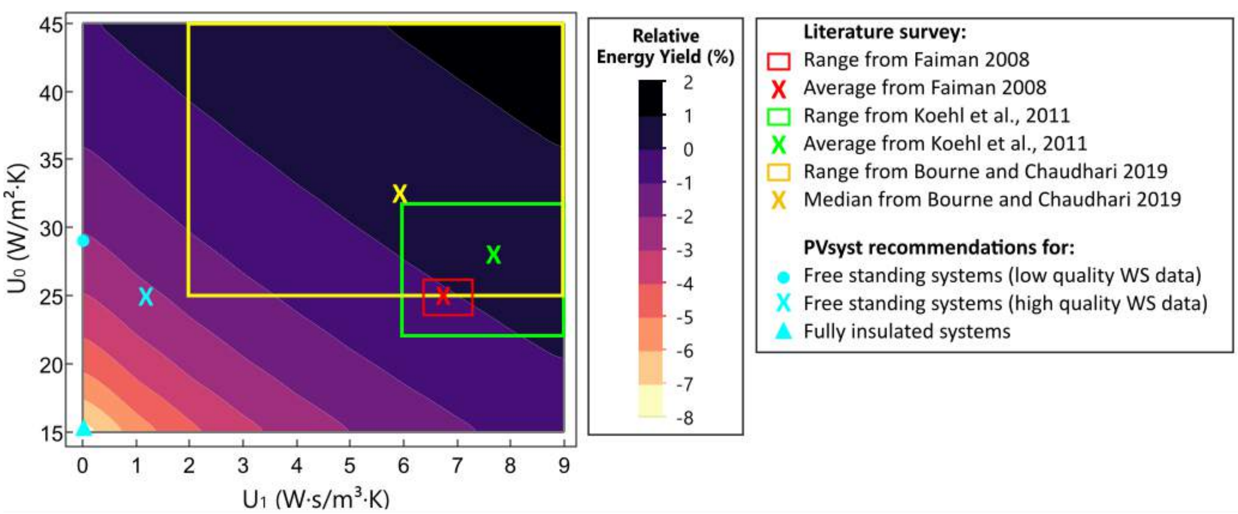

Figure 1.7: Heat map showing the sensitivity of annual energy yield on the values of thermal coefficients. Values of thermal coefficients published in the scientific literature, as well as the recommendations given by the software company PVsyst are shown. The meteo file used for this simulation is the temperate coastal climate in IEC 61853-4. Note that Faiman [73] and Koehl et al. [111] published U_0/U_1 values (Equation 1.7) whereas Bourne and Chaudhari [113] and PVsyst [114] provide U_C/U_V values (Equation 1.8).

Annotated on Figure 1.7 are the range of U_0/U_1 values for c-Si modules mounted on open fixed-tilt racks reported by Faiman and Koehl et al., the U_C/U_V reported by Bourne and Chaudhari, and the U_C/U_V values recommended by PVsyst. The color scale in Figure 1.7 shows the annual energy yield normalized to the yield obtained when the average U_0/U_1 values in Faiman 2008 are used in the simulation (marked with the red 'x'). Although parameter values for the Faiman and PVsyst thermal models are not directly interchangeable, a PV modeler using these models may weigh information from the literature to help them choose coefficient values for a given simulation. The color scale in Figure 1.7 shows that use of one set of coefficient values over another set leads to a non-negligible influence on the simulated energy yield. For example, the median values reported by Bourne and Chaudhari consider that windspeed has a stronger effect on T_{MOD} than the recommendations from PVsyst, but use of the Bourne and Chaudhari values result in 3% higher energy yield than the PVsyst recommended values. This represents one possible source of uncertainty at a single modeling step. Given that the output of one submodel is the input to another submodel, uncertainty at any individual step will propagate into uncertainty in the modeled energy.

Electrical Modeling

The information on PV module datasheets is presently insufficient to complete the PV modeling process, not only because they lack information such as the thermal coefficients shown in the previous example, but also because datasheets contain current-voltage (I-V) measurements at just two conditions: standard test conditions (*STC*, 1000 W/m^2, 25° C, AM1.5G) and nominal module operating temperature (*NMOT*, 800 W/m^2, 20° C ambient, 1 m/s windspeed). I-V measurements at low-irradiance (200 W/m^2, 25° C, AM1.5G) were common on datasheets in years past, but manufacturers have recently stopped reporting these data [115]. It is widely accepted that the accuracy of PV energy yield modeling can be improved when high-quality I-V measurements recorded over the range of irradiance and temperature conditions that modules are exposed to in the field [116] – [118].

There are numerous models to fit I-V measurements made at multiple irradiance and temperature (G-T) conditions, but these approaches can be categorized into one of two general groups: point models or equivalent circuit models. Point models only provide information at discrete points on the I-V curve such as the short-circuit current (I_{SC}), open-circuit voltage (V_{OC}) and the maximum power point (P_{MAX}). Examples of point models include the Sandia Array Performance Model (SAPM) [119], the PVGIS model [120], the MotherPV model [121], and the Heydenreich model [122]. Equivalent or 'lumped' circuit models such as the single diode equation (SDE) [123] – [125] or double-diode model [126] can simulate the full I-V curve of a PV device. The five free model parameters in the SDE are the photogenerated current I_L, the diode quality factor n, the reverse saturation current I_O, the series resistance R_S, and the shunt (or parallel) resistance R_{SH}. Additional parameters to the SDE have been proposed to describe how some of the original five parameters change with G-T conditions (e.g., [116], [127])

PV Modeling Uncertainty

Several authors have attempted to answer the question "what is the uncertainty of PV energy modeling?" using various approaches and perspectives. The previous example illustrated the sensitivity attributable to unknown model parameter values and the absence of experimental data, but additional sources of uncertainty exist, and have been analyzed in detail such as: measurement uncertainty of irradiance [128] [129], measurement uncertainty of module calibration [130] [131], measurement uncertainty of temperature coefficients [132], uncertainty in model equations [133] [134], uncertainty due to varied implementation of published algorithms [135], and uncertainty of model parameters extracted from regressions on measurements [136]. Meanwhile, some authors analyze the residual error between measured energy yield and modeled values to estimate modeling uncertainty. For example, Muller et al., compared measured data of 26 PV systems against long-term yield predictions and concluded that uncertainty of PV energy modeling is about 8% when using recent solar radiation data [137]. Other authors have used the principles within the guide to expression of uncertainty in measurement (GUM) to estimate uncertainty in energy yield. For example, Dirnberger et al. estimated the expanded uncertainty of DC-side performance ratios are between 3.0–4.4% depending on the PV technology and climate [138].

User variability is a lesser studied source of uncertainty. Round-robin style modeling intercomparisons can help fill this gap because when modelers are provided with the same simulation task, and the same starting information, the differences in the modelers' results reveal a great deal about their assumptions as well as highlight the submodeling steps where the PV community needs to improve [1], [139] – [141]. Friesen et al. circulated timeseries G_{POA} and T_{MOD} data to eight European institutions who then simulated module-level performance of different PV technologies in various climates [139]. Each participant ran a different electrical model, so the exercise revealed differences in the models rather than inconsistencies of the modelers themselves, but they found that the group's modeling accuracy was within ±5%. Stein's 2010 blind modeling study provided meteorological data and PV system design information to 20 participants and found a 20% spread in the annual energy reported by the modelers [140]. This study by Stein was one of the first to demonstrate that even the same model run by different users may produce different answers. Moser et al. analyzed the long-term yield predictions provided by six expert modelers for a PV system in an Italian and an Australian site [141]. These modelers were required to independently obtain meteorological data for their simulations which, for the Italian site, lead to 6% differences in GHI, 20% differences in G_{POA}, and ultimately nearly 30% differences in AC energy.

The second half of **Chapter 2** addresses the issue of user-induced variability within the PV modeling process. To this end, the results of a round-robin style modeling intercomparisons are presented (**Publication III**). This study tests the ability of nine expert agencies to implement the set of 20 equations provided in the IEC 61853-3 standard and derive DC performance ratios in various climates.

1.2.2 Bifacial-specific loss factors

Global plane of array irradiance (G_{POA}) is the most important parameter for PV system performance because PV power output is nearly linear with irradiance [142]. The parameter that distinguishes bPV systems from mPV counterparts is the rear plane of array irradiance (R_{POA}), which increases the total irradiance received by the system. If R_{POA} could be modeled as accurately as G_{POA}, then the accuracy of bPV simulations would approximate that of mPV simulations. Therefore, efforts have been made in this thesis to characterize nuanced aspects of R_{POA} with the motivation that a greater understanding of these effects could serve as a starting point for improved bPV modeling.

R_{POA} consists primarily of scattered light from multiple sources including the ground, sky, and neighboring PV rows (Figure 1.8). The intensity of R_{POA} depends mostly on the albedo beneath the PV array and the fraction of diffuse light in the sky hemisphere. Research has shown that R_{POA} on the back of a 37° fixed tilt system above light sandy soil is 130–150 W/m^2 when the frontside is illuminated with the air mass 1.5 global (AM1.5G) reference spectrum (1000 W/m^2) [143] – [145]. Therefore, about 12% of the total irradiance received by a bPV system under reference conditions is R_{POA}, most of which is ground-reflected light. Indeed, the frontside of a PV array also receives a portion of ground-reflected light, but it is a much smaller fraction than that received by the backside [100].

G_{POA} and R_{POA} are both subject to nonuniformity patterns and to spectral shifts, but the two sides experience these phenomena to different extents and for different reasons. For example, nonuniform irradiance patterns are created on the backside from scattering of direct beam irradiance near array edges and from shading by structural support members. Frontside irradiance is also nonuniform by nature, but it is mostly caused by preceding rows that always block part of the sky diffuse light (i.e., diffuse masking [146]) and can occasionally obscure the direct beam light. Finally, the spectral distribution of irradiance on the backside deviates from the AM 1.5G reference spectrum more than the front side because the spectral albedo of most natural materials is significantly different than the distribution of the incident solar spectrum [58], [144], [147].

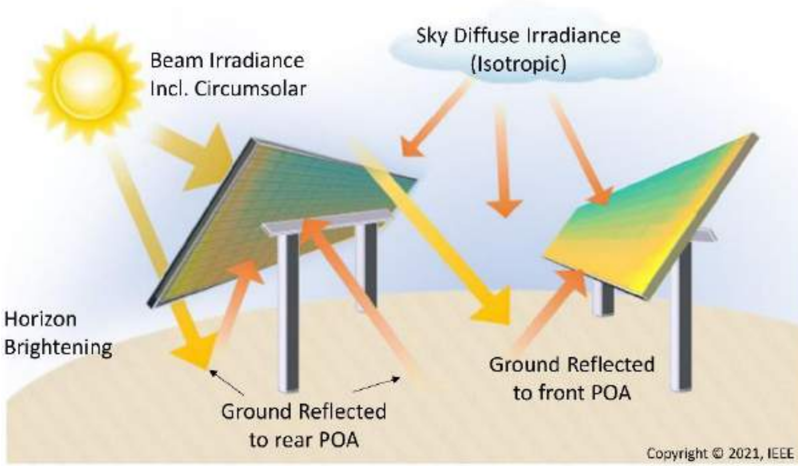

Figure 1.8: Contributions to illumination of the front and rear of bifacial PV modules including direct, sky diffuse, and ground reflected radiation. Original figure from [148] (Copyright © 2021, IEEE). Annotations of irradiance components added by author.

Recall that the optical set of modeling steps shown in Figure 1.5 culminate at the effective irradiance step. The effective irradiance is classically defined as the broadband G_{POA} adjusted for optical effects including the spectral distribution of light, transmission loss due to soiling, non-linear shading losses, and angular-dependent reflection losses at the glass-air interface [119]. In other words, the effective irradiance is the solar energy that a PV system has available for photovoltaic conversion. The same loss mechanisms that reduce frontside G_{POA} into effective irradiance must also be considered for the backside (see dashed blue box of Figure 1.5). However, because the nature of these mechanisms differs on the front versus backside of a PV array, so too will the magnitude of the derates applied to each side. This thesis only investigates backside shading and spectral effects, the topics of backside soiling and reflection losses a left for future studies.

Heterogeneity of rear irradiance

Nonuniformity of R_{POA} is a complicated function of ground albedo, array height, tilt angle, and sky conditions. Field measurement campaigns of R_{POA} have been carried out on fixed-tilt systems [143] [149] – [151] and several studies examined R_{POA} nonuniformity via simulation [84], [86], [88], [93], [152]. These studies have demonstrated that the nonuniformity of R_{POA} is caused by brightening at array edges (e.g., the east and west edges of an equator facing fixed-tilt system) as well as dimming in areas that are shaded by structural support members. Sensitivity studies have shown that the homogeneity of R_{POA} tends to improve with increasing array height and with an increased fraction of sky diffuse irradiance. The nonuniformity of R_{POA} tends be highest for low ground clearance systems above high albedo during clear sky conditions.

R_{POA} nonuniformity creates current mismatch between cells and thus potential for power loss. For this reason, some solar tracker manufacturers have gone to great lengths to develop and advertise structural designs that minimize backside shading. However, Compaan and Cormican [153] conducted side-by-side tests of five equivalent bPV systems mounted on different racking structures – some of which avoided backside shade while others were legacy mPV substructures that induced considerable backside shading. Their results showed that the bPV systems mounted on custom racks with minimal backside shading generated 1–1.5% more energy than the bPV systems mounted on standard monofacial racks. This modest energy gain indicates that spending additional money on bifacial-enhanced mounting systems may not always make financial sense.

Extensive raytracing simulations by Deline et al. led to correlations of electrical mismatch losses with R_{POA} nonuniformity [57]. Figure 1.9 shows two fit lines, Fit #1 is the correlation proposed by Deline et al., and Fit #2 is a correlation proposed by [154]. The correlation proposed by Deline et al., was validated with measurements on a tabletop solar simulator and it can be used by PV modelers to estimate backside electrical mismatch losses when only R_{POA} nonuniformity is known.

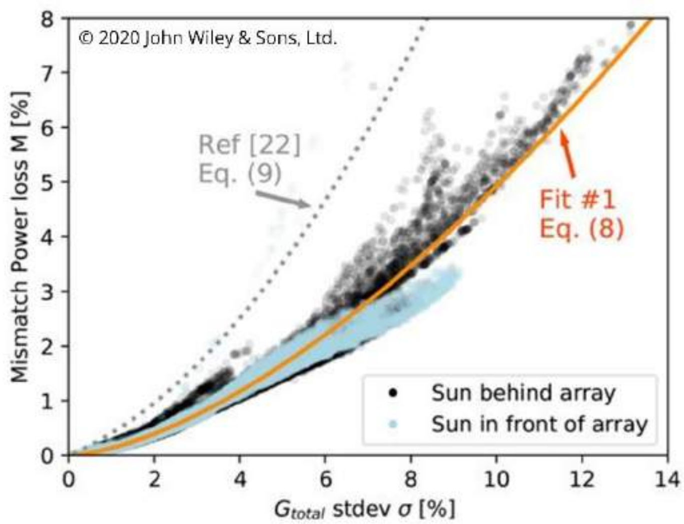

Figure 1.9: Hourly simulations showing instantaneous electrical mismatch (Equation 1.9) as a function of the spatial variation of total irradiance (Equation 1.10). The figure is from [57] with permissions from the publisher.

The y-axis in Figure 1.9 shows the power loss due to nonuniform R_{POA}, which is calculated with Equation 1.9.

$$MM\ [\%] = \left(1 - \frac{P_{Array}}{\sum P_{Cells}}\right) \cdot 100 \tag{1.9}$$

Where P_{Array} is the maximum power point (P_{MAX}) of the bifacial PV array and P_{Cells} is the P_{MAX} of an individual bifacial cell within the array. The concept is that P_{Array} incorporates electrical losses due to current mismatch between series cells, whereas the summation of isolated cells does not. Indeed, derivation of P_{Array} requires an electrical model that incorporates the effect of bypass diodes within the array of bPV modules. Possible approaches to do this include SPICE circuit modeling or direct summing of calculated I-V curves. In this thesis, P_{Array} and P_{Cells} are calculated with the open-source python library *pvmismatch* [155], which uses Bishop's explicit method to solve the SDE [156].

The x-axis in Figure 1.9 shows the standard deviation of *total* irradiance (G_{Total}) received by each cell *i* within the array, which is calculated with Equation 1.10.

$$G_{Total,i} = G_{POA} + \varphi \cdot R_{POA,i} \tag{1.10}$$

Where G_{POA} is the frontside irradiance (assumed here to be uniform), $R_{POA,i}$ is the rear irradiance incident at each cell, and φ is the bifaciality coefficient. The bifaciality coefficient represents the rear to frontside efficiency and is typically about 0.7 for PERC technology.

Field investigations of R_{POA} nonuniformity have been done for fixed-tilt systems and even vertical E-W systems [157]. However, we are not aware of any R_{POA} non-uniformity investigations of HSAT systems with two modules in portrait (2P). **Chapter 3** therefore presents a novel measurement system that was deployed on a large-scale 2P HSAT to continuously monitor the RPOA nonuniformity. The backside electrical mismatch under low and high albedo was then estimated from the high-resolution measurements and from optical simulations (**Publication IV**). This study used procedures comparable to those used in Deline et al. [57], which allowed us to compare results between works. It is worth mentioning that a similar work to **Publication IV** was presented by McIntosh et al. [158] during the same conference.

Spectral distribution of rear irradiance

Flat plate PV modules intended for terrestrial use are calibrated under the global air mass 1.5 (AM1.5G) reference spectrum [159]. Since the spectrum of broadband light sources such as Xenon (Xe) lamps does not replicate AM1.5G, spectral mismatch (SMM) corrections [160] are necessary to report I-V measurements at STC. Furthermore, because AM1.5G is a simulated clear-sky spectrum [161] and rarely observed in the field, PV characterizations performed outdoors also require SMM adjustments before reporting at STC. The SMM formula comes in two forms, the first of which is shown in Equation 1.11.

$$SMM = \frac{\int G_{Ref}(\lambda) * SR_{Ref}(\lambda)\, d\lambda}{\int G_{Meas}(\lambda) * SR_{Ref}(\lambda) d\lambda} \frac{\int G_{Meas}(\lambda) * SR_{DUT}(\lambda) d\lambda}{\int G_{Ref}(\lambda) * SR_{DUT}\,(\lambda) d\lambda} \qquad 1.11$$

Where G_{Ref} is the reference AM1.5G spectrum, SR_{Ref} is the spectral responsivity of a reference device, G_{Meas} is the spectrum of the measured (observed) spectrum and SR_{DUT} is the spectral responsivity of the device under test (DUT). The reference device is typically a crystalline-silicon (c-Si) reference cell that has a similar external quantum efficiency[3] (eQE) as the DUT. When the eQE of the DUT differs significantly from the reference device (e.g., thin-film PV), c-Si reference cells with optical filters can be used to improve the spectral matching. Reference cells made of thin-film materials (e.g., CdTe or CIGS) are not advisable due to the metastable behavior of such devices [162].

Equation 1.11 can be viewed as the ratio of photocurrent densities under measured and reference conditions. In this sense, the SMM factor describes the performance of a specific PV device under an observed spectrum with respect to how the PV device would have performed if illuminated with the AM1.5G spectral distribution. For example, SMM greater than one indicates spectrally induced photocurrent gains while SMM less than one indicates photocurrent losses.

When a spectrally flat pyranometer is used as a reference device, Equation 1.11 is simplified to Equation 1.12. This form of the SMM equation assumes that SR_{Ref} of the pyranometer is one at all active wavelengths, which is not true in practice because UV light is absorbed by a pyranometer's glass dome, and because thermopile sensitivity is significantly reduced at wavelengths greater than 2800–3000 nm.

[3] The external quantum efficiency describes the ratio of charge carriers generated by the PV device versus the number of photons incident on the PV device. The internal quantum efficiency adjusts the external quantum efficiency for the reflection of photons at the device's surface.

However, pyranometers are essentially spectrally flat within the spectrally active range of c-Si PV (i.e., 300–1200 nm).

$$SMM = \frac{G_{Ref} \cdot \int SR_{DUT}(\lambda) \cdot G_{Meas}(\lambda)\, d\lambda}{G_{Meas} \cdot \int SR_{DUT}(\lambda) \cdot G_{Ref}(\lambda)\, d\lambda} \quad 1.12$$

Continuous SMM calculations require solar spectral measurements from a spectroradiometer, which is a cost-prohibitive instrument for most PV applications except for a few highly instrumented systems found at research institutes. Continuously measured solar spectra are therefore uncommon. SMM correlations with common variables such as AM and sky diffuse fraction are useful because they permit the broader PV community to model spectral effects in the absence of costly spectral data [119], [163] – [166]. These spectral models, however, only describe the effect of spectrum on the frontside of PV modules and systems. A simplified model that describes spectral effects on the backside of the array could improve the accuracy of R_{POA} modeling.

Figure 1.10 shows the normalized SR of a pyranometer, compared to that of a typical PERC cell, as well as the reference spectrum AM1.5G, and the spectral albedo of three common materials that include soil, gravel, and grass. Albedo is a Latin term meaning ‘whiteness’ and it is a measure of how well a material reflects incoming light – albedo of zero represents a perfect absorber and albedo of one is a perfect reflector. Except for water, snow and ice, the spectral albedo of earthen materials tends to increase at wavelengths greater than 700 nm [167]. Figure 1.10 shows the different spectral peaks and distributions between common spectral albedos and the AM1.5G calibration spectrum. The AM1.5G reference spectrum has a peak wavelength near 500 nm, whereas the albedos have peak wavelengths closer to 1000 nm. Since the shifts in peak wavelength and spectral distribution occur within the active region of c-Si PV, theory tells us that a c-Si PV device will generate notably different photocurrent densities when illuminated with AM1.5G or spectral albedo.

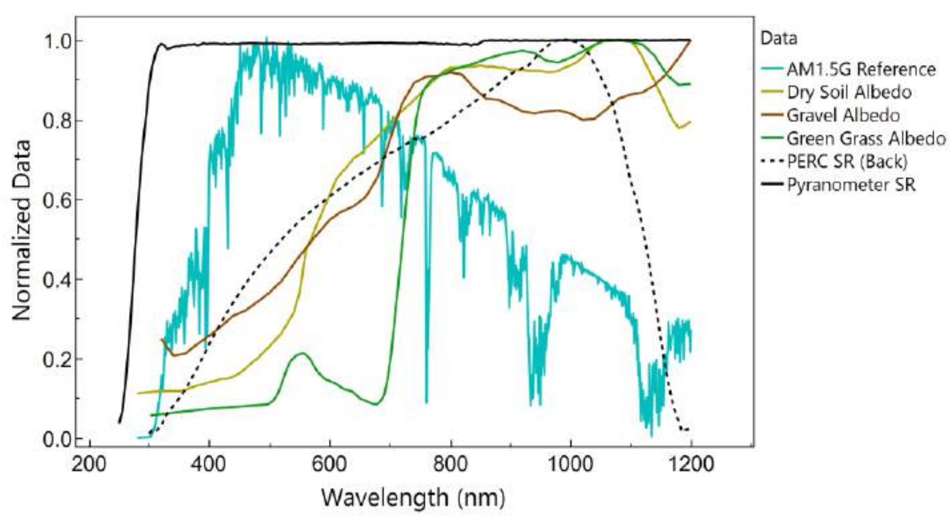

Figure 1.10: Normalized spectral data including the AM1.5G spectrum, three common albedos, the spectral response of a bifacial PERC cell and a pyranometer.

Several researchers have studied spectral albedo on bPV performance [58], [144], [147], [168] – [170]. Gostein et al. calculated spectral mismatch factors for Si bPV devices under different spectral albedos from the SMARTs database [58], the experimental component of Russel et al. measured Si bPV devices in a flash solar simulator and varied the spectral reflectance received by the backside [169], and Blakesley et al. proposed a method to adjust R_{POA} for spectral effects using MODIS satellite albedo products [147]. In all studies, except Blakesley et al., the spectral distribution of R_{POA} is assumed constant with time. Another shortcoming of all the previous spectral albedo studies, except Monokroussos et al. [144], is that they use spectral albedo as a proxy for spectral R_{POA}. This is flawed because, by definition, albedo is measured on a horizontal surface while most bPV systems are not at static horizontal (0°) tilts. Therefore, the second half of **Chapter 3** investigates the temporal nature of spectral albedo and RPOA using high-resolution spectral measurements and 2D VF modeling (**Publication V** and **Publication VI**). In these works, we generated multi-variate correlations of backside SMM with sky diffuse fraction and with $VF_{PV\ Backside \rightarrow sky}$ for three common albedos. These correlations could serve as simplified models for describing spectral effects on the backside of the array.

1.2.3 Rating of bifacial photovoltaic modules and measurement of rear irradiance

Internationally recognized procedures for monofacial PV current-voltage (I-V) characterizations at STC are described in the first ten parts of the IEC 60904 series. These standards describe requirements and protocols for critical elements such as reference cell packages, the reference solar spectrum, cell temperature measurements, spectral responsivity measurements, and reference module handling. Standardization of bPV characterization was lacking until the technical specification (TS) IEC 60904-1-2 was published in 2019 [171]. Although a standardized method for bPV cell characterization was referenced as early as 2010 [172], earnest work toward the international approval of IEC TS 60904-1-2 did not begin until around 2015 [173].

IEC TS 60904-1-2 describes three procedures to measure I-V curves of bPV cells and modules that include outdoors in natural sunlight, indoors with simultaneous dual-side illumination, and indoors with single-side illumination. It is impractical to perform PV characterizations outdoors in Denmark because the solar resource in Denmark is frequently dominated by clouds. Meanwhile, the indoor dual illumination method requires specialized upgrades to standard solar simulators such as a second light source, either steady state [174] or a synchronized pulse [175], or two vertical mirrors at ±45° from the DUT placed between them [176]. Therefore, indoor bPV measurements in this thesis were made with the single-side illumination method described in IEC TS 60904-1-2, also known as the equivalent irradiance method. Figure 1.11 demonstrates the principle of the single-side illumination approach and Figure 1.12 shows how the method is implemented in practice at DTU.

The non-irradiated module side must receive negligible stray light (< 3 W/m^2), which is why IEC TS 60904-1-2 recommends baffles around the module under test. Additionally, bPV modules have transparent or semi-transparent cell gaps, which necessitates a non-reflective background material to minimize the influence of light passing through the cell gaps. Liang et al. demonstrated that the distance between the DUT and the non-reflective back panel plays a critical role in measurement uncertainty. Their analysis showed that uncertainty in P_{MAX} measurements is minimized when the distance is greater than 10 cm [177]. DTU's solar simulator has a 75 cm distance between the DUT and black background. Irradiance measurements on the rear plane were less than 1 W/m^2 when the frontside was illuminated with 1000 W/m^2 and baffles were placed around the DUT.

Figure 1.11 shows that two I-V measurements are required to determine the module's bifaciality: one I-V measurement of the module's frontside at STC and a second of the module's backside at STC. From these measurements, the bifaciality coefficients for I_{SC}, V_{OC} and P_{MAX} are calculated (Equation 1.13–1.15).

Depending on the DUT's frame thickness, the distance between the light source and cells within the DUT can change when the DUT is flipped around. This is accounted for in the DTU system by placing 5 mm wood risers below the module as needed.

$$\varphi_{ISC} = \frac{I_{SC\_rear}}{I_{SC\_front}} \tag{1.13}$$

$$\varphi_{VOC} = \frac{V_{OC\_rear}}{V_{OC\_front}} \tag{1.14}$$

$$\varphi_{PMAX} = \frac{P_{MAX\_rear}}{P_{MAX\_front}} \tag{1.15}$$

Bifaciality coefficients vary with cell technology. For example, the P_{MAX} of bifaciality on cell-level is around 0.65–0.75 for PERC, 0.8–0.9 for n-PERT, and 0.9–0.95 for SHJ [35]. PV manufacturers price modules according to their frontside power rating, so white ceramic coatings between the cell gaps are a common feature. Such white coatings partially shade the backside active area and boost frontside power by 2–5% due to internal light scattering – both effects decrease the bifaciality of bPV modules. A module's I_{SC} bifaciality and P_{MAX} bifaciality are typically very similar, except when there is significant rear-shading (e.g., from a junction box), in which case the I_{SC} bifaciality is usually greater. Bifaciality is reported at STC, but bifaciality can change with irradiance [178], especially in bPV devices that have a non-linear current-irradiance relationship [176].

Once the bifaciality at STC is established, the bifacial rating (BiFi) can be determined. The BiFi rating is determined by regression of P_{MAX} at multiple equivalent irradiances (G_E), wherein Ge is calculated according to Equation 1.16.

$$G_E = 1000\, Wm^{-2} + \varphi_{ISC} \cdot R_{POA} \tag{1.16}$$

IEC TS 60904-1-2 recommends that G_E be calculated with R_{POA} levels between 0 W/m^2 and 200 W/m^2. All G_E measurements are performed on the module's *frontside*. For example, when testing a module with I_{SC} bifaciality of 0.7 at R_{POA} of 100 W/m^2, the solar simulator's light intensity must be set to G_E = 1070 W/m^2. In **Section 4.2**, we present BiFi ratings for three bPV module types measured at DTU and at five other European laboratories as part of an international round robin.

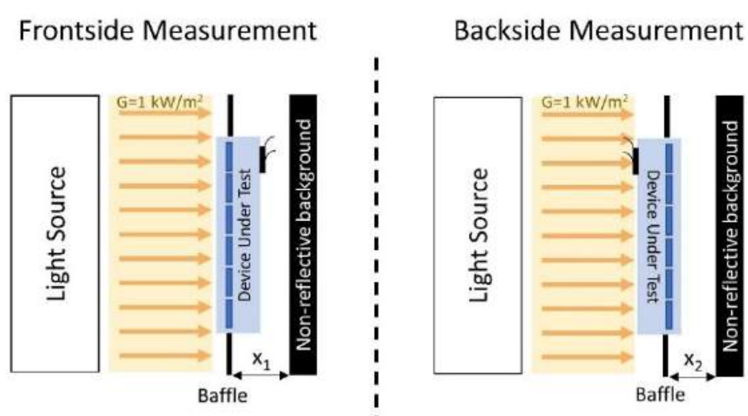

Figure 1.11: Block diagrams of the single side equivalent procedure for the characterization of bifacial PV according to IEC TS 60904-1-2.

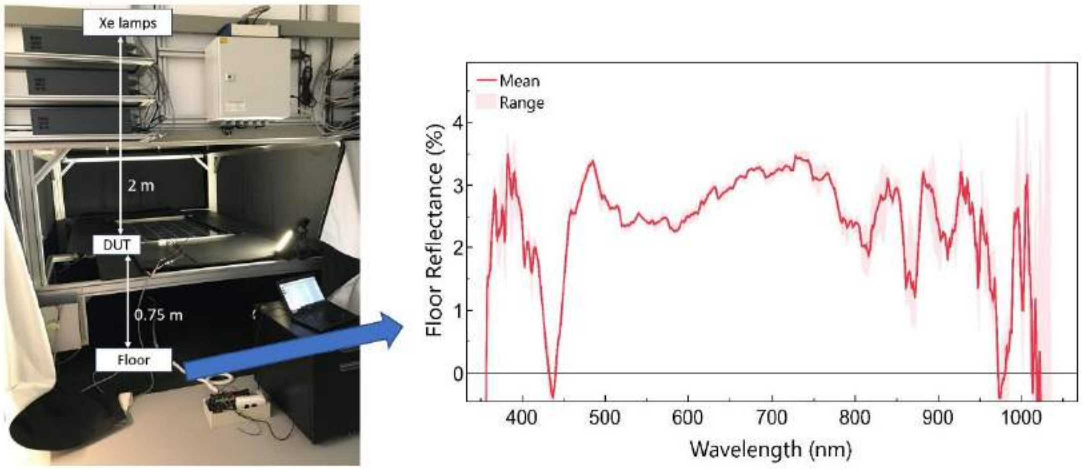

Figure 1.12: Practical implementation of IEC TS 60904-1-2 in the Endeas flash solar simulator at DTU, the graph to the right shows the measured spectral reflectance of the black floor.

Some studies have reported that measurements are not always reproducible across the three approaches laid out in IEC TS 60904-1-2 [174], [176], [179] – [181]. Lopez-Garcia et al. recently compared the three methods at the European Solar Test Installation (ESTI) and found power measurements were within 0.8%, which was below the uncertainty of the reference system [179]. Roest et al. compared single-side and dual-side indoor illumination methods and found differences between -1.2% to +1.8% [174]. This difference was considerably larger than that found by Lopez-Garcia et al. but may have been caused by additional reflections from the second light source that were not corrected for. Rauer et al. demonstrated that comparability between the two indoor methods depends on the DUT's level of rear-shading (e.g., junction boxes, labels, or frames) wherein differences of more than 2% can occur when the DUT has significant rear-shading [176].

Two extensive interlaboratory comparisons of bPV measurements have been conducted since IEC TS 60904-9 was published in 2019 [180] [181]. These efforts helped to establish measurement comparability between accredited and non-accredited labs and to identify sections of the TS that require clarifications. It was important for DTU to participate in these efforts because the measurement system shown in Figure 1.12 was modified to accommodate bPV modules in 2020, which created a need to establish confidence in our new test procedures. Therefore, the first part of **Chapter 4** reports on DTU's results in the bPV round-robin led by the National Physical Laboratory (NPL), which allowed us to compare bPV measurements with participating labs such as TUV Rheinland and Fraunhofer ISE.

Detailed PV Characterizations

The PV community has long since recognized that ratings at STC provide module buyers with insufficient information regarding their expected output under realistic conditions. This is because fielded PV systems are exposed to a wide range of solar positions, irradiance, temperature, and windspeed conditions beyond those at STC. The IEC 61853 series attempts to fill this gap by providing standardized procedures for calculating an energy rating of mPV modules. The 61853 series accomplishes this with PV module characterizations that go beyond STC, six diverse meteorological datasets, and a standardized set of formulae to derive an annual module-level performance ratio (PR), also known as the climate specific energy rating (CSER). Part 1 of the standard describes measurement procedures for I-V measurements at 23 irradiance and cell temperature combinations (100 W/m^2 – 1100 W/m^2, 15°C – 75°C), which covers most operating conditions seen in the field; Part 2 of the standard describes procedures to measure incident angle modifier (IAM), spectral responsivity (SR), and the U_0/U_1 thermal coefficients of Equation 1.7; Part 3 describes the algorithm; and Part 4 provides the timeseries meteorological data.

Figure 1.13 shows the operating conditions (T_{MOD} and G_{POA}) calculated for a standard c-Si module in the six standard climates provided in IEC 61853-4. The 23 irradiance and temperature conditions measured in the laboratory as part of IEC 61853-1 are drawn as black crosses. Curiously, the c-Si module in this example rarely operates at the maximum temperature of 75°C required by IEC 61853-1. On the other hand, there are a significant number of points where T_{MOD} is lower than the minimum temperature of 15°C required by IEC 61853-1 – particularly in the high elevation and temperature continental climates.

It took nearly 20 years to publish the four-part IEC 61853 series [182]. The first committee draft in 2002 received more than 100 pages of comments, which directed the standard to be split into four parts. The first two parts describing the measurement protocols (Part 1 and Part 2) were published in 2011 and 2016, and the two parts describing the calculations (Part 3 and Part 4) were published in 2018. The IEC TC 82 working group 2 (WG2) is currently amending the IEC 61853 series so that it includes procedures for bPV modules. Gracia-Amillo et al. suggested that energy rating calculations for bPV modules should be made for the same six standard climates, but in three additional configurations: fixed-tilt with 20% albedo, fixed-tilt with 60% albedo, and vertical east-west [49]. As far as we are aware, WG2 has not yet made their recommended measurement procedures for Part 1 and Part 2 publicly available.

Of the three characterizations described in IEC 61853-2, the PV laboratories at DTU's Department of Electrical Engineering are only equipped to perform the IAM test [183]. The IAM describes angular-dependent losses, which are primarily due to reflection at the glass–air interface. The IAM is measured taking I_{SC} measurements from 0° to 90° angle of incidence (AOI).

$$IAM(\theta) = \frac{I_{SC}(\theta)}{I_{SC}(0°) \cdot \cos\theta} \quad 1.17$$

In Equation 1.17, θ represents the AOI and $I_{SC}(0°)$ represents the I_{SC} measured at normal incidence. In essence, the IAM is a measure of how well a PV device follows a cosine response. A hypothetical device with an IAM of one from AOI 0° to 90° would be a perfect cosine receiver. Class A pyranometers approximate such a response, but the IAM of PV modules decreases rapidly at AOIs greater than 50°.

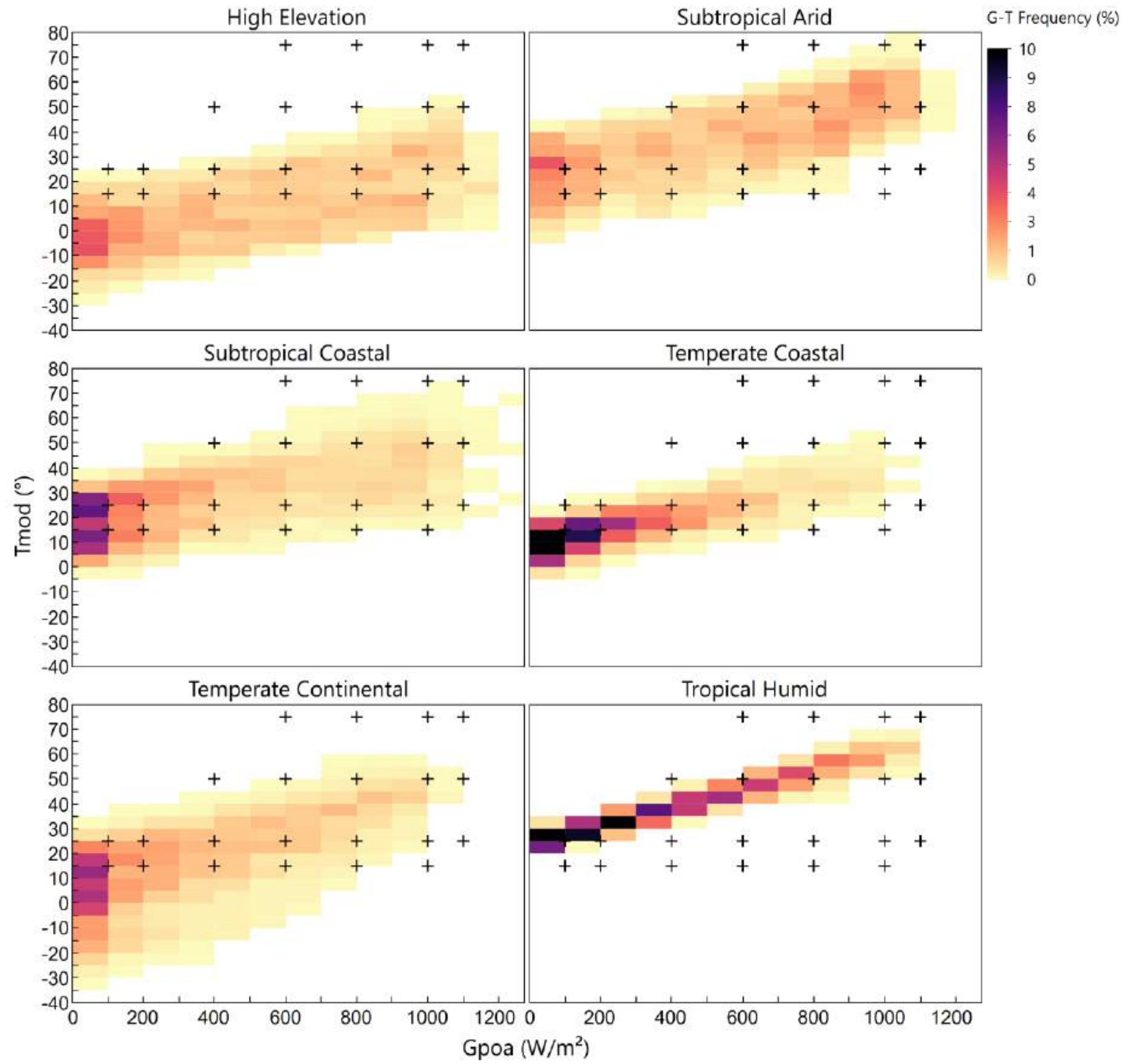

Figure 1.13: Heatmaps showing the density of module temperatures and AOI-corrected plane of array irradiances calculated for a standard c-Si module in the six standard climates of IEC 61853-4. The black crosses show the 23 irradiance and temperature conditions that are required to be measured by IEC 61853-1. The U_0/U_1 values used in the calculation are 26.4 W/m^2·K and 6.3 W·s/m^3·K.

Accurate IAM characterizations are important because fixed-tilt PV systems with standard PV glass lose 3-4% of their annual energy production due to angular-dependent reflections [184], [185]. Anti-reflective coatings (ARC) reduce such reflection losses to 2-3% and have become standard for frontside PV module glasses in recent years [17]. Because backside PV glass rarely has an ARC, the front and backside IAM responses of bPV modules will likely be different. The Marion 2D VF model provides an example for how IAM losses could be applied to R_{POA} (Equation 1.5). For IAM measurements to be useful in PV systems modeling, the data are commonly first fit to a mathematical model such as that of SAPM [119], ASHRAE [186], or Martin and Ruiz [187]; the coefficients extracted from these models are likely to be different for the front and backside of a bPV module.

A detailed investigation of IAM measurement uncertainty was presented by Plag et al. who used GUM principles to propagate uncertainty for a laser based IAM measurement system [188]. Nevertheless, the scientific literature lacks an assessment of how IAM measurement uncertainty impacts energy yield estimates, which is why in 2018 we initiated the first ever international IAM measurement round-robin on PV cells. This effort compared the IAM measurement protocols employed at twelve laboratories and used the resulting data to estimate the effect of IAM measurement variability on energy rating (**Publication VII**).

Irradiance Monitoring in bPV Systems

The first pyranometers dating back to the early 20th century were designed to measure solar radiation on horizontal surfaces (e.g., the Moll-Gorczynski pyranometer sold by Kipp and Zonen in 1927). Measurements of global *tilted* irradiance (G_{POA}) were not studied extensively until the need to measure solar thermal collector performance arose in the early 1980s [189]. Today's best practice guidelines for frontside G_{POA} measurements have therefore benefited from nearly four decades of collective experience across academia and industry [190]. Studies on R_{POA} measurement approaches have appeared only within the last few years [148] [191] – [193], and as such, best practice guidelines for irradiance monitoring in bPV systems are still evolving. Much of the PV community's present knowledge surrounding R_{POA} measurement practices and considerations is codified in the latest revision of IEC 61724-1 [194]. The key recommendations made by the IEC standard for R_{POA} measurements include:

- Sensors should be mounted at the same tilt angle as the modules while minimizing shade on the modules.
- Sensors should be positioned as to avoid end-row brightening effects, localized shading, or enhanced illumination phenomena.
- Multiple sensors should be installed to measure the non-uniform illumination profile throughout the day.

The IEC standard does not recommend a specific number of R_{POA} sensors per array, but only specifies a minimum number of sensors for the entire park depending on the bPV system size. In Class A PV monitoring systems, the minimum number of R_{POA} sensors is three times higher than G_{POA}. For example, 12 R_{POA} sensors are needed for a 200 MWp bPV park. The lack of clear advice for the number of R_{POA} sensors per array is reasonable because R_{POA} non-uniformity depends on the array's height, tilt angle, and pitch, which makes general recommendations difficult. The IEC standard states that bifacial reference cells can be used to determine the effective rear to front irradiance ratio, but it does not recommend the use of any specific sensor type for R_{POA} measurements (i.e., pyranometers vs. reference cells). The standard states that spectrally corrected R_{POA} is optional but does not provide clear guidance on how or when to make such a correction.

In the present era of multi-MW bPV projects, the industry needs more research into R_{POA} measurement practices because any uncertainty in irradiance measurement has direct negative impacts on the financials of PV projects. Therefore, the last section of **Chapter 4** presents a simplified method for conducting RPOA measurements in large bPV plants (**Publication VIII**). This method inherently accounts for the heterogeneity and spectral effects studied in **Chapter 3** and could provide guidance for future revisions of IEC 61724.

1.2.4 Albedo and bifacial energy gain

Similar to R_{POA}, in-depth studies on albedo have been published by PV researchers only in recent years. Some notable works include that of Tuomiranta et al. who compared 20 different albedo models to ground measurements at 26 sites [195], and that of Gueymard et al. who compared albedo from five different satellite sources to ground measurements [55]. But unlike R_{POA} research, there is a plethora of albedo studies from other fields (e.g., remote sensing and climate science), which the PV community can potentially benefit from.

As mentioned in **Section 1.2.2**, albedo describes the fraction of incoming solar radiation that a surface reflects. It has historically been measured by two spectrally flat pyranometers, one facing the sky to measure GHI and one facing the ground to measure the reflected horizontal irradiance (RHI). The albedo ρ is calculated with the ratio of upward and downward fluxes (Equation 1.18).

$$\rho = \frac{RHI}{GHI} \tag{1.18}$$

Marion collected ground-based albedo measurements from nearly 40 locations and created an open access dataset that was intended to increase the PV community's understanding of albedo [56]. DTU contributed to this effort with one-year of measurements from the albedometer shown in Figure 1.14, and in our report[4], we stated the annual average albedo of the grass at the DTU test site is 0.22 with low monthly variability (±0.025). After analyzing ground-measured albedo from nearly 40 sites, Marion notably found that a default albedo value of 0.2 is reasonable, except when a location experiences snow, or is a desert location in which case the albedo is usually greater. Similar findings were obtained by Patel et al. who studied the effect of monthly versus annual average albedo values in bPV performance simulations [196]. Their results showed minimal difference between the albedo assumptions and suggested that a constant albedo approximation is suitable for most bPV simulations, except for sites where snow is present.

Figure 1.14: Broadband albedometer at the DTU outdoor test site (left) and albedometer view from cardinal directions (right).

The broadband albedometer installed at DTU is shown in Figure 1.14 to demonstrate how albedo measurements can be made in bPV parks. It was installed in April 2020 and consists of two Kipp and Zonen SMP10 instruments with a 5° field-of-view limiter on the RHI instrument to prevent direct beam

[4] This report was a private correspondence with Bill Marion, but a summary of the DTU albedo measurements is provided in his peer reviewed publication https://doi.org/10.1016/j.solener.2020.12.050

light from reaching the detector at low sun angles. The images in the righthand side of Figure 1.14 are cardinal direction views and reveal the obstructions that could affect measurements – namely the PV array to the east. This albedometer was designed to be moveable throughout test facility so spatial albedo variations could be captured. As such, it has a 50 m long sensor cable, and the mounting structure is affixed to the ground with earth-screws intended to be hand removable. However, the albedometer's position has never once changed because moving it proved to be an inconvenience, and interesting spatial variations in the grass field never emerged. The height of the two pyranometers is adjustable from 1 to 2m. This was originally set to 1.8 m to match the torque tube height of the trackers, but instrument leveling proved difficult at this height, and was reduced to 1.5 m in July 2021.

Direct beam and diffuse light are scattered differently, which is why computational modeling of albedo requires decoupling the albedo in terms of its black-sky (i.e., directional) and white-sky (i.e., isotropic) components. As far as we are aware, such approaches to albedo modeling are primarily used in fields of study outside PV (e.g., remote sensing). Black-sky albedo describes directional reflections and can be approximated from albedo measurements made on clear and cloudy days that are just a few days apart [197]. The key to this approximation is that the surface's reflectance should not change significantly between the two days. Figure 1.15 shows an example of black-sky albedo estimation from broadband albedo measurements on a cloudy (18/03/2020) and clear day (21/03/2020). Here, the black-sky albedo is calculated using albedo measurements from the Figure 1.14 setup and Equation 1.19. Note the morning dip in the clear sky albedo measurements is caused by the PV array to the east.

$$\rho_{black\_sky} = \frac{RHI - \rho_{white\_sky} \cdot GHI}{DNI \cdot cos\, \theta_Z} \qquad 1.19$$

The white-sky albedo ρ_{white_sky} is taken from the albedo recorded on the cloudy day, which should in theory show no solar angle dependence, but is about 0.20 ±0.02 on the cloudy day shown in Figure 1.15. Coakley estimated a ±0.02 uncertainty for albedo measurements [198], which could be the reason for the variation in cloud day albedo. The black-sky albedo shown in Figure 1.15 (clear day) has a minimum value of 0.03 when the sun is highest in the sky (θ_Z=55°), and a maximum value of 0.25 when the sun is lowest in the sky (θ_Z=85°). Once the surface's black-sky and white-sky albedo are known, then the solar zenith dependence of albedo can be modeled. For example, a model such as Equation 1.20 can be used [198], but there are several other models in the literature [195].

$$\rho = \left(1 - \frac{DfHI}{GHI}\right) \cdot \rho_{black\_sky\_60^\circ} \cdot \frac{1+d}{1+2d\, cos\, \theta_Z} + \frac{DfHI}{GHI} \cdot \rho_{white\_sky} \qquad 1.20$$

In Equation 1.20, DfHI is the diffuse irradiance measured on a horizontal plane, $\rho_{black\_sky\_60^\circ}$ is the black-sky albedo measured at a solar zenith angle of 60°, and *d* is a fitting coefficient adjusted to give the desired angular-dependent albedo behavior (typically 0.1–0.4 depending on the surface and wavelength). Equation 1.20 is a simplification because the anisotropy of reflectance is not just a function of solar zenith angle, but also the solar azimuth angle and the viewing angle. The bi-directional reflectance distribution function (BRDF), defined by Nicodemus in 1965, describes how a surface scatters light as a function of incident and viewing angles [199]. BRDF is not studied in this thesis, but it is important to note that BRDF measurements integrated over a 2π hemisphere should equal the albedo measured by a dual pyranometer albedometer (e.g., that in Figure 1.14).

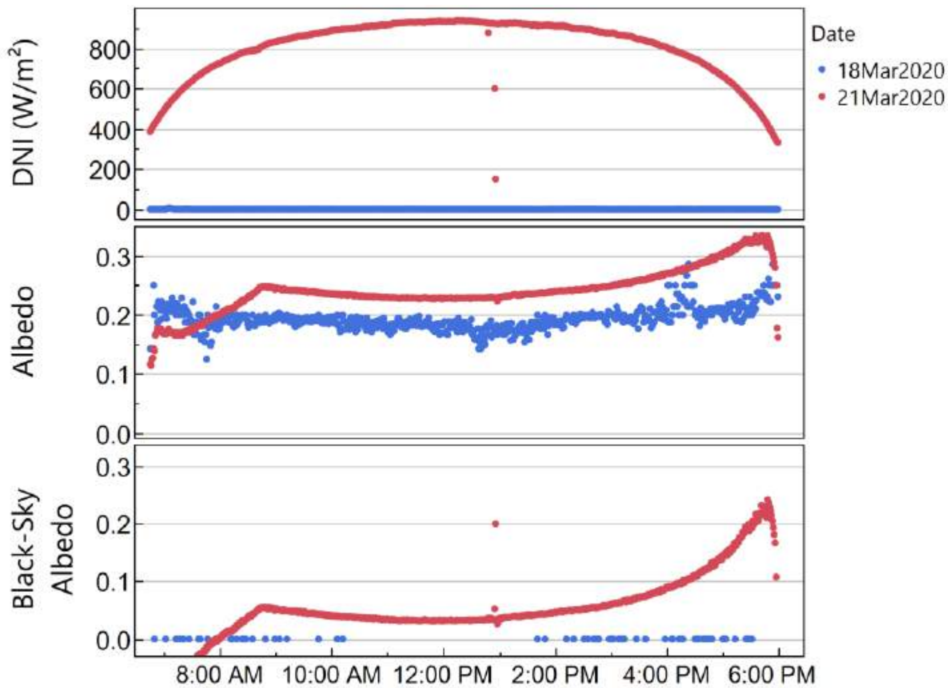

Figure 1.15: Direct normal irradiance (top), broadband albedo (center) and black-sky albedo (bottom) recorded on a cloudy and sunny day at the DTU outdoor test site.

Bifacial Energy Gain

The bifacial energy gain is defined as the additional energy produced by a bPV system over its monofacial equivalent and it is the reason investors pay a premium for bPV modules. If measurements from collocated bPV and mPV systems with identical frontside ratings are available, then bifacial gain is estimated simply as the ratio of electrical output from the two systems. Normalization for the frontside ratings of the two systems must be made if they are not equivalent. If electrical production data (measured or modeled) are not available, then a back-of-the-envelope calculation of bifacial energy gain (BEG) can be made with Equation 1.21.

$$BEG \approx \rho \cdot \varphi_{PMAX} \cdot \Delta \tag{1.21}$$

Where ρ is the albedo, φ_{PMAX} is the module bifaciality, and Δ is a geometrical factor describing how much light the backside can receive. The empirical Kutzer model proposed a complicated algebraic term for Δ that included array height, collector width and pitch [200]. Empirical models have so far proved unreliable in their ability to predict bifacial gain [149], which is why VF or raytrace modeling (**Section 1.2.1**) are the preferred methods for accurate bPV modeling.

Asgarzadeh et al. showed that bifacial gain is linear with albedo, but that the slope of bifacial gain versus albedo is steeper when bPV modules are installed at greater heights [152]. Many efforts to modify the ground below bPV systems have been made to see how bifacial gain can be boosted – examples of such trials are shown in Figure 1.16.

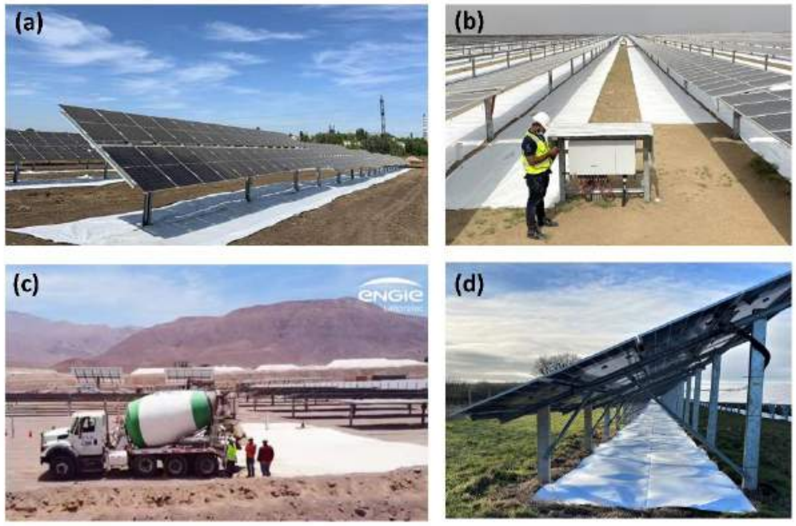

Figure 1.16: Examples of albedo enhancement in large bifacial plants in (a) Ukraine [201], (b) Oman [202], (c) Chile [203], and (d) United Kingdom [204].

The electrical data from experiments such as those shown in Figure 1.16 are rarely available to the public. The 2018 Bifacial Book collected bifacial gain data from 25 systems reported in the literature [205]. Four of the systems found in their review had high albedo (0.5–0.8), wherein bifacial gain was 13–24% for these systems. These data, however, were from small arrays where bifacial gain may have been higher than in utility-scale bPV systems. IEA PVPS Task 13 collected bifacial gain data from 27 bPV systems, but only one system had albedo greater than 0.5 [1]. Interestingly, this was a dual axis tracker bPV system and the bifacial gain was only 6%. Clearly, there is a lack of publicly available bifacial gain data from large-scale systems, and information regarding whether such gains make economic sense was completely absent before 2020. **Chapter 5** therefore contributes a technoeconomic study that assesses the value of albedo enhancement in large-scale bPV plants (**Publication IX**). It is worth noting that two useful studies on this topic were contributed by other authors around the same time [206], [207].

1.3 Project Objectives

i. To identify approaches that can improve the accuracy of PV energy yield modeling, with particular emphasis on the optical subset of models, and the best practices for modelers.

ii. To quantify how the mechanisms that are unique to bifacial PV systems, such as rear irradiance nonuniformity and spectral albedo contribution, impact the energy output.

iii. To develop a method for monitoring irradiance in large bifacial PV plants that incorporates the nuanced effects of rear plane-of-array irradiance such as nonuniformity and spectrum.

iv. To examine strategies that can enhance energy output of bifacial PV systems and provide bottom-line recommendations to developers of large bifacial PV plants.

1.4 Project Limitations

- The PV simulation software tested in **Chapter 2** were benchmarked using operational PV system data from the Danish climate. A comprehensive study would have included similar PV systems in a dissimilar climate (e.g., equatorial). However, such data were not available.

- The rear spectral shift correlations presented in **Chapter 3** were not incorporated into bPV energy yield simulations. Therefore, its potential value to the PV energy modeling chain is not directly assessed. However, **Chapter 3.4** proposes practical methods to integrate a rear spectral shift correlation into the PV modeling process.

- The electrical mismatch due to nonuniformity of R_{POA} in **Chapter 3** was only estimated for trackers. We did not investigate this for other substructure types such as equator facing fixed-tilt or vertical E-W designs.

- The IAM round robin presented in **Chapter 4** included only samples with standard PV glasses. Future works on this topic should include samples with different glasses, including those with various structures and coatings.

- Alternative approaches to the albedo enhancement experiments in **Chapter 5** could have yielded results with more favorable economics. For example, the use of alternative reflector materials and/or alternative positioning of the materials. However, such approaches were not examined in detail due to lack of time and resources.

- The literature suggests that operating temperatures of mPV and bPV devices will vary with environmental conditions [208]. However, this thesis does not investigate differences in operating temperature between monofacial and bPV modules. Back-of-module temperature sensors were installed on mPV and bPV modules at DTU to investigate this effect, but the experiment lacked a structured proposal, and the initial data revealed that the thermal contact between the sensors and back of modules may have been suboptimal.

- It is well-known that the module BoM is critical for reliability. And since the BoMs of mass-produced bPV entered the market only recently, it is necessary to understand if they are susceptible to new failure modes. However, this thesis does not investigate any reliability issues that may face bPV such as potential induced degradation (PID), light and elevated temperature degradation (LeTID), or possible hot spot formation due to partial shading of rear irradiance.

1.5 Main Contributions

The most important contributions that this PhD project offers the field are the following:

1) A benchmarking study on the accuracy of state-of-the-art bifacial energy yield models

This study uses high quality data including standard meteorological parameters, plane-of-array irradiance, module temperature, electrical power, and laboratory measurements to assess how well bifacial yield software can predict electrical power, in-plane irradiance, and module temperature. The study compared PV modeling packages that are used across academia and industry. The entire data set is open access thereby allowing energy modelers to benchmark the accuracy of their own PV simulations.

2) An in-depth study of spectral albedo and its impact on bifacial PV energy output

The PV community has an intuitive sense that spectral albedo shifts ought to affect the electrical output of bPV systems, but there is very little information about how spectral albedo changes with environmental conditions, and how such changes could alter the energy output of different bPV system designs. This study changes that by directly monitoring high-resolution spectral albedo of four ground surfaces over a 15-month duration and by using the data to simulate the performance of three bPV cell concepts on two structure types. The spectral albedo and spectral irradiance measurements are open access to foster reproducibility in science and to stimulate further insights on the topic.

3) The most extensive interlaboratory comparison of IAM measurements to date

The so-called IAM is an important optical loss factor in PV yield modeling. PV energy modelers may use default assumptions for IAM, or they may use measured IAM data from a test lab. In the latter case, there is not much information to guide modelers on the uncertainty of IAM measurements and to help them identify suspicious IAM data. This work circulated encapsulated PV cells to twelve test labs (including accredited and non-accredited) for IAM measurements. The data were used in yield simulations in which 1.0%–1.5% variations in energy were found due to the IAM curves reported by the labs. This work also provided the measurement data in open access form to the PV community.

4) A simplified method to measure bifacial irradiance

The complexities of rear irradiance can frustrate designers of bPV monitoring systems. This method proposes the use of calibrated bPV and mPV reference modules to monitor rear and total effective irradiance. The measurement approach avoids the complexities of identifying representative rear irradiance sensor locations and adjusting for spectral effects, thereby offering accurate measurements with low effort.

5) A technoeconomic case study of albedo enhancement in large bPV systems

Here we monitored the electrical performance of fixed tilt and tracked bPV systems above low and high albedo conditions. The electrical production data were coupled with the real-time spot prices of the Nordpool power market, which formed the basis of the economic model. The levelized cost of energy (LCOE) of bPV systems above natural and reflectivity-enhanced ground surfaces is calculated. The study finds that the current uncertainty in upfront (CAPEX) and ongoing (OPEX) expenditures makes the albedo enhancement unadvisable.

1.6 Thesis Outline

This is an article-based PhD thesis in which **Chapter 2** through **Chapter 5** summarize a previously published paper or a collection of papers. **Chapter 1** first reviews the present status of the bifacial PV market and describes the state-of-the-art in bifacial PV characterization and simulation techniques. This review forms the basis for the research questions and problems that the PhD project focuses upon. The nine research articles produced during the 3-year PhD project period are then summarized in the following four chapters:

Chapter 2: Evaluation of bifacial photovoltaic models and simulation software gives a high-level overview of the capabilities at the outdoor PV testing facility at DTU. Then, we review how these capabilities were utilized, with data quality assessment routines, to conduct a benchmarking study of eight PV simulation software packages. The data analysis deliberately focuses on rear plane-of-array irradiance simulations to quantify how the accuracy of bifacial simulations can be improved. An intercomparison of individual PV modelers implementing the IEC 61853-3 energy rating algorithm is also presented in this chapter. The chapter summarizes Publications I, II, and III.

Chapter 3: Analysis and simulation of bifacial-specific performance factors studies the nuanced effects of irradiance nonuniformity and spectrum in the backside of bifacial PV arrays. The chapter begins by briefly describing two experimental setups that were custom-built to study these performance mechanisms. Then, we show how the high spatial resolution irradiance measurements can be used to estimate electrical mismatch losses on bifacial tracking systems. The high-resolution spatial irradiance measurements are also compared to raytracing simulations. Finally, we use high-resolution spectral albedo measurements and two-dimensional view factor modeling to calculate spectral shifts on the backside of common bifacial system designs. This chapter summarizes Publications IV, V, and VI

Chapter 4: Characterization and performance monitoring of bifacial PV modules and systems analyzes results from two international laboratory comparisons of PV measurements. The first is a comparison of bifacial PV measurements made according to IEC TS 60904-1-2, and the second is a comparison of incident angle modifier (IAM) measurements made according to IEC 61853-2. The data from the IAM round-robin effort are used in the IEC 61853-3 algorithm to derive energy yield, thereby estimating the level of uncertainty that measured IAM data has on the PV model chain. Finally, the IEC TS 60904-1-2 procedures are used to calibrate bifacial reference panels that can be used in continuous field operation for effective irradiance monitoring. This chapter summarizes Publications VII and VIII.

Chapter 5: Methods for enhancing bifacial energy gain reports on the field trials of testing high reflectance materials below the bifacial systems at DTU's outdoor PV test site. The technoeconomic analysis in our case study shows that, out of the six PV designs studied, bifacial PV on trackers above white ground covers provides the lowest LCOE. However, uncertainties in installation and operations costs lead us to discourage modifying the ground of large-scale bifacial plants with albedo enhancements. The chapter concludes with proposals for how such albedo enhancements may be optimized in large-scale bifacial plants. This chapter summarizes Publication IX.

Finally, **Chapter 6** highlights the most important results from the compendium of research articles.

1.7 List of appended publications

I. **Riedel-Lyngskær, N.**, Berrian, D., Alvarez Mira, D., Aguilar Protti, A. C. D., Thorsteinsson, S., Poulsen, P. B., Libal, J., & Vedde, J. (2020). Large-Scale Bifacial PV Test Field Performance Compared to Simulations Using Commercially Available Software, Research-Based and Open-Source Tools. In *Proceedings of 37th European Photovoltaic Solar Energy Conference and Exhibition* (pp. 1324-1329) https://doi.org/10.4229/EUPVSEC20202020-5CO.10.4

II. **Riedel-Lyngskær, N.**, Berrian, D., Alvarez Mira, D., Aguilar Protti, A. C. D., Poulsen, P. B., Libal, J., & Vedde, J. (2020). Validation of Bifacial Photovoltaic Simulation Software against Monitoring Data from Large-Scale Single-Axis Trackers and Fixed Tilt Systems in Denmark. *Applied Sciences*, *10*(23), [8487]. https://doi.org/10.3390/app10238487

III. Vogt, R.M., Riechelmann, S., Gracia-Amillo, A. M., Driesse, A., Kokka, A., Maham, K., Karha, P., Kenny, R., Schinke, C., Bothe, K., Blakesley, J., Music, E., Plag, F., Friesen, G., Corbellini, G., **Riedel-Lyngskær, N.**, Valckenborg, R., Schweiger, M., & Herrmann, W. (2021) PV Module Energy Rating Standard IEC 61853-3 Intercomparison and Best Practice Guidelines for Implementation and Validation. *IEEE Journal of Photovoltaics*. https://doi.org/10.1109/JPHOTOV.2021.3135258

IV. **Riedel-Lyngskær, N.**, Petit, M., Berrian, D., Poulsen, P. B., Libal, J., & Jakobsen, M. L. (2021). A Spatial Irradiance Map Measured on the Rear Side of a Utility-Scale Horizontal Single Axis Tracker with Validation using Open-Source Tools. In *Proceedings of 2020 IEEE Photovoltaic Specialists Conference*. Conference Record of the IEEE Photovoltaic Specialists Conference https://doi.org/10.1109/PVSC45281.2020.9300608

V. **Riedel-Lyngskær, N.**, Ribaconka, M., Po, M., Thorsteinsson, S., Thorseth, A., Dam-Hansen, C., & Jakobsen, M. L. (2021). Spectral Albedo in Bifacial Photovoltaic Modeling: What can be learned from Onsite Measurements? In *Proceedings of 48th IEEE Photovoltaic Specialists Conference* (pp. 0942-0949). IEEE. https://doi.org/10.1109/PVSC43889.2021.9519085

VI. **Riedel-Lyngskær, N.**, Ribaconka, M., Pó, M., Thorseth, A., Thorsteinsson, S., Dam-Hansen, C., & Jakobsen, M. L. (2021). The effect of spectral albedo in bifacial photovoltaic performance. *Solar Energy*, *231*, 921-935. https://doi.org/10.1016/j.solener.2021.12.023

VII. **Riedel-Lyngskær, N.**, Santamaria Lancia, A. A., Plag, F., Kröger, I., Vogt, M. R., Schinke, C., Davidsen, R. S., Amdemeskel, M. W., Jansen, M. J., Manshanden, P., Slooff, L. H., Carr, A. J., Bliss, M., Betts, T., Mayo, M. E., Jauregui, I. P., Balenzategui, J. L., Roldan, R., Bellenda, G., ... Benatto, G. A. D. R. (2021). Interlaboratory comparison of angular-dependent photovoltaic device measurements: Results and impact on energy rating. *Progress in Photovoltaics*, *29*(3), 315-333. https://doi.org/10.1002/pip.3365

VIII. **Riedel-Lyngskær, N.**, Bartholomäus, M., Vedde, J., Poulsen, P. B., & Spataru, S. Measuring Irradiance with Bifacial Reference Panels. (2022). *IEEE Journal of Photovoltaics.* https://doi.org/10.1109/JPHOTOV.2022.3201468

IX. **Riedel-Lyngskær, N.**, Poulsen, P. B., Jakobsen, M. L., Nørgård, P. B., & Vedde, J. (2021). Value of bifacial photovoltaics used with highly reflective ground materials on single-axis trackers and fixed-tilt systems: a Danish case study. *IET Renewable Power Generation*, *14*(9), 3946-3953. https://doi.org/10.1049/iet-rpg.2020.0580

1.8 Related Publications

The work conducted during the 3-year PhD project period led to two research outputs on solar spectral measurements and modeling. Three additional publications were generated with data from the DTU Risø bifacial PV test, the most notable of these was the international PV modeling comparison that was presented during the plenary session of the 8th WCPEC. However, none of the five publications listed below are included in this thesis.

R.1. Theristis, M., Stein, J.S., **Riedel-Lyngskær, N.,** Deville L.M., Barrie D., Campanelli, M., Daxini, R., Driesse, R., Hobbs, W.B., Hodges, H., … Zhao, C. (2022). Blind Photovoltaic Modeling Intercomparison. In *Proceedings of the 8th World Conference on Photovoltaic Energy Conversion*

R.2. Stein, JS, Reise, C, Castro, JB, Friesen, G, Mauger, G, Urrejola, E, Ranta, S, Alam, MA, Anoma, MA, Pelaez, SA, Berrian, D, Bertrand, E, Chiodetti, M, Chudinzow, D, Colin, H, Devoto, I, French, R, Fuentealba, E, Haffner, F, Halm, A, Haysom, J, Hinzer, K, Horvath, IT, Huerta, H, Khan, MR, Klenk, M, Kopecek, R, Libal, J, Lindh, M, Marion, B, Mikofski, M, Molinero, RR, Monarch, M, Neubert, A, Patel, MT, Petersson, AM, Poulin, GN, Ramesh, S, Rhazi, OL, **Riedel-Lyngskær, N**, Riley, D, Russell, ACJ, Schneider, A, Stark, CT, Timofte, T, Tune, D, Tymchak, J, Valdivia, CE, Valencia, F & Wang, M 2021, *Bifacial Photovoltaic Modules and Systems: Experience and Results from International Research and Pilot Applications: Report IEA-PVPS T13-14:2021*. International Energy Agency.

R.3. Clasing, L., Schaaf, S., Blieske, U., **Riedel-Lyngskær, N.,** Santamaria Lancia, A. A., & Reiners, N. (2021). Calculation of the Short-Circuit Current of Colored BIPV Modules under Field Conditions by Application of Spectrally and Angle Resolved Measurement Data. In *Proceedings of the EU PVSEC 2021* (pp. 803-807)

R.4. Looney, E. E., Liu, Z., Classen, A., Liu, H., **Riedel, N.,** Braga, M., Balaji, P., Augusto, A., Buonassisi, T., & Peters, I. M. (2021). Representative Identification of Spectra and Environments (RISE) using K-means. *Progress in Photovoltaics*, *29*(2), 200-211. https://doi.org/10.1002/pip.3358

R.5. **Riedel N**, Aguilar Protti ACD, Jakobsen ML, Pedersen HC, Thorsteinsson S, Poulsen PB et al. (2019). The Outdoor Bifacial Test Facility at Technical University of Denmark. In *Proceedings of the 2019 Bifacial PV Workshop*, Amsterdam, Netherlands.

Chapter 2. Evaluation of bifacial photovoltaic models and simulation software

"All models are wrong, but some are useful." – **George Box**

2.1 Introduction

The first part of this chapter summarizes the results of a PV software benchmarking study with particular attention to the R_{POA} modeling step. Several bPV modeling papers referenced in **Section 1.2.1** contain some form of validation, but this was done mostly on small bPV systems whose performance may not be representative of utility-scale bPV systems. In the study presented here, eight PV software packages with bifacial simulation capabilities were used to model the large-scale systems installed at DTU Risø. The specific system types modeled were monofacial fixed-tilt, monofacial tracked, bifacial fixed-tilt and bifacial tracked. The work was presented at the 2020 EU PVSEC conference (**Publication I**), and at other venues such as the COST-PEARL PV WG3 webinar and First Solar's Plant Predict webinar. A detailed manuscript was ultimately published in the journal Applied Sciences (**Publication II**). The analysis in **Publication II** focuses primarily on rear irradiance simulation accuracy, and it is concluded that the state-of-the-art rear irradiance models are reasonably accurate with average absolute errors of 2–5 W/m^2. Errors of such magnitude contribute roughly 0.5% uncertainty to annual energy estimates, which is a difficult figure to reduce.

The second part of this chapter presents results from an international PV modeling intercomparison. **Publication III** is an interlaboratory comparison of energy rating calculations per IEC 61853-3. Nine European institutes, including DTU, provided their energy rating calculations to the intercomparison. The activity was funded by the European Metrology Program for Innovation and Research (EMPIR) within the 19ENG01 Metro-PV project. DTU participated as a collaborator, not as a funded member of the project consortium. The results from the participants were collected by Malte Vogt and analyzed in detail by Malte Vogt, Ana Gracia-Amillo, Stefan Riechelmann, and Anton Driesse. The nine participants received the same module characterization data, meteorological datasets, and were tasked to calculate climate specific energy ratios (CSER). The characterization data were measured at TUV Rheinland, which included the G-T performance matrix per IEC 61853-1, the IAM per IEC 61853-2 and the spectral responsivity per IEC 61853-2. The first blind comparison revealed CSER differences up to 14%. It took five rounds of calculations—and discussions among the participants—for the nine participants' CSER calculations to agree within 0.1%. This study ultimately demonstrated how user-induced variability can be reduced when modelers are provided with clear procedures for implementing key steps of the PV model chain.

2.2 Input and validation datasets

The outdoor test facility at DTU consists of eight horizontal single-axis trackers (HSATs), labelled T1–T8 in Figure 2.1 and eight south-facing static-tilt structures, labelled T9–T16 in the figure. All 16 substructures (including the south-facing units) are HSATs from the same manufacturer, but T9–T16 have been oriented southward and programmed for a static-fixed tilt. The tracker articulation limits are from -60° (pointing east) to +60° (pointing west). Each PV substructure holds 88 PV modules, either monofacial or bifacial. Please note that the layout shown in Figure 2.1 only applies to the period August 2018 to November 2020. The outdoor test facility at DTU is continuously modified for experimentation of new PV technologies. For example, in November 2020 some of the strings on T7 and T15 were swapped for bPV modules with half-cut cells, and in July 2021 all modules on T16 were swapped for a string of high-power (600 Wp) bPV modules.

In Figure 2.1, the cell types within modules are all 156 mm x 156 mm PERC, but some are mPV PERC (blue boxes) and some are bPV PERC (green boxes). The 88 modules on each substructure are divided into 4 strings, where each string consists of 22 series connected modules. There is one 50 kW dual MPPT inverter for every two trackers (i.e., for every 8 strings) and therefore the operating point of the 88 panels on each substructure is determined by a single MPPT. The DC to AC ratio is 1.07 for the mPV systems and 1.04 for the bPV systems, which leads to negligible inverter clipping. As a further advantage, all substructures at this site have dimensions analogous to those found in utility-scale PV installations.

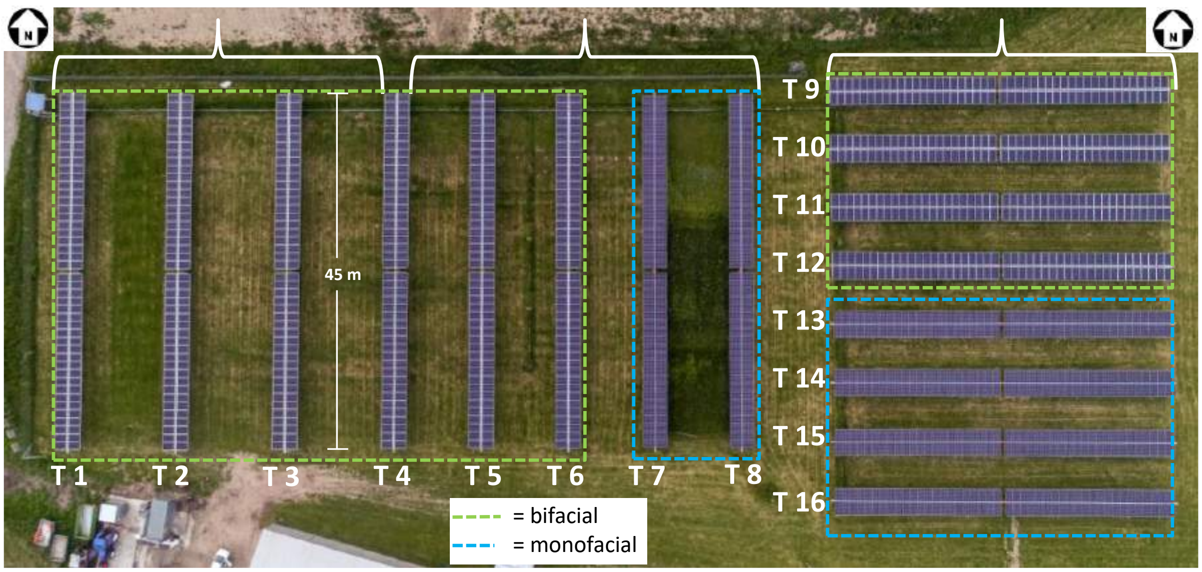

Figure 2.1: Aerial view of the bifacial test facility at DTU. Annotations show the tracker number, substructure type and PV module type. Note that T1–T3 have a 15m pitch, T3–T8 have a 12m pitch, and T9–T16 have a 7.6m pitch.

Broadband DfHI, DNI, and GHI measurements from spectrally flat class A sensors are made onsite at the DTU solar radiation monitoring station located roughly 400 m south of the test site (Figure 2.2a). These high-quality irradiance measurements – in conjunction with ambient temperature and wind speed – are used to create meteorological files for PV simulations of the test site. The solar radiation data are filtered according to the Baseline Surface Radiation Network's (BSRN's) recommended quality checks before being aggregated into the hourly meteorological file [209]. The two R_{POA} sensors located on T11 (Figure 2.2b) are used as a reference when comparing modeled R_{POA} from the different software. Note that T5 has a similar R_{POA} setup for comparing the HSAT simulations. The two R_{POA} sensors on T5 and T11 are mounted ±40% from the center torque tube to sample the nonuniform R_{POA} gradient, and the sensors are located roughly 10 m away from the nearest edge to avoid edge brightening.

Multi-irradiance I-V measurements were performed on a sample of monofacial and bifacial PV modules in the flasher system shown Figure 1.12. These I-V measurements were made before the flasher was upgraded with black baffles and background for optimized bPV testing, and therefore, the backside of the bPV modules were covered with a black backsheet material to prevent stray light from reaching the panels during testing. The multi-irradiance I-V measurements were used to estimate parameter values for the diode models in the various software. Measurements were performed on the panels one year later to check for first year degradation, which was found to be approximately 1%.

(a) **(b)**

Figure 2.2: (a) Direct normal, diffuse horizontal, and global horizontal radiation measured at the DTU solar radiation monitoring station. (b) Spectrally flat class C pyranometers installed on the backside of fixed array T11.

2.3 Testing PV models and software

The objectives of the benchmarking study are to use a consistent set of parameters and meteorological data as input to different bifacial PV software, and to analyze the modeled outputs at various steps of the PV performance model chain including R_{POA}, G_{POA}, T_{MOD} and DC power. The variability that can be introduced by different users of the same software will be investigated in **Section 2.4**.

The PV modeling software tested fall into the categories of commercially available, freeware and open source. A description of each software used in the comparison is provided in Table 2.1. Seven of the models use a 2D VF method to calculate R_{POA} and one model uses a 3D RT based method. We believe that the software programs in Table 2.1 are representative of the tools presently used within the industry and research communities to simulate bifacial PV performance. The column names in Table 2.1 represent some of the most important steps of the PV modeling process (see Figure 1.5). There are several instances in Table 2.1 where multiple software packages use the same model for a particular modeling step. For example, the Perez diffuse model is used in all software packages to transpose horizontal solar radiation data to the plane of array (G_{POA}), and most software use either the PVsyst [51] or Faiman [73] cell temperature models. For this reason, the modeled outputs at the G_{POA} and T_{MOD} steps are similar across the software. G_{POA} and T_{MOD} are the two most important factors that influence PV energy yield, which leads to comparable annual energy yield estimates from the different software. Specifically, the software in Table 2.1 are within 4–5% of each other for annual energy yield, regardless of the modeled PV system type.

Table 2.1: Descriptions of the bifacial performance tools compared in the benchmarking study. All tools implement the Perez transposition model for calculating G_{POA}.

PV Simulation Tool	Sun Position Algorithm	Data used for transposition	R_{POA} Method	IAM Model	Electrical Model	Thermal Model
bifacialvf (0.1.7)	Michalsky	DNI and DfHI	2D VF	Physical	N.A.	N.A.
MoBiDiG VF (0.2.4)	NREL SPA	DNI and DfHI	2D VF	Physical	5 param. De Soto	Faiman
MoBiDiG Hybrid (RT)	Michalsky	DNI and DfHI	3D RT	N.A.	5 param. De Soto	Faiman
PlantPredict (8.7.0)	NREL SPA	GHI and DfHI	2D VF	ASHRAE	PVsyst	PVsyst
pvfactors (1.4.1)	NREL SPA	DNI and DfHI	2D VF	Sandia	N.A.	N.A.
PVsyst (7.0.5)	US Navy	GHI and DfHI	2D VF	Physical	PVsyst	PVsyst
NREL SAM (2020.2.29)	Michalsky	DNI and DfHI	2D VF	Physical	6 param. De Soto	NOCT
SolarFarmer (1.0.187.0)	NREL SPA	GHI and DfHI	2D VF	Martin & Ruiz	PVsyst	PVsyst

Figure 2.3 shows hourly timeseries of measured and modeled R_{POA} on a clear day near the spring equinox. The modeled values have not been adjusted for bifaciality or for derates such as nonuniform illumination or spectral effects. Reflection losses are applied to the modeled R_{POA} according to the software's IAM model shown in Table 2.1. The R_{POA} values modeled by *bifacialvf*, *pvfactors*, and *MoBiDiG* are the average of R_{POA} at five discrete points. The documentation of *PlantPredict*, *PVsyst*, *SAM* and *SolarFarmer* is not clear whether these software segment the rear plane and report an average R_{POA}, or if they simply report R_{POA} at a single location. The error bars around the R_{POA} measurements in Figure 2.3 show the maximum and minimum value recorded by the two sensors mounted on the backside. The difference between the two R_{POA} sensors on the fixed tilt system is significant – about 30 W/m^2 midday. Although the modeled R_{POA} of the fixed tilt system is mostly within the boundaries of measured R_{POA}, the accuracy of the validation depends heavily on where the R_{POA} sensor is mounted on the array's backside. Furthermore, the HSAT results show how the R_{POA} sensor type can influence the results of the R_{POA} comparison, wherein the midday Si photodiode measured R_{POA} is about 10 W/m^2 higher than the pyranometer measured R_{POA}. Considerations regarding how R_{POA} location and R_{POA} sensor type could have consequences for capacity testing or performance guarantees will be discussed in **Section 4.3**.

Figure 2.4 summarizes the R_{POA} modeling error in terms of mean absolute error (MAE) and mean bias error (MBE). The results show that seven of the eight software cluster together with MAE of 2–5 W/m^2 and MBE of -3–5 W/m^2. It will be shown that this error has a small effect on the overall accuracy of energy yield simulations. *SolarFarmer* is an outlier, but its developers have since updated the VF algorithm such that the R_{POA} estimates are more in agreement with other software [210].

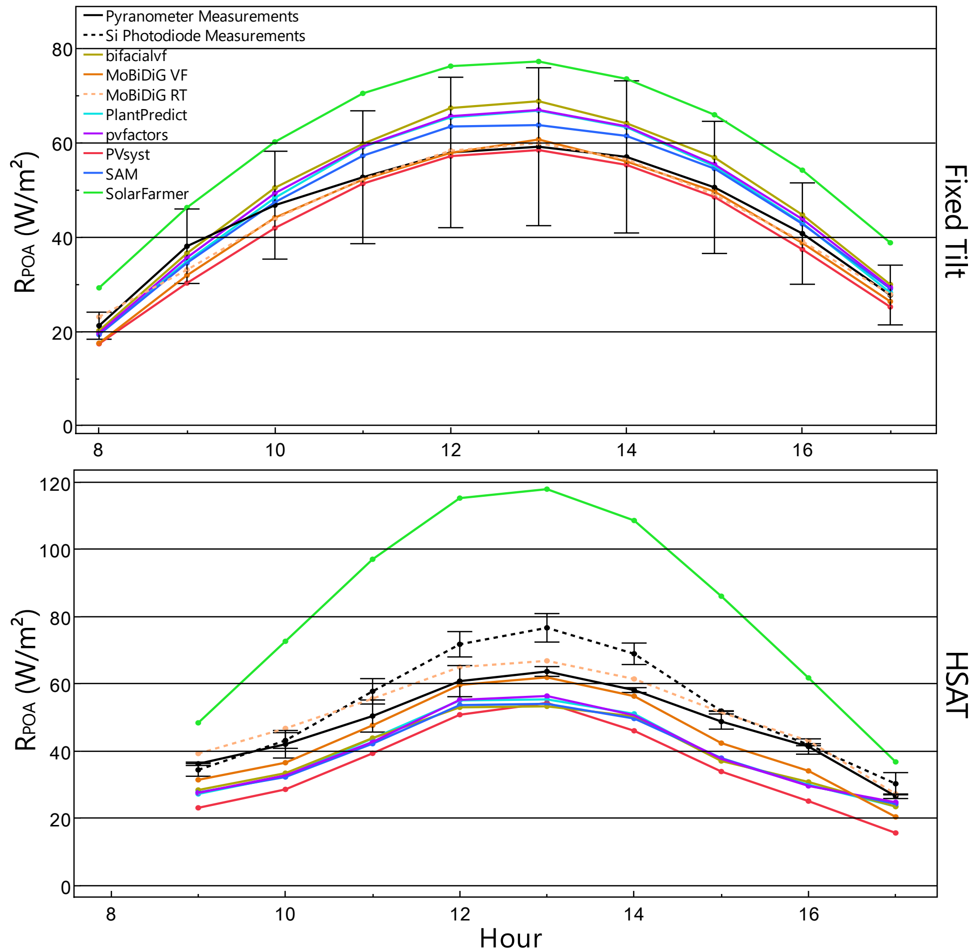

Figure 2.3: Timeseries of modeled and measured R_{POA} on a clear day (26 March 2020). The error bars around the R_{POA} measurements show the max and min values measured by two sensors on the backside of the array. The upper plot shows results for the fixed tilt system (T12) and the bottom plot shows results for the tracker (T5).

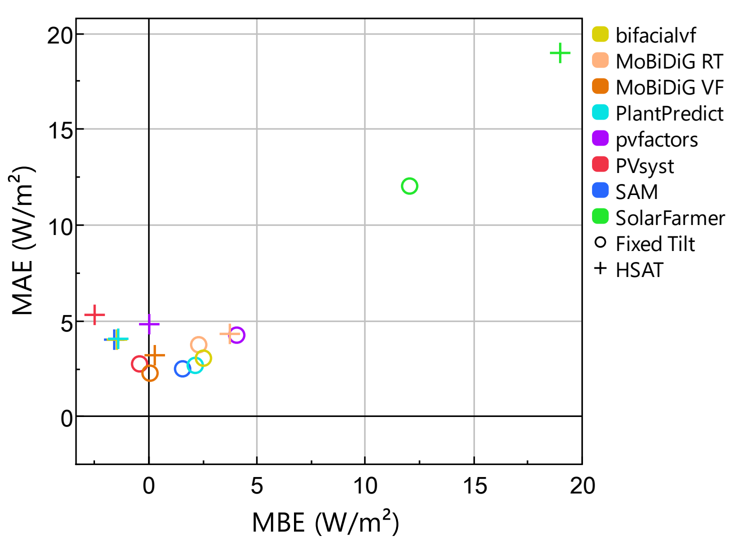

Figure 2.4: R_{POA} mean absolute errors versus R_{POA} mean bias errors for eight software tested. The two marker shapes represent the two modeled PV structures of fixed tilt and single axis tracker.

Figure 2.5 shows the MBE and 95% confidence interval (CI) of modeled R_{POA} from the eight software packages. The distributions are constructed from the hourly R_{POA} errors observed between 21 February 2021 and 31 March 2021 (N = 286). The R_{POA} results from the software are considered significantly different when their CIs do not overlap, which is made evident with the connecting letters shown at the bottom of Figure 2.5. When software do not share the same connecting letter, their R_{POA} error distributions are considered significantly different. For example, the fixed tilt *bifacialvf* error distribution has the connecting letter 'C', which is therefore statistically similar to *MoBiDiG* RT and PlantPredict because these two software have connecting letter 'CD'.

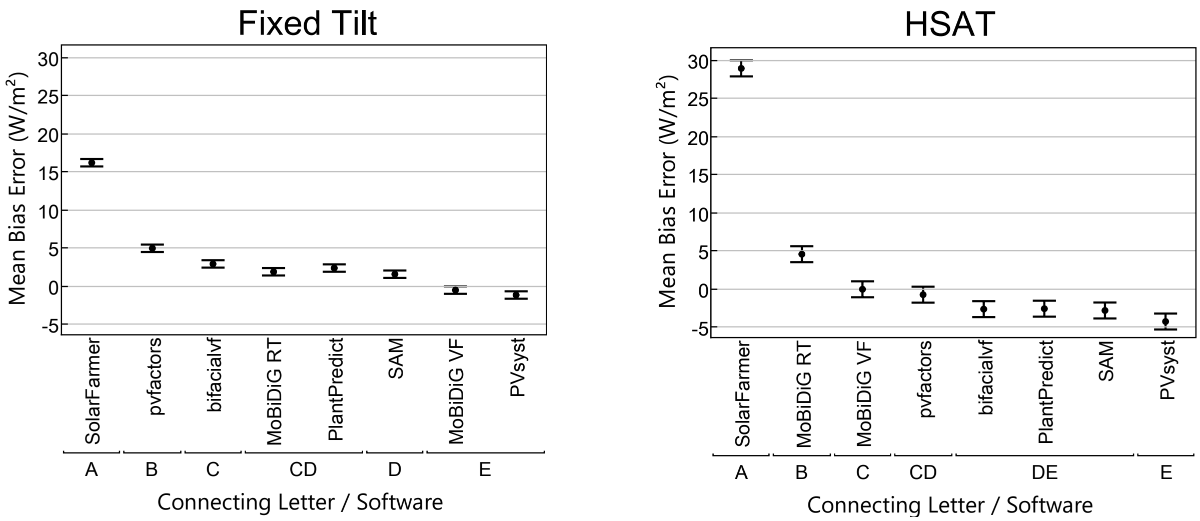

Figure 2.5: Comparison of mean R_{POA} errors for eight different software. The black dots show the mean R_{POA} error, and the error bars show the 95% confidence interval of the mean. R_{POA} errors are considered significantly different when confidence intervals do not overlap and do not share the same connecting letter.

Figure 2.6 shows correlation matrices of modeled and measured R_{POA} for two bPV system types. The color gradient shows the correlation coefficient between two R_{POA} sources. In the fixed tilt simulations, seven of eight software compare well to each other (r = 0.985–0.999) wherein *SolarFarmer* is the outlier with r < 0.95. The HSAT results reveal lower correlation between modeled and measured R_{POA} wherein the best correlation to measurements is the *MoBiDiG* raytrace tool (r = 0.98). It makes sense that the HSAT scenario shows poorer R_{POA} agreement to measurements, and to respective software, because tracking introduces additional complexity at two levels. First, the tracker algorithm[5] implemented by the software is introduced into the comparison and second, the VFs in HSAT simulations are calculated for each change in tilt angle whereas the VFs in fixed-tilt simulations are calculated once for the entire simulation. Despite the lower correlation in modeled HSAT R_{POA}, the MAE in modeled R_{POA} is about 1 W/m^2 different in the HSAT and fixed tilt scenarios.

[5] Backtracking is a standard tracker control algorithm used to prevent row to row shading at low solar elevation angles. We found that the modeled tracker angles agreed well outside of backtracking periods (< 0.5° max difference). However, during backtracking periods, the modeled angles varied by as much as 15°. Data was removed from the analysis when solar elevation < 5°, but this data filter did *not* completely remove backtracking periods from the analysis.

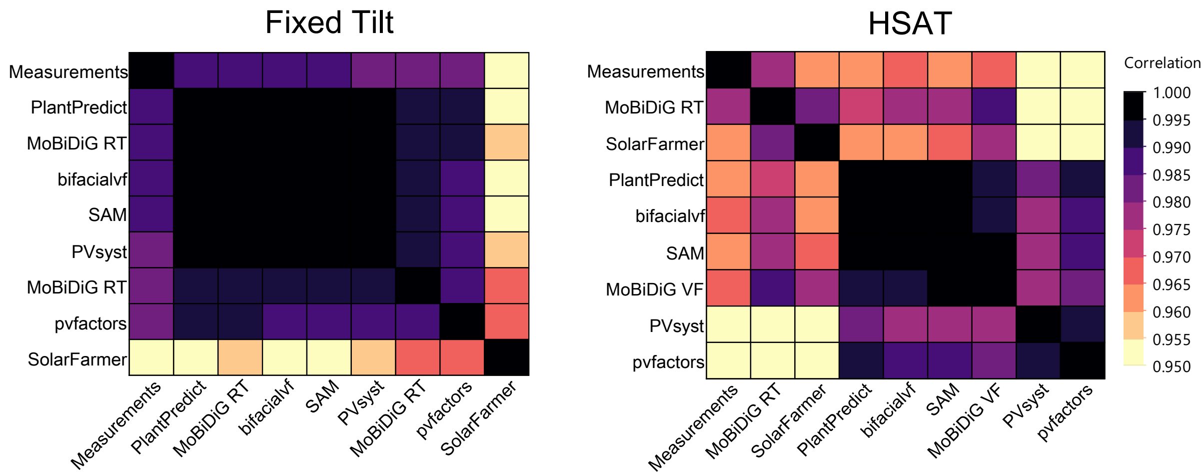

Figure 2.6: Correlation matrices of modeled and measured R_{POA}. The color scale is Pearson's r coefficient.

Now we show differences of measured and modeled DC-side energy yield for the four system types studied. Please see **Publication II** for G_{POA}, T_{MOD} and bifacial gain results. Only six of the eight software are analyzed here because *bifacialvf* and *pvfactors* do not have built in electrical models. In Figure 2.7, the monthly and yearly errors in energy predictions across all four PV system types are shown. Note that roughly 75% of the total annual energy is produced between April and August. With just 25% of the annual energy produced between September and March, errors during these months tend to be larger on a percentage scale. On a monthly basis, *PlantPredict*, *PVsyst*, *SAM*, and *SolarFarmer* fluctuate between negative and positive bias relative to the measurements, sometimes with monthly deviations greater than 5%. However, on an annual basis, all tools simulate the four PV systems within 3.5% or less of measurements, and in some cases, the annual error is less than 1%. This is a positive result considering he uncertainty of the solar radiation measurements and the electrical monitoring system.

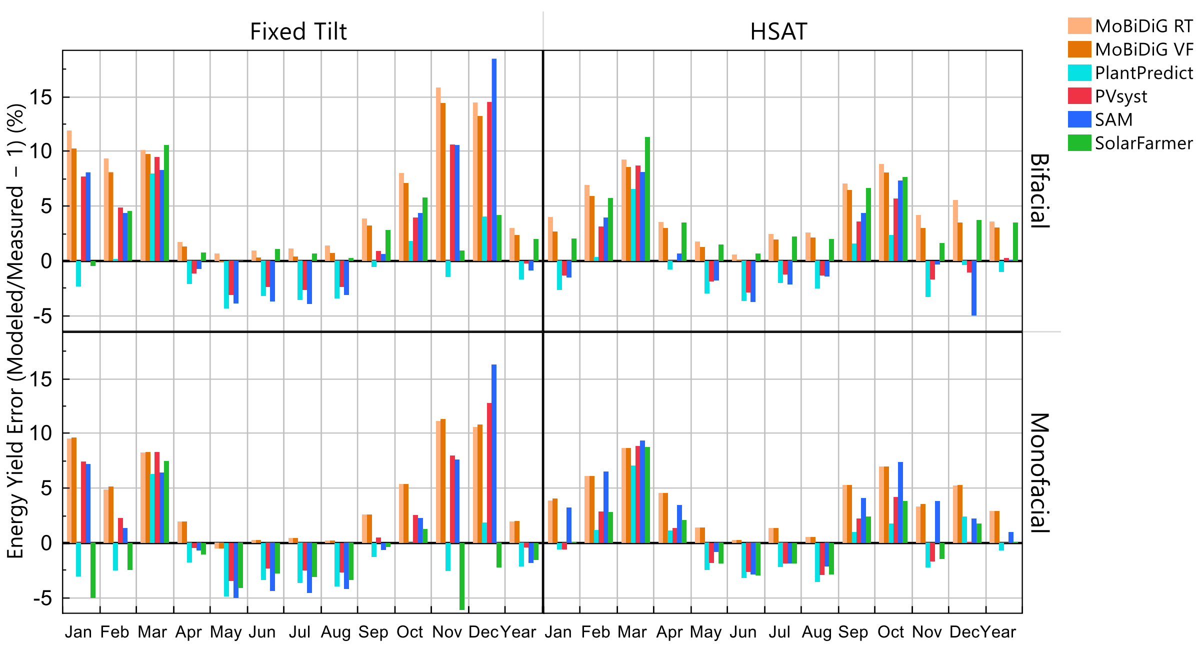

Figure 2.7: Monthly and annual errors in energy yield predictions from six software and four PV system types.

Figure 2.8 shows the MBE and 95% CI of modeled daily energy from the eight software. The distributions are constructed from daily errors in DC energy observed during one-year from 01 April 2020 to 31 March 2021 (N = 323). Like in Figure 2.5, the errors from the various software are considered significantly different when CI's do not overlap, which is indicated by the connecting letters on the x-scale. In the monofacial fixed tilt scenario, all six software share the same letter, and therefore, the error distributions are not considered significantly different (all p-values > 0.09). Adding complexity in the tracking or bifacial simulations leads to only one significant difference between two software, that is MoBiDiG VF/RT and PlantPredict.

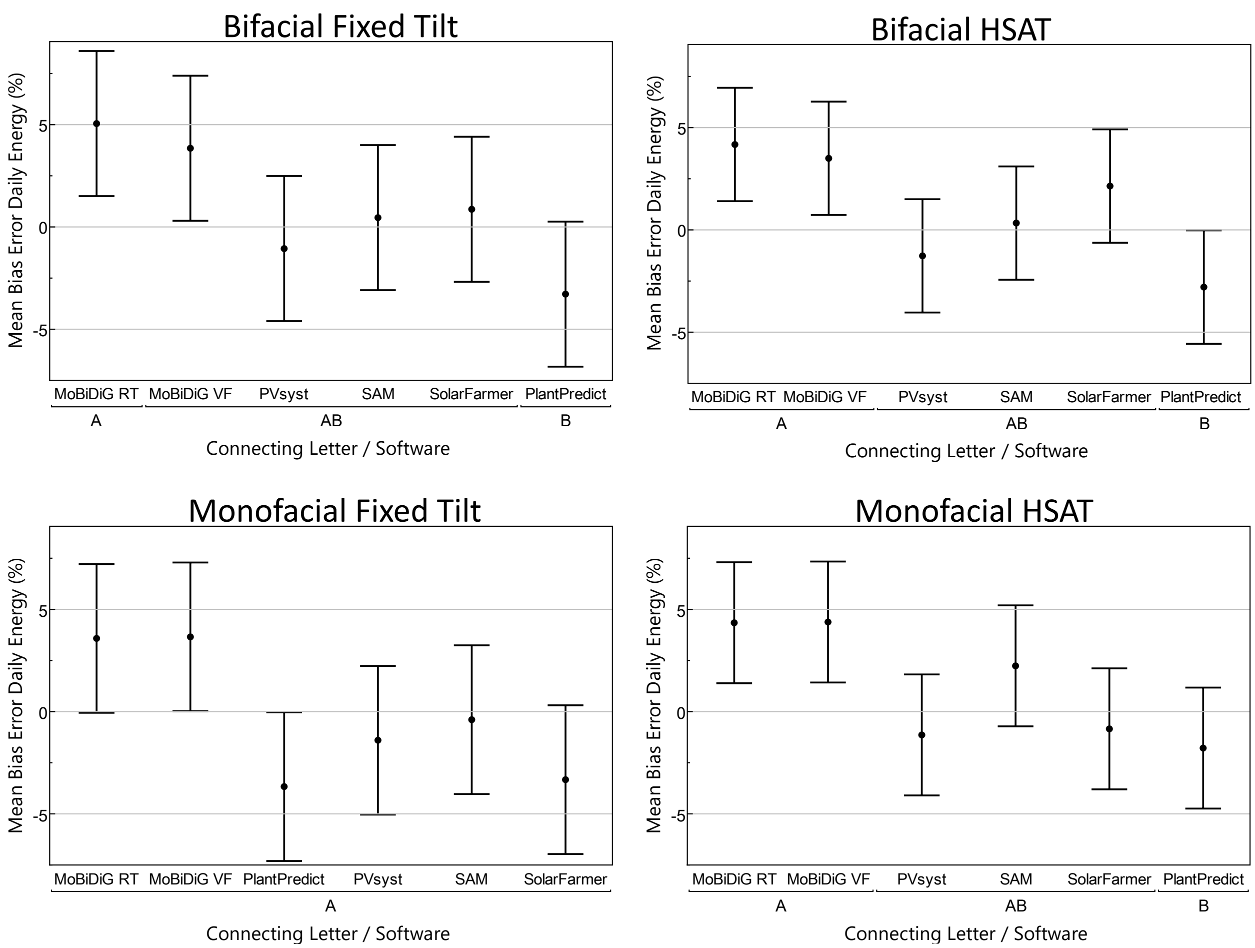

Figure 2.8: Comparison of daily energy yield errors using six different software to model four PV system types. The black dots show the MBE of daily energy prediction, and the error bars show the 95% confidence interval. Energy prediction errors between software are significantly different when their confidence intervals do not overlap and do not share the same connecting letter.

SolarFarmer provides an interesting example where energy predictions are accurate despite having large R_{POA} discrepancies. Presumably, this is because SolarFarmer has low errors for the most important modeling steps of G_{POA} and T_{MOD} and because R_{POA} represents about 10% of the total irradiance.

Finally, within **Publication II** a sensitivity of the albedo was performed wherein albedo was varied by ±3% of the DTU measured average. This resulted in a ±0.5% variation in annual energy yield.

2.4 Testing the users of PV models and software

The eight software programs benchmarked in the previous section were run by two individuals (Nicholas Riedel-Lyngskær and Djaber Berrian) who were in close collaboration to ensure that their assumptions were equivalent at each step of the model chain. This section presents the results of a PV modeling studies that compared results of individual PV modelers implementing IEC 61853-3.

The meteorological data collected in **Publication II**, and details of the four PV system types at DTU Risø, were eventually circulated to 29 PV modelers that spanned academia and industry. This blind intercomparison activity was led by Marios Theristis of Sandia National Laboratories (SNL). The 29 PV modelers were asked to simulate the four operational PV systems at DTU and two operational systems at SNL. DTU contributed to this study with high-quality PV measurements as well as with some data analysis conducted by Nicholas Riedel-Lyngskær's during his external research stay at SNL. The manuscript of this modeling intercomparison is under preparation and results are not presented here.

2.4.1 IEC 61853-3 PV module energy rating comparison led by EMPIR Metro-PV consortium

The ultimate outcome of the four-part IEC 61853 Energy Rating standard is the determination of a PV module's climate specific energy rating (CSER). The CSER is essentially a DC level performance ratio (PR) of a single module that describes the annual deviation in energy production in each standard climate, relative to what the module could have produced if it were operating at its STC performance. Unlike the classic definition of PR, the CSER does not incorporate losses due to soiling, shading, degradation, or any inverter specific losses such as efficiency of power conversion, maximum power point tracking efficiency or clipping losses. The CSER is calculated per Equation 2.1.

$$CSER = \frac{E \cdot G_{STC}}{P_{STC} \cdot H} \qquad 2.1$$

Where E (Wh) is the annual energy produced by the PV device, G_{STC} is the reference irradiance of 1000 W/m^2, P_{STC} is the PV device maximum power at standard conditions, and H (Wh/m^2) is the annual in plane insolation before correction for angular losses and spectral effects.

The CSER is intended to provide PV module buyers with an intuitive metric that assesses the relative performance of commercial PV technologies across climates. The partners in the IEC 61853-3 intercomparison wanted to quantify the CSER variations that could arise from different interpretations and implementations of the 20 equations within the standard. We found that CSER variations among participants could be substantial – up to 14.7%. A CSER difference of this magnitude is, in many cases, greater than a CSER difference due to different properties of two PV modules.

Explanations for the discrepancies among participants fall into two categories. The first category is bugs caused by simple mistakes from transcribing the standard's equations into code. For example, this included relatively easy fixes like missing signs or incorrect balancing of parentheses within equations. The second category is different interpretations of the standard due to ambiguities in the text. This was by far the more difficult category to reconcile. We found that the irradiance-temperature (G-T) extrapolation step, and the spectral irradiance correction step had the most room for interpretation.

The module efficiency data used for the intercomparison is shown in Figure 2.9. The participants were only provided with data at the 23 points marked with circles, which were measured by TUV Rheinland. For each hour of the year, participants had to interpolate or extrapolate efficiency to numerous G-T conditions that were not measured in the lab. This process *could* be done with equations 9 – 17 of IEC 61853-3, but since the standard says these equations "*or equivalent*" may be used, we learned that some participants implemented their own approaches. For example, DTU's initial model extracted a temperature coefficient from the measurements at 1000 W/m^2 and used this to fill in many of the missing temperature values. Methods to fill in the efficiency values within the 61853 G-T matrix were described in detail by [211].

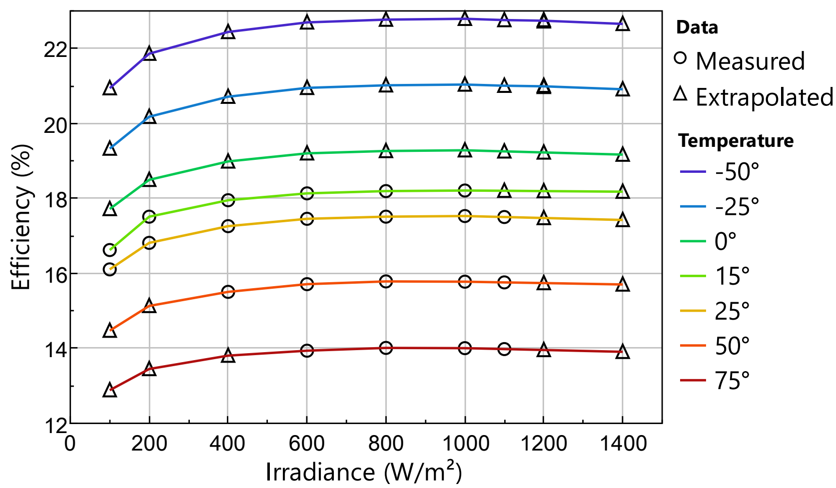

Figure 2.9: Efficiency versus irradiance for a standard monocrystalline silicon module. The circle markers show the 23 measured irradiance and temperature conditions per IEC 61853-1. The triangle markers show extrapolated points using equations in IEC 61853-3. The measured points were provided by TUV Rheinland within the EMPIR funded 19ENG01 Metro-PV project.

The spectral correction of IEC 61853-3 was the second most challenging step to solve before arriving at comparable CSER results. IEC 61853-3 uses Equation 1.12 for the spectral correction formula. IEC 61853-4 provides hourly spectral irradiance from 306–3991 nm for this purpose, but these data are provided in integrated bands whose widths range from 10–760 nm. An example of such binned spectral data (after interpolation) is shown in Figure 2.10. The differences in the participants spectral corrections were due to different definitions of band edges, different numerical integration approaches, and different values of the spectrally integrated reference spectrum (i.e., some participants used 1000 W/m^2, while others calculated a lower value).

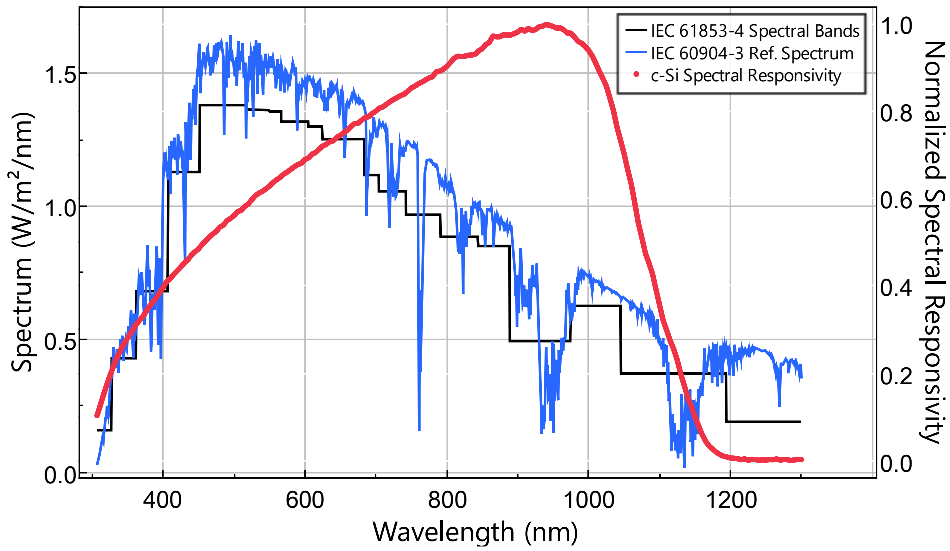

Figure 2.10: Example of spectrally binned irradiance provided in IEC 61853-4 for one hour of one standard climate. The binned spectral data shown here have been normalized for the bin width and interpolated. The IEC 60904-3 reference spectrum and spectral responsivity of the PV module used for the study are also shown. The spectral responsivity was provided by TUV Rheinland within the EMPIR funded 19ENG01 Metro-PV project.

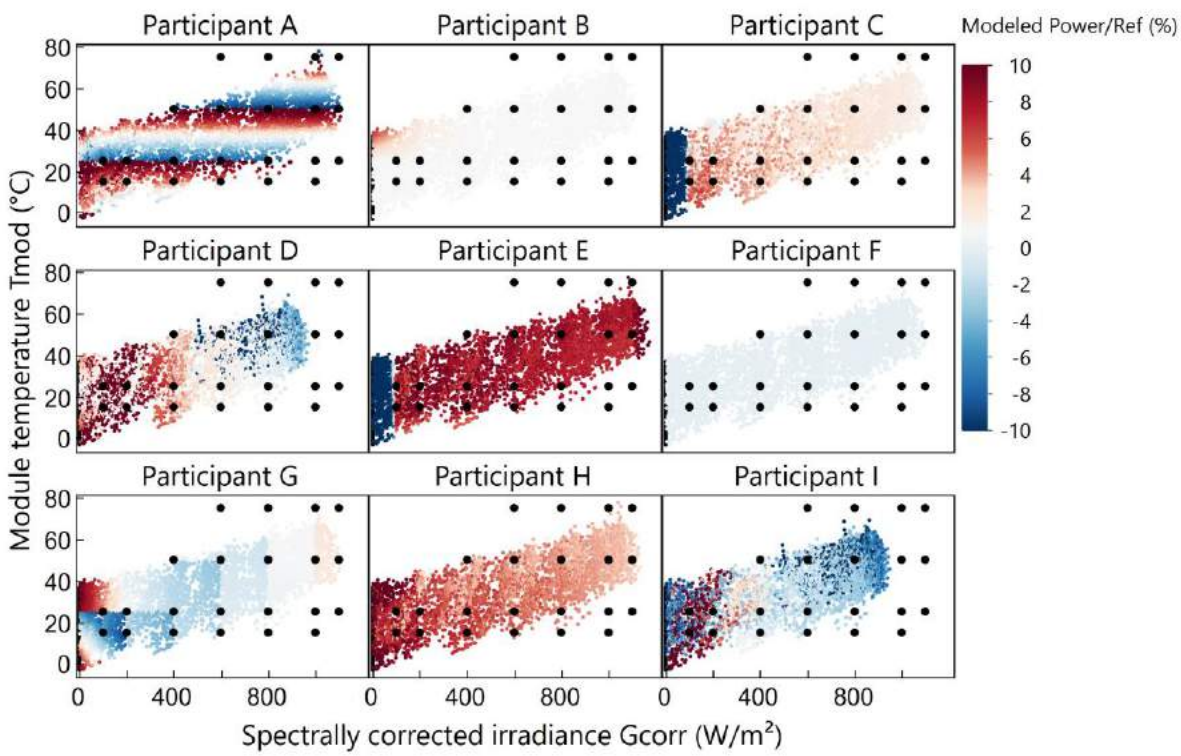

Figure 2.11: Detailed results of calculated power from the first out of five intercomparisons. Participant F was used as a reference here. Deviations to Participant F are shown in the color scale. DTU was designated 'Participant A'. The results here are from the subtropical arid climate, but the error trends were similar for the other five climates.

Figure 2.11 compares all nine participants hourly simulated power values in the initial blind round. These data and the results from rounds two and three are open access (DOI: 10.5281/zenodo.5750185). The color scale shows the deviation of calculated power values relative to Participant F's results, who was chosen as a reference in this case because they were close to the median CSER value. Figure 2.11 shows that no two participants had equivalent results across the entire G-T solution space.

DTU was designated 'Participant A' throughout the comparison. DTU's results in this round showed oscillating biases (high-low) relative to the reference. The reason for this peculiar result was an inadvertent swapping of two terms in the temperature interpolation formula. Interestingly, DTU's CSER results in this round were still near the middle of the group as shown in Figure 2.12a. It is likely that the alternating high-low bias scale canceled out to some extent when integrating hourly power values to annual energy.

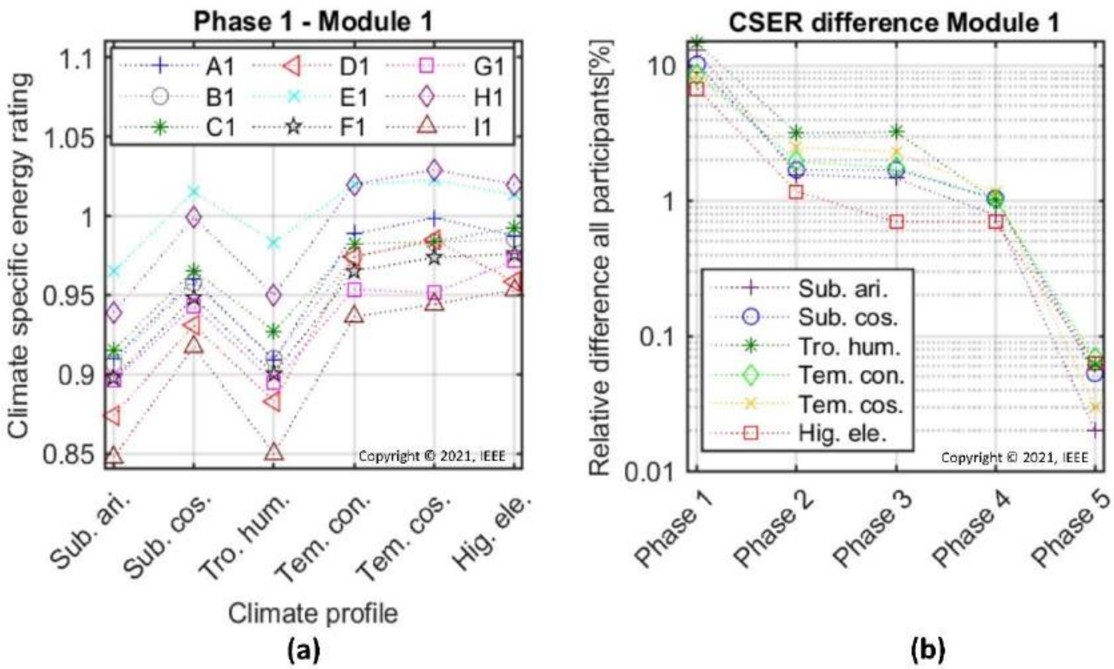

Figure 2.12: (a) CSER comparisons for all participants and climate profiles for the first round of the intercomparison. DTU is designated as 'A1'. (b) The largest relative differences between any two participants in each climate. The difference decreases from 14.7% in phase 1 to 0.07% in phase 5. Original figures are from [212].

After the initial blind round, the participants began a series of regular group discussions to identify reasons for the discrepancies. Errors, bugs, and/or doubts were uncovered at almost every step of the IEC 61853-3 equations. Figure 2.12b shows that the issues that contributed most to the CSER disagreement were caught after the first round, wherein agreement in round two was reduced to 1–3%. Some of the issues uncovered in the discussion rounds included: participants using different fitting approaches to model the IAM data, which was remedied by requiring all participants to use the same angular loss coefficient; some participants interpreting the solar elevation timeseries as solar zenith, which resulted in incorrect projection of direct irradiance; some participants using spectrally corrected instead of angularly corrected irradiance for module temperature; participants using the reference spectra of IEC 60904-3 or ASTM-G-173, which was remedied with mandatory use of IEC 60904-3; and perhaps most importantly, we uncovered that equations in the standard are unclear about how to handle the edge cases of the G-T matrix (e.g, G < 100 W/m^2 or G > 1100 W/m^2). The point about unclear edge cases is demonstrated with Participant C and Participant E's results shown in Figure 2.11, where their agreement to the reference has a distinct shift below 100 W/m^2. This led the core project group to develop supplemental formulae to handle such edge cases, which were made available in the appendix of **Publication III** [212].

2.5 Summary and conclusions

In this chapter, we benchmarked eight software packages for simulating bPV performance. The modeled R_{POA} timeseries from eight software were compared to each other, and to R_{POA} measurements on fixed-tilt and HSAT substructures. Except for one outlier model, we found that R_{POA} modeling errors were small across all software with MAE between 2.5 W/m^2 and 5.0 W/m^2. Irradiance errors of this magnitude constitute roughly 0.5% uncertainty in PV energy modeling. This result suggests that simplified 2D VF models are a suitable approach for bPV simulations, and that long term energy yield predictions do not always necessitate the use of more advanced optical methods like raytracing.

The six software packages with electrical models were benchmarked against DC power measurements from four PV systems that included monofacial fixed-tilt, bifacial fixe-tilt, monofacial HSAT and bifacial HSAT. The error distributions of daily energy yield almost always showed overlapping confidence intervals, which indicates that the software examined here have minimal differences in accuracy. This result makes sense because the software packages often use the same algorithm for the most important modeling steps (e.g., G_{POA}, T_{MOD}, and diode-model). The commercial significance of this result is that PV project developers like European Energy A/S need not over rely on a single software such as PVsyst. This is important because many PV software packages have at least a feature or two that sets them apart from their counterparts. For example, SolarFarmer can model PV plants situated on uneven terrain, SAM has a well-documented software development kit, and the MoBiDiG hybrid model can simulate complex structural features. The results provided here therefore allow companies like European Energy A/S to use the right software for a given simulation task.

Finally, we presented results from an international round robin on IEC 61853-3 energy rating calculations. The initial blind round showed CSER differences up to 14% thereby revealing that the energy rating standard is not so straightforward to implement. A series of discussions among the participants led to development of supplemental procedures that can aid future users of the IEC 61853-3 standard transcribe the 20 standard equations into code. When these procedures were followed, the CSER calculations of nine participants agreed within 0.1% or better. Such reproducibility in CSER calculations will be essential if energy rating labels are ever adopted by solar panel manufacturers or accreditation bodies.

Chapter 3. Analysis and simulation of bifacial-specific performance factors

"The irradiance incident in the plane of the array on the rear side of a bifacial module is determined by a series of factors that have little or no impact on the energy yield of monofacial modules." – **Radovan Kopecek and Joris Libal in Bifacial Photovoltaics 2021: Status, Opportunities and Challenges**

3.1 Introduction

This chapter summarizes the methods used and the key results obtained in **Publications IV**, **V**, and **VI**. These publications investigated the influence of R_{POA} nonuniformity and R_{POA} spectral distribution on bPV performance. Researchers have begun to examine these factors only in recent years and in the wake of ever-growing bPV deployments. At the start of this PhD project in 2019, we hypothesized that the accuracy of bPV energy yield modeling could be improved through understanding and parametrization of R_{POA} nonuniformity and R_{POA} spectral distribution. The works summarized here find that both factors have a small, yet non-negligible, influence on total PV energy yield.

Through measurement and simulation, **Publication IV** finds that the maximum electrical mismatch losses (MML) due to nonuniform R_{POA} is roughly 0.2% for common two-in-portrait (2P) HSAT designs on clear days. Additional raytracing simulations of one-in-portrait (1P) HSATs find that the max MML for this design is about 0.4% on clear days. The additional 1P HSAT simulations look at the sensitivity of MML due to torque tube (TT) shape, TT color, and TT distance from the bPV array. This sensitivity study finds that the MML can be reduced from 0.4% to 0.3% if the TT vertical gap is increased from 7 cm to 15 cm *and* the TT shape is changed from square to round. However, the cost of such redesign is likely to outweigh the economic value of the extra energy produced.

In terms of backside POA spectral effects, **Publication VI** finds that healthy (green) vegetation causes the largest backside spectral mismatch factor (SMM_{Back}), producing backside photocurrent gains as high as 25%. Indeed, the effect of SMM_{Back} is reduced by an order of magnitude when considering the frontside irradiance, which contributes roughly 90% of the total irradiance. Nonetheless, this chapter proposes the first SMM_{Back} correlations, which are a steppingstone toward a simplified R_{POA} spectral model. Finally, the high-resolution spectral albedo measurements collected in **Publication VI** are used to identify 4-6 ideal wavelengths for monitoring spectral albedo with broadband multi-filter instruments. The work was presented at the 2021 International Spectroradiometer Comparison (ISRC) Winter Workshop, and at an IEA PVPS Task 16 meeting before it was submitted to a peer reviewed journal.

The importance of accurate albedo data is seldom discussed in the context of monofacial PV modeling. However, quality albedo data is of high importance to bPV. This chapter concludes by summarizing the results from a cross comparison of five albedo data sources that was performed in **Publication V**. These albedo sources include timeseries measurements from pyranometers, Si-photodiodes and spectroradiometers, as well as a static assumption of 0.2 (constant), and time invariant spectral albedo from the ASTER library. We find that bifacial gain differs by as much as 3% using the three albedo sensors and can deviate by 7% from the ground truth when an incorrect static spectral albedo assumption is used. **Publication V** proudly won the Best Student Presentation Award in Area 11 at the 48th IEEE PVSC.

3.2 Measurement Systems

3.2.1 Mini-modules for Estimating Rear Light Intensity Nonuniformity (MERLIN)

Within the EUDP funded project BiSun Boost, DTU built a custom measurement system to monitor the distribution of R_{POA} on the back of a 2P HSAT. Four minimodules each containing a single column of 10 c-Si cells were laminated such that the electrical contacts of each cell were accessible. Two panels were placed on the south edge, to capture the maximum R_{POA}, and two panels place in the center, to capture the minimum R_{POA}. This setup was dubbed the mini-modules for estimating rear light intensity nonuniformity (MERLIN). As the name suggests, the measurement system permits investigation of edge-brightening effects, R_{POA} nonuniformity, and subsequently, MML (Figure 3.1).

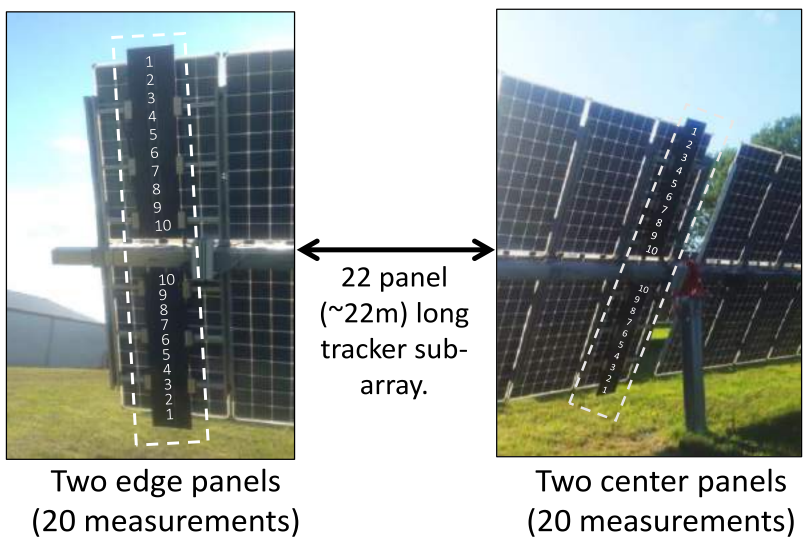

Figure 3.1: Left) Two 1x10 cell panels mounted on the east and west edges of the tracker. Right) the same panel type in the center of the tracker. The black backsheet makes it difficult to see individual cells within panels.

All 40 cells in MERLIN are connected to separate 0.1 Ω resistors, which force the cells to operate near I_{SC}. Thus, a calibration factor is needed to convert the raw measurements from amps to irradiance (W/m^2). For this reason, all 40 cells were calibrated with an Oriel Sol2A class ABA light source and a ReRa c-Si reference cell. Consistent alignment of the individual cells within the test plane proved to be a tedious process (Figure 3.2a) but was critical because of the light source's nonuniformity. Figure 3.2b shows the distribution of I_{SC} values measured on the 40 cells where both the mean and median are 5.37 A at STC. This average I_{SC} value was ultimately used to convert the I_{SC} measurements of all 40 cells in MERLIN into W/m^2.

An uncertainty model for the calibration was made that included contributions such as cell alignment (5.7%, rectangular), displacement between test cells and reference cell (2.5%, normal), reference cell uncertainty (2%, rectangular), datalogger uncertainty (0.8%, rectangular), spectral mismatch (0.5%, rectangular), and the statistical distribution of the 40 cell measurements (1.1%, normal). The expanded uncertainty (k =1.96) was 6.7% using a root sum squared approach.

The 40 shunted PV cells in MERLIN are connected to two separate Campbell Scientific AM16/32B multiplexers and are measured every minute with a single channel on a Campbell Scientific CR6 datalogger.

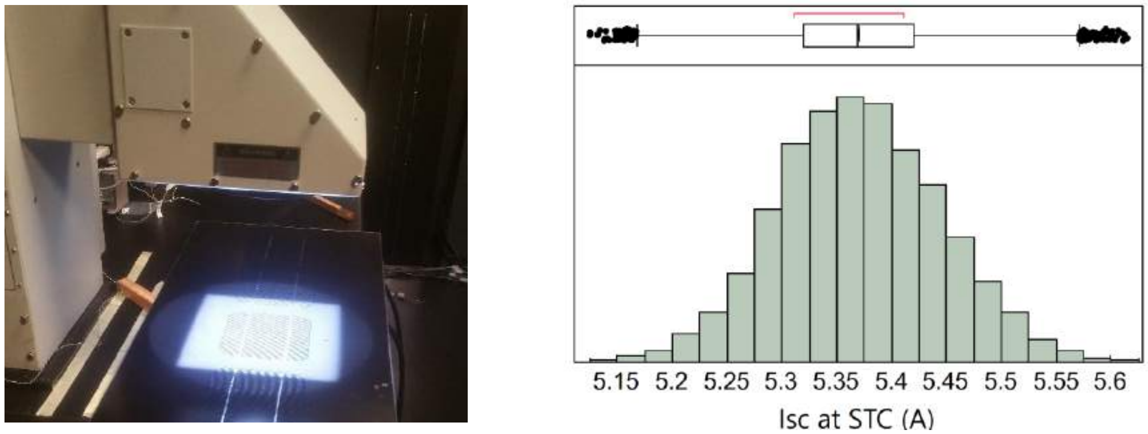

(a) (b)

Figure 3.2: (a) Example of single cell calibration in DTU PV labs with room lights on for visual clarity. (b) distribution of I_{SC} measurements at STC of the 40 cells within MERLIN (μ = 5.37 A, σ = 0.07 A).

3.2.2 Albedo test stands

Ground-based albedo measurements have historically been made with upward and downward facing pyranometers (e.g., Figure 1.14). However, when albedo data is used in bPV applications, questions arise over whether spectrally selective instruments are appropriate.

DTU installed three albedometers with pairs of low-cost EKO ML-02 photodiodes, two albedometers with spectrally flat pyranometers (one with Class A Kipp & Zonen SMP10s, one with Class C EKO MS40-Ms), and a single spectral albedometer with a pair of EKO MS-711 spectroradiometers. The introduction of **Publication VI** describes how the spectrometers were calibrated in DTU's lighting lab before field deployment. The Si-photodiodes have a Teflon diffuser that improves the instrument's directional response, which make the angular-dependent response more comparable to a pyranometer's rather than a reference cell with a flat glass cover. Leveling of the Si-Photodiode instrument proved particularly challenging due to its integrated cylindrically shaped mounting arm. Six separate albedo test stands were curated for 15 months with periodic leveling checks, cleaning, and removal of unwanted weeds. Five different albedos were tested during the 15 months including green grass, dry grass, gravel, a white tarp, and snow.

The largest differences between pyranometer and Si-photodiode albedo measurements were observed when measuring green grass (Figure 3.3). Green grass albedo was roughly 10% higher when measured with Si-photodiodes than when measured with pyranometers. The bottom frames of Figure 3.3 reveal that the higher albedo measured by Si-photodiodes is mostly due to measured RHI, wherein the downward facing Si-photodiode reports RHI values up to 50 W/m^2 higher than the downward facing pyranometer. The large discrepancy in RHI values is caused by the spectral reflectance of green grass. Specifically, it is the significant redshift in the spectral albedo that causes the Silicon photodetector to produce more photocurrent than it would have if illuminated with the AM1.5G calibration spectrum. The pyranometer is spectrally flat and does not respond to such spectral effects. However, bPV modules based on c-Si would respond to reflectance spectra similarly as the Si-photodiode shown in Figure 3.3.

Publication V uses the various albedo datasets collected at DTU to model bifacial gain of the large-scale bPV systems installed at the test facility to provide insight regarding the suitability of Si-based albedometers in bPV applications.

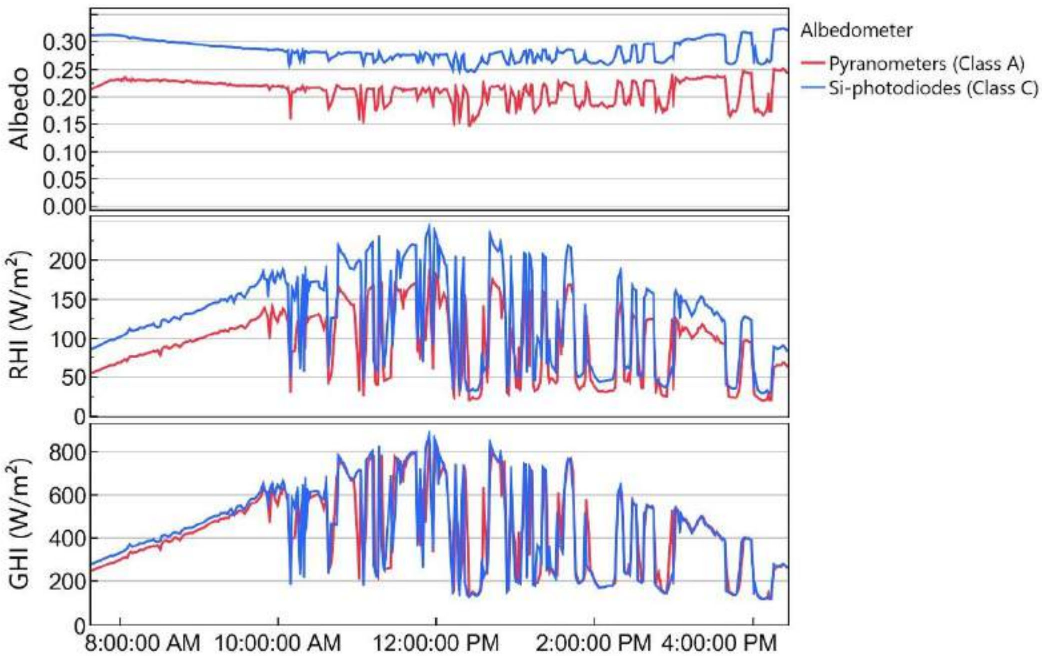

Figure 3.3: Top) Example of diurnal albedo measurements of green grass using spectrally flat pyranometers and spectrally selective Si-photodiodes. Center) Ground reflected irradiance measured by downward facing instruments. Bottom) Global horizontal irradiance measured by upward facing instruments.

3.3 Electrical mismatch induced by nonuniform rear irradiance on trackers

3.3.1 Two-in-portrait single axis trackers (2P HSAT)

Publication IV uses experimental and theoretical approaches to calculate MML due to nonuniform R_{POA} on a 2P HSAT. In the experimental case, the high-resolution R_{POA} measurements from MERLIN are passed to Bishop's [156] electrical model implemented in the *pvmismatch* [155] Python library. In the theoretical case, high-resolution R_{POA} measurements are generated using the *bifacial_radiance* [95] Python library and then passed to *pvmismatch* to calculate MML. Both methods were done for the natural albedo of green grass, and for a high albedo (0.6) white tarp that was placed beneath the 2P HSAT. The paper also presents comparisons of R_{POA} measurements from MERLIN and simulated R_{POA} from *bifacial_radiance* and the *bifacialvf* [82] 2D VF model.

The continuous measurements from the MERLIN setup provide insights regarding the spatial nonuniformity of R_{POA} on 2P HSATs. Figure A.1 and Figure A.2 in the appendix show heatmaps of R_{POA} measured by the center and edge modules on a clear day and cloudy day, respectively. The color legend shows how the irradiance of all 40 cells varies relative to the average total irradiance (i.e., relative to the sum of the G_{POA} front and average R_{POA}). The data reveals several interesting trends, many of which have been discussed in the literature. For example, on the clear day (Figure A.1) the reduction in irradiance due to the torque tube is most apparent at solar noon when the DNI is highest. Also observable on the clear day is that edge modules show *lower* spatial non-uniformity than inner modules

Figure A.2 shows the high-resolution R_{POA} measurements on a cloudy day. On such days where the diffuse fraction (DfHI/GHI) is near 100%, there is little difference in the spatial irradiance measured by the edge and inner panels. In other words, the edge brightening effect is not observed on cloudy days. In the morning and evening, the panel closest to the sky receives more irradiance than the panel closest to the ground, which indicates that bifacial panels mounted on the eastern and western sides should be connected in separate strings to prevent additional MML. Finally, the string closest to the sky experiences more electrical MML than the side closer to the ground. This is consistent with the findings in [158], which was presented at the same conference as **Publication IV**.

Figure 3.4 shows MML results under clear and cloudy skies and under low and high albedo conditions. The clear sky index (K_T) is written on the top of the plots to indicate the sky conditions. The MML shown here was calculated with Equation 1.9, which was discussed in **Section 1.2.2**. The results in Figure 3.4 illustrate how MML changes with conditions, which means that PV simulation packages that use static MML values (e.g., PVsyst) are susceptible to inaccurate effective R_{POA} modeling. The MML values reported here consider the combined effect of rear and frontside irradiance, wherein the frontside irradiance is assumed to be homogeneous. The MML calculations used 5-minute averages of R_{POA} measurements, or simulated values from *bifacial_radiance* with 5-minute resolution. The DfHI and DNI measurements used in the *bifacial_radiance* RT simulation were time-synchronized with the R_{POA} measurements to ensure comparable results between the theoretical and experimental approaches.

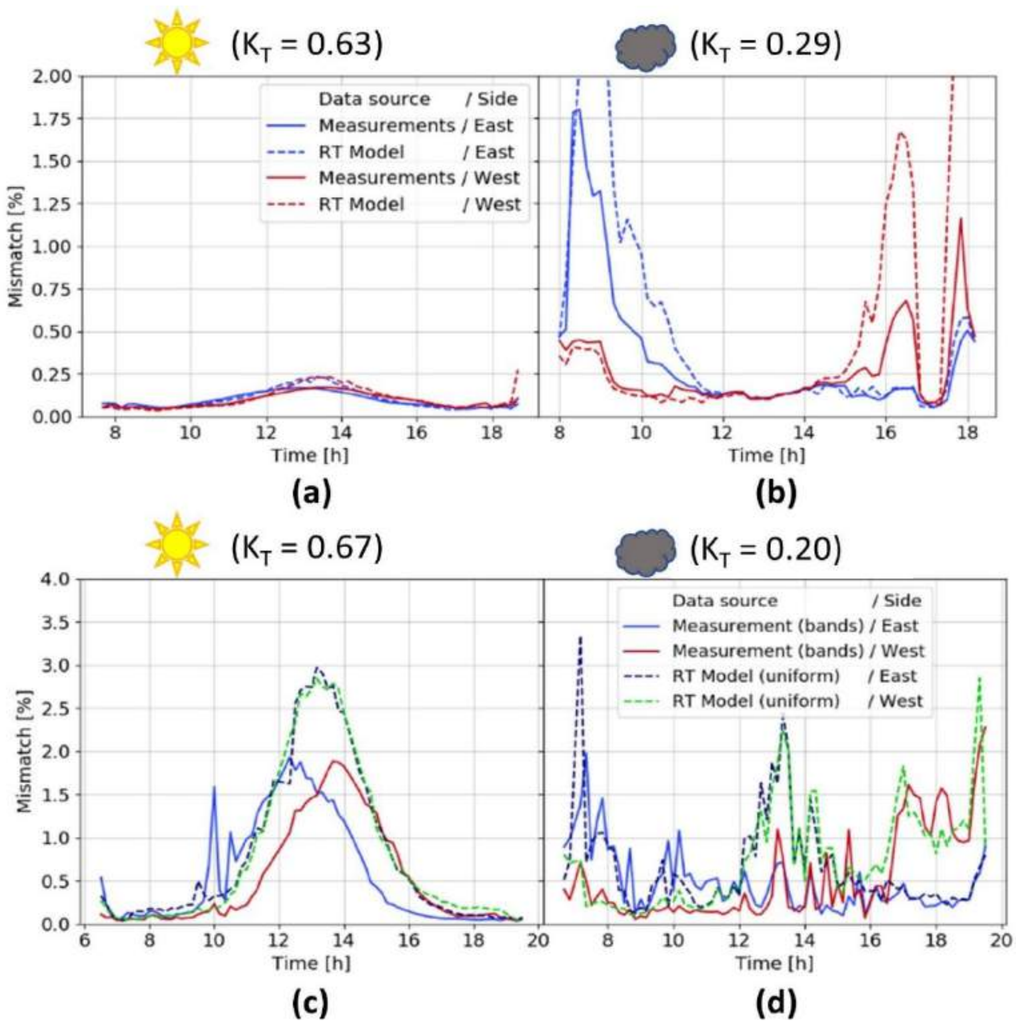

Figure 3.4: Array-level mismatch losses on a 2P HSAT using measured and simulated rear irradiances. The different frames show diurnal mismatch trends under different sky and albedo conditions: a) sunny sky with grass albedo, b) cloudy sky with grass albedo, c) sunny sky with white tarp albedo, and d) cloudy sky with white tarp albedo.

Figure 3.4a shows MML on a clear day with green grass albedo. Here, MML peaks at around 0.25% midday, and is comparable whether measured or modeled R_{POA} is used. Figure 3.4b shows MML on a cloudy day and above green grass. Here, the lowest MML of 0.15% occurs midday but increases above 1% in the morning and afternoon when the GHI is less than 100 W/m^2.

Figure 3.4c and Figure 3.4d show MML during the high albedo test. The simulated albedo in the white tarp scenario assumed uniform coverage whereas the measured albedo was a narrow 5 m wide strip of material, and for this reason, MML in Figure 3.4c is higher when using R_{POA} from raytracing simulations. The albedo of the white tarp is about three times higher than the albedo of the green grass, but the clear sky MML is nearly an order of magnitude higher (i.e., MML is 2–3% depending on R_{POA} source). This occurs because albedo has a nonlinear effect on backside nonuniformity. In **Publication IV,** we used results from the low and high albedo tests to correlated MML and R_{POA} nonuniformity (Figure 18 and 19). Our correlations showed better agreement to the model proposed by [57] than to that proposed by [154].

Interestingly in Figure 3.4a and Figure 3.4c, the raytracing model shows that the MML of the eastern and western arrays peaks midday, but the measurements show that the eastern array MML peaks just before solar noon and the western array MML peaks just after solar noon. This phenomenon is most apparent in Figure 3.4c, but it is also present in Figure 3.4a. The reason for the discrepancy is still unclear. The raw R_{POA} measurements from the east and west halves of MERLIN show similar asymmetrical profiles as the MML Figure 3.4a and Figure 3.4c, thereby suggesting that the actual cell locations of MERLIN are not accurately represented within the raytracing model. However, to the best of our knowledge, the geometry and coordinate references in the raytracing model are consistent with the MERLIN sensor positions.

Figure 3.5 shows error distributions of raytraced and measured R_{POA} at 40 cell locations. The MBE for all locations is -8.2 W/m^2, indicating that the raytracing model consistently underpredicts the measurements. The MAE of all locations is 10.4 W/m^2. Both the MBE and MAE are approximately double the R_{POA} errors from the software tested in **Section 2.3**, which were compared to pyranometer data. The MoBiDiG RT model also used *bifacial_radiance* for R_{POA} estimates and showed MBE and MAE of approximately 4.0 W/m^2. Two likely reasons for the higher R_{POA} errors shown in Figure 3.5 are the high (±6.7%) uncertainty of the laboratory calibration, and the spectral mismatch factor of the c-Si cells inside MERLIN. The spectral mismatch hypothesis is backed up by the findings in **Publication VI**, which show spectral mismatch factors (MMF)[6] of 1.25 when c-Si devices (incl. PERC, n-PERT and IBC) are mounted on the back of trackers and above grass. We did explore spectral simulations using *bifacial_radiance*, wherein we performed simulations iteratively for a single wavelength[7] of light at a time. However, this process was time intensive, and we found that spectral simulations with the 2D VF model *pvfactors* were comparable to those from *bifacial_radiance* with a fraction of the computational requirements.

[6] Recall from **section 1.2.2** that MMF above 1 indicate spectrally induced gains in photocurrent relative to the AM1.5G calibration spectrum. For example, MMF of 1.25 means 25% more photocurrent is produced than if illuminated with the AM1.5G spectral distribution.

[7] Radiance allows RGB reflectance values to be defined for the ground. This would lead one to believe that simulations could be performed three wavelengths at a time. However, a private correspondence with Silvana Oviatt from NREL recommended simulating a single wavelength at time. Furthermore, the Radiance command *gendaylit* only allows for a single DfHI and DNI value to create a description of the sky's luminance.

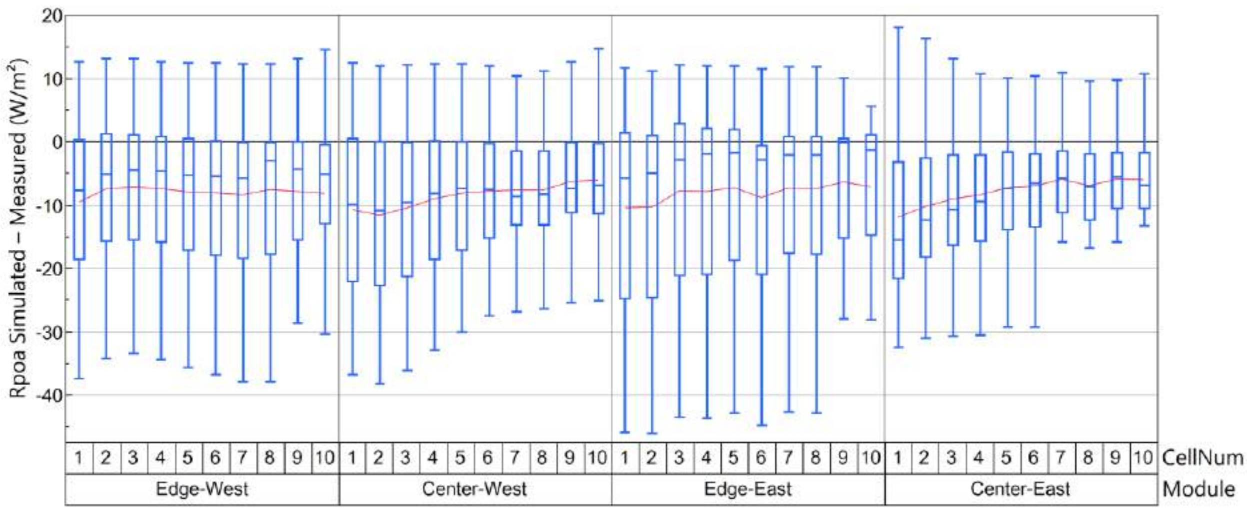

Figure 3.5: Box plots showing the distribution of errors between modeled and measured R_{POA} at 40 locations on a 2P HSAT. The red lines connect the mean error at each cell location within a mini-module. Cell 10 is closest to the torque tube, Cell 1 is the farthest from the torque tube.

3.3.2 One-in-portrait single axis trackers (1P HSAT)

Here we examine MML due to nonuniform R_{POA} on 1P HSATs. In these simulations, the geometry of the European Energy A/S tracker design was recreated using *bifacial_radiance*. The stringing architecture of the *pvmismatch* electrical model was updated to simulate a 144-cell module with half-cut cells. Such half-cell modules still have three bypass diodes, but the upper and lower module halves are paralleled. This design improves partial shade tolerance and makes modules with half-cells ideal for 1P HSAT applications where the TT directly shades the center of the module's backside. The results here are purely theoretical because a MERLIN system was never custom-built for 1P HSATs.

Figure 3.6 shows the midday MML on a 1P HSAT with different TT modifications. The midday MML is shown because this is the time at which MML peaks on clear days (e.g., Figure 3.4a and Figure 3.4c). European Energy's standard design has a 12 cm wide square TT with a 7 cm gap between the TT and rear module plane. This base case design results in 0.44% MML, which is the highest MML out of all cases shown in Figure 3.6. Although this is almost double the midday MML observed on 2P trackers above grass, it does not represent a major loss factor.

The largest decreases in MML are achieved when increasing the TT gap from 7 to 15 cm (~0.07% decrease) and when changing the TT shape from square to round or octagonal (~0.05% decrease). Painting the galvanized steel TT with high reflectivity (0.9) white paint has a negligible effect on MML (~0.01% decrease). These results indicate that redesigning the European Energy tracker with any variant shown in Figure 3.6 would not make economic sense in sight of the possible MML reductions. For this reason, European Energy still offers the base case 1P tracker design with unpainted, square TT, and 7 cm gap.

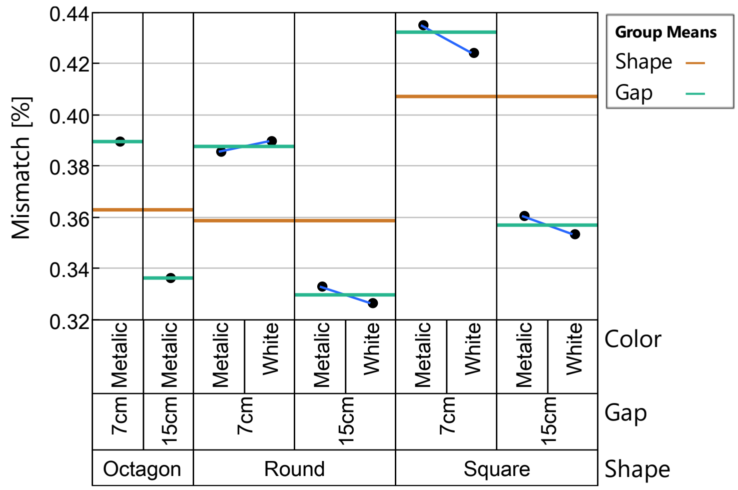

Figure 3.6: Variability of mismatch losses due to torque tube design on 1P trackers. The ‘gap’ refers to the distance between the torque tube and the back of the bPV array.

The performance engineers at European Energy A/S need to simulate the 1P tracker in PVsyst. Therefore, annual simulations were run to calculate the backside mismatch loss factor and structural shading factors required by PVsyst. The annual results for backside (MML_{Rear}) as a function of frontside G_{POA} in a sunny and temperate climate are shown in Figure 3.7. Additional raytracing simulations without the TT were run to estimate the structural shading factor, but these results are not shown here.

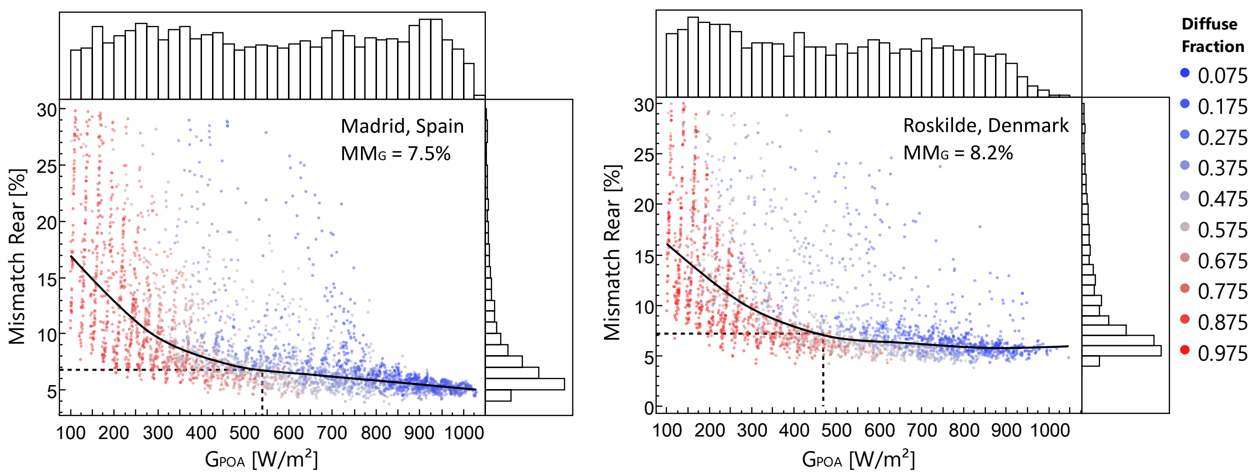

Figure 3.7: Hourly backside irradiance mismatch losses over one-year for 1P HSAT (with square torque tube, and 7 cm module gap). The lefthand plot shows results in Madrid and the righthand plot shows results in Roskilde. The dashed lines show the mean shade loss and mean frontside plane of array irradiance.

The y-axis in Figure 3.7 only considers the electrical losses from *backside* irradiance, which is why the magnitude is higher than previously presented MML results. Figure 3.7 shows that the MML has a strong dependency on G_{POA} and the diffuse fraction. However, PVsyst and other bifacial simulation software currently only allow for a single static value. The average MML value may not be representative of annual losses because the distribution is skewed as shown by the histograms on the right side of Figure 3.7. Therefore, the recommended MML value for use in PVsyst is an annual irradiance weighted MML

(MM_G) shown in Equation 3.1. The irradiance weighted MM_G for the Roskilde site is 8.2%, but shows some dependency on solar resource with 7.5% in Madrid.

$$MM_G = \frac{\sum_{i=1}^{8760} MML_{Rear}(i) \cdot G_{POA}(i)}{\sum_{i=1}^{8760} G_{POA}(i)} \quad 3.1$$

3.4 The effect of spectral albedo on bifacial PV performance

The albedo of natural and synthetic materials is known to vary as a function of wavelength, but most PV simulation tools to date do not incorporate the spectral properties of albedo into their algorithms. This is because ground reflected irradiance constitutes less than 2% of the total frontside G_{POA} for most traditional monofacial installations (i.e., an array tilt angle from horizontal ≤ 30° and albedo ≤ 0.25). In contrast, ground reflected irradiance contributes significantly to the energy produced by bPV systems because the backside R_{POA} is comprised primarily of ground reflected light. For example, the R_{POA} and G_{POA} measurements at DTU showed an average rear-to-frontside irradiance ratio of 8.0% (σ±5.8%) over one-year on fixed tilt systems.

Publication VI uses 15-months of high-resolution spectral albedo measurements to calculate backside spectral mismatch (SMM_{Back}) of three bPV cell concepts mounted on HSAT and fixed-tilt systems. High-resolution spectral data were recorded every 5 minutes and under four albedo scenarios, which included green grass, dry grass, gravel, and snow. Multivariate correlations were generated from this robust dataset, which allow the estimation of SMM_{Back} as a function of more commonly available parameters such as albedo, sky view factor, and sky diffuse fraction.

Spectrally resolved GHI, RHI, and DNI were measured within a 300–1100 nm spectral range for 15 months. The availability of spectral GHI and DNI allowed calculating spectral DfHI. Timeseries R_{POA} spectra were then simulated one wavelength at a time using the 2D VF model *pvfactors*. We selected *pvfactors* as the engine for 2D VF modeling due to its open-source nature and because it showed good agreement to broadband R_{POA} measurements in **Publication II**. HSAT and fixed-tilt systems were chosen for the simulations because they are common among large-scale bPV systems and are the same configuration as the bPV systems collocated at the DTU site.

Figure 3.8 shows daily timeseries of SMM_{Back} calculated with Equation 1.12. The error bars show the range of SMM_{Back} calculated for bifacial PERC, n-PERT and IBC cells. The differences in SMM_{Back} between the three devices were small (±0.01) because they are all single junction silicon cells with similar bandgaps. Recall that SMM values above 1 indicate spectrally induced I_{SC} gains relative to AM1.5G, while SMM values below 1 indicate spectrally induced I_{SC} losses. For example, SMM_{Back} peaks midday at about 1.25 in the HSAT simulations above grass, which means that a bPV's backside will produce 25% more photocurrent in this condition than it would have if illuminated with the calibration spectrum. Curiously, the shape and magnitude of the diurnal SMM_{Back} profile for HSAT above green grass shown Figure 3.8, is nearly identical the diurnal backside MML profile shown in Figure 3.4a. Such overlap implies that the max MML observed midday on clear days is nearly canceled by the midday SMM_{Back} gains.

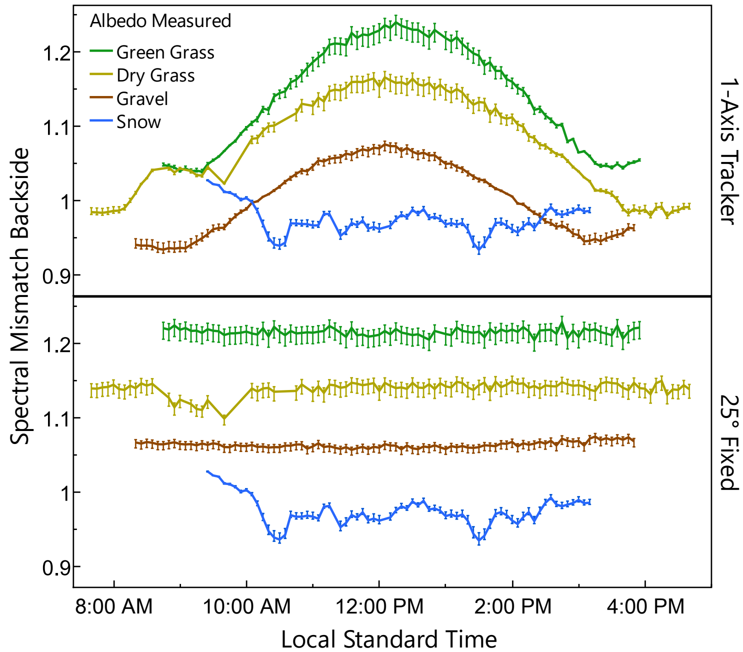

Figure 3.8: Backside spectral mismatch on mostly clear sky days. The error bars around each timeseries show the range of spectral mismatch values for three difference bifacial cell concepts.

Figure 3.9 illustrates the dependency of backside spectral shifts on the view factor from the sky to the array's backside ($VF_{Sky\rightarrow PV,Rear}$) and on the view factor from the ground to the array's backside ($VF_{Ground\rightarrow PV,Rear}$). Except for the snow albedo case, the data shown in Figure 3.8 were recorded under clear skies. As expected, the lowest SMM_{Back} values on the HSAT occur in the morning and afternoon when $VF_{Sky\rightarrow PV,Rear}$ is highest, and the highest SMM_{Back} values occur midday when $VF_{Ground\rightarrow PV,Rear}$ is close to one. We expect the HSAT system to show the lowest spectral mismatch at the beginning/end of the day when at a 60° tilt because the sky diffuse spectrum is blue shifted on clear days [213]. The daily SMM_{Back} values on the static 25° FT system do not change significantly, which follows the expected trend given the constant view factors $VF_{Sky\rightarrow PV,Rear}$ and $VF_{Ground\rightarrow PV,Rear}$.

As mentioned in **Section 1.2.2**, the literature contains several spectral models for mPV that are based largely on correlations with air mass. However, we found air mass to be a poor indicator of SMM_{Back}. We used a bootstrap forest model to identify the most significant predictors of SMM_{Back} from our available weather and tracker position data. We found that a simplified predictive model for SMM_{Back} should at minimum include the backside array sky view factor (VF_{Sky}), the sky diffuse fraction (DF), and a classification of the albedo. Figure 3.9 shows such SMM_{Back} multi-variate correlations using results from the HSAT simulations. The simulated SMM_{Back} values follow the regression lines with a root mean squared error (RMSE) between 0.01 and 0.02. As far as we are aware, this is the first SMM_{Back} model based on commonly found ground measurements and PV system geometry.

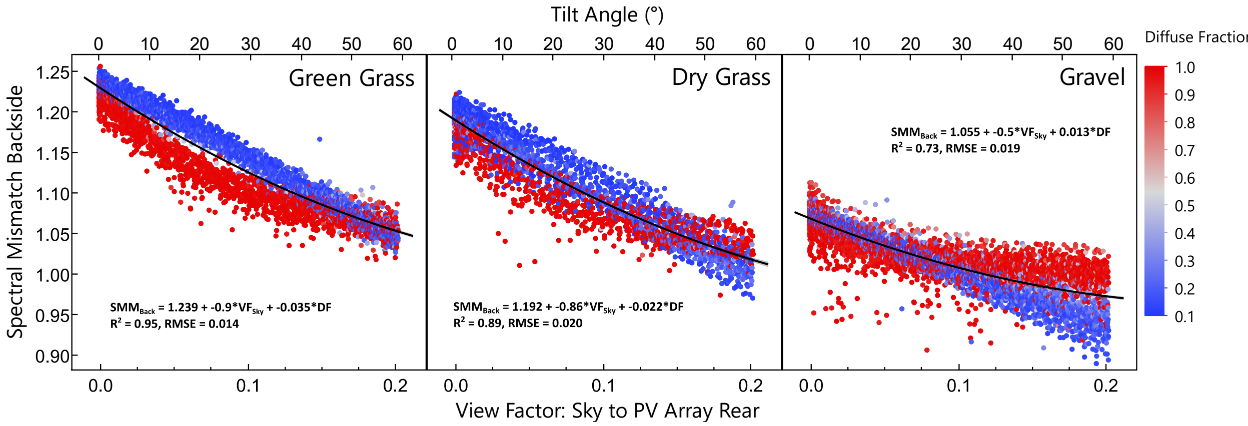

Figure 3.9: Backside spectral mismatch of bifacial PERC versus sky view factor for three measured albedo conditions. The tilt angle of the 2P HSAT is shown on the secondary x-axis above.

The three frames of Figure 3.9 demonstrate how a simplified SMM_{Back} model depends on the ground albedo. A more thorough SMM_{Back} model would require correlations of additional materials such as sand and snow. However, spectral albedo measurement campaigns such as those done in **Publication VI** may be too resource intensive for this purpose. Instead, derivation of SMM_{Back} at a 0° tilt (e.g., using spectral albedo from SMARTS) may be sufficient to simply replace the offset term and use the average coefficient values for the VF_{Sky} and DF parameters shown in Figure 3.9.

In any case, hypothetical users of such a SMM_{Back} model would first need to classify the albedo at the site in question (e.g., dry, or green grass), and then, they would need to select the appropriate correlation for that ground type. More research is needed to develop a method that integrates such a model into PV performance software. For example, how should classification of the ground surface be performed? The necessary information could potentially be obtained with measurements from a multifilter radiometer, or from remote sensing observations (satellite albedo).

Spectral albedo curves are not highly structured like the sun's spectrum [197]. The 0.4 nm wavelength resolution of the spectroradiometers used **Publication VI** therefore resulted in oversampling of the spectral albedo. The benefit of the high-resolution spectral albedo setup, however, is that down sampling can be conducted to identify when spectral mismatch factors show large discrepancies relative to those calculated with the high-resolution data. To this end, we truncated the 2048-pixel measurements down to 2–8 wavelength channels and repeated the SMM_{Back} calculations. Table 3.1 shows the different wavelength bands tested. In all these cases, the down sampled albedo spectra use the 7 nm full-width half maximum optical resolution of the MS-711 spectroradiometer. The spectral albedo between narrow band channels is interpolated with a first order spline fit. Values outside the wavelength ranges shown in Table 3.1 are extrapolated, with the condition that 0.001 and 1.0 are the minimum and maximum spectral albedo values allowed. See **Publication VI** for a discussion on how the different wavelength channel combinations were selected.

Table 3.1: Summary of wavelength channels used in the different down sampling tests of the high-resolution spectral albedo measurements. A 7 nm full width half maximum resolution was used in all scenarios.

N Channels	Center wavelengths (nm)
2	500, 940
3	500, 870, 940
4	415, 615, 870, 940
5	469, 555, 645, 858, 1050
6	415, 500, 615, 673, 870, 940
7	415, 500, 615, 673, 870, 940, 1050
8	415, 555, 615, 673, 762, 870, 940, 1050

Figure 3.10 shows selected daily timeseries of SMM_{Back} calculated with the seven down sampling cases and with the high-resolution spectral albedo measurements. The detailed error summary presented in **Publication VI** indicates that SMM_{Back} can be reasonably approximated using spectral albedo measurements with just 4–8 narrow band channels.

The two and three-channel down sampled cases show notably higher errors, especially in green grass and gravel albedo conditions. Given that many PV parks globally are constructed at sites where the spectral albedo is comparable to the green grass and gravel albedo conditions measured here, our down sampled SMM_{Back} results indicate that four narrow band channels is likely the bare minimum to monitor spectral albedo in bifacial PV applications. Multifilter Instruments with the 6–8 wavelengths shown in Table 3.1 could be advantageous in agricultural PV applications because they would also sample photosynthetically active radiation (PAR).

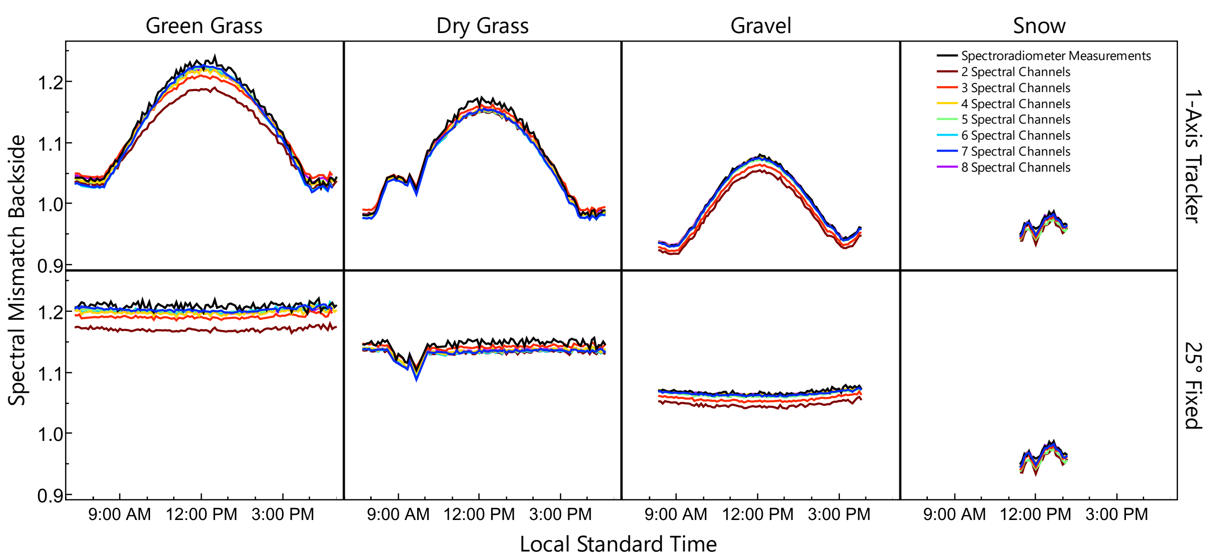

Figure 3.10: Backside spectral mismatch of the PERC cell calculated with down sampled spectral albedos and high-resolution measurements.

3.5 How the choice of albedo dataset influences bifacial gain simulations

Here we analyze the differences in bifacial energy gain that can occur due to different albedo data sources. The albedo data sources investigated include:

1. Measured spectral albedo from spectroradiometers,
2. Measured broadband albedo from thermopile pyranometers,
3. Measured broadband albedo from Si photodiodes,
4. Constant spectral albedo from ASTER data base, and
5. Constant albedo assumption of 0.2.

The spectral albedo measurements are from the EKO MS711 setup described previously. The broadband albedo measurements are from Class C thermopile pyranometers and Silicon-photodiodes. Each of the five albedo data sources is used to generate timeseries R_{POA} and G_{POA} spectra using *pvfactors*. In the case of the Si-photodiode and pyranometer measured albedo, the albedo passed to pvfactors is the same at all wavelengths, proportional to the measurements at each timestamp (i.e., a 'flat' spectral albedo curve is produced). In the case of constant spectral albedo data, the data originates from the ASTER library [214], which is the source of the spectral albedo files in SMARTS. In all five cases studied, the same spectral DNI and spectral DfHI are input to *pvfactors*. This ensures that differences in modeled POA spectra are attributable to the albedo data source.

The front and back POA spectra are summarized using a spectrally weighted bifacial gain (BEG_λ), which is calculated with Equation 3.2.

$$BEG_\lambda = \frac{\int_a^b SR_{Rear}(\lambda) \cdot R_{POA}(\lambda)\, d\lambda}{\int_a^b SR_{Front}(\lambda) \cdot G_{POA}(\lambda)\, d\lambda} \cdot 100\% \qquad 3.2$$

Where SR_{Front} and SR_{Rear} are the bPV cell's spectral response of the front and backside, with measurements of a bifacial PERC cell used here. The integration limits *a* to *b* are 300 to 1200 nm, with data from 1050 to 1200 nm filled in by SMARTS. The BEG_λ in Equation 3.2 is simply the ratio of short-circuit current density (J_{SC}) generated by the backside relative to the J_{SC} generated by the frontside. This equation does not include adjustments for structural shading on the backside of the array, or any possible thermal differences between mPV and bPV cells that could affect voltage. Nonetheless, Equation 3.2 is still useful for our objective, which is to understand the differences in bifacial gain that can occur due to different albedo data sources.

Figure 3.11 shows modeled bifacial gains for PERC on fixed-tilt and HSAT systems above green grass. The daily bifacial gains of the 50 kWp bPV arrays during the same four-month period is also shown. Please see **Publication V** for results from the other albedo scenarios tested. The green grass albedo scenario is shown here because it is the only condition where onsite measurements of large-scale monofacial and bifacial PERC systems are available. The diamonds within each box plot show the 95% confidence interval of the mean, which are small because of the large number of observations. Recall that the pyranometer, Si-photodiode and spectroradiometer albedo data are continuous measurements whereas the constant albedo (0.2) and SMARTS spectral albedo do not change with time.

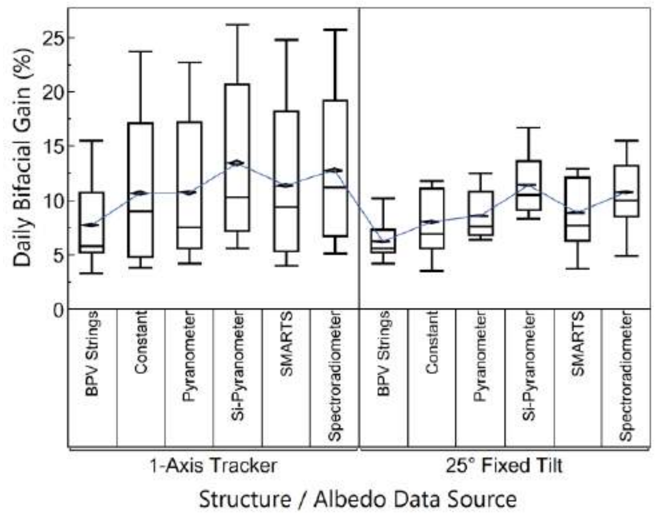

Figure 3.11: Variability of simulated bifacial gain during the four-month green grass albedo period using five different albedo sources. The 'bPV Strings' column shows the distribution of daily bifacial gains measured by 50 kWp inverters during the same period. The SMARTS spectral file used is 'GrazingFields.dat'.

The bifacial gain calculated with Si-photodiode albedo data is about 3% higher than when calculated with pyranometer data. This positive bias is consistent with results shown in Figure 3.3 and is again explained by the large 'red shift' of the grass albedo spectrum relative to AM1.5G. Figure 3.11 shows that the five albedo data sources cause the simulated bifacial gain to change by as much as 3%. The measurements are shown in Figure 3.11 to help identify which of these albedo sources is most representative of bPV performance. However, a fair comparison of the model and measurement requires at least two adjustments: 1) the model would need to account for structural shade losses, and 2) the spectral responsivity used in the model would need to be of a full-size module (i.e., with junction boxes, frame etc.), not an individual cell. If such adjustments were implemented, the bifacial gain in all simulations would be reduced.

Figure 3.12 shows multivariate correlations of simulated BEG_λ (Equation 3.2) and measured bifacial gain. These plots, along with their associated p-values and confidence intervals, were created to identify which albedo data source yields bifacial gain results that best correlate with the measurements. The *r* values shown in the color scales show that simulated bifacial gains correlate well in all cases, irrespective of the albedo dataset used. However, the correlation of simulated and measured bifacial gains is significantly lower with fixed-tilt r values of roughly 0.65, and HSAT *r* values of roughly 0.80. The bottom row of Figure 3.12 shows that no single albedo source results in significantly higher correlation over any other with respect to the measured bifacial gain. This leads to an unsettled conclusion regarding our initial question whether spectrally selective albedometers are more suitable than broadband albedometers in bPV applications.

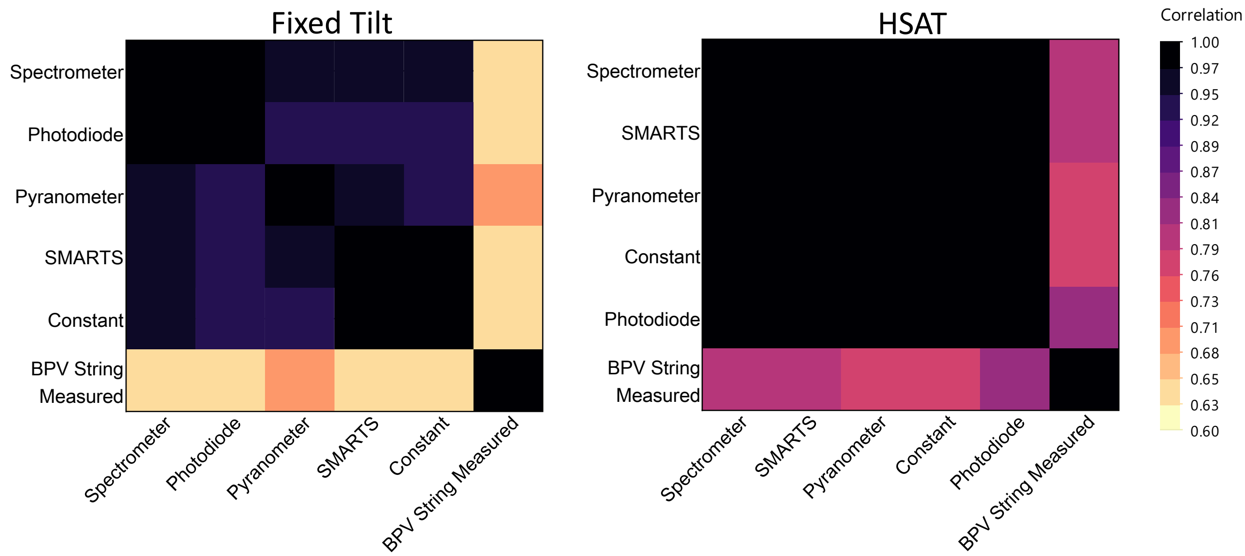

Figure 3.12: Correlation matrices of bifacial energy gain using five different albedo data sources. The bifacial gain from inverter-level electrical measurements is shown on the bottom of the graphs. The color scale shows Pearson's *r* coefficient between two data streams.

When selecting one albedometer type over the other, the accuracy of the sensors must be considered. Si-photodiodes tend to have higher measurement uncertainty than thermopile pyranometers because of their higher spectral errors during field operation and during laboratory calibration. For example, Reda et al. found that typical Si-photodiodes have an expanded uncertainty of about 8% whereas thermopile pyranometers have an uncertainty of about 4% [215]. Furthermore, the use of Si-photodiodes in albedo monitoring would go against decades of precedent. For example, albedo databases such as the Surface Radiation Budget network (SURFRAD) are populated with measurements from thermopile pyranometers. Finally, PV simulation software typically expect irradiance measurements (e.g., GHI, DNI) from broadband pyranometers, although NREL's SAM does allow use of G_{POA} measured by reference cells [216]. These considerations lead us to recommend that spectrally flat pyranometers be used for albedometers within bPV parks. However, project developers and owners who wish to understand the influence of spectral albedo effects are recommended to *additionally* install a spectrally selective albedometer, such as the Si-photodiode instruments used in **Publication V**.

3.6 Summary and conclusions

This chapter presented investigations on how the nonuniformity and spectral distribution of R_{POA} affects bPV performance. In the first section, we showed that nonuniform R_{POA} leads to modest MML on common bPV configurations such as 2P trackers (MML ≈ 0.2% midday) and 1P trackers (MML ≈ 0.4% midday). The magnitude of MML shown here is consistent with the theoretical and measured MML published by other authors for common bPV system designs (e.g., [151], [217]). Our tests with a high reflectance sheet showed that albedo has a nonlinear effect on MML. The high-resolution R_{POA} measurements and simulations performed over various albedo and sky conditions allowed us to create MML correlations, which ultimately showed good agreement to the model proposed by [57]. The MML model validation presented in **Publication IV** is particularly useful if the model proposed in [57] is ever implemented within PV simulation software such as NREL's SAM.

A sensitivity study was performed on 1P trackers to identify possible design changes that could reduce MML. This was a difficult task considering that MML due to nonuniform R_{POA} is already small in the base case design. With raytracing and electrical modeling, we identified that increasing the TT gap from 7 to 15 cm has the largest potential to decrease MML (~0.07% decrease), and that changing the TT shape from square to round or octagonal has similar potential (~0.05% decrease).

In the second part of this chapter, we used high-resolution spectral albedo measurements and 2D VF modeling to calculate SMM_{Back} for the most common bPV cell concepts and mounting configurations. This work demonstrated the dynamic nature of SMM_{Back} on daily and seasonal timescales. On clear days, it was observed that spectrally induced performance gains peak mid-day wherein backside spectral gains were 25%, 15%, and 5% for green grass, dry grass and gravel, respectively. We found that SMM_{Back} tends to be lower on tracked versus fixed tilt systems because the backside of trackers see a larger fraction of the sky hemisphere and because the blue-shifted nature of the clear sky diffuse spectrum offsets some of the red-shifted nature of the spectral albedos studied. The SMM_{Back} values simulated in the various albedo cases at 5-minute resolution were used to create reduced order models in the form of correlations with sky diffuse fraction and sky view factor. However, additional work is needed to develop a procedure to integrate said correlations into bPV performance modeling.

Finally, we modeled bifacial gain with timeseries albedo measurements from three unique sensor types and with static assumptions for spectral and broadband albedo. We found that these five albedo data sources caused substantial variability in modeled bifacial gain. Specifically, we found bifacial gain above green grass was 3% higher when using Si photodiode measured albedo than when using thermopile pyranometer albedo. If frontside irradiance is assumed to be 10-times the backside irradiance, this 3% positive bias in bifacial gain corresponds well to the 25% photocurrent gains calculated in **Publication VI** for horizontally mounted c-Si bPV cells above grass. Correlations of modeled and measured bifacial gains from collocated bifacial PERC arrays did not reveal a clear answer regarding whether spectrally selective albedo measurements are more accurate than broadband albedo measurements in bPV applications. Additional considerations for instrument accuracy and historical albedo measurement practices led us to the conclusion that *spectrally flat* pyranometers should form the basis for albedo measurements within bPV parks, but spectrally selective albedo measurements remain optional for any stakeholders interested in understanding spectral effects.

Chapter 4. Characterization and performance monitoring of bifacial PV modules and systems

"The interplay of measurements and computational modeling has been important to PV rating from its earliest days." **Keith Emery in his 2013 IEEE Cherry Award keynote talk**

4.1 Introduction

This chapter begins with a summary of two interlaboratory comparisons (ILCs) of PV measurements. The first is led by the EMPIR PV-Enerate consortium, with DTU as a participant, and is one of the first ever ILCs on bPV measurements. DTU's results within this ILC were never published but are presented here with the consortium's permission. The second ILC presented here is on incident angle modifier (IAM) measurements and was orchestrated by DTU (**Publication VII**). The measurands studied in both ILCs play a fundamental role in PV energy yield modeling. In the IAM study, we demonstrate how the state-of-the-art IAM measurement methods affect energy yield modeling uncertainty.

The results of the EMPIR led bPV measurement comparison dovetail with **Publication VIII**, where we show how calibrated bPV modules can be used to monitor outdoor bPV performance. Specifically, it is shown how bPV modules measured indoors with the IEC TS 60904-1-2 procedures can be used outdoors as large-area sensors that measure effective irradiance. The proposed method for R_{POA} monitoring in **Publication VIII** was conceptualized as a result of studying the bifacial-specific loss factors discussed in **Chapter 3**. The method potentially simplifies the design of bPV monitoring systems because the large-area reference modules inherently capture backside nonuniformity and spectral effects. **Publication VIII** was presented at the 2022 IEEE PVSC and was an invited contribution to the IEEE Journal of Photovoltaics.

4.2 Interlaboratory comparisons to decrease uncertainty in measurement and modeling

Interlaboratory comparisons (ILCs), sometimes referred to as round-robins, play an essential role in establishing confidence in measurements. For example, ISO 17025 accredited laboratories are required to participate regularly in ILCs to ensure that their measurements are consistent with other accredited laboratories. ILCs can also be used to assess the clarity and accuracy of novel measurement protocols and procedures. This later reason was a key motivator for testing the IEC measurement protocols examined here.

The IEC TS 60904-1-2 procedure for rating of bPV modules and cells was published in 2019. Discussions are presently being held by TC 82 as to whether this technical specification will become an IEC standard. The results of the EMPIR led bPV round-robin, and that presented by [181], will undoubtedly be discussed by the TC 82 (WG 2) members during their decision-making process.

The IEC 61853-2 procedure to measure incident angle effects was published in 2016—two years before we started the IAM ILC in 2018 (**Publication VII**). The NMOT and IAM sections of the IEC 61853-2 standard are presently being amended, and within this revision effort, a second IAM ILC is already in progress. The knowledge obtained in the initial IAM ILC has helped shape the design of the second ILC effort regarding the type of test samples distributed, and the laboratories (i.e., measurement systems) included. Furthermore, the results of the initial IAM ILC provide a baseline to which all future ILCs can compare and improve upon.

4.2.1 Bifacial reference module calibration led by EMPIR PV-Enerate consortium

DTU learned of this ILC effort during the 2021 EUPVSEC, when George Koutsourakis presented the first results from Fraunhofer ISE, TUV Reinland, Physikalisch-Technische Bundesantalt (PTB), and University of Applied Sciences of Italian Switzerland (SUPSI) [180]. George concluded his talk by mentioning that the effort was still on going, so we immediately reached out to him, and the modules were sent to DTU for testing. The test modules in the comparison included bifacial PERC, n-PERT and SHJ.

The I_{SC} and P_{MAX} BiFi curves of each device measured at DTU are shown in Figure 4.1. According to IEC TS 60904-1-2, the BiFi rating is the linear slope of these regressions and the offset (i.e., R_{POA} = 0 W/m^2) is the STC rating. The BiFi rating was intended to provide a standardized and meaningful way for manufacturers to report bPV electrical performance, but so far as we are aware, manufacturers are still not implementing the BiFi rating on their datasheets. The error bars in Figure 4.1 show the expanded measurement uncertainty at 1000 W/m^2.

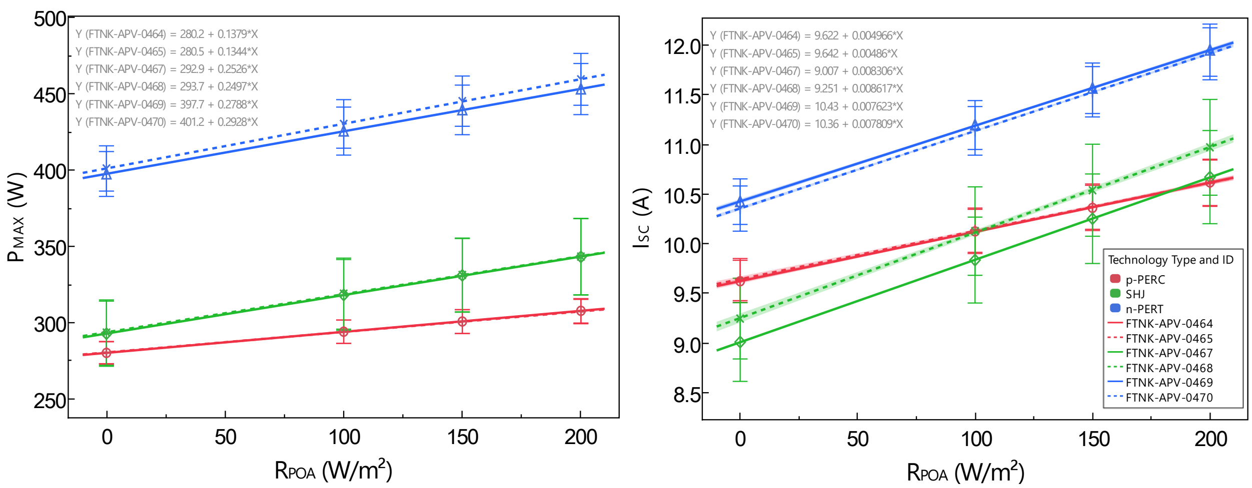

Figure 4.1: BiFi curves of I_{SC} and P_{MAX} measured on three different bPV technology types. The slope is the BiFi rating and the offset is the frontside measurement at STC. The error bars show the measurement uncertainty at STC.

Figure 4.2 shows P_{MAX} results from six participating laboratories wherein DTU's results are labeled 'Partner 6'. The I_{SC}, V_{OC}, bifaciality, and BiFi results are presented in the Appendix (Figure A.3, Figure A.4, and Figure A.5). All but three of the 21 frontside P_{MAX} results are within ±1% of the group median, the exceptions being DTU's measurements on module 3/4 and Partner 2's measurements on module 6. Backside measurements are promising, but agreement among the six labs is not as good as for the front. Discussions with George Koutsourakis revealed that not all participants applied a backside SMM correction, which could cause some of the differences. The backside P_{MAX} agreement was generally within ±2% of the group median with few exceptions such as module 1, DTU's module 3/4 measurements and Partner 2's module 5 measurements.

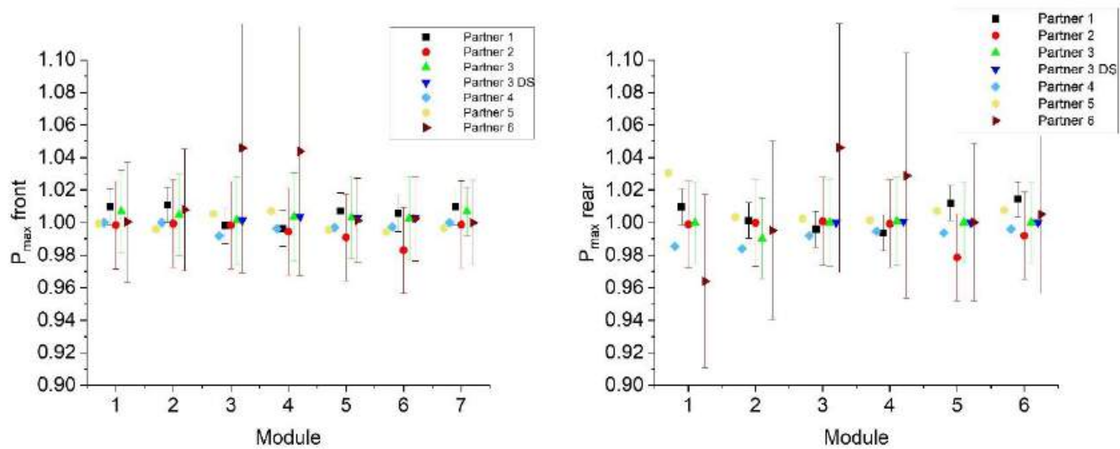

Figure 4.2: Front and back P_{MAX} results normalized to the group median. These graphs were prepared by George Koutsourakis of NPL within the EMPIR funded PV-Enerate project (https://www.pv-enerate.ptb.de/). DTU is partner number six. Modules 1 and 2 are bifacial n-PERT, modules 3 and 4 are bifacial SHJ, and modules 5 and 6 are bifacial PERC. Module 7 is monofacial PERC.

DTU's measurements of the n-PERT (Module 1 and 2) and PERC (Module 5 and 6) modules are within ±1% of the group median. Our electroluminescence (EL) images of Module 1 showed cell damage upon arrival, which is likely why DTU's backside P_{MAX} measurement on this module is 4% lower than the median. DTU's measurements of the SHJ devices (Module 3 and 4) were about 4% higher than the other five labs, but the error bars still overlap with the group median. DTU's uncertainty model is based on the principles laid out in [130]. Within this model, there are uncertainty contributions that are device-specific, such as the module's frame thickness and the hysteresis of forward and reverse I-V sweeps. Although the uncertainty of SHJ measurements is nearly double that of n-PERT and PERC measurements, the measurement uncertainty always overlaps with the group medians. This gives indication that the uncertainty model accurately represents how well we know the true measurand.

The SHJ module was challenging to measure due to the combination of 1) the Endeas solar simulator's short (~4 ms) voltage sweep, and 2) the high minority carrier lifetime of SHJ cells. PV cells with high carrier lifetimes are associated with increased V_{OC} and efficiency but are challenging to measure accurately with short-pulsed solar simulators [218]. The accumulation of charges in a PV device can be represented in the SDE with a capacitor in parallel with the diode. Hence, PV modules with high efficiency (carrier lifetime) are often labeled as 'high capacitance' devices. PV modules with large capacitance can show notable differences between their I-V curves swept in the forward direction (i.e., $I_{SC} \rightarrow V_{OC}$) and reverse direction (i.e., $V_{OC} \rightarrow I_{SC}$). For example, P_{MAX} of the SHJ modules differed by ±5% when measured in forward and reverse directions. DTU's Endeas solar simulator uses a patented Capacitance Compensation (CAC) method [219] to reduce transient artefacts generated during the fast voltage sweep. When the flash pulse is roughly 5 ms, as is the situation in the DTU system, the CAC method length can minimize errors of cells with V_{OC} less than approximately 700 mV. The V_{OC} of cells within the SHJ module, however, is roughly 720 mV. According to calculations by [218], a 100 ms pulse duration is required to minimize SHJ errors to less than 1% with direct I-V measurements (i.e., no capacitance corrections). Despite DTU's low proficiency in SHJ measurements, the excellent agreement of the PERC measurements gives us confidence that this module type can be calibrated using the DTU solar simulator.

4.2.2 Incident angle modifier (IAM)

The IAM function plays a fundamental role in estimating the effective irradiance received by a PV module or array. The IAM accounts for reflections at the glass-air interface that change with AOI. Angular-dependent absorption and spectral effects are also present in PV systems, but reflection is the primary optical loss embedded in an IAM function. The IAM function can be measured indoors or outdoors, but in either case, care must be taken to suppress, or correct for, diffuse light. This is because the AOI term in the IAM formula (Equation 1.17) assumes that all impinging photons come from the same direction (i.e., photons are collimated). Accurate measurement of the AOI, and precise alignment of the test device within the optical axis of rotation, are additional requisites for accurate IAM measurements.

PV system modelers may choose to use default IAM profiles in their simulations, or they may choose to use measured IAM data from a test laboratory. A PV project developer like European Energy A/S faces such a question regularly. Figure 4.3 shows IAM profiles extracted from eight test reports that were provided to European Energy A/S by three laboratories during 2020. The figure also shows three theoretical IAM curves generated with the ASHRAE model [186] and with the Fresnel equations using assumptions for non-coated and anti-reflective coated (ARC) glass. Figure 4.3 uses a value of 0.056 for the angular loss coefficient b_o. PVsyst uses a default value of 0.05 for b_o, which would increase the IAM shown in Figure 4.3 by 0.01–0.02 (1-2%). The procedure used to calculate IAM with the Fresnel equations essentially follows that used by [110].

The eight laboratory measurements shown in Figure 4.3 were performed on modules produced by Eging (N=1), JA Solar (N=1), Longi (N=3), and Risen (N=3). The modules have power class ratings of 380–525W. TUV Reinland tested two modules, TUV SUD tested four modules, and Dekra tested two modules, but *no two labs tested the same module*. Details of the modules' ARC are mostly missing. We reached out to Eging about why Dekra's IAM measurements of the Eging module are so optimistic—well above the simplified models for single layer ARC glass. Their response was that the modules they produced for IAM testing had a double layer ARC (DLARC). As far as we are aware, DLARC on PV module glass is not yet commercially available.

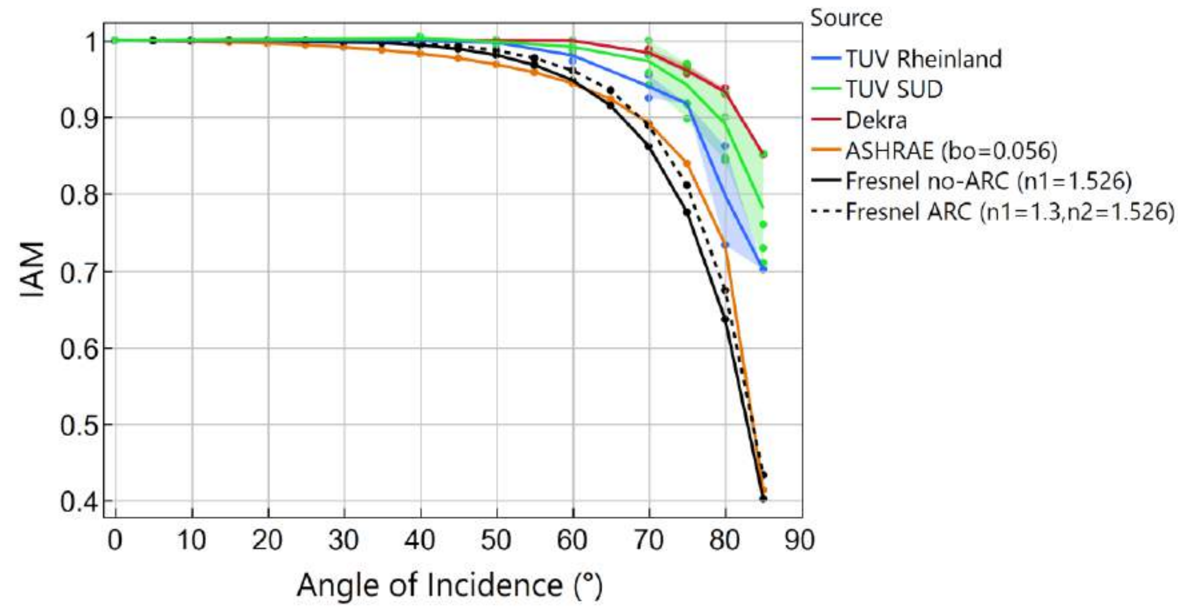

Figure 4.3: Incident angle modifier measurements provided by three laboratories on eight separate modules, wherein no laboratory measured the same two modules. The solid blue, green and red lines show the mean measurement at the test labs. The transparent bands around each solid lines show the range of measurements obtained at each lab. Theoretical curves from the ASHRAE model and the Fresnel equations are also shown.

Although no two labs in Figure 4.3 tested the same PV module, the data lead one to speculate that significant IAM discrepancies can be caused by the test methodology used. The concern around comparability of methodologies was a key motivator for organizing the extensive IAM ILC that ultimately became **Publication VII**. An additional motivator for DTU was the IAM measurement system had been recently developed [220], but was never sanity checked against measurements at other labs. DTU's novel laser driven light source (LDLS) approach to IAM measurements heightened our curiosity regarding its comparability to other labs.

The IAM ILC invited 12 laboratories representing seven countries and two continents. Most importantly, the participating laboratories employed various approaches to IAM measurements, which included five unique light sources and various types of rotation stages. The light sources used were mostly Xe lamps (N=5) and sunlight (N=3), but other light sources were used and included tuneable lasers (N=1), Halogen lamps (N=1), modulated LEDs (N=1) and DTU's LDLS (N=1). The test samples sent to the labs were encapsulated in uncoated PV glass. The different cells measured were a mono-Si Al-BSF cell, and two multi-Si cells with different surface textures. In the end, only the mono-Si cell and the multi-Si cell with reactive ion etching (bSi RIE) were used for analysis due their distinctive IAM profiles. See Table 2 within **Publication VII** for more information on the test samples.

ILCs require a reference value (X_{Ref}), and optionally a reference uncertainty (UC_{Ref}), to assess the participating labs' proficiency. These values can come from an accredited or national laboratory, or from some predetermined source. In this work, we used a weighted averaging approach to determine both X_{Ref} and UC_{Ref}, in which we weighted the IAM measurements according to the uncertainty reported by the participants. Such a weighting approach can bias the proficiency test results if the laboratories have uncertainty models that are oversimplified or too conservative. Although we did not review the uncertainty models of participants, their reputations as expert agencies gave us confidence that they had thorough uncertainty models. The weighted averaging approach we used to derive the X_{Ref} and UC_{Ref} values essentially follows that used in [131], [221], [222]. The reference values at each AOI were then used to derive the so-called E_n proficiency metric [223], which is commonly used by the metrology community to assess how well measurements agree within their stated uncertainty. DTU and five other labs with uncertainty models showed $|E_n| \leq 1$ for both test devices at all AOIs. When $|E_n|$ is less than one, it demonstrates that measurements are within the stated uncertainty. See **Publication VII** for more details of the uncertainty models reported by the participants and the E_n performance statistics.

The top frame of Figure 4.4 shows the median IAM measurements of the mono-Si and BSi RIE sample types. The BSi RIE sample type shows less reflection loss than the mono-Si sample, but the difference between the two sample types is always < 0.015. The modest improvement in angular-dependent performance could be due to a combination of the BSi nanostructure and the white backsheet. The bottom frame of Figure 4.4 shows box plot distributions of the differences between each lab's IAM measurement and the weighted mean (X_{ref}), which is calculated with IAM measurements from seven labs that reported uncertainty.

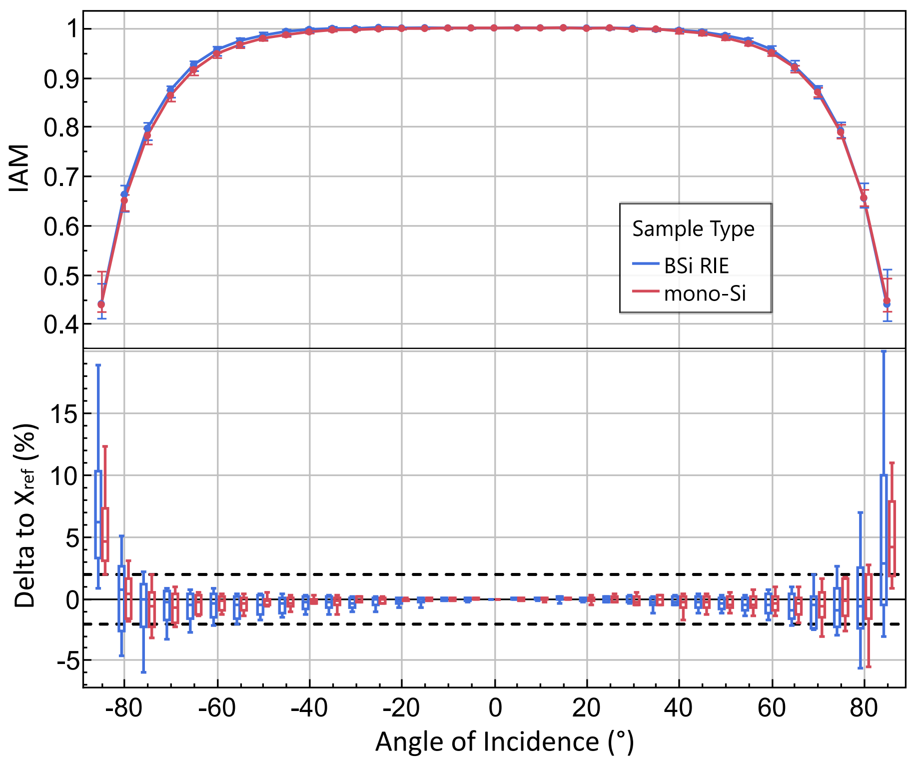

Figure 4.4: Top) Median IAM at each AOI for two sample types. The error bars at each AOI show the interquartile range. Bottom) Box plots showing the differences to the weighted mean X_{ref}. The dashed reference lines are ± 2%.

The IAM measurement agreement is within ±2% until about AOI = 65°, but from 70° to 85° the range—excluding outliers—increases rapidly from 2.5% to 23%. There are four outliers not shown in Figure 4.4 that occur at ± 85°. These outliers are between 44% and 24% low to the weighted mean X_{ref}. All four extreme outliers at ± 85° were reported by the same lab. Finally, at large AOIs in both the positive and negative direction, we observed that the range of IAM measurements is higher for the BSi RIE sample than for the mono-Si sample. This could be due to the nature of the BSi nanostructures, which create a graded refractive index at the Si-EVA interface.

The laboratories' IAM measurements were then used to simulate energy yield in the six standard climates of IEC 61853-4. The code used for this was debugged previously during the early intercomparison rounds presented in **Section 2.4.1** (**Publication III**). IEC 61853-3 uses the Martin and Ruiz IAM model with its single angular loss coefficient a_r, but here we additionally test the ASHRAE model with its single angular loss coefficient b_o. The participants' IAM measurements were fit to these models to extract the a_r and b_o values of each IAM profile. Simple multiplication of the IAM model with the cosine adjusted DNI allows one to calculate the effective POA beam component. It is more complex to derive the reflectance-adjusted diffuse POA component, but this can generally be done in one of two ways. The first approach is to integrate the IAM losses over a 2π hemisphere and the second is to use an analytical expression that approximates the double integral. Martin and Ruiz derived the closed-form expression for their model [184], whereas the closed-form of the ASHRAE model we took from [224]. The numerical integration of diffuse IAM losses followed the procedure described by [225].

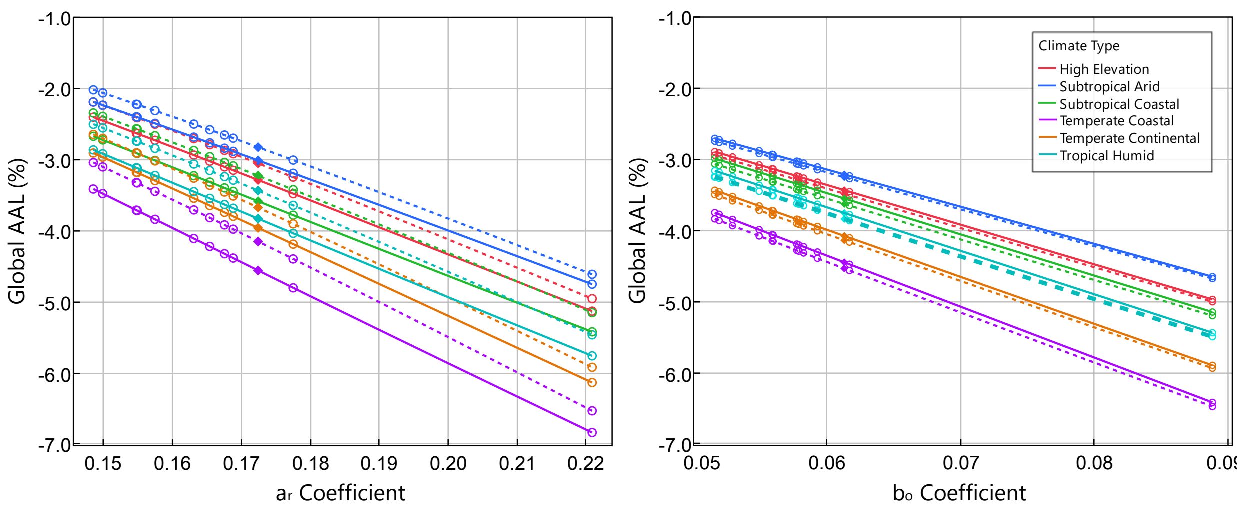

Figure 4.5: Annual angular losses of global irradiance using the Martin and Ruiz IAM model (left) and ASHRAE IAM model (right). Each circle marker represents a single a_r or b_o coefficient extracted from a participant's measurement. The dotted lines show the results using the closed-form equation to apply the angular-dependent losses and the solid lines show the results using integration to apply the losses.

Figure 4.5 shows the annual angular losses (AAL) of global irradiance when using the Martin and Ruiz and ASHRAE IAM models. The dotted lines show the climate-specific AAL when the closed-form approximation and the solid lines show the AAL when the calculation is performed by means of numerically integrating the angular-dependent losses across 1° isotropic sky segments. The closed-form approximation results in 0.2% to 0.4% higher AAL across all climates, but only when using the Martin and Ruiz IAM model.

When using the ASHRAE IAM model, the two methods of applying diffuse losses cause AAL variations below 0.1%. The climate-specific AAL using the ASHRAE model follows the same relative order as that of the Martin and Ruiz model, but the magnitude of the losses tends to be slightly higher (< 0.5%) when the ASHRAE fitting model is used instead of the Martin and Ruiz model. This could be because the

ASHRAE model tends to underpredict the physically measured angular-dependent losses by 2% to 3% between 40° and 65° AOI.

Figure 4.5 shows that more AAL occurs in climates with higher average AOIs (e.g., Temperate Coastal). The range of global AAL is highest for the most northern climates with high diffuse ratios and higher annual average AOIs, and lowest in southern climates where lower diffuse ratios and lower average AOIs are observed. For example, in the case of the Temperate Coastal climate (56°N), global AAL varies from 3.2% to 6.7%, whereas in the Subtropical Arid climate (33°30′N) global AAL varies from 2.1% to 4.7%.

We also used the participants IAM measurements to calculate CSER (Equation 2.1). The range of IAM measurements reported in the IAM ILC resulted in a 1.0% to 1.8% range in CSER values, depending on the climate. This result corresponds well with the rough estimation presented in [138] that the uncertainty of AOI measurements will lead to a 1% uncertainty in CSER. Finally, we calculated the differences in annual energy yield due to the different IAM profiles and we found a range from 1.0% to 1.5%, depending on the climate. It should be emphasized that the incident angle test is one of four measured characteristics in the IEC 61853 series and the uncertainty of the other three characterizations (i.e., performance matrix, spectral responsivity, and thermal behavior) should also be considered when considering the overall uncertainty of the energy rating standard. Refer to **Publication VII** for more details on the CSER results.

We collaborated with the Institute for Solar Energy Research in Hamelin (ISFH) at the end of the IAM ILC. We provided them with detailed data regarding the optoelectrical properties of the test samples (e.g., glass spectral transmittance, backsheet spectral reflectance, grid finger spacing etc.) and asked them to simulate the IAM with their raytracing model [85] [226]. The results obtained using the ISFH ray tracing simulations were all within the inner quartile range of IAM measurements. This result suggests that IAM profiles need not be measured in the lab. So long as the detailed optoelectrical properties are known, the IAM can be simulated with a suitable raytracing framework. Simulations have an advantage over measurements, especially at AOI ≥ 85°, because measurements at these oblique angles are subject to high uncertainty and poor reproducibility. Pease refer to **Publication VII** for more details on raytracing simulations.

4.3 Small-area sensors versus large-area reference module for rear irradiance monitoring

The most basic parameters to measure in PV monitoring systems include irradiance (in-plane, and horizontal), temperature (back-of-module and ambient), electrical output (DC and AC), and windspeed. In-plane irradiance (G_{POA}) is the most important factor influencing PV output, and for this reason, high-quality PV monitoring systems require great diligence concerning the G_{POA} instruments' alignment, soiling mitigation, dew and frost mitigation, and recalibration. Although the backside irradiance R_{POA} represents a fraction of the frontside G_{POA}, the R_{POA} must also be considered as a resource worthy of continuous monitoring.

Figure 4.6 shows one-year of back-to-front irradiance ratios (BFIR) for the two bPV system types installed at DTU Risø. R_{POA} in these diagrams is the average of two pyranometers mounted on the back of the system (i.e., two on HSAT and two on the fixed tilt). The histogram boarders show the annual distributions of BFIR and G_{POA} for each system type. The color scale shows the density of BFIR and G_{POA} observations clustered into ten quantiles. The mean BFIR of both system types is skewed because of the high BFIRs that can occur at low G_{POA}. The annual median BFIR is 9.1% and 7.4% for the HSAT and fixed tilt systems, respectively. The HSAT has a wider pitch than the fixed tilt system (i.e., 12 m vs. 7.6 m), which results in less self-shading and a higher median BFIR. The BFIR is of course dependent on the albedo. The broadband albedo at the DTU Risø site is about 0.2, which is comparable to most natural ground surfaces. Therefore, the distributions of annual BFIR shown in Figure 4.6 are likely to be similar in most utility-scale bPV parks.

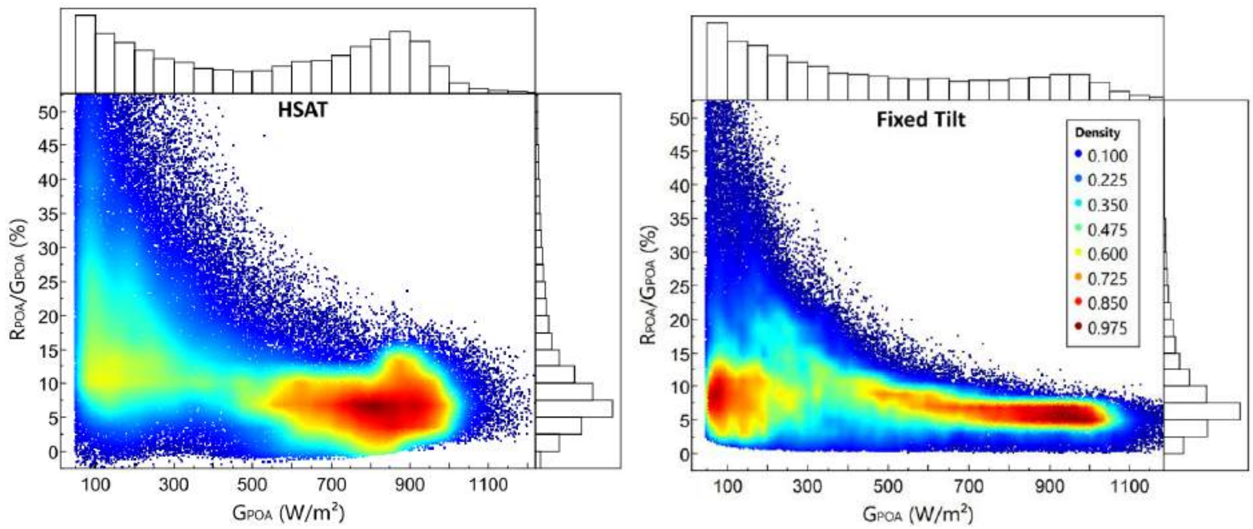

Figure 4.6: Rear to frontside irradiance ratio versus frontside irradiance for two system types: trackers (left) and 25° fixed tilt (right). Measurements shown here are made with thermopile pyranometers. Each plot contains roughly one-year of measurements at DTU Risø.

IEC 61724-1 states that R_{POA} measurements are not required in Class B rated monitoring of bPV systems. Figure 4.6 shows that in Class B monitoring systems, roughly 7–9% of the annual solar resource is simply not recorded. In other words, Class B systems only monitor 91–93% of the available resource. The distributions of annual BFIR in Figure 4.6 can demonstrate the value of adding R_{POA} measurements to a bPV monitoring system. When R_{POA} sensors are deployed, the data allows owners and operators to have a full picture of the key performance indicators (KPIs) that are frequently used for performance guarantees and/or condition monitoring.

Class A monitoring systems must have R_{POA} measurements at multiple locations, with the exact number of R_{POA} sensors dependent on the bPV plant's capacity. IEC 61724-1 provides a bifacial performance ratio (PR_{BIFI}) formula, which requires R_{POA} data. The PR_{BIFI} adjusts the reference yield for R_{POA} with a bifacial irradiance factor (BIF) as shown in Equation 4.1.

$$PR_{BIFI} = \frac{P_{out}/P_{STC}}{G_{POA} \cdot BIF/1000\ W/m^2} \qquad 4.1$$

Where P_{OUT} is the power output of the system, P_{STC} is the rated capacity at standard conditions, G_{POA} is the frontside irradiance, and 1000 W/m^2 is the reference irradiance. In practice, PR and PR_{BIFI} are typically integrated over some predetermined timescale such as days or months. The BIF term in Equation 4.1 adjusts the frontside irradiance for the rear-side irradiance according to Equation 4.2.

$$BIF = (1 + \varphi_{pmax} \cdot \frac{R_{POA}}{G_{POA}}) \quad 4.2$$

Where φ_{pmax} is the bifaciality factor of P_{MAX} and R_{POA} is the rear-side irradiance. Without the BIF term, the PR of bPV systems is frequently above 1. Such a result is peculiar because PR greater than 1 indicates no energy losses were incurred during field operation, relative to reference conditions. Although this result is easily explained by the bifacial energy gain, PR greater than 1 is nonintuitive for most PV professionals. Hence, the advantage of PR_{BIFI} is that bPV system PRs become more comparable to those of mPV systems. However, since IEC 61724-1 is unclear regarding how R_{POA} averaging should be done, a potential pitfall of PR_{BIFI} is that it is influenced by R_{POA} sensor sampling (i.e., R_{POA} nonuniformity), and the type of sensor used (i.e., R_{POA} spectral effects).

Publication VIII investigated how bifacial reference panels used as large-area irradiance sensors can circumvent the complexities involved in R_{POA} measurements. The premise is that the reference modules have the same irradiance-current response as the power producing modules in the array. Hence, monitoring the I_{SC} of a calibrated reference module should capture the heterogeneity and spectral albedo effects that were studied in **Chapter 3**.

A 14.2 kWp array of recently produced high power (595 Wp) modules was used for testing the bifacial reference panel method. Before the modules were deployed in the field, ten panels were randomly selected for flash testing at DTU according to the single-side illumination method described in IEC TS 60904-1-2. Two reference modules were then mounted within the 14.2 kWp string. One of the reference modules was made monofacial by applying several spray-on layers of air-dry Plasti Dip® rubber to the back glass. The other reference module was not modified and thus had the same properties as the bifacial modules in the 14.2 kWp string. The monofacial and bifacial reference panels allowed us to decouple the total irradiance into frontside G_{POA} and rear-side R_{POA} contributions. A two-channel EKO PV-Blocks system measured I-V curves of both reference panels every five minutes and held them at P_{MAX} between I-V scans. We also performed continuous inverter-level I-V scans on three select days to estimate the effective irradiance received by the 14.2 kWp string.

An R_{POA} sensor plate was constructed with an array of Si-photodiodes, Si reference cells, and thermopile pyranometers (Figure 1.1). The measurements from these small-area sensors were compared against those from the large-area reference modules and the 14.2 kWp string. The naming convention for the highest to lowest sensor is A to D. Additionally, we calculated R_{POA} at these locations using the 2D view factor model *pvfactors* because IEC 61724-1 states that an optical model can be used as an alternative to direct R_{POA} measurement. Finally, effective irradiance (G_E) comparisons between the large-area modules and small-area sensors were done using a standard formula (Equation 1.16).

Figure 4.7 shows exemplary R_{POA} and G_E measurements on three mostly sunny days. The diurnal profiles in Figure 4.7 were selected to demonstrate results under different solar zenith angles, and to show two days when string-level measurements were performed for G_E estimation (May 2nd and May 5th). The semi-transparent bands around the R_{POA} timeseries represent the range of values measured at 3–4 locations. The photodiode measurements show a positive bias relative to other R_{POA} and G_E methods, which is due to spectral albedo effects and consistent with the results shown in **Sections 3.2** and **3.4**. There are other reasons for the differences in R_{POA} measurement that were never quantified including the different calibration sources and the nonlinearity of signal-to-irradiance relationships. Finally, the string-level G_E measurements show good agreement to reference cells indicating that I-V data from inverters could be used for effective irradiance monitoring.

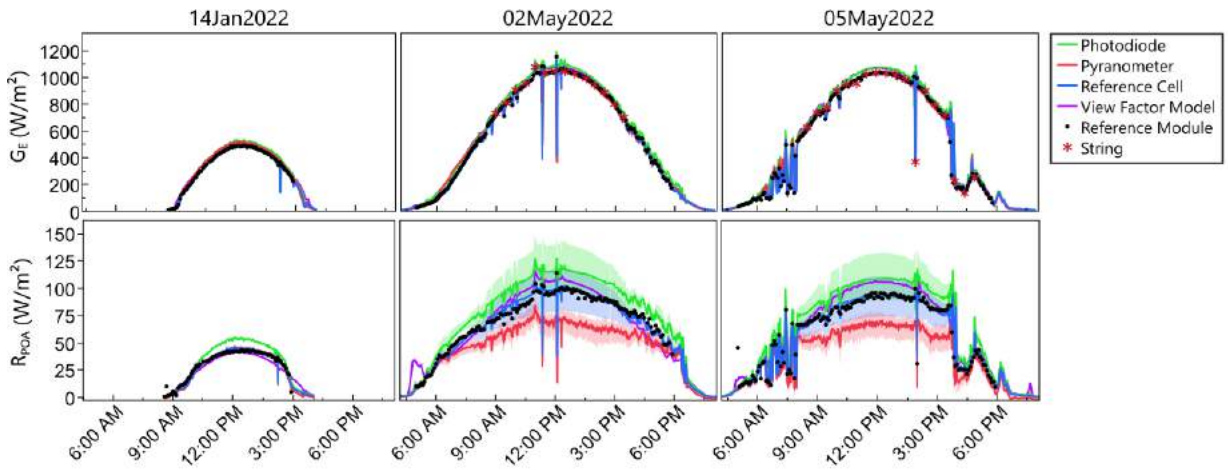

Figure 4.7: Timeseries of effective irradiance (G_E) and rear irradiance (R_{POA}) on three mostly sunny days. The semi-transparent bands around R_{POA} timeseries represent the range of values measured at 3-4 sensor positions. The reference cells, pyranometers, and photodiodes are sampled every minute. The reference modules are sampled every five minutes. The string I-V is performed every 30 minutes on the selected days.

Figure 4.8 shows the 14.2 kWp system's PR_{BIFI} calculated over a 5-month period with the five R_{POA} methods and four rear-side locations studied in **Publication VIII**. Frontside G_{POA} from the same Class A pyranometer is used in all calculations, which means that all variation of PR_{BIFI} in Figure 4.8 is caused by the R_{POA} measurement used. Figure 4.8 shows that PR_{BIFI} differs up to 3% with the R_{POA} methods considered here. The spread of possible PR_{BIFI} values is likely to increase with lower ground clearance because nonuniformity of R_{POA} will be higher.

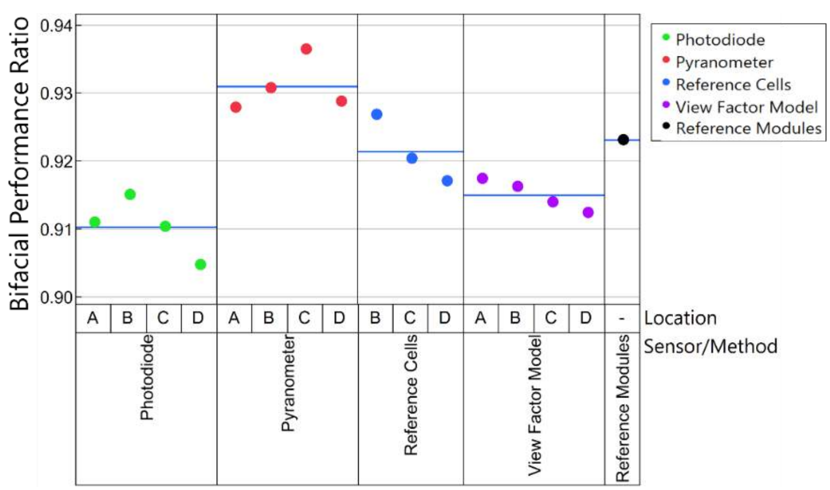

Figure 4.8: Variability of the bifacial performance ratio calculated according to the IEC 61724-1 using three small-area sensor types, an optical model, and a reference module pair.

Figure 4.8 also shows that PR_{BIFI} calculated with reference module R_{POA} is within 0.1% of PR_{BIFI} calculated with the average reference cell R_{POA}. We believe that PR_{BIFI} calculated with reference module R_{POA} has the advantage in that possible variations caused by spatial sampling errors are avoided. Our results indicate that bifacial reference panels can reduce variations in PR_{BIFI} calculations because they circumvent the need to identify representative small-area sensor locations and the need to adjust R_{POA} for spectral effects. At the end of **Publication VIII,** we use the R_{POA} and G_E data from the different sensor types to simulate DC power of the 14.2 kWp array. A residual error analysis between the simulation and string-level measurements showed that mean average percentage errors were comparable between reference cells, pyranometers, and reference modules (2.9–3.4%). These three sensor types have different calibration sources, and measurement principles, but the good agreement among them suggests that reference modules are a suitable approach to irradiance measurement in bPV systems.

Figure 4.9 shows the differences between R_{POA} measured with the various small-area sensors and R_{POA} measured with the large-area reference modules. Roughly five months of measurement data are shown here and the modeled R_{POA} and the differences between methods are shown as cumulative distribution functions (CDFs).

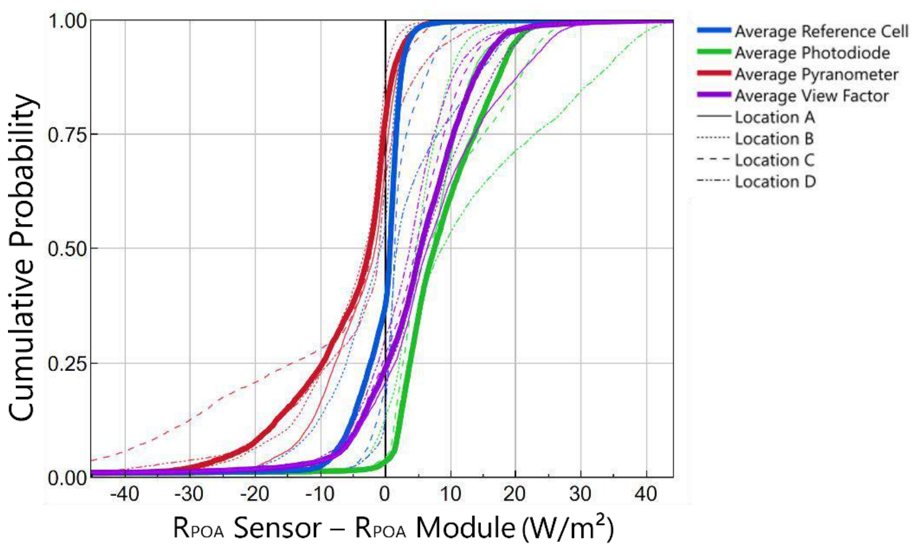

Figure 4.9: Cumulative distribution functions of the R_{POA} differences between four small-area measurement\simulation methods and the reference modules. The thick solid lines show the average of 3–4 locations within a given method.

CDF curves with steeper slopes indicate distributions with lower variances. The reference cell group shows the steepest slope of all groups with 80% of the measurements agreeing to the reference module measurements within ±5 W/m^2. The reference cell group also shows the lowest median bias (0.7 W/m^2) of all small-area methods tested. The good agreement of the reference cell and reference module approaches is not surprising given that the two device types share similar—but not identical—spectral, directional, thermal, and temporal responsivities. The lowest MAE was achieved when the reference cell is placed at location B (+30% from center) or location C (−30% from center). This suggests that a reference cell placed at one, or both, locations could serve as a representative location of the effective rear-side irradiance – so long as the fixed-tilt substructures are geometrically similar to that used here.

Please see **Publication VIII** for a deeper analysis into the differences between reference cell and reference module R_{POA} and G_E measurements, and for discussions on how the V_{OC} data from the I-V curves can be used to derive module temperature (T_{MOD}) of modules and arrays.

4.4 Summary and conclusions

In this chapter we presented the results of two international round robin campaigns on PV measurements. The first effort was conducted with six European participant labs who measured electrical performance of bifacial n-PERT, SHJ and PERC modules. The results were encouraging wherein most deviations were within their stated uncertainties. DTU demonstrated proficiency in bifacial n-PERT and PERC module measurements, which gives us confidence in future measurements of these module types. Most importantly, the results gave us confidence that we could reliably calibrate the bifacial PERC reference panel concept that was demonstrated at the end of this chapter.

The second round robin presented here was among twelve laboratories from Europe and the United States who measured the IAM response of monofacial PV coupons. The agreement was within ±2% until AOI = 65°, but discrepancies rapidly increased with AOI, and at AOI = 85° we observed deviations upward of 30%. The results indicated that the PV community should place minimal reliance on AOI measurements made at oblique angles until improvements can be demonstrated. The raytracing simulations performed by ISFH were always within the inter quartile range of measured IAM values, thereby suggesting that laboratory measurements are not the only way to obtain IAM profiles of PV devices. We then used the IAM data from the twelve participants and performed energy yield assessments in six climates. These results showed that the different IAM profiles cause energy yield estimates to vary by 1.0–1.5%, depending on the climate. This uncertainty is remarkably high considering that the IAM correction represents just one step in the PV model chain.

Finally, this chapter demonstrated a novel method for measuring rear and total irradiance, which involves taking continuous I-V curves of a calibrated pair of reference panels (monofacial and bifacial). We showed how reference modules calibrated per the single-side equivalent irradiance method of IEC TS 60904-1-2 can be used as large-area sensors that measure R_{POA} and G_E. We compared the reference module measurements to three types of commonly used small-area sensors, and out of all the small-area sensors tested, we found that reference cell measurements of R_{POA} and G_E had the best agreement to those made by reference modules. We found that the choice of small-area sensor type and mounting location adds at least ±1.5% uncertainty to bifacial performance ratio calculations. DC yield predictions made using G_E data from pyranometers, reference cells, and modules were within 2.9%–3.4% of measured string-level power, thereby demonstrating the absolute accuracy of the bifacial reference module approach.

Chapter 5. Methods for enhancing bifacial energy gain

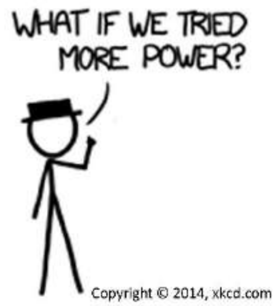

– Randall Munroe contemplating methods for enhancing illumination on the Moon in *What If?*

5.1 Introduction

This final chapter summarizes the methods and results obtained in **Publication IX**, wherein we studied the technoeconomic implications of artificially increasing the ground surface albedo below utility-scale bifacial arrays. The method that we used to increase albedo was simple: fasten a white cloth material directly below the array. This approach minimizes ecological impacts compared to methods like paving the ground and/or painting it white. The white tarp material we used had a hemispherical reflectance of 75%—roughly triple that of the green grass at the DTU test site. We did not have enough of this material to uniformly cover the test site. Instead, we placed a 4 m wide strip directly below the length of select fixed tilt and HSAT systems. With this limited coverage, we observed average bifacial energy gains of 11% for the fixed tilt and 15% for the HSAT, which was roughly double the bifacial gain of systems above grass.

The cash flow in our economic model was calculated with spot prices from the Nordpool power market and with electrical production data from six system types, which included a combination of fixed-tilt/HSAT, mPV/bPV, and white tarp/natural albedo scenarios. The white tarp scenarios increased income of the bifacial systems by roughly 4% during 2019–2020. However, the additional operations and maintenance (O&M) costs assumed for the white tarp scenarios resulted in a 1.8% lower 30-year levelized cost of energy (LCOE), relative to the LCOE of bifacial with natural albedo. This modest decrease in LCOE led us to the conservative conclusion that such a white tarp solution is not recommendable at utility scale, until the economics surrounding O&M become more favorable. However, we do not believe that the results of **Publication IX** are the final word on albedo enhancement. This chapter therefore concludes with recommendations that could have improved the economics of our study, which include increased material reflectivity, wider reflector material coverage, and/or more strategic placement of the reflector material.

5.2 Economic indicators and modeling

The Nordpool power market was established in 2000, and today it includes countries within Scandinavia, the Baltics, and others such as France, Germany, the Netherlands, and Poland. Nordpool offers both day-ahead and intraday (spot) electricity trading. Nordpool created their spot market due to the growing capacity of variable generators such as wind and solar. In our study, we used the hourly Nordpool spot price of electricity at the back-feed location (DK2) to determine the economic value generated by the six systems.

The value of the energy generated by the six systems was not estimated and compared solely based on hourly Nordpool spot power market prices and income. We additionally used the value factor as used in [227] and [228], which is the ratio of the income generated by a specific PV system relative to the average spot price during the period analysed. The value factor would equal one if a PV system generated a flat (i.e., time invariant) production curve during the period analyzed. A value factor less than one means that the value of electricity produced is less than what a constant production profile would earn. When comparing the production curves of two or more generating technologies, increasing *VF* simply indicates that the power production curve is better aligned with high spot prices.

Additionally, we use the LCOE to compare the different system types in terms of their upfront and ongoing (i.e., lifecycle) costs and the electricity generated during a 30-year project period. The LCOE model we used is described in Annex 2 of [229], but the basic form of the LCOE calculation is shown in Equation 5.1.

$$LCOE = \sum_{t=1}^{N} \frac{C_t / (1+d)^t}{E_t / (1+d)^t} \tag{5.1}$$

Where C_t is the total expenditures (capital, operation and maintenance, debt and equity service etc.) in year t and E_t is the energy generated in year t. All cashflows are discounted by the discount rate d. Many input values within the LCOE equation are highly project-specific (e.g., cost of capital and debt, land costs, local taxes etc.) and as such, the absolute LCOE values published here will vary for PV projects in different regions. However, the LCOE remains a practical and intuitive tool for assessing the costs and economic benefits of different energy generation technologies relative to each other.

5.3 Results of bifacial boost experiments at DTU

Pictures of the test setups after the white tarp was installed are shown in Figure 5.1a and Figure 5.1b. The manufacturer designed the material for use in greenhouses and states that it has a five-year outdoor lifetime. This replacement cost was accounted for in the economic model. Figure 5.1c shows the white tarp after three years in the field. The material has become less reflective and is covered by grass clippings. However, the economic model did not take the loss of reflectivity into account. Our albedo measurements showed that the material’s reflectivity reduced by roughly 5% in the first year. If we had accounted for this degradation, it would have made the economics of the white tarp scenarios less favorable.

Figure 5.1a and Figure 5.1b show HSAT and fixed tilt bPV systems with two different types of gravel below them. The idea behind gravel was that it was sourced locally and would not blow away like sand. We did not study the economics of the gravel systems because the broadband albedo was comparable to grass, and the installation was labor intensive. The bifacial gains of the gravel systems are published in [1]. However, the gravel turned into an ongoing problem because gardeners mowing the grass picked up small stones that broke several panels. Finally, we also tested a micro-structured reflector material with visual appearance like Mylar. The setup is partially visible in the background of Figure 5.1b and hemispherical reflectance measurements in the lab are shown in Figure 5.2. The reflectivity is about 65% in the visible light spectrum, about 10% less than the white tarp. The problems with this reflector were that the specular reflectance was concentrated in a local area of the large array resulting in a modest bifacial gain of 7%, and the material was easily damaged by strong winds.

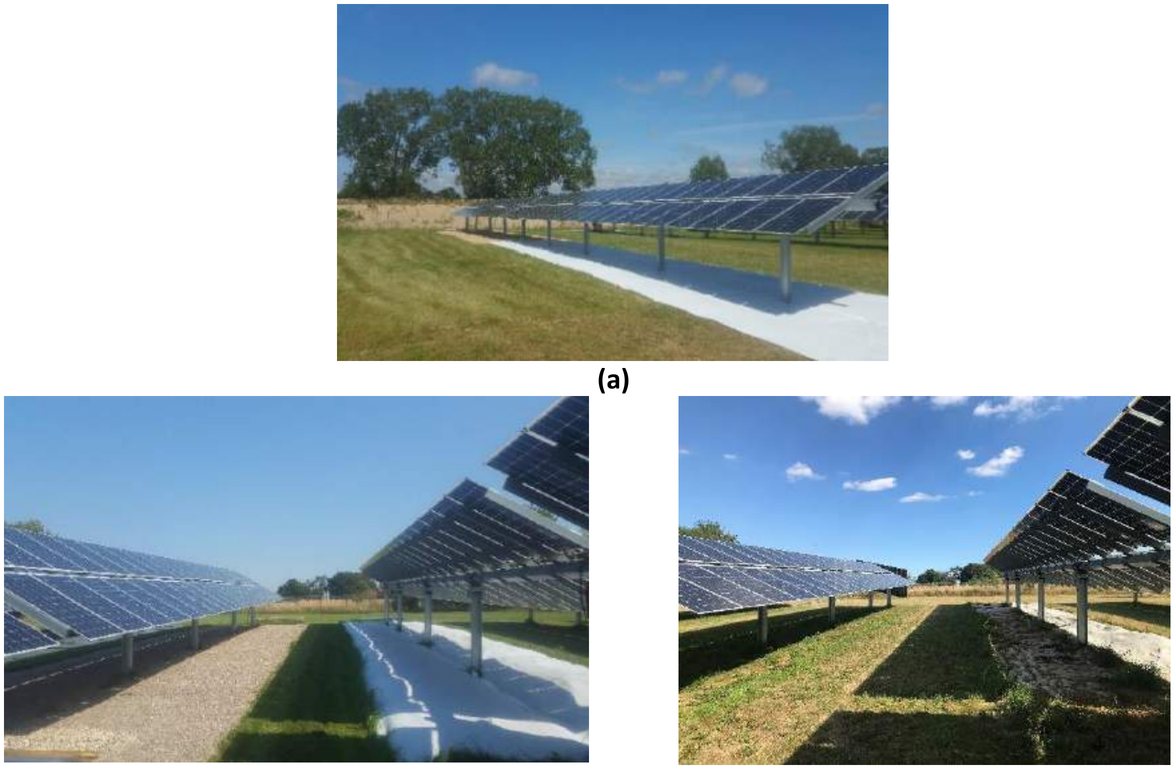

(a) **(b)** **(c)**

Figure 5.1: a) Recently mounted white tarp under bifacial single axis tracker. b) Recently mounted white tarp under bifacial fixed tilt rows. c) white tarp under fixed tilt three years after deployment. Note that the white tarp coverage is approximately ±2 m from the torque tube.

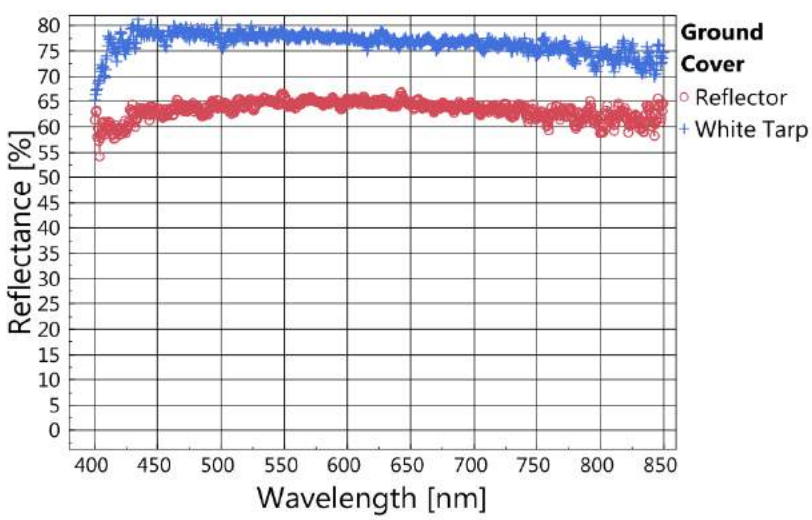

Figure 5.2: Spectrally resolved hemispherical reflectance of ground covers measured in the lab before field deployment.

Figure 5.3 shows specific yields of the six PV systems and a statistical display of daily spot prices at the test site location. The average production profiles are illustrated for each month. The performance of HSAT systems tend to have wider diurnal generation profiles than fixed tilt systems, especially in summer months when the sun's path is higher in the sky and spans a wider range of azimuth angles. The HSAT systems show higher generation in the morning/evening, but lower generation during midday when the tracker is oriented horizontally, and the sun's AOI is higher to the HSAT plane than it is to the fixed plane.

The HSAT production profile corresponds well to the typical variation of the power market prices over the day – wherein relatively high prices are observed in the morning/evening and relative low prices observed during midday. Little difference is observed in fixed versus HSAT production on cloudy days when 100 % of the solar irradiance comes from diffuse light. Under such conditions similar income is expected among all PV systems. The income from each system is calculated by simply multiplying the energy generation (MWh) by the spot price (DKK/MWh) at the time the energy was generated. Please see **Publication IX** for more details on the annual energy yield and income of the six system types.

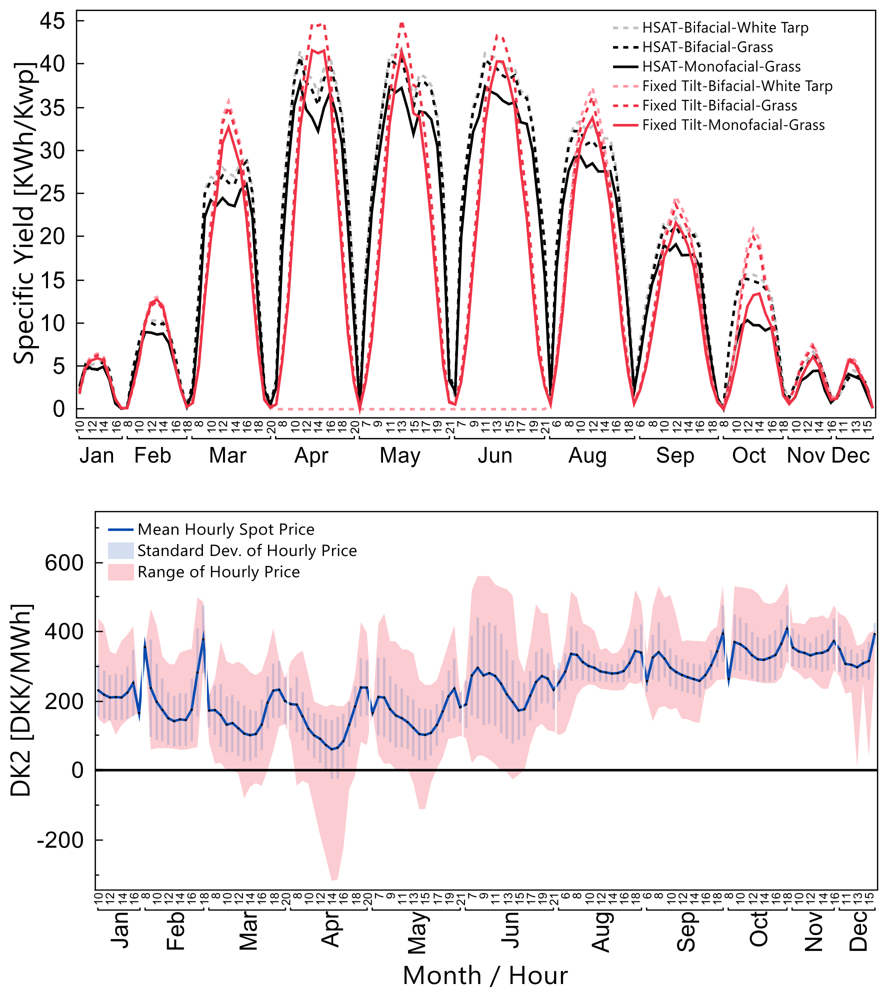

Figure 5.3: Top) Specific yield (kWh/kWp) generated by the six different PV systems during each hour of the test period. These plots can be interpreted as the average daily profiles within a given month. Bottom) Hourly Nord Pool spot prices within each month where solid line shows the mean, blue bars show one standard deviation, and red bands show the range of hourly prices within a given month.

Figure 5.4 shows the internal rate of return (IRR) plotted as a function of LCOE. The IRR is shown in conjunction with LCOE because the IRR is oftentimes a more meaningful metric for investors while the LCOE is mostly used by technical experts to compare different technologies. A clear negative correlation is observed, wherein the IRR decreases as the LCOE increases. Notably, whether the value factor or LCOE is used as a figure of merit, the relative ranking of the six system types is largely the same.

In Figure 5.4, the missing energy production data from the fixed tilt bifacial white tarp system have been imputed from months with a similar solar resource (e.g., missing April data is filled in with measured August data). Cost assumptions for all cases are based on discussions with suppliers. We have multiplied the expected capital cost of the white tarp by a factor of four to account for installation costs, which makes the white tarp approximately 15% of the total hard capital costs. This capital cost of the white tarp recurs every five years to account for replacement. Additional assumptions in the model include: a 20-year mortgage with 0.5% interest that covers 80% of the total (i.e., soft and hard) capital expenditures, spot prices from 2018 as a baseline with inflation of 1.3%/year, linear depreciation over 30 years, a tax rate of 22%, system degradation of 0.5%/year and unavailability of 0.5%/year.

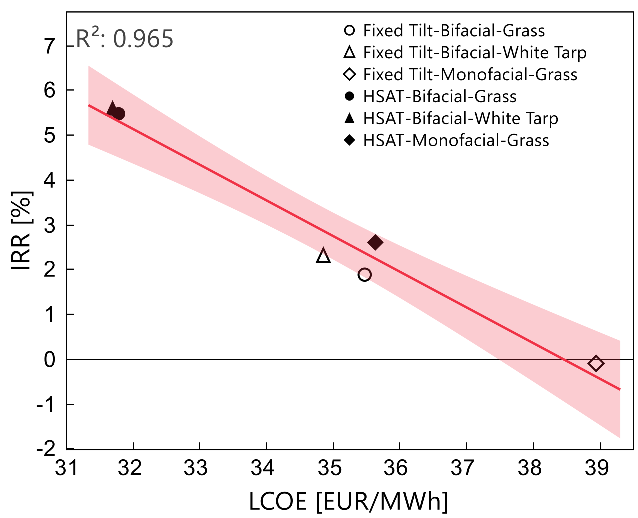

Figure 5.4: Internal rate of return versus levelized cost of energy calculated for a 30-year period in Denmark. The shaded areas around the red regression line show the 95 % confidence interval of the regression line.

The results show that there are similar decreases in LCOE (and thus increases in IRR) between fixed and HSAT systems and between monofacial and bifacial systems (3.5 – 4.0 EUR/MWh). There is a small, but notable decrease in LCOE between bifacial above grass and bifacial above white tarp cases. In the FT bifacial grass versus FT bifacial white tarp case, there is a 0.6 EUR/MWh LCOE decrease and a 0.4 % IRR increase. While the comparison of the HSAT bifacial grass and HSAT bifacial white tarp systems shows a smaller difference: a 0.1 EUR/MWh decrease in LCOE and a 0.1 % increase in IRR. The different result obtained for fixed and HSAT systems could be due to use of data imputation.

For both the bifacial FT and bifacial HSAT system, the extra cost of the white tarp is compensated by the additional energy production. The LCOE and IRR differences between bifacial grass and bifacial white tarp are, however, small. Therefore, the uncertainty in the capital expenditure and O&M parameters leads to the prudent conclusion that the white tarp is not advisable until O&M and/or CAPEX of such an albedo enhancement solution comes down. For example, an O&M increase of just 10 % in the bifacial white tarp cases increases the LCOE and decreases IRR to levels less favorable than bifacial cases without ground albedo enhancement.

5.4 Alternative approaches to increase bifacial energy gain

The results of the case study presented in **Publication IX** ultimately advise against modifying the albedo in large-scale bPV parks. However, the last word on the topic is not spoken. Here we discuss the factors that may have led to more favorable economic outcomes in our case study.

We had little experience with installing the white tarp and no experience installing it in a utility-scale system. Therefore, we had a conservative assumption that the installation cost was 15% of the total system cost. If an automated process for rolling out the white tarp could be devised, it could improve the economics. The use of white pavement or asphalt has been proposed for this purpose (e.g., **Section** 1.2.4), but we found that such solutions were non-starters for Danish municipalities because of concerns surrounding the increased storm water runoff.

Three additional factors could have been optimized to improve the results obtained in **Publication IX**:

1) Use of a material with reflectivity higher than 75%,
2) Use of a wider strip of material, and
3) Better placement of the material.

With respect to 1), a white tarp with 85% reflectivity was provided to us in November 2019. However, the hardware we used to affix this role of material to the ground was not as robust as the 20 cm U-bolts used to mount the tarps shown in Figure 5.1. Therefore, it quickly blew away in the wind, became muddy, and lost its high reflectance.

With respect to 2), we made a reflection coverage model only *after* the white tarps shown in Figure 5.1 were mounted. The model used trigonometry to determine how much light received by a downward facing point above a reflecting surface comes from that surface, and how much of the reflected light comes from the area beyond the surface.

Figure 5.5 shows the output of the model for different sensor heights. This model was especially useful for designing the spectral albedo test stand used in **Publication V** and **Publication VI**. The dashed dotted lines in Figure 5.5 are drawn at 2 m material radius (i.e., half the white tarp width) and 2 m sensor height (i.e., half the array height). Approximately 54% of the ground reflected light received at this point comes from the white tarp, and 46% comes from the grass. However, the parametric study performed by [206] found that the first square meter of material below a bPV array has the greatest influence on bifacial gain. This makes sense, considering that reflectance from additional material will be reduced by cosine of the viewing angle. Similar findings were obtained in the sensitivity analysis of [97], where they showed a reflecting material with area 1000-times that of the array, yields only 3% more energy than if the reflection material is 10-times the area of the array. Although the literature indicates our results in **Publication IX** may not have been improved with using more white tarp material, without running the sensitivity within the Danish context, we cannot be sure that we optimized for this parameter.

With respect to 3), the parametric study of [206] provides indication that the location of our white tarp was poorly selected. The authors of [206] used their raytracing model PVNOV to simulate 52 different configurations for an albedo enhancing material which included various, material sizes, heights from array, and ground coverages. Figure 5.6 shows the configuration that resulted in the highest bifacial energy gain. In this configuration, the reflector covers 70% of the ground and is placed 3 m (~33%) north of the table's low side, not directly below the table as in Figure 5.1. Placement such as shown in Figure 5.6 makes sense considering that reflector material in front of the array can scatter direct beam light to the back of the array, whereas the material shown in Figure 5.1 scatters more diffuse light.

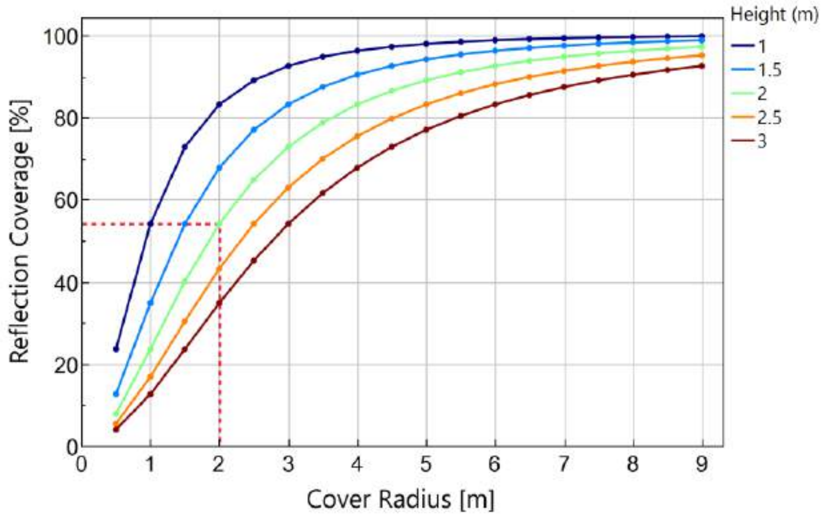

Figure 5.5: Percentage of total reflectance received by a downward facing sensor relative to the total reflectance available within a 180° field-of-view. The color scale shows the calculation at various sensor heights.

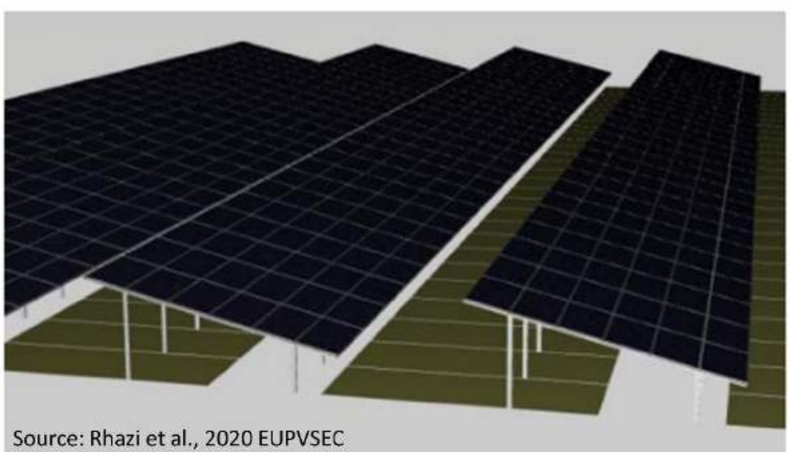

Figure 5.6: Optimal reflector material coverage and placement as determined by [206] for fixed tilt systems.
Summary and conclusions

5.5 Summary and conclusions

In this chapter we assessed the energy gains and economic implications of six different PV designs installed at the DTU Risø test site. One-year of energy production data showed a 26% difference between the system with the lowest output (fixed-tilt monofacial) and the highest output (HSAT bifacial with white tarp). Comparisons between fixed tilt and tracker systems allowed us to estimate a tracker gain (10.5–12.7%) while comparisons between monofacial and bifacial systems above grass provided bifacial gain estimates (7.2–10.5%) for the location. The bifacial energy boost of using the white sheet was about 3%, but as we demonstrated in **Section 5.4**, the 4 m wide strip of material may not have been ideally situated. LCOE calculations provided insight to the economic value of the six system types. Roughly a 10% reduction in LCOE was found in single-axis tracking designs over fixe-tilt designs, and a similar LCOE reduction (~10%) was found in bifacial designs over monofacial counterparts. This made bifacial on trackers above the natural ground surface the second most optimized design in terms of LCOE. This result is in line with that of Rodriguez-Gallegos et al. who found that bifacial PV on trackers is the PV design with the lowest LCOE across 93% of the world's land surface [104]. Our case study that bifacial PV modules on trackers above a highly reflective white tarp has the lowest LCOE of all six designs studied. However, the LCOE of bPV on trackers above white tarp was only 0.3% lower than bifacial on trackers above the natural ground surface. This marginal difference in LCOE was not enough for us to recommend the white tarp solution, at least in the fashion that it was applied in **Publication IX**. We concluded this chapter with suggestions for future work on the topic of albedo enhancements, namely the use of higher reflectance material, use of more material, and more strategic placement of material.

Chapter 6. Conclusions

6.1 Thesis Summary

This thesis summarized the main research outputs produced during the PhD project entitled "Characterization and Modeling of Bifacial Photovoltaic Modules and Systems.". The main project objectives were to assess the accuracy of bifacial modeling approaches, and to identify possible approaches for improvement. Additional objectives were to identify optimal methods for continuous irradiance and albedo monitoring in bifacial power plants, and to recommend practical methods for boosting bifacial energy gain. All these objectives were approached through a collection of field experiments as well as computational modeling.

In **Chapter 2**, we demonstrated that rear irradiance modeling in large-scale bifacial systems can be accurate within 2–5 W/m^2 when 2D view factor and raytracing approaches are used. We concluded that this level of error adds an extra 0.5% uncertainty to PV energy modeling. However, as the EMPIR-led energy rating model comparison showed, even expert PV modelers can implement the same algorithm differently. Therefore, the 2–5 W/m^2 mean absolute accuracy figure is likely to vary between PV modelers. Our benchmarking study of eight PV simulation software and four large-scale PV systems showed that the median accuracy in hourly PV energy modeling is between -3% and -1%, depending on the PV system design. Indeed, user-variability may lead to different results, and for this reason, the data set used in Publication II has been circulated to 29 modelers as part of a PVPMC-led modeling comparison effort. Full results from the PVPMC-led effort will be published in mid-2023.

In **Chapter 3**, we examined the subtle properties of the light on the backside of PV arrays. Namely, we investigated the spatial nonuniformity and spectral distribution of rear plane-of-array irradiance, but a comparison of various albedo data sources was also made at the end of the chapter. We found that, under typical albedo scenarios, the electrical mismatch due to nonuniform irradiance is small on common single-axis tracker designs. For 1P designs, we showed that mismatch losses peak at 0.4% midday on clear-sky days. We simulated design modifications that could reduce this mismatch loss. We found the design with largest potential to decrease the losses from 0.4% to 0.32%, is not likely to be economically advantageous given the modest nature of the losses in the base case. The spectral albedo investigations of five ground materials showed that backside bifacial performance can be improved by as much as 20% due to the reflected light's spectral distribution. The spectral data from the field measurements and simulations resulted in multiple linear regressions that can be used as a simplified spectral model for rear irradiance. Finally, we performed bifacial energy gain simulations with five different albedo sources and compared the results to electrical performance data. We determined that, out of the five albedo sources considered, the optimal solution for albedo monitoring in bifacial PV parks is a compulsory pair of thermopile pyranometers, and an optional pair of spectrally selective radiometers to study spectral effects.

In **Chapter 4**, we studied the relationship between laboratory measurements and energy yield modeling. Incidence angle modifier (IAM) measurements from 12 state-of-the-art laboratories were found to cause a 1.0–1.5% variation in modeled energy yield, depending on the climate. This intercomparison only looked at IAM measurements of single-sided monofacial PV cells–IAM measurements of dual-sided bifacial devices could result in greater deviations. Therefore, Singapore lab SERIS is leading a second IAM round-robin, in which DTU is participating, that includes two bifacial PV devices. The research conducted in Chapter 3 inspired us to test bifacial reference panels as a method to measure rear and total effective irradiance. We found that bifacial modules calibrated with the IEC TS 60904-1-2 procedures can be used to measure total effective irradiance in large-scale PV parks. Furthermore, a complementary monofacial module permits rear irradiance measurements that are comparable in accuracy to those from calibrated reference cells. The advantages of the bifacial reference panel approach are: 1) PV system designers need not expend great effort identifying suitable locations for small-area sensors, 2) PV analysts need not correct for backside spectral effects, 3) variations in bifacial performance ratio calculations are reduced when measuring irradiance over a large-area, and 4) the equivalent cell temperature can be calculated from open-circuit voltage data.

Finally, in **Chapter 5** we assessed the energy gains and economics of bifacial PV and ground covers with white fabric and reflective foil. Our case study that bifacial on trackers above a highly reflective white tarp has the lowest levelized cost of energy (LCOE) of all six designs studied. However, the LCOE of bifacial on trackers above a white tarp was only 0.3% lower than bifacial on trackers above the natural (grass) ground surface. We found that small variations in the capital and/or operations cost of the white tarp could easily reverse the financial appeal of this albedo augmentation solution. Therefore, it is our recommendation to not advise such ground albedo enhancements until definite cost reductions are achieved.

References

[1] J. Stein, C. Reise, J. Castro, G. Friesen, G. Maugeri, E. Urrejola and S. Ranta, "Bifacial Photovoltaic Modules and Systems: Experience and Results from International Research and Pilot Applications," International Energy Agency PVPS Task 13 - Performance, Operation and Reliability of Photovoltaic Systems, 2021.

[2] H. Mori, "Radiation energy transducing device". US/JAPAN Patent US3278811A·1966-10-11/JP4074860A·1960-10-04, 1966.

[3] G. Grigorieva, M. Kagan, K. Zviagine, V. Kalikasuskas, L. Kreinin, N. Bordin and N. Eisenberg, "Future of Bifacial Si Solar Cells for Space Applications," in *23rd European Photovoltaic Solar Energy Conference and Exhibition*, Valencia, Spain, 2008.

[4] A. Luque-Lopez, "Procedure for obtaining bifacial solar cells". Spain Patent ES458514A1·1978-04-16, 1977.

[5] J. Ledesma, R. Almeida, F. Martinez-Moreno, C. Rossa, J. Martín-Rueda, L. Narvarte and E. Lorenzo, "A simulation model of the irradiation and energy yield of large bifacial photovoltaic plants," *Solar Energy,* vol. 206, p. 522–538, 2020.

[6] C. Zhou, P. Verlinden, R. Crane, R. Swanson and R. Sinton, "21.9% efficient silicon bifacial solar cells," in *26th IEEE Photovoltaic Specialists Conference*, Anaheim, CA, 1997.

[7] T. Mishima, M. Taguchi, H. Sakata and E. Maruyama, "Development status of high-efficiency HIT solar cells," *Solar Energy Materials and Solar Cells,* vol. 95, no. 1, pp. 18-21, 2011.

[8] T. Nordmann, T. Vontobel and L. Clavadetscher, "15 Years of Practical Experience in Development and Improvement of Bifacial Photovoltaic Noise Barriers Along Highways and Railway Lines in Switzerland," Frankfurt, Germany, 2012.

[9] R. Hezel, "Novel Applications of Bifacial Solar Cells," *Progress in Photovoltaics,* vol. 11, p. 549–556, 2003.

[10] International Energy Agency (IEA), "Special Report on Solar PV Global Supply Chains," 2022.

[11] VDMA, "International Technology Roadmap for Photovoltaics (ITRPV): Seventh Edition," 2016.

[12] VDMA, "International Technology Roadmap for Photovoltaics (ITRPV): Eighth Edition," 2017.

[13] VDMA, "International Technology Roadmap for Photovoltaics (ITRPV): Ninth Edition," 2018.

[14] VDMA, "International Technology Roadmap for Photovoltaics (ITRPV): Tenth Edition," 2019.

[15] VDMA, "International Technology Roadmap for Photovoltaics (ITRPV): Eleventh Edition," 2020.

[16] VDMA, "International Technology Roadmap for Photovoltaics (ITRPV): Twelfth Edition," 2021.

[17] VDMA, "International Technology Roadmap for Photovoltaics (ITRPV): 2021 Results," 2022.

[18] N. Ishikawa and S. Nishiyama, "World First Large Scale 1.25MW Bifacial PV Power Plant on Snowy Area in Japan," in *3rd Bifi PV Workshop*, Miyazaki, Japan, 2016.

[19] Canadian Solar, "Bifacial BiKu Module 100 MW Utility Solar Plant," 2018. [Online]. Available: https://www.canadiansolar.com/project-wuhai-china-biku/. [Accessed 10 October 2022].

[20] P. Fath and F. Es, "Establishment of a 1.3 GWp Solar Power Plant and 500 MWp Integrated Manufacturing Facility in Turkey," in *38th European Photovoltaic Solar Energy Conference*, 2021.

[21] P. Wolfe, "The world's largest solar parks," PV Magazine, 23 September 2021. [Online]. Available: https://www.pv-magazine.com/2021/09/23/the-worlds-largest-solar-parks/. [Accessed 10 October 2022].

[22] D. Feldman, K. Dummit, J. Zuboy, J. Heeter, K. Xu and R. Margolis, "Spring 2022 Solar Industry Update," NREL Report# PR-7A40-82854, 2022.

[23] S. Chunduri and M. Schmela, "Bifacial Solar Technology 2021 Edition - Part 1," Taiyang News, 2021.

[24] J. Stein and D. Jordan, "Glass-Glass Photovoltaic Modules - Overview of Issues," in *Fall DuraMAT Workshop*, Palo Alto, CA, 2018.

[25] H. Bahar and J. Moorhouse, "Renewable Energy Markey Update: Outlook for 2021 and 2022," International Energy Agency (IEA), 2021.

[26] J. Singh, S. Guo, I. Peters, A. Arbele and T. Walsh, "Comparison of Glass/Glass and Glass/Backsheet PV Modules Using Bifacial Silicon Solar Cells," *IEEE Journal of Photovoltaics,* vol. 5, no. 3, pp. 783 - 791, 2015.

[27] H. Yin, Y. Zhou, S. Sun, W. Tang, W. Shan, X. Huang and X. Shen, "Optical enhanced effects on the electrical performance and energy yield of bifacial PV modules," *Solar Energy,* vol. 217, p. 245–252, 2021.

[28] B. Jaekel, G. Voldber, C. Monokroussos, G. Muelhoffer and A. Roth, "TYPE APPROVAL AND SAFETY CONSIDERATIONS FOR BIFACIAL PV MODULES: REQUIREMENTS FOR IEC 61215 AND IEC 61730," in *35th EU PVSEC*, Brussels, Belgium, 2018.

[29] P. Thorat, S. Waghmare, A. Sinha, A. Kumar and G. Tamizhmani, "Reliability Analysis of Field-aged Glass/Glass PV Modules: Influence of Different Encapsulant Types," in *47th IEEE PVSC*, 2020.

[30] A. Patel, A. Sinha and G. Tamizhmani, "Field-Aged Glass/backsheet and Glass/Glass PV Modules," *IEEE Journal of Photovoltaics,* vol. 10, no. 2, pp. 607-615, 2020.

[31] A. Sinha, M. Owen-Bellini, D. Sulas-Kern and L. Spinella, "Glass/Glass Photovoltaic Module Reliability and Degradation: A Review," *Journal of Physics D: Applied Physics ACCEPTED,* 2021.

[32] T. Dullweber and J. Schmidt, "Industrial Silicon Solar Cells Applying the Passivated Emitter and Rear Cell (PERC) Concept—A Review," *IEEE Journal of Photovoltaics,* vol. 6, no. 5, p. 1366–1378, 2016.

[33] T. Dullweber, C. Kranz, R. Peibst, U. Baumann, H. Hannebauer, A. Fülle, S. Steckemetz, T. Weber, M. Kutzer, M. Müller, G. Fischer, P. Palinginis and H. Neuhaus, "PERC+: industrial PERC solar cells with rear Al grid enabling bifaciality and reduced Al paste consumption," *Progress in Photovoltaics,* vol. 24, p. 1487–1498, 2016.

[34] A. Blakers, A. Wang, M. Adele, J. Zhao and M. Green, "22.8% efficient silicon solar cell," *Applied Physics Letters,* vol. 55, p. 1363–1365, 1989.

[35] I. Romijn, G. Janssen, T. Dullweber, B. van-Aken, N. Eisenberg, L. Kreinin, M. Despeisse, V. Mihailetchi, J. Lossen, W. Jooss and R. Kopecek, "Chapter 2: Bifacial cells," in *Bifacial Photovoltaics: Technology, applications and economics*, J. Libal and R. Kopecek, Eds., London, The Institution of Engineering and Technology, 2018, p. 17–71.

[36] R. Kopecek and J. Libal, "Bifacial Photovoltaics 2021: Status, Opportunities and Challenges," *Energies,* vol. 14, no. 2076, 2021.

[37] J. Svarc, "Most Efficient Solar Panels 2022," Clean Energy Reviews, 28 July 2022. [Online]. Available: https://www.cleanenergyreviews.info/blog/most-efficient-solar-panels. [Accessed 22 September 2022].

[38] A. Rehman and S. Lee, "Advancements in n-type base crystalline silicon solar cells and their emergence in the photovoltaic industry," *The Scientific World Journal,* 2013.

[39] US Federal Registrar, "Determination on the Exclusion of Bifacial Solar Panels From the Safeguard Measure on Solar Products," Trade Representative Office of the United States, 17 April 2020. [Online]. Available: https://www.federalregister.gov/documents/2020/04/17/2020-08189/determination-on-the-exclusion-of-bifacial-solar-panels-from-the-safeguard-measure-on-solar-products. [Accessed 12 September 2022].

[40] E. Merchant, "US Reverses Course on Tariff Exclusion for Bifacial Solar Modules," Greentech Media, 07 October 2019. [Online]. Available: https://www.greentechmedia.com/articles/read/us-reverses-course-on-tariff-exclusion-for-bifacial-solar-modules. [Accessed 12 September 2022].

[41] J. John, "Whiplash: Bifacial Solar Modules to Retain US Tariff Exemption," Greentech Media, 05 December 2019. [Online]. Available: https://www.greentechmedia.com/articles/read/court-order-will-retain-tariff-exemption-for-bifacial-solar-modules. [Accessed 12 September 2022].

[42] E. Merchant, "Trump Administration Removes Tariff Exemption for Bifacial Solar Panels — Again," Greentech Media, 17 April 2020. [Online]. Available:

https://www.greentechmedia.com/articles/read/trump-admin-removes-tariff-exemption-for-bifacial-solar-panels-again. [Accessed 12 September 2022].

[43] Solar Energy Industries Association (SEIA), "The Adverse Impact of Section 201 Tariffs: Lost Jobs, Lost Deployment and Lost Investments," December 2019. [Online]. Available: https://www.seia.org/sites/default/files/2019-12/SEIA-Tariff-Analysis-Report-2019-12-3-Digital_0.pdf. [Accessed 12 September 2022].

[44] Solar Energy Industries Association (SEIA), "SEIA Supports Biden Administration's Effort to Find Balanced Solution on Section 201 Tariffs," 04 February 2022. [Online]. Available: https://www.seia.org/news/seia-supports-biden-administrations-effort-find-balanced-solution-section-201-tariffs. [Accessed 12 September 2022].

[45] D. Jordan, N. Haegel and T. Barnes, "Photovoltaics module reliability for the terawatt age," *Progress in Energy,* vol. 4, 2022.

[46] J. Weaver, "World has installed 1TW of solar capacity," PV Magazine, 15 March 2022. [Online]. Available: https://www.pv-magazine.com/2022/03/15/humans-have-installed-1-terawatt-of-solar-capacity/ . [Accessed 13 September 2022].

[47] International Renewable Energy Agency (IRENA), "IRENASTAT Online Data Query Tool: Installed renewable electricity capacity (MW) by Region/country/area, Technology and Year," [Online]. Available: https://pxweb.irena.org/pxweb/en/IRENASTAT/IRENASTAT__Power%20Capacity%20and%20Generation/RECAP_2022_cycle2.px/. [Accessed 13 September 2022].

[48] M. Waters, C. Deline, J. Kemnitz and J. Webber, "Suggested Modifications for Bifacial Capacity Testing," in *IEEE 46th Photovoltaic Specialists Conference (PVSC)*, Chicago, IL, 2019.

[49] A. Gracia-Amillo, R. P. Kenny, G. Friesen, C. Reise and J. Lopez-Garcia, "Extension of energy rating to bifacial modules – proposals from the PV-enerate project," JRC Technical Report, 2020.

[50] N. Dioro and C. Deline, "Bifacial Simulation in SAM System Advisor Model (SAM)," in *Bifacial PV Workshop*, Lakewood, 2018.

[51] A. Mermoud and B. Wittmer, "Bifacial Shed Simulation with PVsyst," in *Bifacial PV Workshop*, Konstanz, 2017.

[52] J. Carolus, A. Heide, E. Voroshazi, W. Ceunick, M. Daenen and I. Tsanakas, "Physics of potential-induced degradation in bifacial p-PERC solar cells," *Solar Energy Materials and Solar Cells,* vol. 200, 2019.

[53] J. Karas, I. Repins, K. Berger and H. Maaroufi, "Results from an international interlaboratory study on light- and elevated temperature-induced degradation in solar modules," *Progress in Photovoltaics,* vol. 30, no. 11, pp. 1255-1269, 2022.

[54] S. Dittmann, H. Sanchez, L. Burnham, R. Gottschalg, S.-Y. Oh, A. Benlarabi, B. Figgis, A. Abdallah, C. Rodriguez, R. Rüther and C. Fell, "Comparative Analysis of Albedo Measurements at Multiple Sites Worldwide," in *36th European Photovoltaic Solar Energy Conference and Exhibition*, Marseille, 2019.

[55] C. A. Gueymard, V. Lara-Fanego, M. Sengupta and Y. Xie, "Surface albedo and reflectance: Review of definitions, angular and spectral effects, and intercomparison of major data sources in support of advanced solar irradiance modeling over the Americas," *Solar Energy,* vol. 182, pp. 194-212, 2019.

[56] B. Marion, "Measured and Satellite-derived albedo data for estimating bifacial photovoltaic system performance," *Solar Energy,* vol. 215, p. 321–327, 2021.

[57] C. Deline, S. A. Pelaez, S. MacAlpine and C. Olalla, "Estimating and parameterizing mismatch power loss in bifacial photovoltaic systems," *Progress in Photovoltaics,* vol. 28, no. 7, 2020.

[58] M. Gostein, B. Marion and B. Stueve, "Spectral Effects in Albedo and Rearside Irradiance Measurement for Bifacial Performance Estimation," in *IEEE Photovoltaic Specialists Conference (PVSC)*, Virtual, 2020.

[59] J. Stein, "Energy Prediction and System Modeling," in *Photovoltaic Solar Energy: From Fundamentals to Applications 1st Edition*, John Wiley and Sons, 2016, pp. 564-578.

[60] C. Demian, M. Journee and C. Bertrand, "Evaluation of different models to estimate the global solar radiation on inclined surfaces," *Renewable Energy,* vol. 50, pp. 710-721, 2013.

[61] A. Noorian, I. Moradi and G. Kamali, "Evaluation of 12 models to estimate hourly diffuse irradiation on inclined surfaces," *Renewable Energy,* vol. 33, pp. 1406-1412, 2008.

[62] G. Chowdhury, A. Kladas, B. Herteleer, J. Capelle and F. Catthoor, "Performance Analysis of Highly Cited Silicon Photovoltaic Module Temperature Estimation Methods: A Critical Review," *Solar SRRN,* 2022.

[63] E. Skoplaki and J. Palyvos, "On the temperature dependence of photovoltaic module electrical performance: A review of efficiency/power correlations," *Solar Energy,* vol. 83, pp. 614-624, 2009.

[64] M. Prilliman, J. Stein, D. Riley and G. Tamizhmani, "Transient Weighted Moving-Average Model of Photovoltaic Module Back- Surface Temperature," *IEEE Journal of Photovoltaics,* vol. 10, no. 4, pp. 4153-1060, 2020.

[65] P. Gilman, "SAM Photovoltaic Model Technical Reference," National Renewable Energy Laboratory Report (NREL/TP-6A20-64102), 2015.

[66] S. Kalagirou, "Applications of artificial neural-networks for energy systems," *Applied Energy,* vol. 67, no. 2, pp. 17-35, 2000.

[67] F. Almonacid, C. Rus, P. Perez and L. Hontoria, "Estimation of the energy of a PV generator using artificial neural network," *Renewable Energy,* vol. 34, no. 12, pp. 2743-2750, 2009.

[68] D. Pombo, P. Backer, C. Ziras, H. Binder, S. Spataru and P. Sørensen, "Benchmarking physics-informed machine learning-based short term PV-power forecasting tools," *Energy Reports,* vol. 8, pp. 6512-6520, 2022.

[69] K. Passow, L. Ngan, B. Littman, M. Lee and A. Panchula, "Accuracy of energy assessments in utility scale PV power plant using PlantPredict," in *42nd IEEE Photovoltaic Specialists Conference*, New Orleans, 2015.

[70] M. Mikofski, R. Darawali, M. Hamer, A. Neubert and J. Newmiller, "Bifacial Performance Modeling in Large Arrays," in *46th IEEE Photovoltaic Specialists Conference (PVSC)*, Chicago, 2019.

[71] R. Perez, P. Ineichen, R. Stewart and D. Menicucci, "A new simplified version of the Perez diffuse irradiance model for tilted surfaces," *Solar Energy,* vol. 44, no. 2, pp. 271-289, 1987.

[72] J. Hay and J. Davies, "Calculations of the solar radiation incident on an inclined surface," in *Proc. of First Canadian Solar Radiation Data Workshop*, 1980.

[73] D. Faiman, "Assessing the Outdoor Operating Temperature of Photovoltaic Modules," *Progress in Photovoltaics,* pp. 307-315, 2008.

[74] A. Duffie and B. W.A., "Chapter 23: Design of Photovoltaic Systems," in *Solar Engineering of Thermal Processes 3rd Edition*, John Wiley and Sons, 2006.

[75] C. Cameron, W. Boyson and D. Riley, "Comparison of PV system performance-model predictions with measured PV system performance," in *33rd IEEE PVSC*, 2008.

[76] C. Gueymard, "Direct and indirect uncertainties in the prediction of tilted irradiance for solar engineering applications," *Solar Energy,* vol. 83, pp. 432-444, 2009.

[77] P. Loutzenhiser, H. Manz, C. Felsmann, P. Strachan, T. Frank and G. Maxwell, "Empirical validation of models to compute solar irradiance on inclined surfaces for building energy simulation," *Solar Energy,* vol. 81, pp. 254-267, 2007.

[78] R. Mubarak, M. Hofmann, S. Riechelmann and G. Seckmeyer, "Comparison of Modelled and Measured Tilted Solar Irradiance for Photovoltaic Applications," *Energies,* vol. 10, 2017.

[79] U. Gross, K. Spindler and E. Hahne, "Shapefactor-equations for radiation heat transfer between plane rectangular surfaces of arbitrary position and size with parallel boundaries," *Letters in Heat and Mass Transfer,* vol. 8, pp. 219-227, 1981.

[80] I. Shoukry, D. Berrian, J. Libal and F. Haffner, "Chapter 4: Simulation models for energy yield prediction of bifacial systems," in *Bifacial Photovoltaics - Technology, Applications and Economics*, Institution of Engineering and Technology, 2018.

[81] D. Grobgeld, "View factor two differential areas illustration.svg," 2010. [Online]. Available: https://en.wikipedia.org/w/index.php?curid=28020281. [Accessed 10 October 2022].

[82] B. Marion, S. MacAlpine, C. Deline, A. Asgharzadeh, F. Toor, D. Riley, J. Stein and C. Hansen, "A Practical Irradiance Model for Bifacial PV Modules," in *IEEE Photovoltaic Specialists Conference*, Washington D.C., 2017.

[83] A. Krenzinger and E. Lorenzo, "Estimation Of Radiation Incident On Bifacial Albedo-Collecting Panels," *International Journal of Solar Energy,* vol. 4, no. 5, pp. 297-319, 1986.

[84] L. Kreinin, N. Bordin, A. Karsenty, A. Drori, D. Grobgeld and N. Eisenberg, "PV module power gain due to bifacial design. Preliminary experimental and simulation data," in *35th IEEE Photovoltaic Specialist Conference*, 2010.

[85] C. Schinke, M. R. Vogt and K. Bothe, "Optical Modeling of Photovoltaic Modules with Ray Tracing Simulations," in *Photovoltaic Modeling Handbook*, Wiley, 2018.

[86] S. A. Pelaez, C. Deline, P. Greenberg, J. S. Stein and R. K. Kostuk, "Model and Validation of Single-Axis Tracking with Bifacial PV," *IEEE Journal of Photovoltaics,* vol. 9, no. 3, pp. 715-721, 2019.

[87] K. McIntosh, "How the PVSyst inputs for bifacial systems depend on conditions," in *Bifi PV Workshop*, Virtual, 2020.

[88] C. W. Hansen, R. Gooding, N. Guay, D. M. Riley, J. Kallickal, D. Ellibee, A. Asgharzadeh, B. Marion, F. Toor and J. S. Stein, "A Detailed Model of Rear-Side Irradiance for Bifacial PV Modules," in *44th IEEE Photovoltaic Specialists Conference (PVSC)*, Washinton D.C., 2017.

[89] M. Anoma, D. Jacob, B. Bourne, J. Scholl, D. Riley and C. Hansen, "View Factor Model and Validation for Bifacial PV and Diffuse Shade on Single-Axis Trackers," in *44th IEEE Photovoltaic Specialist Conference (PVSC)*, Washington D.C., 2017.

[90] G. Janssen, A. B. A. Burgers, A. Carr, B. R. I. van Aken, M. Klenk, H. Nussbaumer and T. Baumann, "How to maximize the kWh/kWp ratio: simulations of single-axis tracking in bifacial systems," in *35th European Photovoltaic Solar Energy Conference and Exhibition*, Brussels, 2018.

[91] D. Berrian, J. Libal, M. Klenk, Nussbaumer and R. Kopecek, "Performance of Bifacial PV Arrays With Fixed Tilt and Horizontal Single-Axis Tracking: Comparison of Simulated and Measured Data," *IEEE Journal of Photovoltaics,* vol. 9, no. 6, 2019.

[92] I. Horvath, H. Goverde, P. Manganiello, A. Schils, A. Heide, J. Govaerts and E. Voroshazi, "Next Generation Tools for Accurate Energy Yield Estimation of Bifacial PV Systems – Best Practices, Improvements and Challenges," in *36th European Photovoltaic Solar Energy Conference and Exhibition*, 2021.

[93] K. McIntosh, M. Abbott, B. Sudbury and J. Meydbray, "Mismatch Loss in Bifacial Modules Due to Nonuniform Illumination in 1-D Tracking Systems," *IEEE Journal of Photovotaics,* vol. 9, no. 6, pp. 1504-1512, 2019.

[94] M. Chiodetti, A. Lindsay and Dupeyrat, "A ray-tracing based 3D tool for accurate prediction of PV plants yield," in *36th EU PVSEC*, Marseille, 2019.

[95] C. Deline and S. Pelaez, "bifacial_radiance: a python package for modeling bifacial solar photovoltaic systems.," *Journal of Open Source Software,* vol. 5, no. 50, 17 Dec 2020.

[96] G. Ward, "The RADIANCE Lighting Simulation and Rendering System," 1994.

[97] U. Yusufoglu, T. Pletzer, L. Koduvelikulathu, C. Comparotto, R. Kopecek and H. Kurz, "Analysis of the Annual Performance of Bifacial Modules and Optimization Methods," *IEEE Journal of Photovoltaics,* vol. 5, no. 1, p. 320–328, 2015.

[98] J. Appelbaum, "The role of view factors in solar photovoltaic field," *Renewable and Sustainable Energy Reviews,* vol. 81, pp. 161-171, 2018.

[99] H. Ziar, F. Sönmez, O. Isabella and M. Zeman, "A comprehensive albedo model for solar energy applications: Geometric spectral albedo," *Applied Energy,* vol. 255, 2019.

[100] D. Chudinzow, J. Haasb, G. Díaz-Ferránc, S. Moreno-Leivaa and L. Eltrop, "Simulating the energy yield of a bifacial photovoltaic power plant," *Solar Energy ,* vol. 183, p. 812–822, 2019.

[101] A. Russell, C. Valdiva, C. Bohemier, J. Haysom and K. Hinzer, "DUET: A Novel Energy Yield Model With 3-D Shading for Bifacial Photovoltaic Systems," *IEEE Journal of Photovoltaics,* 2022.

[102] J. Robledo, L. Leloux, E. Lorenzo and C. Gueymard, "From video games to solar energy : 3D shading simulation for PV using GPU," *Solar Energy,* 2019.

[103] K. Jager, P. Tillmann and C. Becker, "Detailed illumination model for bifacial solar cells," *Optics Express,* vol. 28, 2020.

[104] C. Rodriguez-Gallegos, H. Liu, O. Gandhi, J. Singh, V. Krishnamurthy, A. Kumar, J. Stein, S. Wang, L. Li, T. Reindl and I. M. Peters, "Global Techno-Economic Performance of Bifacial and Tracking Photovoltaic Systems," *Joule,* vol. 4, pp. 1514-1541, 2020.

[105] M. Ernst, C. G.E.J. and C. Asselineau, "Accelerating the simulation of annual bifacial illumination of real photovoltaic systems with ray tracing," *iScience,* 2022.

[106] C. Zhao, J. Xiao, Y. Yu and J.-N. Jaubert, "Accurate shading factor and mismatch loss analysis of bifacial HSAT systems through ray-tracing modeling," *Solar Energy Advances,* vol. 1, 2021.

[107] W. Herrmann, C. Monokroussos and L. Kyumin, "COMPARISON OF DIFFERENT APPROACHES TO DETERMINE THE NOMINAL PV MODULE OPERATING TEMPERATURE (NMOT)," in *38th European Photovoltaic Solar Energy Conference and Exhibition*, 2021.

[108] B. King, C. Hansen, D. Riley, C. Robinson and L. Pratt, "Procedure to Determine Coefficients for the Sandia Array Performance Model (SAPM)," Sandia National Laboratories Report # SAND2016-5284, 2016.

[109] D. Jordan and S. Kurtz, "The Dark Horse of Evaluating Long-Term Field Performance—Data Filtering," *IEEE Journal of Photovoltaics,* vol. 4, no. 1, 2014.

[110] J. Fatehi and K. Sauer, "Modeling the incidence angle dependence of photovoltaic modules in PVsyst," in *40th IEEE Photovoltaic Specialists Conference*, 2014.

[111] M. Koehl, M. Heck, S. Weismeir and J. Wirth, "Modeling of the nominal operating cell temperature based on outdoor weathering," *Solar Energy Materials and Solar Cells,* vol. 95, no. 7, pp. 1638-1646, 2011.

[112] A. Driesse, J. Stein and M. Theristis, "Improving Common PV Module Temperature Models by Incorporating Radiative Losses to the Sky," Sandia National Laboratories Report # SAND2022-11604, 2022.

[113] B. Bourne and C. Chaudhari, "Deriving Thermal Response Coefficients for PVsyst," in *PV Performance Modeling Collaborative Workshop*, Albuquerque, NM, 2019.

[114] PVsyst, "Array Thermal Losses," [Online]. Available: https://www.pvsyst.com/help/thermal_loss.htm. [Accessed 11 October 2022].

[115] Google Groups, "pvlib-python@googlegroups.com," March 2021. [Online]. Available: https://groups.google.com/g/pvlib-python/c/_ZFDH9by6O8/m/if9lH63YBgAJ. [Accessed 11 October 2022].

[116] K. Sauer, T. Roessler and C. Hansen, "Modeling the Irradiance and Temeprature Dependence of Photovoltaic Modules in PVsyst," *IEEE Journal of Photovoltaics,* vol. 5, no. 1, pp. 152-158, 2015.

[117] K. Lee, "PAN Files from IEC 61853-1 Data: Why using Datasheet I-V Values is a bad Idea," in *11th PV Performance Modeling and Monitoring Workshop*, Albuquerque, 2018.

[118] A. Driesse, M. Theristis and J. Stein, "A New Photovoltaic Module Efficiency Model for Energy Prediction and Rating," *IEEE Journal of Photovoltaics,* vol. 11, no. 2, pp. 527-534, 2021.

[119] D. King, B. Boyson and J. Kratochvill, "Photovoltaic Array Performance Model," Sandia Report (SAND2004-3535), 2004.

[120] T. Huld, G. Friesen, A. Skoczek, R. Kenny, T. Sample, M. Field and E. Dunlop, "A power-rating model for crystalline silicon PV modules Thomas," *Solar Energy Materials & Solar Cells,* vol. 95, pp. 3359-3369, 2011.

[121] A. Guérin de Montgareuil, L. Sicot, J.-L. Martin, F. Mezzasalma, Y. Delesse and J. Merten, "A New Tool for the MotherPV Method: Modeling of the Irradiance Coefficient of Photovoltaic Modules," in *24th European Photovoltaic Solar Energy Conference*, Hamburg, 2009.

[122] W. Heydenreich, B. Muller and C. Reise, "Describing the World with three Parameters: A new Approach to PV Module Power Modelling," in *23rd European Photovoltaic Solar Energy Conference and Exhibition*, Valencia, 2008.

[123] W. De Soto, S. Klein and W. Beckman, "Improvement and validation of a model for photovoltaic array performance," *Solar Energy,* vol. 80, pp. 78-88, 2006.

[124] V. Lo Brano, A. Orioli, G. Ciulla and A. Di Gangi, "An improved five-parameter model for photovoltaic modules," *Solar Energy Materials and Solar Cells,* vol. 94, pp. 1358-1370, 2010.

[125] M. de Blas, J. Torres, E. Prieto and A. Garcia, "Selecting a suitable model for characterizing photovoltaic devices," *Renewable Energy,* vol. 25, pp. 371-380, 2002.

[126] D. Chan and J. Phang, "Analytical Methods for the Extraction of Solar-Cell Single- and Double-Diode Model Parameters from I- V Characteristics," *IEEE Transactions of Electron Devices,* vol. 34, no. 2, 1987.

[127] A. Dobos, "An Improved Coefficient Calculator for the California Energy Commission 6 Parameter Photovoltaic Module Model," *Journal of Solar Energy Engineering,* vol. 2, p. 134, 2012.

[128] L. Vuilleumier, M. Hauser, C. Félix, F. Vignola, P. Blanc, A. Kazantzidis and B. Calpini, "Accuracy of ground surface broadband shortwave radiation monitoring," *Journal of Geophysical Research: Atmospheres,* vol. 119, no. 13, pp. 838-860, 2014.

[129] A. Habte, M. Sengupta, I. Reda and A. Andreas, "Calibration and Measurement Uncertainty Estimation of Radiometric Data," NREL/CP-5D00-62214, 2014.

[130] D. Dirnberger and U. Kräling, "Uncertainty in PV Module Measurement—Part I: Calibration of Crystalline and Thin-Film Modules," *IEEE Journal of Photovoltaics,* vol. 3, no. 3, pp. 1016-1026, 2013.

[131] D. Dirnberger, U. Kralling, H. Mullejans, E. Salis, K. Emery, Y. Hishikawa and K. Kiefer, "Progress in photovoltaic module calibration: results of a worldwide intercomparison between four reference laboratories," *Measurement Science and Technology,* vol. 25, 2014.

[132] B. Mihaylov, T. Betts, A. Pozza, H. Mullejans and R. Gottschalg, "Uncertainty Estimation of Temperature Coefficient Measurements of PV Modules," *IEEE Journal of Photovoltaics,* vol. 6, no. 6, pp. 1554-1564, 2016.

[133] C. Hansen and A. Pohl, "Which Models Matter: Uncertainty and Sensitivity Analysis for Photovoltaic Power Systems," in *40th IEEE Photovoltaic Specialists Conference*, 2014.

[134] C. Hansen and C. Martin, "Photovoltaic System Modeling: Uncertainty and Sensitivity Analyses," Sandia Report (SAND2015-6700), 2015.

[135] A. Driesse and N. Patel, "Cross-validation of PV System Simulation Software," in *35th European Photovoltaic Solar Energy Conference*, Marseille, 2019.

[136] C. Hansen, J. Stein, S. Miller, B. Boyson, J. Kratochvil and D. King, "PARAMETER UNCERTAINTY IN THE SANDIA ARRAY PERFORMANCE MODEL FOR FLAT-PLATE CRYSTALINE SILICON MODULES," in *IEEE Photovoltaic Specialists Conference*, 2011.

[137] B. Muller, L. Hardt, A. Armbruster, K. Kiefer and C. Riese, "Yield predictions for photovoltaic power plants: empirical validation, recent advances and remaining uncertainties," *Progress in Photovoltaics,* vol. 24, no. 4, 2015.

[138] D. Dirnberger, B. Muller and C. Reise, "PV module energy rating: opportunities and limitations," *Progress in Photovoltaics,* vol. 23, pp. 1754-1771, 2015.

[139] G. Friessen, R. Gottschalg, H. Beyer, S. Williams, W. van Sark, T. Huld, B. Muller and Y. Niu, "Intercomparison of Different Energy Prediction Methods Within the European Project "Performance" - Results of the 1st Round Robin," in *22nd European Photovoltaic Solar Energy Conference*, Milan, 2007.

[140] J. Stein, "The Photovoltaic Performance Modeling Collaborative (PVPMC)," in *IEEE Photovoltaic Specialists Conference*, 2012.

[141] D. Moser, S. Lindig, M. Herz, B. Muller, I. Horvath, A. Schils, S. Ramesh, M. Green, J. Vedde, D. Barnard, J. Ascencio-Vasquez and M. Richter, "BENCHMARKING YIELD ASSESSMENT EXERCISE IN DIFFERENT CLIMATES WITHIN AN INTERNATIONAL COLLABORATION FRAMEWORK," in *37th European Photovoltaic Solar Energy Conference and Exhibition TOPIC*, 2020.

[142] A. Dobos, "PVWatts Version 5 Manual," National Renewable Energy Laboratory, 2014.

[143] C. Deline, S. MacAlpine, B. Marion, F. Toor, A. Asgharzadeh and J. Stein, "Assessment of Bifacial Photovoltaic Module Power Rating Methodologies—Inside and Out," *IEEE Journal of Photovoltaics,* vol. 7, no. 2, 2017.

[144] C. Monokroussos, Q. Gao, X. Zhang, E. Lee, Y. Wang, C. Zou, L. Rimmelspacher, J. B. Castro, M. Schweiger and W. Herrmann, "Rear-side spectral irradiance at 1 sun and application to bifacial module power rating," *Progress in Photovoltaics,* 2020.

[145] International Electrotechnical Commission, "IEC 61215-1 Terrestrial photovoltaic (PV) modules - Design qualification and type approval," 2021.

[146] D. Tschopp, A. Jensen, J. Dragsted, P. Ohnewein and S. Furbo, "Measurement and modeling of diffuse irradiance masking on tilted planes for solar engineering applications," *Solar Energy,* vol. 231, pp. 365-378, 2022.

[147] J. C. Blakesley, G. Koutsourakis, S. Douglas, J. Holder, J. Torry, F. Mukadam, Schmid, Alexandra and R. Abrams, "Effective spectral albedo from satellite data for bifacial gain calculations of PV systems," in *European Photovoltaic Solar Energy Conference (EUPVSEC)*, Virtual, 2020.

[148] M. Gostein, S. Ayala, C. Deline, A. Habte, C. Hansen, B. Marion, J. Newmiller, M. Sengupta, J. Stein and I. Suez, "Measuring Irradiance for Bifacial PV Systems," Virtual, 2021.

[149] S. Pelaez, C. Deline, S. MacAlpine, B. Marion, J. Stein and R. Kostuk, "Comparison of Bifacial Solar Irradiance Model Predictions With Field Validation," *IEEE Journal of Photovoltaics,* vol. 9, no. 1, pp. 82-88, 2019.

[150] R. P. Kenny, E. G. Menendez, J. Lopez-Garcia and B. Haile, "Characterizing the Operating Conditions of Bifacial Modules," in *8th Internation Conference on Crystalline Silicon Photovoltaics*, 2018.

[151] C. Rossa, F. Martinez-Moreno and E. Lorenzo, "Experimental observations in mismatch losses in monofacial and bifacial PV generators," *Progress in Photovoltaics,* 2021.

[152] A. Asgharzadeh, B. Marion, C. Deline, C. Hansen, J. Stein and F. Toor, "A Sensitivity Study of the Impact of Installation Parameters and System Configuration on the Performance of Bifacial PV Arrays," *IEEE Journal of Photovoltaics,* vol. 8, no. 3, p. 798–805, 2018.

[153] D. Compaan and J. Cormican, "Quantifying the impacts of racking structure on bifacial gain," in *NREL Photovoltaic Reliability Workshop*, 2022.

[154] G. Janssen, R. Gali, K. deGroot, A. J. Carr, B. B. Van Aken and I. Romijn, "Impact of inhomogenous irradiance at the rear of bifacial panels on modelled energy yield," in *33rd European Photovoltaic Solar Energy Conference and Exhibition*, Amsterdam, 2017.

[155] B. Meyers and M. Mikofski, "Accurate Modeling of Partially Shaded PV Arrays," in *44th IEEE Photovoltaic Specialists Conference*, 2017.

[156] J. Bishop, "Computer simulation of the effects of electrical mismatches in photovoltaic cell interconnection circuits," *Solar Cells,* vol. 25, no. 1, pp. 73-89, 1988.

[157] M. M.C., R. Kenny, T. Lyubenova, A. Gracia-Amillo and J. Lopez-Garcia, "Analysis of the Irradiance Non-Uniformity on the Performance of Vertical and Tilted Bifacial PV Module Arrays," in *38th European Photovoltaic Solar Energy Conference*, 2021.

[158] K. McIntosh, M. Abbott, B. Sudbury, C. Zak, G. Loomis, A. Mayer and J. Meydbrey, "Irradiance on the upper and lower modules of a two-high bifacial tracking system," in *47th IEEE Photovoltaics Specialist Conference (PVSC)*, Virtual Meeting, 2020.

[159] International Electrotechnical Commision, "IEC 60904-3 Ed. 4.0," 2019.

[160] International Electrotechnical Commision, "IEC 60904-7 Ed. 4.0," 2019.

[161] D. Myers and C. Gueymard, "Description and availability of the SMARTS spectral model for photovoltaic applications," in *Proceedings of SPIE - The International Society for Optical Engineering #5520*, 2004.

[162] M. Deceglie, T. Silverman, K. Emery, D. Dirnberger, A. Schmid, S. Barkaszi, N. Riedel, L. Pratt, S. Doshi, G. Tamizhmani, B. Marion and S. Kurtz, "Validated Method for Repeatable Power Measurement of CIGS Modules Exhibiting Light-Induced Metastabilities," *IEEE Journal of Photovoltaics,* vol. 5, no. 2, pp. 607-612, 2015.

[163] T. Huld, T. Sample and E. Dunlop, "A simple model for estimating the influence of spectrum variations on PV performance," in *24th European Photovoltaic Solar Energy Conference*, Hamburg, 2009.

[164] M. Lee and A. Panchula, "Spectral correction for photovoltaic module performance based on air mass and precipitable water," Portland, OR, 2016.

[165] B. Duck and C. Fell, "Improving the spectral correction function," in *43rd IEEE Photovoltaic Specialists Conference*, Porland, OR, 2016.

[166] S. Pelland, C. Beswick, D. Thevenard, A. Côté, A. Pai and Y. Poissant, "Development and Testing of the PVSPEC Model of Photovoltaic Spectral Mismatch Factor," Calgary, Canada, 2020.

[167] M. Iqbal, "Chapter 9: Ground Albedo," in *An Introduction to Solar Radiation*, New York and London, Academic Press, 1983, p. 281–293.

[168] M. R. Vogt, T. Gewohn, K. Bothe, C. Schinke and R. Brendel, "Impact of using spectrally resolved ground albedo data for performance simulations of bifacial modules," in *European Photovoltaic Solar Energy Conference (EUPVSEC)*, Brussels, 2018.

[169] T. C. R. Russel, R. Saive, A. Augusto, S. G. Bowden and H. A. Atwater, "The Influence of Spectral Albedo on Bifacial Solar Cells: A Theoretical and Experimental Study," *IEEE Journal of Photovoltaics,* vol. 7, no. 6, pp. 1611-1619, 2017.

[170] A. Mekemeche and M. Beghdad, "Impact of the Environmental Effective Albedo on the Performance of PERC + Solar Cells," *Silicon,* vol. 29, 2020.

[171] International Electrotechnical Commision, "IEC TS 60904-1-2 "Measurement of current-voltage characteristics of bifacial photovoltaic (PV) devices"," 2019.

[172] J. Hohl-Ebinger and W. Warta, "Bifacial Solar Cells in STC Measurement," in *25th European Photovoltaic Solar Energy Conference* , 2010.

[173] V. Fakhfouri, "IEC 60904-1-2: Measurement of current-voltage characteristics of bifacial photovoltaic devices," in *bifiPV Workshop*, Konstanz, 2017.

[174] S. Roest, W. Nawara, B. Van-Aken and E. Goma, "Towards Developing a Standard for Testing Bifacial PV Modules: Single-Side versus Double-Side Illumination Method I-V Measurements Under Different Irradiance and Temperature," in *IEEE 44th Photovoltaic Specialist Conference (PVSC)*, Washington D.C., 2017.

[175] K. Ramspeck, D. Dzafic, S. Zimmermann, C. Krober and M. Meixner, "Measurement techniques for bifacial solar cells," in *bifiPV Workshop*, Konstanz, 2017.

[176] M. Rauer, A. Schmid, F. Guo, F. Neuberger, P. Gebhardt and J. Hohl-Ebinger, "Comprehensive evaluation of IEC measurement procedures for bifacial solar cells and modules," in *37th European PV Solar Energy Conference*, Lisbon, 2020.

[177] T. Liang, M. Pravettoni, J. Singh and Y. Khoo, "A Metrological Study of Accurate Indoor," *IEEE Journal of Photovoltaics,* vol. 10, no. 5, 2020.

[178] C. Reise, G. Baarah, E. Schabel, U. Kraling and B. Muller, "From Bifaciality to Yield: Different Bifacial Cell Technologies May Differ Even More in Annual Outdoor Performance," in *35th EUPVSEC*, Brussels, 2018.

[179] J. Lopez-Garcia, E. Ozkalay, R. Kenny, L. Pinero-Prieto, D. Shaw, D. Pavanello and T. Sample, "Implementation of the IEC TS 60904-1-2 Measurement Methods for Bifacial Silicon PV Devices," *IEEE Journal of Photovoltaics,* vol. 12, no. 3, 2022.

[180] G. Koutsourakis, M. Rauer, A. Schmid and S. Winter, "Results of the Bifacial PV Cells and PV Modules Power Measurement Round Robin Activity of the PV-Enerate Project," 2021.

[181] M. Pravettoni, "Testing the Tests: Conclusions of the International Bifacial Round-Robin," in *bifiPV workshop*, Virtual, 2020.

[182] R. Gottschalg, "Overview of Energy Rating Standard (IEC 61853 parts 1-4)," in *7th PV Performance Modeling Workshop*, Lugano, Switzerland, 2017.

[183] M. Babin, S. Thorsteinsson, A. Santamaria, P. Poulson, A. Thorseth and J. M, "Dependency of IAM Losses in Colored BIPV Products on the Refractive Index of Colorants," in *38th European Photovoltaic Solar Energy Conference*, 2021.

[184] N. Martin and J. Ruiz, "Annual angular reflection losses in PV modules," *Progress in Photovoltaics,* vol. 13, pp. 75-84, 2005.

[185] Y. Khoo, J. Singh, T. Walsh and A. Arbele, "Comparison of Angular Reflectance Losses Between PV Modules With Planar and Textured Glass Under Singapore Outdoor Conditions," *IEEE Journal of Photovoltaics,* vol. 4, no. 1, pp. 362-367, 2014.

[186] A. Souka and H. Safwat, "Determination of the optimum orientations for the double-exposure, flat-plate collector and its reflectors," *Solar Energy,* vol. 10, no. 4, pp. 170-174, 1966.

[187] N. Martin and J. Ruiz, "A new model for PV modules angular losses under field conditions," *International Journal of Solar Energy,* vol. 22, no. 1, pp. 19-31, 2002.

[188] F. Plag, I. Kroger, T. Fey, F. Witt and S. Winter, "Angular-dependent spectral responsivity-Traceable measurements on optical losses in PV devices," *Progress in Photovoltaics,* vol. 26, no. 3, 2017.

[189] F. Vignola, J. Michalsky and T. Stoffel, in *Solar and Infrared Radiation Measurements, Second Edition*, Boca Raton, CRC Press, 2019, pp. 80-83;137-144.

[190] M. Sengupta, A. Habte, S. Wilbert, C. Gueymar and J. Remund, "Best Practices Handbook for the Collection and Use of Solar Resource Data for Solar Energy Applications: 3rd Edition," NREL/TP-5D00-77635, 2021.

[191] P. Babal, M. Korevaar, S. Franken, J. Mes, T. Bergmans and K. Wilson, "Uncertainties in irradiance measurements of sensors to POA-rear of bifacial solar panels," in *IEEE 47th Photovoltaic Specialists Conference (PVSC)*, Calgary, 2020 .

[192] J. Braid, J. Stein, B. King, C. Raupp, J. Mallineni, J. Robinson and S. Knapp, "Effective Irradiance Monitoring Using Reference Modules," in *IEEE Photovoltaic Specialists Conference (PVSC)*, Philadelphia, PA, 2022.

[193] M. Korevaar, P. Babal, S. van Nieuwkerk, K. Wilson and J. Mes, "Simulation and Validation of Bifacial Irradiance Sensor Mounting Position," in *37th European Solar Energy Conference (EUPVSEC)*, Lisbon, 2020.

[194] International Electrotechnical Commision, "IEC 61724-1 Edition 2 Photovoltaic system performance - Part 1: Monitoring," 2021.

[195] A. Tuomiranta, A. Pierre-Jean, C. Ballif and H. Ghedira, "Worldwide performance evaluation of ground surface reflectance models," *Solar Energy,* vol. 224, pp. 1063-1078, 2021.

[196] T. Patel, R. Khan, A. Alnuaimi, O. Albadwawwi, J. John and M. Alam, "Implications of Seasonal and Spatial Albedo Variation on the Energy Output of Bifacial Solar Farms: A Global Perspective," in *46th IEEE Photovoltaic Specialists Conference (PVSC)*, Chicago, IL, 2019.

[197] F. Vignola, J. Michalsky and T. Stoffel, "Chapter 9: Albedo," in *Solar Radiation and Infrared Radiation Measurements*, Boca Raton, FL, CRC Press, 2017, p. 193–204.

[198] J. Coakley, "Reflectance and Albedo, Surface," in *Encyclopedia of Atmospheric Sciences*, 2003, p. 1914–1923.

[199] F. Nicodemus, "Directional Reflectance and Emissivity of an Opaque Surface," *Applied Optics,* vol. 4, no. 7, pp. 767-775, 1965.

[200] M. Kutzer, "Ertragssteigerung durch bifaciale Modultechnologie," in *Symposium Photovoltaische Solarenergie*, 2016.

[201] V. Janulevicius, LinkedIn, [Online]. Available: https://www.linkedin.com/feed/update/urn:li:activity:6574540002976415744/. [Accessed 11 October 2022].

[202] R. Krishnan, LinkedIn, [Online]. Available: https://www.linkedin.com/posts/rahul-krishnan-58321218a_sungrow-sg250hx-oman-activity-6887742008786472960-Q-XX/. [Accessed 11 October 2022].

[203] Laborelec, LinkedIn, [Online]. Available: https://www.linkedin.com/posts/engie-laborelec_boosting-bifacial-pv-plant-yield-by-harnessing-ugcPost-6924256991527763968-QxB5/.

[204] Lightsource BP, LinkedIn, [Online]. Available: https://www.linkedin.com/posts/lightsourcebp_innovation-solar-activity-6907689477582770176-Er1e/. [Accessed 11 October 2022].

[205] M. Klenk, Y. Veschetti, R. Kopecek, H. Nussbaumer, H. Hildebrandt and R. Kreiter, "Chapter 5: Bifacial PV sysems and yield data," in *Bifacial Photovoltaics: Technology, Applications, and Economics*, The Institution of Engineering and Technology, 2018.

[206] O. Rhazi, M. Chiodetti, J. Dupuis, S. Benyakhlef, K. Radouane and P. Dupeyrat, "Optimising the Utilisation of Reflective Materials for Bifacial Plants," in *37th European Photovoltaic Solar Energy Conference and Exhibition* , 2020.

[207] V. Durkovic and Z. Durisic, "Impact of a horizontal reflector on the techno-economic characteristics of large VPV power plants," *Solar Energy,* vol. 220, no. 15, pp. 650-659, 2021.

[208] M. Lamers, E. Ozkalay, R. Gali, G. Janssen, A. Weeber, I. Romijn and B. Van Aken, "Temperature effects of bifacial modules: Hotter or cooler?," *Solar Energy Materials and Solar Cells,* vol. 185, pp. 192-197, 2018.

[209] C. Long and E. Dutton, "BSRN Global Network recommended QC tests v2," Baseline Surface Radiation Network, 2010.

[210] A. Neubert, Interviewee, *DTU validation data.* [Interview]. 5 May 2022.

[211] A. Driesse and J. Stein, "From IEC 61853 power measurements to PV system simulations," Sandia National Laboratories (Report # SAND2020-3877), 2020.

[212] M. Vogt, S. Riechelmann, A. Gracia-Amillo and A. Driesse, "PV Module Energy Rating Standard IEC 61853-3 Intercomparison and Best Practice Guidelines for Implementation and Validation," *IEEE Journal of Photovoltaics,* vol. 12, no. 3, pp. 844-852, 2021.

[213] B. Kirn and M. Topic, "Diffuse and direct light solar spectra modeling in PV module performance rating," *Solar Energy,* vol. 150, p. 310–316, 2017.

[214] A. Baldridge, S. Hook, C. Grove and G. Rivera, "The ASTER spectral library version 2.0," *Remotes Sens Environment,* vol. 113, p. 711–715, 2009.

[215] I. Reda, "Method to Calculate Uncertainties in Measuring Shortwave Solar Irradiance Using Thermopile and Semiconductor Solar Radiometers," National Renewable Energy Laboratory Report (NREL/TP-3B10-52194), 2011.

[216] J. Freeman, D. Freestate, C. Riley and W. Hobbs, "Using Measured Plane-of-Array Data Directly in Photovoltaic Modeling: Methodology and Validation," in *43rd IEEE Photovoltaic Specialists Conference (PVSC)*, Portland, OR, 2016.

[217] Y. Zhang, Y. Yu, F. Meng and Z. Liu, "Experimental Investigation of the Shading and Mismatch Effects on the Performance of Bifacial Photovoltaic Modules," *IEEE Journal of Photovoltaics,* vol. 10, no. 1, 2020.

[218] M. Pravettoni, D. Poh, J. Singh, J. Ho and M. Nakayashiki, "The effect of capacitance on high-efficiency photovoltaic modules: a review of testing methods and related uncertainties," *Journal of Physics D: Applied Sciences,* 2021.

[219] H. Vahlman, "Accurate flash testing ofhigh-efficiency solar cellsand modulesusingCapacitance Compensation," Endeas Oy - Application Note, 2018.

[220] M. Amdemeskel, G. Benatto, N. Riedel, B. Iandolo, R. Davidsen, P. Poulsen, S. Thorsteinsson, A. Thorseth and C. Dam-Hansen, "Indoor measurement of Angle resolved light absorption by antireflective glass in solar panels," in *34th EUPVSEC*, Amsterdam, 2017.

[221] E. Salis, D. Pavanello, M. Field, U. Kraling, F. Neuberger and H. Mullejans, "Improvements in world-wide intercomparison of PV module calibration," *Solar Energy,* vol. 155, pp. 1451-1460, 2017.

[222] C. Monokroussos, S. Dittmann, T. Herbrecht, H. Müllejans, E. Salis, D. Etienne, G. Friesen, J. Stang, V. Fakhfouri, N. Rebeaud and D. Pavanello, "Electrical characterization intercomparison of high-efficiency c-Si modules within Asian and European laboratories," *Progress in Photovoltaics,* vol. 27, pp. 603-622, 2019.

[223] ISO/IEC 17043, "Conformity assessment – General requirements for proficiency testing," 2010.

[224] D. J. Wright, "Closed-Form, Analytic Solution for Diffuse Irradiance on a Tilted, Photovoltaic Collector," *IEEE Journal of Photovoltaics,* vol. 9, no. 2, pp. 391-396, 2019.

[225] B. Marion, "Numerical method for angle-of-incidence correction factors for diffuse radiation incident photovoltaic modules," *Solar Energy,* vol. 147, pp. 344-348, 2017.

[226] H. Holst, M. Winter, M. R. Vogt, K. Bothe, M. Kontges, R. Brendel and P. Altermatt, "Application of a New Ray Tracing Framework to the Analysis of Extended Regions in Si Solar Cell Modules," *Energy Procedia,* vol. 38, pp. 86-93, 2013.

[227] L. Hirth, "The benefits of flexibility: The value of wind energy with hydropower," *Applied Energy ,* vol. 181, pp. 210-223, 2016.

[228] D. Chudinzow, S. Nagel, J. Gusewell and L. Eltro, "Vertical bifacial photovoltaics – A complementary technology for the European electricity supply?," *Applied Energy,* vol. 264, 2020.

[229] D. Moser, S. Lindig, M. Richter, J. Ascencio-Vásquez, I. Horvath, B. Müller, M. Green, J. Vedde, M. Herz, B. Herteleer, W. Karl-Anders and B. Stridh, "Uncertainty in Yield Assessments and PV LCOE (IEA-PVPS T13-18:2020)," International Energy Agency (IEA), 2020.

Appendix

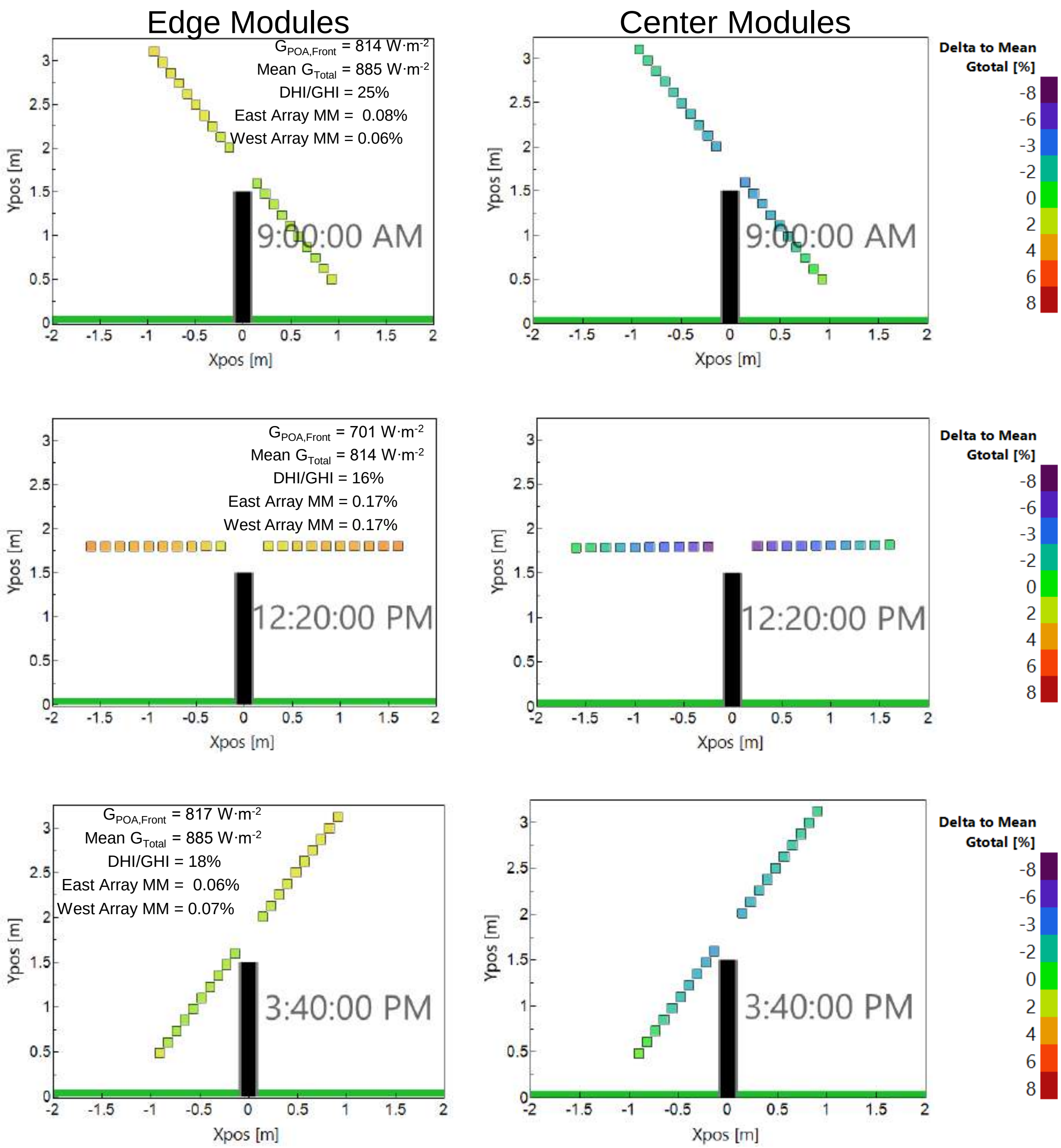

Figure A.1: High resolution rear POA measurements on the back of a 2-in-portrait HSAT during a clear-sky day (albedo = 0.22). The left column of images show measurements from the edge panels and the right column shows measurements from the center panels. The color scale shows the irradiance of each cell location relative to the *total* average irradiance. The dimensions are representative of the tracker position at each timestamp. The array-level non-uniformity induced electrical mismatch for the eastern and western arrays is displayed in the text boxes.

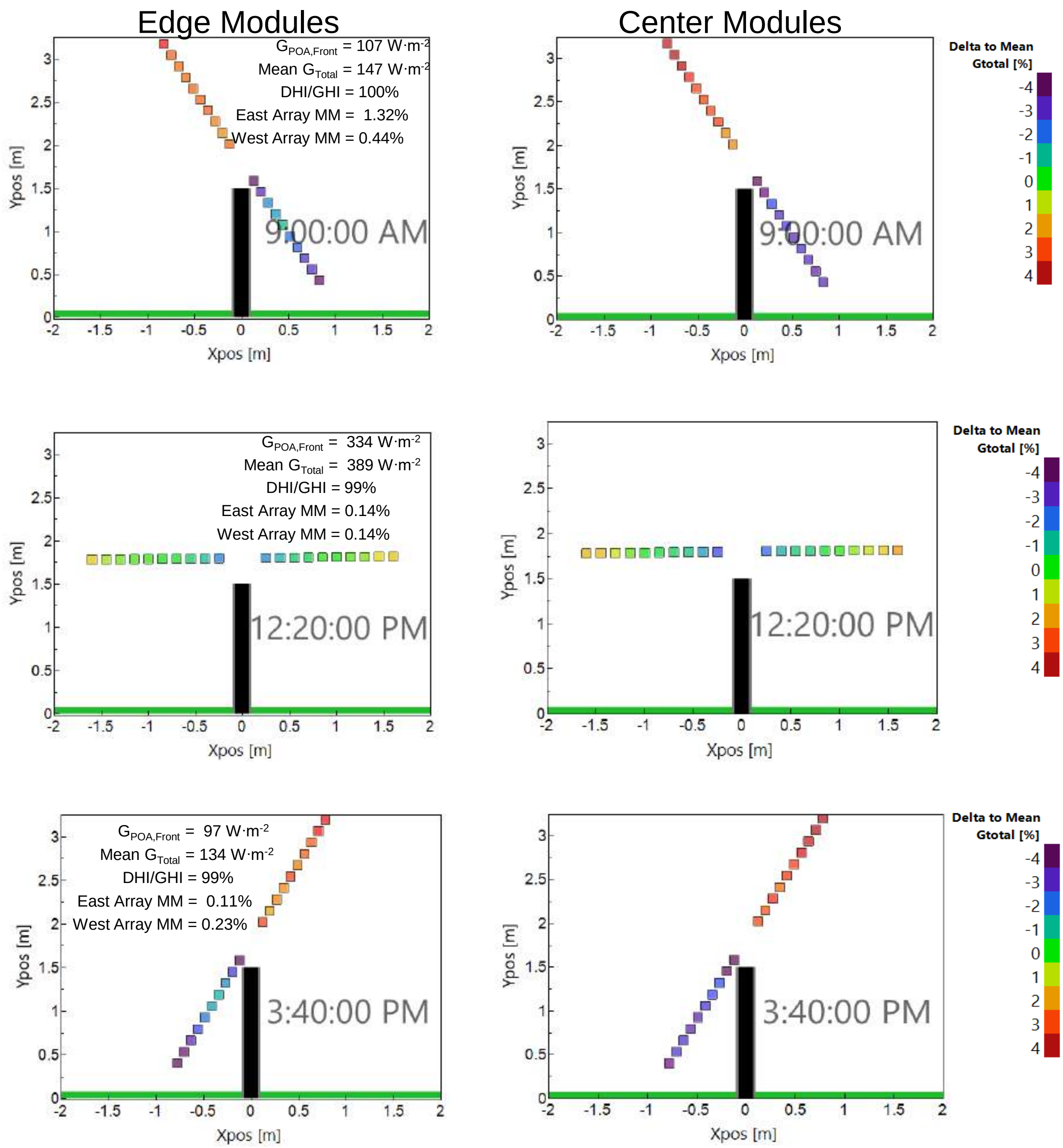

Figure A.2: High resolution rear POA measurements on the back of a 2-in-portrait HSAT during a cloudy day (albedo = 0.22). The left column of images show measurements from the edge panels and the right column shows measurements from the center panels. The color scale shows the irradiance of each cell location relative to the *total* average irradiance. The dimensions are representative of the tracker position at each timestamp. The array-level non-uniformity induced electrical mismatch for the eastern and western arrays is displayed in the text boxes.

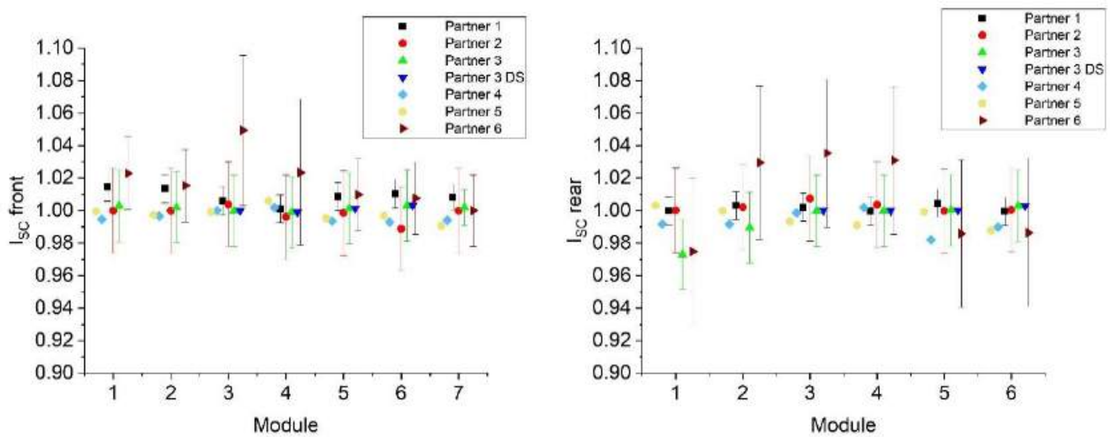

Figure A.3: Front and back I_{SC} results normalized to the group median. These graphs were prepared by George Koutsourakis of NPL within the EMPIR funded PV-Enerate project. DTU is partner number six. Modules 1 and 2 are bifacial n-PERT, modules 3 and 4 are bifacial SHJ, and modules 5 and 6 are bifacial PERC.

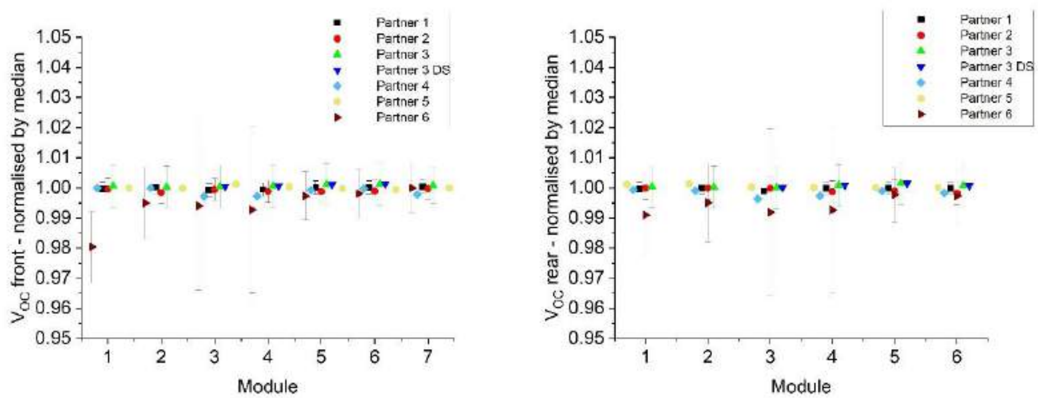

Figure A.4: Front and back V_{OC} results normalized to the group median. These graphs were prepared by George Koutsourakis of NPL within the EMPIR funded PV-Enerate project. DTU is partner number six. Modules 1 and 2 are bifacial n-PERT, modules 3 and 4 are bifacial SHJ, and modules 5 and 6 are bifacial PERC.

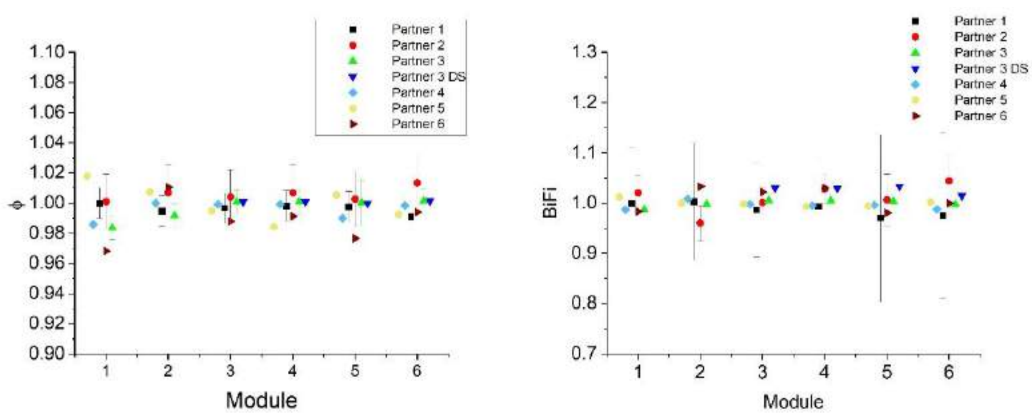

Figure A.5: Bifaciality and BiFi rating results normalized to the group median. These graphs were prepared by George Koutsourakis of NPL within the EMPIR funded PV-Enerate project. DTU is partner number six. Modules 1 and 2 are bifacial n-PERT, modules 3 and 4 are bifacial SHJ, and modules 5 and 6 are bifacial PERC.

Appended Publications

The nine papers that were summarized in Chapters 2 through 5 are provided here in full. Six of the papers are peer-reviewed (five as first author), and three are conference proceedings (all first author). The signed coauthor statements as required by DTU have been submitted separately. Please note that some of the publications appended here are author copies due to copyright.

I. **Riedel-Lyngskær, N.** et al., (2020). Large-Scale Bifacial PV Test Field Performance Compared to Simulations Using Commercially Available Software, Research-Based and Open-Source Tools. In *Proceedings of 37th European Photovoltaic Solar Energy Conference and Exhibition* (pp. 1324-1329)

II. **Riedel-Lyngskær, N.**, et al., (2020). Validation of Bifacial Photovoltaic Simulation Software against Monitoring Data from Large-Scale Single-Axis Trackers and Fixed Tilt Systems in Denmark. *Applied Sciences*, *10*(23),

III. Vogt, R.M., et al., (2022). PV Module Energy Rating Standard IEC 61853-3 Intercomparison and Best Practice Guidelines for Implementation and Validation. *IEEE Journal of Photovoltaics*.

IV. **Riedel-Lyngskær, N.**, et al., (2020). A Spatial Irradiance Map Measured on the Rear Side of a Utility-Scale Horizontal Single Axis Tracker with Validation using Open-Source Tools. In *Proceedings of 47th IEEE Photovoltaic Specialists Conference*

V. **Riedel-Lyngskær, N.**, et al., (2021). Spectral Albedo in Bifacial Photovoltaic Modeling: What can be learned from Onsite Measurements? In *Proceedings of 48th IEEE Photovoltaic Specialists Conference* (pp. 0942-0949).

VI. **Riedel-Lyngskær, N.**, et al., (2021). The effect of spectral albedo in bifacial photovoltaic performance. *Solar Energy*, *231*, 921-935. https://doi.org/10.1016/j.solener.2021.12.023

VII. **Riedel-Lyngskær, N.**, et al., (2021). Interlaboratory comparison of angular-dependent photovoltaic device measurements: Results and impact on energy rating. *Progress in Photovoltaics*, *29*(3), 315-333.

VIII. **Riedel-Lyngskær, N.**, et al., (2022). Measuring Irradiance with Bifacial Reference Panels. *IEEE Journal of Photovoltaics.* https://doi.org/10.1109/JPHOTOV.2022.3201468

IX. **Riedel-Lyngskær, N.**, et al., (2021). Value of bifacial photovoltaics used with highly reflective ground materials on single-axis trackers and fixed-tilt systems: a Danish case study. *IET Renewable Power Generation*, *14*(9), 3946-3953. https://doi.org/10.1049/iet-rpg.2020.0580

Publication I. Large-Scale Bifacial PV Test Field Performance Compared to Simulations Using Commercially Available Software, Research-Based and Open-Source Tools

Authors:

Nicholas Riedel-Lyngskær, Djaber Berrian, Daniel Alvarez Mira, Alexander Aguilar Protti, Sune Thorsteinsson, Peter Poulsen, Joris Libal, and Jan Vedde

Published in:

37th European Photovoltaic Solar Energy Conference (EUPVSEC) 2020

LARGE-SCALE BIFACIAL PV TEST FIELD PERFORMANCE COMPARED TO SIMULATIONS USING COMMERCIALLY AVAILABLE SOFTWARE, RESEARCH-BASED AND OPEN SOURCE TOOLS

Nicholas Riedel-Lyngskær[1], Djaber Berrian[2], Daniel Alvarez Mira[1], Alexander A. Protti[1], Sune Thorsteinsson[1], Peter B. Poulsen[1], Joris Libal[2], Jan Vedde[3]

[1]Technical University of Denmark, Department of Photonics Engineering, Roskilde, Denmark
[2]ISC Konstanz, Konstanz, Germany
[3]European Energy A/S, Søborg, Denmark

ABSTRACT — The aim of this work is to provide the photovoltaic (PV) community with a validation study of eight tools used to simulate bifacial PV performance. We simulate real 26 kWp bifacial p-PERC arrays located within a 420 kWp site located in Northern Europe (55.6°N, 12.1°E). The substructures investigated include horizontal single axis trackers (HSATs) and fixed tilt racks that have dimensions analogous to those found in utility-scale PV installations. Each bifacial system has a monofacial reference system with similar front side power. We use on-site solar radiation (global, diffuse and beam) and albedo measurements from spectrally flat class A sensors as inputs to the simulation tools, and compare modeled values to field measurements of string level DC power and rear plane of array irradiance. Our results show that state-of-the-art bifacial performance models add ~0.5% uncertainty to the PV modeling chain. For the site investigated, 2D view factor fixed tilt simulations are within ±1 % of measured monthly bifacial gain. However, simulations of single axis tracker systems are less accurate, wherein 2D view factor and 3D ray tracing are within approximately 2% and 1% of measured bifacial gain, respectively.

1 INTRODUCTION

In this work we compare eight bifacial PV modeling tools to 1 year of field measurements (April 2019 to March 2020) made on kW scale bifacial and monofacial systems located in Roskilde, Denmark (55.6°N, 12.1°E) (Figure 1). The performance models tested fall into the categories of commercially available (licensed), freeware and open source - a description of each is provided in Table 1. The software often use different models for key steps of the PV modeling chain, which means that differences in simulated energy – and thus bifacial gain –are to be expected. Seven of the software use a 2D view factor (2D VF) method to calculate the rear plane of array irradiance ($G_{POA,Rear}$) and one model uses 3D ray-tracing (3D RT).

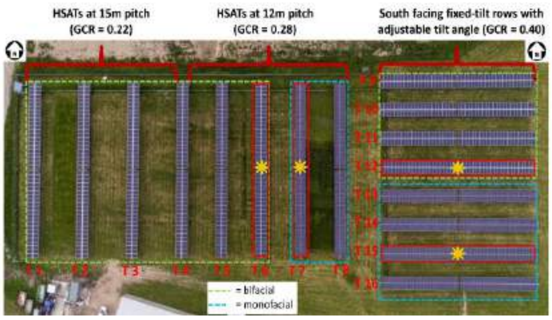

Figure 1: Aerial view of the 420 kWp test site consisting of 45 meter long two-in-portrait substructures. The annotations show the substructure type, pitch and PV module type. The systems where electrical performance and bifacial gain are simulated (T6, T7, T12, and T15) are boxed in red with sun symbols in the middle.

2 FIELD TEST DETAILS

The site includes eight HSATs and eight south facing fixed tilt 45 m long substructures as shown in Figure 1. All 16 substructures (including the south facing units) are Soltec SF7 trackers with two modules in portrait (2P). The inclination of the south facing units is adjustable from 0° to 60°, but the tilt has been programmed to remain at 25° during the period studied here. On each substructure there are mounted 88 PV modules wired into four parallel strings, each containing 22 panels in series. The panels on each substructure are either 60 cell monofacial p-PERC, or 60 cell bifacial p-PERC. The four strings on each substructure are kept at their maximum power point (P_{MP}) by a single maximum power point tracker (MPPT). The DC to AC ratio is 1.04:1, which is substantially lower than what is found in typical utility scale PV installations. The advantage of a this comparatively low DC:AC ratio is that no inverter clipping is observed and that the DC performance at full solar irradiance can be studied.

We make our results comparable to previous studies by including modeled versus measured bifacial energy gain per Eq. (1). Where E_{BF} and E_{MF} are the energy produced by the bifacial and monofacial systems, respectively and $P_{STC,BF}$ and $P_{STC,MF}$ are the front side power ratings of the bifacial and monofacial systems, respectively. The P_{STC} values are obtained from measurements made at DTU using the single lamp front and rear measurement method specified in IEC TS 60904-1-2 [1].

$$BG\,[\%] = \left(\frac{E_{BF}/P_{STC,BF}}{E_{MF}/P_{STC,MF}} - 1\right) \cdot 100 \qquad (1)$$

Note that *bifacialvf* and *pvfactors* (Table 1) do not incorporate cell temperature models or electrical models. Therefore, we also present bifacial gain in terms of rear to frontside irradiance ratios, in order to compare results from all software.

$$BG\,[\%] = \frac{G_{POA,Rear}}{G_{POA,Front}} \cdot BF \cdot (1 - Bifi_{loss}) \cdot 100 \qquad (2)$$

In Eq. (2), *BF* is the rear to frontside efficiency at STC $\eta_{STC,rear}$ / $\eta_{STC,front}$) known as the “bifaciality factor”, which is 0.67 according to the DTU measurements. The $Bifi_{loss}$ term accounts for the electrical losses induced by non-uniform backside illumination and structural shading. In a previous work we studied the backside mismatch of bifacial PV on single axis trackers [2]. From ray tracing and field measurements done in this work, we use 0.025, which is the estimated mismatch on a clear-sky day at solar noon. The tracker manufacturer Soltec published a white paper [3] that recommends 0.007 as a value for structural shading, which is used here. The $Bifi_{loss}$ value used in this work therefore amounts to 0.032.

TABLE I: Descriptions of the bifacial performance tools compared in this study. All tools implement the Perez transposition model for calculating $G_{POA,Front}$ irradiance, although some use DNI and DHI for the transposition while others use GHI and DHI. Also note that the sun position algorithm used among the tools is not always the same.

Bifacial PV Simulation Tool	Version Used	Accessibility	$G_{POA,Rear}$ Method	IAM Model	Electrical Model	Thermal Model	Ref.
bifacialvf	0.1.7	Open source	2D VF	Physical	N.A.	N.A.	[10]
MoBiDiG VF	0.2.4	Proprietary	2D VF	Physical	De Soto 1-diode	Faiman	[14]
MoBiDiG Hybrid (RT)	0.2.4	Proprietary	3D RT	N.A.	De Soto 1-diode	Faiman	[9]
PlantPredict	8.7.0	Freeware	2D VF	ASHRAE	PVsyst 1-diode	Faiman	[10]
pvfactors	1.4.1	Open source	2D VF	Sandia	N.A.	N.A.	[15]
PVsyst	7.0.5	Licensed	2D VF	Physical	PVsyst 1-diode	Faiman	[12]
Solar Advisor Model (SAM)	2020.2.129	Freeware	2D VF	Physical	De Soto 1-diode	NOCT	[10] [13]
SolarFarmer	1.0.187.0	Licensed	2D VF	Martin/Ruiz	PVsyst 1-diode	Faiman	[11]

2.1 *Model Input Data*

Measurements of the broadband diffuse horizontal irradiance (*DHI*), direct normal irradiance (*DNI*), global horizontal irradiance (*GHI*) and albedo are collected onsite with spectrally flat class A sensors. The *DHI*, *DNI*, and *GHI* are filtered according to recommendations published by the Baseline Surface Radiation Network (BSRN) [4]. We have calculated the expanded U_C of each sensor following the Guide to the Uncertainty in Measurement (GUM). Measurement uncertainty (U_C) of pyranometers and pyrheliometers is not a constant value, but rather changes according to the prevailing environmental conditions (e.g. diffuse ratio, sun position, solar variability index etc.). The U_C of the *GHI* is heavily affected by the instrument's cosine response, but only when direct beam light is present. Therefore, the *GHI* increases with decreasing sun elevation angles. We estimate that the expanded (k = 2) U_C of the hourly averaged *GHI* is about ±4.0 % at solar noon on a clear summer solstice, and about ±7.3 % on a clear winter solstice. The uncertainty of the hourly averaged *DNI*, on the other hand, is significantly affected by inter-hour irradiance variability. During hours with little to no variability, the uncertainty of hourly averaged *DNI* is as low as ±2.2 %, but under high solar variability the uncertainty can be as high as ±10.0 %. Such uncertainties of the meteorological data ought to be considered when validating PV performance models, which will be done in a future work.

The seasonal albedo at the site shows little seasonal variation, but monthly average albedo is used in the simulations nonetheless (*min* = 0.192, *mean* = 0.214, *max* = 0.229). Some tools shown in Table 1 are capable of sub-hourly simulations, whereas others are limited to hourly resolution. Hence all simulations shown here are performed using hourly averages of the *GHI*, *DHI*, *DNI*, ambient temperature and wind speed measured onsite.

For the bifacial performance tools that include an electrical model, we use the following data and assumptions for DC performance, AC performance and DC losses. Low irradiance efficiency is determined by the 1-diode parameters used in each performance tool (fitting of I-V data is only at STC). The inverter performance behavior is taken from the manufacturer's datasheet. In each simulation, the total DC loss applied is 2.3 %. This includes losses from light-induced degradation (LID), wiring, and module mismatch.

2.2 *Model Validation Data*

The electrical monitoring system at the test site is independent of the inverter measurements. Every minute the maximum power current (I_{MP}) and voltage (V_{MP}) of each string are measured. Digital filters are applied to the data to remove noise. The expanded uncertainty of the P_{MP} measurement is 0.5 % of full scale.

3 RESULTS

3.1 *Rear Plane of Array Irradiance*

The fundamental challenge in bifacial – as compared to monofacial – PV performance modeling is estimating $G_{POA,Rear}$. Therefore, the discrepancies in simulated bifacial energy production are likely to occur in the derivation of $G_{POA,Rear}$ values. Figure 2 shows one year of simulated $G_{POA,Rear}$ values as a function of the average simulated value. The dispersion of simulated values is nearly the same for the fixed tilt and HSAT system. The range of simulated values among software correlates with the frontside irradiance (R^2 = 0.81–0.85). The range of simulated $G_{POA,Rear}$ values is approximately 20 W·m^{-2} at 1000 W·m^{-2} frontside *POA* irradiance. In other words, the range of $G_{POA,Rear}$ is about 2 % of $G_{POA,Front}$. SolarFarmer is highest in this comparison because its integrated approach does not currently consider the obstruction of sky diffuse irradiance caused by neighboring PV rows. Therefore, the ground reflected irradiance between PV rows is over estimated. To our knowledge, this detail is currently being revised and is expected to be implemented in SolarFarmer versions greater than 1.0.191.2.

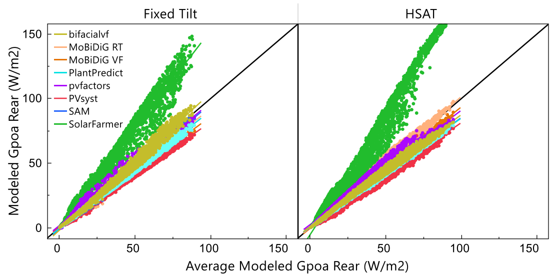

Figure 2: Simulated rear plane of array irradiance as a function of the average of the eight simulation tools. The solid black line is unity to the average.

A comparison of modeled $G_{POA,Rear}$ during five weeks (Feb 21st – Mar 30th, 2020) where measured $G_{POA,Rear}$ data are available on the fixed tilt and HSAT system are shown in Figure 3 and Figure 4, respectively. The simulated results include reflection losses at the PV glass-air interface according to the IAM model implemented in each software. The solid black 45° degree lines in Figure 3 and Figure 4 represent unity to the measurements. The measurements are the average of two EKO MS-40 pyranometers mounted on the backside of the structure: east and west in the case of the HSAT, top and bottom for the fixed tilt. Figure 5 shows an image of the pyranometers (and Si photodiodes) mounted on the backside of tracker T5, twelve panels North of the south edge. Ray trace simulations made by [5] have shown that this 12 m distance into the 45 m long array should be sufficient to remove edge brightening effects and to be representative of the semi-infinite assumption that is common among 2D VF models.

We see that trendlines from seven of the eight software agree well to pyranometer measurements. The mean absolute error (MAE) of said group is 2.3–5.2 W·m^{-2}. The peak total irradiance (i.e. sum of $G_{POA,Front}$ and $G_{POA,Rear}$) measured during this period was approximately 1000 W·m^{-2}. When the magnitude of total irradiance is considered, the MAE of $G_{POA,Rear}$ contributes roughly 0.5 % uncertainty to the bifacial PV modeling chain.

During clear sky (i.e. low diffuse fraction) days, we observed that the bottom pyranometer can receive nearly twice as much irradiance as the top pyranometer. Therefore, the black unity line in Figure 3 – which represents the average measurement from two sensors – can at times have error bars on the order of ±15 W·m^{-2}. On such clear sky days, seven of the eight software studied give $G_{POA,Rear}$ results that are within that range. In other words, when the vertical spatial non-uniformity of irradiance is considered, the reduced-order complexity 2D VF models perform reasonably well for fixed tilt simulations.

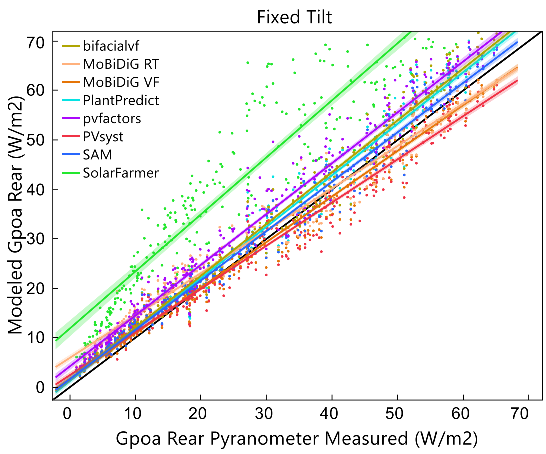

Figure 3: Simulated rear plane of array irradiance on the fixed tilt sytem as a function of measured for a 5-week period. The solid black line represents unity to the measurements. The shaded areas around each regression line indicate the 95 % confidence intervals. The measurements are made 17 m into T11 (Figure 1).

The simulated $G_{POA,Rear}$ values on the single axis tracker mostly under estimate the pyranometer measurements. Additionally, the agreement to measurements is not as good as the fixed tilt scenario. The MAE of the 3D RT model and six out of seven 2D VF models is between 3.5–6.7 W·m^{-2}. This result makes sense considering that the HSAT system introduces additional complexity – and thus additional degrees of freedom for error – at two levels. First, the tracker algorithm implemented by the software is introduced to the comparison and second, the VFs in HSAT simulations are calculated for each change in tilt angle whereas the VFs in fixed tilt simulations are calculated once for the entire simulation. Note that the 3D RT simulation over predicts $G_{POA,Rear}$ in the HSAT scenario, which could be due to the fact that this model currently does not incorporate backside IAM losses.

Our $G_{POA,Rear}$ measurements over grass have shown that – under most conditions – the tracker side that is farthest from the ground receives more irradiance than the side closest to the ground. In other words, in the morning the western sensor typically reports higher measurements than its eastern counterpart, whereas the trend reverses in the afternoon. We found that the differences between eastern and western $G_{POA,Rear}$ pyranometer measurements on the HSAT system were not as extreme as differences between the top and bottom $G_{POA,Rear}$ measurements on the fixed tilt system. On a clear sky day, we observed differences on the order of 10 W·m^{-2} between western and eastern pyranometers. Although five of eight software agree within 5 W·m^{-2} of each other, none of the same five tools overlap the measurement uncertainty bars. This result likely could change if alternative backside pyranometer locations were chosen. Therefore, the PV industry could benefit from a standardized best-practice protocol for mounting rear plane of array irradiance sensors in bifacial PV monitoring systems.

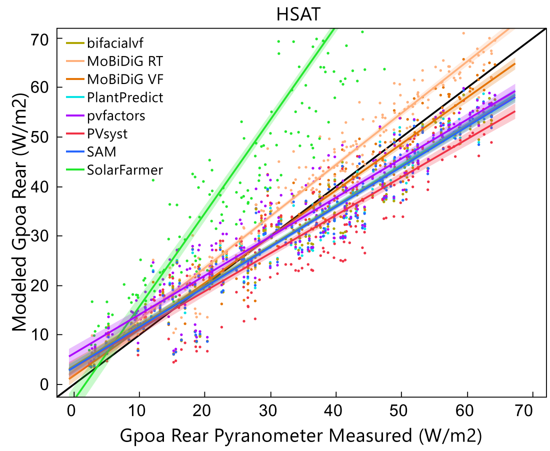

Figure 4: Simulated rear plane of array irradiance on the HSAT as a function of measured for a 5-week period. The solid black line represents unity to the measurements. The shaded areas around each regression line indicate the 95 % confidence intervals. The measurements are made 12 m into T5 (Figure 1).

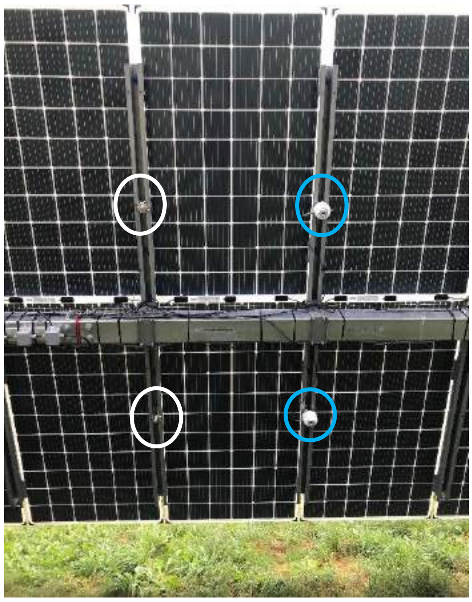

Figure 5: Optical sensors mounted on the backside of T5. The Si photodiodes are circled in white and the pyranometers are circled in blue. The sensors are located 11 modules North of the array's south edge. Note that sensor placement is similar on the fixed tilt system (T11).

3.2 *Bifacial Gain*

Figure 6 shows the monthly bifacial gain from software with capability of simulating electrical performance. The black lines in each plot show the results from the DC string measurements. Recall that the measured results are normalized with the I-V measurements made at DTU per equation (1). If the normalization were instead made using the manufacturer's nameplate rating, the measured bifacial gain according to

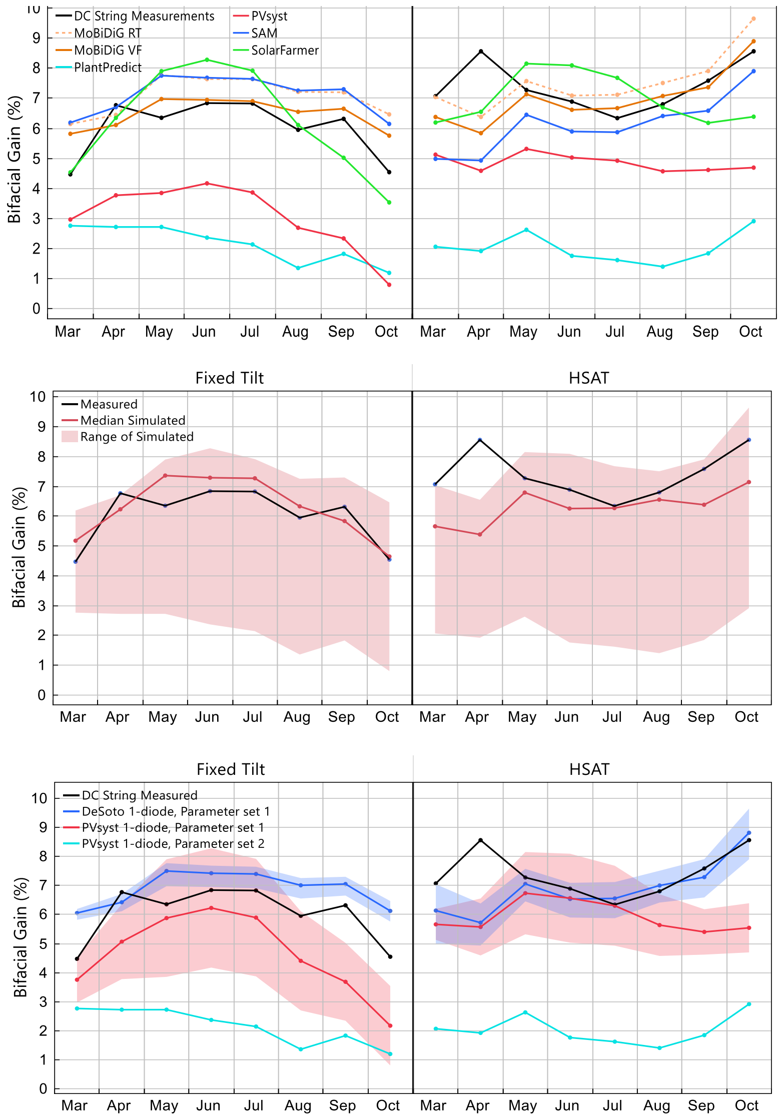

Figure 6: Monthly bifacial gain from DC power simulated by six software and from DC string measurements. The left column shows results from the fixed tilt system, and the right column shows the single axis tracker results. Each row shows the same data but grouped in different ways. The first row shows the results grouped by software (Table 1), the second row is grouped by measurement/simulation, and the third row groups results by which 1-diode model and parameter set was used.

Eq. (1) would be 1.5 % higher than what is shown. This difference can significantly affect the economics of project decisions that are made based on an expected bifacial energy gain.

The results in Figure 6 (and Figure 7) only include datapoints where sun elevation is greater than 15°. This filter is why November through February are not shown: the sun elevation in Denmark is too low during these months. During winter months, there is a significant amount of inter-row shading on the fixed tilt system and even some shading on the HSAT from surround objects. We chose to exclude periods of severe shade-loss because during such times, the simulated results become heavily affected by the shade-model and by the backtracking model used by each software. It was not this work's objective to assess the performance of the shading and backtracking models.

The measured bifacial gain on the fixed tilt system is between 4.5–7.0 %. Meanwhile, the bifacial gain on the tracker is consistently higher - between 6.3–8.5 %. This is likely due to the wider 12 m spacing between rows on the HSAT (GCR = 0.28) versus the narrower 7.6 m spacing on the fixed tilt system (GCR = 0.4), which creates more self-shading within the inner rows of the PV park.

The simulated bifacial gain values mostly follow the trends of the measurements, except for April when a small spike in bifacial gain is observed on both the fixed tilt and HSAT system. Since the measured albedo data from April 2019 were higher than any other month studied here (0.229), and since the spike in bifacial gain is observed in both systems, it could be that the measurements from the onsite albedometer were not representative of the overall site during this month. If this is true, then it could mean that a best-practice for bifacial PV monitoring systems is the implementation of redundant albedometers throughout the park – similar to the well-known best practice for frontside plane-of-array pyranometers.

One notable outcome in Figure 6 is the results from SolarFarmer are frequently within 1 % of the measured bifacial gain, despite the deviations in $G_{POA,Rear}$ shown previously. This is due to the fact that the rear irradiance constitutes 8 % or less of the total irradiance for half of the timestamps studied here. Of course, the higher the albedo and/or the higher the module bifaciality factor, the larger influence modeled $G_{POA,Rear}$ is expected to contribute to the overall model accuracy.

The bottom row of Figure 6 shows the simulated bifacial gains grouped into which of the two electrical models was used and – in the case of the PVsyst 1-diode model – which of two parameter sets was used. Recall that the parameters used within each electrical model were determined by a fit to measured I-V data at STC – i.e. low irradiance measurements were not considered. We found that the six parameters used in the DeSoto 1-diode model

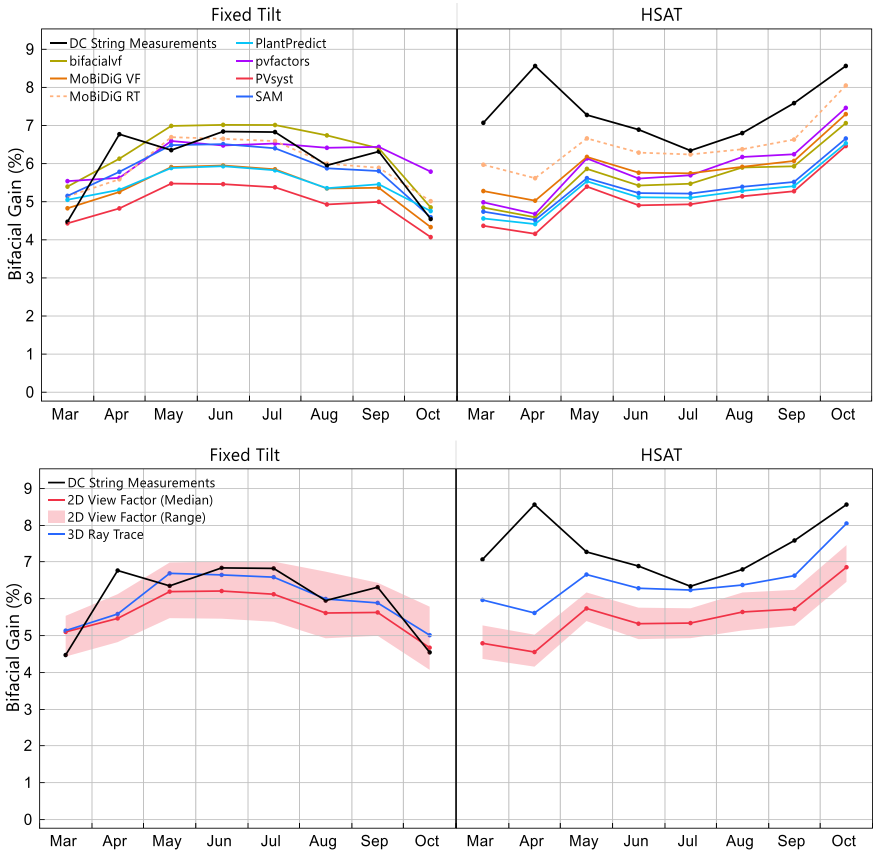

Figure 7: Monthly bifacial gain from modeled rear to front side irradiance ratios (equation 2) from seven software and from DC string measurements. The left column shows results from the fixed tilt system, and the right column shows the single axis tracker results. Both rows show the same data but grouped in different ways. The first row shows the results grouped by software (Table 1), the second row is grouped by whether a 2D view factor or 3D ray trace approach was used to calculate back side irradiance.

(used by MoBiDiG and SAM) more accurately predicted measured low light performance than did the five parameters used in the PVsyst 1-diode mode (used by PVsyst, PlantPredict and SolarFarmer). Therefore, we believe this is why the software that used the DeSoto 1-diode model, more accurately predicted the measured bifacial gain. Future work should use 1-diode parameters that are optimized for a range of irradiance and temperature conditions, for example as done in [6]. The reason there are two parameter sets used among software implementing the PVsyst 1-diode model is that PlantPredict sets limits based on what its developers consider to be realistic. Specifically, series resistance of the module must be ≥ 100 mΩ. Due to this restriction, the series resistance used in the PlantPredict bifacial module file was ten times higher than the 10 mΩ extracted from fitting the I-V data, and used in the PVsyst and SolarFarmer models. Therefore, the modeled voltages of bifacial systems in PlantPredict were lower than in PVsyst and SolarFarmer, which resulted in the lowest simulated bifacial gain of all software.

Figure 7 shows the simulated bifacial gain according to the $G_{POA,Rear}$ to $G_{POA,Front}$ ratio (Eq. 2). The modeled results show better agreement with each other when the bifacial gain is calculated using the optical gain as in Eq. (2), as opposed to using the simulated energy as in Eq (1). The agreement among software shown in Figure 7 is within 2 % or better for both system types. The bottom row of Figure 7 shows the results grouped by whether $G_{POA,Rear}$ is calculated using a 2D VF or 3D RT approach. When visualized in this manner, it becomes clear that the 3D RT approach follows the measured bifacial gain most closely for the HSAT simulation - within 0.5 % of measurement for most months. The 3D RT model also matches well – typically within 0.5 % – to bifacial gain measurements on the fixed tilt system. However, 2D VF models such the one integrated in SAM compared equally well to field measurements. Indeed, the measured bifacial gain shown in Figure 7 are influenced by the value of $Bifi_{loss}$. The static $Bifi_{loss}$ values used here, in actuality change dynamically over the day with the prevailing conditions [2], [7], [8]. However, all the software tested here have the capability to use only a single value. This simplification offers room to improve the accuracy of the bifacial PV performance software used in industry today.

4 SUMMARY

We have assessed eight bifacial PV performance tools to $G_{POA,Rear}$ and to DC P_{MP} measurements made at a 420 kWp test site in Roskilde, Denmark. Our results show that state-of-the-art bifacial performance models add ~**0.5% uncertainty** to the PV modeling chain. This finding was demonstrated using $G_{POA,Rear}$ measurements, but in a future more detailed report, we will show how the modeled and measured DC P_{MP} substantiate this finding.

Our results further show that – for the site investigated – 2D view factor fixed tilt simulations are within ±1 % of measured monthly bifacial gain. Simulations of single axis tracker systems are less accurate with 2D view factor simulations within approximately 2% and 3D ray tracing within approximately 1% of measured bifacial gain, respectively. These results are published with the motivation that similar studies from other parts of the globe are published, and a comprehensive review of those studies be made in the near future.

5 ACKNOWLEDGEMENTS

The work made on behalf of DTU, ISC Konstanz, and European Energy A/S was made possible by the Danish Energy Technology Development and Demonstration Program (EUDP) under project contract 64018-0624. We thank Mark Mikofski and Anja Neubert from DNV GL, Kendra Conrad of First Solar and Chris Deline of NREL for reviewing parts of this work.

This publication is based upon work from COST Action CA16235 PEARL PV supported by COST (European Cooperation in Science and Technology). We thank the members of WG3 for the substantive discussions on bifacial PV performance.

6 REFERENCES

[1] IEC TS, "Measurement of current-voltage characteristics of bifacial photovoltaic (PV) devices," *60904-1-2*, 2018.

[2] N. Riedel-Lyngskær, M. Petit, D. Berrian, P. Poulsen, J. Libal and M. Jakobsen, "A Spatial Irradiance Map Measured on the Rear Side of a Utility-Scale Horizontal Single Axis Tracker with Validation using Open Source Tools," in *47th IEEE PVSC*, 2020.

[3] J. Guerrero-Perez and J. N. Berbel, "BiTEC : How to simulate bifacial projects ? BiTEC Results 2 - Fall 2018 - Winter 2019," *Soltec Whitepaper*, 2019.

[4] C. Long and E. Dutton, "BSRN Global Network recommended QC tests v2," Baseline Surface Radiation Network, 2010.

[5] S. A. Pelaez, C. Deline, S. M. Macalpine, B. Marion, J. S. Stein and R. K. Kostuk, "Comparison of Bifacial Solar Irradiance Model Predictions with Field Validation," *IEEE Journal of Photovoltaics*, vol. 9, no. 1, pp. 82-88, 2019.

[6] K. Sauer, T. Roessler and C. Hansen, "Modeling the Irradiance and Temeprature Dependence of Photovoltaic Modules in PVsyst," *IEEE Journal of Photovoltaics*, vol. 5, no. 1, pp. 152-158, 2015.

[7] C. Deline, S. Pelaez, S. MacAlpine and C. Olalla, "Estimating and parameterizing mismatch power loss in bifacial photovoltaic systems," *Progress in Photovoltaics Res. Appl.*, pp. 1-13, 2020.

[8] K. McIntosh, M. Abbott, B. Sudbury and J. Meydbray, "Mismatch Loss in Bifacial Modules Due to Nonuniform Illumination in 1-D Tracking Systems," *IEEE Journal of Photovotaics*, vol. 9, no. 6, pp. 1504-1512, 2019.

[9] D. Berrian, J. Libal, M. Klenk, H. Nussbaumer and R. Kopecek, "Performance of Bifacial PV Arrays With Fixed Tilt and Horizontal Single-Axis Tracking: Comparison of Simulated and Measured Data," *IEEE Journal of Photovoltaics*, vol. 9, no. 6, pp. 1583-1589, 2019.

[10] B. Marion, S. MacAlpine, C. Deline, A. Asgharzadeh, F. Toor, D. Riley, J. Stein and C. Hansen, "A Practical Irradiance Model for Bifacial PV Modules," no. June, pp. 1537-1542, 2018.

[11] M. Mikofski, "SolarFarmer Bifacial Modelling," *PV Systems Symposium Albuquerque New Mexico.*

[12] A. Mermoud and B. Wittmer, "Bifacial shed simulation with PVSyst," *Bifacial Workshop 2017, Konstanz, Germany.*

[13] N. Diorio and C. Deline, "Bifacial Simulation in SAM System Advisor Model (SAM)," *Bifi PV 2018 Workshop – Lakewood, Colorado*, 2018.

[14] D. Berrian, J. Libal and S. Glunz, "MoBiDiG Simulations and LCOE," in *Bifacial Workshop*, Konstanz, 2017.

[15] M. Anoma, D. Jacob, B. Bourne, J. Scholl, D. Riley and C. Hansen, "View Factor Model and Validation for Bifacial PV and Diffuse Shade on Single-Axis Trackers," in *44th IEEE Photovoltaic Specialist Conference*, 2017.

Publication II. Validation of bifacial photovoltaic simulation software against monitoring data from large-scale single-axis trackers and fixed tilt systems in Denmark

Authors:

Nicholas Riedel-Lyngskær, Djaber Berrian, Daniel Alvarez Mira, Alexander Aguilar Protti, Peter Poulsen, Joris Libal, and Jan Vedde

Published in:

Applied Sciences 2020, 10(23), 8487

Validation of Bifacial Photovoltaic Simulation Software against Monitoring Data from Large-Scale Single-Axis Trackers and Fixed Tilt Systems in Denmark

Riedel-Lyngskær, Nicholas; Berrian, Djaber; Alvarez Mira, Daniel ; Aguilar Protti, Alexander Corazon de; Poulsen, Peter Behrensdorff; Libal, Joris; Vedde, Jan

Published in:
Applied Sciences

Link to article, DOI:
10.3390/app10238487

Publication date:
2020

Document Version
Publisher's PDF, also known as Version of record

applied sciences

MDPI

Article

Validation of Bifacial Photovoltaic Simulation Software against Monitoring Data from Large-Scale Single-Axis Trackers and Fixed Tilt Systems in Denmark

Nicholas Riedel-Lyngskær [1,*], Djaber Berrian [2], Daniel Alvarez Mira [1], Alexander Aguilar Protti [1], Peter Behrensdorff Poulsen [1], Joris Libal [2] and Jan Vedde [3]

1 Department of Photonics Engineering, Technical University of Denmark, 4000 Roskilde, Denmark; damir@fotonik.dtu.dk (D.A.M.); s172151@student.dtu.dk (A.A.P.); ppou@fotonik.dtu.dk (P.B.P.)
2 ISC Konstanz, 78467 Konstanz, Germany; djaber.berrian@isc-konstanz.de (D.B.); joris.libal@isc-konstanz.de (J.L.)
3 European Energy A/S, 2860 Søborg, Denmark; jve@europeanenergy.dk
* Correspondence: nrie@fotonik.dtu.dk

Received: 02 November 2020; Accepted: 24 November 2020; Published: 27 November 2020

Featured Application: This work can assist photovoltaic (PV) project developers and financiers with bankability assessments and due diligence of PV simulation software. In addition, the real-world bifacial gains presented here can inform PV developers' expectations in pre-construction phases.

Abstract: The size and number of utility-scale bifacial photovoltaic (PV) installations has proliferated in recent years but concerns over modeling accuracy remain. The aim of this work is to provide the PV community with a validation study of eight tools used to simulate bifacial PV performance. We simulate real 26 kilowatt-peak (kW_P) bifacial arrays within a 420-kW_P site located in northern Europe (55.6° N, 12.1° E). The substructures investigated include horizontal single-axis trackers (HSATs) and fixed tilt racks that have dimensions analogous to those found in utility-scale PV installations. Each bifacial system has a monofacial reference system with similar front side power. We use on-site solar radiation (global, diffuse, and beam) and albedo measurements from spectrally flat class A sensors as inputs to the simulation tools, and compare the modeled values to field measurements of string level power, rear and front plane of array irradiance, and module temperature. Our results show that state-of-the-art bifacial performance models add ~0.5% uncertainty to the PV modeling chain. For the site investigated, 2-D view factor fixed tilt simulations are within ±1% of the measured monthly bifacial gain. However, simulations of single-axis tracker systems are less accurate, wherein 2-D view factor and 3-D ray tracing are within approximately 2% and 1% of the measured bifacial gain, respectively.

Keywords: bifacial PV; PV performance; model validation; bifacial gain; single-axis trackers

1. Introduction

Bifacial photovoltaics (PV) has entered the mainstream market in recent years due to enhanced energy yields, which are enabled by the conversion of light impinging on the module's backside into useable photocurrent. A testament to the widespread adoption of bifacial PV is that multi-megawatt-scale bifacial PV projects are now being deployed in latitudes as far north as Denmark (56° N) in technology neutral auctions [1]. However, the validation of the modeled bifacial performance to the actual performance of fielded systems remains an ongoing task for the PV industry [2–6]. As more bifacial model validation studies are published from sites around the globe, the expectations that PV buyers and investors have regarding bifacial field performance will be in better alignment with actual field performance. If such validations of bifacial simulations are found to be within acceptable agreement, this has the potential to de-risk bifacial PV investments and thus lower soft costs. A key aim of this study is to contribute to this ongoing bifacial performance model validation effort.

The recent bifacial modeling literature contains several studies that include some form of model validation [7–24]. Most bifacial performance model validation to date has been done using small PV systems. A shortcoming of studies on small-scale bifacial systems is that the observed bifacial gains are not representative of bifacial gains at the utility scale. This is because the long and repetitive rows in utility-scale systems lead to a significant amount of self-shading, and since utility-scale strings consist of many modules in series, the backside irradiance enhancement at array edges increases bifacial gain to a much lower extent than on small standalone systems with far less self-shading.

Nevertheless, the bifacial validation results reported to date mostly show good agreement to field measurements. For example, the authors in [16] compared the measured irradiance gain and bifacial gain on horizontal single-axis trackers (HSATs) in Eastern Oregon, USA and Albuquerque, USA to view factor (VF) and ray-trace (RT) simulations. They found that the measurements matched their modeled values within the measurement uncertainty. A separate validation study performed by [13] looked at the rear plane of array irradiance ($G_{POA,Rear}$) from four simulation tools (pvfactors, bifacialvf, bifacial_radiance, and PVsyst) and compared them to measurements on a fixed-tilt system in Albuquerque, USA and an HSAT system in Davis, USA. Their results showed that the long-term (3 to 12 months) irradiance gain as modeled by these four tools agreed within 1% of their measurements when the ground albedo varied from 0.16 to 0.56. The authors in [20] compared modeled and measured daily energy (kWh) of a single panel within a mechanically maneuverable 12-panel setup in Switzerland. They reported agreement mostly within ±1% for static tilt angles from 0° to 45°. However, the authors mention that a short-coming of their study is that it was only performed over a 3-day period, and go on to conclude that definitive error correlations could emerge if the data were analyzed over longer time scales. The need for bifacial PV model validation on large-scale systems and on long timescales is addressed in this paper.

Our objective was to use a consistent set of parameters and meteorological data as input to different bifacial PV software and to analyze the modeled outputs at various steps of the PV performance modeling chain. It was not our intent to analyze the variability that can be introduced by different users of the same software, as this has been studied by other authors [25,26]. These studies revealed that even expert users can make widely different assumptions for the same parameter or loss factor, and for this reason, we performed a sensitivity analysis on key parameters at the end of this paper. Please note that we presented a preliminary version of this work in [27] but expand on it here with consideration for the uncertainty of the onsite-measured solar radiation input data and deeper analyses of the modeling sub-steps and performance metrics.

2. Materials and Methods

2.1. PV Simulation Software Tested

The performance models tested in this work fall into categories of commercially available (licensed), freeware, and open source. A description of each software used in the comparison is provided in Table 1. Seven of the models use a 2-D VF method to calculate $G_{POA,Rear}$ and one model uses a 3-D RT-based method. The 3-D RT method can simulate detailed features of the mounting structure, such as the torque tube and mounting rails, whereas the 2-D VF method simplifies the structural geometry to drastically reduce computation time. The 3-D RT simulations performed in this work required more than 12 h to complete a full-year simulation without a cumulative sky approach. In contrast, the 2-D VF simulations required between 10 s and 5 min to complete a full-year simulation of one PV system. Specifically, annual simulations were completed in less than 10 seconds in PlantPredict (First Solar Inc., Tempe, Arizona, USA), PVsyst (PVsyst SA, Satigny, Switzerland, System Advisor Model (SAM) (National Renewable Energy Laboratory, Golden, Colorado, USA), and SolarFarmer (DNV GL, Bristol, UK). Annual simulations in bifacialvf (National Renewable Energy Laboratory, Golden, Colorado, USA), pvfactors (SunPower Corporation, San Jose, California, USA), and MoBiDiG VF (ISC Konstanz, Konstanz, Germany) were completed in <1, <3, and <5 min, respectively. Simulations were performed using a Dell 7400 (Round Rock, Texas, USA) laptop with an Intel i7-8665U processor (Santa Clara, CA, USA) and 16 GB of RAM, or similar.

We believe that the software shown in Table 1 are representative of the state-of-the-art tools used within the industry and research community to simulate bifacial PV performance. We do not report on the useability of the different PV software, as this was outside the scope of the present work and is currently being assessed by the members of working group 3 (WG3) within the Pearl PV CA16235 project funded by the European Cooperation in Science and Technology (COST) program. There are several instances in Table 1 where multiple software use the same model for a particular modeling step. For example, all software use the Perez diffuse model to transpose horizontal solar radiation data to the plane of array ($G_{POA,Front}$). It has been demonstrated by [28] that the implementation of the same model can vary among software, which will be considered in the results section that follows.

Table 1. Descriptions of the bifacial performance tools compared in this study. All tools implement the Perez transposition model for calculating global irradiance on the frontside plane of array.

PV Simulation Tool	Sun Position Algorithm	Irradiance Input	$G_{POA,Rear}$ Method	IAM Model	1-Diode Electrical Model	Thermal Model	Ref.
bifacialvf (0.1.7)	Michalsky	DNI, DHI	2-D VF	Air-glass [1]	N.A.	N.A.	[8]
MoBiDiG VF (0.2.4)	NREL SPA	DNI, DHI	2-D VF	Air-glass [1]	5 param. De Soto	Faiman	[14]
MoBiDiG Hybrid (RT)	Michalsky	DNI, DHI	3-D RT	N.A.	5 param. De Soto	Faiman	[29,30]
PlantPredict (8.7.0)	NREL SPA	GHI, DHI	2-D VF	ASHRAE	PVsyst	Faiman	[8,31]
pvfactors (1.4.1)	NREL SPA	DNI, DHI	2-D VF	Sandia	N.A.	N.A.	[9]
PVsyst (7.0.5)	US Navy	GHI, DHI	2-D VF	Air-glass [1]	PVsyst	Faiman	[32]
System Advisor Model (2020.2.29)	Michalsky	DNI, DHI	2-D VF	Air-glass [1]	6 param. De Soto	NOCT	[33]
SolarFarmer (1.0.187.0)	NREL SPA	GHI, DHI	2-D VF	Martin & Ruiz	PVsyst	Faiman	[34,35]

[1] IAM losses calculated using a "slab" approach similar or identical to that described in [36].

2.2. PV Test Facility at Technical University of Denmark (DTU)

We compared the outputs from eight bifacial PV modeling tools to 12 months of field measurements (April 2019 to March 2020) made on kilowatt-scale bifacial and monofacial systems located in Roskilde, Denmark (55.6° N, 12.1° E). The site includes eight HSATs and eight south-facing fixed-tilt 45-m-long substructures as shown in Figure 1.

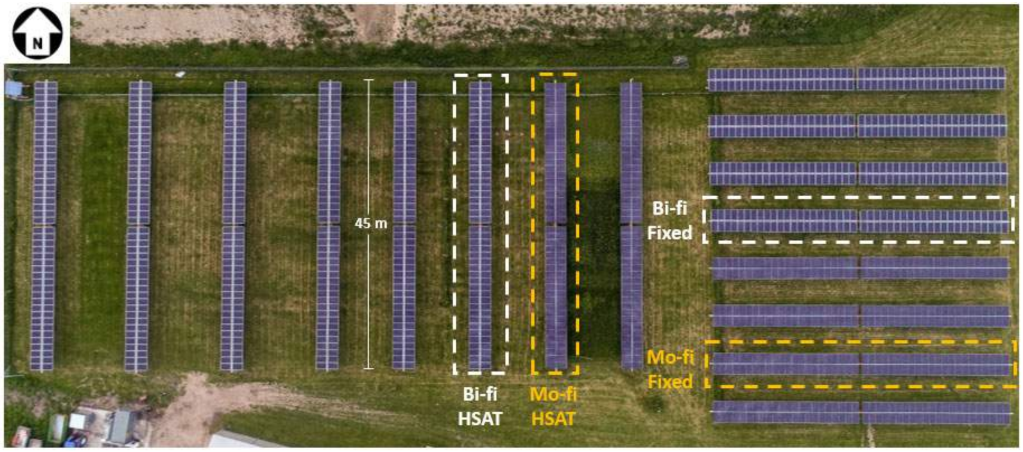

Figure 1. Aerial view of the test facility. There are eight horizontal single-axis trackers (HSATs) and eight fixed-tilt rows. The bifacial (bi-fi) and monofacial (mo-fi) systems investigated in this paper are highlighted in white and orange, respectively.

All 16 substructures (including the south facing units) are SF7s (Soltec, Madrid, Spain) with 2 modules in portrait. The bifacial substructures feature a torque tube and mounting rails that do not directly cover the backside of the PV modules (Figure 2a). The inclination of the south-facing structures is adjustable from 0° to 60°, but the tilt was programmed to remain at 25° during the 12-month period studied here. On each substructure, 88 PV modules are mounted, wired into four series strings (i.e., 22 panels per string). The panels on each substructure are either 60 cell monofacial with a 305-W_P rating, or 60 cell bifacial with a 295-W_P front side rating. The cell technology in both module types is passivated emitter and rear contact (PERC). The four strings on each substructure are kept at their maximum power point (P_{MP}) by a single maximum power point tracker. The ratio of direct current (DC) to alternating current (AC) capacity is 1.04:1, which is substantially lower than what is found in typical utility-scale PV installations. The advantage of this comparatively low DC:AC ratio is that no inverter clipping is observed and that the DC performance at full solar irradiance can be studied. The ground cover ratio (GCR) is 0.28 for the HSAT field and 0.40 for the field of fixed-tilt field systems, both of which are slightly lower than in typical utility-scale systems with limited land area. The irradiance sensors are cleaned approximately on a weekly basis. Although the PV arrays are never cleaned—other than by rainfall events—our soiling measurements made at a 50 MW utility-scale PV site in Hanstholm, Denmark show very low (<0.25%) soiling ratios. Therefore, 0.25% soiling losses are applied in the simulations.

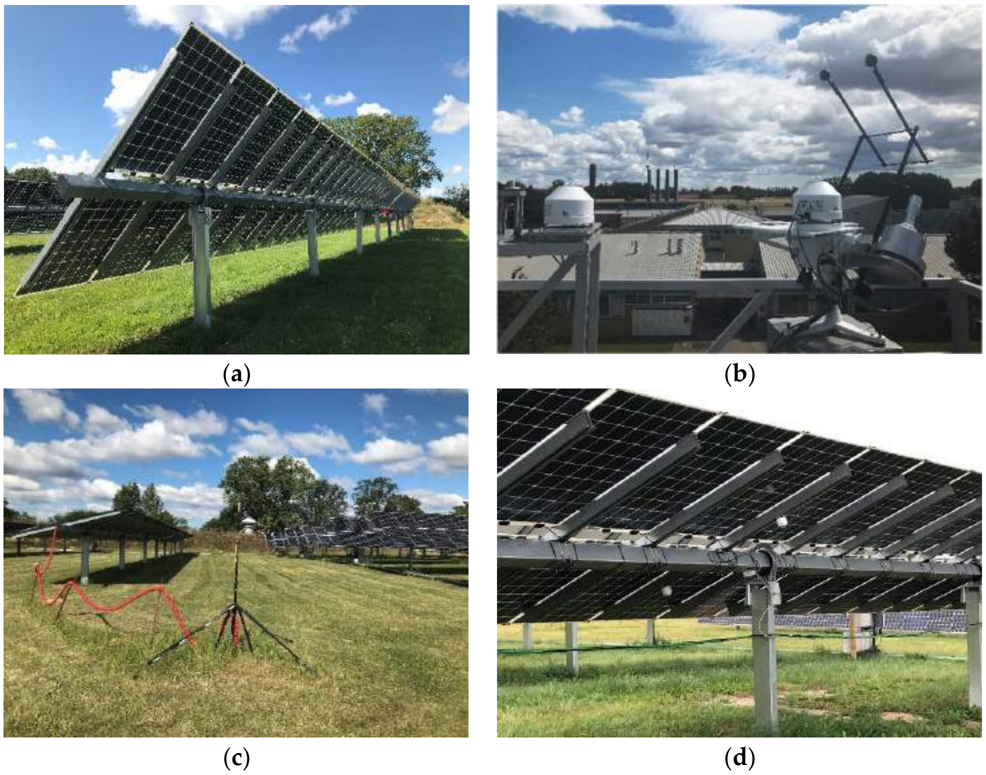

Figure 2. (**a**) Ground-level view of the bifacial HSAT system; (**b**) Onsite solar radiation monitoring tower where the broadband global horizontal (GHI), diffuse horizontal (DHI), and direct normal irradiance (DNI) measurements are recorded. (**c**) Onsite albedometer. (**d**) Two rear plane of array pyranometers (top and bottom circled in blue) on the fixed-tilt bifacial system; Sensors are placed 17 m from the nearest array edge.

2.3. *Input Data for Simulations*

In this section, we describe the methods to compile the input data used in the simulations. The values of selected parameters are summarized in Appendix A.

2.3.1. Electrical Performance and Direct Current (DC) Losses

For the bifacial performance tools that include an electrical model, we used the following data and assumptions for DC performance, AC performance, and DC losses. The current-voltage (I-V) characteristics of the PERC panels were measured before field deployment in an QuickSun Xe-arc flasher (Endeas, Espoo, Finland) using the single lamp front and rear side measurement method specified in IEC TS 60904-1-2 [37]. The modules are temperature stabilized in the flash chamber within ±1 °C of 25 °C, which ensured that the PV cells are close to the ambient room temperature. Measurements of the ambient (i.e., room) temperature are then used as a surrogate for cell temperature (i.e., cell temperature is not directly measured). The calibration module is a cell-technology-matched PERC module with traceability to Fraunhofer ISE's CalLab.

The average front-side P_{MP} measurements of the samples were roughly 8 W low (−2.7%) to the manufacturer's rating. The literature review presented in [38] shows that such divergence from the manufacturer's nameplate rating is common among external testing laboratories. I–V curves at multiple irradiances (200–1000 W·m^{-2}) were also acquired in the DTU flasher system. We used the multi-irradiance I–V data, and a method described by [39] implemented in pvlib python [40] to extract the 1-diode model parameters that are used in PlantPredict, PVsyst, and SolarFarmer. The 1-diode model parameters used in SAM and MoBiDiG were extracted using a method described by [41] and incorporated into SAM's user interface [42] (see Table A3). The inverter performance was taken from the manufacturer's datasheet. After 14 months of field exposure, we repeated the indoor flash I-V tests on a sample of monofacial modules (n = 25). The results from the tests showed P_{MP} losses of 1% or less due to first-year degradation. These losses are most likely due to light-induced degradation (LID) since the electroluminescence images showed no signs of cell cracking or potential-induced degradation (PID). In each simulation, the total DC losses applied amount to 2.3% (see Table A5). This figure includes losses from LID, wiring, soiling, and module mismatch.

2.3.2. Solar Radiation Measurements and Uncertainty

Some modeling tools shown in Table 1 are capable of sub-hourly simulations, whereas others are limited to an hourly resolution. Hence, all simulations shown here were performed using hourly averages of the global horizontal irradiance (GHI), diffuse horizontal irradiance (DHI), direct normal irradiance (DNI), ambient temperature (T_{AMB}), and wind speed measured onsite. Measurements of broadband GHI, DHI, DNI, and albedo were collected onsite with spectrally flat class A sensors, with ventilation units underneath the GHI and DHI sensors (Figure 2b,c). The ventilation unit consists of a fan below the sensor base, which mitigates the accumulation of dust, snow, and ice on the glass dome. The DHI, DNI, and GHI are sampled every 10 s and are filtered according to recommendations published by the Baseline Surface Radiation Network (BSRN) before calculating the hourly averages that are input to the PV simulation software. The BSRN data quality checks ensure that the measurements are within both physical and reasonable limits. In some cases, our implementation is more stringent than the BSRN recommendations. For example, in our implementation, the sum of DHI and direct horizontal irradiance must always be within ±5% of the GHI whereas the BSRN tolerance is ±8% for most solar zenith angles. For more information on the quality checks, we refer the reader to [43].

The literature shows that the solar resource assessment (e.g., GHI) and the transposition of horizontal data to plane-of-array irradiance ($G_{POA,Front}$) are the highest sources of uncertainty when modeling PV energy yield [39,44–. The present study therefore considers how the expanded uncertainty (U_C) of the onsite GHI, DHI, and DNI irradiance measurements impact the simulated energy yield and thus the comparisons to measured electrical data. We calculated the expanded uncertainty U_C of the DHI, GHI, and DNI measurements following principles in the Guide to the Uncertainty in Measurement and best-practice guidelines published within the field of solar radiation measurements [48,49]. Measurement uncertainty of pyranometers and pyrheliometers is not constant but changes according to the prevailing environmental conditions (e.g., diffuse ratio, sun position, etc.) [49]. When the solar zenith angle is greater than 70°, the largest source of uncertainty in the *GHI* measurements is the cosine error. Since this cosine error is considered systematic, it could be significantly reduced by characterizing the angular-dependent response of the instrument and then applying a device-specific correction to the measurements [47]. However, such corrections were not performed here largely due to the complexity of executing such an approach with high accuracy. Figure 3 demonstrates how the U_C of the GHI is most heavily affected by the instrument's cosine response when the sky diffuse fraction is low (i.e., cloudless skies), and when the sun is close to the horizon (i.e., early morning, late afternoon). We estimate that the expanded (k = 2) U_C of the hourly averaged GHI is about ±4% at solar noon on a clear summer solstice, and about ±7.3% on a clear winter solstice. The uncertainty of the hourly averaged DNI, on the other hand, is most significantly affected by inter-hour irradiance variability.

While it is well-established that the uncertainty of pyrheliometer (DNI) measurements is lower than global pyranometer (GHI) measurements due to the non-ideal cosine response of pyranometers [50], this is not always the case in the present work because hourly averages are used for the simulations. During periods of high cloud variability, the variance of hourly DNI is significantly higher than the variance of hourly GHI. The uncertainty due to this variation is included in the uncertainty model using the standard error of the hourly averaged value. Figure 3 shows that the uncertainty of hourly averaged DNI is as low as ±2.2% during hours with little to no cloud variability, but under high solar variability, the uncertainty can exceed ±15%. Please note that the hourly DNI tends to be low in absolute ($W \cdot m^{-2}$) terms during such times of passing clouds.

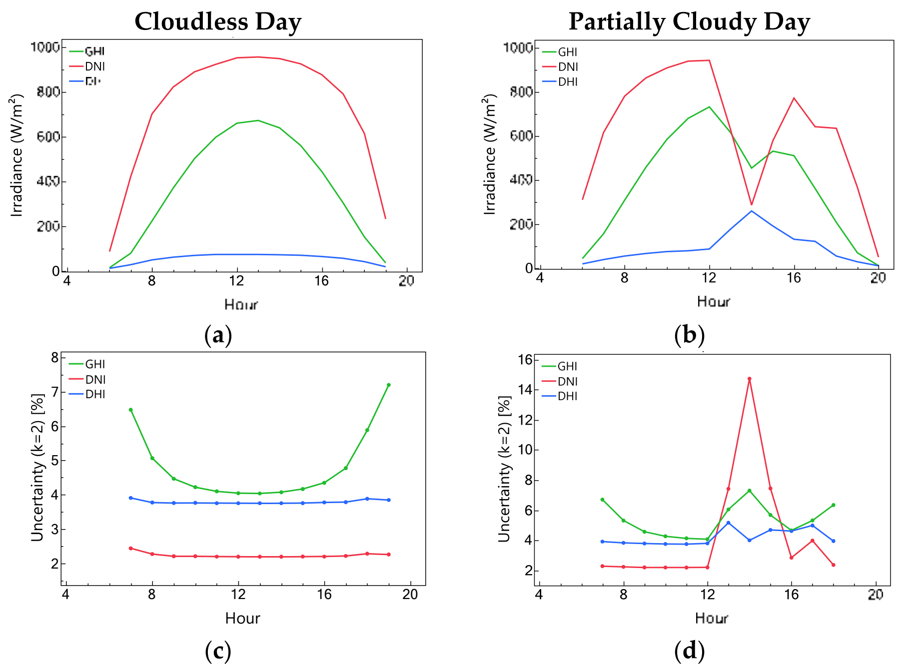

Figure 3. Uncertainty of the hourly GHI, DHI, and DNI measurements performed onsite from two example days in April 2019. A cloudless day is shown in (**a**) and (**c**) and a partially cloudy day is shown in (**b**) and (**d**). The top row shows the absolute uncertainty (in W/m^2) as shaded bands around the measured value. The bottom row shows the uncertainty in percentage.

As illustrated in Figure 3, the uncertainty of a PV performance simulation is dependent on which combination of GHI, DHI, and/or DNI is used as input. Table 1 shows which two components each software uses to calculate $G_{POA,Front}$ and $G_{POA,Rear}$—some use GHI and DHI, while others use DHI and DNI. When simulations use hourly GHI and DHI, only under clear sky conditions will this simulation be associated with higher uncertainty than simulations that use hourly DNI and DHI. Under variably cloudy sky conditions, simulations that use hourly DNI and DHI are likely to be associated with higher uncertainty.

2.3.3. Albedo Measurements

During the 12-month period shown here, the average annual albedo of the grass is 21.6% (Figure 4). The average monthly albedo shows little variation at the location where the albedometer is placed (Figure 2c). The lowest average monthly albedo (19.3%) occurs in December, which is possibly due to the moist ground in winter. Six days with snowfall events were observed during the test period, but because Denmark is in a temperate climate, the snowfall did not accumulate substantially or remain on the ground for more than one day. The average monthly albedo is used in all modeling tools except for bifacialvf and pvfactors, which use the annual average albedo. A sensitivity analysis on albedo is provided in the discussion section of this paper. Please note that the raw albedo data shown here are openly available as part of the National Renewable Energy Laboratory's albedo project [51].

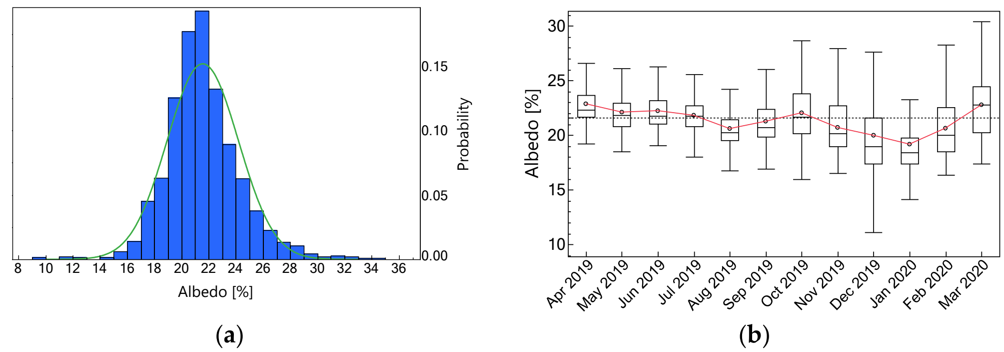

Figure 4. (**a**) Distribution of albedo measurements made during the one-year period; (**b**) Box and whisker plots of the monthly albedo, the red line connects the mean monthly albedo, the dashed reference line shows the annual average of 21.6%.

2.3.4. Thermal Performance

A white paper from solar tracker manufacturer Soltec [52] provides recommended values for the conductive and convective heat transfer coefficients (U_0/U_1) of bifacial modules mounted on their trackers, which are derived from field measurements made in Livermore, USA. In the absence of measured coefficients for the modules at the DTU site, we used the manufacturer-recommended values of 31 and 1.6 $W{\cdot}m^{-3}K{\cdot}m^{-1}{\cdot}s$ in the simulations here (Table A1). Similar U_0 coefficients were determined in [53] for glass-glass bifacial n-PERT, which provides justification for the use of these values. However, the use of one set of thermal coefficients for all bifacial module types and all projects is likely not ideal given that the climatic region and module-specific bill of materials are known to influence the value of the U_0/U_1 coefficients [54]. The thermodynamic behavior of monofacial PV modules has been shown to deviate from that of bifacial modules in side-by-side tests [53,55] and therefore a U_0 coefficient of 29.5 $W{\cdot}m^{-2}{\cdot}K^{-1}$ was used for these simulations. Finally, as [56] concludes in their review paper on bifacial PV simulation, more experimental validation of bifacial PV thermal coefficients is needed. Due to the uncertainty of these coefficients for the modules at the DTU site, we perform a sensitivity analysis on the results in the discussion section.

2.4. Analysis of Measured and Simulated Bifacial Energy Gain (BG)

We make our results comparable to previous studies by including modeled versus measured bifacial energy gain per Equation (1, where E_{BF} and E_{MF} are the energy produced by the bifacial and monofacial systems, respectively, and $P_{STC,BF}$ and $P_{STC,MF}$ are the front side power ratings of the bifacial and monofacial systems, respectively. The P_{STC} values are obtained from I-V measurements made at DTU:

$$BG\ [\%] = \left(\frac{E_{BF}/P_{STC,BF}}{E_{MF}/P_{STC,MF}} - 1 \right) \times 100 \tag{1}$$

Note that bifacialvf and pvfactors (Table 1) do not incorporate cell temperature models or electrical models. Therefore, we also present bifacial gain in terms of the rear to frontside irradiance ratios, in order to compare results from all software:

$$BG\ [\%] = \frac{G_{POA,Rear}}{G_{POA,Front}} \times BF \times (1 - Bifi_{loss}) \times 100 \tag{2}$$

where, in Equation (2), BF is the bifaciality factor defined as the ratio of rear to frontside efficiency at standard test conditions (STC), which is 0.67 according to the DTU indoor flash I-V measurements. The $Bifi_{loss}$ term here accounts for two separate parameters: The electrical losses induced by non-uniform backside illumination and the losses due to structural profiles that shade the backside of the array. The electrical mismatch caused by non-uniform backside irradiance is not a constant value but varies with the prevailing environmental conditions [19,57,58]. In our previous work [19], we determined that on a clear day at solar noon, the irradiance nonuniformity-induced mismatch for the bifacial arrays at our site is roughly 0.025 (without considering the front-side irradiance contribution), and is used to calculate $Bifi_{loss}$. The aforementioned Soltec white paper [52] that recommends 0.007 as a value for structural shading loss, which is subsequently used here. The $Bifi_{loss}$ value used in this work therefore amounts to 0.032. Note that the performance models tested here sometimes consider additional parameters, such as the transparency of the PV array and the reflectivity of the PV array's back and front side (see Table A4).

Validation of bifacial performance models requires measurements of the rear plane-of-array irradiance ($G_{POA,Rear}$). Figure 2d shows a photograph of two pyranometers that are used for this purpose. The instruments shown are mounted on the backside of the fixed-tilt system, 17 panels east of the western array edge. The rear facing pyranometers on the HSAT are located 12 panels north of the southern array edge. Ray trace simulations made by [17] have shown that this distance into the 45-m-long array should be sufficient to remove edge-brightening effects and to be representative of the semi-infinite assumption that is common among 2-D VF models.

3. Results

3.1. Rear Plane-of-Array Irradiance ($G_{POA,Rear}$)

The fundamental challenge in bifacial—as compared to monofacial—PV performance modeling is estimating $G_{POA,Rear}$. Therefore, the discrepancies in simulated bifacial energy production are likely to occur in the derivation of $G_{POA,Rear}$ values. Figure 5 shows one year of simulated $G_{POA,Rear}$ values as a function of the average simulated value. The dispersion of simulated values is nearly the same for the fixed-tilt and HSAT system. The range of simulated values among software correlates with the front-side irradiance (R^2 = 0.81–0.85). The range of simulated $G_{POA,Rear}$ values is approximately 20 W·m^{-2} at 1000 W·m^{-2} frontside irradiance. In other words, the range of $G_{POA,Rear}$ is about 2% of $G_{POA,Front}$. SolarFarmer is highest in this comparison because its integrated approach does not currently consider the obstruction of sky diffuse irradiance caused by neighboring PV rows. Therefore, the ground-reflected irradiance between PV rows is over estimated. To our knowledge, this detail is currently being revised and is expected to be implemented in SolarFarmer versions greater than 1.0.191.2.

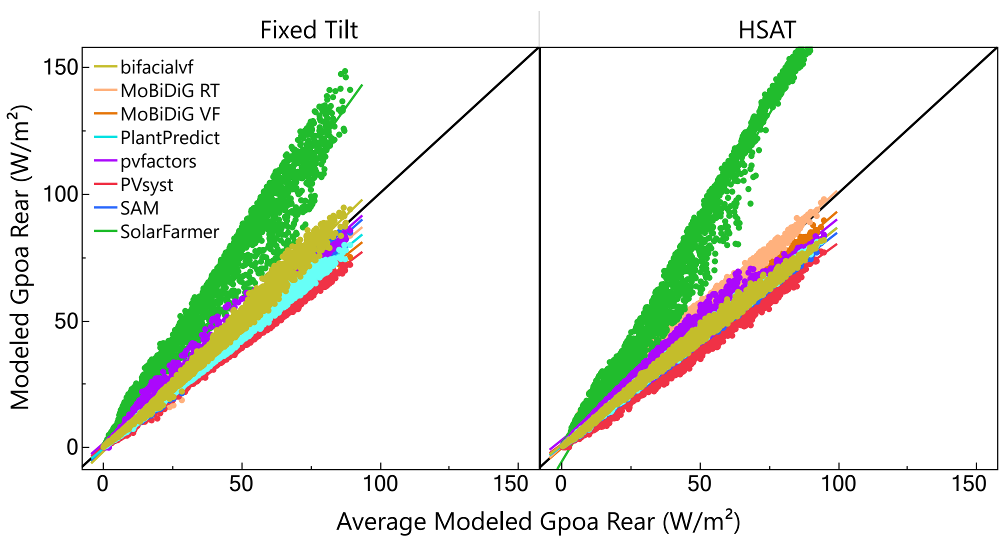

Figure 5. Simulated rear plane of array irradiance as a function of the average of the eight simulation tools. The solid black line is unity to the average.

A comparison of the modeled $G_{POA,Rear}$ during five weeks (21 February–30 March 2020) where measured $G_{POA,Rear}$ data are available on the fixed-tilt and HSAT system is shown in Figure 6. The simulated results include reflection losses at the PV glass–air interface according to the IAM model implemented in each software. The solid black 45° lines in Figure 5 represent unity to the measurements. The measurements are the average of two MS-40 pyranometers (EKO Instruments, Tokyo, Japan) mounted on the backside of the structure: east and west in the case of the HSAT, top and bottom for the fixed tilt (Figure 2d).

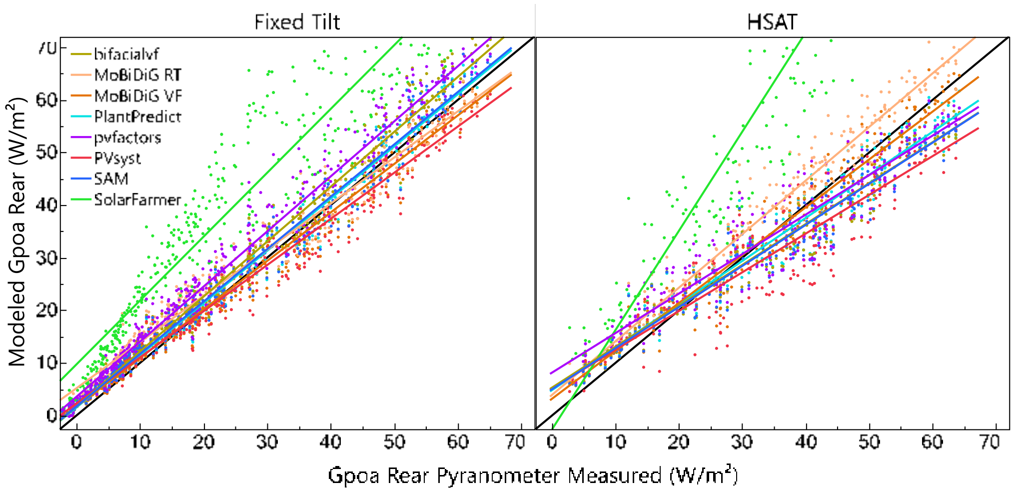

Figure 6. Simulated rear plane of array irradiance on the fixed-tilt and horizontal single-axis trackers (HSAT) systems as a function of being measured over a 5-week period. The solid black 45° line represents unity to the measurements. The measurements are the average of two pyranometers located a minimum of 12 m from the nearest array edge. The shaded areas around each regression line indicate the 95% confidence intervals.

The trendlines from seven of the eight software agree well with the pyranometer measurements. The mean absolute error (MAE) of these seven software is 2.3–5.2 W·m^{-2} for the fixed-tilt system and slightly higher at 3.5–6.7 W·m^{-2} for the HSAT system. We analyzed the model residuals as a function of the sun position $G_{poa,front}$ and diffuse fraction and found no systematic trends, other than a tendency towards higher percentage errors in $G_{POA,Rear}$ when $G_{POA,Front}$ is low.

The peak total irradiance (i.e., sum of $G_{POA,Front}$ and $G_{POA,Rear}$) of both system types was approximately 1000 W·m^{-2} during the five-week period shown in Figure 6. When the magnitude of total irradiance is considered, the MAE of $G_{POA,Rear}$ contributes roughly 0.5% uncertainty to the bifacial PV modeling chain. The 3-D MoBiDiG RT simulation over predicts $G_{POA,Rear}$ in the HSAT scenario, which could be due to its use of the Perez all-weather luminance model [59], which is unique among all software tested. The overall poorer model agreement with measurements in the HSAT scenario makes sense considering that tracking introduces additional complexity—and thus additional degrees of freedom for error—at two levels. First, the tracker algorithm implemented by the software is introduced into the comparison and second, the VFs in HSAT simulations are calculated for each change in tilt angle whereas the VFs in fixed-tilt simulations are calculated once for the entire simulation.

An inclinometer sensor mounted on the back of the tracker continuously recorded the tracker roll angle during the test period. We found that the modeled tracker angle was within ±1° of the measured angles 50% of the time, but deviations were as high as 5° during periods of backtracking. We used pvfactors to test the effect that this difference in the roll angle had on simulated $G_{POA,Rear}$ values. When the measured—as opposed to calculated—angular position was used in the simulation, we found that the mean bias error (MBE) improved slightly from −1.1 to −0.7 W·m^{-2}, but the MAE, however, changed by less than 0.1 W·m^{-2}.

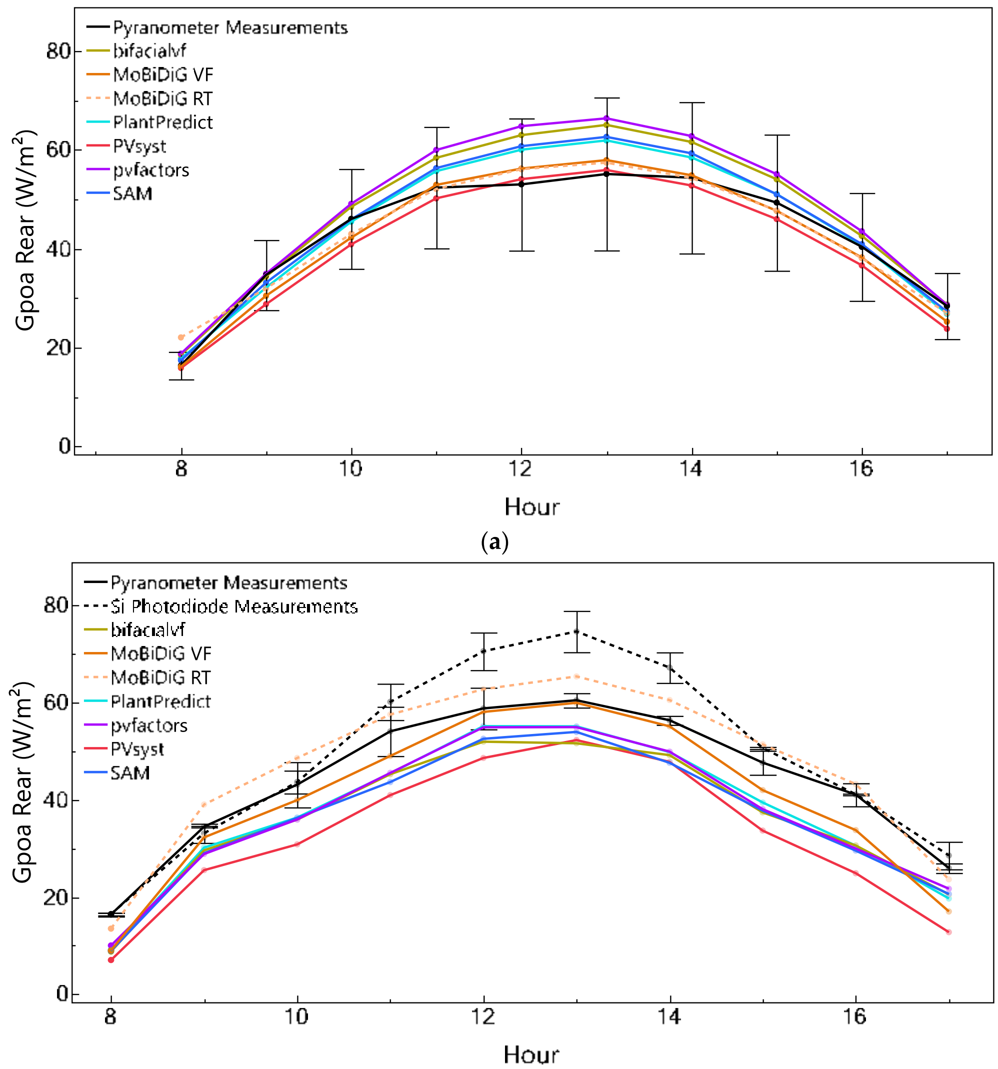

(**a**)

(**b**)

Figure 7. Timeseries plots of modeled and measured rear plane of array irradiance ($G_{POA,Rear}$) on a cloudless day (23 March 2020). The error bars around the measured values show the maximum and minimum measurements made by two sensors. (**a**) Fixed-tilt system where rear-facing POA pyranometer measurements are made 17 m from the western array edge. (**b**) HSAT system where rear-facing silicon photodiode and pyranometer measurements are made 12 m from the southern array edge.

The spatial non-uniformity of irradiance on the backside of a bifacial PV array makes it difficult to identify a position for a backward-facing irradiance sensor that is representative of the entire array. Fortunately, research is being conducted on this topic by other authors, although it is still in an early stage [60]. During clear sky (i.e., low diffuse fraction) days, we observed that the bottom pyranometer can receive nearly twice as much irradiance as the top pyranometer. Therefore, the black unity line in Figure 6, which represents the average measurement from two sensors, can at times have error bars on the order of ±15 W·m^{-2}. On such clear sky days, seven of the eight software studied give $G_{POA,Rear}$ results that are within this range (Figure 7a). In other words, when the vertical spatial non-uniformity of irradiance is considered, the reduced-order complexity 2-D VF models perform reasonably well for fixed-tilt simulations.

In the HSAT scenario, we do not see the same level of model agreement (Figure 7b). We observed that the irradiance sensor closest to the sky (i.e., western sensor in the morning, eastern sensor in the afternoon) typically receives more irradiance than the pyranometer closest to the ground, which is consistent with the findings of [22]. We found that the differences between eastern and western $G_{POA,Rear}$ measurements on the HSAT system were not as extreme as differences between the top and bottom $G_{POA,Rear}$ measurements on the fixed-tilt system. On a clear sky day, we observed differences on the order of 10 W·m^{-2} between western and eastern pyranometers. Although five of eight software agree within 5 W·m^{-2} of each other, none of the same five tools overlap with the measurement uncertainty bars in Figure 7b. This result could likely change if alternative backside pyranometer locations were chosen. Therefore, the PV industry could benefit from a standardized best-practice protocol for mounting the rear plane of array irradiance sensors in bifacial PV monitoring systems.

The difference between Si photodiode $G_{POA,Rear}$ measurements and pyranometer $G_{POA,Rear}$ measurements is most apparent at midday, when the tracker is at or near a horizontal tilt. This could be because the Si photodiodes used in this work are calibrated under the air-mass 1.5 global reference spectrum (AM1.5G), but the spectral reflectance of grass deviates strongly from the spectral distribution of AM1.5G [61]. Particularly, healthy grass has high reflectance in the near-infrared spectrum and very little reflectance in the visible spectrum where the AM1.5G spectrum peaks. It is well known that the output of silicon PV devices calibrated under the AM1.5G spectrum will increase as the observed spectrum "red shifts" [62,63]. This can explain why the Si photodiode measurements are higher than the pyranometer measurements around midday when the tracker is near horizontal, and the sensor's field of view is primarily encompassed by grass, not the sky. However, the spectral response of the Si photodiodes is reasonably well matched to that of the bifacial PERC module's rear side, and for this reason, the readings from this sensor type could be more representative of the effective irradiance received at the backside of the PV array. Indeed, further research is needed on the benefits of silicon radiometers (reference cells) versus pyranometers in bifacial PV monitoring applications.

3.2. DC Power

Figure 8 shows one year of modeled versus measured DC string power of four PV configurations as simulated by six software. Good correlation is observed in all 24 regressions ($R^2 = 0.99$), but residual errors can exceed 5 kW (20%) in some cases. When such large errors are observed, the error is similar for all six software, which indicates an unidentified issue with the meteorological measurements and/or the electrical monitoring system. The DC electrical monitoring system measures string-level voltage and current independently of the inverter. The galvanically isolated data acquisition boards are a commercially available string.bloxx solution from Gantner Instruments (Rodgau, Germany). From the specifications, we determined the uncertainty of the DC power measurements as ±0.5% at the full scale. The dashed black lines in Figure 8 are drawn at ±4.5% from the solid black unity line and depict the GHI measurement uncertainty on a clear day at solar noon (±4%) and the uncertainty of the power measurements (±0.5%). All 24 trend lines in Figure 8 are within this boundary at measured power levels greater than 7 kW.

Figure 9 shows the model errors from Figure 8 in the form of cumulative distribution functions (CDFs). The slopes of all 24 CDFs in Figure 9 are steepest around approximately ±500 W, which indicates that the majority of errors are within this range. CDF shifts in the positive X-axis direction indicate that a modeling tool has a tendency toward higher DC power predictions, while shifts in the negative x-axis direction indicate a tendency toward more conservative DC power predictions. With this in mind, the bifacial fixed-tilt and HSAT simulations reveal two groups: PlantPredict, PVsyst, and SAM showing nearly identical CDFs; and MoBiDiG RT, MoBiDiG VF, and SolarFarmer showing very similar CDFs. The former group has a tendency toward negative bias and the latter group a tendency toward positive bias. In the case of the bifacial HSAT simulation, the reason for this two-group split could be attributed to the latter group yielding the highest estimates of $G_{POA,Rear}$ (Figure 6). In the case of the bifacial fixed-tilt simulation—and both monofacial simulations—the explanation is not so clear and therefore likely not attributable to a single difference in submodeling steps but rather due to the differences accumulated in multiple submodels. We performed regressions of the DC power residuals as a function of measured variables, such as diffuse light fraction (*DHI*/*GHI*), sun position (zenith and azimuth), and $G_{POA,Front}$. This exercise revealed no significant correlations (R^2 <

0.25) or systematic trends, other than a trend of larger absolute errors during times of high solar irradiance.

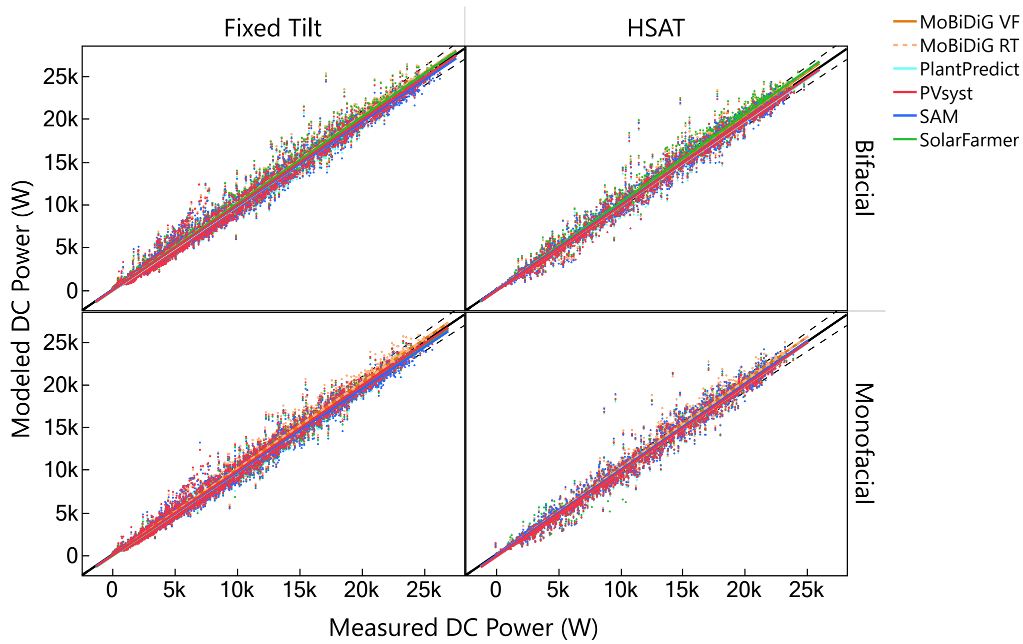

Figure 8. Regressions of hourly modeled versus hourly measured DC power of four the four PV system types studied. Result from six different software are shown. Data points recorded when the sun elevation was less than 5° above the horizon were removed from these plots.

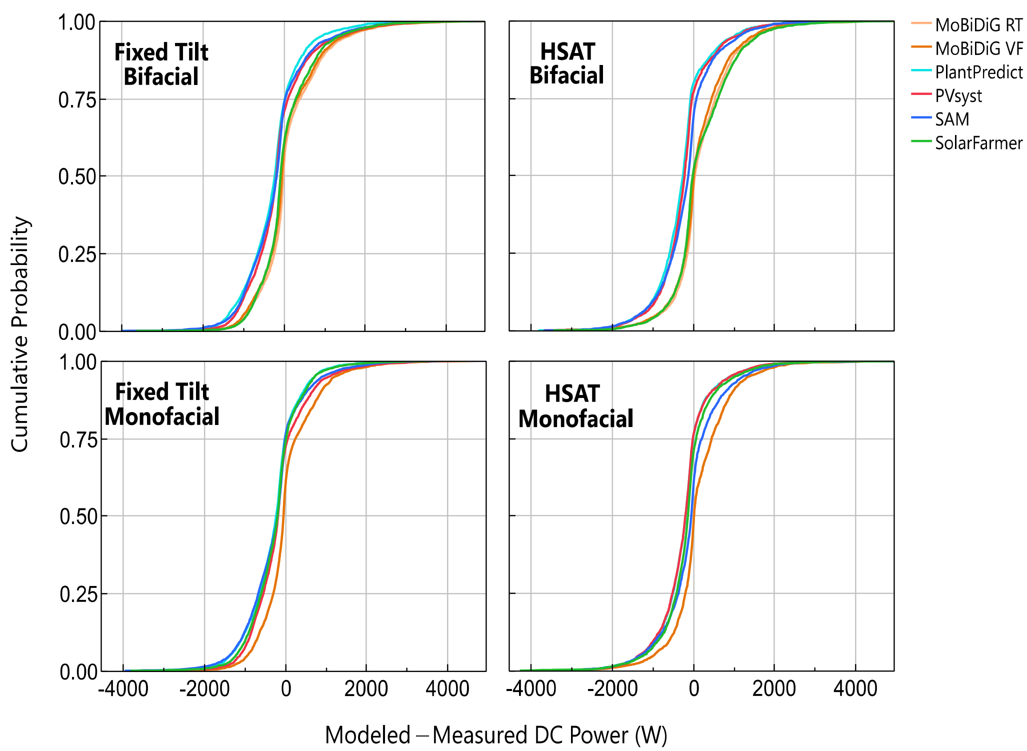

Figure 9. Cumulative distribution functions of the modeling error observed in DC power. Results from four system types and six software are shown. These plots are generated using the residuals from Figure 8.

Figure 10 shows two variability plots that summarize the annual mean absolute errors (MAEs) and mean bias errors (MBEs) of the four PV system types simulated by six software. The dashed orange lines in each variability plot represent the average modeling error of the bifacial and monofacial system types and indicate a 30 W higher MAE in bifacial simulations. The slightly higher MAE can be explained simply by the fact that the bifacial arrays produce about 5% more energy on an annual basis than the monofacial arrays. When the MAE is normalized to the average power produced by each system type over the year, we found that the normalized error is about 0.25% higher for bifacial simulations versus monofacial simulations. This difference is likely driven by the contribution of $G_{POA,Rear}$. In terms of the average MBE, bifacial simulations are about 90 W higher than monofacial simulations but closer to zero bias than the monofacial simulations. Within the context of the results obtained from the site studied here, we conclude that the accuracy of bifacial PV simulations is not significantly different than monofacial PV simulations.

Figure 10a shows the MAE calculated using two approaches: (1) without error weighting and (2) by weighting the error with the inverse uncertainty (1/U_C) of the solar radiation measurements during each hour of energy production. In approach (2), the errors are weighted by either the *GHI* uncertainty or DNI uncertainty, depending on the data used in the transposition step, and the sum of all error weights equals one. The rationale behind the 1/U_C weighting in approach (2) is that uncertainty in solar radiation measurements directly impacts simulated PV power, which ought to be accounted for in error analyses. As expected, weighting the error by a factor of 1/U_C reduces the MAE, but the reduction is small at about 20 W, or 0.2%.

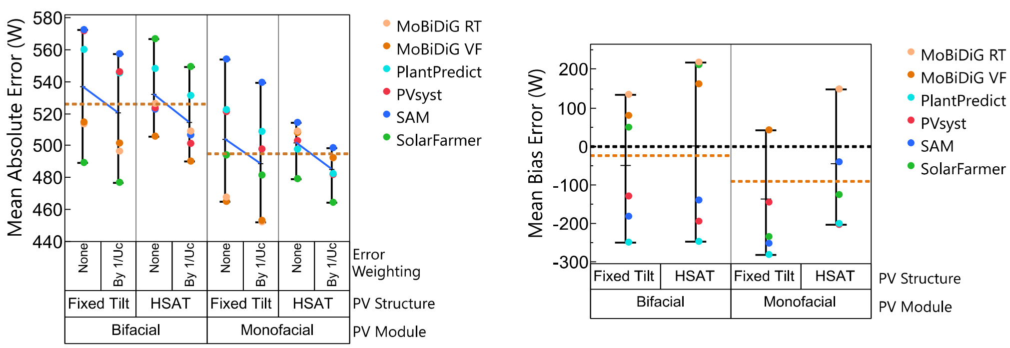

(**a**) (**b**)

Figure 10. (**a**) Variability plot showing the mean absolute error of DC power for the four PV system types as simulated by six software. The chart displays unweighted error and error weighted by the inverse of the uncertainty of the solar radiation measurements. (**b**) Variability plot showing the mean bias error of DC power. Only the unweighted error is shown in these plots. The dashed orange lines show the mean error of the bifacial and monofacial arrays.

3.3. Bifacial Gain

Figure 11 shows the monthly bifacial gain from five software that are capable of simulating electrical performance. The black lines in each plot show the monthly results from the DC string measurements. The error bars show the inner quartile range of daily measured bifacial gains observed in each month. The daily bifacial gains in winter fluctuate greatly because the daily energy production in winter can be an order of magnitude less than in summer months: This variability is illustrated with the wider error bars in winter. Recall that the measured results are normalized with the I-V measurements made at DTU per Equation (1). If the normalization was instead made using the manufacturer's nameplate rating, the measured bifacial gain according to Equation (1) would be 1.5% higher than what is shown. This difference can significantly affect the economics of project decisions that are made based on an expected bifacial energy gain.

The measured monthly bifacial gain on the fixed-tilt system is between 4.3% and 7.3% from March to October. Meanwhile, the bifacial gain on the tracker is consistently higher, between 6.6% and 8.5% during the same months. The higher bifacial gains observed on the HSAT are likely due to the wider 12-m spacing between rows (GCR = 0.28) versus the narrower 7.6-m spacing on the fixed-tilt system (GCR = 0.4), which creates more self-shading within the inner rows of the fixed-tilt field.

From November to February, the measured bifacial gain on the two system types shows opposing trends, wherein the HSAT system shows an increase and the fixed-tilt system shows a decrease. These months were characterized consistently as cloudy skies with mean monthly diffuse fractions between 88% and 94%. The works of other authors have demonstrated that bifacial gain will increase as the fraction of diffuse light increases [64], which can explain the higher bifacial gain on the HSAT system in winter. It also been shown that bifacial PV systems require higher tilt angles to capture the benefit of such diffuse conditions [65]. This can explain why the simulations and the measurements in winter show lower bifacial gains on the fixed-tilt system (25°) than the HSAT system (±60°).

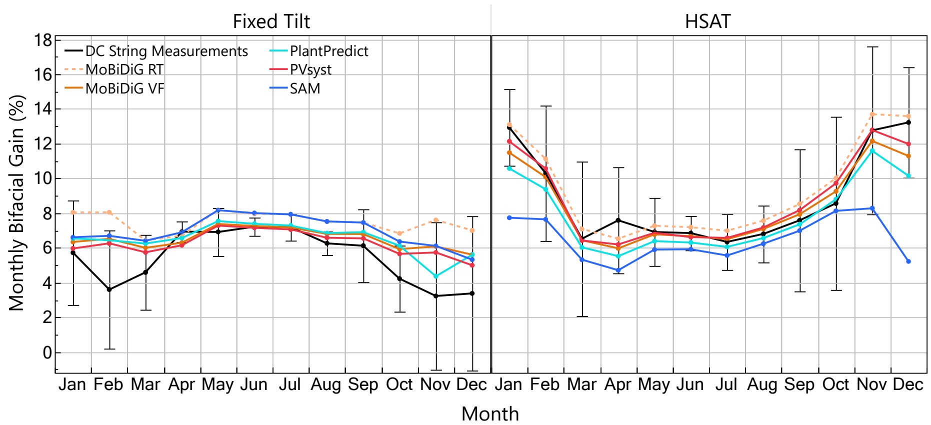

(**a**)

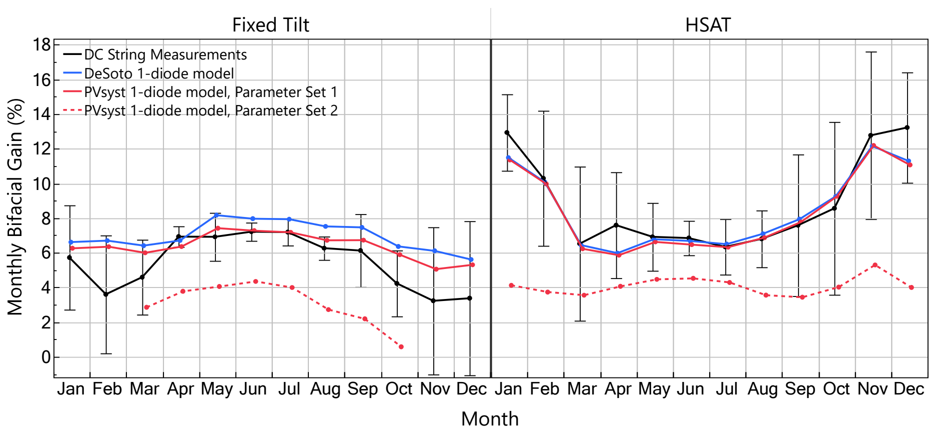

(**b**)

Figure 11. Monthly bifacial gain on fixed-tilt and HSAT systems calculated with Equation (1). All plots show bifacial gain as simulated by five software and from DC string measurements. The black error bars show the inner quartile range of daily bifacial gain measurements within each month. Datapoints when sun elevation is lower than 5° above the horizon are not included in these plots. (**a**) Results grouped by software (Table 1). (**b**) Results grouped by which 1-diode model and parameter set was used. PVsyst Parameter Set 1 is based on laboratory I-V measurements at multiple irradiances while PVsyst Parameter Set 2 is based on only STC measurements.

The simulated bifacial gain values largely follow the trends of the measurements, but the most notable exception is the fixed-tilt system in winter (November through February). This discrepancy is likely due to the significant amount of inter-row shading on the fixed-tilt system from November to February. The fixed-tilt system has a shade angle (at solar noon) of 16°, but on the winter solstice, the sun elevation peaks at 12°. Therefore, the fixed-tilt rows are partially shaded at practically all times in December and January. In fact, negative bifacial gains were measured in November and December on the fixed-tilt systems. Such an incongruous result points toward issues in the measurements rather than the shade-loss models. A visual inspection on a clear winter day near solar noon confirmed that there was more inter-row shading on the bifacial arrays than on the monofacial arrays. This is attributed primarily to the torque tube gap on the bifacial arrays, and the lack of such a gap on the monofacial arrays. The torque tube gap on the bifacial arrays (Figure 2a) places the bifacial modules approximately 5 cm higher than modules on the monofacial arrays that completely cover the torque tube (Figure A2). This slight differentiation in structural geometry may not have been simulated sufficiently in the software.

Another notable discrepancy between the model and measurement is seen in April when a small spike in bifacial gain is observed on both the fixed-tilt and HSAT system. The trend in modeled bifacial gains from March to May indicate that the measured bifacial gain in April is overstated by as much as 1.5%. We believe the higher measured bifacial gain in April was caused largely by extraordinarily high pollen counts in late April 2019, which caused non-uniform soiling on the PV arrays, and ultimately more power loss in the monofacial than bifacial systems. We observed that the daily bifacial gains were between 10% and 20% from 23–26 April 2019, which corresponds to the dates of the soiling event (Figure A2). A significant rainfall event occurred on 27 April 2019 at which point more modest and typical bifacial gains resumed. This artifact highlights the challenge of curating high-quality data acquisition in large-scale PV test sites.

Please note that the bifacial gain results from SolarFarmer are not presented in Figure 11 because the overestimation of $G_{POA,Rear}$ shown in Figure A2 causes a 2–4% upward bias in bifacial gain as compared to the other tools, which use the PVsyst 1-diode model (i.e., PlantPredict and PVsyst). This result conflicts with our previous work [27], which showed SolarFarmer results mostly within 1% of the measured bifacial gain, while PlantPredict and PVsyst results were 3–4% low to the measured bifacial gain. The reason for this discrepancy is that the present work uses a 1-diode model parameter set based on laboratory measurements made at irradiances from 200–1000 W·m^{-2} (noted as 'Parameter Set 1' in Figure 11b) while our previous work used a parameter set based on measurements made only at STC (noted as 'Parameter Set 2' in Figure 11b). The improved agreement of 'Parameter Set 1' shown here is attributed to the fact that this parameter set more accurately predicts performance at low-light conditions (<400 W·m^{-2}) than does 'Parameter Set 2'. This finding is in agreement with the findings and recommendations of other authors [66,67].

Figure 12 shows the simulated bifacial gain according to the $G_{POA,Rear}$ to $G_{POA,Front}$ ratio (Equation (2)). The agreement among the different software is similar regardless of whether the bifacial gain is calculated using the optical gain (Equation (2)) or the electrical performance (Equation (1)), with the exception of HSAT results in winter, where better agreement among software is seen using Equation (2). The larger discrepancies between HSAT simulations in winter using Equation (1) could be due to the different backtracking and shade-loss algorithms used by the software. Equation (2) results in better agreement with the fixed-tilt system measurements in winter, which indicates that inaccuracies in the shade-loss models are likely the result of the significant winter deviations shown in Figure 11.

Figure 12b shows the results grouped by whether $G_{POA,Rear}$ is calculated using a 2-D VF or 3-D RT approach. When visualized in this manner, it becomes clear that the 3-D RT approach follows the measured bifacial gain most closely for the HSAT simulation, within 0.5% of measurement for most months outside of winter. The 3-D RT model also matches well, typically within 0.5%, with the bifacial gain measurements on the fixed-tilt system. However, 2-D VF models, such as the one integrated in SAM, compared equally well to field measurements. Indeed, the measured bifacial gain shown in Figure 12 is influenced by the value of $Bifi_{loss}$. The static $Bifi_{loss}$ values used here, in actuality, change dynamically over the day with the prevailing conditions [19,57,58]. All the commercial software tested here has the capability to use only a single value. This simplification offers room to improve the accuracy of the bifacial PV performance simulation tools used in industry today.

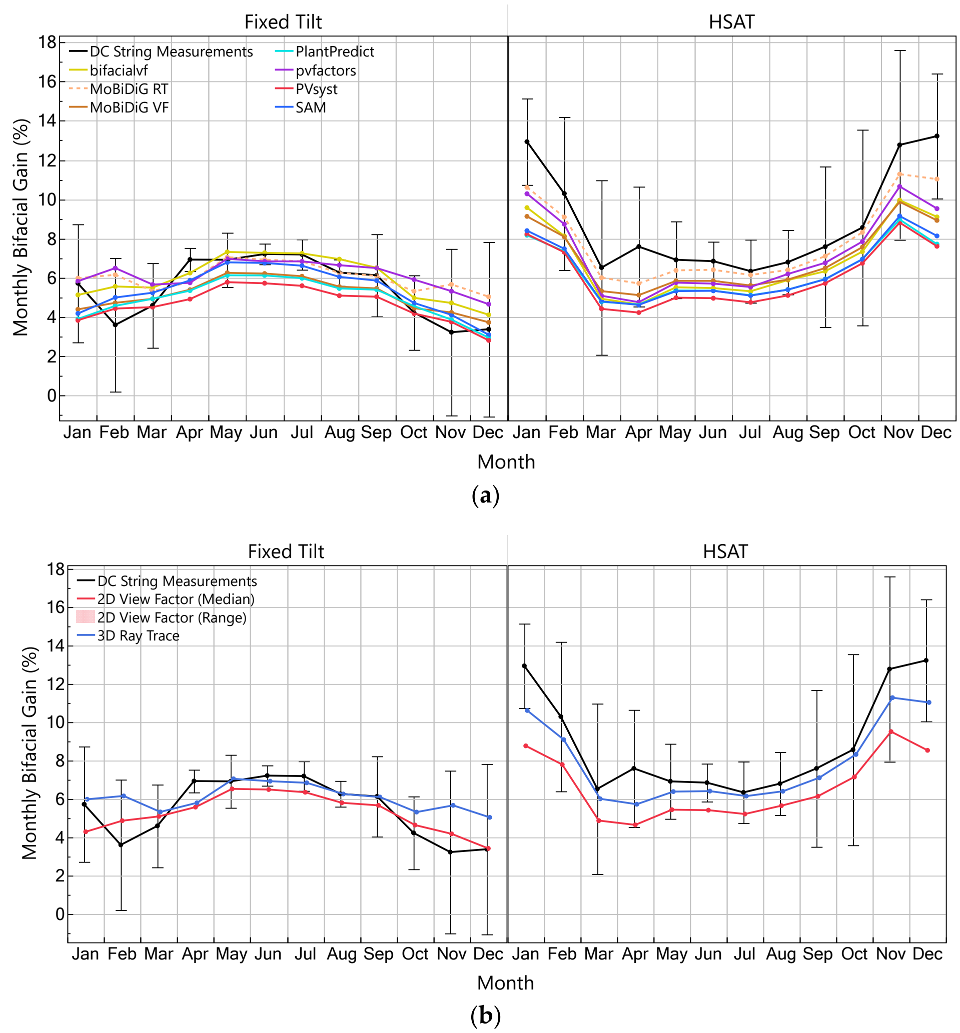

Figure 12. Monthly bifacial gain on fixed-tilt and HSAT systems calculated with Equation (2). All plots show bifacial gain as simulated by seven software and from DC string measurements. The black error bars show the inner quartile range of daily bifacial gain measurements within each month. Datapoints when sun elevation is lower than 5° above the horizon are not included in these plots. (**a**) Results grouped by software (Table 1). (**b**) Results grouped by whether a 2-D view factor or 3-D ray trace approach was used to calculate back side irradiance.

3.4. Frontside Plane-of-Array Irradiance ($G_{POA,Front}$) and Module Temperature (T_{MOD})

PV project developers and investors are often interested in bottom-line figures, such as performance ratios, specific yields, and, in the case of bifacial PV, the bifacial gain. However, comparing simulations to measurements at such a high level is often not meaningful without first analyzing the performance of key submodeling steps. This section builds on this analysis, which started in Section 3.1 with an assessment of $G_{POA,Rear}$, and shows how the simulations compare to onsite front-side plane-of-array irradiance ($G_{POA,Front}$) and back of module temperature (T_{MOD}) measurements.

Figure 13 shows an overlay of the simulated and measured $G_{POA,Front}$ on a cloudless day. The trends shown here are representative of the results from clear sky days within the test period. The plot is color coated by which the combination of solar radiation measurements is used in the Perez transposition model. Lower $G_{POA,Front}$ estimates (≈40 W·m^{-2}) are seen at midday when *DNI* is used in the transposition step. On an annual basis, the MBE is between 11 and 13 W·m^{-2} when *GHI* is used in transposition, and when *DNI* is used in the transposition step, the MBE is between −7 and 5 W·m^{-2}. These rather large differences in results using *DNI* and *DHI* versus *GHI* and *DHI* could be the result of measurement issues with either the *GHI* pyranometer or *DNI* pyrheliometer. However, it is worth reiterating that weekly maintenance is performed at the weather station, and that the *GHI*, *DHI* and *DNI* data passed the quality checks recommended by the BSRN [46]. Additionally noteworthy in Figure 13 is how there are considerable deviations among the tools that use the same *DNI* and *DHI* data as input, a result that is similar to that of other authors [28].

Since the front-side irradiance constitutes 92% or more of the total irradiance for half of the timestamps in the bifacial simulations, one would suppose that software that uses *DNI* in the transposition step would tend to underpredict DC power. However, this turns out to not always be the case. For example, MoBiDiG is one such tool that uses *DNI*, and this tool was shown in the CDF plots of Figure 9 to *overpredict* DC power of all PV system types compared to the other five software. SAM is another such tool that uses *DNI*, but the results in Figures 8 and 9 show that SAM tends to predict marginally higher DC power values than the tools that use *GHI* but only in HSAT simulations. The underprediction of $G_{POA,Front}$ by MoBiDiG and SAM could be compensated by their tendency to overpredict electrical performance at irradiance conditions <400 W·m^{-2}, which is due to their use of the De Soto versus PVsyst 1-diode model (Figure A1). This demonstrates how analyzing the accumulated errors at various submodeling stages and their subsequent impact on energy yield is not always a straightforward process.

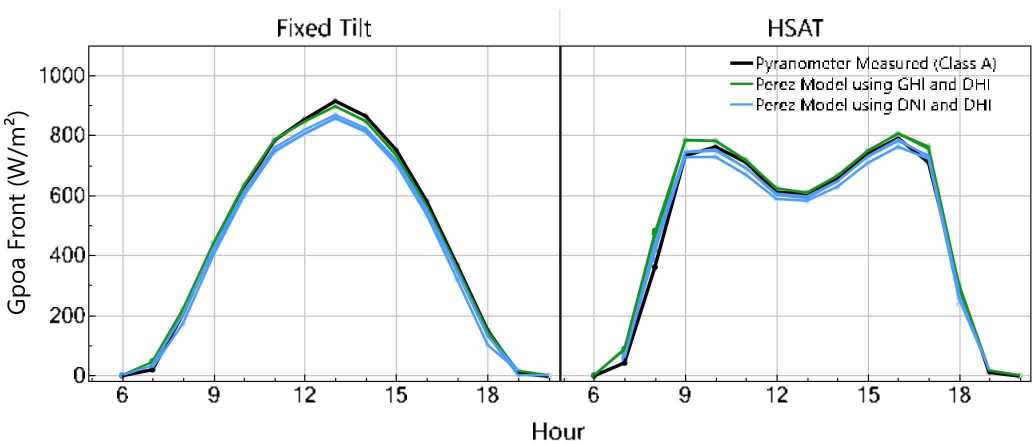

Figure 13. Overlay of simulated and measured frontside global POA irradiance on fixed-tilt and HSAT structures. The data shown are from a clear sky day (23 March 2020) and are grouped by which solar radiation data were used as input to the simulations.

Figure 14 shows the difference between module temperature and ambient temperature versus $G_{POA,Front}$. This difference between module and ambient temperature is known to be essentially linear with respect to the in-plane irradiance with a slope proportional to the U_0 coefficient used. The variations around are due to the assumptions for convective heat transfer in the U_1 coefficient. A notable difference in Figure 14 is the module temperature predicted by SAM, which is simply due to SAM's use of the NOCT versus Faiman model. The T_{MOD} measurement comes from one 4-wire resistance temperature device (RTD) affixed to a single cell on the backsheet of a module within the array; no translation from back of module (backsheet) to cell temperature is made in Figure 14. The monofacial results of Figure 14 show that the simulations tend to underpredict the measured back of module temperature by 2–3 °C, but errors are often greater than 5 °C. Unfortunately, T_{MOD} sensors were never installed on the bifacial arrays, and as such, only monofacial temperature measurements are available.

All software studied here implement simplified steady-state thermal models that assume the PV array operates at a homogenous temperature, which can lead to discrepancies with measured values. Although healthy (i.e., non-damaged) modules are typically assumed to have homogenous temperatures within an array [68], cell temperatures are known to vary within a healthy module [69].

Therefore, the cell on which the RTD is placed may not be representative of the average cell temperature within the array, which is a potential source of error when comparing to modeled values.

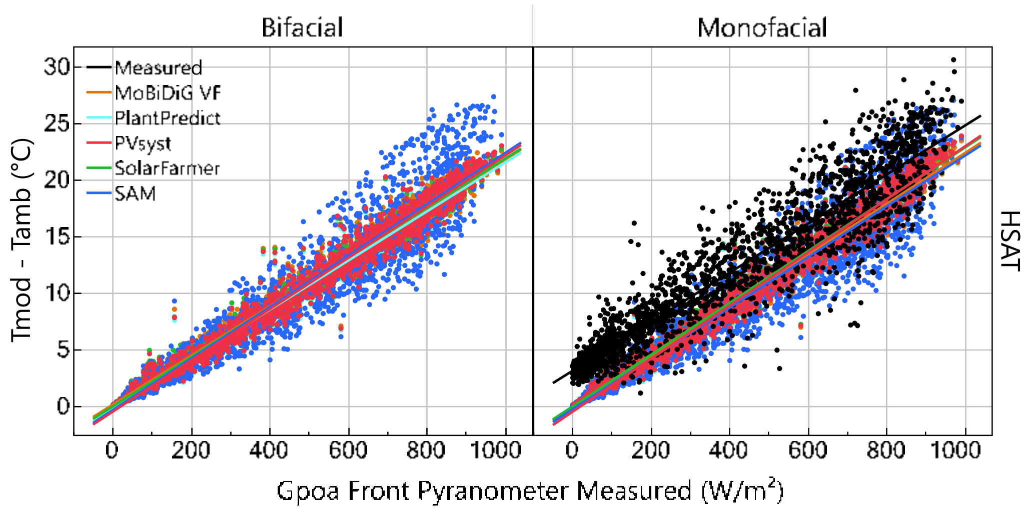

Figure 14. Temperature difference of the PV module and ambient versus frontside global POA irradiance on the HSAT system. Back of module temperature measurements are shown in black and were only available for the monofacial HSAT system.

Appropriate values for device-specific thermal parameters, and the methods to acquire them from measurements, have been the subject of discussion and debate in the PV community [70]. Therefore, we performed a sensitivity analysis of the U_0 and U_1 thermal coefficients using the MoBiDiG VF tool. Our sensitivity found that the MBE of simulated monofacial DC power was minimized using U_0 and U_1 parameter values of 24 and 1.6 $W \cdot m^{-3} \cdot K^{-1} \cdot s$, respectively. The sensitivity analysis showed that the best agreement between themodeled and measured module temperature would require U_0 and U_1 values near 20 and 0 $W \cdot m^{-3} \cdot K^{-1} \cdot s$, respectively. Since these values are below the lower boundary of published values that we are aware of for open-air mounted PV systems [54,71], it seems that the cell on which the RTD is placed is not representative of the average cell temperature within the array.

3.5. Sensitivity Analysis of the Albedo

While the bifacial gain is known to increase linearly with increases in albedo [65,72,73], uncertainties in albedo measurements have been shown to have a non-negligible effect on bifacial performance [74]. Therefore, we performed a sensitivity analysis with the MoBiDiG VF tool using annual albedo values from 18% to 24% (±3% of measured annual average) in place of the monthly measured albedo data that were used in previous sections. The results from this analysis are shown in Figure 15, with winter months excluded for clarity.

Figure 15 shows that differences in simulated bifacial gain are very small (<0.3%) when annual average albedo data are used in place of monthly averages. However, during the high solar resource months of May through August, using monthly albedo in the simulation tends to match the measured bifacial gain more closely. This demonstrates that monthly albedo data is preferred over annual albedo data, even at sites where the albedo does not vary greatly throughout the year, such as the site studied here.

Figure 15 shows only few instances where the measured bifacial gain is outside the boundaries of the sensitivity. One such example occurs in April, where unusually high bifacial gain was measured. In the case of the HSAT, nearly 30% albedo would be needed to recreate the measured bifacial gain in that month. Since such uncertainty in the measured albedo is unlikely, this lends credence to our hypothesis that abnormally high pollen counts (i.e., soiling) in April caused the spikes in bifacial gain. Another instance where the measured bifacial gain is outside the sensitivity boundaries occurs in the fixed-tilt system in March and October. Since the fixed-tilt array experiences the most shading in these months, it is likely that power losses due to shading are not accurately accounted for in the simulation.

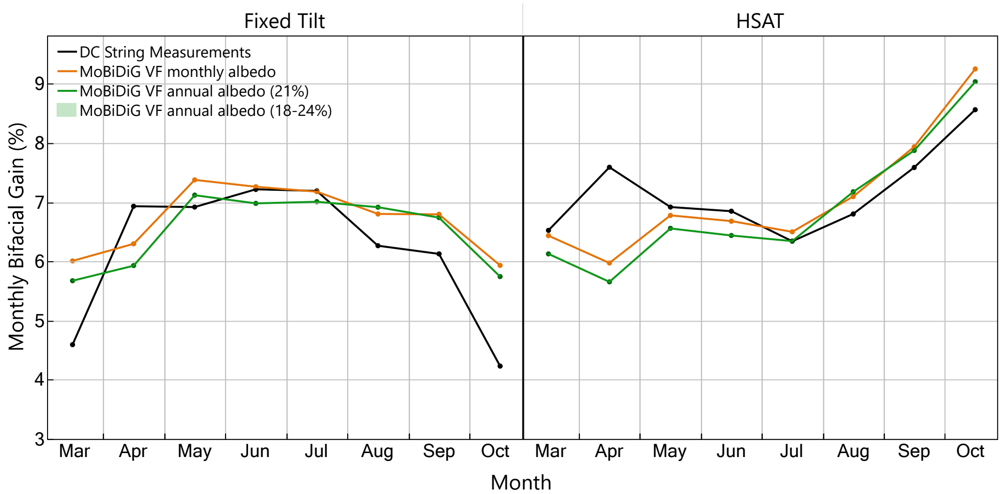

Figure 15. Sensitivity of albedo on the monthly bifacial gain (Equation (1)). All simulations here are performed with the MoBiDiG VF model. The orange curve shows the base case that uses monthly albedo (Figure 11), the green curve shows results using 21% annual average albedo, and the shaded green regions show the range of results obtained using annual albedo values of 18% to 0.24%.

3.6. Monthly and Annual Energy Production

With the results from several key intermediary modeling steps presented, we conclude the results section with a comparison of the modeled and measured monthly DC energy. In Figure 16, the monthly and yearly errors in energy predictions across all four PV system types are shown. Please note that roughly 75% of the total annual energy is produced between April and August. With just 25% of the annual energy produced between September and March, errors during these months tend to be larger on a percentage scale. An interesting result in Figure 16 is that on a monthly basis, PlantPredict, PVsyst, SAM, and SolarFarmer fluctuate between negative and positive bias relative to the measurements, sometimes with monthly deviations greater than 5%. However, on an annual basis, all tools simulate the four PV systems within 3.5% or less of measurements, and in some cases, the annual error is less than 1%. This is a rather positive result considering the uncertainty of the solar radiation measurements and the electrical monitoring system.

The accuracy of annual results from PVsyst and SAM shown in Figure 16 are in fact better than those published by [75], which could be because the parameters and loss factors used here were thoroughly calculated rather than using default values. On an annual basis, results from PlantPredict match PVsyst within 0.7% to 2.0%, which is a slightly larger deviation than that presented in [31] for Cadmium Telluride technology, but the larger differences here could be due to the use of different IAM models to describe reflection losses and/or the introduction of $G_{POA,Rear}$. The annual MoBiDiG results are between 2% and 3% above measurements, which is higher than the ±1% published in [14] for most static-tilt configurations, but agreement could improve if, for example, the DeSoto parameter set was modified such that the modeled DC efficiency was lowered at low-light conditions (Figure A1).

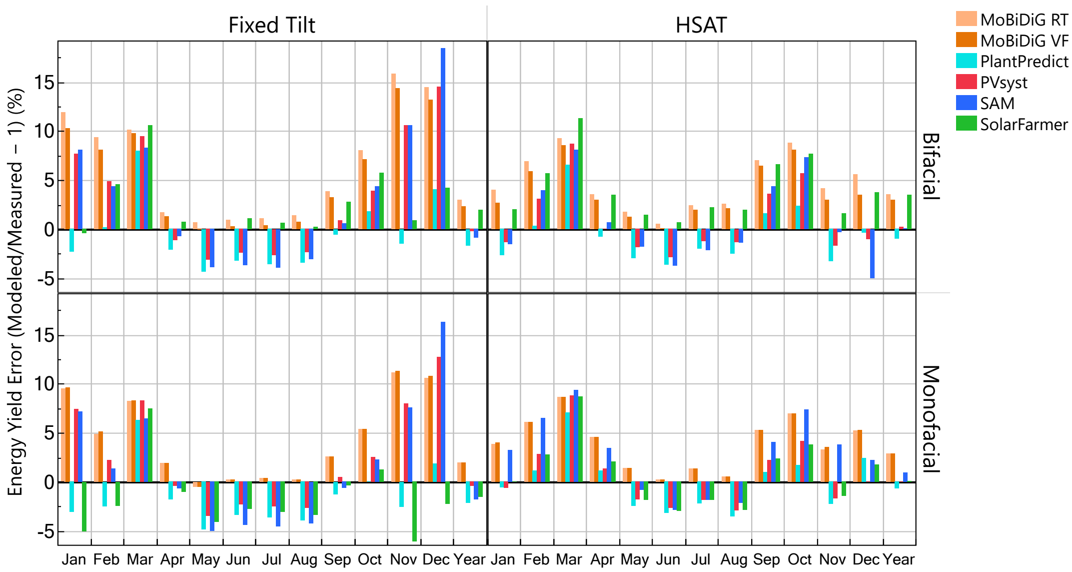

Figure 16. Monthly and yearly errors in energy yield (MWh) predictions from six software simulating four PV system types.

Finally, a word on the accuracy of bifacial versus monofacial simulations: The difference between the annual energy yield error in bifacial versus monofacial simulations is 1% or less, for five of six software. The outlier is SolarFarmer, which shows larger differences between its bifacial and monofacial simulations, but this is simply due to the overestimate of $G_{POA,Rear}$ mentioned previously. The annual errors in bifacial and monofacial simulations are no more than 0.5% different when performed in MoBiDiG VF, PlantPredict, and PVsyst. This result is in accord with the results presented in Section 3.1, which showed a deviation of roughly 0.5% between modeled and measured $G_{POA,Rear}$ values when considering the contribution of $G_{POA,Front}$.

4. Discussion and Conclusions

We assessed eight bifacial PV simulation software against $G_{POA,Rear}$, $G_{POA,Front}$, T_{MOD}, DC P_{MP}, bifacial gain, and energy measurements made at a 420-kW$_P$ test site in Roskilde, Denmark. Our results show that state-of-the-art bifacial performance models add approximately 0.5% uncertainty to the PV modeling chain. This finding was demonstrated in the analysis of modeled and measured $G_{POA,Rear}$ and DC P_{MP} values. Although 0.5% may seem small, an uncertainty of 0.5% in a 500-MW power plant translates into 2.5 MW, which translates into substantial risk in economic models. Therefore, continued efforts in reducing error in bifacial PV simulations should continue. One suggestion is the implementation of models that describe how $Bifi_{loss}$ parameters change with prevailing conditions rather than the use of static $Bifi_{loss}$ parameters as used in this work.

Our results further show that, outside of winter months, 2-D view factor fixed-tilt simulations are within ±1% of the measured monthly bifacial gain. Simulations of single-axis tracker systems are less accurate with 2-D view factor simulations within approximately 2% and 3-D ray tracing within approximately 1% of the measured bifacial gain, respectively.

When comparing modeled $G_{POA,Rear}$ to measurements, the accuracy is highly dependent on the location and type of the optical sensor. We therefore recommend future research efforts to develop standardization and/or best practice guidelines for the placement of rear POA sensors. We observed significant differences between $G_{POA,Rear}$ measurements made with thermopile pyranometers and Si-based sensors. As such, future work should aim to improve the PV community's understanding of how the spectral distribution of albedo impacts rear-facing pyranometer reference cell versus measurements, in the framework of bifacial PV performance assessment.

An objective of this study was to assess the accuracy of reduced-order bifacial PV simulations, and we found good agreement with measurements considering the uncertainty of the solar radiation input data. Because of this finding, and the fact that the rear irradiance contribution constitutes roughly 8% of the total irradiance for the site studied here, we suggest that the PV modeling community do not forget the importance of improving the accuracy of all parts of the PV modeling chain, including, but not limited to, shade loss models, cell temperature models, and diffuse sky models.

A shortcoming of this validation study is that it was performed at one site, with its specific conditions and equipment. We therefore recommend that future work includes a comprehensive review of all bifacial PV simulation validation studies performed to date. Such a study can inform the decisions of PV project developers and investors of bifacial PV assets.

Author Contributions: Conceptualization, N.R.-L., D.B., J.V., and J.L.; PV modeling, N.R.-L. and D.B.; Uncertainty modeling, D.A.M. and N.R.-L.; Engineering and design of test site, J.V. and N.R.-L.; Data analysis and visualization, N.R.-L.; Research assistance, A.A.P.; Data curation, N.R.-L., D.A.M, and J.V.; Writing—original draft, N.R.-L.; Writing—review and editing, D.B., D.A.M., A.A.P., P.B.P., J.L., J.V.; Supervision, J.V., J.L.; Project administration, J.V., P.B.P., J.L.; Funding acquisition, J.V., J.L., N.R.-L., and P.B.P. All authors have read and agreed to the published version of the manuscript.

Funding: This research was funded by the Danish Energy Technology Development and Demonstration Program (EUDP) under project contract 64018-0624.

Acknowledgments: This publication is based upon work from COST Action CA16235 PEARL PV supported by COST (European Cooperation in Science and Technology). We thank the members of WG3 for the substantive discussions on PV performance modeling. We thank Sune Thorsteinsson of DTU for assisting with the mechanical design of the albedometer stand and Martynas Ribaconka of DTU for assisting the installation of the rear POA pyranometers. We would also like to acknowledge Mark Mikofski and Anja Neubert of DNV GL, Kendra Conrad of First Solar, Marc Anoma of SunPower and Chris Deline of NREL for the technical insights they provided us on SolarFarmer, PlantPredict, pvfactors and SAM, respectively.

Conflicts of Interest: The authors declare no conflict of interest.

Nomenclature

Term	Description
BF	Bifaciality factor (%)
BG	Bifacial gain (%)
$Bifi_{loss}$	Loss of effective $G_{POA,Rear}$ (%)
BSRN	Baseline Surface Radiation Network
DHI	Diffuse horizontal irradiance (W·m^{-2})
DNI	Direct normal irradiance (W·m^{-2})
DTU	Technical University of Denmark
E	Electrical energy (Wh). Subscripts *BF* or *MF* indicate bifacial or monofacial PV, respectively
GCR	Ground cover ratio
GHI	Global horizontal irradiance (W·m^{-2})
G_{POA}	Global irradiance on the PV array (W·m^{-2}). Subscripts *front* or *rear* indicate PV Array frontside or backside
HSAT	Horizontal single axis tracker
IAM	Incident angle modifier
LID	Light induced degradation
MAE	Mean absolute error
MBE	Mean bias error
NOCT	Nominal operating cell temperature
PERC	Passivated emitter and rear contact
P_{MP}	PV module maximum power (W)
P_{STC}	Power at standard test conditions (W)
POA	Plane of array
PID	Potential induced degradation
RT	Ray tracing
RTD	Resistance temperature device
T_{AMB}	Ambient temperature (°C)

T_{MOD}	PV module temperature (°C)
U_0	Coefficient describing the effect of radiation on module temperature (W·m^{-2}·K^{-1})
U_1	Coefficient describing the effect of wind speed on module temperature (W·m^{-3}·K^{-1}·s)
U_C	Expanded uncertainty
VF	View factor

Appendix A. Model Parameters and Supplemental Data

This section provides the parameter and loss values used for the main modeling steps in the base case scenario.

Table A1. Thermal coefficients used in simulations. The NOCT of 42°C was used because this value gave a comparable thermal response as the selected U_0/U_1 coefficients with the 1-year of meteorological data used in this study.

Parameter	Monofacial	Bifacial	Unit	Model	Source
U_0	29.5	31.0	W·m^{-2}·K^{-1}	Faiman	[53]
U_1	1.6	1.6	W·m^{-3}·K^{-1}·s	Faiman	[52,71]
NOCT	42.0	42.0	°C	NOCT	
NOCT Adjust	0.0	0.0	°C	NOCT	

Table A2. Incident angle modifier coefficients used in simulations. All model coefficients—Except for the Physical model—Were extracted using a Gauss-Newton fitting algorithm and an IAM curve of a PV module with anti-reflective coating.

Parameter	PV Front Side	Model
ar	0.155	Martin & Ruiz
bo	0.056	ASHRAE
n2	1.290	Air-glass
n3	1.526	Air-glass
b0	1.029	Sandia
b1	-9.130×10^{-4}	Sandia
b2	8.507×10^{-6}	Sandia
b3	-8.464×10^{-8}	Sandia
b4	-8.713×10^{-8}	Sandia
b5	-1.711×10^{-9}	Sandia

Table A3. Electrical parameters for the two different versions of the 1-diode model used in the simulations. Please note that the parameter set used for the DeSoto model was extracted from DTU laboratory I-V measurements at STC and that the parameter set used for the PVsyst model was extracted from DTU laboratory measurements at multiple irradiances (200–1000 W·m^{-2}).

Parameter	Model	Monofacial	Bifacial	Unit
$I_{SC,STC}$	DeSoto	9.745	9.642	A
	PVsyst	9.573	9.629	
I_O	DeSoto	0.007	0.005	nA
	PVsyst	1.381	5.682	
R_{SER}	DeSoto	0.304	0.382	Ω
	PVsyst	0.192	0.255	
R_{SHUNT}	DeSoto	3.539×10^2	1.891×10^3	Ω
	PVsyst	2.035×10^3	3.821×10^3	
a	DeSoto	1.533	1.518	
Adjust	DeSoto	9.010	6.311	
$R_{SHUNT,0}$	PVsyst	8.856×10^3	2.971×10^4	Ω
Gamma	PVsyst	1.126	1.21	

Table A4. Bifacial-specific coefficients used in the simulations.

Parameter	Value	Source
Bifaciality	0.6700	DTU I-V Measurements
Transmission fraction	0.0375	DTU Calculations
Mismatch loss factor [1]	0.0025	[19]
Structure shading factor	0.0070	[52]
Front PV surface reflectivity	0.0100	[9]
Rear PV surface reflectivity	0.0300	[9]

[1] Includes front side irradiance contribution.

Table A5. DC losses used in the simulations.

Loss Factor	Value	Unit	Source
Light induced degradation	0.5	%	DTU I-V Measurements
Module Mismatch	0.1	%	[76]
DC wiring (at STC)	1.5	%	Wire-gauge and length
Soiling	0.2	%	Danish Field Measurements

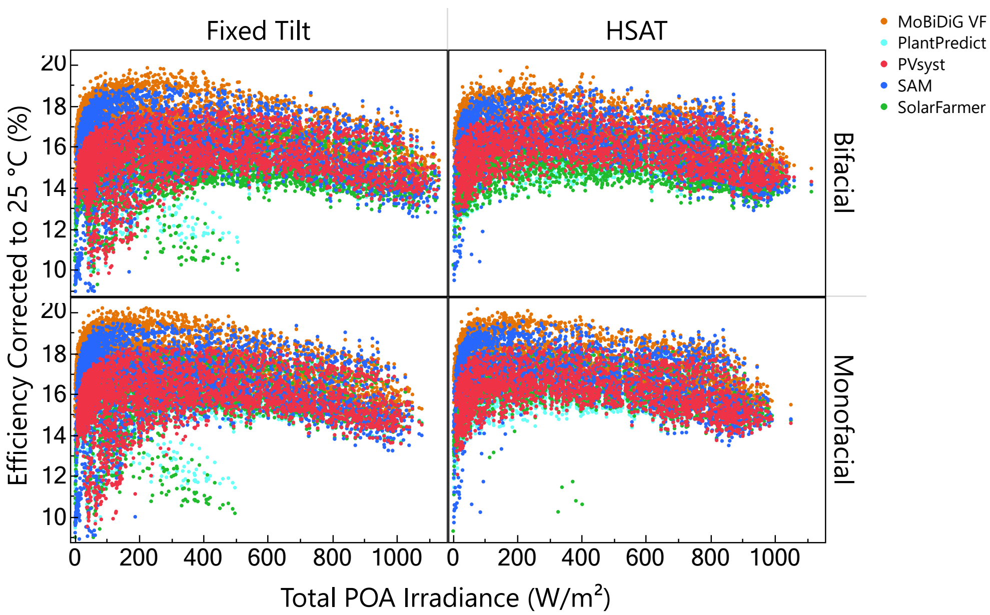

Figure A1. Modeled DC efficiency versus total POA irradiance. Note that in the monofacial cases, the x-axis does not include backside irradiance ($G_{POA,Rear}$). Data are corrected to 25 °C using the module temperature coefficient for P_{MP}.

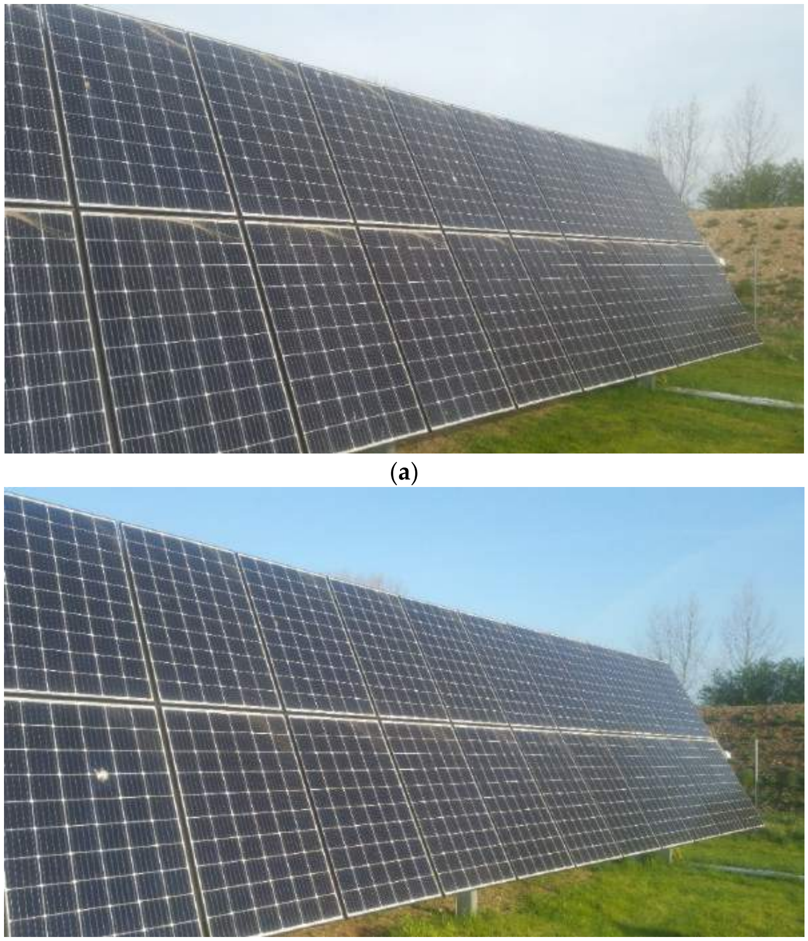

(**a**)

(**b**)

Figure A2. Monofacial HSAT array before and after a rainfall event in late April. The unusually high bifacial gains in April are attributed to the soiling present before the rainfall event. (**a**) Soiling from pollen (26 April 2019). (**b**) Reduced soiling after rainfall event (29 April 2019).

References

1. L. Stoker, EUROPE ROUND-UP: Denmark's First Bifacial Solar Farm is Sold, RWE to Pocket French Solar. Available online: (accessed on 31 October 2020).
2. EPRI. Bifacial Solar Photovoltaic Modules. Program on Technology Innovation. Available online: https://www.epri.com/research/products/3002009163 (accessed on 10 October 2019).
3. Kopecek, R.; Libal, J. Towards large-scale deployment of bifacial photovoltaics. *Nat. Energy* **2018**, *3*, 443–446, doi:10.1038/s41560-018-0178-0.
4. Meydbray, J. *Outdoor Testing for Model Validation*; BifiPV Workshop: Amsterdam, The Netherlands, 2019.
5. Wilson, G.M.; Al-Jassim, M.; Metzger, W.K.; Glunz, S.W.; Verlinden, P.; Xiong, G.; Mansfield, L.M.; Stanbery, B.J.; Zhu, K.; Yan, Y.; et al. The 2020 photovoltaic technologies roadmap. *J. Phys. D: Appl. Phys.* **2020**, *53*, 493001, doi:10.1088/1361-6463/ab9c6a.
6. Urrejola, E.; Valencia, F.; Vidal, E.F.; Deline, C.; Pelaez, S.A.; Meydbray, J.; Clifford, T.; Kopecek, R.; Stein, J. *bifiPV2020 Bifacial Workshop: A Technology Overview*; Technical Report: *NREL/TP-5K00-77817;* National Renewable Energy Laboratory, Golden, Colorado, USA, 2020.
7. Hansen, C.W.; Gooding, R.; Guay, N.; Riley, D.M.; Kallickal, J.; Ellibee, D.; Asgharzadeh, A.; Marion, B.; Toor, F.; Stein, J.S.; et al. A detailed model of rear-side irradiance for bifacial PV modules. In *Proceedings of the 2017 IEEE 44th Photovoltaic Specialist Conference (PVSC)*; Institute of Electrical and Electronics Engineers (IEEE): Washington, DC, USA, June 25–30, 2017; pp. 1543–1548.
8. Marion, B.; MacAlpine, S.; Deline, C.; Asgharzadeh, A.; Toor, F.; Riley, D.; Stein, J.; Hansen, C.; Lundberg, O.; Wallin, E.; et al. A practical irradiance model for bifacial PV modules. In *Proceedings of the 2017 IEEE*

44th Photovoltaic Specialist Conference (PVSC); Institute of Electrical and Electronics Engineers (IEEE): Washington, DC, USA, 2017; pp. 1537–1542.

9. Anoma, M.; Jacob, D.; Bourne, B.; Scholl, J.; Riley, D.; Hansen, C. View factor model and validation for bifacial PV and diffuse shade on single-axis trackers. In Proceedings of the 44th IEEE Photovoltaic Specialist Conference (PVSC), Washington, DC, USA, 25–30 June 2017.
10. Molin, E.; Stridh, B.; Molin, A.; Wackelgard, E. Experimental Yield Study of Bifacial PV Modules in Nordic Conditions. *IEEE J. Photovolt.* **2018**, *8*, 1457–1463, doi:10.1109/jphotov.2018.2865168.
11. Chiodetti, M.; Kang, J.; Reise, C.; Lindsay, A. Predicting yields of bifacial PV power plants: What accuracy is possible? In Proceedings of the 35th European Photovoltaic Solar Energy Conference (EUPVSEC), Brussels, Belgium, 24–28 September 2018.
12. Bonilla, J.; Herz, M.; Monokroussos, C.; Schweiger, M. Energy yield comparison between bifacial and monofacial PV modules: Real world measurements and validation with bifacial simulations. In Proceedings of the 35th European Photovoltac Solar Energy Conference (EUPVSEC), Brussels, Belgium, 24–28 September 2018.
13. Asgharzadeh, A.; Toor, F.; Bourne, B.; Anoma, M.A.; Hoffman, A.; Chaudhari, C.; Bapat, S.; Perkins, R.; Cohen, D.; Kimball, G.M.; et al. A benchmark and validation of bifacial PV irradiance models. In Proceedings of the 46th IEEE Photovoltaic Specialist Conference (PVSC), Chicago, IL, USA, 16–21 June 2019.
14. Berrian, D.; Libal, J.; Klenk, M.; Nussbaumer, H.; Kopecek, R. Performance of Bifacial PV Arrays with Fixed Tilt and Horizontal Single-Axis Tracking: Comparison of Simulated and Measured Data. *IEEE J. Photovolt.* **2019**, *9*, 1583–1589, doi:10.1109/jphotov.2019.2924394.
15. Nussbaumer, H.; Klenk, M.; Morf, M.; Keller, N. Energy yield prediction of a bifacial PV system with a miniaturized test array. *Sol. Energy* **2019**, *179*, 316–325, doi:10.1016/j.solener.2018.12.042.
16. Pelaez, S.A.; Deline, C.; Greenberg, P.; Stein, J.S.; Kostuk, R.K. Model and Validation of Single-Axis Tracking With Bifacial PV. *IEEE J. Photovolt.* **2019**, *9*, 715–721, doi:10.1109/jphotov.2019.2892872.
17. Pelaez, S.A.; Deline, C.; MacAlpine, S.M.; Marion, B.; Stein, J.S.; Kostuk, R.K. Comparison of Bifacial Solar Irradiance Model Predictions With Field Validation. *IEEE J. Photovolt.* **2019**, *9*, 82–88, doi:10.1109/jphotov.2018.2877000.
18. Berrian, D.; Libal, J. A comparison of ray tracing and view factor simulations of locally resolved rear irradiance with the experimental values. *Prog. Photovolt. Res. Appl.* **2020**, *28*, 609–620, doi:10.1002/pip.3261.
19. Riedel-Lyngskær, N.; Petit, M.; Berrian, D.; Poulsen, P.; Libal, J.; Jakobsen, M. A spatial irradiance map measured on the rear side of a utility-scale horizontal single axis tracker with validation using open source tools. In Proceedings of the IEEE 47th Photovoltaic Specialists Conference (PVSC), Calgary, Canada,15 June–21 August 2020.
20. Nussbaumer, H.; Janssen, G.; Berrian, D.; Wittmer, B.; Klenk, M.; Baumann, T.; Baumgartner, F.; Morf, M.; Burgers, A.; Libal, J.; et al. Accuracy of simulated data for bifacial systems with varying tilt angles and share of diffuse radiation. *Sol. Energy* **2020**, *197*, 6–21; doi:10.1016/j.solener.2019.12.071.
21. Beardsworth, G.; Asgharzadeh, A. *Quantifying your Bifacial Gains*; NexTracker White Paper, Fremont, California, USA, 2020.
22. McIntosh, K.; Abbott, M.; Sudbury, B.; Zak, C.; Loomis, G.; Mayer, A.; Meydbrey, J. Irradiance on the upper and lower modules of a two-high bifacial tracking system. In Proceedings of the 47th IEEE Photovoltaics Specialist Conference (PVSC), Calgary Canada, 15 June–21 August, 2020.
23. Rodríguez-Gallegos, C.D.; Liu, H.; Gandhi, O.; Singh, J.P.; Krishnamurthy, V.; Kumar, A.; Stein, J.S.; Wang, S.; Li, L.; Reindl, T.; et al. Global techno-economic performance of bifacial and tracking photovoltaic systems. *Joule* **2020**, *4*, 1514–1541; doi:10.1016/j.joule.2020.05.005.
24. Durusoy, B.; Ozden, T.; Akinoglu, B.G. Solar irradiation on the rear surface of bifacial solar modules: A modeling approach. *Sci. Rep.* **2020**, *10*, 1–10, doi:10.1038/s41598-020-70235-3.
25. Richter, M.; Tjengdrawira, C.; J. Vedde, M. Green, L. Frearson, B. Herteleer, U. Jahn, M. Herz and M. Kontges, *Technical Assumptions Used in PV Financial Models: Review of Current Practices and Recommendations*; IEA-PVPS T13-08:2017; The International Energy Agency (IEA), Paris, France, 2017.
26. Moser, D.; Lindig, S.; Herz, M.; Müller, B.; Horvath, I.; Schils, A.; Ramesh, S.; Green, M.; Vedde, J.; Barnard, D.; et. al. Benchmarking yield assessment exercise in different climates within an international collaboration framework. In Proceedings of the 37th European Photovoltaic Solar Energy Conference (EUPVSEC), Lisbon, Portugal, 7–11 September, 2020.

27. Riedel-Lyngskær, N.; Berrian, D.; Protti, A.; Alvarez, D.; Thorsteinsson, S.; Poulsen, P.; Libal, J.; Vedde. J. Large-scale bifacial PV test field performance compared to simulations using commercially available software, research-based, and open-source tools. In Proceedings of the 37th European Photovoltaic Solar Energy Conference (EUPVSEC), Lisbon, Portugal, 7–11 September 2020.
28. Driesse, A.; Patel, N. Cross-validation of PV System Simulation Software. In Proceedings of the 36th European Photovoltaic Solar Energy Conference (EUPVSEC), Marseille, France, 9–13 September 2019.
29. Berrian, D.; Libal, J.; Glunz, S. MoBiDiG simulations and LCOE. In *Bifacial PV Workshop*; Konstanz, Germany, 2017.
30. Deline, C.; Ayala, S. Bifacial_Radiance. Computer Software. USDOE Office of Energy Efficiency and Renewable Energy (EERE), Solar Energy Technologies Office (EE-4S). Available online: https://github.com/NREL/bifacial_radiance (accessed on 31 October 2020).
31. Passow, K.; Ngan, L.; Littman, B.; Lee, M.; Panchula, A. Accuracy of energy assessments in utility scale PV power plant using PlantPredict. In Proceedings of the 42nd IEEE Photovoltaic Specialists Conference, New Orleans, LA, USA, 14–19 June 2015.
32. Mermoud, A.; Wittmer, B. Bifacial shed simulation with PVsyst. In *Bifacial PV Workshop*; Konstanz, Germany, 2017.
33. Dioro. N.; Deline, C. Bifacial Simulation in SAM System Advisor Model (SAM). In *Bifacial PV Workshop*; Lakewood, CO, USA, 2018.
34. Mikofski, M.; Darawali, R.; Hamer, M.; Neubert, A.; Newmiller, J. Bifacial performance modeling in large arrays. In Proceedings of the 46th IEEE Photovoltaic Specialist Conference (PVSC), Chicago, IL, USA, 16–21 June 2019.
35. Mikofski, M. SolarFarmer bifacial modelling. In Proceedings of the 12th PV Performance Modeling and Monitoring Workshop, Albuquerque, NM, USA, 14–15 May 2019.
36. Sjerps-Koomen, E.; Alsema, E.A.; Turkenburg, W. A simple model for PV module reflection losses under field conditions. *Sol. Energy* **1996**, *57*, 421–432, doi:10.1016/s0038-092x(96)00137-5.
37. IEC 60904-1-2 TS. *Measurement of Current-Voltage Characteristics of Bifacial Photovoltaic (PV) Devices*; International Electrotechnical Commision, Geneva, Switzerland 2018.
38. Garcia, J.L.; Sample, T. Evolution of measured module characteristics versus labelled module characteristics of crystalline silicon based PV modules. *Sol. Energy* **2018**, *160*, 252–259, doi:10.1016/j.solener.2017.12.018.
39. Hansen, C.W.; Martin, C.E. *Photovoltaic system modeling. Uncertainty and sensitivity analyses*; Sandia Report (SAND2015-6700); Sandia National Laboratories Albuquerque, NM, USA 2015; pp. 2015–6700.
40. Holmgren, W.F.; Hansen, C.W.; Mikofski, M.A. pvlib python: A python package for modeling solar energy systems. *J. Open Source Softw.* **2018**, *3*, doi:10.21105/joss.00884.
41. Dobos, A.P. An Improved Coefficient Calculator for the California Energy Commission 6 Parameter Photovoltaic Module Model. *J. Sol. Energy Eng.* **2012**, *134*, 021011, doi:10.1115/1.4005759.
42. Gilman, P. SAM *Photovoltaic Model Technical Reference. National Renewable Energy Laboratory Report;* (NREL/TP-6A20-64102); National Renewable Energy Laboratory, Golden, CO, USA 2015.
43. Long, C.; Dutton, E. BSRN Global Network recommended QC tests v2. Baseline Surface Radiation Network, 2010. Available online: https://bsrn.awi.de/data/quality-checks/ (accessed on 31 October 2020).
44. Thevenard, D.; Driesse, A.; Pelland, S.; Turcotte, D.; Poissant, Y. *Uncertainty in Long-Term Photovoltaic Yield Predictions*; CanmetENERGY Report # 2010-122 (RP-TEC), 2010; Natural Resources Canada, Ottawa, Canada, 2010.
45. Belluardo, G.; Herz, M.; Jahn, U.; Richter, M.; Moser, D.Evaluation of uncertainty in PV project design: Definition of scenarios and impact on energy yield predictions. In Proceedings of the 44th IEEE Photovoltaic Specialist Conference (PVSC), Washington, DC, USA, 25–30 June 2017.
46. Muller, B.; Hardt, L.; Armbruster, A.; Kiefer, K.; Riese, C. Yield predictions for photovoltaic power plants: Empirical validation, recent advances and remaining uncertainties. *Prog. Photovolt.* **2015**, *24*, 15 April 2015; https://doi.org/10.1002/pip.2616.
47. Myers, D.; Reda, I.; Wilcox, S.; Stoffel, T. Uncertainty analysis for broadband solar radiometric instrumentation calibrations and measurements: An Update. In Proceedings of the World Renewable Energy Congress VIII, Denver, CO, USA, 2004.

48. Reda, I. *Method to Calculate Uncertainties in Measuring Shortwave Solar Irradiance Using Thermopile and Semiconductor Solar Radiometers*, National Renewable Energy Laboratory Report (NREL/TP-3B10-52194), Golden, CO, USA, 2011.
49. Vuilleumier, L.; Hauser, M.; Félix, C.; E Vignola, F.; Blanc, P.; Kazantzidis, A.; Calpini, B. Accuracy of ground surface broadband shortwave radiation monitoring. *J. Geophys. Res. Atmos.* **2014**, *119*, 13838, doi:10.1002/2014jd022335.
50. Vignola, F.; Michalsky, J.; Stoffel, T. *Solar and Infrared Radiation Measurements*, 2nd ed.; CRC Press: Boca Raton, FL, USA, 2019; pp. 80–83, 137–144.
51. Marion, B. Albedo data for bifacial PV systems. In *PV Reliability Workshop*; Lakewood, CO, USA, 26–28 February 2019
52. Guerrero-Perez, J.; Berbel, J.N. *BiTEC: How to Simulate Bifacial Projects? BiTEC Results 2 - Fall 2018 - Winter 2019*. Soltec Whitepaper, Madrid, Spain, 2019.
53. Lamers, M.; Özkalay, E.; Gali, R.; Janssen, G.; Weeber, A.; Romijn, I.; Van Aken, B. Temperature effects of bifacial modules: Hotter or cooler? *Sol. Energy Mater. Sol. Cells* **2018**, *185*, 192–197, doi:10.1016/j.solmat.2018.05.033.
54. Koehl, M.; Heck, M.; Wiesmeier, S.; Wirth, J. Modeling of the nominal operating cell temperature based on outdoor weathering. *Sol. Energy Mater. Sol. Cells* **2011**, *95*, 1638–1646, doi:10.1016/j.solmat.2011.01.020.
55. Wang, H.; Cheng, X.; Yang, H. Temperature coefficients and operating temperature. *IEEE J. Photovolt.* **2020**, *10*, 729–740.
56. Liang, T.S.; Pravettoni, M.; Deline, C.; Stein, J.; Kopecek, R.; Singh, J.P.; Luo, W.; Wang, Y.; Aberle, A.; Khoo, Y.S. A review of crystalline silicon bifacial photovoltaic performance characterization and simulation. *Energ. Environ. Sci.* **2019**, *116*.
57. McIntosh, K.R.; Abbott, M.D.; Sudbury, B.A.; Meydbray, J. Mismatch Loss in Bifacial Modules Due to Nonuniform Illumination in 1-D Tracking Systems. *IEEE J. Photovolt.* **2019**, *9*, 1504–1512, doi:10.1109/jphotov.2019.2937217.
58. Deline, C.; Pelaez, S.A.; MacAlpine, S.; Olalla, C. Estimating and parameterizing mismatch power loss in bifacial photovoltaic systems. *Prog. Photovolt. Res. Appl.* **2020**, *28*, 691–703, doi:10.1002/pip.3259.
59. Perez, R.; Seals, R.; Michalsky, J. All-weather model for sky luminance distribution—Preliminary configuration and validation. *Sol. Energy* **1993**, *50*, 235–245, doi:10.1016/0038-092x(93)90017-i.
60. Korevaar, M.; Babal, P.; van Nieuwkerk, S.; Wilson, K.; Mes, J. Simulation and validation of bifacial irradiance sensor mounting position. In Proceedings of the 37th European Solar Energy Conference (EUPVSEC), Lisbon, Portugal, 7–11 September, 2020.
61. Andrews, R.W.; Pearce, J.M. The effect of spectral albedo on amorphous silicon and crystalline silicon solar photovoltaic device performance. *Sol. Energy* **2013**, *91*, 233–241, doi:10.1016/j.solener.2013.01.030.
62. King, D.; Kratochvil, J.; Boyson, W. Measuring solar spectral and angle-of-incidence effects on photovoltaic modules and solar irradiance sensors. In Proceedings of the Conference Record of the Twenty Sixth IEEE Photovoltaic Specialists Conference, Anaheim, CA, USA, 29 September – 3 October 1997.
63. Myers, D.R. Quantitative analysis of spectral impacts on silicon photodiode radiometers. In Proceedings of the 40th ASES National Conference, 2011.
64. Shoukry, I.; Libal, J.; Kopecek, R.; Wefringhaus, E.; Werner, J. Modelling of Bifacial Gain for Stand-alone and in-field Installed Bifacial PV Modules. *Energy Procedia* **2016**, *92*, 600–608, doi:10.1016/j.egypro.2016.07.025.
65. Asgharzadeh, A.; Marion, B.; Deline, C.; Hansen, C.W.; Stein, J.S.; Toor, F. A Sensitivity Study of the Impact of Installation Parameters and System Configuration on the Performance of Bifacial PV Arrays. *IEEE J. Photovolt.* **2018**, *8*, 798–805, doi:10.1109/jphotov.2018.2819676.
66. Sauer, K.; Roessler, T.; Hansen, C. Modeling the irradiance and temeprature dependence of photovoltaic modules in PVsyst. *IEEE J. Photovoltaics* **2015**, *5*, 152–158.
67. Lee, K. PAN Files from IEC 61853-1 Data: Why using Datasheet I-V Values is a bad idea. In Proceedings of the 11th PV Performance Modeling and Monitoring Workshop, Albuquerque, NM, USA, 1–3 May 2018.
68. Tsanakas, J.A.; Ha, L.; Buerhop, C. Faults and infrared thermographic diagnosis in operating c-Si photovoltaic modules: A review of research and future challenges. *Renew. Sustain. Energy Rev.* **2016**, *62*, 695–709, doi:10.1016/j.rser.2016.04.079.

69. Hansen, C.W.; Farr, M.; Pratt, L. Correcting bias in measured module temperature coefficients. In Proceedings of the 2014 IEEE 40th Photovoltaic Specialist Conference (PVSC); Institute of Electrical and Electronics Engineers (IEEE), Denver, CO, USA, 8–13 June 2014; pp. 2651–2655.
70. Muller, M.; Marion, B.; Rodriguez, J. Evaluating the IEC 61215 Ed.3 NMOT procedure against the existing NOCT procedure with PV modules in a side-by-side configuration. In Proceedings of the 2012 38th IEEE Photovoltaic Specialists Conference, Austin, TX, USA, June 3–8 2012.
71. Chaudhari, C.; Bourne, B. Deriving Thermal Response Coefficients for PVsyst. In Proceedings of the 12th PV Performance Modeling and Monitoring Workshop, Albuquerque, NM, USA, 14–16 May 2019.
72. Chiodetti, M.; Lindsay, A.; Dupeyrat, P.; Binesti, D.; Lutun, E.; Raduane, K. Mousel, S.PV Bifacial Yield simulation with a Variable Albedo Model. In Proceedings of the 33rd European Photovoltaic Solar Energy Conference (EUPVSEC), Munich, Germany, 21–24 June 2016.
73. Yusufoglu, U.A.; Pletzer, T.M.; Koduvelikulathu, L.J.; Comparotto, C.; Kopecek, R.; Kurz, H. Analysis of the Annual Performance of Bifacial Modules and Optimization Methods. *IEEE J. Photovolt.* **2015**, *5*, 320–328, doi:10.1109/jphotov.2014.2364406.
74. Grommes, E.; Blieske, U.; Muller-Ost, J. The impact of Albedo measurements on power density calculations of bifacial models. In Proceedings of the 37th European Photovoltaic Solar Energy Conference (EUPVSEC), Lisbon, Portugal, 7–11 September, 2020.
75. Freeman, J.; Whitmore, J.; Blair, N.; Dobos, A. Validation of Multiple Tools for Flat Plate Photovoltaic Modeling Against Measured Data. National Renewable Energy Laboratory Technical Report (NREL/TP-6A20-61497), 2014, accessed on 31 October 2020, https://www.nrel.gov/docs/fy14osti/61497.pdf.
76. Evans, R.; Boreland, M.; Green, M.A. A holistic review of mismatch loss: From manufacturing decision making to losses in fielded arrays. *Sol. Energy Mater. Sol. Cells* **2018**, *174*, 214–224, doi:10.1016/j.solmat.2017.08.041.

Publication III. PV module energy rating standard IEC 61853-3 intercomparison and best practice guidelines for implementation and validation

Authors:

Malte Ruben Vogt, Stefan Riechelmann, Ana Maria Gracia-Amillo, Anton Driesse, Alexander Kokka, Kinza Maham, Petri Kärhä, Robert Kenny, Carsten Schinke, Karsten Bothe, James C. Blakesley, Esma Music, Fabian Plag, Gabi Friesen, Gianluca Corbellini, **Nicholas Riedel-Lyngskær**, Roland Valckenborg, Markus Schweiger, and Werner Herrmann

Published in:

IEEE Journal of Photovoltaics 2022, 12(3), pp. 844-852

PV Module Energy Rating Standard IEC 61853-3 Intercomparison and Best Practice Guidelines for Implementation and Validation

Ruben Vogt, Malte; Riechelmann, Stefan; Gracia-Amillo, Ana Maria; Driesse, Anton; Kokka, Alexander; Maham, Kinza; Karha, Petri; Kenny, Robert; Schinke, Carsten; Bothe, Karsten

Total number of authors:
19

Published in:
IEEE Journal of Photovoltaics

Link to article, DOI:
10.1109/JPHOTOV.2021.3135258

Publication date:
2022

Document Version
Peer reviewed version

This article has been accepted for inclusion in a future issue of this journal. Content is final as presented, with the exception of pagination.

PV Module Energy Rating Standard IEC 61853-3 Intercomparison and Best Practice Guidelines for Implementation and Validation

Malte Ruben Vogt, Stefan Riechelmann, Ana Maria Gracia-Amillo, Anton Driesse, Alexander Kokka, Kinza Maham, Petri Kärhä, Robert Kenny, Carsten Schinke, Karsten Bothe, James C. Blakesley, Esma Music, Fabian Plag, Gabi Friesen, Gianluca Corbellini, Nicholas Riedel-Lyngskær, Roland Valckenborg, Markus Schweiger, and Werner Herrmann

***Abstract*—The IEC 61853 standard series aims to provide a standardized measure for photovoltaic (PV) module energy rating, namely the Climate Specific Energy Rating (CSER). For this purpose, it defines procedures for the experimental determination of input data and algorithms for calculating the CSER. However, some steps leave room for interpretation regarding the specific implementation. To analyze the impact of these ambiguities, the comparability of results, and the clarity of the algorithm for calculating the CSER in Part 3 of the standard, an intercomparison is performed among research organizations with ten different implementations of the algorithm. We share the same input data, obtained by measurement of a commercial crystalline silicon PV module, among the participating organizations. Each participant then uses their individual implementations of the algorithm to calculate the resulting CSER values. The initial blind comparison reveals differences of 0.133 (14.7%) in CSER. After several comparison phases, a best practice approach is defined, which reduces the difference by a factor of 210 to below 0.001 (0.1%) in CSER for two independent PV modules. The best practice presented in this article establishes clear guidelines for the numerical treatment of the spectral correction and power matrix extrapolation, where the methods in the standard are not clearly defined. Additionally, we provide input data and results for the PV community to test their implementations of the standard's algorithm. To identify the source of the deviations, we introduce a climate data diagnostic set. Based on our experiences, we give recommendations for the future development of the standard.**

***Index Terms*—Energy performance, energy rating, energy yield, photovoltaic (PV) module.**

I. Introduction

THE IEC 61853 standard series "Photovoltaic (PV) module performance testing and energy rating" was completed in 2018 with the publication of Parts 3 and 4 [1], [2]. This followed the publication of Part 1 dealing with power rating and Part 2 dealing with incidence angle effects and module operating temperature, in 2011 and 2016, respectively [3], [4]. The series aims to provide a standardized measure for PV module performance, namely the Climate Specific Energy Rating (CSER), which is calculated in Part 3.

Manuscript received August 11, 2021; revised November 3, 2021; accepted December 1, 2021. This work was supported in part by the Project 19ENG01 (Metro-PV) from the EMPIR program cofinanced by the Participating States and in part by the European Union's Horizon 2020 research and innovation program. *(Corresponding author: Malte Ruben Vogt.)*

Malte Ruben Vogt was with the Institute for Solar Energy Research Hamelin, 31860 Emmerthal, Germany, Now he is with Photovoltaic Materials and Devices, Delft University of Technology, 2628 CD Delft, The Netherlands (e-mail: m.r.vogt@tudelft.nl).

Stefan Riechelmann and Fabian Plag are with the Physikalisch-Technische Bundesanstalt, 38116 Braunschweig, Germany (e-mail: stefan.riechelmann@ptb.de; fabian.plag@ptb.de).

Ana Maria Gracia-Amillo and Robert Kenny are with the Joint Research Centre, European Commission, 21027 Ispra, Italy (e-mail: ana.gracia-amillo@ec.europa.eu; robert.kenny@ec.europa.eu).

Anton Driesse is with the Photovoltaic Performance Labs, 79110 Freiburg, Germany (e-mail: anton.driesse@pvperformancelabs.com).

Alexander Kokka, Kinza Maham, and Petri Kärhä are with the Metrology Research Institute, Aalto University, 02150 Espoo, Finland (e-mail: alexander.kokka@hehkulab.fi; kinza.maham@aalto.fi; petri.karha@aalto.fi).

Carsten Schinke is with the Institute for Solar Energy Research Hamelin, 31860 Emmerthal, Germany, and also with the Institute for Solid State Physics, Leibniz University Hannover, 30167 Hannover, Germany (e-mail: schinke@isfh.de).

Karsten Bothe is with the Institute for Solar Energy Research Hamelin, 31860 Emmerthal, Germany (e-mail: bothe@isfh.de).

James C. Blakesley is with the National Physical Laboratory, TW11 0LW Teddington, U.K. (e-mail: james.blakesley@npl.co.uk).

Esma Music is with the Physikalisch-Technische Bundesanstalt, 38116 Braunschweig, Germany, and also with the Institut za mjeriteljstvo Bosne i Hercegovine, BA-71000 Sarajevo, Bosnia and Herzegovina (e-mail: esma.music@met.gov.ba).

Gabi Friesen and Gianluca Corbellini are with the SUPSI-PVLab, University of Applied Sciences and Arts of Southern Switzerland, 6850 Mendrisio, Switzerland (e-mail: gabi.friesen@supsi.ch; gianluca.corbellini@supsi.ch).

Nicholas Riedel-Lyngskær is with the Department of Photonics Engineering, Technical University of Denmark, 4000 Roskilde, Denmark (e-mail: nrie@fotonik.dtu.dk).

Roland Valckenborg is with the TNO, 5656 AE Eindhoven, The Netherlands (e-mail: roland.valckenborg@tno.nl).

Markus Schweiger and Werner Herrmann are with the TÜV Rheinland Energy GmbH, 51101 Cologne, Germany (e-mail: markus.schweiger@de.tuv.com; werner.herrmann@de.tuv.com).

This article has supplementary material provided by the authors and color versions of one or more figures available at https://doi.org/10.1109/JPHOTOV.2021.3135258.

Digital Object Identifier 10.1109/JPHOTOV.2021.3135258

It is important to distinguish between the two related but different concepts of energy yield prediction and energy rating since they have two very different objectives. Energy yield prediction is an estimate of the energy produced by a particular PV system constructed in a particular way in a particular location. It typically needs at least ten years of location-specific data to consider site-specific climatic characteristics as well as intra- and interannual climatological variability. The energy yield estimation requires taking into consideration many parameters, including the specific location and mounting conditions, the local environment, and climate. Energy rating is a simplified measure of how a given module type will tend to perform in different climates. It can be estimated based on one single year of data and it allows a quantitative comparison between module types. The energy rating datasets and methods are not intended to predict energy yield at any particular location.

For the purpose of energy rating, six reference climate datasets [5] describing the most representative working conditions that PV installations worldwide are subjected to are specified in Part 4 of the standard. The CSER relates the module energy efficiency in the reference climates to the module power efficiency under Standard Testing Conditions (STC: 25°C, 1000 W·m^{-2}, AM1.5G) [6] and thus aims to be a practical measure of performance in real conditions. The detailed procedure for the calculation of CSER is contained in Part 3, using input data from the other three parts. Part 3 contains 20 equations additionally the user has to derive another 18 equations to cover all extrapolation possibilities surrounding the power matrix. Thus, many calculation steps are required and the specific implementation of the calculation is left to the user, and some steps in the procedure may be subject to different interpretations. Both of these factors mean that there is a risk that different CSER results may be obtained by different laboratories and institutions. Without a reference parameter set available to the PV community, it is impossible to verify the correctness of the implementation of the CSER calculation.

This article reports comparisons of CSER calculation implementations at ten different institutions. Different programming languages were employed including Python, MATLAB, and JSL. At least one participant provides the code in open source [7]. Significant differences in results were found in the first intercomparison round [8], demonstrating that even for experienced users, the standard is not straightforward to implement. Five intercomparison rounds were needed to resolve issues, ranging from programming bugs to interpretation difficulties. These intercomparison rounds culminated in a robust implementation and very close results for all participants, when tested on an independent module dataset. It was found that the spectral correction and extrapolation of module power are the two calculation steps that cause the most issues with the interpretation of the standard. The former can be traced back to the standard not defining the exact procedure and method for numerical integration and for dealing with different spectral resolutions in the spectral correction step. The latter can be traced back to the standard not defining the exact procedure and method for extrapolation of the module power or rather efficiency table for some cases.

To establish best practice guidelines for the PV community, the detailed steps and potential pitfalls are described, as well as the reasoning behind the interpretation considered most appropriate where some ambiguity of calculation steps is found.

A reference parameter set is provided, which will allow users to test their implementation and compare their results with those of this group. The dataset includes a complete definition of all the module parameters needed (measured as defined in Parts 1 and 2 of the standard series), as well as the resulting CSER values for the six climate profiles. To aid debugging of implementations, a climate data diagnostic set is also provided that contains a small number of hourly climate data in the format of Part 4 of the standard series, chosen to highlight specific issues, along with appropriate intermediate output data.

Finally, the intensive work performing the intercomparisons involving all four parts of the standard series has enabled identification of several areas for possible improvements. Some recommendations are made, which focus on the calculation steps in Part 3, but since all four parts are closely related, it is advantageous to ensure that any proposed changes are made consistently in all four parts.

A. *IEC 61853 Standard Series Overview*

The IEC 61853 Standard series "Photovoltaic (PV) module performance testing and energy rating" establishes requirements for determining PV module performance in terms of power (watts), specific module energy rating (kWh/kW), and CSER (dimensionless). The methodology does not take into account either progressive degradation or transient behavior such as light-induced changes and/or thermal annealing. The standard presently applies to monofacial modules only. No other technologies are explicitly excluded, so it is possible to rate PV modules with all types of absorber materials and cell architectures. The standard series consists of the following four parts.

IEC 61853 Part 1 "Irradiance and temperature performance measurements and power rating" [3] describes requirements for evaluating PV module performance in terms of power (watts) rating over a range of irradiances from 100 to 1100 W·m^{-2} and module temperatures from 15°C to 75°C. This part is used to determine the so-called power matrix, which is one of the main input data required in the calculation methods applied in Part 3.

IEC 61853 Part 2 "Spectral responsivity, incidence angle and module operating temperature measurements" [4] describes test procedures to obtain the effect of varying angle of incidence (AOI) between the received irradiance and the module's surface. Part 2 also details the impact of irrdiance with wavelengths (i.e., spectral responsivity) on the PV module's effectively absorbed irradiance. The angular-loss (a_{r}) coefficient is extracted from the AOI test data, which is based on the Martin and Ruiz model [9], [10]. The higher the a_{r} coefficient, the greater the angular-dependent losses. Part 2 also describes the experimental procedures to obtain the u_{o} and u_1 thermal coefficients that are required to calculate the module temperature $T_{\mathrm{mod},j}$ from in-plane irradiance $G_{\mathrm{corr,AOI},j}$, ambient temperature $T_{\mathrm{amb},j}$, and wind speed v_j. The u_{o} and u_1 coefficients are taken from the Faiman model [11], and describe the effect of radiation and wind cooling on module temperature.

IEC 61853 Part 3 "Energy rating of PV modules" [1] describes the calculation steps needed for PV module ratings. The

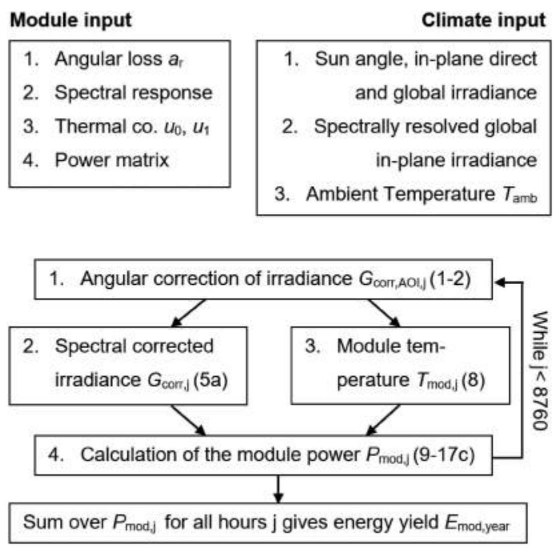

Fig. 1. Main steps and input parameters for each step of the IEC61853-3 algorithm and the equation number in this article.

input data to these calculations include the measurements and parameters obtained in Parts 1 and 2 and the meteorological conditions available in Part 4. The calculation steps are shown schematically in Fig. 1.

IEC 61853-4 Part 4 "Standard reference climatic profiles" [2] contains six standard reference climatic profiles describing the most representative working conditions of PV installations worldwide. The six standard reference climatic profiles are subtropical arid (sub. ari.), subtropical coastal (sub. cos.), tropical humid (tro. hum.), temperate continental (tem. con.), temperate coastal (tem. cos.), and high elevation (hig. ele.). The mounting condition is defined to be a free standing fixed rack, equator facing with an inclination angle β, which is fixed at 20°. Each dataset contains 8760 hourly values of several climatological variables over a year, including irradiance, ambient temperature, and wind speed. Several irradiance parameters are provided: horizontal, in-plane global, and direct broadband irradiance, as well as in-plane spectrally resolved global irradiance from 307 to 4606 nm integrated into 29 discrete bands [12].

B. Calculating CSER

For each of the six reference climatic profiles, the calculations steps in Part 3 are as follows.

The first step of the calculation algorithm is correcting the in-plane beam B_j and sky diffuse D_j irradiation for angular losses at the PV module interface due to oblique AOI θ_j. For this purpose, the model of Martin and Ruiz [9], [10] is used (1)-(2), based on the angular loss coefficient a_r of the PV module. Please note that we use the same equation numbers as the 2018 version of the IEC 61853-3 standard to simplify comparison and add letters to the equation numbers, if we introduce modified versions.

The second step is spectral correction [4] of the angular corrected irradiance $G_{\mathrm{corr,AOI},j} = B_{\mathrm{corr},j} + D_{\mathrm{corr},j}$ for the mismatch between the spectrally resolved global irradiance given in the climate data set and AM1.5G reference spectrum [13]. The result is the corrected global irradiance $G_{\mathrm{corr},j}$, for which we propose (5a).

The third step is the calculation of the module temperature $T_{\mathrm{mod},j}$, for which the Faiman model is used [11] (8).

$$B_{\mathrm{corr},j} = B_j \left[\frac{1 - \exp\left(-\frac{\cos(\theta_j)}{a_r}\right)}{1 - \exp\left(-\frac{1}{a_r}\right)} \right] \tag{1}$$

$$D_{\mathrm{corr},j} = D_j \left\{ 1 - \exp\left[-\frac{1}{a_r}\left(\frac{4}{3\pi}\left(\sin\beta + \frac{\pi - \beta - \sin\beta}{1+\cos\beta}\right) + (0.5a_r - 0.154)\left(\sin\beta + \frac{\pi-\beta-\sin\beta}{1+\cos\beta}\right)^2 \right) \right] \right\} \tag{2}$$

$$T_{\mathrm{mod},j} = T_{\mathrm{amb},j} + \frac{G_{\mathrm{corr,AOI},j}}{u_0 + u_1 v_j}. \tag{8}$$

The fourth step is the calculation of the module power output for the given hour. For this purpose, the module power is measured according to [3] at different module temperatures (15–75°C) and irradiances (100–1100 W·m^{-2}). These results form a power matrix consisting of 22 power values, converted into module efficiency through dividing by irradiance. Two-dimensional (2-D) bilinear interpolation is then used to determine the module efficiency at the corrected global irradiance $G_{\mathrm{corr},j}$ and the module temperature $T_{\mathrm{mod},j}$ values. Afterward, the obtained module efficiency value is used to calculate power output $P_{\mathrm{mod},j}$ for the given hour *j* and the process (Steps 1–4) is repeated for every hour of the year. The energy produced by the module is the sum of the hourly values. The CSER is then calculated using the following equation (20):

$$\mathrm{CSER} = \frac{E_{\mathrm{mod,year}}/H_{p,\mathrm{year}}}{P_{\mathrm{max,STC}}/G_{\mathrm{ref,STC}}} \tag{20}$$

where $E_{\mathrm{mod,year}}$ is the total energy produced, relative to the total yearly irradiation in the module plane $H_{p,\mathrm{year}}$ and the module's maximum power under STC $P_{\mathrm{max,STC}}$ and the irradiance of the reference spectrum $G_{\mathrm{ref,STC}}$. The CSER may be interpreted as the annual energy conversion efficiency in the climate relative to STC power conversion efficiency, or as a PV module performance ratio (MPR) [5], [14]–[17]. A CSER of 1 means that the PV module operates as efficient in the climate as under STC, whereas CSER values below 1 indicate lower efficiency in the reference climate and vice versa.

II. Test Module Input Data

The Module 1 dataset uses the thermal coefficients $u_0 = 25$ W/(m^2×K) and $u_1 = 6.84$ W/(m^3×s×K) taken from the literature [11]. All other module parameters are measured at TÜV Rheinland, and the results are presented in Table I and Fig. 2. All the module data are available in csv format in Appendix B–Input data module 1 and Appendix C–Input data module 2 as well as for download from https://www.metro-pv.ptb.de/home/ (see Supplementary Material). A standard c-Si module with 60

TABLE I
MODULE POWER [W] FOR MODULE 1 AT THE SPECIFIED TEMPERATURES AND IRRADIANCES IN IEC 61853-1 MEASURED FOR THIS STUDY

	Temperature [°C]			
Intensity [W/m²]	**15°C**	**25°C**	**50°C**	**75°C**
100	26.60	25.77	NA	NA
200	56.04	53.80	NA	NA
400	114.89	110.46	99.24	NA
600	174.09	167.57	150.84	133.80
800	232.89	224.16	202.05	179.35
1000	291.36	280.47	252.45	224.08
1100	NA	308.05	277.36	246.06

TABLE II
MODULE POWER [W] FOR MODULE 2 AT THE SPECIFIED TEMPERATURES AND IRRADIANCES IN IEC 61853-1 TAKEN FROM [19]

	Temperature [°C]			
Intensity [W/m²]	**15°C**	**25°C**	**50°C**	**75°C**
100	28.83	27.71	NA	NA
200	59.26	57.01	NA	NA
400	120.65	115.95	104.72	NA
600	182.0	175.04	157.86	140.13
800	242.05	233.19	209.93	186.43
1000	301.23	289.88	260.73	231.39
1100	NA	317.58	285.20	253.47

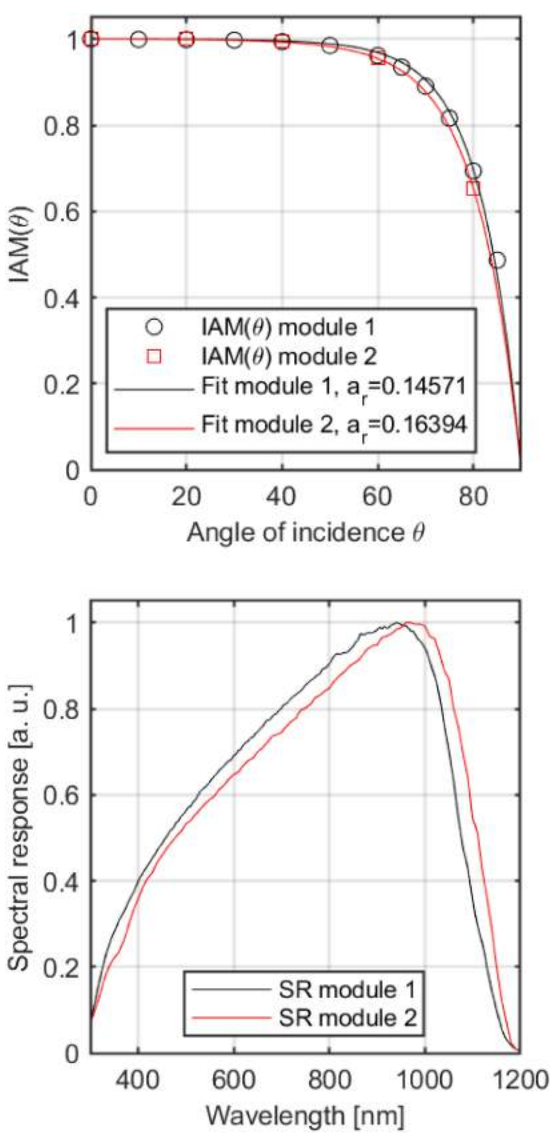

Fig. 2. IAM (top) and spectral responsivity (bottom) of the two modules used in the intercomparison campaign. Please note that the values for module 1 are measured, whereas the values for module 2 are obtained via simulation.

cells is used as the test module 1. A pulsed solar simulator, class AAA according to IEC 60904-9 [18], is used to measure the power matrix according to IEC 61853-1 [3]. The results are shown in Table I, listing the $P_{\mathrm{max,STC}}$ value as 280.47 W. The spectral responsivity (as shown in Fig. 2, bottom) is measured according to IEC 61853-2 using a monochromator system with bias light source. A pulsed solar simulator, class AAA according to IEC 60904-9, is used for the incidence angle modifier (IAM) measurement according to IEC61853-2. The measured values are the black symbols in Fig. 2 (top). In the first phase of the intercomparison campaign, participants determined their own a_{r} angular loss coefficient by fitting the measurement data themselves using different fitting methods. This lead to deviations of up to 0.008 in a_{r}. As this study is focused on Part 3 of the series and not Part 2, it was decided to use $a_{\mathrm{r}} = 0.14571$ (black line, Fig. 2 left) for all other phases.

Since no complete set of PV module input parameters for IEC 61853-3 was available in the literature, input parameters from different literature sources, all describing c-Si modules, are combined to form a second data set. This collection of PV module input parameters will be referred to as "module 2," to simplify descriptions. The module 2 dataset uses the thermal coefficients $u_0 = 26.4$ W/(m$^2\times$K) and $u_1 = 6.25$ W/(m$^3\times$s$\times$K) taken from the literature [11]. The module power matrix as shown in Table II is taken from [19]. The spectral response and angular behavior of module 2 are simulated using the Daidalos cloud ray tracer [20], which demonstrated good agreement with measurements in several studies [21]–[24]. The results are shown in red in Fig. 2.

III. INTERCOMPARISON RESULTS

In the first phase of the intercomparison [8], each participant calculated the results for module 1 without knowledge of the other participants' results. The results from phase 1 are shown in Fig. 3 for all six climate profiles. The largest difference between two participants was 0.133 (14.7%) in the tropical humid profile, but even the high elevation climate with the lowest difference of 6.7% still showed a significant deviation. Please note that result J1 was excluded due to the use of input parameters from

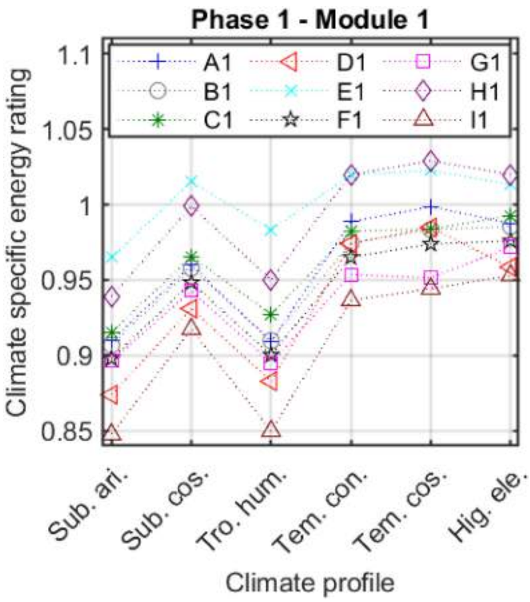

Fig. 3. CSERs for all participants and climate profiles for the same module in the initial blind comparison.

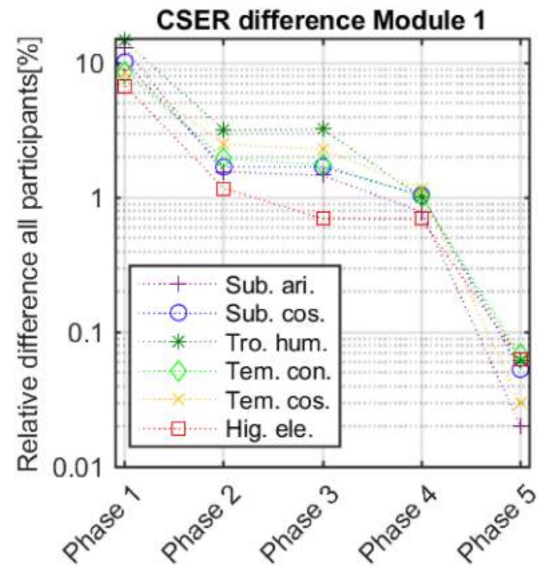

Fig. 5. Largest relative difference between any two participants for module 1 in each climate and phase declines from 14.7% to 0.07%.

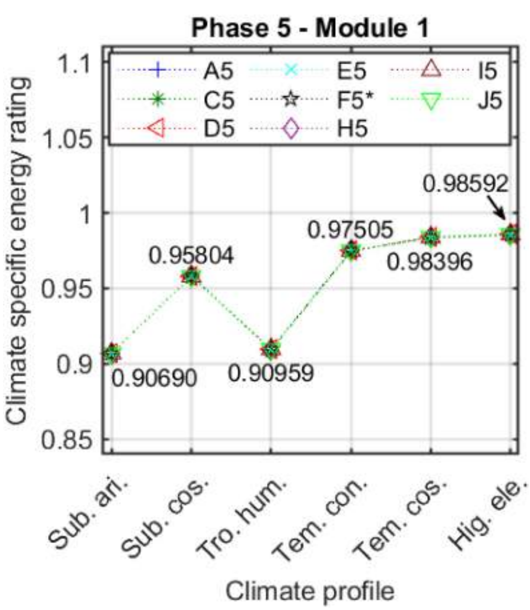

Fig. 4. CSERs for all participants and climate profiles for the same module in the final comparison round. The median of all participants' values is the respective number shown for each climate.

a different module and that the star next to participant F in phase 5 signifies that 2-D inter- and extrapolation functions build into a python software package are used rather than the explicit equations given in Appendix A (see Supplementary Material). Also note that the results including hourly data will be available for download from https://zenodo.org/record/5750185 and https://www.metro-pv.ptb.de/home/.

The results of the final comparison round (phase 5, Fig. 4) show a difference of 0.00066 (0.07%) in CSER for the temperate continental climate and less in all other climate profiles (down to 0.00018 (0.02%) in CSER for the subtropical arid climate profile).

Fig. 5 shows the development of the largest relative difference between any two participants for each climate profile through all five phases. This difference declines from 14.7% in phase 1, to 3.2% in both phases 2 and 3, to 1.2% in phase 4 and down to 0.07% in phase 5. This is a reduction by a factor of 210 between of the highest relative difference in phase 1 and 5. The relative differences shown in Fig. 5 are defined by the two most disagreeing participants, if we discard the results for the half of the participants, which are furthest from the median: We would get a difference of 4.8% in phase 1, to 0.33% in phase 2, to 0.20% in phase 3, to 0.022% in phase 4 and down to 0.0042% in phase 5. This is an even greater reduction (factor of 1152) for the core results surrounding the median of each phase. Signifying that the improvements are achieved by all participants. Please note that participants B and G stopped contributing results in phases 4 and 5 due to other work priorities; the deviation of their phase 3 results from the final median CSER is 0.21% or less for all climate profiles.

IV. Best Practice

During the intercomparison, we identified three main sources for errors [8], namely the AOI correction based on the determination of a_r values from AOI measurements, the spectral correction of in-plane irradiance, and the determination of instantaneous module power through inter- and extrapolation. In the following, we present additional guidance in interpreting the standard in a way that will provide consistent results.

A. Recommendations for the AOI Correction Procedure

The correction of AOI effects requires the a_r factor that represents the angular responsivity of the device under test. In

IEC 61853-2, it is described that this factor has to be determined by "an appropriate fitting procedure." We here recommend to use a least square fit optimization with measurement data and to limit to the range from 0° to 80° incidence angle. Measurements of higher incidence angles are increasingly prone to systematic measurement errors and therefore measurements at 85° should be rejected [24]. In the CSER calculation, the angular loss coefficient should be specified with an accuracy of five digits to prevent the impact of the fitting and rounding on the calculation.

B. Recommendations for the Spectral Correction of In-Plane Irradiance

The spectral correction is based on spectrally resolved global irradiance data given in the IEC 61853-4 and is performed by (5)–(7) of IEC 61853-3. In our analysis of the spectral correction [8], we noticed that this step is a main source for the deviations. One of the origin for that is that the spectral correction factor, defined by (6) of IEC 61853-3, does not give the value of 1, if one corrects with the reference spectrum R_{STC}. Several participants rectified this by replacing the 1000 with their value for $\int_{\lambda_s}^{\lambda_e} R_{\mathrm{STC}}(\lambda) \cdot d\lambda$. By substituting (7) into (6), we eliminate the spectral correction factor and thus a deviation source and derive:

$$G_{\mathrm{corr},j} = 1000 \cdot \frac{\int_{\lambda_s}^{\lambda_e} S(\lambda) \cdot R_{\mathrm{corr,AOI},j}(\lambda) \cdot d\lambda}{\int_{\lambda_s}^{\lambda_e} S(\lambda) \cdot R_{\mathrm{STC}}(\lambda) \cdot d\lambda}. \quad (5a)$$

Another origin of the spectral deviation is the steps and limits of the numerical integration. While the standard states that the integration limits are $\lambda_s = 300$ nm and $\lambda_e = 4000$ nm, the spectrally resolved global irradiance data in Part 4 is given in 29 so-called Kato bands [12], ranging from 306.8 to 4605.65 nm. In addition, the spectral responsivity $S(\lambda)$ and the spectral intensity of the AM1.5 spectrum have different resolutions compared to the Kato bands. We suggest to perform the following steps to harmonize the input data and solve (5a).

1) To get $S(\lambda)$ to the Kato grid, first use linear interpolation to add data points to the existing grid at the wavelength edges of the corresponding Kato band. If, for example, the initial wavelength grid of your $S(\lambda)$ is $\lambda = 300, 305, 310, 315, 320, 325, 330, \ldots, 1200$ nm, then perform a linear interpolation to $\lambda = 306.8, 310, 315, 320, 325$, and 327.8 nm.
2) Apply the trapezoidal rule for numerical integration with the now extended wavelength grid (via the previous step) to derive an $S(\lambda)$ value corresponding to the first Kato waveband.
3) Repeat 1 and 2 until you have values for 28 Kato bands. Some of these bands will have an value of zero, since $S(\lambda)$ is typically 0 beyond 1200 nm. Kato band 29 is skipped, since the last Kato band ranges from 3991 to 4605.65 nm, where the AM1.5 standard spectrum is not defined.
4) Repeat Steps 1–3 for $R_{\mathrm{STC}}(\lambda)$. Again, only 28 Kato bands are calculated.
5) Now, $S(\lambda)$, $R_{\mathrm{STC}}(\lambda)$, and $R_{\mathrm{corr,AOI},j}(\lambda)$ all have exactly 28 values, corresponding to the Kato bands. Use them as an input in (5) and calculate the products in the integrals.
6) Now, sum up the values in the integrals and multiply with 1000 to derive $G_{\mathrm{corr},j}$.

C. Recommendations for the Determination of Instantaneous Module Power

For the determination of instantaneous module power, the standard recommends converting the power matrix into an efficiency matrix. Calculation of the efficiency at arbitrary irradiance and temperature levels defined by the working conditions using 2-D bilinear interpolation or equivalent is recommended. In the round-robin, the focus remained on the bilinear approach and alternative methods were not investigated. A recent report on bilinear and alternative methods points out that for a typical PV efficiency matrix, bilinearly interpolated values will always be underestimated and extrapolated values will always be overestimated [25]. Other PV-specific methods are available that would reproduce the module efficiency characteristics with greater accuracy, and would also be suitable for the energy rating task [26]. However, allowing different methods could introduce a bias in CSER related to the method, therefore it is more important to agree on a single method even if is perhaps not the best.

Bilinear interpolation is a well-known method whereby an interpolation in two dimensions is made by performing linear interpolation along one dimension, followed by a linear interpolation along the other dimension. The order in which this is done does not affect the interpolated value. Extrapolation is done by changing one or both of the linear interpolation steps into linear extrapolation from the nearest grid points. Normally, a bilinear interpolation or extrapolation calculation requires four distinct known points on the rectangular grid formed by the two dimensions, in this case, temperature and irradiance. Unfortunately, around the irregular perimeter of the power/efficiency matrix, it is not obvious everywhere which known points (measured temperatures and irradiances) should be used for the extrapolation. Thus, some additional guidance is required to avoid inconsistent results.

First, not all extrapolation equations needed for deriving *P*(*G*, *T*) are formulated explicitly in the standard. A visual overview of the various interpolation and extrapolation cases occurring when *P(G,T)* is derived from the G-T matrix is given in Fig. 6. The standard provides (9)–(11) for interpolation of *P(G,T)* values inside the range of the G-T matrix. For extrapolating *P(G,T)*, (12)–(14) are given in the standard if 100 W/m^2 $< G <$ 1100 W/m^2 and $T >$ 75°C. If both $G >$ 1100 W/m^2 and T $>$ 75°C, (15)–(17) of the standard shall be applied. All other extrapolation equations, e.g., for $G <$ 100 W/m^2, have to be derived from the given equations, which is prone to errors. Therefore, we added all formulas necessary for extrapolation of irradiance and temperature to Appendix A (see Supplementary Material). Note that variations of the standard equations are marked by an extra letter, e.g., (14a) for extrapolation for *P(G,T)* with $G <$ 100 W/m^2. For easier reading, we use the same equation numbers (9)–(17) as in the standard.

Second, missing G-T matrix values lead to ambiguous extrapolations. A total of six data points of the G-T matrix are left blank to reduce measurement effort in IEC 61853-1. In

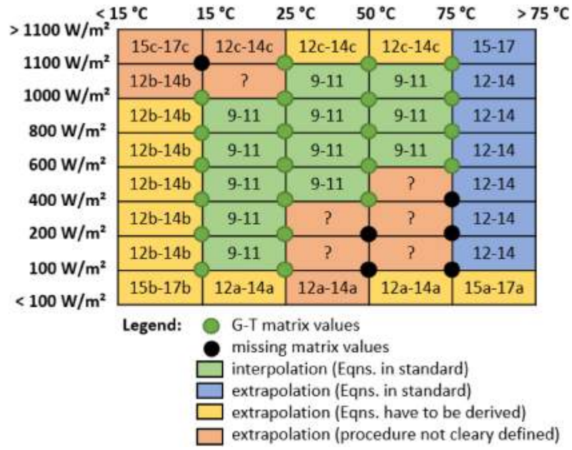

Fig. 6. Visualization of all inter- and extrapolation regions of the G-T-matrix used to derive $P(G, T)$ in the IEC 61853-3 standard. Annotations in the boxes specify the equations needed for deriving $P(G, T)$ values here. Question marks signal the possibility of ambiguous solutions.

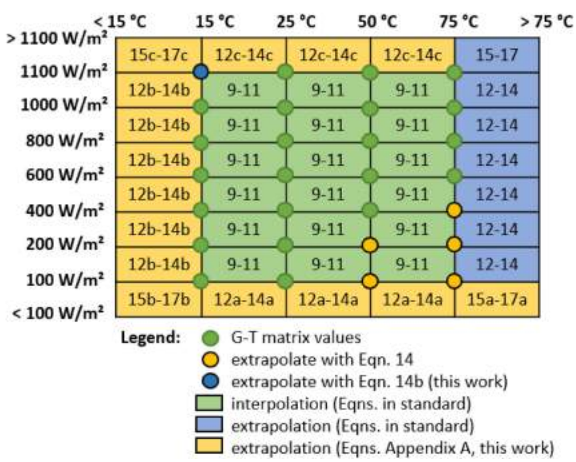

Fig. 7. Visualization of our approach to derive $P(G, T)$ based on equations of the IEC 61853-3 standard. Before $P(G, T)$ can be extrapolated, the missing data values in the G-T matrix are filled up with formula (14) of the standard and its deviation formula (14a), respectively.

this case, a $P(G,T)$ data point has three known neighbors. It is not specified which equation is applicable for this case. Possible options are an extrapolation along the temperature axis by applying (12)–(14), an extrapolation along the irradiance axis by applying (12a)–(14a), or a flat plane extrapolation with (15a)–(17a). Before starting the determination of $P(G, T)$, we recommend to fill up missing measurements in the matrix. Of the three possible options, linear extrapolation along the irradiance axis produced the least plausible efficiency values, whereas extrapolation along the flat plane formed by the nearest known grid points produced the most realistic trends. For simplicity, however, it is recommended to use the third option, which is linear extrapolation along the temperature axis with (14b) when $T = 15°\text{C}$ and with (14) when $T >= 50°\text{C}$, respectively (see Fig. 7).

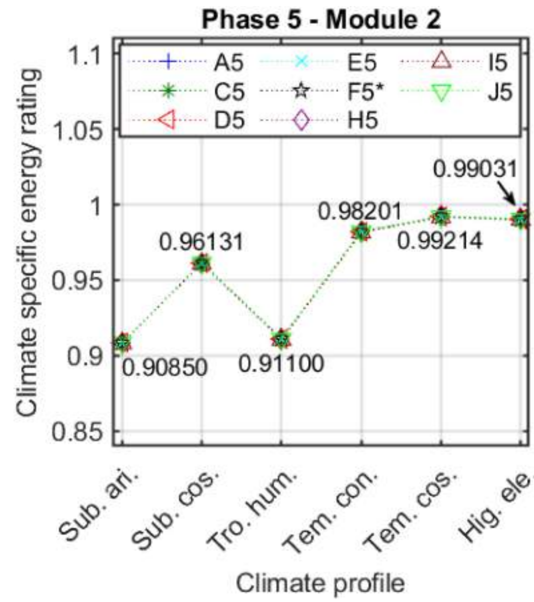

Fig. 8. Median of all participants' values is the respective number shown for each climate. The highest difference among all participants for module 2 is 0.00091 (0.095%) in CSER. This verifies, in another blind comparison round, that the improvements in agreement achieved are reproducible with other modules.

V. Verification With Independent Module Data

To verify that the improved agreement is not only limited to module 1, another blind comparison round is conducted with a new module (module 2). As in the initial blind comparison, the participants calculated the CSER values without the knowledge of the other participants' results.

The results are shown in Fig. 8. The highest difference among all participants for module 2 is 0.00091 (0.095%) in CSER for the subtropical coastal profile and less in all other climate profiles down to 0.00044 (0.044%) in CSER for the high elevation climate profile. In conclusion, a deviation of less than 0.1% between the different implementations is maintained for all climate profiles, which is significantly lower than the typical measurement uncertainty for the input parameters.

VI. Climate Data Diagnostic Set

During the intercomparison, we recognized the need to easily identify the source of differences in the CSER calculation. To achieve this purpose, the climate data diagnostic set given in Appendix D (see Supplementary Material) is created. It has the same format as the climate data given in Part 4 of the standard, but just 96 rows instead of 8760. Additionally, the climate data are artificially created for testing the following five different aspects of the CSER algorithm.

1) The first aspect tested is the treatment of direct and diffuse irradiation. This is done by the data in Appendix D rows 1–6 (month 1) (see Supplementary Material), where the direct fraction of the irradiation is increased from 0 to 100%.

2) The second aspect tested is the treatment of different incidence angles. This is done by the data in Appendix D rows 7–16 (month 2) (see Supplementary Material), where the angles of incidence are increased from 0° to 90°.
3) The third aspect tested is the treatment of different spectral bands. This is done by the data in Appendix D rows 17–45 (month 3) (see Supplementary Material), where all irradiance is concentrated in one band scanning through all 29 individual bands row by row.
4) The next aspect tested is the temperature behavior. This is done by the data in Appendix D rows 46–56 (month 4) (see Supplementary Material), where the wind speed is increased from 0 to 10 m/s.
5) The last aspect tested is the module power with respect to whole temperature as well as irradiance range. This is done by the data in Appendix D rows 57–96 (month 5) (see Supplementary Material). The artificial climate data force the algorithm to calculate the module power for each field in Figs. 6 and 7 from top left to bottom right, thus covering all inter- and extrapolation scenarios. Even some, which are nonexistent in the climate data of Part 4.

When using the climate data diagnostic set, the best practice approach with the respective module input data, we calculate a CSER of 0.86528 for module 1 and 0.86644 for module 2 or within 0.1% of this value. As discussed in Section III, at least half of the participants are within 0.005% of these values, thus we recommend to aim for an agreement in this range. The hourly results for AOI corrected irradiation, spectral correct irradiation, module temperature, and power for each hour/row are given in Appendixes E and F (see Supplementary Material).

VII. Summary and Conclusion

The practical implementation of IEC 61853-3 is more complicated than one might expect as demonstrated by the initial comparison with differences of 0.133 (14.7%) in CSER. However, after several comparison phases, a best practice approach is defined, which reduces the difference in CSER to below 0.001 (0.1%) for two independent modules.

The best practice approach establishes clear guidelines for the numerical treatment of the spectral correction and power matrix extrapolation, where the standard is not clearly defined. According to the best practice approach, the spectral correction step should use the 28 Kato bands between 306.8 and 3991 nm. In the spectral correction term, linear interpolation should be performed to generate points at band edges. Afterward, the trapezoidal rule should be used for integration. For the power matrix extrapolation, explicit equations are given in Appendix A (see Supplementary Material) for all possible combinations of temperature and irradiance.

The climate data diagnostic set introduced in this article is created to identify the source of the following deviations: Differences in the treatment of direct and diffuse irradiation as well as their angular correction, testing the module temperature based on wind as well as irradiation changes, comparing the spectral correction for each Kato band individually, and revealing differences in the inter- or extrapolation in any of the 40 regions inside as well as surrounding the power matrix points.

For future versions of the IEC 61853-3 standard, we recommend that all calculation steps are clearly defined by equations for all cases, integration limits, and numerical methods. However, from a software development perspective, the use of build-in software functions for certain tasks such as interpolation should be allowed. Of course, there is a wide range of software development packages with built-in functions, thus it should be tested on a case-by-case basis that the used function is comparable to the explicit equation in the standard. In addition to the guidelines established in this work for Part 3, the mathematical fit algorithm for determining the angular loss coefficient should be defined by future versions of 61853-2. We here recommend to use a least square fit optimization with measurement data limited to the incidence angle range from 0° to 80° and that angular loss coefficient should be specified with an accuracy of five digits to reduce the impact of the fitting and rounding in CSER calculation.

Acknowledgment

The authors would like to thank Harald Müllejans for discussions concerning (5) and its implications. Malte Ruben Vogt, Stefan Riechelmann, Ana Maria Gracia-Amillo, and Anton Driesse are the members of the taskforce for analyzing the results and investigating the inconsistencies.

References

[1] *PV Module Performance Testing and Energy Rating - Part 3: Energy Rating of PV Modules*, IEC61853-3, Oct. 2018.
[2] *PV Module Performance Testing and Energy Rating - Part 4: Standard Reference Climatic Profiles*, IEC61853-4, Nov. 2018.
[3] *PV Module Performance Testing and Energy Rating - Part 1: Irradiance and Temperature Performance Measurements and Power Rating*, IEC61853-1, Jan. 2011.
[4] *PV Module Performance Testing and Energy Rating - Part 2: Spectral Responsivity, Incidence Angle and Module Operating Temperature Measurements*, IEC61853-2, Sep. 2016.
[5] T. Huld, E. Salis, A. Pozza, W. Herrmann, and H. Müllejans, "Photovoltaic energy rating data sets for Europe," *Sol. Energy*, vol. 133, pp. 349–362, Aug. 2016, doi: 10.1016/j.solener.2016.03.071.
[6] *Solar Photovoltaic Energy Systems - Terms, Definitions and Symbols*, IEC61836, Dec. 2016.
[7] A. Driesse, "PV performance labs tools for python," 2020. [Online]. Available: https://github.com/adriesse/pvpltools-python
[8] M. R. Vogt *et al.*, "Interlaboratory comparison of the PV module energy rating standard IEC 61853-3," in *Proc. Eur. Photovolt. Sol. Energy Conf. Exhib.*, 2020, pp. 811–816.
[9] N. Martin and J. M. Ruiz, "Calculation of the PV modules angular losses under field conditions by means of an analytical model," *Sol. Energy Mater. Sol. Cells*, vol. 70, pp. 25–38, 2001.
[10] N. Martin and J. M. Ruiz, "Corrigendum to calculation of the PV modules angular losses under field conditions by means of an analytical model," *Sol. Energy Mater. Sol. Cells*, vol. 110, 2012, Art. no. 154, doi: 10.1016/j.solmat.2012.11.002.
[11] D. Faiman, "Assessing the outdoor operating temperature of photovoltaic modules," *Prog. Photovolt. Res. Appl.*, vol. 16, no. 4, pp. 307–315, Jun. 2008, doi: 10.1002/pip.813.
[12] S. Kato, T. P. Ackerman, J. H. Mather, and E. E. Clothiaux, "The k-distribution method and correlated-k approximation for a shortwave radiative transfer model," *J. Quant. Spectrosc. Radiative Transf.*, vol. 62, no. 1, pp. 109–121, May 1999, doi: 10.1016/S0022-4073(98)00075-2.

[13] *Photovoltaic Devices - Part 3: Measurement Principles for Terrestrial Photovoltaic (PV) Solar Devices With Reference Spectral Irradiance Data*. IEC 60904-3, Feb. 2019.

[14] D. Dirnberger, B. Müller, and C. Reise, "PV module energy rating: Opportunities and limitations: PV module energy rating: Opportunities and limitations," *Prog. Photovolt. Res. Appl.*, vol. 23, no. 12, pp. 1754–1770, Dec. 2015, doi: 10.1002/pip.2618.

[15] M. Schweiger, "Performance of PV modules with different technologies and the impact on energy yield in four climatic zones," Ph.D. dissertation, Technischen Hochschule Aachen, Aachen, Germany, 2017.

[16] J. C. Blakesley *et al.*, "Accuracy, cost and sensitivity analysis of PV energy rating," *Sol. Energy*, vol. 203, pp. 91–100, Jun. 2020, doi: 10.1016/j.solener.2020.03.088.

[17] J. Bonilla Castro and M. Schweiger, "Climatic rating of photovoltaic modules: Different technologies for various operating conditions," 2021.

[18] *Photovoltaic Devices - Part 9: Solar Simulator Performance Requirements*, IEC60904-9, Oct. 2007.

[19] CFV Labs, "19074 PAN file report: Hanwha q CELLS Q.Peak-G4.1 300 module," Dec. 2019. [Online]. Available: https://pvpmc.sandia.gov/pv-research/pv-lifetime-project/pv-lifetime-modules/

[20] M. R. Vogt *et al.*, "Boosting PV module efficiency beyond the efficiency of its solar cells – A ray tracing study with Daidalos now available to the scientific community," in *Proc. Eur. Photovolt. Sol. Energy Conf. Exhib.*, 2019, pp. 795–800.

[21] H. Holst *et al.*, "Application of a new ray tracing framework to the analysis of extended regions in Si solar cell modules," *Energy Procedia*, vol. 38, pp. 86–93, 2013, doi: 10.1016/j.egypro.2013.07.253.

[22] H. Holst *et al.*, "Increased light harvesting by structured cell interconnection ribbons: An optical ray tracing study using a realistic daylight model," *Energy Procedia*, vol. 92, pp. 505–514, Aug. 2016, doi: 10.1016/j.egypro.2016.07.134.

[23] M. Köntges *et al.*, "Measuring the light recovery factor of backsheets in photovoltaic modules," *Sol. Energy Mater. Sol. Cells*, vol. 186, pp. 175–183, Nov. 2018, doi: 10.1016/j.solmat.2018.06.028.

[24] N. Riedel-Lyngskær and A. A. Santamaría Lancia, "Interlaboratory comparison of angular-dependent photovoltaic device measurements: Results and impact on energy rating," *Prog. Photovolt., Res. Appl.*, vol. 29, no. 3, pp. 315–333, doi: 10.1002/pip.3365.

[25] A. Driesse and J. Stein, "From IEC 61853 power measurements to PV system simulations," 2020. [Online]. Available: https://www.osti.gov/biblio/1615179

[26] A. Driesse, M. Theristis, and J. S. Stein, "A new photovoltaic module efficiency model for energy prediction and rating," *IEEE J. Photovolt.*, vol. 11, no. 2, pp. 527–534, Mar. 2021.

Publication IV. A spatial irradiance map measured on the rear side of a utility-scale horizontal single axis tracker with validation using open-source tools

Authors:

Nicholas Riedel-Lyngskær, Manon Petit, Djaber Berrian, Peter Poulsen, Joris Libal, and Michael Linde Jakobsen

Published in:

IEEE 47th Photovoltaic Specialists Conference (PVSC) 2020

DTU Library

A Spatial Irradiance Map Measured on the Rear Side of a Utility-Scale Horizontal Single Axis Tracker with Validation using Open Source Tools

Riedel-Lyngskær, Nicholas Chistopher; Petit, Manon; Berrian, Djaber; Poulsen, Peter Behrensdorff; Libal, Joris; Jakobsen, Michael Linde

Published in:
Proceedings of 2020 IEEE Photovoltaic Specialists Conference

Link to article, DOI:
10.1109/PVSC45281.2020.9300608

Publication date:
2021

Document Version
Peer reviewed version

A Spatial Irradiance Map Measured on the Rear Side of a Utility-Scale Horizontal Single Axis Tracker with Validation using Open Source Tools

Nicholas Riedel-Lyngskær
Dept. of Photonics Engineering, Technical University of Denmark
Roskilde, Denmark nrie@fotonik.dtu.dk

Manon Petit
Dept. of Photonics Engineering, Technical University of Denmark
Roskilde, Denmark

Djaber Berrian
International Solar Energy Research Center Konstanz
Konstanz, Germany

Peter B. Poulsen
Dept. of Photonics Engineering, Technical University of Denmark
Roskilde, Denmark

Joris Libal
International Solar Energy Research Center Konstanz
Konstanz, Germany

Michael L. Jakobsen
Dept. of Photonics Engineering, Technical University of Denmark
Roskilde, Denmark

***Abstract*—This work presents measurements from 40 individual 125 mm x 125 mm crystalline silicon (c-Si) cells placed on the backside of a horizontal single axis tracker (HSAT) located in Roskilde, Denmark (55.6°N, 12.1°E). The measurements are used to validate a general set of conclusions gathered from recent literature, to compare to simulated backside irradiance results from view factor and ray-trace based methods, and to estimate the electrical losses caused by nonuniform illumination at the module and array level. In this work, all simulations are performed using the open source tools *bifacialvf*, *bifacial_radiance*, and *pvmismatch*. The tracker studied is 45 m long with 60-cell bifacial photovoltaic (PV) modules mounted "two-in-portrait" - a configuration commonly implemented in utility scale PV parks. Our measurements corroborate the conclusions from several simulation-based studies made by other authors. The measurements and simulations indicate that the irradiation-nonuniformity-induced electrical mismatch of the bifacial array is not higher than 0.25% when mounted above grass (albedo 0.22) on a clear sky day. But the array-level mismatch can go up to 3% when the PV park is *uniformly* covered by a white polymeric material (albedo 0.60). During a cloudy day, the mismatch of the bifacial system over grass is as high as 1%, but is lower than 0.25% around solar noon. Above the white ground cover on a cloudy day, the mismatch is around 1-2%, even at solar noon.**

Keywords*—*bifacial, electrical mismatch, single axis tracking

I. Introduction

A well-known challenge in bifacial photovoltaic (PV) performance modeling is accounting for the spatial non-uniformity reaching the backside of the PV array. To this end, the recent years have shown several studies where view factor (VF) and/or ray-trace (RT) based methods are used to understand how the nonuniformity changes with sky conditions and with site specific criteria such as module height, tilt angle and ground reflectance (albedo) [1] - [5]. Some of these studies include model validation and report spatial rear plane of array irradiance ($G_{POA,Rear}$) measurements, typically on static tilt systems using between two and ten irradiance sensors. From these papers a few conclusions regarding the spatial distribution of irradiance on the backside of bifacial PV arrays can be made:

1. Edge modules are brighter than inner modules.
2. Better homogeneity is observed under cloudy (high diffuse) than under clear sky conditions.
3. The closer a cell is to the tracker torque tube, the more shade loss it will experience.
4. Module-level mismatch losses are greatest in the middle of the day during a clear day, and constant over time when it is cloudy.
5. Mismatch losses are higher under high albedo than for low albedo conditions.
6. Homogeneity improves as a function of array height from the ground.

This work uses detailed $G_{POA,Rear}$ measurements collected on a two-in-portrait (2P) horizontal single axis tracker (HSAT) under clear and cloudy sky conditions and under two albedo conditions (0.22 and 0.60). With this measurement system, the aforementioned conclusions 1 - 5 can be validated in the context of Northern Europe using a HSAT configuration. We cannot validate conclusion number 6 because the tracker height is not adjustable. The movability of the sensors can also support answering open questions in the bifacial literature, such as where is the ideal location within an array to place a single backward-facing reference cell? For example, in the case of capacity testing or performance monitoring [6].

II. Methods

The Technical University of Denmark (DTU) in partnership with European Energy A/S operates a 260 kWp bifacial test facility in Roskilde, Denmark (55.6°N, 12.1°E) [7]. The facility contains various measurement systems that investigate the parameters known to influence bifacial gain (e.g. albedo, tracker pitch, tilt angle etc.). Of these is a measurement system that provides information on the non-homogeneity of light reaching the backside of a horizontal single axis tracker (HSAT). The first measurement series begins in July 2019 and

This work was funded by the Danish Energy Technology Development and Demonstration Program (EUDP) under project contract 64018-0624.

is made above the natural grass with an albedo around 0.22. On May 9th, 2020, we mounted a white polymer sheet underneath the tracker to investigate empirically the effect of albedo on electrical mismatch. Our onsite measurements indicate that the albedo of this material is approximately 0.60. The second measurement series was acquired only from May 10th to May 25th. The installation of the white sheet was delayed due to the pandemic-related situation, and therefore reduced the data acquisition period.

A. Measurement System

The HSAT studied here is a 45 m long Soltec SF7 with a 2P module mounting configuration. The tracker is situated in the middle of an eight-tracker field, with a ground cover ratio of 0.28 (Fig. 1). The tracker has a square shape (15 cm x 15 cm) torque tube with 10 cm "z-gap" from the module plane. The tracker hub height is 1.95 m.

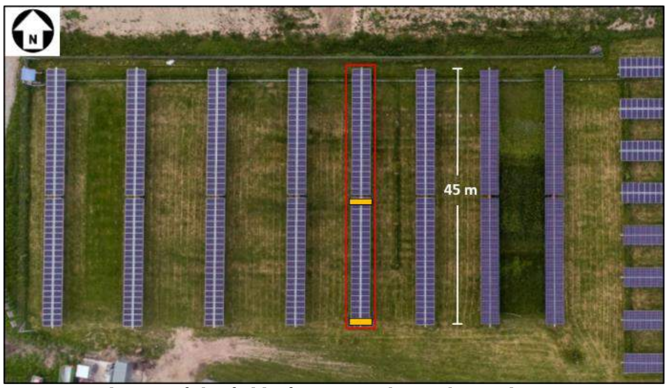

Fig. 1. Aerial view of the field of HSATs. The tracker under investigation is boxed in red. The orange rectangles show the most extreme distances (center and edge) tested. Views from the ground are shown in Fig. *2* and Fig. *3*.

On the backside of this tracker we have mounted four custom 1x10 cell panels. These panels have been assembled by MG Solar using DTU's PV module prototyping facilities. Each panel consists of ten 156.3 cm^2 mono-silicon Al-BSF cells wherein each cell's electrical contacts are accessible through the polymeric backsheet. The low-iron glass is 3.2 mm thick and does not have an anti-reflective (AR) coating. The short circuit current (I_{SC}) of each cell within the laminate is monitored using shunt resistors with ohmic values sized for the expected cell-level current-voltage (I-V) behavior at low light conditions. The expanded measurement uncertainty was estimated at ±9.3% (k = 2). The three principal components driving the uncertainty are the lab calibration (light source irradiance), the angular response, and spectral mismatch observed in the field.

The measurement panels and Radiance renderings are shown in Fig. 2 and Fig. 3. Note the 0.5 m motor gap adjacent to the inner modules has not been replicated in the Radiance simulations. The individual cells within the panels are difficult to see because the backsheet is black. On May 9th, 2020, a white polymer sheet was mounted underneath the studied tracker and is pictured in Fig. 4. The white cover is 5 m wide with 2.5 m of material on each side of the tracker. A similar scene was simulated in *bifacial_radiance* and is visualized in Fig. 5.

To make sure that our field experiment is representative of a scene where the ground is uniformly covered by an albedo of 0.60, one additional scene is simulated in *bifacial_radiance* where the ground albedo is set to 0.60 for the entire field surface.

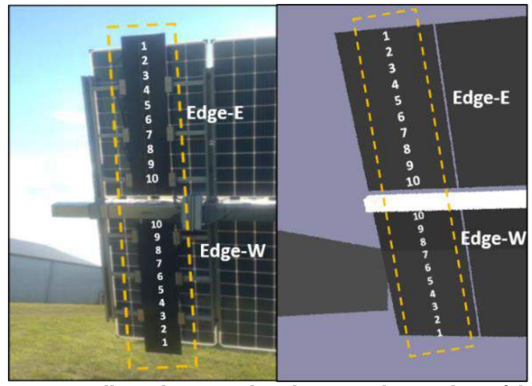

Fig. 2. Two 1x10 cell panels mounted on the east and west edges of the tracker along with the cell numbering convention. The left image shows the physical panels, the right image shows the Radiance rendering with the sensor locations.

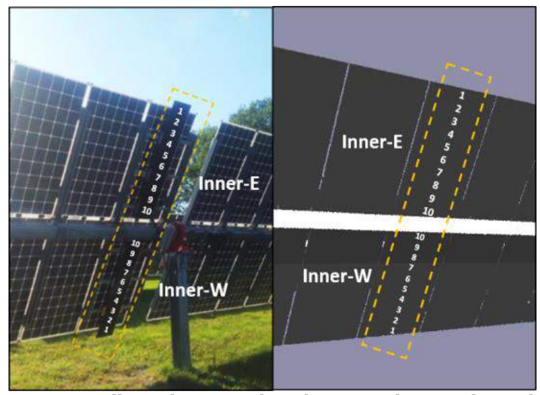

Fig. 3. Two 1x10 cell panels mounted on the east and west sides in the center of the tracker along with the cell numbering convention. The left image shows the physical panels, the right image shows the Radiance rendering.

Fig. 4. Picture of the white sheet mounted under the investigated tracker.

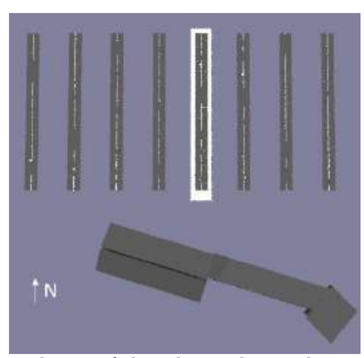

Fig. 5. Radiance rendering of the white polymer sheet mounted under the tracker considered from a top-view perspective.

B. *Backside Irradiance and Electrical Mismatch Models*

We simulate the spatial irradiance on the backside of the HSAT using two open source tools developed by the U.S. National Renewable Energy Laboratory (NREL). The first is *bifacial_radiance* [8], which is based on the Radiance ray-trace engine. The second is *bifacialvf* [9], which is a 2D VF model that implements the logic described by *Marion et al* [10]. We update the meteorological input files with 10-minute averages of onsite broadband diffuse horizontal irradiance (*DHI*), direct normal irradiance (*DNI*), global horizontal irradiance (*GHI*) recorded by spectrally flat class A sensors (per ISO 9060:2018). The onsite *GHI* - which includes all incident light - and ground reflected horizontal irradiance (*RHI*) measurements provide the albedo of the natural grass, and white surface. For each measurement series, two days are investigated: one clear sky day and one overcast day (Fig. 6 and Fig. 7). The daily clearness indexes (K_T) on the two sunny days are 0.63 and 0.67 for the first and second series, respectively. The daily K_T on the two cloudy days are 0.29 and 0.20, respectively.

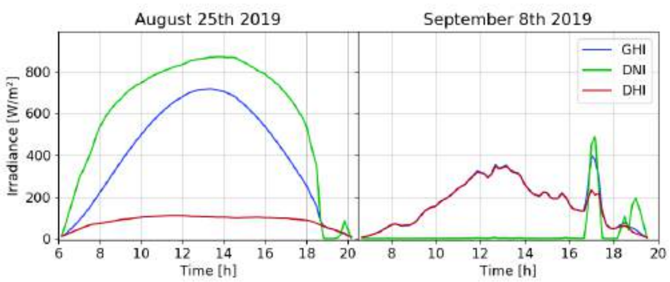

Fig. 6. Broadband irradiance (*GHI*, *DHI*, and *DNI*) from a clear sky day (08/25/2019) and overcast day (09/08/2019) in the first measurement series.

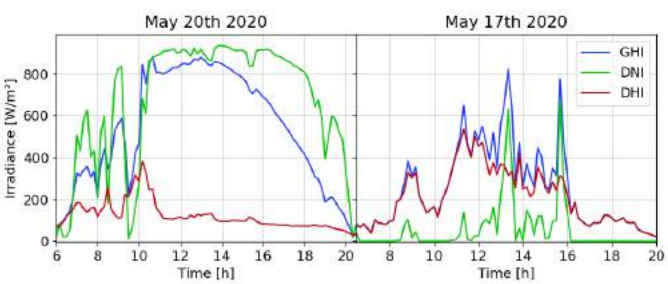

Fig. 7. Broadband irradiance (*GHI*, *DHI*, and *DNI*) from a clear sky day (05/20/2020) and overcast day (05/17/2020) in the second measurement series.

The electrical mismatch losses resulting from the nonuniform illumination are calculated using the open source code *pvmismatch* developed by SunPower [11]. The mismatch calculations are performed for conventional 60-cell (1.6 m x 1.0 m) panels with three bypass diodes per substring. We assume that the rear irradiances observed in cell locations 1 through 10 are constant along the 1.0 m horizontal width of the 60-cell panels. We calculate electrical mismatch within the four modules (Edge-E, Edge-W, Inner-E, and Inner-W) using two different inputs for $G_{POA,Rear}$: the measurements from the custom panels, and the *bifacial_radiance* simulations that contain the 40 "sensors" placed in locations representative of the cells within the custom measurement panels. In all cases the electrical mismatch at each timestamp is calculated per (1).

$$Mismatch\ [\%] = 1 - \frac{P_{Mod}}{\sum P_{Cells}} \qquad (1)$$

Where P_{Mod} is the maximum power point (P_{MP}) of the 60-cell module. This value is affected by electrical mismatch from nonuniform rear side illumination. P_{Cell} is the P_{MP} of an individual cell within the 60-cell module. For each timestamp in our *pvmismatch* model, we apply the total effective irradiance (G_{Total}) for each cell *i* as shown in (2). The front and rear side irradiance rear $G_{POA,Front}$ and $G_{POA,Rear,i}$ are calculated using either the field measurements or the *bifacial_radiance* simulation outputs, with $G_{POA,Front}$ assumed to be homogenous across the array. The total effective irradiance becomes:

$$G_{Total,i} = G_{POA,Front} + \varphi \cdot G_{POA,Rear,i} \qquad (2)$$

Where φ is the technology-specific bifaciality factor calculated as the ratio of backside efficiency to front side efficiency ($\eta_{STC,rear}$ / $\eta_{STC,front}$). In this work we have used a φ value of 0.7, which is representative of contemporary bifacial PERC modules on the market.

We have calculated the array-level mismatch using the simplified assumption that the modules in the center of the array are illuminated by the average irradiance between the Edge and Inner cases, separated by the cell numbers, as shown in Fig. 8.

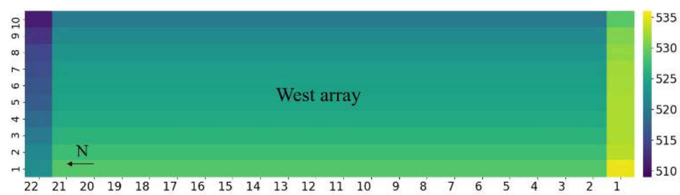

Fig. 8. Measured average $G_{Total,i}$ [W·m^{-2}] from July to November 2019 for the south-western half of an interior row of 44 modules surrounded by 7 HSATs. The numbers 1-10 on the y-axis represent cell positions, and the numbers 1-22 on the x-axis represent module positions.

III. Results

A. *Rear irradiance spatial distribution over grass surface*

The measured and modeled backside irradiance of the 4 different modules during the first measurement series is studied here. Fig. 9 displays the average measured rear irradiance within each module for a sunny and a cloudy day.

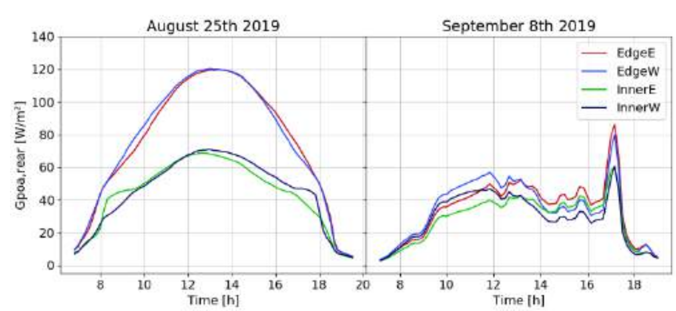

Fig. 9. Average rear irradiance of the ten cells measured within a module on a sunny (08/25/2019) and an overcast day (09/08/2019) over **grass**.

Fig. 9 confirms conclusion 1: especially during the sunny day, the edge module rear side is brighter than the inner one. On the sunny day, it is easy to see that the cells within the two edge panels receive nearly twice as much irradiance as the cells within the two inner panels. On the cloudy day, the irradiance indeed becomes more uniform and irradiance values observed within the array are within 10 W·m^{-2}. Hence, conclusion 1 and 2 – that the edge module rear side is brighter than the inner one and that homogeneity improves on the cloudy day – are validated.

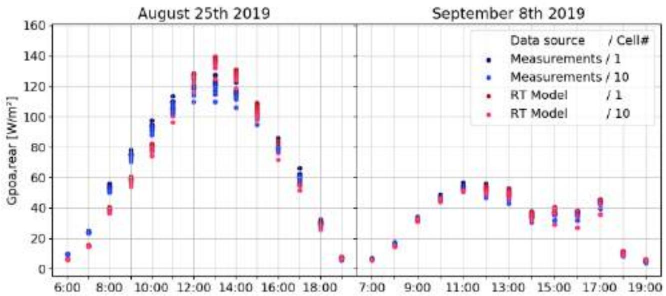

Fig. 10. Hourly average of measured/ simulated $G_{POA,Rear}$ on the **edge** module, west side of the HSAT on a sunny and an overcast day over **grass**.

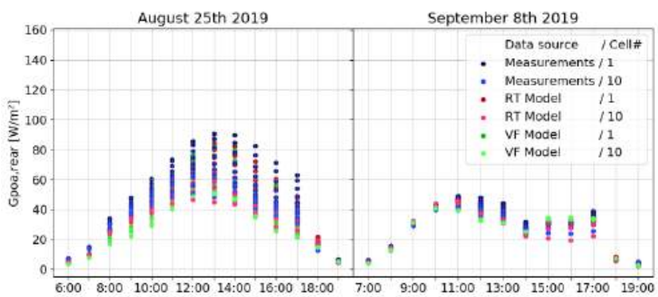

Fig. 11. Hourly average of measured/ simulated $G_{POA,Rear}$ on the **inner** module, west side of the HSAT on a sunny and an overcast day over **grass**.

Fig. 10 and Fig. 11 overlay the hourly averaged measurements, *bifacial_radiance* and *bifacialvf* simulations for the west side of the tracker at the inner and edge module locations. The *bifacialvf* results are only shown in the inner module plot, since *bifacialvf* does not consider edge effects. Ten data points are shown at each hourly timestamp and group, which represent the ten cells measured within the module.

Color shades have been applied to differentiate between cells 1 to 10. The lighter color means cell 10, which is located closest to the torque tube. The #10 cells can receive as much as 20% lower $G_{POA,Rear}$ values than the #1 cells on the sunny day and up to 10% lower on the cloudy day. This validates conclusion 3, and conclusion 2 again – that the backside irradiance is spread over a larger gradient during sunny days.

bifacial_radiance simulations reproduce well the measured inner and edge module rear irradiances. The poorest agreement of measured to modeled values is observed on the sunny day on the edge module. In the case of the west module, the model tends underestimate the irradiance in the morning, and to overestimate it around solar noon. In the morning, the error is larger than the estimated measurement uncertainty (±9.3%), but around solar noon the error becomes smaller than the uncertainty. During the cloudy day, the simulated absolute values are within the measurement uncertainty 76% of the time - considering all 40 sensors. Also, the model agrees with observed measurement trends such as: during the cloudy day, the module the closest to the sky receives more irradiance and during the sunny day, the inner module the closest to the ground receives more irradiance.

A daily root mean squared error (RMSE) was calculated individually for all 40 sensors. The cloudy day RMSE is between 1-3 W·m^{-2} with no clear trend for higher errors occurring at any particular sensor location. The sunny day RMSE, however, is between 4-10 W·m^{-2} wherein the 20 inner panel sensors show a systematic trend of lowest RMSE nearest the torque tube (4 W·m^{-2}) and highest RMSE farthest from the torque tube (10 W·m^{-2}). This could be due to an imprecise definition of the tracker motor gap in the Radiance scene. The 20 sensors on the edge panels all have a sunny day RMSE between 8-10 W·m^{-2}.

Our *bifacialvf* simulation results are slightly less accurate than *bifacial_radiance* simulations of the inner modules, which makes intuitive sense as it is a reduced order model. The VF model tends to underestimate the $G_{POA,Rear}$ irradiance during the sunny day by as much as 20 W·m^{-2}, but the discretized mean bias error (MBE) for the 20 segments is between -6 W·m^{-2} and -10 W·m^{-2} on the clear sky day. The daily RMSE is 3-5 W·m^{-2} on the cloudy day and 8-12 W·m^{-2} on the sunny day. Larger errors are again observed for cells farthest away from the torque tube. The errors could be because the structural elements of the tracker are not properly accounted for in the model (e.g. shed transparency factor, structure shading factor etc.). The *bifacialvf* model is not used for the remainder of the article since it accounts for fewer geometry details and does not capture edge effects, a key element for mismatch computations.

B. Influence of albedo on the backside irradiance

In this section, the effect of the white ground cover on the backside irradiance is studied on a clear and an overcast day. The intent is to compare to the results made over low albedo grass that were shown in section A. Using *bifacial_radiance*, two different scenes are simulated: one similar to the field experiment with a 2.5 m wide white (albedo 0.60) band on grass, and one with a uniform 0.60 albedo over the entire surroundings.

Fig. 12. Hourly average of measured/ simulated $G_{POA,Rear}$ on the **edge** module, west side of the HSAT on a sunny and an overcast day over different scenarios of **white ground cover**.

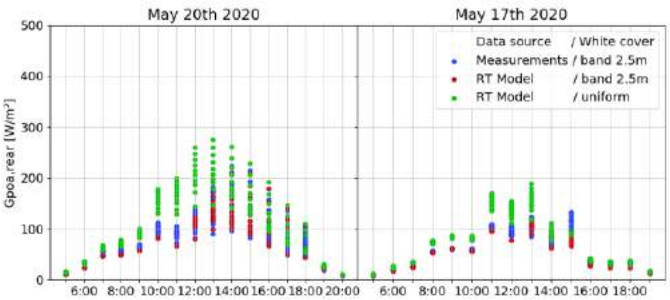

Fig. 13. Hourly average of measured/ simulated $G_{POA,Rear}$ on the **inner** module, west side of the HSAT on a sunny and an overcast day over different types of **white ground cover**.

The backside irradiance levels of the edge and inner modules of the west side are displayed in Fig. 12 and Fig. 13, respectively. First, the measurements are used to validate the accuracy of *bifacial_radiance* for the high albedo condition. Indeed, the 2.5 m wide band simulation is very close to the measurement irradiance values, within 10% precision.

Now comparing the 2.5 m band case with the uniform albedo case, it appears that the band is not wide enough to be representative of a uniform 0.60 albedo. In other words, we have reason to believe that a large quantity of ground reflected light reaching the cells comes from the grass, not the white cover. Imagine a scenario early in the morning when the west module is far from the ground: At such a moment, $VF_{GND \rightarrow PV}$ on cell 1 on the tracker west side includes a considerable portion of the grass area. An additional *bifacial_radiance* simulation showed that a 5 m band (~2.5x torque tube height) on each side of the tracker would lead to results similar to a uniform 0.60 albedo. This much additional white cover material could not be provided nor mounted yet due to pandemic-related restrictions.

The daily RMSE of the *bifacial_radiance* simulations (2.5 m band case) are between 5-10 W·m^{-2} on the cloudy day and between 9-17 W·m^{-2} on the sunny day. We again observed that the RMSE is lower for cells nearest the torque tube as was the case in the low albedo simulations. As the outdoor measurements seem to validate *bifacial_radiance* in simulating $G_{POA,Rear}$ under different albedo conditions, we will compare the bifacial gain under both conditions. Here the RT model is used for the high albedo case because the bifacial gain observed over our white cover in the field is not truly representative of a uniformly covered field. Furthermore, the $G_{POA,Rear}$ levels in W·m^{-2} are not directly comparable because the daily *GHI* profiles are different between the sunny and cloudy days of the two measurement series. The average bifacial irradiance (optical) gain is defined in (3) where $G_{POA,Rear}$ stands for the average rear irradiance within a module.

$$BG_{irr} = \frac{G_{POA,Rear}}{G_{POA,Front}} \qquad (3)$$

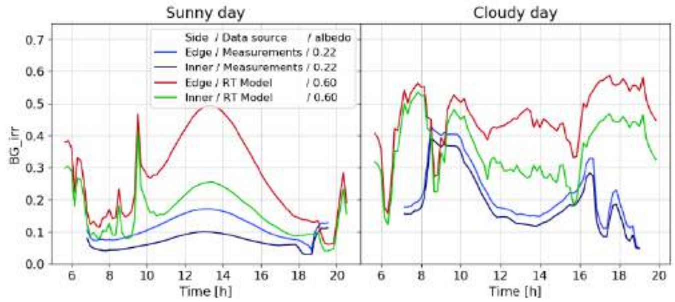

Fig. 14. Mean bifacial gain within the edge and inner modules of the west side on a sunny and a cloudy day over an albedo of 0.22 (measured, 08/25/2019 and 09/08/2019) and over albedo of 0.60 (RT model, 05/20/2020 and 05/17/2020).

The irradiance gains on the edge and the inner modules during cloudy and sunny are plotted in Fig. 14. The average bifacial irradiance gain is up to 2.5 times higher under an albedo of 0.60 than under grass albedo. As a result, the bifacial gain varies linearly with the albedo on average. Also apparent in Fig. 14 is how the bifacial gain can be overestimated by as much as 2x when edge panels - as opposed to inner panels - are used for the calculation.

C. Power mismatch losses over different ground albedos

The electrical mismatch calculated using inputs from the onsite measurements and the *bifacial_radiance* simulations during the first measurement series over grass is shown below. Fig. 15 shows electrical mismatch at the module-level and Fig. 16 at the array-level.

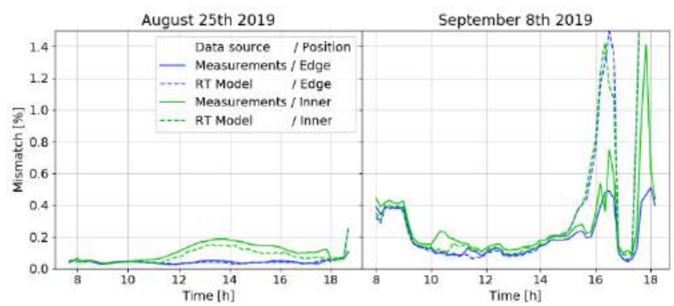

Fig. 15. **Module**-level mismatch losses of the west side modules using the measured and simulated rear irradiance values on a sunny and a cloudy day during the first measurement series over **grass**.

When used to estimate module-level mismatch losses, the RT model agrees very well with the measurements, except late in the cloudy day when some direct beam light was observed. The large discrepancy late in the day could be due to passing clouds and a lagged response from the thermopile (pyranometer) sensors - although the sensors implemented here do have response times < 5 seconds. During the sunny day, the module-level mismatch is lower than 0.2%. And during the cloudy day, the module-level mismatch losses are mostly lower than 0.2%, except at the beginning and at the end of the day. Conclusion 4 is validated here, since the module-level mismatch is highest in the middle of the day when it is sunny and is quite constant throughout the day if it is cloudy.

Please note that the results from the Eastern panels are not shown here to maintain clarity in the figures. An interesting observation we found when comparing East and West sides during the sunny day is that the module closest to the ground suffers higher mismatch losses than the top module.

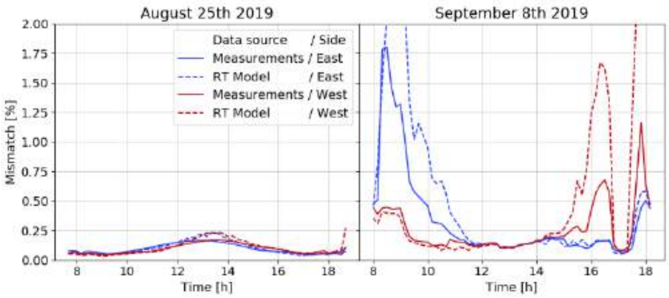

Fig. 16. **Array**-level mismatch losses using the measured and simulated rear irradiance values on a sunny and a cloudy day during the first measurement series over **grass**.

At the array-level now in Fig. 16, the RT model tends to overestimate the mismatch but follows the same trends as the measurements. During the sunny day, both the simulated and measured mismatch are lower than 0.25% and the mismatch losses are again highest in the middle of the day. During the cloudy day in the middle of the day the mismatch is < 0.15%, but in the morning and afternoon the mismatch increases on the array the closest to the ground up to 1% for periods with meaningful levels of irradiance (*GHI* > 100 W·m^{-2}).

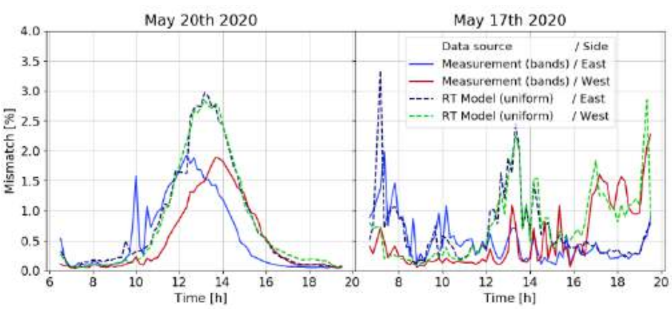

Fig. 17. **Array**-level mismatch losses using the measured and simulated data points of the HSAT for a sunny and a cloudy day of the second measurement series over an albedo of 0.60. The measurement consists of two 2.5 m bands of white cover material and the RT simulations used a uniform 0.60 albedo.

The electrical mismatch calculated using inputs from the second measurement series is studied in Fig. 17. Two different conditions are compared. The measurements made over 2.5 m wide bands of white material on each side of the tracker, and the RT scene with a uniform 0.60 albedo. During the sunny day, the modeled mismatch is similar for the east and west arrays, with a significantly higher mismatch in the middle of the day. In contrast, the measurements show that the array closest to the ground experience a higher mismatch, which is likely due to the inhomogeneous albedo. For analyzing the effect of albedo on the mismatch, the RT model calculations are used instead of the measurement, since the comparison should be done over a uniform albedo for both the grass and white-cover albedo.

Fig. 17 validates conclusion 5 – mismatch losses are higher under high albedo than for low albedo conditions. Indeed, the highest array-level mismatch during the sunny day increases from 0.25% over an albedo of 0.22 to 3% over an albedo of 0.60, i.e. by an order of magnitude.

The electrical mismatch is now studied as a function of the relative standard deviation, also termed the coefficient of variation, of the total irradiance as defined in (4) with $\mu = mean(G_{POA,total})$ from (2). A similar study has recently been carried out by *Deline et al*. [12] where RT simulations were performed of a 10° fixed tilt system above a high reflective surface and ground clearances of 0.15 m to 1.0 m. Their work resulted in a simplified model that describes electrical mismatch loss as a function of irradiance non-uniformity. *Janssen et al*. proposed a similar model in [13] for a fixed-tilt system. The module-level mismatch is shown in this section to compare our outcomes to their fitted curves. Indeed, the interpolated data used previously to calculate the array-level mismatch is not exactly true to reality. We estimate that this assumption does not affect mismatch losses much, but can significantly affect the array-level standard deviation (non-uniformity), which thus makes it unsuitable for building predictive models based on the standard deviation. Finally, only timestamps when *GHI* > 150 W/m² are considered here.

$$std_r[\%] = \frac{1}{\mu} \cdot \sqrt{\sum_{i=1}^{N} \frac{\left(G_{Total,i} - \mu\right)^2}{N}} \cdot 100\% \qquad (4)$$

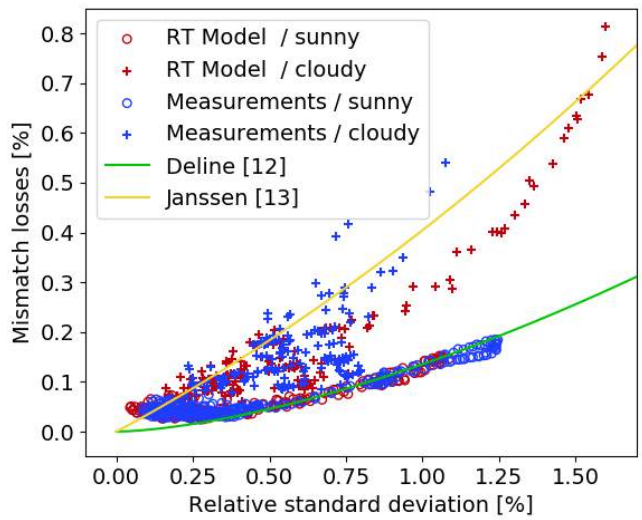

Fig. 18. **Module**-level electrical mismatch vs. the relative standard deviation. Results from the measurements and Radiance simulations are shown for all 4 modules over **grass** and compared to the literature [12] [13]. Data points are filtered when *GHI<150 W/m²*.

Module-level mismatch losses vs. relative standard deviation over grass is shown in Fig. 18. During the sunny day, both the measurements and the RT model fit quite well to the exponential curve of *Deline et al.* in [12] specified in (5). In fact, the edge modules are very uniform and correspond to a large amount of data points with $std_r[\%] < 0.25\%$. While the data from the inner modules best fits the *Deline* correlation (5).

$$M[\%]_{fit1} = e^{-2} \cdot std_r[\%]^{1.57} \qquad (5)\ [12]$$

$$M[\%]_{fit2} = 0.33 \cdot std_r[\%] + 0.075 \cdot std_r[\%]^2 \qquad (6)\ [13]$$

During the cloudy day, the correlation between mismatch and standard deviation is less obvious. Some measured data points, and even more RT modeled data points are closer to

Janssen polynomial curve [13] detailed in (6). This suggests that the effect of diffuse light ought to be accounted for when modeling mismatch losses in this range. However, one must keep in mind that the mismatch values obtained in this study are on the very low end of possible values that bifacial PV systems - particularly low ground clearance systems - can incur.

Fig. 19 again shows module-level mismatch vs. relative standard deviation, but for the second measurement series over the white cover of albedo 0.60. As a reminder, the measurements were done over a 2.5 m wide tarp under each side of the tracker, whereas the RT model considers a uniform 0.60 albedo for comparison. Both the measurements and the model fit well to the exponential curve specified in (5), for both the sunny and cloudy day. However, during the cloudy day, most of the data points are still gathered in a cluster where the relative standard deviation is lower than 1%. The sunny day data points follow the exponential curve more evenly, with relative deviations up to 3% and module-mismatch losses up to 0.9%.

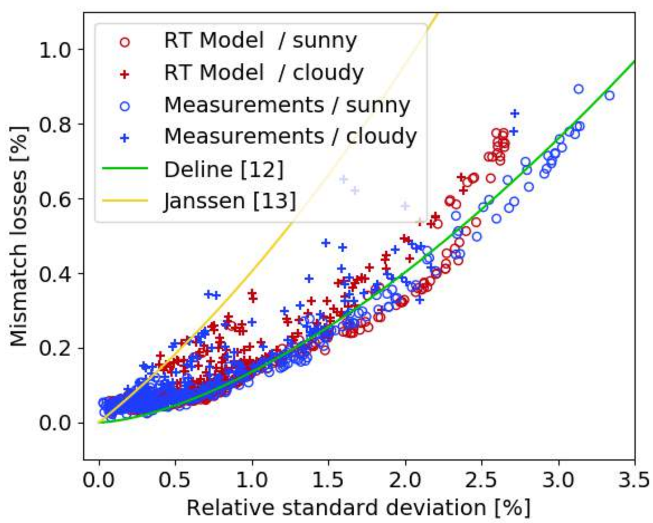

Fig. 19. **Module**-level electrical mismatch vs. the relative standard deviation. Results from the measurements and Radiance simulations are shown for all 4 modules over **white cover** and compared to the literature [12] [13]. Data points are filtered when *GHI<150 W/m²*.

IV. Summary

We have presented high resolution irradiance measurements on the back of a 2P HSAT, compared them to VF and RT simulations and calculated electrical mismatch using open source tools. The RT and VF models has been validated during a typical sunny and cloudy day over natural grass (albedo 0.22) and over a white polymer sheet (albedo 0.60), but the VF approach is less accurate as one would expect. Moreover, the effect of albedo on the backside irradiance, bifacial gain and irradiance-nonuniformity-induced power mismatch losses have been analyzed. Please note that the mismatch results shown here are expected to be different when the torque tube shape and module gap differ significantly from the tracker studied here.

References

[1] L. Kreinin, N. Bordin, A. Karsenty, A. Drori, D. Grobgeld and N. Eisenberg, "PV module power gain due to bifacial design. Preliminary experimental and simulation data," *Conference Record of the IEEE Photovoltaic Specialists Conference*, 2010.

[2] S. A. Pelaez, C. Deline, P. Greenberg, J. S. Stein and R. K. Kostuk, "Model and Validation of Single-Axis Tracking with Bifacial PV," *IEEE Journal of Photovoltaics*, vol. 9, no. 3, pp. 715-721, 2019.

[3] A. Asgharzadeh, B. Marion, C. Deline, C. Hansen, J. S. Stein and F. Toor, "A sensitivity study of the impact of installation parameters and system configuration on the performance of bifacial PV arrays," *IEEE Journal of Photovoltaics*, vol. 8, no. 3, pp. 798-805, 2018.

[4] C. W. Hansen, R. Gooding, N. Guay, D. M. Riley, J. Kallickal, D. Ellibee, A. Asgharzadeh, B. Marion, F. Toor and J. S. Stein, "A Detailed Model of Rear-Side Irradiance for Bifacial PV Modules," *44th IEEE Photovoltaic Specialists Conference*, 2017

[5] K. R. McIntosh, M. D. Abbott, B. A. Sudbury and J. Meydbray, "Mismatch Loss in Bifacial Modules Due to Nonuniform Illumination in 1-D Tracking Systems," *IEEE Journal of Photovoltaics,* vol. 9, no. 6, pp. 1504-1512, 2019.

[6] M. Waters, C. Deline, J. Kemnitz, J. Webber, M. Waters, C. Deline, J. Kemnitz and J. Webber, "Suggested Modifications for Bifacial Capacity Testing," *46th IEEE Photovoltaic Specialists Conference*, 2019.

[7] N. Riedel et al."The Outdoor Bifacial PV Testing Facility at Technical University of Denmark," *BifiPV Workshop, Amsterdam,* 2019.

[8] C. Deline and S. Ayala, Bifacial_Radiance. Computer Software. https://github.com/NREL/bifacial_radiance. USDOE Office of Energy Efficiency and Renewable Energy (EERE), Solar Energy Technologies Office (EE-4S). 17 Dec. 2017. Web. doi:10.11578/dc.20180530.16.

[9] NREL, "bifacialvf," 2019. [Online]. Available: http://github.com/ NREL/bifacialvf.

[10] B. Marion, S. MacAlpine, C. Deline, A. Asgharzadeh, F. Toor, D. Riley, J. Stein and C. Hansen, "A Practical Irradiance Model for Bifacial PV Modules," *44th IEEE Photovoltaic Specialists Conference*, 2017.

[11] M. Mikofski, B. Meyers and C. Chaudhari, "PVMismatch Project," SunPower Corporation, Richmond, CA, 2018. [Online]. Available: https://github.com/SunPower/PVMismatch.

[12] C. Deline, S. Ayala Pelaez, S. MacAlpine, C. Olalla "Estimating and parameterizing mismatch power loss in bifacial photovoltaic systems," *Prog Photovolt Res Appl.* 2020;1-13.

[13] G. Janssen, R. Gali, K. de Groot, A. Carr, B. Van Aken and I. Romijn, "Impact of inhomogeneous irradiance at

the rear of bifacial panels on modeled energy yield," in *33rd European Photovoltaic Solar Energy Conference and Exhibition*, Amsterdam, the Netherlands, 2017.

Publication V. Spectral albedo in bifacial photovoltaic modeling: what can be learned from onsite spectral measurements?

Authors:

Nicholas Riedel-Lyngskær, Martynas Ribaconka, Mario Po, Anders Thorseth, Carsten Dam Hansen, Sune Thorsteinsson, and Michael Linde Jakobsen

Published in:

IEEE 48th Photovoltaic Specialists Conference (PVSC) 2021

DTU Library

Spectral Albedo in Bifacial Photovoltaic Modeling: What can be learned from Onsite Measurements?

Riedel-Lyngskar, Nicholas; Ribaconka, Martynas; Po, Mario; Thorsteinsson, Sune; Thorseth, Anders; Dam-Hansen, Carsten; Jakobsen, Michael L.

Published in:
Proceedings of 48th IEEE Photovoltaic Specialists Conference

Link to article, DOI:
10.1109/PVSC43889.2021.9519085

Publication date:
2021

Document Version
Peer reviewed version

Citation (APA):
Riedel-Lyngskar, N., Ribaconka, M., Po, M., Thorsteinsson, S., Thorseth, A., Dam-Hansen, C., & Jakobsen, M. L. (2021). Spectral Albedo in Bifacial Photovoltaic Modeling: What can be learned from Onsite Measurements? In *Proceedings of 48th IEEE Photovoltaic Specialists Conference* (pp. 0942-0949). IEEE. https://doi.org/10.1109/PVSC43889.2021.9519085

Spectral Albedo in Bifacial Photovoltaic Modeling: What can be Learned from Onsite Measurements?

Nicholas Riedel-Lyngskær[1], Martynas Ribaconka[1], Mário Pó[2], Sune Thorsteinsson[1], Anders Thorseth[1], Carsten Dam-Hansen[1], Michael L. Jakobsen[1]

[1]Technical University of Denmark, Department of Photonics Engineering, Roskilde, Denmark

[2] EKO Instruments B.V., The Hague, the Netherlands

***Abstract*—This contribution reports on a yearlong spectral albedo measurement campaign performed in Roskilde, Denmark. Four albedo scenarios are monitored using three sensor types. The ground surfaces include green grass, dry grass, gravel, and snow – all of which have been monitored with albedometers based on spectroradiometers, silicon-pyranometers, and thermopile pyranometers. Implications of using the various albedo data sources/assumptions in bifacial PV modeling are assessed with the spectrally weighted bifacial energy gain (BEG). We find that BEG differs by as much as 3% with the different albedo sensors and BEG can deviate by as much as 7% from the ground truth when an incorrect static spectral albedo assumption is used. Finally, the spectral mismatch factor (SMM) is calculated to summarize rear plane of array (POA) spectral shifts. Our measurements show midday backside POA spectral shifts as high as 25% for Silicon bifacial PV devices mounted on single axis trackers above grass.**

***Keywords*—Albedo, Spectrum, Bifacial, Photovoltaic, Tracker**

I. Introduction

The albedo of a surface is defined as the percentage of incident sunlight that it reflects. The albedo of natural and synthetic materials is known to vary as a function of wavelength, but most photovoltaic (PV) simulation tools to date do not incorporate the spectral properties of albedo into their algorithms. This is because ground reflected irradiance constitutes less than 2% of the total frontside plane-of-array (POA) irradiance for most traditional monofacial installations (i.e., an array tilt angle from horizontal ≤ 30° and albedo ≤ 0.25). However, ground reflected irradiance contributes significantly to the energy produced by bifacial PV systems because the rear POA irradiance is comprised primarily of ground reflected light. With the rapid increase in bifacial PV module adoption — and the forecasted majority market share of bifacial cells by 2023 [1] — a better understanding of spectral albedo in bifacial PV applications is necessary to improve performance modeling accuracy and reduce perceived risk by investors.

Previous works on spectral albedo in bifacial PV applications come to a common conclusion that spectral effects must be accounted for in bifacial PV simulation [2] – [5]. A shortcoming of these and other works [6] – [8] is that they use a single spectral albedo curve (with the exception of [5]) for timeseries simulations when it is well-known that the spectral albedo distribution changes with conditions such as solar angle, sky diffuse fraction, surface roughness and surface moisture content [9]. We use continuous spectral albedo measurements and 2D view factor modeling to put the constant spectral albedo assumption under a microscope. Additionally, we analyze the differences in modeled rear POA irradiance ($G_{POA,Rear}$) and bifacial gain that can occur due to different albedo data sources, which in this work include:

1. Measured spectral albedo from spectroradiometers,
2. Measured broadband albedo from pyranometers,
3. Measured broadband albedo from Si-pyranometers,
4. Constant spectral albedo from data base, and
5. Constant albedo assumption of 0.2.

Our previous work demonstrated that $G_{POA,Rear}$ modeling contributes approximately 0.5% uncertainty to annual energy yield estimates when using state-of-the-art bifacial PV simulation tools [10]. A motivation of the present work is to identify approaches that can reduce this uncertainty.

II. Methods

A. Field Measurements

Spectral irradiance data in the range of 300 – 1100 nm are recorded every five minutes by three EKO MS711 spectroradiometers. Two MS711s are horizontally mounted: one upward facing instrument records the global horizontal spectral irradiance GHI_λ and one downward facing instrument records the ground reflected horizontal spectral irradiance RHI_λ (Fig. 1). The third MS711 records the direct normal spectral irradiance DNI_λ. This instrument is installed on a dual-axis tracker and has a 5° field-of-view (FOV) collimation tube – as used in [11]. The spectral albedo α_λ is calculated as the ratio of the downward facing RHI_λ and upward facing GHI_λ measurements:

$$\alpha(\lambda) = \frac{RHI(\lambda)}{GHI(\lambda)} \tag{1}$$

The diffuse horizontal spectral irradiance $DfHI_\lambda$ is calculated (2) from the difference between the measured GHI_λ and the measured DNI_λ adjusted by Lambert's cosine law with the zenith angle (θ_Z):

$$DfHI(\lambda) = GHI(\lambda) - DNI(\lambda) \cdot \cos\theta_Z \tag{2}$$

This work was funded by the Danish Energy Technology Development and Demonstration Program (EUDP) under project contract 64018-0624.

The field measurement campaign investigates the diurnal and seasonal variations in spectral albedo under four surfaces/conditions: green grass (Fig. 1a), dry grass (Fig. 1b), gravel (Fig. 1c), and snow (Fig. 1d). Broadband albedo measurements from Class C thermopile pyranometers and Silicon-photodiode pyranometers are acquired onsite at 1-minute intervals. The pyranometers albedo stand is located 12 m from the spectral albedo setup and the Si-Pyranometer albedo stand is located ~100 m away.

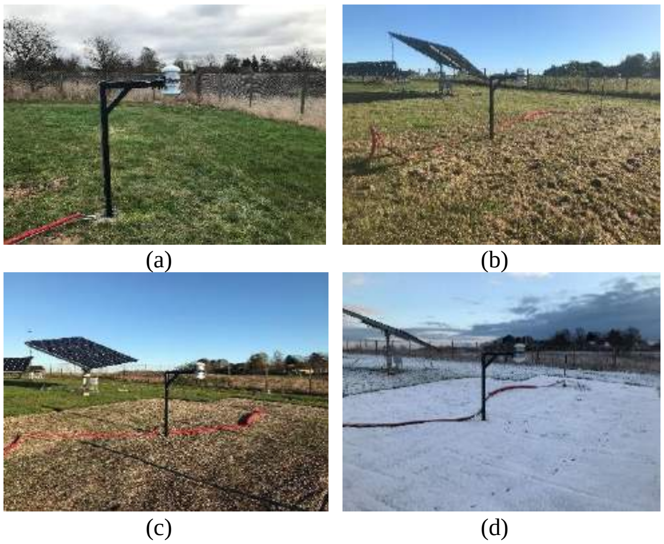

Fig. 1. Various albedo conditions tested: (a) Healthy grass from Feb – May 2020, (b) dry grass from Jul – Sep 2020, (c) 5 – 8 mm gravel from Sep 2020 – Apr 2021, and (d) snow in Jan 2021.

B. Laboratory Calibration and Uncertainty

Calibration of all three EKO MS711 spectroradiometers was performed inhouse at DTU Fotonik's DOLL laboratories in January 2020 just before the field measurement campaign began. The calibration setup consists primarily of a NIST traceable FEL lamp on an alignment jig 50 cm from the device under test with measures to mitigate stray light. A second measurement of the FEL reference lamp was performed in May 2021 immediately after the measurement campaign concluded. These final measurements served to check for any calibration and/or wavelength drifts that occurred during the field measurements. The spectroradiometers used for DNI_λ and GHI_λ measurements deviated by less than 5% relative to the reference lamp between 400 and 1050 nm and showed mean bias errors (MBE) less than 3%. The spectroradiometer used for RHI_λ measurements showed deviations as high as 9% at some wavelengths, but the MBE was 3%, comparable to the other two spectroradiometers. This instrument showed pronounced wavelength shifts at 645 and 670 nm, which were not observed in the other two instruments.

The expanded calibration uncertainty is wavelength and instrument dependent. Fig. 2 shows the calibration uncertainty during the May 2021 calibration event. The uncertainty is estimated using uncertainty contributions from: lamp sensor distance (0.8%), signal to error estimation (mean 2.2%, max 8%), lamp current stability (0.1%), lamp drift estimate (0.5%), repeatability of measurement (0.5%) and readout noise (max 2.2%).

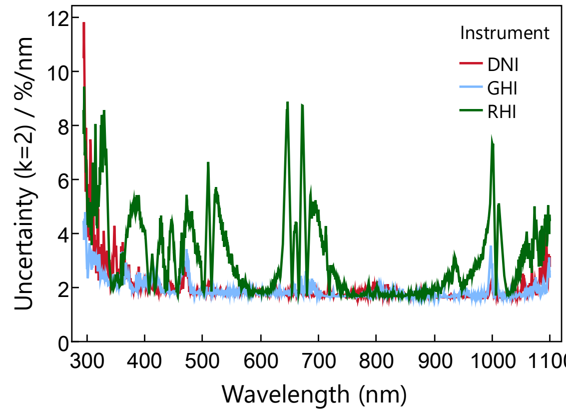

Fig. 2. Measurement uncertainty (k=2) of the spectral calibration. The spikes are appearing where gradients in the spectral throughput cause responsivity to change drastically with wavelength shifts.

The angular response of the upward and downward facing MS711s follow a cosine response within 3% or better when the solar zenith angle is greater than 80°. This cosine error will primarily affect the upward facing (GHI) instrument at high solar zenith angles in direct sunlight.

C. Handling of Spectral Data

The upward and downward facing spectroradiometers do not acquire measurements in parallel because a single datalogger records data from both units. We have observed up to ~15 second delays between when the first spectroradiometer begins its measurement and when the second unit completes its measurement. This delay is due to the data processing time in the logger and the exposure times in each sensor, which take 10 to 5000 ms each depending on the light intensity. An irradiance stability check is needed because the calculated spectral albedo values assume a constant condition during the GHI_λ and RHI_λ measurements. The stability check is performed for each measurement using a variability index (VI) [12]. GHI data recorded every 10 seconds by a Class A pyranometer are used to calculate a VI within a 2-minute period: approximately 1 minute before and after the measurement. Measurements are removed when the VI > 1.1. Data recorded on detector edges (λ < 300 nm and λ > 1050 nm) are also removed as they are often prone to measurement noise.

The bifacial cells studied in this work are spectrally sensitive to light between 300 and 1200 nm. Since the useful detector range is limited to 1050 nm, the spectral irradiance gap (1050 – 1200 nm) is completed using SMARTS 2.9.5 [13]. We use the real-time solar zenith angle (air mass proxy), ambient temperature and atmospheric pressure to generate SMARTS clear sky spectra that correspond to each spectral measurement. The simulated clear sky spectra are scaled using a procedure described by [14], which uses the broadband global and diffuse fluxes to account for cloud cover. The RHI_λ data are extended by scaling the SMARTS spectral albedo file that shows the most similar relative profile to the measurements. For example, the spectral albedo measurements of grass are extended using the 'GrazingField.dat' file. The spectral extension carries minimal effect on the results, however, because the spectral responsivity is low between 1050 and 1200 nm, and because sunlight can be significantly absorbed by atmospheric water vapor between 1100 and 1200 nm.

Handling of continuous solar spectral measurements can be challenging owing to the sheer volume of data generated over yearly timescales. For example, our three spectroradiometers with 2048 pixels each measuring every 5 minutes over 15 months generated a data frame with over 22 million rows. We have found the hierarchical data format (HDF5) to be particularly useful in organizing and working with such datasets.

D. Optical Model

The measured and calculated spectral irradiance data (α_λ, GHI_λ, DNI_λ, and $DfHI_\lambda$) are passed to the open-source Python-based 2D view factor model *pvfactors* [15] running in full simulation mode. Two principal assumptions inherent in 2D view factor models are that surfaces scatter light isotropically (i.e., Lambertian scattering) and that the PV rows are infinitely long (i.e., edge brightening effects are ignored). Most natural surfaces, however, are non-Lambertian scatterers, at least to some extent.

With pvfactors, we calculate the front and rear POA spectral irradiances ($G_{POA,Front,\lambda}$ and $G_{POA,Rear,\lambda}$) for 25° fixed-tilt and horizontal single-axis tracking (SAT) systems (Table 1), which are the two types of large-scale bifacial PV systems collocated at the site [10]. In both cases, a five-row system is simulated and results from the middle row are reported.

Table 1. Configuration of the 2-in-portrait bifacial PERC systems installed on site and modeled in this work. Systems are installed above grass (see Fig. 1a).

	Fixed-Tilt	**Single Axis Tracker**
Tilt Angle	25°	± 60°
Hub (center) Height (m)	2.3	2.0
Ground Cover Ratio	0.40	0.28

The spectral irradiance data at each wavelength λ are processed in pvfactors using the same approach as if broadband irradiance data were used. In other words, instead of passing broadband irradiance in $W{\cdot}m^{-2}$, as a pvfactors user would do ordinarily, our implementation passes *spectral* irradiance in $W{\cdot}m^{-2}{\cdot}nm^{-1}$. The model then accounts for the interreflections between scene surfaces using spectrally resolved light for wavelengths between 300 and 1200 nm. Front and rear side angular reflection losses are accounted for using the Sandia incident angle modifier (IAM) model [16].

E. Analysis

The spectral POA irradiance $G_{POA,Front,\lambda}$ and $G_{POA,Rear,\lambda}$ are summarized using a spectrally weighted bifacial energy gain (BEG), which is calculated as:

$$BEG = \frac{\int_a^b SR_{Rear}(\lambda) \cdot G_{POA,Rear}(\lambda)\, d\lambda}{\int_a^b SR_{Front}(\lambda) \cdot G_{POA,Front}(\lambda)\, d\lambda} \cdot 100\% \qquad (3)$$

Where SR_{Front} and SR_{Rear} are the PV cell's spectral response of the front and backside. The integration limits *a* to *b* are 300 to 1200 nm. The BEG in (3) is simply the ratio of short-circuit current (I_{SC}) generated by the backside relative to the I_{SC} generated by the frontside. This equation does not include adjustments for structural shading on the backside of the array, or any possible thermal differences between monofacial and bifacial cells that could affect voltage. Nonetheless, (3) is still useful for our objective, which is to understand the differences in bifacial gain that can occur due to different albedo data sources. In the case of the Si-pyranometer and pyranometer measured albedo, the albedo passed to pvfactors is the same at all wavelengths, proportional to the measurements at each timestamp (i.e., a 'flat' spectral albedo curve is produced). In the case of constant spectral albedo data, the data originates from the ASTER library [17], which is the source of the spectral albedo files in SMARTS used here. In all cases, the same DNI_λ and $DfHI_\lambda$ spectra are input to pvfactors.

The Results section also reports backside POA spectral mismatch (SMM) factors (4). Equation (4) is taken from (7) in IEC 60904-7 [18], where G_{Ref} is the AM1.5G reference spectrum defined in IEC 60904-3 [19].

$$SMM = \frac{G_{Ref} \cdot \int_a^b SR_{rear}(\lambda) \cdot G_{POA,rear}(\lambda)\, d\lambda}{G_{POA,rear} \cdot \int_a^b SR_{rear}(\lambda) \cdot G_{Ref}(\lambda)\, d\lambda} \qquad (4)$$

The SMM factor captures spectral shifts relative to the AM1.5G rating wherein SMM > 1 indicates spectrally induced I_{SC} gains and SMM < 1 indicates spectrally induced I_{SC} losses. The backside SMM also serves as a meaningful way to summarize the large amount of spectral albedo data recorded.

The BEG and SMM are calculated for a standard bifacial p-type passivated emitter and rear contact (PERC) cell. The PERC cell was procured from Blue Sun solar and encapsulated in 3 mm PV glass and EVA at DTU. Fig. 3 shows the measured spectral responsivity on front and backside. The choice to analyze PERC was made because this technology is presently the most common bifacial cell type deployed in large systems.

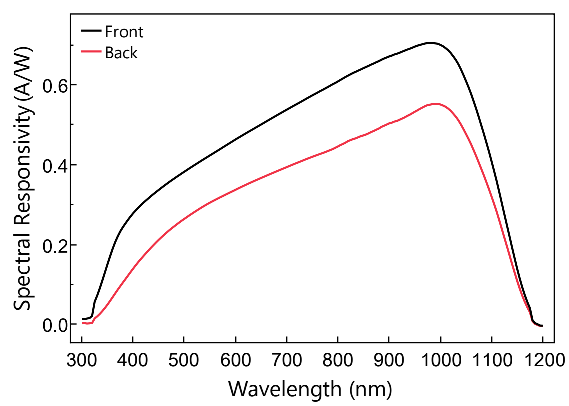

Fig. 3. Absolute spectral responsivity of the PERC cell (front and back). The cell is encapsulated in standard PV glass and measured using a PV Measurements QEXL quantum efficiency measurement system.

III. Results

A. Diurnal and Seasonal Spectral Albedo

Fig. 4, Fig. 5, and Fig. 6 show spectral albedo measurements recorded on clear sky days above green grass, dry grass, and gravel, respectively. Note that the sky conditions in the pictures shown in Fig. 1 do not represent those during the measurements in Fig. 4 to Fig. 6**,** but the ground conditions are essentially the same. As there were no sunny days when snow cover was recorded, a 100% diffuse day is shown for the daily snow spectral albedo in Fig. 7. The histogram borders in each plot show the daily density of spectral albedo measurements in the range of 300 to 1050 nm. The red reference lines within the histograms show the daily mean spectral albedo.

In instances where the spectral albedo curve is smooth (e.g., Fig. 6 and Fig. 7), we observe kinks (e.g., at 675 nm) which are measurement artifacts that were not present immediately after the calibration in January 2020. The fact that these kinks occurred after less than 1 year of deployment demonstrates how sensitive the alignment of the internal optical bench (i.e., mirrors and grating) is to field conditions and highlights the need for regular calibration.

The clear sky measurements demonstrate that there are notable shifts in spectral albedo over the course of a day. Specifically, there is a minimum spectral albedo around solar noon when the sun elevation is at its peak. The color gradient in the plots highlights this solar zenith dependency. The clear sky solar zenith dependency, with its early morning and late afternoon peaks, is of course typical of broadband albedo measurements [20]. In the case of spectral albedo measurements, however, the solar zenith dependency is not equal across all wavelengths. The tendency is for near infrared (NIR) wavelengths to show greater solar zenith dependency than visible (VIS) or UV wavelengths. This is because the spectral distribution of the sun's beam component shifts toward NIR wavelengths in the morning and afternoon, and because some surfaces reflect more NIR light than UV or VIS (e.g., grass).

A comparison between Fig. 4 and Fig. 5 reveals the seasonal spectral albedo variations going from spring into summer, and a comparison to Fig. 7 demonstrates the dramatic shifts that can occur in winter. If previous works [2] – [5] are correct in that spectral albedo ought to be implemented in bifacial PV modeling, then the seasonal shifts shown here offer scenarios where onsite measurements could advise a performance model that uses spectral albedo data.

One or more spectral albedo curves from SMARTS are shown in Fig. 4 to Fig. 7. When spectral albedo is accounted for in PV modeling (e.g., [6] – [8], [21], [22]) such static assumptions are used, almost exclusively. One unsurprising take away from comparing the measurements to static assumptions is that the static spectral albedo curves often fail to agree with the measured albedo curves' shape and magnitude across all wavelengths. In other words, static spectral albedo assumptions are not likely to be physically correct. The SMARTS documentation indicates that for all materials except snow, the spectral albedo curves were measured at a solar zenith angle of about 53°.

The largest differences between measurements and the database assumption occur in the VIS region of Fig. 5. (Dry grass). This is likely because the grass at the site retained some chlorophyl (visible in the greenness of Fig. 1b), even during the driest summer period.

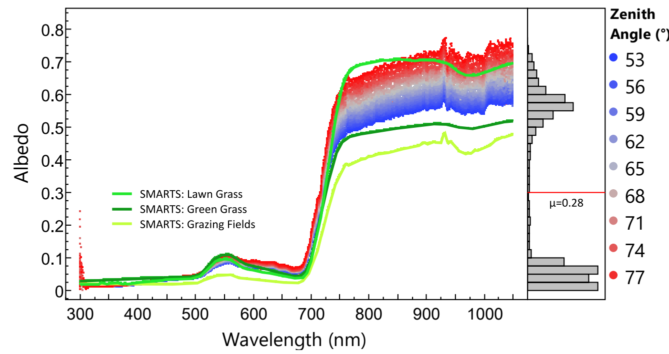

Fig. 4. One day of clear sky measurements recorded above *green* grass (25.03.2020). Three of the most similar SMARTS albedo curves are shown.

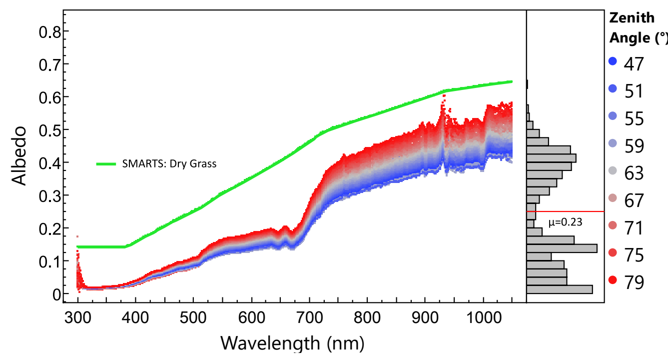

Fig. 5. One day of clear sky measurements recorded above *dry* grass (31.08.2020). The most similar SMARTS spectral albedo is also shown.

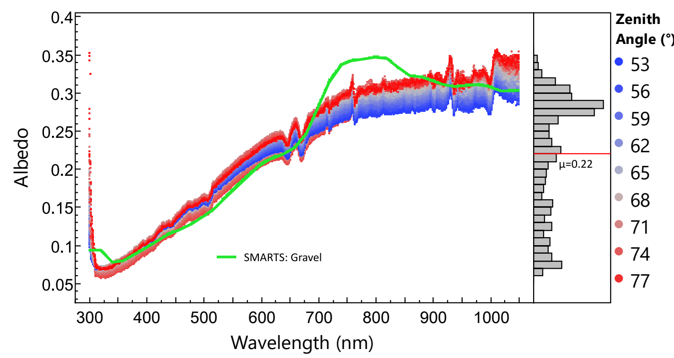

Fig. 6. One day of clear sky measurements recorded above gravel (18.09.2020). The most similar SMARTS albedo is also shown.

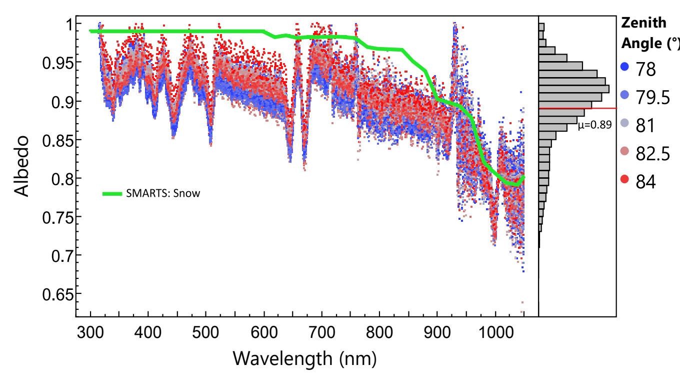

Fig. 7. One day of cloudy sky measurements recorded above snow (06.01.2021). The most similar SMARTS is also shown.

In the gravel albedo case, the spectral albedo from SMARTS aligns well to the measurements for all wavelengths except 700 – 900 nm. The differences in this spectral region are likely because the mineral content of the onsite gravel mixture deviates from that of the database assumption. For example, iron content is known to absorb solar radiation between 900 and 1000 nm [23], but the reasons for the discrepancy at 700 – 900 nm remain unclear.

Finally, the measured snow albedo case is shown in Fig. 7. The spectral albedo of snow is complex as it not only depends on solar zenith angle and diffuse ratio, but it also depends on the snow's freshness (age), grain size (roughness), snow depth, and whether the surface below the snow can be seen (coverage) [24]. Based on local weather measurements, we estimate that the snow depth during the measurements in Fig. 7. was less than 5 cm, that the snow fell within 24 hours of measurement, and that the gravel below was completely covered by snow. A particular challenge of snow albedo measurements is that the upward facing instrument will become covered in snow without some form of sensor heating or ventilation. The spectroradiometers used here contain thermoelectric cooling elements to maintain a detector temperature of 25°C ±0.5°C, which subsequently melts any snow deposited on the instruments. The SMARTS documentation indicates the spectral albedo files for snow are recorded at a zenith angle of about 20°, but in principle, the solar zenith angle should have very little effect on the albedo during a 100% diffuse day like the one shown.

B. *Bifacial Gain with Different Albedo Data Sources*

Fig. 8, Fig. 9, Fig. 10 show modeled bifacial gains for PERC on fixed tilt and tracked systems above green grass, dry grass, and gravel, respectively. Each figure shows the variability of modeled bifacial gain using five albedo data sources. The diamonds within each box plot show the 95% confidence interval of the mean, which are small because of the large number of observations. Recall that the pyranometer, Si-pyranometer and spectroradiometer albedo data are continuous measurements whereas the constant albedo (0.2) and SMARTS spectral albedo do not change with time. The duration of each albedo scenario is two, four and eight months for dry grass, green grass, and gravel, respectively.

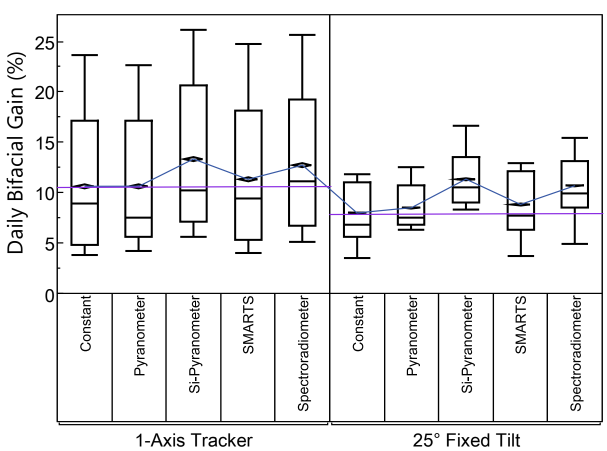

Fig. 8. Variability of simulated bifacial gain during the four month green grass albedo period using five different albedo data sources. The horizontal purple lines show the measured bifacial gain on large-scale PERC systems above grass during the same period. The SMARTS spectral file used is 'GrazingFields.dat'.

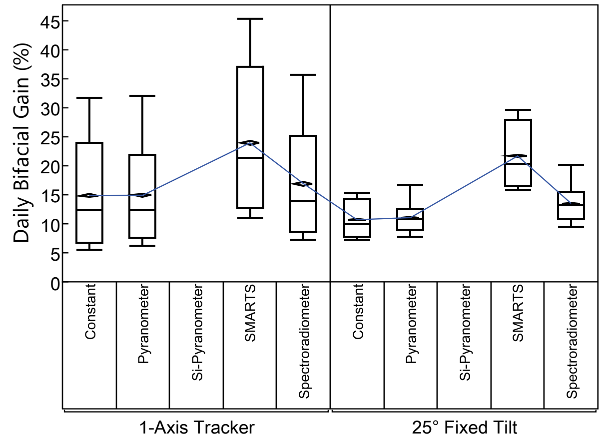

Fig. 9. Simulated bifacial gain results for the two month dry grass albedo period using four different albedo data sources. The Si-Pyranometer results are not shown because the ground surface under this sensor was not comparable to the others during this time. The SMARTS spectral file used is 'DryGrass.dat'.

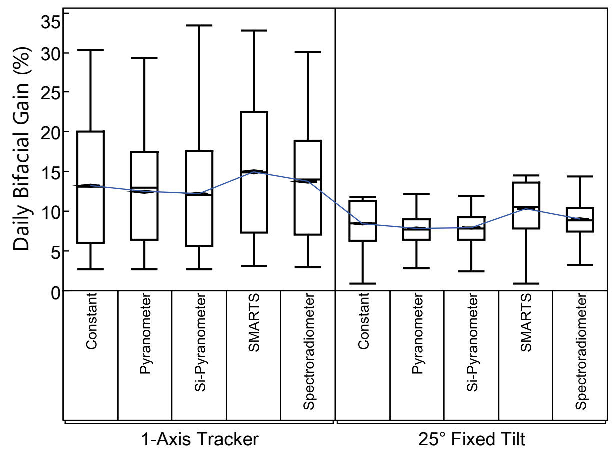

Fig. 10. Simulated bifacial gain results for the five month gravel albedo period using five different albedo data sources. The SMARTS spectral file used is 'Gravel.dat'.

In the green grass and gravel albedo cases shown Fig. 8 and Fig. 10, we see that the five albedo data sources cause the simulated bifacial gain to change by as much as 3%. In the dry grass albedo case shown in Fig. 9, the range of modeled bifacial gain values is 10%. The larger range of bifacial gains in the dry grass simulations is primarily caused by the SMARTS spectral albedo that results in 7% higher bifacial gain than when measured spectral albedo are used. Clearly, the SMARTS 'drygrass.dat' file is not a good approximation of the dry grass albedo, at this location (see Fig. 5).

In the green grass and gravel albedo cases, the bifacial gain changes by about 1.5%–2.0% if continuous spectral albedo measurements or SMARTS spectral albedo are used. Grazing Fields SMARTS albedo was used in the grass case because its relative shape was a near match to our measurements, thus leading us to believe that this vegetation was of a similar or same genus and species as the grass onsite. We also ran the simulations using the 'LawnGrass.dat' and 'GreenGrass.dat' SMARTS files. We found that bifacial gain was 7% higher and 1% lower, respectively, than when spectral albedo measurements were used.

Notable in the green grass albedo case of Fig. 8 is the bifacial gain calculated with Si-pyranometer albedo data is about 3% higher than when calculated with pyranometer data. This positive bias can be explained by the large 'red shift' of the grass albedo spectrum relative to AM1.5G (see Fig. 4). It is well known that the output of Silicon devices calibrated under the AM1.5G spectrum will increase when exposed to red shifted spectra [25]. Hence, the albedo of vegetation will tend to be higher when measured by Si-pyranometers or reference cells than with pyranometers. Similar results were reported by [26].

Green grass albedo (Fig. 8) is the only condition where onsite measurements of large-scale monofacial and bifacial PERC systems are available. The mean bifacial gain of these systems during the four-month period are shown with horizontal purple lines. Curiously, the constant albedo assumption of 0.2 yields the best agreement to the measurements. However, a fair comparison of the model and measurement requires at least two adjustments: 1) the model would need to account for structural shade losses, and 2) the spectral responsivity used in the model would need to be of a full-size module (i.e., with junction boxes, frame etc.), not an individual cell. If such adjustments were implemented, we estimate that the bifacial gain in all simulations would be reduced by at least 1%.

C. *Backside Spectral Mismatch*

Fig. 11 shows the backside spectral mismatch (SMM) of the PERC device during the four albedo periods studied on two structure types. We also calculated backside SMM for bifacial n-PERT and IBC cells, but because all devices are single junction silicon cells with similar bandgaps, the differences in SMM between the three devices were small (±0.01), likely within the uncertainty of the SMM calculation itself.

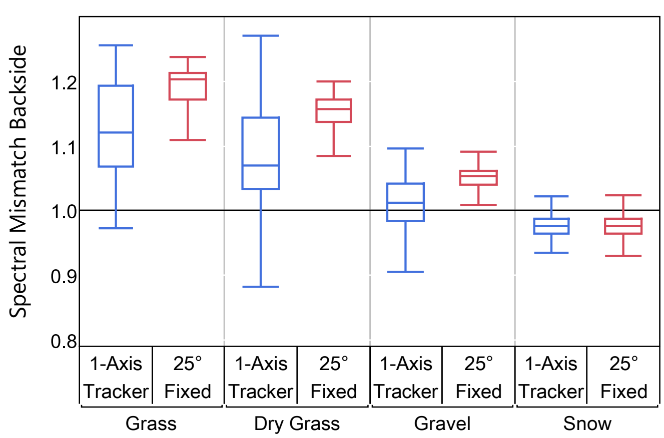

Fig. 11. Box and whisker plots showing spectral mismatch factors for the backside of the PERC cell on two structure types: trackers (blue), fixed (red). Mismatch is calculated for four albedo periods corresponding to Fig. 1.

The single axis tracker SMM results show a wider range of values than the 25° fixed tilt SMM results. This is explained by the tracker's continuously changing tilt angles, which are steepest in the early morning and late afternoon (±60°). The steeper the tilt angle, the greater the contribution of sky diffuse light to rear POA irradiance. For albedos that increase with wavelength (i.e., grass and gravel), backside tracker SMM always peaks midday. At midday, the tracker is horizontal, and the backside only receives reflected light from the ground. The green grass albedo has the largest red shift (i.e., ratio of NIR to VIS light) than the other three ground surfaces, which likely causes the highest SMM. The grass reflects more VIS light as it dries, which decreases the backside SMM by about 0.07 (7%) at the end of summer.

The median backside SMM of the grass and dry grass albedos is between about 1.1 and 1.2. Although these SMM factors correspond to I_{SC} gains of 10 to 20% relative to the AM1.5G rating, one must remember that frontside irradiance is approximately an order of magnitude greater than backside irradiance. Thus, performance models of bifacial systems above grass could suffer inaccuracies of 1–2% if spectral albedo effects are not properly accounted for.

D. *Rear Plane-of-array (POA) Spectra*

Fig. 12 and Fig. 13 show discretized rear POA spectral irradiance ($G_{POA,Rear,\lambda}$) on the single axis tracker above green grass during the morning and afternoon of a cloudless day (25.03.2020). The $G_{POA,Rear,\lambda}$ is simulated at 20 equally spaced segments, which correspond to the 20 vertical cell locations on the 2-in-portrait tracker. Segment 1 is the western most cell and segment 20 is the eastern most cell.

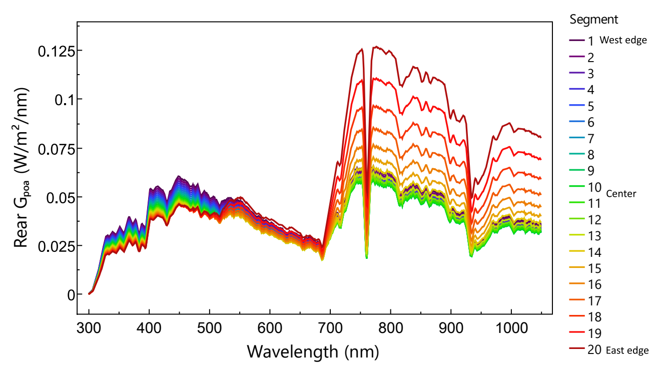

Fig. 12. Simulated rear spectral irradiance of the tracker system on a clear sky day in the morning at 20 discrete segments. At this time the tracker is tilted at 60° from horizontal and facing east (surface azimuth = 90°).

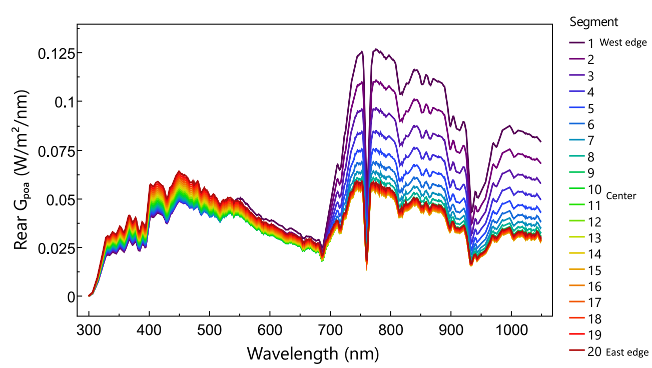

Fig. 13. Simulated rear spectral irradiance on the tracker system on a clear sky day in the afternoon at 20 discrete segments. At this time the tracker is tilted at 60° from horizontal and facing west (surface azimuth = 270°).

The 20 $G_{POA,Rear,\lambda}$ spectra in Fig. 12 (morning) and Fig. 13 (afternoon) show mirrored trends. In the morning when the tracker is pointing east, segment 1 (west) is highest in the sky and segment 20 (east) is lowest to the ground. Thus, segment 1 receives the largest contribution of sky diffuse irradiance and segment 20 the largest contribution of ground reflected irradiance. In the afternoon, the height of the segments is reversed with 1 lowest to the ground and 20 highest in the sky.

Because the clear sky diffuse spectrum is blue shifted (due to Rayleigh scattering), and the green grass albedo is heavily red shifted (see Fig. 4), the western most and eastern most cells can see notably different spectral distributions in the morning and afternoon. This can cause the SMM within the array to vary by as much as ±0.075 (7.5%). Midday when the tracker is horizontal, the spectral distributions at the 20 segments are the same, and thus there is no SMM gradient at solar noon.

Fig. 14 shows $G_{POA,Rear,\lambda}$ under the same clear sky and grass albedo conditions as in Fig. 13, but for the 25° fixed tilt system. The $G_{POA,Rear,\lambda}$ is again simulated at 20 cell locations within the 2-in-portrait array where segment 1 corresponds to the top most cell and segment 20 corresponds to the bottom most segment.

The backside light intensity is greater at the bottom than at the top of the fixed tilt system, but the relative spectral distribution among the 20 segments varies less than the 20 segments within the single axis tracker. This is because the top segment in the 25° fixed tilt system receives less sky diffuse light than an array at 60° as is the case in Fig. 12 and Fig. 13. So long as the sun is in front of the array, the backside SMM does not vary with solar position.

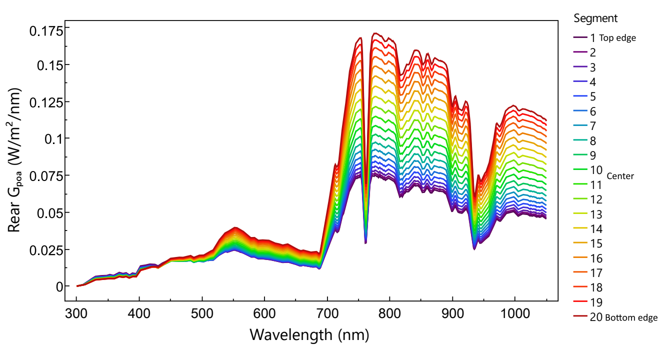

Fig. 14. Simulated rear spectral irradiance on the 25° south facing fixed tilt system on a clear sky day in the afternoon at 20 discrete segments.

IV. Discussion and Conclusions

Our measurements show that the albedo at bifacial PV sites can be highly spectrally dynamic over daily and seasonal timescales. The bifacial gains calculated with pyranometer, Si-pyranometer and spectroradiometer albedo varied by as much as 3% for the systems and ground surfaces studied.

If spectral albedo from a database shall be used in a bifacial performance model, then detailed information about the ground's type and condition are required. For example, SMARTS 2.9.5 contains seven files for grass and the present ASTER (ECOSTRESS) library contains at least nine files classified as grass. Knowledge that the ground is simply 'grass' may not be sufficient: Additional information such as genus, species, water content and growth state is likely required to correctly select spectral albedo from a database. Differences in bifacial gain up to 7% were observed when the static spectral albedo curve was not representative of actual conditions.

The large backside spectral mismatch values of 1.1 to 1.2 lead us to recommend spectral albedo measurements in some capacity. The most basic solution to account for spectral albedo effects would be a rear POA reference cell, but a more robust method would be to sample the albedo at a few carefully selected wavelengths. Such down sampled measurements can be made without significantly affecting the results shown here because spectral albedo is not heavily structured like the sun spectrum.

Acknowledgment

We thank Dennis Corell of DTU for supporting the spectrometer calibration effort, Rasmus Nielsen of DTU for helping with the spectral responsivity measurements, and Dr. Joris Libal of ISC Konstanz for providing us with bifacial n-PERT and IBC cell samples.

V. References

[1] "International Technology Roadmap for Photovoltaics: 2020 Results," ITRPV, 2021.

[2] M. R. Vogt et al., "Impact of using spectrally resolved ground albedo data for performance simulations of bifacial modules," in *36th EUPVSEC*, Brussels, 2018.

[3] C. Monokroussos et al., "Rear-side spectral irradiance at 1 sun and application to bifacial module power rating," *Progress in Photovoltaics*, 2020.

[4] M. Gostein, B. Marion and B. Stueve, "Spectral Effects in Albedo and Rearside Irradiance Measurement for Bifacial Performance Estimation," in *47th IEEE PVSC*, Virtual, 2020.

[5] J. C. Blakesley et al., "Effective spectral albedo from satellite data for bifacial gain calculations of PV systems," in *38th EUPVSEC*, Virtual, 2020.

[6] R. Andrews and J. Pearce, "The Effect of Spectral Albedo on Amorphous Silicon and Crystalline Silicon Solar Photovoltaic Device Performance," *Sol. Energy*, vol. 91, pp. 233-241, 2013.

[7] M. P. Brennan et al., "Effects of spectral albedo on solar photovoltaic devices," *Sol. Energy Mat. & Sol. Cells*, vol. 124, pp. 111-116, 2014.

[8] K. McIntosh et al., "Mismatch Loss in Bifacial Modules Due to Nonuniform Illumination in 1-D Tracking Systems," *IEEE JPV*, vol. 9, no. 6, pp. 1504-1512, 2019.

[9] J. Coakley, "Reflectance and Albedo, Surface," in *Encyclopedia of Atmos. Sciences*, 2003, p. 1914–1923.

[10] N. Riedel-Lyngskær et al., "Validation of Bifacial Photovoltaic Simulation Software," *Applied Sciences*, vol. 10, no. 23, pp. 1-29, 2020.

[11] N. Riedel et al., "Direct Beam and Diffuse Spectral Irradiance Measurements Analyzed With Average Photon Energy," in *7th WCPEC*, Waikoloa, 2018.

[12] J. Stein, C. Hansen and M. Reno, "The Variability Index: A New and Novel Metric for Quantifying Irradiance and PV Output Variability," Sandia Report: SAND2012-2088C, 2012.

[13] D. Myers and C. Gueymard, "Description and availability of the SMARTS spectral model for photovoltaic applications," in *SPIE #5520*, 2004.

[14] M. Ernst et al., "SunCalculator: A program to calculate the angular and spectral distribution of direct and diffuse solar radiation," *Sol. Energy Mat. & Sol. Cells*, vol. 157, pp. 913-922, 2016.

[15] M. Anoma et al., "View Factor Model and Validation for Bifacial PV and Diffuse Shade on Single-Axis Trackers," in *44th IEEE PVSC*, Washington D.C., 2017.

[16] D. King, B. Boyson and J. Kratochvill, "Photovoltaic Array Performance Model," Sandia Report (SAND2004-3535), 2004.

[17] A. Baldridge, S. Hook, C. Grove and G. Rivera, "The ASTER spectral library version 2.0," *Remotes Sens Environment*, vol. 113, p. 711–715, 2009.

[18] "IEC 60904-7 Ed. 4.0 (2019)".

[19] "IEC 60904-3 Ed. 4.0 (2019)".

[20] B. Marion, "Measured and satellite-derived albedo data for estimating bifacial system performance," *Sol. Energy,* vol. 215, p. 321–327, 2021.

[21] T. C. R. Russel et al., "The Influence of Spectral Albedo on Bifacial Solar Cells: A Theoretical and Experimental Study," *IEEE JPV,* vol. 7, no. 6, pp. 1611-1619, 2017.

[22] H. Ziar et al., "A comprehensive albedo model for solar energy applications: Geometric spectral albedo," *Applied Energy,* vol. 255, 2019.

[23] F. Vignola, J. Michalsky and T. Stoffel, "Chapter 9: Albedo," in *Solar Radiation and Infrared Radiation Measurements*, CRC Press, 2017, p. 193–204.

[24] W. Wiscombe and S. Warren, "A Model for the Spectral Albedo of Snow. Part 1," *Journ. of Atmos. Sci.,* 1980.

[25] D. R. Myers, "Quantitative analysis of spectral impacts on silicon photodiode radiometers," in *40th ASES Conference,* pp. 97-102, 2011.

[26] B. Stueve, "Field Albedo Measurements," in *bifiPV Workshop,* Amsterdam, 2019.

Publication VI. The effect of spectral albedo in bifacial photovoltaic performance

Authors:

Nicholas Riedel-Lyngskær, Martynas Ribaconka, Mario Po, Anders Thorseth, Carsten Dam Hansen, Sune Thorsteinsson, and Michael Linde Jakobsen

Published in:

Solar Energy 2022, 231(3), pp. 921-935

The effect of spectral albedo in bifacial photovoltaic performance

Riedel-Lyngskær, Nicholas; Ribaconka, Martynas; Pó, Mário; Thorseth, Anders; Thorsteinsson, Sune; Dam-Hansen, Carsten; Jakobsen, Michael L.

Published in:
Solar Energy

Link to article, DOI:
10.1016/j.solener.2021.12.023

Publication date:
2021

Document Version
Publisher's PDF, also known as Version of record

Link back to DTU Orbit

Citation (APA):
Riedel-Lyngskær, N., Ribaconka, M., Pó, M., Thorseth, A., Thorsteinsson, S., Dam-Hansen, C., & Jakobsen, M. L. (2021). The effect of spectral albedo in bifacial photovoltaic performance. *Solar Energy*, *231*, 921-935. https://doi.org/10.1016/j.solener.2021.12.023

Solar Energy 231 (2022) 921–935

Contents lists available at ScienceDirect

Solar Energy

journal homepage: www.elsevier.com/locate/solener

The effect of spectral albedo in bifacial photovoltaic performance

Nicholas Riedel-Lyngskær [a,*], Martynas Ribaconka [a], Mário Pó [b], Anders Thorseth [a], Sune Thorsteinsson [a], Carsten Dam-Hansen [a], Michael L. Jakobsen [a]

[a] Technical University of Denmark, Department of Photonics Engineering, Roskilde, Denmark
[b] EKO Instruments B.V., The Hague, the Netherlands

ARTICLE INFO

Keywords:
Spectral albedo
Spectral mismatch
Trackers
Bifacial
Normalized difference vegetation index

ABSTRACT

This paper analyzes 15-months of spectral albedo measurements collected at the Technical University of Denmark (55.6°N, 12.1°E). High-resolution spectroradiometers are used to monitor four albedo scenarios, which include green vegetation, dry vegetation, gravel, and snow. Spectral mismatch and spectral impact are calculated for the front and backside of three different bifacial cell concepts mounted on horizontal single axis trackers and fixed-tilt substructures. The spectral nature of albedo is shown to have significant influence on bifacial photovoltaic performance wherein backside spectral impact as high as 1.20 is observed for fixed-tilt systems above green vegetation and as low as 0.98 for systems above snow. The results reveal that spectral impact is always lower on tracked than fixed-tilt systems because a greater fraction of sky diffuse light reaches the backside of tracked systems. Given the variety of albedos tested here, we find that the normalized difference vegetation index is a good predictor of backside spectral effects. When the high-resolution measurements are truncated to 4 to 8 carefully selected wavelengths, we find that this limited measurement resolution sufficiently captures the seasonal spectral albedo fluctuations that influence bifacial photovoltaic energy production. Finally, to alleviate the dearth of spectral datasets presently available to the PV community, the spectral irradiance and albedo measurements are made freely available in open access format (https://doi.org/10.11583/DTU.14695437.v1).

1. Introduction and literature review

In the mid-2010s, the photovoltaic (PV) industry began shifting crystalline-silicon (c-Si) cell production away from aluminum back surface field (Al-BSF) cells toward passivated emitter and rear cell (PERC) technology (Dullweber, et al., 2016); (Dullweber and Schmidt, 2016). The subsequent cost reductions in industrial-scale PERC manufacturing processes paved the way for a revival of bifacial PV cells and modules. Once viewed as a niche technology used in small-scale applications like the sun-shading elements presented in (Hezel, 2003), the noise barriers in (Nordmann, et al., 2012), and the collection of systems displayed in the introduction of (Ledesma, et al., 2020), bifacial PV is now a mainstream technology with over 20 GW deployed worldwide (Kopecek and Libal, 2021). It has been estimated that 70%–90% of PV modules made during the last three decades were produced with Al-BSF cells (Green, 2015); (Wilson, et al., 2020), but this market majority has been quickly replaced by PERC and bifacial PERC cell technology. The 2021 ITRPV report estimates that by 2025 roughly 60% of PV modules produced will contain bifacial cells, and that by this time, the Al-BSF concept will be phased out (VDMA, 2021).

Recent research has characterized many of the nuanced performance effects present in bifacial PV systems and quantified how bifacial energy gains are influenced by installation and environmental conditions. For example, the backside edge brightening effect and electrical losses induced by nonuniformly distributed irradiance were simulated in detail by (Deline, et al., 2020) and (McIntosh, et al., 2019); the susceptibility to power loss from tracker torque tube shading was first described by Pelaez et al. (2019a) with Radiance based ray trace simulations (Ward, 1994) using the opensource Python library bifacial_radiance (Deline and Pelaez, 2017); other researchers later used bifacial_radiance to investigate similar backside shading effects for system types such as equator-facing static tilts (Berrian and Libal, 2020), (Korevaar, et al., 2020), and two-in-portrait trackers (Riedel-Lyngskær et al., 2020a); electrical mismatch losses induced by nonuniform rear irradiance were investigated experimentally on fixed-tilt systems by (Rossa, et al., 2021) and (Zhang, et al., 2020), and on trackers by (McIntosh, et al., 2020) and (Riedel-Lyngskær et al., 2020a)***;*** the dissimilar thermodynamic behavior between monofacial and bifacial PV devices was studied by (Lamers, et al., 2018) and (Wang, et al., 2020); and parametric studies that

* Corresponding author.
E-mail address: nrie@fotonik.dtu.dk (N. Riedel-Lyngskær).

https://doi.org/10.1016/j.solener.2021.12.023
Received 13 September 2021; Received in revised form 1 December 2021; Accepted 13 December 2021
Available online 24 December 2021

Solar Energy 231 (2022) 921–935

Nomenclature

α	Albedo
I_{SC}	Short-circuit current
K_d	Diffuse to global horizontal irradiance fraction
Θ_Z	Solar zenith angle

Subscripts

λ	Wavelength resolved data
Back	Backside device performance
Front	Front side device performance

Abbreviations

Al-BSF	Aluminum back surface field
BEG	Bifacial energy gain
DfHI	Diffuse horizontal irradiance
DNI	Direct normal irradiance
FOV	Field of view
FT	Fixed tilt structure
GHI	Global horizontal irradiance
G_{POA}	Global irradiance in plane-of-array
HSAT	Horizontal single axis tracker
IBC	Interdigitated back contact
MBE	Mean bias error
MFR	Multi-filter radiometer
NDVI	Normalized difference vegetation index
NIR	Near infrared (700 – 1000 nm in this work)
PERC	Passivated emitter and rear cell
PERT	Passivated emitter rear totally diffused
RHI	Reflected horizontal irradiance
SMM	Spectral mismatch factor
SI	Spectral impact
SR	Spectral responsivity
VIS	Visible light (400 – 700 nm in this work)

simulated bifacial energy gains due to module orientation, height, row spacing and diffuse light content were presented in (Asgharzadeh, et al., 2018), (Chudinzow, et al., 2020), (Guo, et al., 2013), (Sun, et al., 2018), and (Yusufoglu, et al., 2015).

No less important than these installation and environmental influences is the ground surface albedo. Defined as the percentage of incident sunlight (beam and sky diffuse) that a surface reflects, the albedo determines the amount of ground reflected radiation available for PV energy conversion. Ground reflected radiation constitutes less than 3% of the total effective irradiance for the majority of monofacial systems and can amount to less than 1% of the total irradiance when the tilt angle from horizontal is less than 25°. In contrast, ground reflected radiation contributes approximately 10% of the effective irradiance received by most bifacial systems worldwide (Pelaez et al., 2019a); (Rodriguez-Gallegos, et al., 2020) and (Sun, et al., 2018). Indeed, the rear irradiance received by bifacial systems is increased to some extent by sky diffuse irradiance, and in some conditions, by beam irradiance reaching the backside. However, the contributions of sky diffuse and beam irradiance to the total rear irradiance are either small or negligible compared to ground reflected contributions (Chiodetti, et al., 2016); (Chudinzow et al., 2019).

The albedo of natural and synthetic materials varies with the wavelength of incident sunlight, which is a property referred to as spectral albedo or spectral reflectance. Some of the earliest spectral albedo measurement campaigns were intended to understand the Earth's energy balance (Krinov, 1953), the spectral properties of plants (Gates et al., 1965), water bodies and snow (Kondratiev et al., 1964). Prior to 2016, spectral albedo was sparsely studied within the context of PV applications (Andrews and Pearce, 2013); (Brennan et al., 2014), which is likely because ground reflected radiation contributes minimally to monofacial PV performance. In the wake of ever-increasing bifacial PV deployments, however, there has been a subsequent upswing in the spectral albedo investigations conducted by PV researchers (Blakesley et al., 2020); (Gostein et al., 2020); (Monokroussos et al., 2020); (Pal et al., 2020); (Russel et al., 2017); (Vogt et al., 2018). One common conclusion we found among these studies is that spectral albedo effects can significantly influence the backside irradiance received by PV bifacial systems—up to 30 % in some cases—and that these effects should be accounted for in bifacial PV simulations (Blakesley et al., 2020); (Gostein et al., 2020); (Vogt et al., 2018). Several works have accordingly incorporated spectral albedo into bifacial PV performance models. All such studies use spectral albedo data from the ASTER spectral library (Baldridge et al., 2009) and the implicit assumption that the distribution of the spectral albedo does not change with time and conditions (Dupre et al., 2020) (McIntosh et al., 2019); (Mekemeche and Beghdad, 2020); (Russel et al., 2017); (Tuomiranta et al., 2020); (Ziar et al., 2019).

To our knowledge, the literature is lacking in contributions where diurnal and seasonal spectral albedo shifts are analyzed within the context of bifacial PV performance. The only work that we are aware of covering this topic is (Blakesley et al., 2020), who calculated spectrally effective albedo for three bifacial PV device types using satellite and ground-based spectral albedo measurements in Namibia and France. The present contribution reports on continuous high spectral resolution albedo measurements made in Roskilde, Denmark (55.6° N, 12.1° E) over a 15-month period. The objectives are to demonstrate how temporal changes in spectral albedo affect the performance of commercially available bifacial PV devices mounted in different orientations, and to provide recommendations for how field measurements can be used to account for spectral albedo shifts that affect bifacial energy output.

2. Methodology

2.1. On site measurements

Spectral irradiance data in the range of 300 – 1100 nm were recorded every 5 min by three EKO MS-711 spectroradiometers. The Si detector inside each spectroradiometer contains 2048 pixels, which provides a wavelength scale with 0.4 nm sampling interval. The optical resolution (full-width half maximum) of the instruments is 7 nm. Two of the spectroradiometers have a 180° field-of-view (FOV) and were horizontally mounted on a measurement stand 1.5 m above the ground (Fig. 1). The upward facing spectroradiometer recorded the global horizontal spectral irradiance (GHI_λ) and the downward facing instrument recorded the ground reflected horizontal spectral irradiance (RHI_λ). The spectral albedo α_λ was calculated according to Eq. (1).

$$\alpha(\lambda) = \frac{RHI(\lambda)}{GHI(\lambda)} \tag{1}$$

The third spectroradiometer has a 5° FOV collimation tube and was mounted on a dual-axis tracker to measure the direct normal spectral irradiance DNI_λ. This is the same instrument used in (Riedel et al., 2018) and is installed nearby in a 15 m tower where horizon shading is negligible. The diffuse horizontal spectral irradiance $DfHI_\lambda$ was calculated from the difference between the measured GHI_λ and the measured DNI_λ adjusted by the zenith angle (θ_Z) according to Lambert's cosine law.

$$DfHI(\lambda) = GHI(\lambda) - DNI(\lambda) \bullet \cos\theta_Z \tag{2}$$

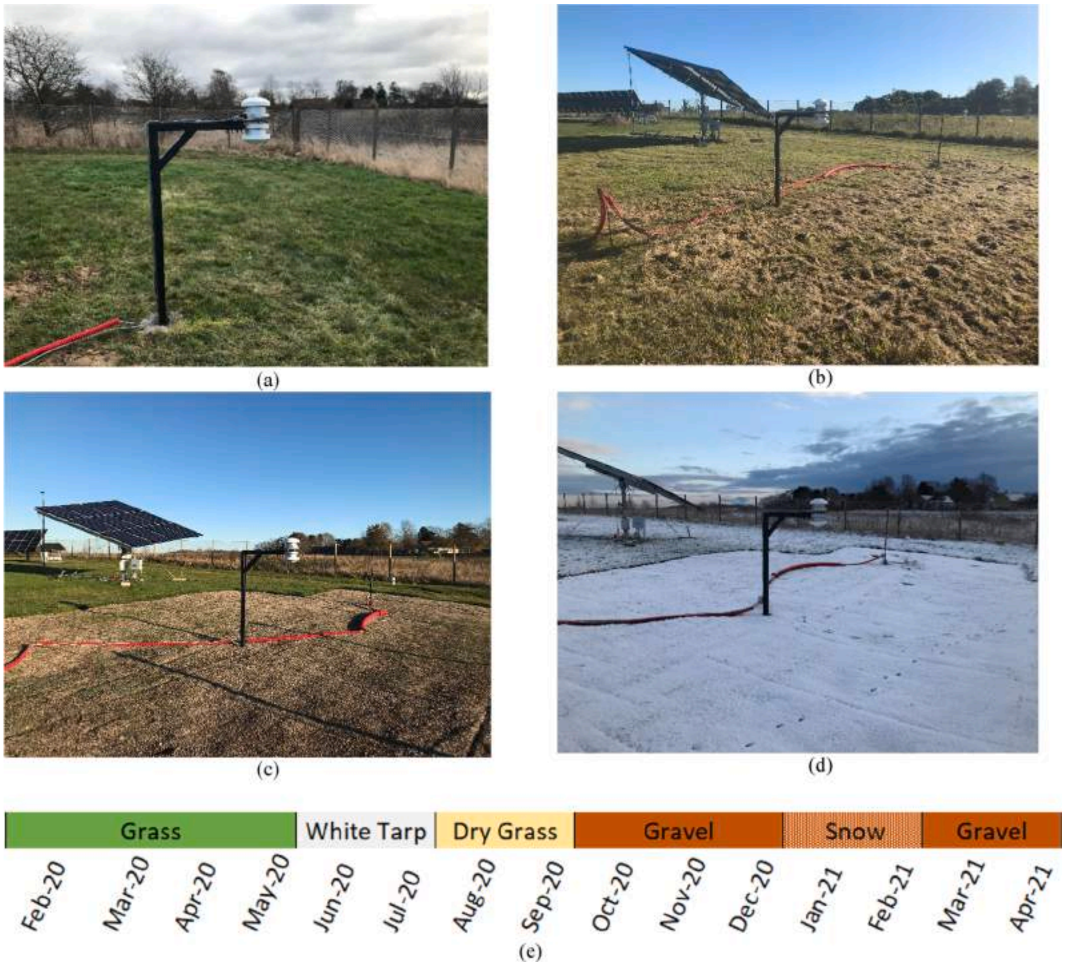

Fig. 1. Spectral albedo measurement stand and the various albedo conditions tested at Technical University of Denmark: (a) Green grass from February to May 2020, (b) dry grass from August to September 2020, (c) 5 – 8 mm gravel from September 2020 to April 2021, (d) snow in January 2021, and (e) timeline of the ground surfaces tested during the campaign. (For interpretation of the references to colour in this figure legend, the reader is referred to the web version of this article.)

The field measurement campaign investigated the diurnal and seasonal variations in spectral albedo under four surfaces/conditions including green grass (Fig. 1a), dry grass (Fig. 1b), gravel (Fig. 1c), and snow (Fig. 1d). A timeline is shown in Fig. 1e. The spectral RHI_λ, GHI_λ and DNI_λ data, as well as the weather data and broadband albedo data recorded during this period are available to the solar energy community in an open access format (https://doi.org/10.11583/DTU.14695437.v1).

Healthy green grass was measured for three months from 05.02.2020 to 06.05.2020. From 07.05.2020 to 27.07.2020 a highly reflective white tarp was affixed to the ground with the spectral albedo stand in the center. The data recorded during the white tarp period are not reported here because the white tarp's area was not large enough to limit the light reflected off the surrounding grass to less than 5% of the total signal received by the downward facing spectroradiometer. However, the spectral albedo measurements from the white tarp albedo period are available in the open access dataset.

The grass began to dry out shortly after the white tarp was removed (Fig. 1b). The period of dry grass albedo measurements spanned from 28.07.2020 to 07.09.2020. On 08.09.2020, a 12 m by 12 m gravel mixture (consisting of 5 – 8 mm diameter stones) was distributed in an area covering the majority of the spectroradiometer's FOV and remained in place until the measurement campaign concluded on 29.04.2021 (Fig. 1c). We estimate that more than 97% of the ground reflected light reaching the downward facing instrument originates from the 144 m^2 gravel area. Periodic snowfall occurred in winter 2021 (Fig. 1d) and was recorded by a Lufft UMB600 weather sensor. There were five days when the daily snowfall was greater than 25 mm. Onsite snow depth data are not available, but snowfall hardly accumulates in Denmark's predominantly humid continental climate (Köppen climate classification Dfb), and the snowfall that we observed melted completely within a day or two.

The albedo measurements reported here are not split into black-sky and white-sky albedo components, but the open access data set allows users to perform such a decomposition if desired. The black-sky and white-sky albedos can be determined with the procedure described by (Michalsky and Hodges, 2013). This method requires measurements from a clear sky day and a cloudy day with the criterion that ground conditions do not change appreciably between the clear sky and cloudy period.

The upward and downward facing spectroradiometers shown in Fig. 1 did not acquire measurements simultaneously because a single datalogger was used to acquire data from both instruments. We observed delays of up to 10–15 s between the time at which the first spectroradiometer began its measurement, to when the second unit completed its measurement. This delay is due to data processing time in the logger and the exposure times in each sensor, which take 10 to 5000 ms each, depending on the light intensity. An irradiance stability check was used because Eq. (1) assumes a constant condition during the GHI_λ and RHI_λ measurements. Broadband GHI data recorded every 10 s were used to calculate a variability index (VI) (Stein et al., 2012) within a 2-minute period: approximately 1 min before and after the spectral albedo measurement. Measurements were removed from the analysis when the VI was greater than 1.1, which served as an irradiance stability filter. Data recorded on detector edges (λ less than 300 nm and λ greater than 1050 nm) were also removed because as these data are prone to measurement noise.

Typically, the spectral sensitivity of Si spectroradiometers is between 300 and 1100 nm, which makes analysis of Si PV devices challenging because the spectral responsivity of contemporary Si PV (e.g., PERC) is between 300 and 1200 nm (Belluardo et al., 2018). Since the useful spectral range is 300 to 1050 nm, and the bifacial devices we analyzed are spectrally responsive between 300 and 1200 nm (Fig. 3), we used the SMARTS model (Gueymard, 1995) to fill the spectral irradiance gap between 1050 and 1200 nm. We used the real-time solar zenith angle as a proxy for air mass, the ambient temperature, and atmospheric pressure to generate a SMARTS clear sky spectrum for each spectral measurement. The simulated clear sky spectra were scaled with the cloud opacity factor of (Ernst et al., 2016), which was calculated with broadband global and diffuse irradiance from two onsite pyranometers. However, we have found that the stochastic nature of cloud cover is nearly impossible to account for with a single cloud coverage factor and therefore, the simulated spectra from 1050 to 1200 nm were scaled with a secondary factor to ensure that the simulated spectra align with the measurements at 1050 nm. It is worth noting that under the AM1.5G reference spectrum (International Electrotechnical Commision, 2019a), the bifacial PV devices we analyzed (Fig. 3) generate approximately 4% of their total photocurrent from light between 1050 and 1200 nm. Therefore, the extension imposes a small effect on the results reported here.

2.2. Spectroradiometer calibration

Calibration of all three spectroradiometers was performed inhouse at DTU Fotonik's DOLL laboratories on 22.01.2020, two weeks before the field measurement campaign began. The calibration setup consists of a NIST traceable Optronics Laboratories FEL-type lamp that is calibrated for spectral irradiance and placed on an alignment jig 50 cm from the device under test with measures to mitigate stray light. The spectral responsivity is calculated as the certified spectral irradiance of the lamp divided by the spectral pixel count and multiplied by the integration time used during calibration. The expanded uncertainty of the calibration is approximately 4.5% for wavelengths between 400 and 1050 nm, but between 300 and 400 nm, the uncertainty can be as high as 10% (Fig. 2a). The primary uncertainty contributions in the setup are the lamp drift (4.0%), and the low signal to noise ratios at the extreme ends of the spectroradiometer sensitivity.

A final measurement of the standard lamp was made on 11.05.2021 to check the spectroradiometers for any drift that occurred during the measurement campaign. The lamp is stored and operated in ways that minimize changes in output, the electrical power applied to the lamp is precisely monitored during calibrations, and the lamp is periodically compared to other in-house reference lamps to detect any drift. Fig. 2b shows each spectroradiometer's measured deviations to the standard lamp spectrum upon completion of the 15-month measurement campaign, and highlights that the magnitude of the measurement drift is dependent on the instrument and wavelength. (Dirnberger et al., 2015a) showed that a comparable spectroradiometer deployed in Freiburg, Germany for two years had less than ± 5% drift between 400 and 1100 nm – a magnitude that is comparable to the DNI and GHI instrument drifts shown in Fig. 2b.

The spectroradiometer used for RHI measurements showed the highest deviations to the reference lamp (mean deviation to reference lamp of + 3.3%, 95% of measurements within ± 5.6%) and showed pronounced kinks at certain wavelengths (e.g., 645 nm and 670 nm). The most pronounced kinks overlap with sharp gradients in the spectral responsivity of the instrument. This means that small changes in the wavelength response will be amplified near the wavelength where these

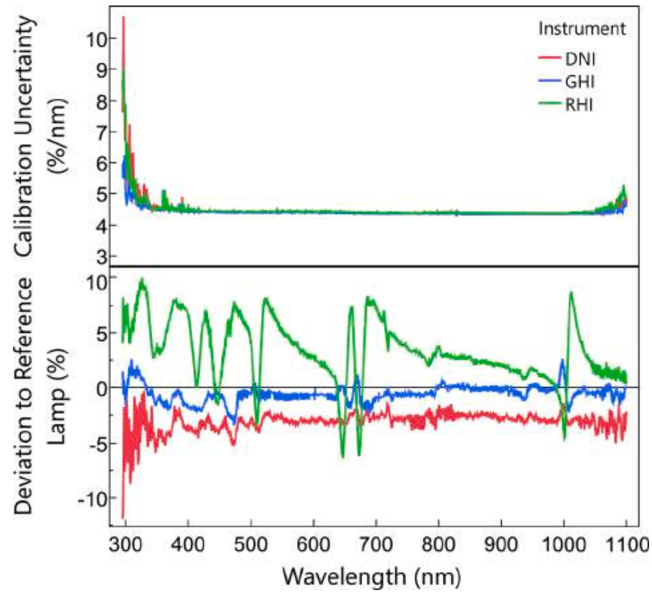

Fig. 2. (a) Uncertainty (k = 2) of the calibration check performed on 11.05.2021, two weeks after completion of the measurement campaign. (b) Measured deviations to the FEL-type reference lamp after 15 consecutive months of field operation. The averages of ten measurements made with each instrument are shown.

gradients reside. The results from the calibration events on 22.01.2020 and 11.05.2021 suggest that the spectral responsivity of the RHI instrument was affected during the outdoor experiments. In Section 3.3 we describe the extent to which the kinks observed in the RHI instrument affected spectral mismatch calculations.

An expanded uncertainty estimation of the continuous outdoor solar spectral irradiance measurements would be a complex task in of its own. Monte-Carlo approaches are commonly used to account for the correlation between spectroradiometer uncertainty components and wavelength (Dirnberger et al., 2015a), (Hohl-Ebinger and Warta, 2011), (Schinke et al., 2020), but the time-dependency of continuous solar spectral measurements introduces additional constraints and complexity that can limit the applicability of the Monte Carlo method. Although expanded uncertainty has not been made for the continuous outdoor measurements performed in this work, the instruments have participated in international laboratory intercomparisons in 2017 (Pravettoni et al., 2018) and 2018 (Galleano et al., 2019) to establish confidence in the calibration and measurement accuracy. The angular response of the horizontally mounted EKO MS-711 spectroradiometers follow a cosine response within 3% or better. This cosine error will primarily affect the upward facing (GHI) instrument at high solar zenith angles in direct sunlight. Finally, all three spectroradiometers contain thermoelectric heating and cooling, which maintained detector temperatures of 25 °C ± 0.5° during approximately 98% of the field measurements.

2.3. Bifacial cell technologies

Fig. 3 shows the front and backside spectral responsivities of the bifacial cells studied. The cell concepts include interdigitated back contact (IBC), n-type passivated emitter and rear totally diffused (n-PERT), and p-type passivated emitter and rear cell (PERC). These were chosen for their varying rear to frontside efficiencies (i.e., bifaciality factors) and availability. Under AM1.5G illumination, the bifaciality factors of the IBC, n-PERT and PERC cells are 62%, 88% and 75%, respectively. Note that bifaciality factors of full-size modules will be lower than on a cell-level because the active backside of modules is commonly shadowed by junction boxes, labels, frames, and/or a glazing printed on the glass between cell spacings.

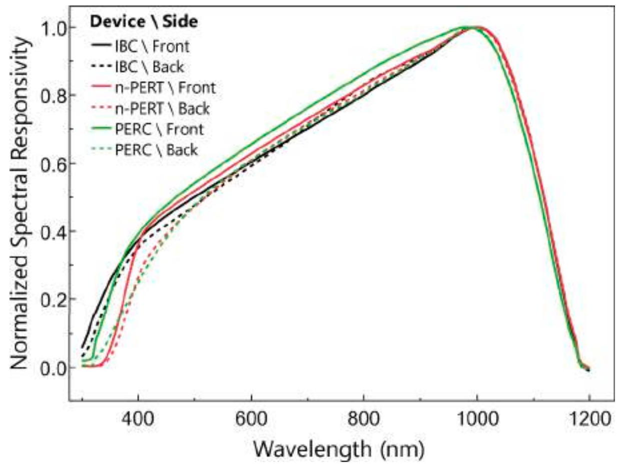

Fig. 3. Normalized spectral responsivity of the three bifacial cell types studied. The cells are encapsulated in standard PV glass.

The spectral responsivity measurements shown in Fig. 3 are of single cells laminated inside 20 × 20 cm PV glass. The measurements were performed with a PV Measurements QEXL quantum efficiency measurement system. The bifacial IBC device is the ZEBRA cell with front surface field (FSF) emitter developed at ISC Konstanz (Kopecek et al., 2020). The bifacial n-PERT device is the BiSoN (bifacial on n-type) concept, also produced by ISC Konstanz (Lossen et al., 2015). The PERC cell was procured from Blue Sun Solar.

2.4. Optical modeling

Most bifacial PV systems are mounted at non-horizontal tilt angles, which allows light from the sky hemisphere to reach the backside. Since sky diffuse light can have a markedly different spectral distribution than the albedo, a thorough study of spectral effects in bifacial systems requires data in the rear plane-of-array (POA). We used the 2D view factor model pvfactors (Anoma et al., 2017) to calculate global frontside and rear POA spectral irradiances ($G_{POA,Front,\lambda}$ and $G_{POA,Rear,\lambda}$). View factors are used in radiative heat transfer theory to describe the fraction of radiation emitted from surface A that strikes surface B, expressed as $F_{A\rightarrow B}$. We selected pvfactors as the engine for 2D view factor modeling due to its open-source nature and because it showed good agreement to broadband $G_{POA,Rear}$ measurements in our previous work (Riedel-Lyngskær et al., 2020b). We performed simulations for two orientations: a 25° south facing fixed-tilt (FT) system and a horizontal single-axis tracking (HSAT) system. These two system types were chosen because they are commonly implemented in large-scale PV systems and are the same configuration as the bifacial PERC systems collocated at the measurement site.

Table 1 summarizes the structural details of the FT and HSAT systems simulated, which correspond to the real 45 m long bifacial PV arrays that are installed onsite. Five-rows of FT and HSAT systems are simulated, and all results reported here are from the center row. The 2D view factor method assumes that rows are infinitely long and thereby neglects edge brightening effects, but the works of Berrian (2020) and Pelaez et al. (2019b) have shown that the performance of the center array within a five-row system, at least 10 m long, is comparable to the performance of an array within a semi-infinite field. In other words, five rows can accurately represent utility-scale installations.

The measured (α_λ, DNI_λ) and calculated ($DfHI_\lambda$) spectral data were passed to the 2D view factor model (pvfactors), one wavelength at a time in 1 nm steps from 300 to 1200 nm. The full simulation mode of the model was used to calculate the spectral radiosity of all surfaces within the modeled scene for each respective wavelength λ. Angular reflection losses at the front and rear module surface are accounted for with the Sandia incident angle modifier (IAM) model (King et al., 2004). An IAM profile for a c-Si module with non-antireflective coated glass was used for the rear side.

Table 1
Structural specifications of the two-in-portrait PV systems simulated in this work.

Specification	Fixed-Tilt	Single Axis Tracker
Tilt Angle from horizontal (°)	25	± 60
Surface azimuth (°)	180	90 or 270
Ground clearance* / Hub height (m)	0.9	2.0
Ground cover ratio	0.40	0.28

*Ground clearance corresponds to the fixed-tilt system while hub height corresponds to the tracker.

2.5. Data analysis

The large volume of data recorded by high-resolution spectral instruments in continuous operation can be challenging to analyze – especially over multi-year timescales. Qualitative metrics such as the average photon energy parameter (Dirnberger et al., 2015)b, (Nofuentes et al., 2017) are useful in this respect because they permit a quick and simple analysis of spectral shifts within a vast dataset that potentially contains several 100 million records, or more. To this end, we used the normalized difference vegetation index (NDVI) to identify significant changes in the spectral albedo distribution during the 15-month campaign. First proposed by (Rouse et al., 1974), the NDVI is commonly used in remote sensing to identify vegetated areas from satellite images. The NDVI is a dimensionless quantity on a scale of −1 to + 1 and is calculated according to Eq. (3).

$$NDVI = \frac{NIR - VIS}{NIR + VIS} \tag{3}$$

In this work, the VIS and NIR quantities are the integral of the spectral RHI from 400–700 nm and 700–1000 nm, respectively. The concept behind NDVI is that healthy green vegetation reflects very little visible light (VIS) light but reflects significantly in the near infrared (NIR) region. Thus, green vegetation has a large difference between NIR and VIS reflectance and has a high positive NDVI value. As vegetation goes through drying stages of senescence to death, it continuously loses chlorophyll, which results in increased VIS reflection and a smaller difference between NIR and VIS. During snow albedo conditions, the NDVI is near zero or slightly negative (Dye and Tucker, 2003).

The spectral POA irradiance $G_{POA,Front,\lambda}$ and $G_{POA,Rear,\lambda}$ were summarized using the spectral mismatch factor (SMM) per Equation 7 in IEC 60904–7 (International Electrotechnical Commision, 2019b). We introduce subscript j to denote the front or rear side of the PV device and POA.

$$SMM_j = \frac{G_{Ref} \bullet \int_a^b SR_j(\lambda) \bullet G_{POA,j}(\lambda) d\lambda}{G_{POA,j} \bullet \int_a^b SR_j(\lambda) \bullet G_{Ref}(\lambda) d\lambda} \tag{4}$$

SR_{Front} and SR_{Back} are the front and backside spectral responsivity, and $G_{Ref,\lambda}$ is the AM1.5G reference spectrum defined in IEC 60904–3 (International Electrotechnical Commision, 2019a). The integration limits a to b are 300 to 1200 nm. As pyranometer data in the POA were not available for each albedo scenario (Fig. 1), G_{POAj} is calculated as the integral of $G_{POA,Front,\lambda}$ or $G_{POA,rear,\lambda}$. and G_{Ref} is calculated as the integral of $G_{Ref,\lambda}$ over the same integration limits. SMM_{Back} was calculated for the three types of bifacial PV cell concepts shown in Fig. 3.

Eq. (4) is simply the ratio of two ratios. The numerator is the short-circuit current (I_{SC}) under the observed spectral condition $G_{POA,j,\lambda}$. divided by the broadband irradiance $G_{POA,rear}$, and the denominator is the I_{SC} under the AM1.5G reference spectrum $G_{Ref,\lambda}$ divided by the broadband irradiance G_{Ref}. SMM values greater than 1 thus indicate spectrally induced gains in I_{SC} relative to AM1.5G, and SMM values less than 1 indicate spectrally induced I_{SC} losses. When analyzing temporal spectral shifts over time, it is typical to report the so-called the 'spectral impact' or 'spectral effect', which is the SMM weighted by broadband POA irradiance during a given period (Alonso-Abella et al., 2014), (Dirnberger et al., 2015b), (Pelland et al., 2020) (Polo et al., 2017). Following this practice, spectral impact (SI) was calculated for the front and backsides according to Eq. (5).

$$SI_j = \frac{\sum SMM_j \bullet G_{POA,j}}{\sum G_{POA,j}} \quad (5)$$

3. Results and discussion

3.1. Diurnal spectral albedo trends

Albedo measurements on clear days show a strong dependency on solar zenith angle (Θ_Z), while albedo measurements remain reasonably constant on cloudy days without precipitation (Coakley, 2003) (Vignola et al., 2017). Fig. 4 shows normalized spectral albedo on selected clear and cloudy days at 100 nm resolution. The data are normalized to the spectral albedo observed at solar noon (180° solar azimuth). These plots are intended to reveal some of the nuanced spectral albedo effects that are embedded in the SMM summary presented in Section 3.3.

The daily horizontal diffuse to global fraction (K_d) on the clear days was less than 0.40, while on cloudy days K_d was greater than 0.95. Albedo increases with decreases in sun height on clear days, but only down to solar elevation angles of about 10° at which point the albedo decreases (Iqbal, 1983). This phenomenon occurs because the fraction of horizontal diffuse to horizontal beam irradiance rapidly increases as the solar elevation angle decreases from 10° toward the horizon. Therefore, we only show measurements when the sun is higher than 10° above the horizon in Fig. 4a, Fig. 4c, and Fig. 4e.

Increases in albedo with solar zenith angle are a familiar characteristic found in broadband albedo observations on clear days (Dittmann et al., 2019), (Marion, 2021). In the case of spectral albedo measurements, however, the solar zenith dependency is not equal across all wavelengths. The tendency shown here is for near infrared (NIR) wavelengths to show greater solar zenith dependency than visible (VIS) or UV wavelengths, which is consistent with measurements reported by (Kondratyev, 1969), (Michalsky and Hodges, 2013). Fig. 4a, Fig. 4c and Fig. 4e show that albedo tends to be higher after solar noon than before solar noon. Other authors have reported such asymmetrical daily trends for spectral albedo (Kondratyev, 1969), (Michalsky and Hodges, 2013) and broadband albedo (Chiodetti et al., 2016) (Minnis et al., 1997) (Stueve, 2019). Since instrument leveling checks were regularly performed, we attribute the asymmetry shown here to the mostly western grade in the albedo stand vicinity (max 4°). The slight westerly slope results in greater ground illumination—and thus reflectance—in the afternoon than in the morning.

The clear sky green grass albedo data recorded on 21.04.2020 (Fig. 4a) show a pronounced dip in the early morning that returned to expected albedo levels once the sun elevation reached about 20°. Shadows cast from objects in the horizon have been ruled out for several reasons: the GHI_λ measurements were unaffected during the albedo dip, our measured skyline profile indicated that there should be no eastern shading when the sun elevation is above 5°, and the gravel albedo data recorded 364 days later—during nearly identical solar angles—showed no such morning dip. The cause for the dip is still uncertain but is presently attributed to possible morning dew formed on the grass, which evaporated as broadband DNI became sufficiently high and relative humidity sufficiently low.

Fig. 4b and Fig. 4f show examples when the cloudy day albedo is not constant. In Fig. 4b, a rainfall event caused a small, but noticeable, wavelength-dependent decrease in grass albedo. During the cloudy day gravel albedo measurements (Fig. 4f), two light snowfall events caused a 50% increase in albedo (e.g., 0.2 to 0.3 at 950 nm). This is roughly consistent with (Marion, 2021) who reported melting snow albedos of 0.4 or less. Note that the thermoelectric elements inside the spectroradiometers maintain the detector temperature at 25 °C ± 0.5 °C, which melts snow deposited on the instruments. However, water droplets from rain and melted snow could affect the measurements during precipitation.

3.2. Seasonal spectral albedo trends

The NDVI is frequently used in remote sensing applications to assess the spectral reflectance of Earth's surface (Huang et al., 2020), but as far

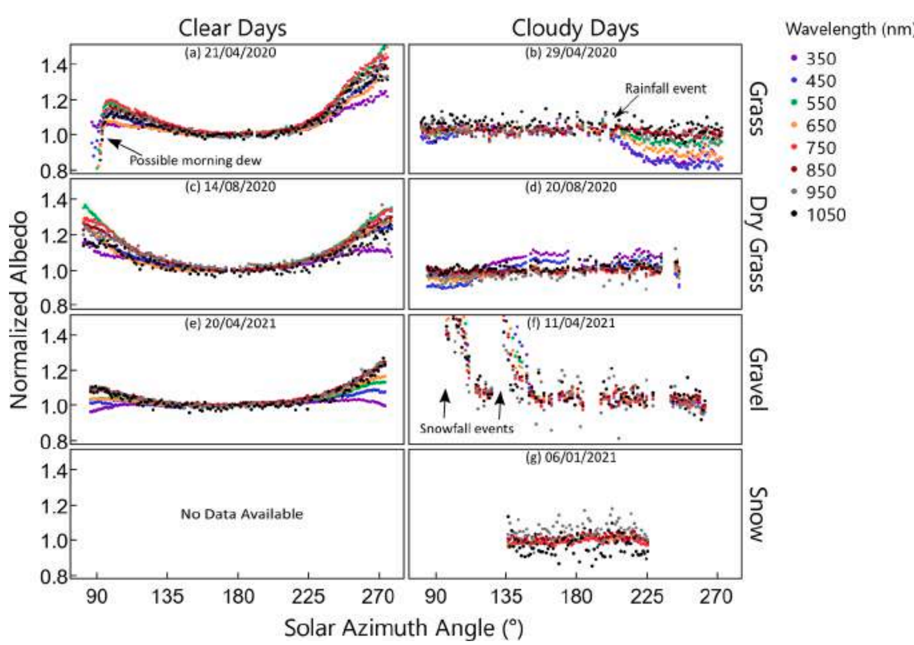

Fig. 4. Spectral albedo for select wavelengths normalized to the albedo observed at solar noon. Figures in the lefthand column contain data recorded during clear sky conditions and figures in the righthand column contain data recorded on cloudy days. The four rows indicate the state of the ground cover during measurement: Green grass, dry grass, gravel and snow. (For interpretation of the references to colour in this figure legend, the reader is referred to the web version of this article.)

as we are aware, the NDVI metric has not yet been applied to bifacial PV applications. Fig. 5 shows the NDVI values observed during the 8-month grass period, excluding the two months when the white tarp was affixed to the ground. The results are typical of seasonal vegetation with maximum NDVIs of approximately 0.7 (green vegetation) and minimum NDVIs of approximately 0.1 (dry vegetation). The NDVI was reasonably stable between 0.6 and 0.7 for the first 3.5 months of the measurement campaign and a rapid decrease in NDVI occurred in summer 2020 when the grass was quickly drying. If the spectral albedo measurements of grass had continued for another year or more, we expect that NDVI would have recovered to approximately 0.6 and followed a cyclical pattern each year, likely with the lowest NDVIs in summer.

The vertical green line and yellow line in Fig. 5 indicate the highest and lowest NDVI values observed on clear days. Fig. 6 displays the albedo measurements on these days and reveals the most extreme seasonal variations recorded. The largest differences between the green grass and dry grass albedo are in the visible light region (400–700 nm). The reflectance and absorption of light in this region is determined by the amount of chlorophyll in the grass: The green grass albedo (Fig. 5a) shows low reflection and high absorption of visible light, while the dry grass albedo (Fig. 5b) shows higher reflection and lower absorption.

Our previous work (Riedel-Lyngskær et al., 2021) showed that spectral albedo curves from databases (e.g., that of (Baldridge et al., 2009)) often fail to agree with the measured albedo curves' shape and magnitude across all wavelengths and days. This observation suggests that information such as genus, species, water content and growth state is likely required to select spectral albedo data that is representative of a given site. The significant shift toward NIR wavelengths in green grass's albedo (Fig. 6a) presents an important implication for its measurement with broadband sensors. Specifically, our previous work (Riedel-Lyngskær et al., 2021) showed that bifacial energy gain calculations can be as much as 3% higher when albedo measurements of vegetation are made with Si devices rather than thermopile pyranometers. Finally, the spectral albedo of vegetation (with open access measurements provided in this work) have significance for the up-and-coming field of agricultural PV, where installations often feature vertically mounted bifacial modules such as those simulated in (Chudinzow et al., 2020) and (Robledo et al., 2021). In such vertically mounted PV systems, the ground reflected irradiance can represent a significant percentage of the total in-plane irradiance.

Fig. 7 shows the NDVI values observed during the 7-month gravel period. The NDVIs recorded during snowfall events are indicated with green markers. The NDVI is mostly between −0.15 and 0.10 when snow is not present, but on days when the gravel was fully covered in snow, the NDVI was as low as −0.3. The lowest NDVI values in Fig. 7 correspond well to those reported by (Dye and Tucker, 2003) for fully snow-covered areas.

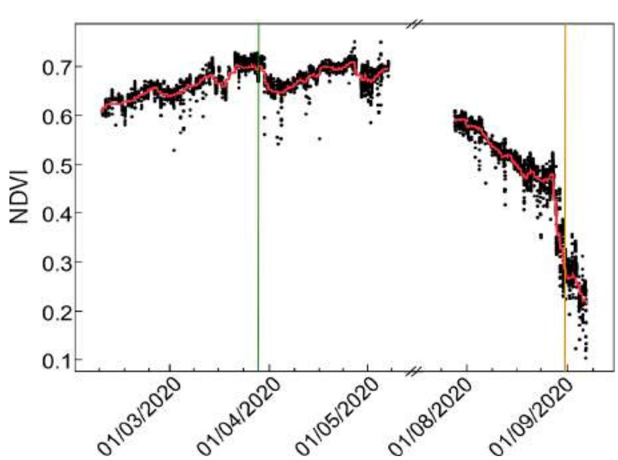

Fig. 5. NDVI from February to September 2020 over grass. The black dots show NDVI measured every five minutes, and the red line shows the one-day rolling average. The vertical green and yellow reference lines indicate the highest and lowest NDVI values recorded on clear days. The spectral albedo recorded on these two days is shown in Fig. 6. (For interpretation of the references to colour in this figure legend, the reader is referred to the web version of this article.)

In Fig. 7, the vertical brown reference line indicates a clear day at the beginning of the gravel albedo period, and the blue reference line indicates one of the most severe snowfall days during the test period. Fig. 8 zooms in to the spectral albedo measurements recorded on these two days. Based on local weather measurements, we estimate that the snow depth during the measurements in Fig. 8b was less than 5 cm, that the snow fell within 24 h of measurement, and that the gravel below was completely covered by snow. Although our test site contains various PV module designs that include bifacial, monofacial, framed, and frameless constructions, we did not receive sufficient snowfall to draw meaningful conclusions about their different snow shedding behaviors. But interestingly, recent literature suggests that bifacial modules in certain configurations can offer improved snow shedding performance over monofacial counter parts. (Burnham et al., 2019) conducted side-by-side tests of bifacial and monofacial systems on dual-axis trackers in Burlington, Vermont (44.5°N) and noted that the bifacial systems tended to shed snow faster than monofacial, which they proffered was because the $G_{POA,Rear}$ exposure caused greater heating of the bifacial arrays. (Riley et al., 2019) observed that the absence of a module frame tends to expedite snow shedding, so long as snow drifts did not accumulate below the array. This phenomenon stands to benefit bifacial systems because they are typically laminated in glass-glass packages, which thereby offers the possibility of frameless construction.

The gravel and snow spectral albedo curves appear smoother than those of vegetation because they do not show the step increase at 700 nm. The smooth shape of the gravel and snow spectral albedos reveal kinks in the measurements (e.g., at 675 nm and 1000 nm) which are artifacts that were not present after the initial calibration on 22.01.2020. A cubic spline fit was applied to obscure the kinks of the binned spectral albedo curves in Fig. 6 and Fig. 8. The fact that these kinks occurred after less than 1 year of deployment demonstrates how sensitive the alignment of the internal optical bench (i.e., mirrors and grating) is to field conditions and highlights the need for regular calibration.

3.3. Spectral mismatch and spectral impact

This section details how the spectral albedo conditions measured at the site impact bifacial PV performance. Fig. 9 shows linear regressions of the daily backside spectral impact (SI_{Back}) versus the daily average NDVI for three bifacial cell concepts and two structures. The datapoints are mostly in two clusters: one for the gravel period without snow, and one for the green grass period. The lowest and highest NDVI values correspond to full snow coverage (-0.3) and green grass (0.7), respectively. The points between the two clusters correspond to the dry grass period in summer.

The shaded areas around the regression lines show the 95% confidence region of the prediction equation, which is about ± 0.04. The prediction equations for the three bifacial cells in Fig. 9 show negligible differences within the same structure type (e.g., tracking or fixed-tilt). The small differences likely arise because all three cell concepts are based on Si and have the same bandgap. This suggests that a single prediction equation would be suitable for all bifacial cell concepts with Si substrates.

The strong correlation between SMM and NDVI (R^2 = 0.90–0.95) suggests that by measuring albedo with just two spectrally sensitive sensors—one covering the VIS and one covering the NIR—it is possible to reasonably quantify seasonal shifts in backside irradiance relative to the AM1.5G rating. This correlation is potentially advantageous for bifacial system planners because satellite networks make NDVI products available with global coverage (European Space Agency, 2021) (NASA,

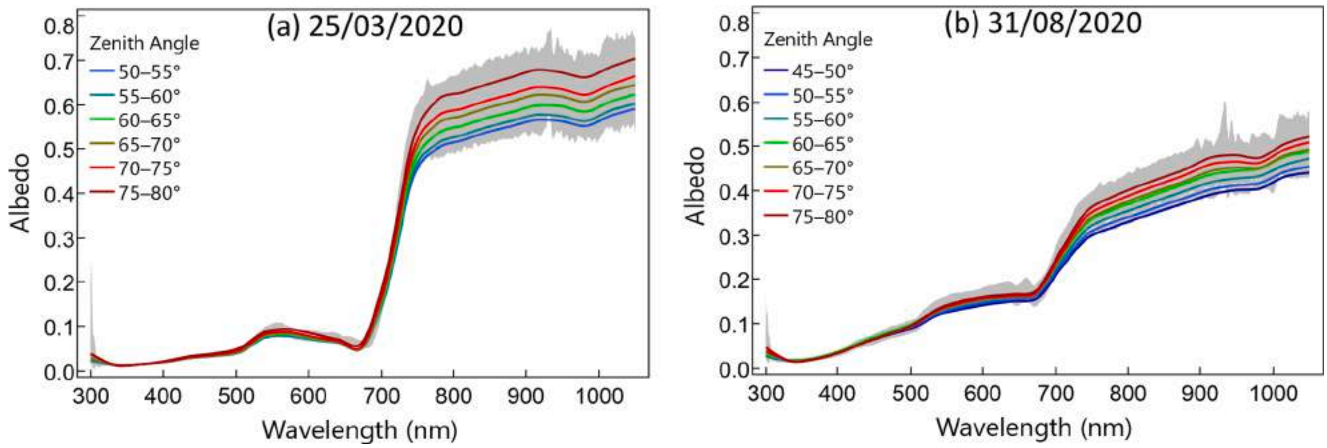

Fig. 6. Spectral albedo measurements on clear days above green grass a) and dry grass b). The solar zenith angle dependency is shown by averaging the spectral albedo data within 5° solar zenith bins. The gray shaded areas represent the range of spectral albedo measurements made on each day. (For interpretation of the references to colour in this figure legend, the reader is referred to the web version of this article.)

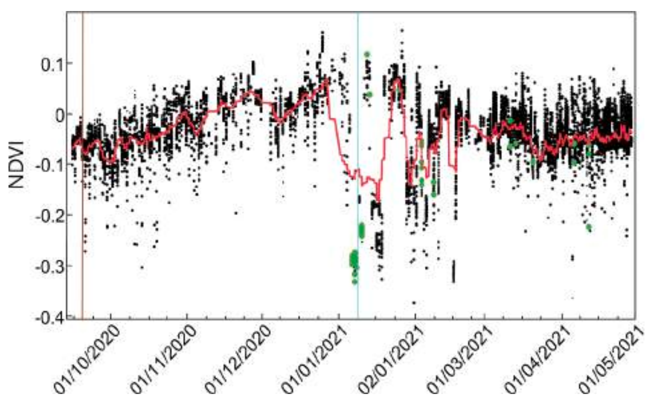

Fig. 7. NDVI from September 2020 to May 2021 over gravel. The black dots show NDVI at 5-minute resolution and the red line shows the one-day rolling average. Green dots indicate the NDVI when snowfall was recorded. (For interpretation of the references to colour in this figure legend, the reader is referred to the web version of this article.)

2021). Although current results indicate that satellite derived NDVI products may be sufficient for estimating seasonal backside POA spectral shifts within about ± 0.04 accuracy, further research is necessary to validate this and to better understand the associated uncertainties.

Table 2 summarizes SI_{Back} on the FT and HSAT systems during the four measured albedo periods. The results for the three cell concepts are averaged because there is little difference among them. We focus on the backside spectral results in this work because spectral shifts of monofacial Si have been reported for static tilt systems in several locations (Alonso-Abella et al., 2014), (Dirnberger et al., 2015b), (Ishii et al., 2013), (Jessen et al 2018), (Polo et al. 2017) and recently for HSATs in the United States (Ripalda et al., 2020). Nonetheless, a brief statement on our observations of SI_{Front} can be made, which is that SI_{Front} is between 0.983 and 1.017 for the three bifacial cells, two structures, and four albedo conditions studied here. These values are consistent with those reported by other authors.

During clear skies, the output of c-Si devices that are calibrated under AM1.5G will increase with air mass, or as the sun's spectral distribution shifts toward NIR wavelengths (King et al., 2004) (Myers, 2011). Since the spectral albedos of green grass, dry grass and gravel increase with wavelength (Fig. 6 and Fig. 8), it is reasonable to expect that the bifacial devices studied here will experience spectrally induced gains in I_{SC} when illuminated with these albedo spectra. The results in Table 2 confirm this because SI_{Back} is always greater than 1 for green grass, dry grass, and gravel albedo. Larger spectral albedo shifts toward NIR wavelengths result in greater SI_{Back} values, which is also demonstrated in the correlations of Fig. 9.

The 25° FT system shows higher SI_{Back} values than the HSAT system except during the brief snow albedo period. The differences in SI_{Back} on the two structure types are explained by the different amounts of sky diffuse and ground reflected light received at the backside POA. The backside of the 25° FT system has a constant sky view factor ($F_{Sky\to PV,Rear}$) of 0.03, meaning that regardless of sun position, 3% of the diffuse

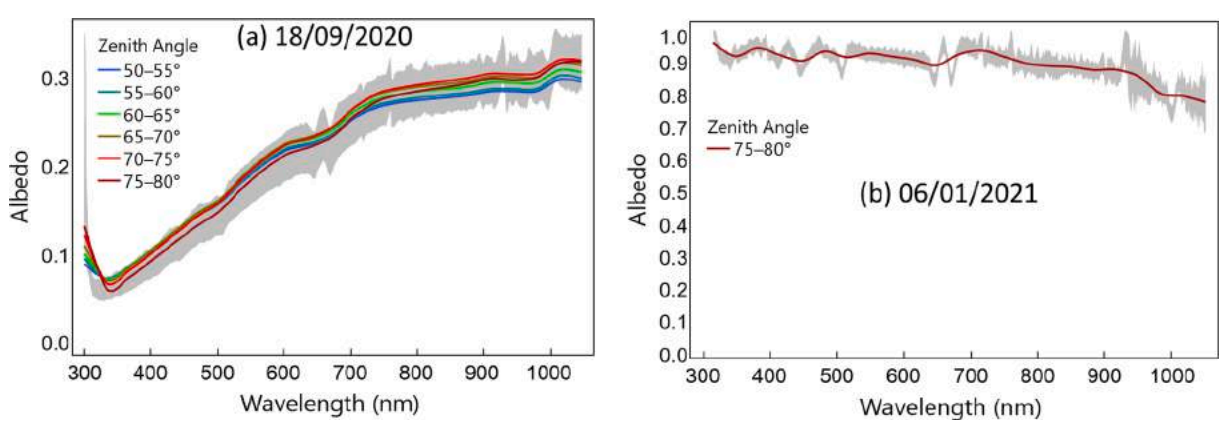

Fig. 8. Spectral albedo measurements of gravel on a clear day a) and of snow on a cloudy day b). The solar zenith angle dependency is shown by averaging the spectral albedo data within 5° solar zenith bins. The gray shaded areas show the range of spectral albedo measurements made on each day.

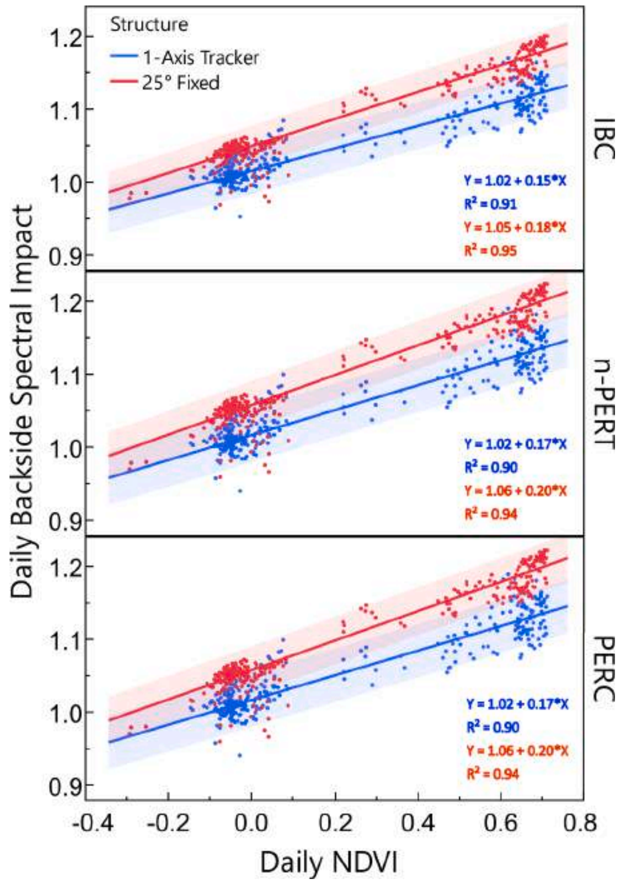

Fig. 9. Correlations of the daily backside spectral impact and normalized difference vegetation index for three bifacial technologies and two structure types. Approximately 15 months of measurements are shown.

light available from the sky hemisphere reaches the backside. In contrast, the sky view factor at the HSAT's backside POA changes continuously with sun position. In the morning and afternoon, the backside has a maximum sky view factor of 0.2 when the tilt is 60°. Midday, the sky view factor is reduced to zero when the tilt is horizontal. Because the sky diffuse spectrum is blue shifted on clear days (Kirn and Topic, 2017), we can expect the HSAT system to show the lowest spectral mismatch at the ends of the day when at a 60° tilt.

Fig. 10 shows daily timeseries of SMM_{Back} to illustrate the dependency of backside spectral shifts on the view factor from the sky to the array's backside ($F_{Sky\rightarrow PV,Rear}$) and on the view factor from the ground to the array's backside ($F_{Ground\rightarrow PV,Rear}$). Except for the snow albedo case, the data shown in Fig. 10 were recorded under clear skies. As expected, the lowest SMM_{Back} values on the HSAT occur in the morning and afternoon when $F_{Sky\rightarrow PV,Rear}$ is highest, and the highest SMM_{Back} values occur midday when $F_{Ground\rightarrow PV,Rear}$ is close to one. The daily SMM_{Back} values on the static 25° FT system do not change significantly, which follows the expected trend given the constant view factors $F_{Sky\rightarrow PV,Rear}$ and $F_{Ground\rightarrow PV,Rear}$.

Fig. 11 shows the density of SMM_{Back} values during the 15-month measurement campaign. The wider dispersion of SMM_{Back} in the HSAT case is attributed to the constantly changing sky view factors. Fig. 12 illustrates this relationship between SMM_{Back} and sky view factor on the backside of the 2-in-portrait HSAT. Snow albedo is not shown in Fig. 12 due to a lack of measured data. The results show a strong correlation with sky view factor and reveal that the diffuse fraction (K_d) is an important secondary effect. Most measurements in Fig. 12 were recorded during very clear days (K_d less than 0.2) or very cloudy days (K_d greater than 0.9). This is because the variability index filter removed most measurements outside these conditions.

The literature contains several spectral models for monofacial PV that are based largely on correlations with air mass (Huld et al., 2009) (King et al., 2004), (Lee and Panchula, 2016), (Pelland et al., 2020). However, we found air mass to be a poor indicator of SMM_{Back}. We used a bootstrap forest model to identify the most significant predictors of SMM_{Back} from our available weather and tracker position data. We found that a simplified predictive model for SMM_{Back} should at minimum include the backside array sky view factor, and the sky diffuse fraction. The third piece of information needed is a classification of the ground surface (e.g., green grass), which could be obtained with measurements from a multifilter radiometer (see Section 3.4) or the NDVI. With simple multiple linear regression techniques, we obtained root mean squared errors (RMSE) for SMM_{Back} between 0.014 and 0.020, depending on the albedo. Although the correlations in Fig. 12 are made with results from single axis tracker simulations, the model is likely to apply to systems with different azimuth orientations when the diffuse light received by the backside is only isotropic diffuse. This would include multi-row equator facing FT systems with several rows behind the array that block the horizon brightening component.

Fig. 10, Fig. 11 and Fig. 12 show that the $G_{POA,rear,\lambda}$ spectral

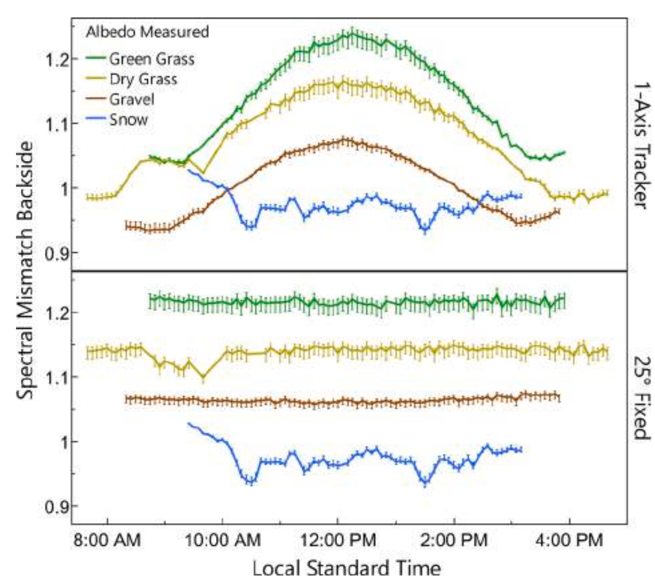

Fig. 10. Backside spectral mismatch on select days for the single axis tracker (top) and fixed-tilt systems (bottom). The raw spectral albedo recorded these days is shown in Fig. 6 and Fig. 8. The error bars around each timeseries show the range of spectral mismatch values of three different bifacial cell concepts.

Table 2
Backside spectral impacts of Si bifacial devices mounted on two structure types above four ground surfaces. The results are the average spectral impacts of bifacial IBC, n-PERT and PERC concepts.

Structure	Green Grass			Dry Grass			Gravel			Snow		
	SI_{Back} Mean	SI_{Back} Range	N	SI_{Back} Mean	SI_{Back} Range	N	SI_{Back} Mean	SI_{Back} Range	N	SI_{Back} Mean	SI_{Back} Range	N
1A Tracker	1.133	0.012	15,648	1.093	0.010	18,792	1.007	0.000	28,698	0.981	0.007	810
25° Fixed	1.196	0.022	15,648	1.155	0.019	18,792	1.046	0.007	28,698	0.980	0.007	810

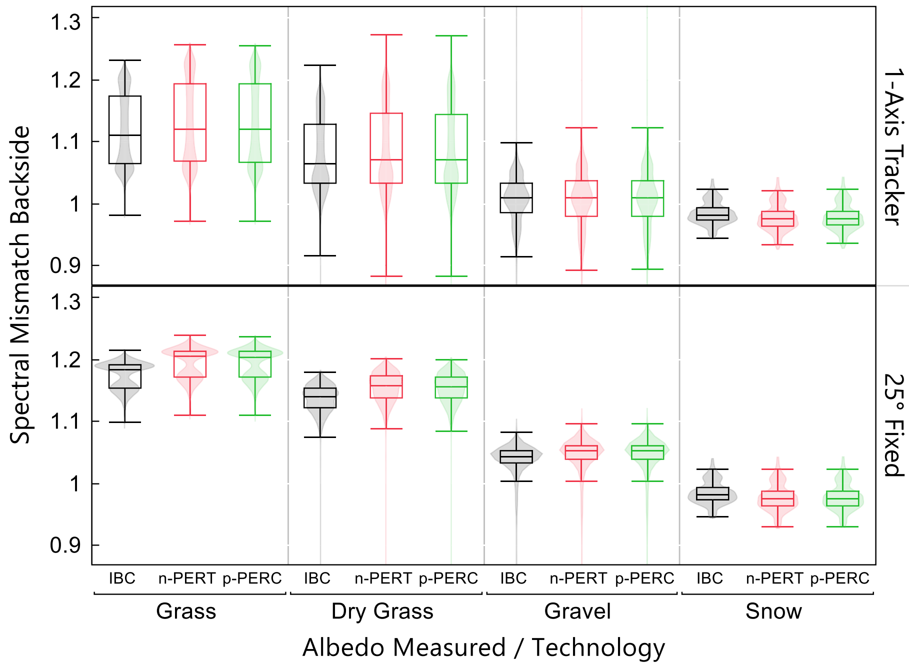

Fig. 11. Box and whisker plots of backside spectral mismatch for single axis tracker (top) and fixed-tilt systems (bottom). The x-axis levels are bifacial cell technology within albedo. The shaded violin plots show the density of spectral mismatch values.

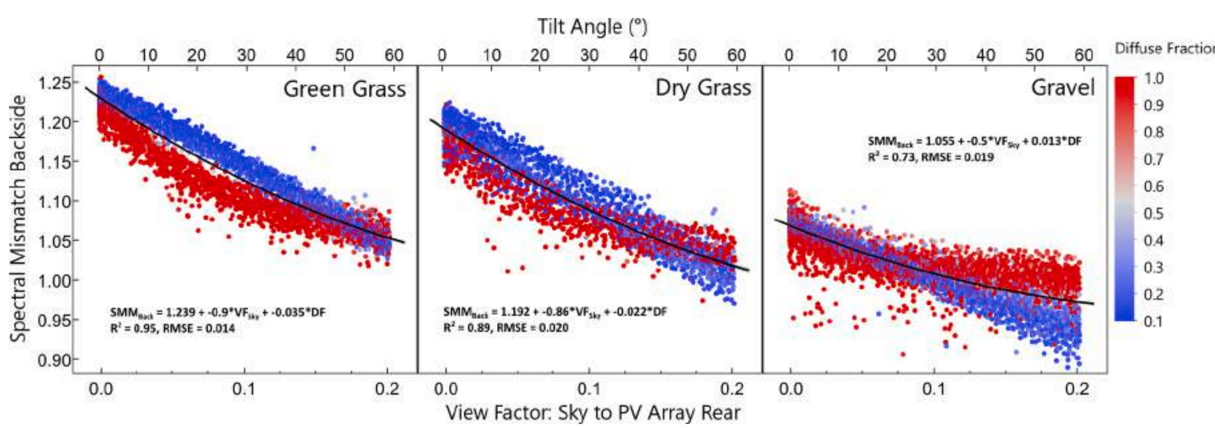

Fig. 12. Backside spectral mismatch of PERC versus sky view factor for three measured albedo conditions: green grass (left), dry grass, (center) and gravel (right). The tilt angle of the 2-in-portrait tracker system is shown on the secondary x-axis above. (For interpretation of the references to colour in this figure legend, the reader is referred to the web version of this article.)

distribution deviates significantly from AM1.5G over daily and seasonal timescales. Indeed, backside spectral gains as high as 25% occur with green grass albedo, but since rear irradiance makes up only 5–15% of total irradiance, such backside spectral gains are reduced to approximately 2% in most conditions. A complementary reference spectrum for backside bifacial PV characterization (i.e., an AM1.5R) could conceivably reduce spectral errors observed in the field. However, (Monokroussos et al., 2020) concluded that the industry-wide complications that would occur after introducing a new standardized spectrum are not worth the reduced spectral errors that can be achieved. Although this reason has not prevented other authors from proposing supplemental spectra to counter the shortcomings of AM1.5G (Jessen et al., 2018) (Kinsey, 2021) (Looney et al., 2020) (Myers et al., 2004), the AM1.5G spectrum is likely to remain the standard for backside bifacial PV characterizations in years to come. The question then becomes, what are the alternatives to reduce the spectral uncertainties encountered in fielded bifacial systems?

Backside spectral mismatch can be minimized using a rear facing reference cell that has a similar spectral responsivity as the backside of the bifacial cells within the array. However, the standardization of such a cell's position within the array is still ongoing and no recommendation has yet been offered in international standards (Gostein et al., 2021). Designers of bifacial PV monitoring systems must presently understand many nuanced effects of rear POA irradiance to optimally select the number and mounting location of reference cells. The nonuniformity of $G_{POA,rear,\lambda}$ is one such effect that is infrequently considered, but can be significant in some cases, as illustrated in Fig. 13.

Fig. 13 shows SMM_{Back} of the PERC device discretized in 20 equally spaced segments, which correspond roughly to the 20 cell locations on the 2-in-portrait HSAT and FT systems. The simulations use spectral data from a cloudless day during the green grass albedo period (25.03.2020). In the HSAT simulation, segment 1 is the western most cell and segment 20 is the eastern most cell. In the FT simulation, segment 1 corresponds to the topmost cell and segment 20 corresponds to the bottom most cell.

The results indicate that a single backward facing reference cell is not likely to represent the effective rear irradiance on an HSAT system

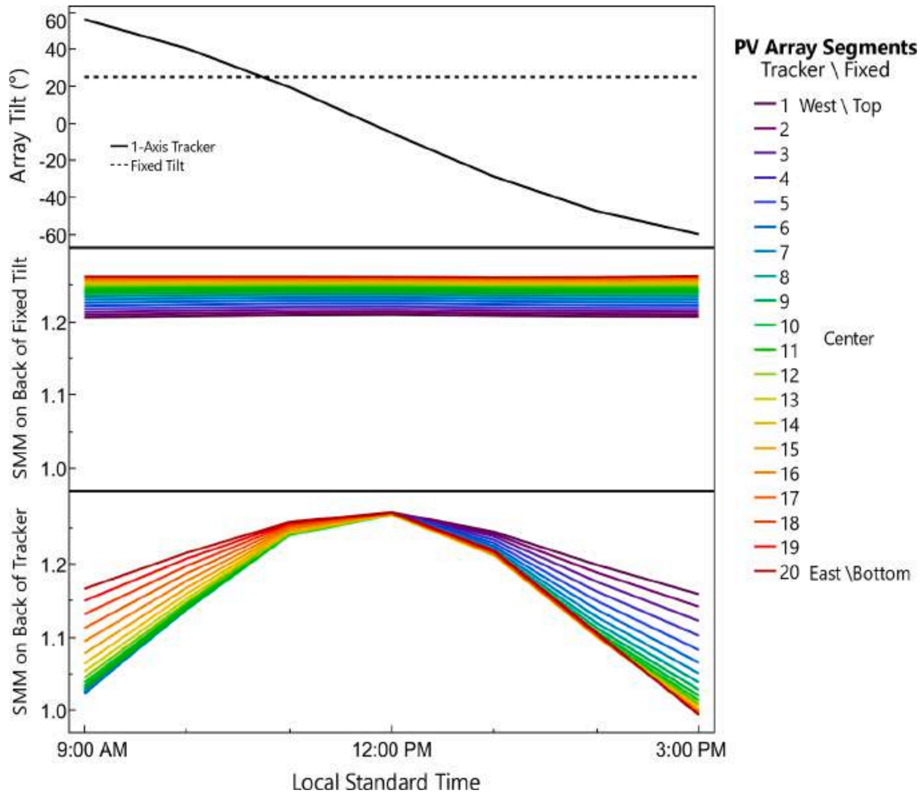

Fig. 13. Simulated nonuniformity of backside spectral mismatch of PERC using spectral albedo measurements of green grass on a clear day near the spring equinox. The two cases shown are 2-in-portrait tracked (bottom figure) and fixed-tilt systems (center figure). (For interpretation of the references to colour in this figure legend, the reader is referred to the web version of this article.)

because SMM_{Back} within the array varies by as much as ± 0.075 (7.5%) in the morning and afternoon. In the morning when the tracker is pointing east, segment 1 (west) is highest in the sky and segment 20 (east) is lowest to the ground. Thus, segment 1 receives the largest contribution of sky diffuse irradiance—resulting in the lowest SMM_{Back}—and segment 20 has the largest contribution of ground reflected irradiance resulting in the largest SMM_{Back}. Midday when the tracker is horizontal, the ground view factor of all 20 segments is unity, and there is no SMM gradient at solar noon.

The dispersion of SMM_{Back} within the 2-in-portrait FT array is about ± 0.03 (3%) throughout the day if the sun is in front of the array. This spectral gradient is large enough to advise two backward facing reference cells – one for the bottom and top halves of the array. The bottom cell in the 25° FT system shows spectral gains 6% higher than the top cell, a difference which is again attributed to the different exposure to sky diffuse and ground reflected light.

We conclude this section with a note on the uncertainty of spectral mismatch (SMM) and spectral impact (SI). As mentioned in Section 2.2 (Fig. 2), the measurement drift of the spectroradiometers used for GHI and DNI measurements were mostly within the uncertainty of the calibration, but the instrument used for RHI measurements drifted significantly beyond the calibration uncertainty at some wavelengths. To understand the implications of these wavelength shifts on the results, we compared SMM_{Back} calculations using calibrations from 22.01.2020 (pre-deployment) and 11.05.2021 (post-deployment). The results showed that SMM_{Back} agreed within 0.004 (0.4%) or better 99% of the time, given the two sets of calibration coefficients and the albedo and sky conditions observed during the test period. The small difference in SMM_{Back} is because the wavelength shifts did not significantly affect the area under the measured spectral albedo curves. Finally, uncertainty of SI can be inferred from the work of (Dirnberger et al., 2015a), who used spectroradiometers from the same manufacturer as used in this work and concluded that the minimum standard uncertainty is 0.009 (0.9%) for monofacial single junction c-Si SI calculations.

3.4. Impact of wavelength sampling reduction on spectral mismatch

Spectral albedo curves are not highly structured like the sun's spectrum as was demonstrated in Fig. 6 and Fig. 8, as well as by others (Vignola et al., 2017). The 0.4 nm wavelength resolution of the spectroradiometers used in this work therefore resulted in oversampling of the spectral albedo. The benefit of the high-resolution spectral albedo setup, however, is that down sampling can be conducted to identify when spectral mismatch, or other spectral factors, show large discrepancies relative to those calculated with the high-resolution data. To this end, we truncated the 2048-pixel measurements down to 2–8 wavelength channels and repeated the SMM_{Back} calculations. Table 3 shows the different wavelength bands tested. In all these cases, the down sampled albedo spectra use the 7 nm full-width half maximum optical resolution of the MS-711 spectroradiometer. The spectral albedo between narrow band channels is interpolated with a first order spline fit. Values outside the wavelength ranges shown in Table 3 are extrapolated, with the condition that 0.001 and 1.0 are the minimum and maximum

Table 3
Summary of wavelength channels used in the different down sampling tests of the high-resolution spectral albedo measurements. A 7 nm full width half maximum resolution was used in all scenarios.

N Channels	Center wavelengths (nm)
2	500, 940
3	500, 870, 940
4	415, 615, 870, 940
5	469, 555, 645, 858, 1050
6	415, 500, 615, 673, 870, 940
7	415, 500, 615, 673, 870, 940, 1050
8	415, 555, 615, 673, 762, 870, 940, 1050

spectral albedo values allowed.

The first four wavelength channels in the five-channel scenario (469 nm, 555 nm, 645 nm, and 858 nm) are the center wavelengths of the first four bands of the MODIS satellite (Schaaf and Wang, 2015); because the fifth MODIS spectral band (1240 nm) is beyond the spectral responsivity of Si, the fifth wavelength channel used here is 1050 nm. The wavelength channels in all other scenarios are selected for their common use in multi-filter radiometer (MFR) applications (Michalsky and Hodges, 2013) (Vladutescu et al., 2013) and because they are similar to those used by (Tatsiankou et al., 2016). The six-channel case uses the same six channels as used in the works of (Michalsky and Hodges, 2013) and (Vladutescu et al., 2013). To select the wavelengths of the two, three and four-channel cases, we down sampled all possible combinations of the six-channel case and identified the combination of wavelengths, for each case, that resulted in the lowest root mean square error (RMSE) across the four measured albedo conditions. The seven-channel case simply adds an NIR channel (1050 nm) to the six-channel case, and the eight-channel case has additional measurements at 555 nm and 762 nm, which are intended to capture the features of green vegetation. Fig. 14 shows examples of spectral albedo curves down sampled according to Table 3 for the four albedo conditions measured onsite.

Fig. 15 shows selected daily timeseries of SMM_{Back} calculated with the seven down sampling cases and with the high-resolution spectral albedo measurements. Table 4 summarizes the SMM_{Back} deviations across the entire 15-month measurement campaign in terms of the mean bias error (MBE) and RMSE.

The results indicate that SMM_{Back} can be reasonably approximated using spectral albedo measurements with just 4–8 narrow band channels. The two and three-channel down sampled cases show notably higher errors, especially in green grass and gravel albedo conditions. Given that many PV parks globally are constructed at sites where the spectral albedo is comparable to the green grass and gravel albedo conditions measured here, our down sampled SMM_{Back} results indicate that four narrow band channels is likely the bare minimum to monitor spectral albedo in bifacial PV applications. However, it is apparent in the four-channel curve of Fig. 14a that the down sampling overestimates the

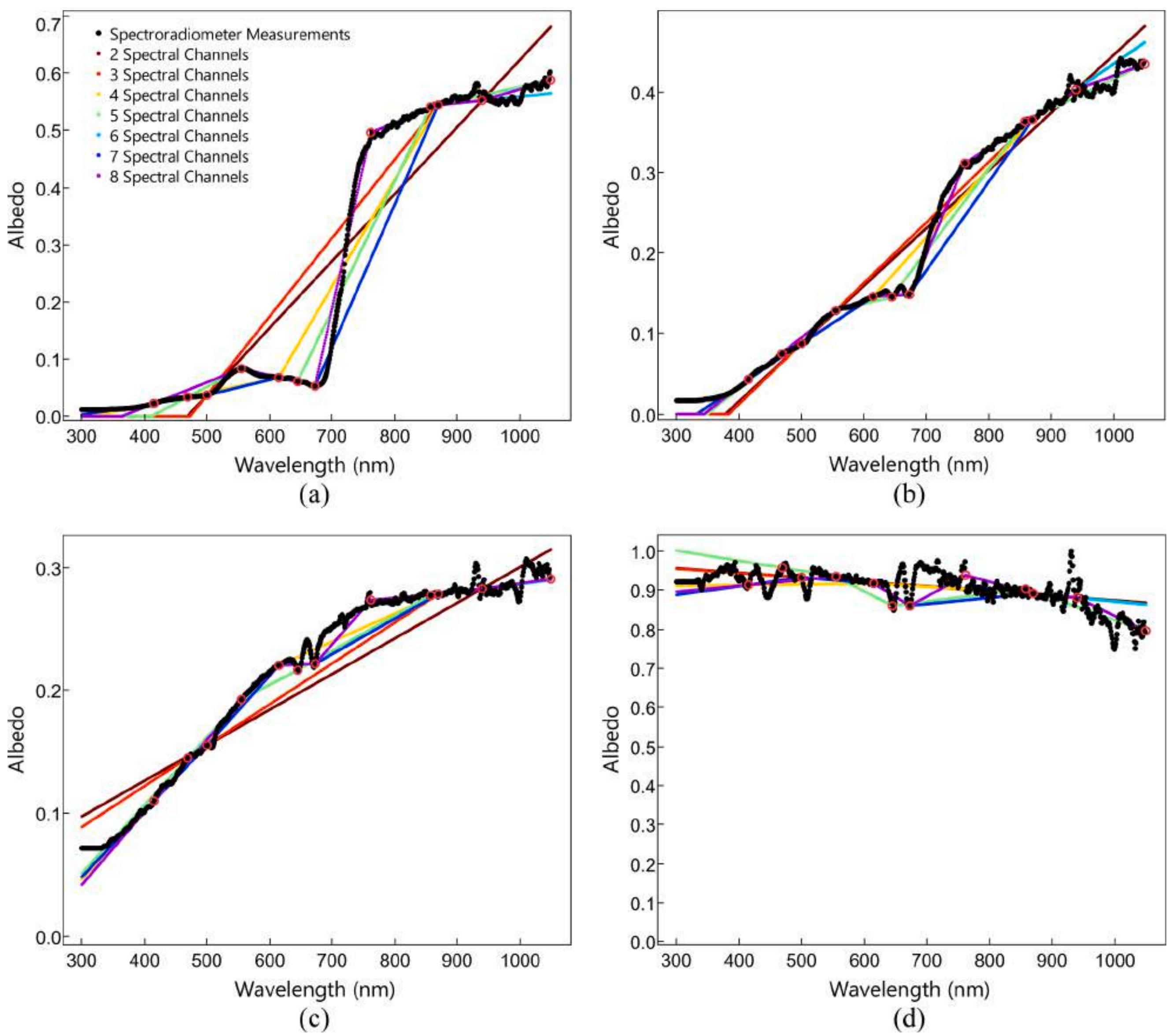

Fig. 14. Comparisons of measured and down sampled spectral albedo during the four albedo conditions: (a) green grass, (b) dry grass, (c) gravel and (d) snow. The example curves shown here are taken at 12:00 noon on the days shown in Fig. 6 and Fig. 8. The red circles correspond to the channels shown in Table 3. The red circles highlight the wavelengths at which the down sampled curves are created from the high-resolution measurements. (For interpretation of the references to colour in this figure legend, the reader is referred to the web version of this article.)

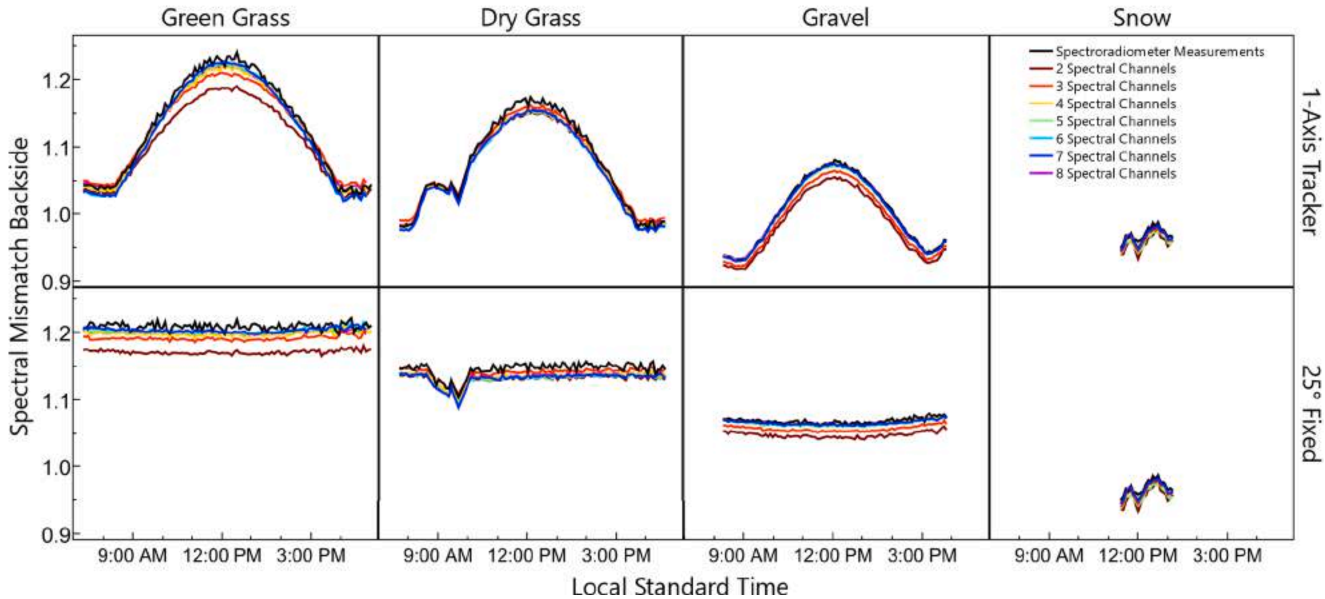

Fig. 15. Backside spectral mismatch of the PERC cell calculated with down sampled spectral albedos and high-resolution measurements. The down sampled calculations are made with the 2–8 narrow band channels shown in Table 4. Backside spectral mismatch is shown for a single axis tracker (top row) and a fixed-tilt system (bottom row). The four measured albedo conditions are displayed column-wise.

Table 4
Error Summary for backside spectral mismatch calculations performed using down sampled spectral albedo.

Structure	N Spectral Channels	Green Grass		Dry Grass		Gravel		Snow	
		MBE	RMSE	MBE	RMSE	MBE	RMSE	MBE	RMSE
1-Axis Tracker	2	−0.0243	0.0297	−0.0139	0.0175	−0.0116	0.0138	−0.0108	0.0122
	3	−0.0080	0.0170	−0.0011	0.0083	−0.0042	0.0072	−0.0056	0.0065
	4	−0.0081	0.0155	−0.0070	0.0097	0.0020	0.0038	−0.0012	0.0029
	5	−0.0056	0.0137	−0.0059	0.0083	−0.0004	0.0052	−0.0104	0.0108
	6	−0.0086	0.0155	−0.0098	0.0114	0.0004	0.0033	−0.0032	0.0042
	7	−0.0082	0.0153	−0.0095	0.0111	−0.0005	0.0035	−0.0030	0.0041
	8	−0.0060	0.0146	−0.0065	0.0098	0.0021	0.0042	−0.0006	0.0035
25° Fixed Tilt	2	−0.0310	0.0329	−0.0199	0.0213	−0.0138	0.0156	−0.0114	0.0128
	3	−0.0124	0.0161	−0.0048	0.0086	−0.0049	0.0079	−0.0059	0.0068
	4	−0.0097	0.0135	−0.0094	0.0115	0.0021	0.0042	−0.0013	0.0030
	5	−0.0064	0.0108	−0.0075	0.0097	−0.0005	0.0058	−0.0109	0.0113
	6	−0.0082	0.0125	−0.0103	0.0123	0.0003	0.0037	−0.0034	0.0043
	7	−0.0077	0.0123	−0.0099	0.0120	−0.0008	0.0040	−0.0032	0.0043
	8	−0.0081	0.0122	−0.0094	0.0115	0.0022	0.0046	−0.0007	0.0035

spectral albedo in some areas and underestimates it in others. Because the SMM calculation is an integrated quantity, it is possible that in cases where the down sampled spectral albedo curves show both high and low biases relative to the ground truth, the differences are effectively cancelled when assessed via the SMM factor. A more robust solution would therefore aim to recreate the spectral albedo curve across the various albedo conditions, which the eight-channel scenario (Fig. 14) does reasonably well.

Nearly all scenarios in Table 4 result in negative MBE relative to the high-resolution measurements, the exception is gravel albedo for which three of the seven scenarios show positive MBE. The RMSE of SMM_{Back} is between 0.0033 and 0.0329 with a trend toward higher errors at lower spectral resolution. The eight-channel case, however, does not always show the lowest RMSE. In fact, the RMSE of the eight-channel case and the 3–7 channel cases are within 0.005 of each other in all albedo conditions except snow. The two-channel case always shows the highest RMSE, with a maximum of 0.0329 (green grass) and a minimum of 0.0122 (snow). Since the two-channel case contains one measurement in the VIS and one in the NIR region, the errors shown in Table 4 coincide with those of Section 3.3 where it was shown that the NDVI can be used to approximate SMM_{Back} with an accuracy of $\pm$ 0.04.

4. Conclusions

We have demonstrated that backside spectral mismatch in bifacial PV systems is dynamic on daily and seasonal timescales, and we have quantified the extent to which it is dependent on the albedo, sky conditions, and mounting structure. On clear sky days, we observed that spectrally induced performance gains peak at mid-day wherein the backside spectral gains were 25%, 15%, and 5% for green vegetation, dry vegetation, and gravel, respectively. Backside spectral effects are significantly lower on tracked versus fixed-tilt bifacial systems because of the larger sky view factors on the array backside. On clear days, when the tracker is tilted at 60° from a horizontal, the spectral effects are reduced to 5%, 0%, and −5% for green vegetation, dry vegetation, and gravel, respectively.

With the variety of albedo conditions tested here, we showed that the normalized difference vegetation index (NDVI) is a reasonable data source to estimate backside spectral effects in bifacial PV systems. Specifically, the strong correlation between SMM_{Back} and NDVI suggests that satellite derived NDVI products could be a simple method to estimate backside spectral effects. However, the small area of our test site in comparison to the pixel resolution of satellite images prevented further examination of this conclusion.

Our 2D view factor simulations of incident backside spectrum discretized at the cell-level showed that backside POA spectral gradients (up to ± 7.5% in the tracked case) make multiple reference cells in the same array advisable, especially in 2-in-portrait configurations. Finally, we demonstrated that high-resolution spectral albedo measurements are neither practical nor necessary for bifacial PV performance monitoring applications. When SMM_{Back} was calculated with 2 to 8 wavelengths that were judiciously sampled between 300 and 1100 nm, we demonstrated that SMM_{Back} values calculated with just 4 wavelength channels are comparable to those calculated with the full spectroradiometer measurements with RMSE ≤ 0.0155. However, 8 spectral channels are recommended for users who are interested in recreating the spectral albedo curves as closely as possible.

Declaration of Competing Interest

The authors declare that they have no known competing financial interests or personal relationships that could have appeared to influence the work reported in this paper.

Acknowledgements

We thank Dennis Corell of DTU for supporting the spectrometer calibration efforts, Rasmus Nielsen of DTU for supporting the spectral responsivity measurements, and Dr. Joris Libal of ISC Konstanz for providing us with bifacial n-PERT and IBC cell samples.

Funding

This work was funded by the Danish Energy Technology Development and Demonstration Program (EUDP) under project contract 64018-0624.

References

Alonso-Abella, M., Chenlo, F., Nofuentes, G., Torres-Ramírez, M., 2014. Analysis of spectral effects on the energy yield of different PV (photovoltaic) technologies: The case of four specific sites. Energy 67, 435–443.

Andrews, R.W., Pearce, J.M., 2013. The Effect of Spectral Albedo on Amorphous Silicon and Crystalline Silicon Solar Photovoltaic Device Performance. Sol. Energy 91, 233–241.

Anoma, M., et al., 2017. View Factor Model and Validation for Bifacial PV and Diffuse Shade on Single-Axis Trackers. Washington D.C, s.n.

Asgharzadeh, A., Marion, B., Deline, C., Hansen, C., Stein, J.S., Toor, F., 2018. A Sensitivity Study of the Impact of Installation Parameters and System Configuration on the Performance of Bifacial PV Arrays. IEEE J. Photovoltaics 8 (3), 798–805.

Baldridge, A.M., Hook, S.J., Grove, C.I., Rivera, G., 2009. The ASTER spectral library version 2.0. Remotes Sens Environ. 113 (4), 711–715.

Belluardo, G., Galleano, R., Zaaiman, W., Pravettoni, M., Halwachs, M., Fucci, R., Drobisch, A., Friederichs, M., Haverkamp, E., Phinikarides, A., Friesen, G., 2018. Are the spectroradiometers used by the PV community ready to accurately measure the classification of solar simulators in a broader wavelength range? Sol. Energy 173, 558–565.

Berrian, D., Libal, J., 2020. A comparison of ray tracing and view factor simulations of locally resolved rear irradiance with the experimental values. Prog. Photovolt. 28 (6), 609–620.

Berrian, D., 2020. Accuracy of Ray Tracing and View Factor Optical Models - PhD Dissertation. Albert-Ludwigs-University, Freiburg im Breisgau, Germany.

Blakesley, J.C., et al., 2020. Effective spectral albedo from satellite data for bifacial gain calculations of PV systems. Virtual, s.n.

Brennan, M.P., Abramase, A.L., Andrews, R.W., Pearce, J.M., 2014. Effects of spectral albedo on solar photovoltaic devices. Sol. Energy Mater. Sol. Cells 124, 111–116.

Chiodetti, M. et al., 2016. *PV Bifacial Yield Simulation with a Variable Albedo Model.* Munich, s.n.

Chudinzow, D., Haas, J., Díaz-Ferrán, G., Moreno-Leiva, S., Eltrop, L., 2019. Simulating the energy yield of a bifacial photovoltaic power plant. Sol. Energy 183, 812–822.

Chudinzow, D., Klenk, M., Eltrop, L., 2020. Impact of field design and location on the techno-economic performance of fixed-tilt and single-axis tracked bifacial photovoltaic power plants. Sol. Energy 207, 564–578.

Coakley, J.A., 2003. Reflectance and Albedo, Surface. In: Encyclopedia of Atmospheric Sciences. Elsevier, pp. 1914–1923, 10.1016/B0-12-227090-8/00069-5.

Deline, C. & Pelaez, S., 2017. *Bifacial_Radiance. Computer Software..* [Online] Available at: https://github.com/NREL/bifacial_radiance.

Deline, C., Ayala Pelaez, S., MacAlpine, S., Olalla, C., 2020. Estimating and parameterizing mismatch power loss in bifacial photovoltaic systems. Progress in Photovoltaics 28 (7), 691–703.

Dirnberger, D., Müller, B., Reise, C., 2015a. On the uncertainty of energetic impact on the yield of different PV technologies due to varying spectral irradiance. Sol. Energy 111, 82–96.

Dirnberger, D., Blackburn, G., Müller, B., Reise, C., 2015b. On the impact of solar spectral irradiance on the yield of different PV technologies. Sol. Energy Mater. Sol. Cells 132, 431–442.

Dittmann, S. et al., 2019. Comparative Analysis of Albedo Measurements at Multiple Sites Worldwide. Marseille, s.n.

Dullweber, T., et al., 2016. PERC+: industrial PERC solar cells with rear Al grid enabling bifaciality and reduced Al paste consumption. Progress in Photovoltaics 24, 1487–1498.

Dullweber, T., Schmidt, J., 2016. Industrial Silicon Solar Cells Applying the Passivated Emitter and Rear Cell (PERC) Concept—A Review. IEEE J. Photovoltaics 6 (5), 1366–1378.

Dupre, O., et al., 2020. Design Rules to Fully Benefit From Bifaciality in Two-Terminal Perovskite/Silicon Tandem Solar Cells. IEEE J. Photovoltaics 714–721.

Dye, D., Tucker, C., 2003. Seasonality and trends of snow-cover, vegetation index, and temperature in northern Eurasia. Geophys. Res. Lett. 30 (7), 58–61.

Ernst, M., Holst, H., Winter, M., Altermatt, P., 2016. SunCalculator: A program to calculate the angular and spectral distribution of direct and diffuse solar radiation. Sol. Energy Mater. Sol. Cells 157, 913–922.

European Space Agency, 2021. *Sentinel VGT S NDVI.* [Online] Available at: https://sentinel.esa.int/web/sentinel/technical-guides/sentinel-3-synergy/vgt-s/ndvi [Accessed 30 6 2021].

Galleano, R. et al., 2019. *Spectroradiometer Comparison under Outdoor Direct Normal Irradiance and Indoor High-Power AM0-Like Conditions.* Marseille, France, 36th European Photovoltaic Solar Energy Conference and Exhibition.

Gates, D., Keegan, H., Schleter, J., Weidner, V., 1965. Spectral Properties of Plants. Appl. Opt. 4, 11–20.

Gostein, M., et al., 2021. Measuring Irradiance for Bifacial PV Systems. Virtual48th IEEE Photovoltaic Specialists Conference.

Gostein, M., Marion, B., Stueve, B., 2020. Spectral Effects in Albedo and Rearside Irradiance Measurement for Bifacial Performance Estimation. Virtual, s.n.

Green, M., 2015. The Passivated Emitter and Rear Cell (PERC): From conception to mass production. Sol. Energy 143, 190–197.

Gueymard, C., 1995. *SMARTS2, A Simple Model of the Atmospheric Radiative Transfer of Sunshine: Algorithms and performance assessment Authors,* s.l.: Florida Solar Energy Center Report (FSEC-PF-270-95).

Guo, S., Walsh, T., Peters, M., 2013. Vertically mounted bifacial photovoltaic modules: A global analysis. Energy 61, 447–454.

Hezel, R., 2003. Novel Applications of Bifacial Solar Cells. Prog. Photovoltaics 11, 549–556.

Hohl-Ebinger, J., Warta, W., 2011. Uncertainty of the spectral mismatch correction factor in STC measurements on photovoltaic devices. Prog. Photovolt. 19.

Huang, S., et al., 2020. A commentary review on the use of normalized difference vegetation index (NDVI) in the era of popular remote sensing. J. For. Res. 32 (5), 1–6.

Huld, T., Sample, T. & Dunlop, E., 2009. *A simple model for estimate the influence of spectrum variations on PV performance.* Hamburg, 24th EUPVSEC.

International Electrotechnical Commision, 2019a. *IEC 60904-3 Ed. 4.0,* s.l.: s.n.

International Electrotechnical Commision, 2019b. *IEC 60904-7 Ed. 4.0,* s.l.: s.n.

Iqbal, M., 1983. Chapter 9: Ground Albedo. In: An Introduction to Solar Radiation. Academic Press, New York and London, pp. 281–293.

Ishii, T., Otani, K., Itagaki, A., Utsunomiya, K., 2013. A simplified methodology for estimating solar spectral influence on photovoltaic energy yield using average photon energy. Energy Science and Engineering.

Jessen, W., et al., 2018. Proposal and evaluation of subordinate standard solar irradiance spectra for applications in solar energy systems. Sol. Energy 168, 30–43.

King, D., Boyson, B. & Kratochvill, J., 2004. *Photovoltaic Array Performance Model,* s.l.: Sandia Report (SAND2004-3535).

Kinsey, G., 2021. Solar cell efficiency divergence due to operating spectrum variation. Sol. Energy 217, 49–57.

Kirn, B., Topic, M., 2017. Diffuse and direct light solar spectra modeling in PV module performance rating. Sol. Energy 150, 310–316.

Kondratiev, K. Y., Mironova, Z. F. & Otto, A. N., 1964. Spectral albedo of natural surfaces. *pure and applied geophysics,* Volume 59, p. 207–216.

Kondratyev, K., 1969. Section 7.1: Spectral Albedo of Natural Underlying Surfaces. In: Radiation in the Atmosphere. Academic Press, New York and London, pp. 411–422.

Kopecek, R., Libal, J., 2021. Bifacial Photovoltaics 2021: Status, Opportunities and Challenges. Energies 14 (2076).

Kopecek, R. et al., 2020. *ZEBRA technology: low cost bifacial IBC solar cells in mass production with efficiency exceeding 23.5%.* Calgary, s.n.

Korevaar, M., et al., 2020. Simulation and Validation of Bifacial Irradiance Sensor Mounting Position. Virtual Meeting, 37th European Solar Energy Conference (EUPVSEC).

Krinov, E., 1953. *Spectral reflectance properties of natural formations.* Technical translation TT-439 by E. Belkov, National Research Council of Canada, Ottawa ed. USSR: Area Methods Laboratory, Academy of Sciences (orginally in Russian, 1947).

Lamers, M., et al., 2018. Temperature effects of bifacial modules: Hotter or cooler? Sol. Energy Mater. Sol. Cells 185, 192–197.

Ledesma, J., et al., 2020. A simulation model of the irradiation and energy yield of large bifacial photovoltaic plants. Sol. Energy 206, 522–538.

Lee, M. & Panchula, A., 2016. *Spectral correction for photovoltaic module performance based on air mass and precipitable water.* Portland, OR, 43rd IEEE Photovoltaic Specialists Conference.
Looney, E., et al., 2020. Representative identification of spectra and environments (RISE) using k-means. Prog. Photovolt. 29, 200–211.
Lossen, J. et al., 2015. *From Lab to Fab: Bifacial n-Type Cells Entering Industrial Production.* Hamburg, Germany, Proceedings of the 31st European Photovoltaic Solar Energy Conference and Exhibition.
Marion, B., 2021. Measured and satellite-derived albedo data for estimating bifacial photovoltaic system performance. Sol. Energy 215, 321–327.
McIntosh, K., Abbott, M., Sudbury, B., Meydbray, J., 2019. Mismatch Loss in Bifacial Modules Due to Nonuniform Illumination in 1-D Tracking Systems. IEEE J. Photovotaics 9 (6), 1504–1512.
McIntosh, K., et al., 2020. Irradiance on the upper and lower modules of a two-high bifacial tracking system. Virtual Meeting, 47th IEEE Photovoltaics Specialist Conference (PVSC).
Mekemeche, A., Beghdad, M., 2020. Impact of the Environmental Effective Albedo on the Performance of PERC + Solar Cells. Silicon 29.
Michalsky, J., Hodges, G., 2013. Field Measured Spectral Albedo-Four Years of Data from the Western U.S Prairie. J. Geophys. Res. Atmospheres 118, 813–825.
Minnis, P., Mayor, S., Smith, W., Young, D., 1997. Asymmetry in the Diurnal Variation of Surface Albedo. IEEE Trans. Geosci. Remote Sens. 35 (4), 879–890.
Monokroussos, C., et al., 2020. Rear-side spectral irradiance at 1 sun and application to bifacial module power rating. Prog. Photovolt.
Myers, D., Emery, K., Gueymard, C., 2004. Revising and Validating Spectral Irradiance Reference Standards for Photovoltaic Performance Evaluation. J. Sol. Energy Eng. 126, 567–574.
Myers, D. R., 2011. Quantitative analysis of spectral impacts on silicon photodiode radiometers. *40th ASES National Solar Conference 2011, SOLAR 2011,* 1(April), pp. 97-102.
NASA, 2021. *MODIS Vegetation Index Products.* [Online] Available at: https://modis.gsfc.nasa.gov/data/dataprod/mod13.php.
Nofuentes, G., et al., 2017. Is the average photon energy a unique characteristic of the spectral distribution of global irradiance? Sol. Energy 149, 32–43.
Nordmann, T., Vontobel, T. & Clavadetscher, L., 2012. 15 Years of Practical Experience in Development and Improvement of Bifacial Photovoltaic Noise Barriers Along Highways and Railway Lines in Switzerland. Frankfurt, Germany, 27th European Photovoltaic Solar Energy Conference and Exhibition.
Pal, S., Reinders, A., Saive, R., 2020. Simulation of Bifacial and Monofacial Silicon Solar Cell Short-Circuit Current Density Under Measured Spectro-Angular Solar Irradiance. IEEE J. Photovoltaics 10 (6), 1803–1815.
Pelaez, S.A., et al., 2019a. Model and Validation of Single-Axis Tracking with Bifacial PV. IEEE J. Photovoltaics 9 (3), 715–721.
Pelaez, S., et al., 2019b. Comparison of Bifacial Solar Irradiance Model Predictions With Field Validation. IEEE J. Photovoltaics 9 (1), 82–88.
Pelland, S. et al., 2020. *Development and Testing of the PVSPEC Model of Photovoltaic Spectral Mismatch Factor.* Calgary, Canada, 47th IEEE Photovoltaic Specialistis Conference.
Polo, J., Alonso-Abella, M., Ruiz-Arias, J., Balenzategui, J., 2017. Worldwide analysis of spectral factors for seven photovoltaic technologies. Sol. Energy 142, 194–203.
Pravettoni, M., et al., 2018. Spectroradiometry in PV: how inter-laboratory comparison may improve measurement accuracy. Waikaloa, Hawaii, 7th World Conference on Photovoltaic Energy Conversion.
Riedel-Lyngskær, N., et al., 2020a. A Spatial Irradiance Map Measured on the Rear Side of a Utility-Scale Horizontal Single Axis Tracker with Validation using Open Source Tools. Virtual Meeting, 47th IEEE Photovoltaics Specialist Conference (PVSC).
Riedel-Lyngskær, N., et al., 2020b. Validation of Bifacial Photovoltaic Simulation Software against Monitoring Data from Large-Scale Single Axis Trackers and Fixed Tilt Systems in Denmark. Applied Sciences 10 (23), 1–29.
Riedel-Lyngskær, N., et al., 2021. Spectral Albedo in Bifacial Photovoltaic Modelling: What can be Learned from Onsite Measurements? Miami, FL, 48th IEEE Photovoltaic Specialists Conference.
Riedel, N., et al., 2018. Direct Beam and Diffuse Spectral Irradiance Measurements in a Nordic Country Analyzed With the Average Photon Energy Parameter. Waikoloa, United States, s.n.
Ripalda, J., Chemisana, D., Llorens, J. & Garcıa, I., 2020. Location-Specific Spectral and Thermal Effects in Tracking and Fixed Tilt Photovoltaic Systems. *iScience,* 23 (101634).
Rodriguez-Gallegos, C., et al., 2020. Global Techno-Economic Performance of Bifacial and Tracking Photovoltaic Systems. Joule 4, 1514–1541.
Rossa, C., Martinez-Moreno, F., Lorenzo, E., 2021. Experimental observations in mismatch losses in monofacial and bifacial PV generators. Progress Photovolt.
Rouse, J., Haas, R., Scheel, J. & Deering, D., 1974. *Monitoring Vegetation Systems in the Great Plains with ERTS.* s.l., s.n., pp. 48-62.
Russel, T.C.R., et al., 2017. The Influence of Spectral Albedo on Bifacial Solar Cells: A Theoretical and Experimental Study. IEEE J. Photovolt. 7 (6), 1611–1619.
Schaaf, C., Wang, Z., 2015. MCD43A3 MODIS. [Online].
Schinke, C., Pollex, H., Winter, S., 2020. Calibrating spectrometers for measurements of the spectral irradiance caused by solar radiation. Metrologia.
Stein, J., Hansen, C. & Reno, M., 2012. *The Variability Index: A New and Novel Metric for Quantifying Irradiance and PV Output Variability,* s.l.: Sandia Report: SAND2012-2088C.
Stueve, B., 2019. *Field Albedo Measurements.* Amsterdam, bifiPV Workshop.
Sun, X., Khan, M., Deline, C., Alam, M., 2018. Optimization and performance of bifacial solar modules: A global perspective. Appl. Energy 212, 1601–1610.
Tatsiankou, V., et al., 2016. Design principles and field performance of a solar spectral irradiance meter. Sol. Energy 133, 94–102.
Tuomiranta, A. et al., 2020. *Comparative Field Performance Assessment of Bifacial Solar Modules.* Calgary, 7th IEEE Photovoltaic Specialists Conference (PVSC), p. 1033–1034.
VDMA, 2021. International Technology Roadmap for Photovoltaics (ITRPV): Twelfth Edition, s.l.: s.n.
Vignola, F., Michalsky, J. & Stoffel, T., 2017. Chapter 9: Albedo. In: *Solar Radiation and Infrared Radiation Measurements.* Boca Raton, FL: CRC Press, p. 193–204.
Vladutescu, D., et al., 2013. Aerosol Transport and Source Attribution Using Sunphotometers, Models and In-Situ Chemical Composition Measurements. IEEE Trans. Geosci. Remote Sens. 5 (7), 3803–3811.
Vogt, M. R. et al., 2018. Impact of using spectrally resolved ground albedo data for performance simulations of bifacial modules. Brussels, s.n.
Wang, H., Cheng, X., Yang, H., 2020. Temperature Coefficients and Operating Temperature Verification for Passivated Emitter and Rear Cell Bifacial Silicon Solar Module. IEEE J. Photovoltaics 10 (3), 729–739.
Ward, G., 1994. The RADIANCE Lighting Simulation and Rendering System. Proceedings of the 21st annual conference on Computer graphics and interactive techniques.
Wilson, G., et al., 2020. The 2020 photovoltaic technologies roadmap. J. Phys. D Appl. Phys. 53 (49).
Yusufoglu, U., et al., 2015. Analysis of the Annual Performance of Bifacial Modules and Optimization Methods. IEEE J. Photovoltaics 5 (1), 320–328.
Zhang, Y., Yu, Y., Meng, F., Liu, Z., 2020. Experimental Investigation of the Shading and Mismatch Effects on the Performance of Bifacial Photovoltaic Modules. IEEE J. Photovoltaics 10 (1).
Ziar, H., Sönmez, F., Isabella, O., Zeman, M., 2019. A comprehensive albedo model for solar energy applications: Geometric spectral albedo. Appl. Energy 255.

Publication VII. Interlaboratory comparison of angular-dependent photovoltaic device measurements: Results and impact on energy rating

Authors:

Nicholas Riedel-Lyngskær, Adrián A. Santamaría Lancia, Fabian Plag, Ingo Kröger, Malte R. Vogt, Carsten Schinke, Rasmus S. Davidsen, Mekbib Amdemeskel, Mark J. Jansen, Petra Manshanden, Lenneke H. Slooff, Anna J. Carr, Martin Bliss, Tom Betts, Mikel E. Mayo, Iñigo P. Jauregui, Jose L. Balenzategui, Ruben Roldan, Giovanni Bellenda, Mauro Caccivio, Ulli Kräling, Frank Neuberger, Daniel Zirzow, Jim Crimmins, Charles Robinson, Bruce King, Wesley Teasdale, Cherif Kedir, John Watts, Ryan Desharnais, Peter B. Poulsen, Michael L. Jakobsen, and Gisele A. dos Reis Benatto

Published in:

Progress in Photovoltaics Res Appl. 2021, 29: 315-333

DTU Library

Interlaboratory comparison of angular-dependent photovoltaic device measurements: Results and impact on energy rating

Riedel, Nicholas; Santamaria Lancia, Adrian Alejo; Plag, Fabian; Kröger, Ingo; Vogt, Malte R. ; Schinke, Carsten; Davidsen, Rasmus Schmidt; Amdemeskel, Mekbib Wubishet; Jansen, Mark J. ; Manshanden, Petra

Total number of authors:
33

Published in:
Progress in Photovoltaics

Link to article, DOI:
10.1002/pip.3365

Publication date:
2021

Document Version
Peer reviewed version

Citation (APA):
Riedel, N., Santamaria Lancia, A. A., Plag, F., Kröger, I., Vogt, M. R., Schinke, C., Davidsen, R. S., Amdemeskel, M. W., Jansen, M. J., Manshanden, P., Slooff, L. H., Carr, A. J., Bliss, M., Betts, T., Mayo, M. E., Jauregui, I. P., Balenzategui, J. L., Roldan, R., Bellenda, G., ... Benatto, G. A. D. R. (2021). Interlaboratory comparison of angular-dependent photovoltaic device measurements: Results and impact on energy rating. *Progress in Photovoltaics*, *29*(3), 315-333. https://doi.org/10.1002/pip.3365

Interlaboratory comparison of angular-dependent photovoltaic device measurements: Results and impact on energy rating

Nicholas Riedel-Lyngskær[1], Adrián A. Santamaría Lancia[1], Fabian Plag[2], Ingo Kröger[2], Malte R. Vogt[3], Carsten Schinke[3,4], Rasmus S. Davidsen[5], Mekbib Amdemeskel[1], Mark J. Jansen[6], Petra Manshanden[6], Lenneke H. Slooff[6], Anna J. Carr[6], Martin Bliss[7], Tom Betts[7], Mikel E. Mayo[8], Iñigo P. Jauregui[8], Jose L. Balenzategui[9], Ruben Roldan[10], Giovanni Bellenda[10], Mauro Caccivio[10], Ulli Kräling[11], Frank Neuberger[11], Daniel Zirzow[12], Jim Crimmins[12], Charles Robinson[13], Bruce King[13], Wesley Teasdale[14], Cherif Kedir[14], John Watts[15], Ryan Desharnais[15], Peter B. Poulsen[1], Michael L. Jakobsen[1], Gisele A. dos Reis Benatto[1]

1. Technical University of Denmark, Department of Photonics Engineering, 4000 Roskilde, Denmark
2. Physikalisch-Technische Bundesanstalt (PTB), 38116 Braunschweig, Germany
3. Institute for Solar Energy Research Hamelin (ISFH), 31860 Emmerthal, Germany
4. Leibniz University Hanover, Institute for Solid State Physics, Solar Energy Department, 30167 Hannover, Germany
5. Technical University of Denmark, National Centre for Nano Fabrication and Characterization, 2800 Lyngby, Denmark
6. TNO Energy Transition, 1755 LE Petten, the Netherlands
7. Centre for Renewable Energy Systems Technology (CREST), Wolfson School of Mechanical, Electronic and Manufacturing Engineering, Loughborough University, Loughborough, LE11 3TU, UK
8. Spanish National Renewable Energy Centre (CENER), 31621 Sarriguren, Spain
9. PVLab, Photovoltaic Solar Energy Unit, CIEMAT, 28040 Madrid, Spain
10. University of Applied Sciences and Arts of Southern Switzerland, Institute for Applied Sustainability to the Built Environment (SUPSI - ISAAC), Campus Trevano, CH-6952 Canobbio, Switzerland
11. Fraunhofer Institute for Solar Energy Systems ISE, CalLab PV Modules, 79110 Freiburg, Germany
12. CFV Laboratories, Albuquerque, NM, 87110, USA
13. Sandia National Laboratories, Albuquerque, NM, 87185-0951, USA
14. Renewable Energy Test Center (RETC), Fremont, CA, 94538, USA
15. PV Evolution Labs (PVEL), Berkeley, CA, 94710, USA

Corresponding Author: Nicholas Riedel-Lyngskær, nrie@fotonik.dtu.dk, Technical University of Denmark, Department of Photonics Engineering, 4000 Roskilde, Denmark

Key words: Angle of incidence, incidence angle modifier, relative transmittance, interlaboratory comparison, optical losses, angular-dependent losses, energy rating, diffuse irradiance

Abstract

This paper presents the results from an extensive interlaboratory comparison of angular-dependent measurements on encapsulated photovoltaic (PV) cells. Twelve international laboratories measure the incident angle modifier of two unique PV devices. The absolute measurement agreement is ±2.0% to the weighted mean for angles of incidence (AOI) ≤ 65°, but from 70°–85° the range of measurement deviations increases rapidly from 2.5%–23%. The proficiency of the measurements is analyzed using the expanded uncertainties published by seven of the laboratories, and it is found that most of the angular-dependent measurements are reproducible for AOI ≤ 80°. However, at 85° one laboratory's measurement do not agree to the weighted mean within the stated uncertainty, and measurement uncertainty as high as 16% is needed for the laboratories without uncertainty to be comparable. The poor agreement obtained at 85° indicates that the PV community should place minimal reliance on angular-dependent measurements made at this extreme angle until improvements can be demonstrated. The cloud-based Daidalos ray tracing model is used to simulate the angular-dependent losses of the mono-Si device and it is found that the simulation agrees to the median measurement within 0.6% for AOI ≤ 70° and within 1.4% for AOI ≤ 80°. Finally, the impact that the angular-dependent measurement deviations have on climate specific energy rating (CSER) is evaluated for the six climates described in the IEC 61853-4 standard. When one outlier measurement is excluded, the angular-dependent measurements reported in this work cause a 1.0%–1.8% range in CSER and a 1.0%–1.5% range in annual energy yield, depending on the climate.

Table 1 Nomenclature

Θ	Angle of incidence (°)
STC	Standard Test Conditions of 1000 W·m^{-2}, 25 °C and AM1.5G
E_n	ISO 17043 proficiency test performance statistic known as the 'E_n number' (dimensionless)
τ	Measured relative light transmittance, also known as the incident angle modifier (dimensionless)
τ_{spec}	Simulated optical losses relative to the AM1.5G reference spectrum at normal incidence
a_r	Angular loss coefficient extracted from Martin and Ruiz model
b_o	Angular loss coefficient extracted from ASHRAE model
F_D	Correction factor for loss of diffuse irradiance due to reflection (dimensionless)
$D_{Corr,AOI}$	Plane of array diffuse irradiance corrected for reflection losses (W·m^{-2})
$B_{Corr,AOI}$	Plane of array beam irradiance corrected for reflection losses (W·m^{-2})
$G_{Corr,AOI}$	Plane of array global irradiance corrected for reflection losses (W·m^{-2})
Global AAL	Annual angular losses of global irradiance (%)

1 Introduction

Angular-dependent losses in photovoltaic (PV) devices are known to increase as function of a light source's angle of incidence (AOI) relative to the normal plane of the PV collector [1] – [3]. For PV modules with unsoiled planar glasses, these optical losses typically increase rapidly for AOI > 50°. Such angular-dependent losses are primarily due to reflection at the glass-air interface, but they also include absorption in the front materials and spectral effects [4]. The works of [5] and [6] have shown that annual angular losses for c-Si devices with cleaned planar glasses are between approximately 3 – 4 % when the PV module is mounted toward the equator with a tilt within 10° of the latitude. Thus, AOI effects represent a major loss mechanism for PV devices.

Angular-dependent losses are not characterized during measurements at Standard Test Conditions (STC), which are performed with the PV device at normal incidence to the light source (AOI = 0°). Unless dual axis tracking is used, the direct beam light that impinges on a PV module in the field will be at an AOI ≠ 0° for most of year. The IEC 61853 series of standards provide guidance on how to characterize PV devices over the breadth of environmental conditions known to influence PV performance, and among these are procedures for conducting AOI measurements [7].

Numerous interlaboratory comparisons have been conducted for PV measurements at STC [8] – [12], but the literature is comparatively sparse when it comes to comparisons of angular-dependent measurements. Our literature review revealed that the intercomparisons of AOI measurements to date have been conducted among few laboratories and have thus compared a limited number of test methods. For example, the authors in [13] compared outdoor measurements performed in real-time at Sandia National Laboratories (SNL) and CFV Labs, which lay roughly 10 km apart from each other. These two labs used unique methods to measure the AOI response of identical 36-cell (0.65 m^2) PV modules and found an acceptable level of agreement between their measurements. The authors in [14] compared AOI measurements — also performed at SNL on full-size (0.72 – 1.6 m^2) PV modules — to relative transmittance data supplied within the commercially available software PVsyst, or to measurements performed at an unnamed third party lab. The authors found that these three sources often had significant deviations for the same module type, and up to a 14 % difference in relative transmittance at large AOIs. Finally, in a white paper published by PV Evolution Labs (PVEL), a comparison of five laboratories' angular-dependent measurements on a commercially available PV module was presented, not of the angular-dependent measurements themselves, but in the form of utility-scale PV energy simulations [15].

To the best of our knowledge, the scientific literature presently contains no published works of intercomparisons or "round-robin" measurement campaigns of angular-dependent measurements on PV devices beyond the aforementioned studies. Therefore, we conclude that an international intercomparison of angular-dependent measurements is needed to establish the present-day comparability of measurements made using various test methods that conform to the IEC 61853-2 standard. We presented a preliminary version of this effort in [16]. An overlapping objective in our previous paper and this work is to assess how well the measurement differences agree within the laboratories' stated expanded uncertainties. This contribution has two additional objectives: to compare the laboratory measurements to simulations performed using the Daidalos ray tracing model [17] [18], and to determine the impact the angular measurement discrepancies have on energy rating when different fitting models and diffuse models are used.

2 Methods

The participating laboratories measure short-circuit current (I_{SC}) on all samples from -85° to 85° AOI, except for two labs that only measured I_{SC} in the positive angular direction. A common temperature coefficient for I_{SC} was provided to the labs so measurements could be temperature corrected. Since the participants were asked to use their standard techniques for AOI measurements, they were afforded discretion concerning specific procedures such as measurement correction techniques and the number of readings to average at each AOI. For example, two labs determined that temperature corrections of I_{SC} had a negligible influence on the overall uncertainty, and therefore chose not to temperature correct their I_{SC} measurements. The same type of judgement was given to participants in applying corrections due to fluctuations in broadband irradiance. Most labs did apply irradiance stability corrections to I_{SC} using readings from a reference device, but in some cases, the correction was not applied because the light source was determined to be stable throughout the test and/or a reference device was not used during the test. Only one laboratory reported implementing a spectral correction to I_{SC} due to the change in spectrum during the test, which was performed outdoors. The labs were also permitted to decide how many I_{SC} measurements at each AOI to average. This varied widely among labs with some labs performing as few as one and other labs performing more than one hundred I_{SC} measurements per AOI. We refer the reader to Appendix 1, Table 5 for more information about the specific test methods employed by each lab.

In the results that follow the angular-dependent I_{SC} measurements are converted to relative transmittance $\tau(\theta)$ (Eq. 1). The relative transmittance describes the photocurrent a PV device generates in the absence of diffuse light at a given AOI relative to the photocurrent the device would have generated if it exhibited a perfect cosine response (i.e. a Lambertian receiver). In this scheme, $\tau(\theta)$ is a dimensionless quantity wherein a value of 1 indicates the relative light transmission to the PV device follows that of a true cosine receiver and any values less than 1 indicate additional reflection and/or absorption. In other words, the quantity 1 - $\tau(\theta)$ is the amount of sunlight reflected and/or absorbed by the PV device's front materials, normalized to how much light is reflected or absorbed by the front materials at normal incidence. In practice the reflectance observed at normal incidence for the samples tested is of approximately 4 %. Note that the definition of $\tau(\theta)$ as it is presented here, is equivalent to the definition of the incident angle modifier (IAM) as described elsewhere in the literature [14], [19], [20].

$$\tau(\theta) = \frac{I_{SC}(\theta)}{I_{SC}(0°)\cdot\cos\theta} \quad (1)$$

2.1 Participating Laboratories and Measurement Systems

Twelve laboratories from seven countries are involved in the measurement comparison. Descriptions of each laboratory, the measurement systems used, and selected methodological details are provided in Appendix 1, Table 5. The indoor measurement systems used at CIEMAT, CREST, Fraunhofer ISE, RETC, SUPSI and TNO are based on a flash system used for full-sized (roughly 1 x 2 m) modules. However, each one of these labs used a different approach to build the rotation stage. The rotation stage at TNO, for example is designed to measure small laminates (roughly 20 x 20 cm), while the CREST, Fraunhofer ISE, and SUPSI rotation stages can accommodate small laminates up to full-sized modules. The DTU system is only capable of testing small laminates and the PTB system can accommodate mini-modules with up to four 156 x 156 mm cells. The outdoor two-axis solar trackers at CENER, CFV Labs, and SNL can accommodate full-sized modules, and since small single cell laminates were used as the devices under test (DUTs) in this intercomparison, they utilized the trackers' area to perform the test on all DUTs at once.

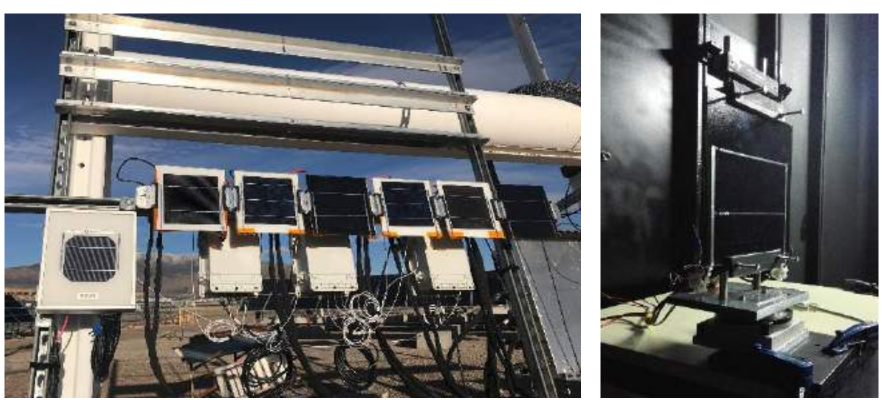

Figure 1: Photos from selected measurement systems. Intercomparison samples mounted on the dual axis tracker at Sandia National Laboratories (left) and a mono-Si sample mounted in the flash tunnel at CIEMAT (right).

The expanded measurement uncertainty provided from eight of the twelve testing partners is shown in Figure 2. Three labs reported expanded uncertainties individually for each of the two DUTs. Figure 2 shows a trend of increasing uncertainty with increasing AOI, wherein a range of 0.2 % – 1.1 % at normal incidence and a range of 2.5 % – 30.7 % at 85° AOI is observed. The specific reasons for this increasing trend will be unique to a given measurement system. Many authors have reported on the challenges and uncertainties encountered when directly measuring angular-dependent losses in PV devices [4], [21] – [26]. Some of these uncertainties exist in all AOI measurement systems, irrespective of the method. For example, common across measurement approaches is the fact that at AOIs approaching → 80°, the I_{SC} of the DUT can be an order of magnitude lower than at normal incidence. At such extreme angles, the I_{SC} of the DUT and the equipment used to measure current can deviate from a linear response and this should be accounted for in the uncertainty budget. Additionally, when AOI > 65°, the main contribution to overall uncertainty is likely to be the uncertainty from the measured angle (θ). Therefore, the wide range of reported measurement uncertainties at 85° shown in Figure 2 is likely driven by the varying levels of accuracy in the measured angle Θ. For example, Lab J determined that the error of Θ in their system at the time of measurement was approximately 2.3°, which was thus the major contributor to the total measurement uncertainty of nearly 30 % at 85°. In contrast, Lab C, Lab D, Lab F and Lab K — all of which reported uncertainty less than 7.0 % at 85° — reported that the error of the measured angle Θ was between < 0.1° and 0.2° in their respective measurement systems.

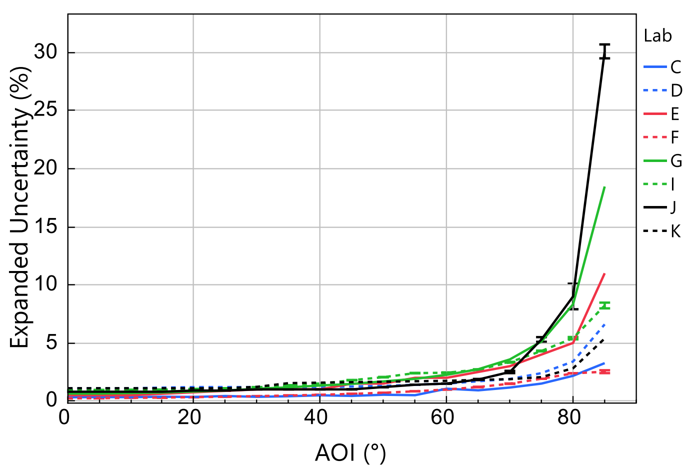

Figure 2: Expanded uncertainty of relative transmission measurements reported by eight laboratories as a function of AOI. The three labs with DUT-specific uncertainty are noted with range bars (Lab F, I, and J).

Some specific difficulties are encountered whether the angular-dependent characteristics are measured indoors or outdoors. The major challenges for indoor measurements include suppression of diffuse light within the test bed (i.e. improving collimation), which can be accomplished using baffles such that the field of view to the module is restricted within 20° to 30° and implementing non-reflective surfaces that minimize reflections within the test bed.

Further challenges indoors include precisely positioning the DUT at the center of the rotational axis and maintaining low spatial irradiance non-uniformity as the device is rotated toward an increasing AOI. The IEC 61853-2:2016 standard specifies that the non-uniformity should remain lower than 5 % throughout the test. However, [25] has demonstrated that when there is a 7.2 m distance from the light source to the DUT's optical axis, this non-uniformity requirement cannot be met when measuring commercially available PV panels that are 1 m in width. Another challenge is ensuring that the angular range of incident light on the DUT does not vary significantly throughout the duration of the test. The current (2016) edition of IEC 61853-2 specifies that the variation of AOI shall not vary by more than 1°, which is presently understood as the difference in AOIs observed between the two active edges of the DUT that are closest and farthest away from the light source. However, [26] has shown that when commercially available solar simulators are used, this requirement can only be met for small-area samples, or when a subarea of a full-size module is investigated either by mechanically isolating a single cell, or by partially shading the cell of interest. An intercomparison of AOI measurements on single cell laminates — as carried out in this work

— should therefore allow participating laboratories to closely comply with the present requirements of the standard. Single cell laminates as DUTs also allows more laboratories and measurement systems to participate in the intercomparison. Specifically, five measurement systems used in this intercomparison are not capable of performing AOI measurements on full-size PV modules.

The primary challenges of performing angular-dependent PV measurements outdoors include correcting for environmental fluctuations during testing and quantifying the diffuse irradiance in the plane of the DUT. The plane of array diffuse irradiance (D_{POA}) contribution can be accounted for indirectly using cosine corrected direct beam measurements from a pyrheliometer and global measurements from a reference device. Alternatively D_{POA} can be measured directly if a specialized solar tracker is available as in [13]. Additionally, the pyranometers that are most often used as reference devices are not true cosine receptors [27]. Therefore, the sensitivity coefficients used should be uniquely calibrated for each value of θ under which the DUT is tested. Failure to apply such a correction could lead to errors of up to 12 % [22], [24].

2.2 Devices under Test (DUTs)

Table 2 summarizes the bill of materials and the testing history of all DUTs distributed in this work. All 12 participating labs received a case of six samples that included three device types (mono-Si, BSi RIE, and BSi ADE). There was a duplicate sample of each type so there would be a backup in the case that any one sample became damaged during the measurement campaign. Before the intercomparison began, all DUTs were light soaked in the open-circuit state to a minimum dose of 10 $kWh \cdot m^{-2}$ to remove initial light induced degradation (LID). A final stability check of I_{SC} was not performed at the end of the intercomparison because the reported quantity $\tau(\theta)$ is calculated using a relative measurement approach. In other words, any minor degradation in the I_{SC} during the measurement campaign would not impact the $\tau(\theta)$ results because these values are referenced to each individual laboratory's I_{SC} measurement at normal incidence. Therefore, the electroluminescence (EL) imaging performed by each laboratory before the AOI tests was considered adequate to detect any changes in cell-level performance that could potentially impact the test results.

The following specifications are common to all DUTs: (i) An active cell area of 156 mm x 156 mm; (ii) full area dimensions of 200 mm x 200 mm; (iii) 3.2 mm thickness, low-iron, non-coated, finely textured PV glass superstrate; (iv) ethylene-vinyl acetate (EVA) encapsulant; (v) two tabs as metal contacts; and (vi) a flat polymeric backsheet with slight curvature around the cell edges. The differences between the samples are the cell type, the cell texturing, and the backsheet color. One sample type has a mono-crystalline Czochralski grown silicon (mono-Si) cell textured by a conventional random pyramid etch using KOH and will be referred to as 'mono-Si' hereafter. The second sample type has a multi-crystalline black silicon (BSi) cell textured under a mask-less reactive ion etching (RIE) process that results in ~400 nm tall conical-like hillocks as described in [28]; this device type will be referred to as 'BSi RIE' hereafter. The third sample type has a multi-crystalline cell textured by atmospheric dry etching (ADE) resulting in ~450 nm rounded cones after a wet-chemical post-etching [29] and is referred to as 'BSi ADE' hereafter. The edges of the DUTs were covered with non-transparent tape to prevent measurement artifacts at large incident angles. All the DUTs have a greater ratio of visible backsheet to active cell area than is typical of commercially available PV modules; this is due to the availability of 20 cm x 20 cm glass sheets and conventional 156 mm x 156 mm PV cells.

Table 2: Descriptions of the DUTs distributed to all participants in the intercomparison. When cells in the 'Testing Outcome and Data Usage' column are highlighted green, this indicates that the angular-dependent measurements of the DUT are reported in this manuscript.

<table>
<tr><th>Serial Number (SN)</th><th>Testing Outcome and Data Usage</th><th>Device Type (Alias)</th><th>Cell Type[1] and Surface Texture</th><th>Glass Specifications[2]</th><th>Encapsulant and Backsheet</th></tr>
<tr><td>0008</td><td>Sent to all 12 labs. Results from 10 of 12 labs presented here. Lab D and Lab L measurements not presented because they were determined as outliers in [16].</td><td rowspan="4">mono-Si</td><td rowspan="4">mono-Si cell with Random pyramids from KOH</td><td rowspan="4">Manufacturer A</td><td rowspan="4">EVA encapsulant / Polymeric black backsheet</td></tr>
<tr><td>0010</td><td>Sent to Lab D for retest. Results are presented here together with 'mono-Si' test results (SN 0008).</td></tr>
<tr><td>0015</td><td>Sent to Lab L for retest. Results are presented here together with 'mono-Si' test results (SN 0008).</td></tr>
<tr><td>0020</td><td>Sent to 12 labs. Damaged glass edge found during visual inspection. τ(ϴ) results not presented.</td></tr>
<tr><td>0025</td><td>Sent to all 12 labs. Results from 10 of 12 labs presented here. Lab D and Lab L measurements not presented because they were determined as outliers in [16].</td><td rowspan="2">BSi RIE</td><td rowspan="2">multi-Si cell with conical-like hillocks from RIE</td><td rowspan="4">Manufacturer B</td><td rowspan="4">EVA encapsulant / Polymeric white backsheet</td></tr>
<tr><td>0026</td><td>Sent to 12 labs. Duplicate DUT of SN 0025. τ(ϴ) results not presented.</td></tr>
<tr><td>0027</td><td>Sent to all 12 labs, but measurements not presented due to lack of dataset completeness and lack of distinctiveness in angular-dependent response compared to mono-Si or BSi RIE devices.</td><td rowspan="2">BSi ADE</td><td rowspan="2">multi-Si cell with rounded cones from ADE</td></tr>
<tr><td>0028</td><td>Sent to all 12 labs. Significant cell cracks found in EL image. τ(ϴ) results not presented here.</td></tr>
</table>

[1] All cells are a 156 mm x 156 mm square (multi-Si) or pseudo square (mono-Si).

[2] The glass specifications are the same for all samples (i.e. 200 mm x 200 mm, 3.2 mm thickness, low-iron, non-coated, finely textured), but they were procured from two different manufacturers noted here as 'Manufacturer A' and 'Manufacturer B'.

The convention regarding the axis of rotation was predefined to allow the results from the different partners to be directly comparable. The definition for which angular direction was positive and negative was made explicitly clear in a memorandum document that all partners received. The document also specified the location of the rotational axis and tolerances for the precise location of the front of the PV cell surface within the laminate. The samples made for this round-robin have an offset of approximately 1.5 mm ± 0.5 mm from the rear side (backsheet) to the front surface of the PV cell.

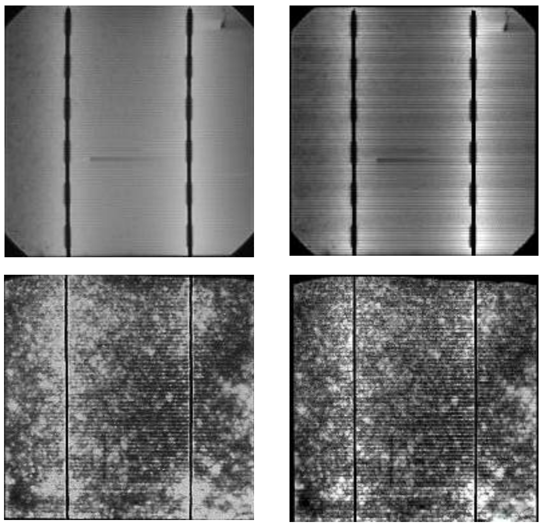

Figure 3: EL images taken before the intercomparison started (left) and EL images of the same devices taken two years later upon completion of the measurement campaign (right). Top images are the mono-Si sample with standard texturing (SN 0008) and bottom images are the BSi RIE nanostructured sample (SN 0026). Two BSi RIE samples were sent to all 12 labs for characterization, and the EL shown here is the highest quality of the two.

EL images were taken before each laboratory started testing to ensure that no damage occurred due to transportation or handling. The glass of one mono-Si sample (SN 0020) was damaged about halfway through the campaign, and one BSi ADE sample (SN 0028) experienced extreme cell cracking near the end of the campaign. These damaged test samples highlight the necessity of duplicate samples in round-robin style measurement campaigns. The labs were asked to measure all six samples that they received, but unfortunately two labs only measured three samples (i.e. they only measured SN 0008, SN 0025, SN 0028, and not the duplicate samples). Of these three, BSi ADE sample SN 0028 was later found to have significant cell damage, which compromised the completeness of the measurement results from that sample type. Furthermore, the reported angular-dependent measurements of the three device types with different cell textures were consistent with previous authors [22] [30] in that they did not significantly differ from each other when encapsulated with similar or identical glass superstrates. Therefore, the results from the BSi ADE sample type are not presented here. Regarding the two sample types that are presented in this work (mono-Si and BSi RIE), the EL images taken before the first lab's measurement and after the final lab's measurement showed that no damage had occurred during the measurement campaign (Figure 3).

In our previous work [16], we determined that Lab D's and Lab L's initial AOI measurements on all samples contained outlier measurements at AOIs between 45° and 85°. Therefore, two additional mono-Si samples were sent to these labs for retests: One sample (SN 0010) was sent to Lab D, and the other sample (SN 0015) was sent to Lab L. Sending new samples allowed the intercomparison to continue as planned while Lab D and Lab L completed their retests in parallel. In the sections that follow, the results from Lab D and Lab L's retests are shown together with measurements on a separate — but equivalent — mono-Si sample (SN 0008). The homogeneity of mono-Si samples SN 0010, SN 0015, SN 0008 was first established given that they were produced in the same batch using identical bills of materials from the same manufacturers. The equivalence of their angular-dependent responses was established with measurements performed at DTU, prior to shipment to Lab D and Lab L. The DTU measurements showed $\tau(\theta)$ deviations less than 0.003 (0.3 %) for most AOIs and a maximum deviation of 0.0046 (0.46 %) that occurred at 85° AOI. Therefore, the results from Lab D and Lab L's retest measurements on SN 0010 and SN 0015 are included with the results from SN 0008; the results from all three samples are reported as the mono-Si device type.

2.3 Analysis

This section describes the main methods used to analyze the angular-dependent measurements.

2.3.1 Statistical Analysis using the E_n Number Approach

The expanded uncertainty of each lab's measurements is critical for establishing comparability through the E_n number calculation (Eq. 2) per ISO 17043 [31]. Therefore, the labs that were not able to provide measurement uncertainty are removed from the E_n number proficiency assessment, and a separate analysis is performed. In this separate analysis, we show the lowest measurement uncertainty that is needed to be comparable to the labs that did provide uncertainty. We use the well-known Tukey outlier box plot to identify outliers in the laboratories' $\tau(\theta)$ measurements prior to calculation of the consensus (i.e. reference) values. This exercise revealed several outliers in the $\tau(\theta)$ values reported by Lab J at AOIs between 10° and 85°. Therefore, Lab J's results were excluded in the derivations of consensus values shown in Eq. 3 and Eq. 4. When measurement uncertainty is available, an E_n number is calculated for each sample at each AOI as:

$$E_n = \frac{x_i - X_{ref,i}}{\sqrt{UC_i^2 + UC_{ref,i}^2}} \tag{2}$$

Wherein x_i is the individual laboratory's measured relative transmittance $\tau(\theta)$ and UC_i is the expanded uncertainty of the lab's measurement of $\tau(\theta)$ with a confidence level of approximately 95 %. The reference value $X_{ref,i}$ is the weighted mean of seven partner´s measured $\tau(\theta)$ values for a given sample at a given angle. Here the measurements are weighted by the uncertainty provided by each partner. Weighting the results in this manner has the consequence of shifting the X_{ref} value towards the measured values (x_i) of the laboratories with lower uncertainty. For every sample and every angle, the $X_{ref,i}$ value is calculated as:

$$X_{ref,i} = \frac{\sum_{i=1}^{N} \frac{x_i}{\sigma_i^2}}{\sum_{i=1}^{N} \frac{1}{\sigma_i^2}} \tag{3}$$

wherein σ_i is the standard uncertainty (k = 1) of the lab's measurement. We assume that the values of σ_i are mutually uncorrelated, and therefore an inverse-variance weighting procedure is used. Finally, $UC_{ref,i}$ is the expanded combined uncertainty of $X_{ref,i}$ and is calculated as:

$$UC_{ref,i} = \frac{2}{\sqrt{\sum_{i=1}^{N} \frac{1}{\sigma_i^2}}} \tag{4}$$

Calculating UC_{ref} in this way yields a value that is always lower than any of the participating labs' declared uncertainties. For example, the lowest reported measurement uncertainty at 0° AOI is 0.2 % while UC_{ref} is 0.1 %; And at 85° AOI, the lowest reported uncertainty is 2.5 % while UC_{ref} is 1.8 %. The relative transmittance measurements from each laboratory are said to be in agreement with each other when $-1 \leq E_n \leq 1$. In other words, the condition $-1 \leq E_n \leq 1$ is met when the difference between a lab's measurement (x_i) and the reference value ($X_{ref,i}$) is less than or equal to the square root of square sum of the lab's declared uncertainty (UC_i) and the reference uncertainty ($UC_{ref,i}$). The sign of E_n provides a convenient way of discerning whether a lab's measurement is high ($E_n > 0$) or low ($E_n < 0$) relative to the weighted group mean.

2.3.2 Comparison of Measurements to Simulations

Given the many challenges with directly measuring the angular-dependent response of PV devices it can be of value to have a simulation model for comparisons and additional analysis. Because it is difficult to model the sub-wavelength BSi texture [32] and much larger DUT features like glass and metal contacts all in one model, we only use the mono-Si sample for comparison where all features can be modeled accurately. We show how the relative transmittance measurements made on the standard mono-Si sample compare to simulated values using the cloud-based version of the Daidalos ray tracing framework, which is developed by ISFH [33] [34] and accessible to the PV scientific community at no cost [35]. Daidalos models the glass cover, the encapsulation, the cell metallization and the cell texture as 3D geometries with spectrally resolved complex refractive index values. As output, Daidalos gives spectrally resolved absorptance and reflection curves for each component of the PV device. These curves are then multiplied with the AM1.5G spectrum in units of photo current and integrated over the wavelength range from 300 nm to 1200 nm to obtain the PV device short-circuit current. As inputs, the measured spectral reflectance of the backsheet before encapsulation, and the measured height and pitch of the silver grid fingers from an optical profilometer are used together with spectrally resolved complex refractive index values for the other components taken from literature [36]. To verify the spectral behavior of the Daidalos model, we use measured external quantum efficiency (eQE) data from PTB's differential spectral responsivity system under 350 W·m^{-2} white light bias irradiation without consideration for device non-linearity.

An advantage of these ray tracing simulations over measurements is that the amount of lost incoming light due to reflection or absorption at specific parts of the PV module can be determined. To investigate the angular behavior of these losses, we use a modified version of the relative transmittance τ_{spec}, where the angle dependent loss current equivalents I_x are used in the numerator and the incoming photo current I_{spec} (0°) is used in the denominator.

$$\tau_{spec}(\theta) = \frac{I_x(\theta)}{I_{spec}(0°)\cdot\cos\theta} \tag{5}$$

2.3.3 Fitting Models to Angular-dependent Measurements

Several authors have described mathematical models for fitting measured angle-dependent transmittance curves of PV devices [19] and [37] – [39]. The IEC 61853-2 and IEC 61853-3 standards adopt the Martin and Ruiz model, which uses a single parameter a_r to describe angular reflection losses [40]. This model is shown in Eq. (6) below.

$$\tau(\theta) = \frac{1-exp(^{-cos\,\theta}/_{a_r})}{1-exp(^{-1}/_{a_r})} \tag{6}$$

In addition to the PV-specific fitting models, a model developed by [39] for solar thermal collectors was developed in the 1960's. This model was adopted by ASHRAE and is still used by PV modelers today [41], [42]. Similar to the Martin and Ruiz model, the ASHRAE model uses single parameter b_0 to describe angular reflection losses as shown below.

$$\tau(\theta) = 1 - b_0\left(\frac{1}{cos\,\theta} - 1\right) \tag{7}$$

The current (2016) edition of IEC 61853-2 provides no specific guidance on how to extract the a_r coefficient from the analytical function (Eq. 6). Since different fitting procedures could lead to disparate coefficients, the participating laboratories did not report angular loss coefficients. Instead, we extracted the angular loss coefficients a_r and b_o at the end of the measurement campaign using a common method for all participant's measurement data. The method uses a Gauss-Newton least squares fitting approach that minimizes the sum of squared errors (SSE) and weights measurements at all AOIs equally. No significant impact was observed on the coefficients or energy rating when using a fitting procedure that weighted the measurements according to the reported uncertainty at each AOI. We obtained coefficients from measurements made in the negative and positive angular directions and the coefficients reported here are the average of the two directions. Once the angular loss coefficients are obtained, the aforementioned formulae can subsequently be used in energy rating and/or energy yield calculations as will be shown below.

2.3.4 Impact of Laboratory Measurement Differences on Energy Rating

The ultimate outcome of the four part series of IEC 61853 Energy Rating standards is the determination of the PV module's climate specific energy rating (CSER) [43]. The CSER is essentially a DC level performance ratio (PR) of a single module that describes the annual deviation in energy production in a given climate, relative to what the module could have produced if it were operating at its STC performance. Unlike the classic definition of PR, the CSER does not incorporate losses due to soiling, shading, degradation, or any inverter specific losses such as efficiency of power conversion, maximum power point tracking efficiency or clipping losses. According to [44] the CSER and annual energy yield are simply intended for PV module buyers and system developers to assess the relative performance of PV technologies across climates. The CSER is calculated per the formula below where *E [Wh]* is the annual energy produced by the PV device, G_o is the reference irradiance of 1000 $W \cdot m^{-2}$, P_{STC} is the PV device maximum power at standard conditions, and H $[Wh \cdot m^{-2}]$ is the annual in plane insolation before correction for angular losses and spectral effects.

$$CSER = \frac{E \cdot G_O}{P_{STC} \cdot H} \tag{8}$$

TÜV Rheinland has provided multi-irradiance and temperature performance data (i.e. the IEC 61853-1 matrix) and spectral responsivity measurements for a conventional crystalline silicon 60-cell PV panel. We use theoretical values for thermal heat transfer coefficients U_0 = 25 $W \cdot m^{-2} \cdot K$ and U_1 = 6.84 $W \cdot m^{-3} \cdot K \cdot s$, which are taken from [45]. With these data, and the relative light transmission data from the participating labs, we calculate CSER for the six climate regions described in the IEC 61853-4 standard. The accuracy of our program that implements the IEC 61853-3 energy rating algorithm has been established in a parallel intercomparison [46].

2.4 Annual Angular Losses Calculated with Different Diffuse Models

As mentioned previously, the IEC 61853 Energy Rating standards use the Martin and Ruiz fitting model. We investigate the impact that the choice of fitting model has on the annual angular performance losses by repeating the calculations using the ASHRAE fitting model. Furthermore, we investigate how two different methods to apply the angular losses to the diffuse radiation component affect the results. These two methods include numerical integration and closed-form analytical approximations. The purpose of these tests is to explore the range of annual angular losses (AAL) that can be obtained due to differences in angular-dependent measurements from the participating labs and due to different approaches used to apply angular-dependent losses to diffuse radiation. The authors in [6] showed that the AAL of diffuse radiation can change by up to 0.5 % based on the model used to transpose horizontal diffuse radiation to a tilted surface. Because this impact is relatively small, we forego investigations into the effect that the choice of transposition model has on AAL calculations by using the in plane irradiance provided in the standard data sets. A summary of the different methods used to calculate AAL are shown in Table 3.

The IEC 61853-3 standard specifies that the angular-dependent losses associated with the diffuse component shall be calculated using the closed-form analytical approximation as proposed in [2] and shown below. The AOI corrected diffuse irradiance in the plane of array $D_{corr,AOI}$ is calculated using the diffuse angular loss factor (F_D).

$$F_D = \left(1 - exp\left[-\frac{1}{a_r}\left(\frac{4}{3\pi} \cdot \Delta + (0.5 \cdot a_r - 0.154) \cdot \Delta^2\right)\right]\right) \tag{9}$$

$$\Delta = \sin\beta + \frac{\pi - \beta - \sin\beta}{1 + \cos\beta} \tag{10}$$

Where β is the PV collector's tilt angle from a horizontal. In all our calculations, we use β = 20°, according to the standard. Once F_D is calculated, the diffuse irradiance in the plane of array (D_{POA}) is corrected for reflection losses using Eq. (11).

$$D_{corr,AOI} = D_{POA} \cdot F_D \tag{11}$$

Eq. (9) can only be used with the a_r coefficient extracted from Eq. (6). Therefore, we calculate $D_{corr,AOI}$ using the b_o coefficient from the ASHRAE model using a closed-form approximation as proposed by [20] and shown in Eq. (12) where DHI is the diffuse irradiance on a horizontal plane.

$$D_{corr,AOI} = D_{POA} \cdot \left(1 - b_0 + 2\,\frac{b_0\,\beta}{\pi}\right) \tag{12}$$

Finally, we calculate $D_{corr,AOI}$ using the spherical integration method as described in [47]. This method permits the calculation of the AOI corrected diffuse radiation using any fitting model, either the Martin and Ruiz model, ASHRAE model, or otherwise. In the spherical integration method, the model specific relative transmittance $\tau(\Theta)$ function is applied at each solid angle viewed by the PV module and weighted by cosine of Θ. Indeed the work of [47] contains a methodology to account for the circumsolar and horizon brightening components of diffuse irradiance, and [48] provides a model that describes the spectral and directional and properties of diffuse irradiance, but we simplify our calculations by assuming an isotropic sky.

Table 3: List of fitting model and diffuse models used in the calculation of global annual angular losses. All methods assume an isotropic sky diffuse component.

Method	**Data Fitting Model**	**Method to Apply Angular-dependent Losses to D_{POA}**	**Ref.**
1	Martin & Ruiz (Eq. 6)	Closed form approximation (Eq. 9)	[2]
2	Martin & Ruiz (Eq. 6)	Numerical integration	[49]
3	ASHRAE (Eq. 7)	Closed form approximation (Eq. 12)	[20]
4	ASHRAE (Eq. 7)	Numerical integration	[49]

In all AAL calculations, we calculate the plane of array beam irradiance corrected for reflection losses via

$$B_{corr,AOI} = B_{POA} \cdot \tau(\theta) \tag{13}$$

Wherein B_{POA} is the beam irradiance in the POA and $\tau(\Theta)$ is the relative transmittance of the PV device using the Martin an Ruiz model (Eq. 6) or ASHRAE model (Eq. 7). AOI corrected global irradiance $G_{corr,AOI}$ is then calculated by summation of the AOI corrected diffuse and beam components.

$$G_{corr,AOI} = D_{corr,AOI} + B_{corr,AOI} \tag{14}$$

Angular losses from ground reflections are not considered in the IEC 61853 Energy Rating normative nor are they considered here. This is because the calculations consider a mono-facial PV module with a static tilt angle of 20°. In this scenario, the module's view factor of the ground is on the order of 3 %, and when this view factor is multiplied by the albedo, the contribution of irradiance from ground reflections is considered negligible. Finally, the AAL of global irradiance in each climate is calculated by the difference of annual hourly $G_{CORR,AOI}$ and G_{POA} as shown below in Eq. 15. G_{POA} refers to the global in irradiance before reflection losses and $G_{CORR,AOI}$ is the effective irradiance available to the PV cells after angular losses have been applied.

$$Global\ AAL\ = \frac{\sum G_{corr,AOI} - \sum G_{POA}}{\sum G_{POA}} \tag{15}$$

3 Results and Discussion

3.1 Comparability of Angular-dependent Measurements among Laboratories

The top frame of Figure 4 shows the median *τ(Θ)* measurements of the mono-Si and BSi RIE sample types. The BSi RIE sample type shows less reflection loss than the mono-Si sample, but the difference between the two sample types is always < 0.015. The modest improvement in angular-dependent performance could be due to a combination of the BSi nanostructure and the white backsheet. The bottom frame of Figure 4 shows box plot distributions of the differences between each lab's *τ(Θ)* measurement and the weighted mean X_{ref}. The y-axis of the bottom graph in Figure 4 shows the numerator of the E_n calculation in Eq. 2, where X_{ref} is calculated based on measurements from only seven of the eight labs that reported uncertainty. The overall agreement is within ± 2 % until about AOI = 65°, but from 70° to 85° the range — excluding outliers — increases rapidly from 2.5 % to 23 %. There are four outliers not shown in Figure 4 that occur at ± 85°. These outliers are between 44 % and 24 % low to the weighted mean X_{ref}. All four extreme outliers at ± 85° were reported by Lab J. As described in Section 2.2, Lab D and Lab L performed retests on two separate mono-Si samples, which were not measured by the other labs, but determined as equivalent test devices. The initial measurements from Lab D and Lab L can be found in our previous work [16]; the improvements shown here are believed to be from a reduction of stray light within the testbed and better alignment of the DUT in the optical axis of rotation.

At large AOIs in both the positive and negative direction, we observed that the range of *τ(θ)* measurements is higher for the BSi RIE sample than for the mono-Si sample. This could be due to the nature of the BSi nanostructures, which create a graded refractive index at the Si-EVA interface. The graded refractive index principle differs fundamentally to the anti-reflection mechanism of the random pyramid structure on the mono-Si sample, where photons are reflected off the pyramid sidewalls and on average are absorbed in adjacent pyramids. Furthermore, the variance of the BSi nanostructure topology may not be similar to that of the conventional random pyramids over large areas. This means at large AOIs the nanostructured surface may still reflect as a graded refractive index, but deviations in collimation and topology across the cell may instead result in the response of a planar Si surface. At small AOIs the BSi has a graded refractive index, which more effectively suppresses broadband light. These factors can make reproducible measurements on BSi challenging, particularly at large AOIs.

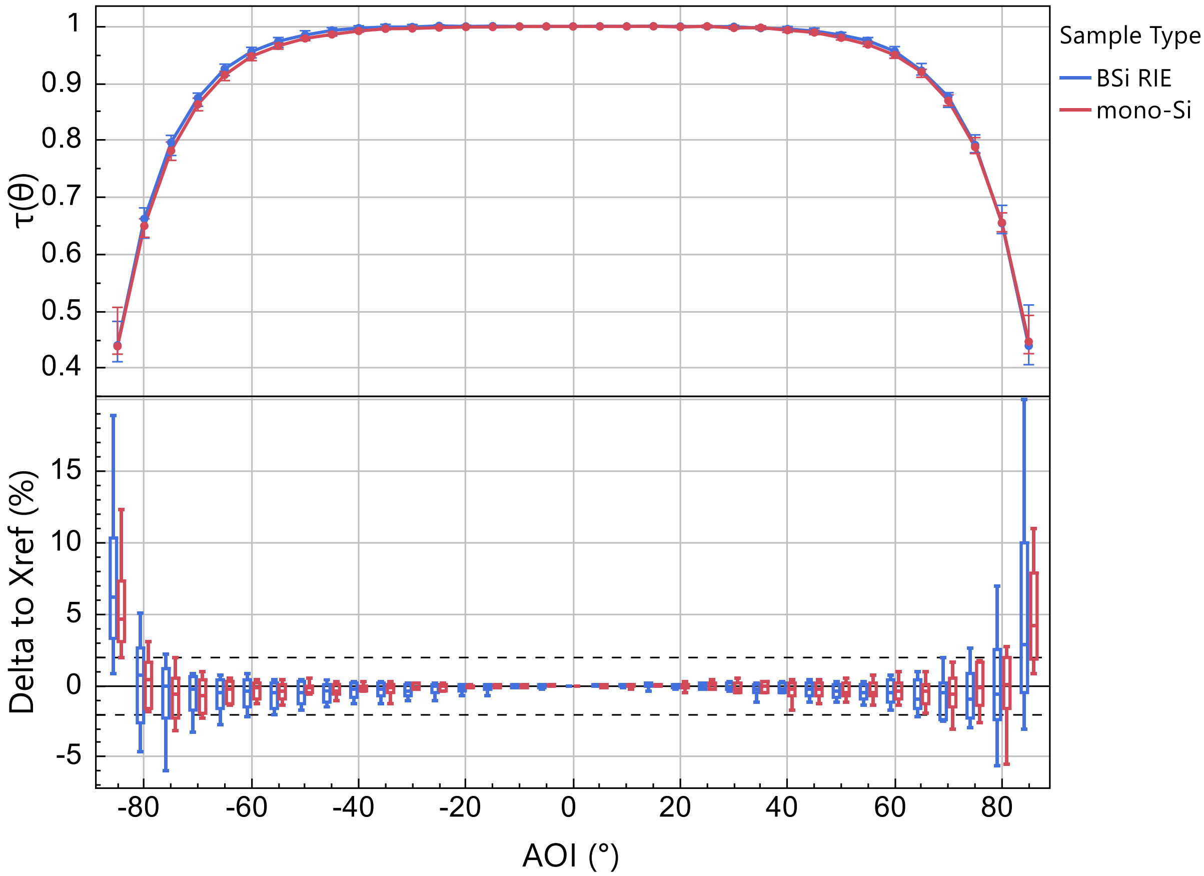

Figure 4: Results from all laboratories. Top – Median measured relative transmission at each AOI for two sample types. The error bars at each AOI show the interquartile range. Bottom - Box plots showing the differences to the weighted mean X_{ref}. The dashed reference lines are drawn at ± 2 %. Note that at ± 85° there are 4 outliers ranging from -44 % to -24 %, which are not shown. X_{ref} is calculated based on the measurements from seven labs that reported expanded uncertainty.

Results for the E_n number proficiency assessment (Eq. 2) are shown in Figure 5. Recall that Lab J has been removed from this analysis and their results are instead assessed in Figure 6. The dashed red lines in Figure 5 indicate the ± 1 conformity boundaries according to ISO 17043. There are only five instances outside this boundary — four of which belong to Lab C and one to Lab E — and all of which occur at AOIs ≥ 50°. The greatest dispersion in E_n values is observed at 85°, which indicates that reproducible angular-dependent measurements at 85° are currently the most challenging to obtain among leading PV laboratories.

The root causes for the measurement discrepancies are difficult to identify because the exact reasons could include any combination of the general challenges and uncertainties that were mentioned in Section 2.1. However, given that the largest discrepancies among labs occur at large AOIs, and that the largest single uncertainty component at such steep angles is typically the uncertainty of the measured angle Θ, a major reason is likely due to mounting errors or inaccurate measurement of Θ. The current (2016) edition of IEC 61853-2 specifies that the accuracy of the AOI between DUT and light source must be ± 1° or better for indoor measurements, and ± 0.5° or better for outdoor measurements. To the best of our knowledge all the participating labs employed rotation stages that meet or go beyond this requirement. This suggests that a more stringent requirement for determination of AOI Θ could be necessary to achieve better reproducibility in angular-dependent measurements at 85°.

Future interlaboratory comparisons of angular-dependent measurements could employ procedures that aim to minimize mounting error. For example, such error could potentially be mitigated by using DUTs with a standardized clamping system, or by using DUTs with frames that are already compatible in all participating labs' measurement systems. During our measurement campaign, some labs reported that they needed to devise custom solutions to mount the 20 x 20 cm frameless DUTs in their measurement systems. Such need for ad hoc solutions should be avoided in future interlaboratory comparisons of angular-dependent measurements to allow the labs to adhere to their standard measurement practices as closely as possible.

Additional actions could be taken to remediate the unsatisfactory agreement at large AOIs. The first is that the labs not meeting the condition $|E_n| \leq 1$ should adopt a more conservative measurement uncertainty. This is particularly true in the case of lab C that reported one of the lowest measurement uncertainties out of the eight labs in Figure 2. The second action is that researchers and PV industry professionals in general should place minimal confidence on angular-dependent measurements made at 85° until improved measurement agreement and reduced uncertainty can be demonstrated. A final possibility is that future revisions of the IEC 61853-2 standard could specify that measurements at 85° AOI are optional. In Section 3.2 we will explore how modeled angular-dependent performance can be used as a substitute to measurements, which can be useful when accuracy is compromised by high measurement uncertainty.

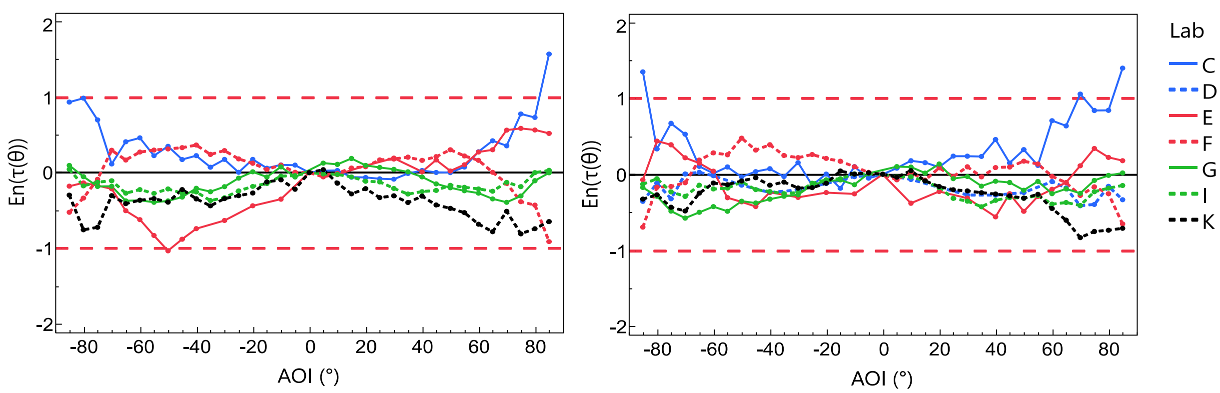

Figure 5: Proficiency of seven labs that reported measurement uncertainty per the En number statistical approach. The left graph shows results of the BSi RIE sample, the right graph shows results of the mono-Si sample.

Shown in Figure 6 are the minimum uncertainties that the remaining five labs would need at each positive AOI to be comparable to the weighted mean $X_{ref,i}$ and weighted uncertainty $UC_{ref,i}$ of the seven labs shown in Figure 5. The results of this calculation show that at 85°, the measurement uncertainty that Lab J needs in order to be considered comparable is between 28 % and 38 %, depending on the DUT. Although this uncertainty is nearly within their stated uncertainty at 85° (Figure 2), there are several measurements at AOI < 50° that are not within their stated uncertainty. Therefore, it is likely that Lab J's test procedure needs to be reviewed and improved. Since Lab J performed the test outdoors, they should check the AOI specific calibration coefficients for the in plane pyranometer, the method for measuring the diffuse irradiance in the plane of array in addition to the accuracy of the AOI Θ measurement. Figure 6 also shows the minimum uncertainties that Lab A, B, H and L would need in order to be comparable to the weighted mean of the seven labs shown in Figure 5. The most notable trends happen again at 85° where Lab H would need a measurement uncertainty as high as 16 % in order to be comparable to the weighted mean. This result again confirms that angular-dependent measurements at 85° are challenging and therefore our recommendation is that future revisions of IEC 61853-2 state that measurements are optional where AOI ≥ 85°.

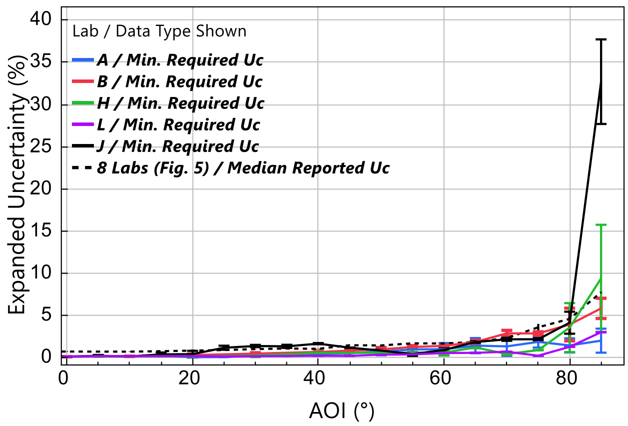

Figure 6: Minimum expanded uncertainty required for labs without measurement uncertainty to obtain |En| ≤ 1. The top and bottom of each range bar show the result for the mono-Si or BSi RIE sample. Only the positive angular direction is shown.

3.2 Comparison of Measured Relative Transmittance to Ray Tracing Simulations with Daidalos

In Figure 7 we show how the relative transmittance measurements for the mono-Si sample compare to the curve simulated in the Daidalos ray tracing model. The results show that the Daidalos model agrees to the group median within ± 0.6 % for AOI ≤ 70°, within ± 1.4 % for AOI ≤ 80° and at -4.1 % for an AOI = 85°. The higher discrepancy at higher AOIs is likely driven by the higher measurement uncertainty.

In Figure 8, we show the relative transmittance relative to the AM1.5G spectrum. At normal incidence, 81.3 % of the incoming photo current I_{spec} is absorbed by the Si cell, while the largest losses are reflection by glass surface 4.1 %, reflection by other parts of the module at 5.8 %, absorption in the full area rear metallization of the cell 5.4 %, absorption in the EVA 2.2 % and in the glass 0.8 %. There is a gradual change to AOI of 60°, where the Si still absorbs 76.9 % of the incoming photo current I_{spec}, the reflection by the glass surface is more than doubled to 9.1 %, while the absorption in the EVA and in the glass increase to their maximum of 2.5 % and 1.0 %, respectively. Our simulations show that the absorption maximum for both the glass and the EVA is formed by two trends with opposite AOI dependence. On the one hand higher AOIs cause longer light path lengths in both materials and on the other hand higher AOIs cause higher reflection at the glass surface, reducing the amount of light which enters both materials. For an AOI of 85°, the Si cell absorbs 32.8 %, while the glass surface reflects 61.4 % of the incoming light. Please recall that the mono-Si sample has no glass anti-reflection coating, which is often used to reduce these surface reflection losses.

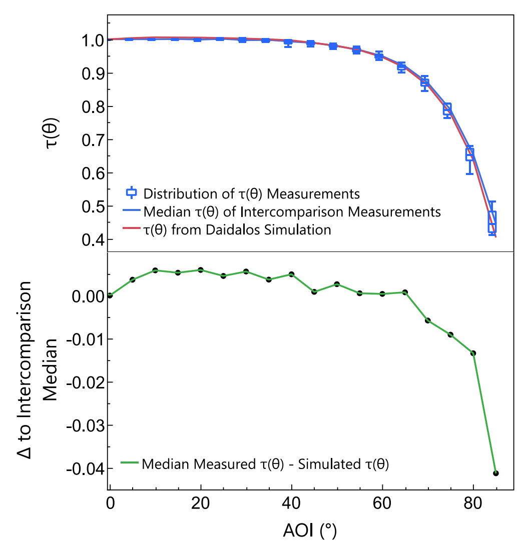

Figure 7: Comparison of measured relative transmittance to ray trace simulations of the mono-Si test sample. The blue box plots show the distribution of twelve laboratories' measurements on the mono-Si DUT at each AOI.

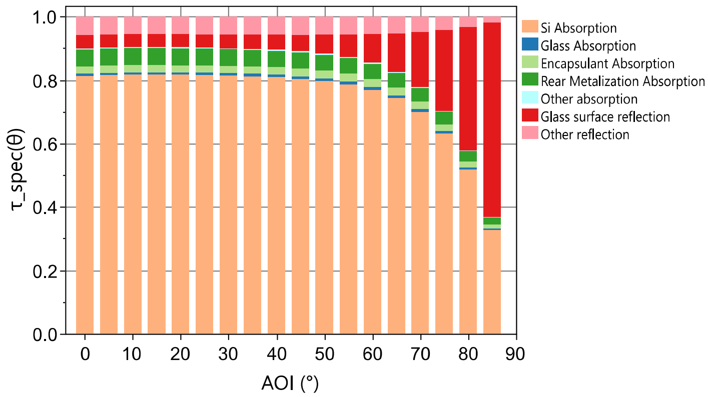

Figure 8: Ray tracing simulation results showing the angular dependence of the optical losses in the mono-Si test sample.

3.3 Comparison of Measurement Systems: Indoor versus Outdoor

There has been conjecture in recent years that the technical challenges encountered during outdoor testing cannot be overcome with contemporary test methods, which thus leads to speculation that angular-dependent measurements performed outdoors are unsuitable for use in PV energy modeling [15] [50]. In this section we share the experience from this intercomparison with an assessment of the angular-dependent measurements from the nine indoor measurement systems and three outdoor systems.

Figure 9 shows the results from the mono-Si sample when the results are grouped by indoor and outdoor measurement systems. The black error bars indicate the full range of measurement differences as reported by the nine labs performing the test indoors. At each AOI there are three red markers that represent measurements reported by the three labs where the test was performed outdoors. When all the red markers are within the black range bars, this means that indoor measurements showed larger deviations to the intercomparison median than did the outdoor measurements.

One of the three outdoor measurements is lab J (shown in red circles as 'Outdoor 1') where many instances of non-conformity were observed previously (Figure 5). When lab J's measurements are excluded, we see that the measurements from the other two outdoor tests are either on or within the black range bars for most AOIs from 0° to 85°. Specifically, the measurements from 'Outdoor 2' are always within the black range bars and those from 'Outdoor 3' are inside the range bars for 10 of the 17 AOIs shown in Figure 9. Although our data set consists mostly of indoor measurements, the results shown here indicate that angular-dependent PV measurements performed outdoors are not inherently more error prone than those made indoors. It is likely that the discrepancies observed are due to the methodology employed, not the specific test location, light source, or equipment used. Figure 9 contains retest measurements from Lab D and Lab L where the AOI test was performed indoors; their original measurements, which we determined as non-proficient in our previous work [16], are not included in Figure 9.

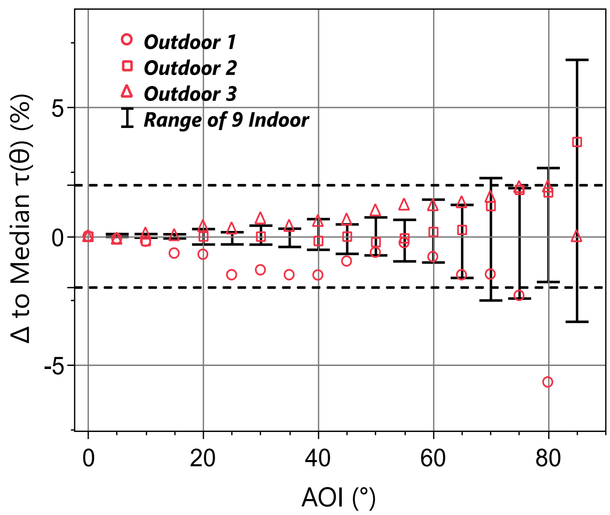

Figure 9: Comparison of indoor versus outdoor measurements made on the mono-Si sample. Dashed reference lines are drawn at ±2 %.

3.4 Impact of Angular-dependent Measurement Deviations on IEC 61853 Energy Rating

Here we follow the procedures stipulated in the IEC 61853-3 standard to determine the CSER and annual energy yield of the mono-Si sample using the a_r angular loss coefficients extracted from the measured data and from the Daidalos simulation. Table 4 shows a description of the six climates. Our calculations result in 13 CSER values per climate region (i.e. one CSER per lab plus the Daidalos simulation), where the differences in CSER values within each climate are driven by the differences in angular-dependent measurements from the participating labs.

Table 4: List of standard data sets with summaries of annual insolation, AOI between the sun and a 20° tilted south oriented surface, and diffuse ratio. The mean AOI and diffuse ratio are calculated only during hours when the sun is above the horizon.

Data Set Number	**Latitude**	**Climate Type**	**Annual global insolation in plane (kWh·m^{-2})**	**Mean Annual AOI θ (°)**	**Mean Annual Diffuse Ratio**
1	1°S	Tropical humid	1677.7	50.4	0.71
2	33°30’N	Subtropical arid	2295.5	49.2	0.41
3	33°22’N	Subtropical coastal	1496.6	49.1	0.75
4	56°N	Temperate coastal	972.9	56.4	0.77
5	34°N	High elevation	2139.1	49.5	0.51
6	57°N	Temperate continental	1266.0	56.5	0.65

Figure 10 shows that when one outlier is excluded, the range of angular-dependent measurements as reported in the intercomparison result in a 1.0 % to 1.8 % range in CSER values, depending on the climate. This result corresponds well with the rough estimation presented in [51] that the uncertainty of AOI measurements will lead to a 1 % uncertainty in CSER. The results obtained using the Daidalos ray tracing simulations are indicated with blue diamond markers and are mostly located at the bottom of the inner quartile range. Since it was demonstrated previously that angular-dependent measurements at 85° are subject to high uncertainty, Figure 10 also shows the energy rating results obtained when the curve fitting (Eq. 6) is done in the limited AOI range of 0° to 80°. The main result from removing measurements at 85° is that no outliers are observed in the energy rating outcomes, although the range of outcomes within the box plot whiskers remains largely unchanged.

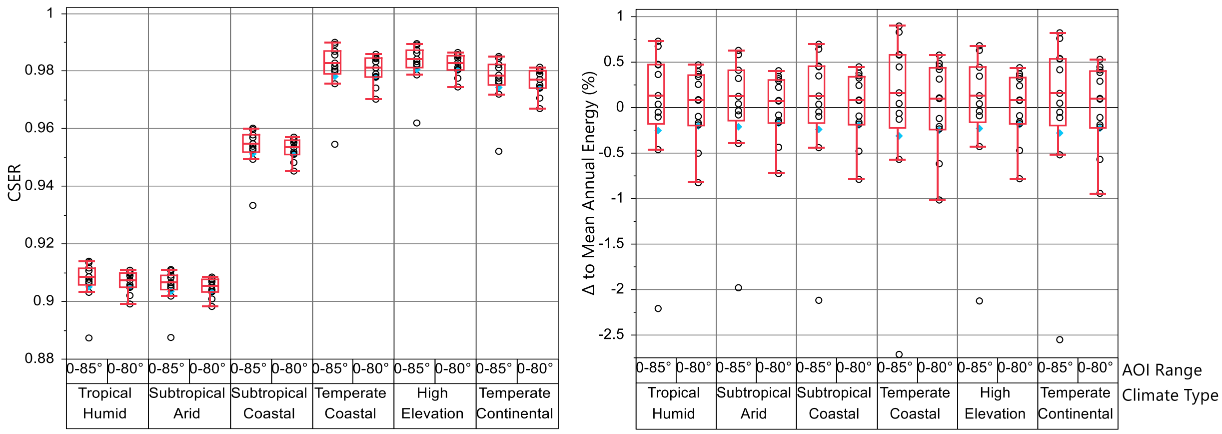

Figure 10: Results of calculating CSER with 12 participating laboratories' relative transmittance data (Left) and variability of the mean annual energy when using the 12 participating laboratories' measurements (right). Each plot shows the results when all relative transmittance measurements are used in the fitting routine (0-85°) and with 85° removed (0-80°). The blue diamonds near the bottom of the inner quartile ranges show the results when CSER and annual energy are calculated using simulated relative transmittance data from Daidalos.

Figure 10 additionally shows the percentage difference to the mean annual energy yield *E* by climate. When the one outlier is excluded, the annual energy difference can range from 1.0 % to 1.5 % depending on the climate. The range of CSER and energy yield values is highest for the most northern climates with high diffuse ratios and higher average AOIs (e.g. Temperature Coastal), and lowest in southern climates where lower diffuse ratios and lower average AOIs are observed (e.g. Subtropical Arid). It should be emphasized that the incident angle test is one of four measured characteristics in the IEC 61853 series and the uncertainty of the other three characterizations (i.e. performance matrix, spectral responsivity, and thermal behavior) should also be considered when considering the overall uncertainty of the energy rating standard.

3.5 Annual Angular Losses Calculated with Different Diffuse Models

In this section we use the relative transmittance data from the intercomparison to calculate the annual angular loss (AAL) of global irradiance in the six standard climates using different approaches for calculating the diffuse radiation component ($D_{Corr,AOI}$). We use the four calculation approaches shown in Table 3 to demonstrate the impact that the AOI fitting model and the application of the fitting model to the diffuse radiation has on global AAL. Similar to Section 3.4, only results from the mono-Si sample are shown.

Figure 11 shows the results using the Martin and Ruiz fitting model. The dotted lines show the climate-specific AAL when the closed-form approximation as prescribed in the IEC 61853-3 standard is used to apply the angular loss a_r coefficient to the diffuse irradiance. The solid lines show the AAL when the calculation is performed by means of numerically integrating the angular-dependent losses across 1° isotropic sky segments. The closed-form approximation results in 0.2 % to 0.4 % higher AAL across all climates. As expected, more AAL is observed in climates with higher average AOIs (e.g. Temperate Coastal). Similar to the results for CSER (Figure 10), the range of global AAL is highest for the most northern climates with high diffuse ratios and higher annual average AOIs, and lowest in southern climates where lower diffuse ratios and lower average AOIs are observed. For example, in the case of the Temperate Coastal climate (56°N), global AAL varies from 3.2 % to 6.7 %, whereas in the Subtropical Arid climate (33°30'N) global AAL varies from 2.1 % to 4.7 %.

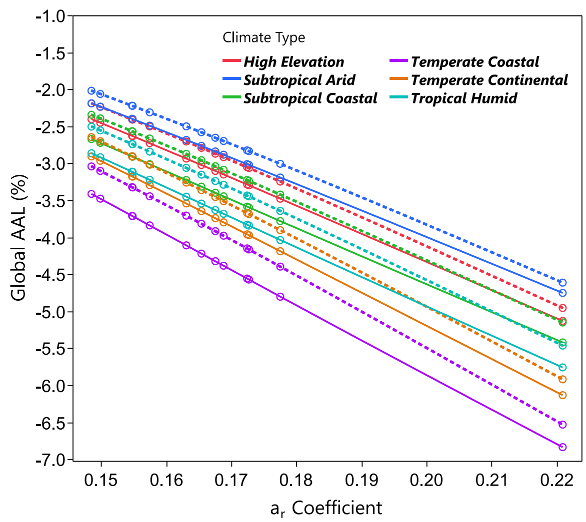

Figure 11: Annual angular losses of global irradiance using the Martin and Ruiz model. Each circle marker represents a single a_r coefficient extracted from a participant's measurement. The dotted lines show the results using the closed-form equation to apply the angular-dependent losses and the solid lines show the results using integration to apply the losses. The a_r coefficient extracted from the Daidalos simulation is 0.17242.

Figure 12 shows the global AAL when the ASHRAE fitting model is used to extract the b_o angular loss coefficient from the participating laboratories' data. The dotted lines show the results when the closed-form approximation in Eq. 11 is used to apply the angular-dependent losses to the diffuse radiation, and the solid lines show the results when integration is used to apply the angular-dependent losses to the diffuse radiation component. The difference in AAL as calculated by these two methods is less than 0.1 % across all climates. The climate-specific AAL follow the same relative order as shown in Figure 11, but the magnitude of the losses tends to be slightly higher (< 0.5 %) when the ASHRAE fitting model is used instead of the Martin and Ruiz model. This could be because the ASHRAE model tends to under predict the physically measured angular-dependent losses by 2 % to 3 % between 40° and 65° AOI.

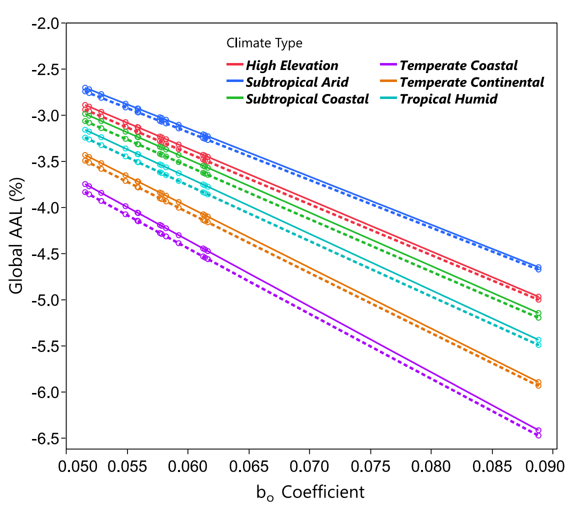

Figure 12: Annual angular losses of global irradiance using the ASHRAE model. Each circle marker represents a single b_o coefficient extracted from a participant's measurement. The dotted lines show the results using the closed-form equation to apply the angular-dependent losses and the solid lines show the results using integration to apply the losses. The b_o coefficient extracted from the Daidalos simulation is 0.06128.

In Section 3.1 we determined that Lab J's results were not comparable to the intercomparison weighted mean and in Section 3.4 it was shown that Lab J's results were outliers when used to calculate energy rating (Figure 10). A key driver of these results is that Lab J's measurements yield the highest a_r and b_o angular loss coefficients out of any participant (a_r = 0.2209 and b_o = 0.0888 for Lab J's mono-Si sample measurements). If Lab J's results are excluded from Figure 11 and Figure 12, we can conclude that the range of a_r and b_o angular loss coefficients across the intercomparison is 0.1485 to 0.1775 and 0.0516 to 0.0617, respectively. When Lab J's results are excluded the range of AAL across labs is reduced from 3.21 % to 1.46 % (averaged across climates) for the Martin and Ruiz model, and for the ASHRAE model the range is reduced from 2.31 % to 0.68 %. Interesting is that the range of AAL is lower when using the ASHRAE model instead of the Martin and Ruiz. This indicates that the ASHRAE fitting model better masks the deviations in angular-dependent measurements when they are applied to PV performance modeling.

A variance components analysis can show whether the differences in the AAL primarily result from the fitting/diffuse model, the standardized climate data set, or the measured relative transmittance $\tau(\Theta)$ data reported by the participating labs. We performed a variance components analysis in the JMP software package that showed that 72 % of the variation in annual diffuse losses is due to the spread of angular loss coefficients, 23 % of the variation is due to the climate data set, and approximately 5 % of the variation is due to the fitting/diffuse model used. In other words, the variability in angular-dependent measurements across laboratories has a far greater impact on PV performance modeling results than the choice of fitting model, diffuse model or meteorological data set. This highlights the importance of accurate angular-dependent measurements in PV energy modeling as variations in $\tau(\Theta)$ can cause significant changes in the annual angular losses of global irradiance. Please note that these results hold true for the fitting models, diffuse models and data sets tested, but we believe these are representative of contemporary modeling practices.

4 Conclusions

We have presented results from a twelve laboratory comparison of angular-dependent measurements on two encapsulated PV devices that took place from autumn 2017 to spring 2020. The proficiency of the measurements was assessed using the E_n number method prescribed in the ISO 17043 standard, but this analysis was only applied to the measurements of seven laboratories that provided uncertainty and showed no outliers in their $\tau(\theta)$ measurements. A separate analysis was conducted for the other five labs wherein the minimum measurement uncertainty required to obtain $| E_n | \leq 1$ was demonstrated. The agreement of all twelve laboratories' measurements was analyzed with a simple difference between their $\tau(\theta)$ measurements and the weighted mean $X_{ref,i}$ as calculated from seven labs with measurement uncertainty.

The E_n number analysis revealed five total instances of unsatisfactory $\tau(\theta)$ measurements — with three such instances occurring at 85° — which indicates corrective actions should be considered such as revising test procedures and uncertainty budgets. One additional suggestion is that measurements at 85° could be deemed optional in future revisions of the IEC 61853-2 standard as it was demonstrated that outliers in energy rating calculations could be prevented simply by removing angular-dependent measurements at 85° from the fitting procedure. The agreement in relative transmittance $\tau(\theta)$ measurements between eleven labs is within ± 2.0 % of the weighted mean for AOI ≤ 65°, but from 70° to 85°, the range of measurement differences increase rapidly from 2.5 % to 23 %. We identified outlier measurements from one lab that performed the characterizations outdoors; in the most extreme case this lab reported measurements that were 44 % low to the weighted mean at 85°.

We grouped the results according to indoor versus outdoor measurement methods. Although this analysis was limited in that only three of the twelve participating labs performed the test outdoors, it was shown that two of the three labs indeed had measurements that were within the range of the nine indoor measurements. Thus indicating that accuracy is not dependent on test location, but rather it is the rigor of the methodology that matters. It was shown that the variability in $\tau(\theta)$ measurements on the BSi RIE sample are 50 % and 100 % higher than the variability observed for the mono-Si sample at 80° and 85°, respectively; the higher variation could be due to the nature of the BSi nanostructures. This work employed two test samples with the same glass type, but with unique cell surface textures. We suggest that future work on angular-dependent measurement comparisons include test samples with various structures on the glass, anti-reflective glass coatings, tandem cell technologies, and full-sized PV panels rather than single cell coupons.

The angular-dependent measurements from the participating laboratories as well as simulations from the cloud-based Daidalos ray tracing software were used as input to the IEC 61853-3 standardized procedure for calculating energy rating. When one outlier is excluded, it was found that the angular-dependent measurements from eleven participating laboratories cause a 1.0 % to 1.8 % range in CSER and a 1.0 % to 1.5 % range in annual energy yield, depending on the climate. When the CSER and energy yield results were viewed as distributions, it was shown that results from the Daidalos ray tracing simulation for all six standard climates were either within or bordering on the inner quartile range thereby demonstrating that the software is a suitable tool for simulating relative transmission curves of PV devices for use in energy rating calculations. The simulations have the benefit of describing the optical losses at each material within the PV device, which is not possible with measurements made according to IEC 61853-2. Finally, the annual angular losses (AAL) of global irradiance were analyzed using four different approaches used to apply angular-dependent losses to the diffuse radiation in six standardized climate data sets. It was shown that the measurement variability among the twelve laboratories caused the largest variation (72 %) in the AAL than did the choice of fitting or diffuse (23 %), or the meteorological data set used (5 %), which highlights the importance of accurate angular-dependent measurements for use in PV performance modeling.

5 Acknowledgements

We thank Dr. Werner Herrmann of TÜV Rheinland Energy GmbH for providing the spectral responsivity and multi-irradiance/temperature matrix measurements of a 60-cell crystalline Silicon module, which allowed us to perform the energy rating calculations. Part of the work made on behalf of DTU was funded by the Danish Energy Technology Development and Demonstration Program (EUDP) project number 64016-0030.

This material is based upon work supported by the U.S. Department of Energy's Office of Energy Efficiency and Renewable Energy (EERE) under Solar Energy Technologies Office (SETO) Agreement Number 34364. Sandia National Laboratories is a multi-mission laboratory managed and operated by National Technology and Engineering Solutions of Sandia LLC, a wholly owned subsidiary of Honeywell International Inc. for the U.S. Department of Energy's National Nuclear Security Administration under contract DE-NA0003525.

6 References

[1] T. W. Sjerps-Koomen EA, Anselma EA, "A simple model for PV module reflection losses under field conditions," *Solar Energy,* vol. 57, no. 6, pp. 421-432, 1997.

[2] N. Martin and J. M. Ruiz, "Calculation of the PV modules angular losses under field conditions by means of an analytical model," *Solar Energy Materials and Solar Cells,* vol. 70, no. 1, pp. 25-38, 2001.

[3] J. L. Balenzategui and F. Chenlo, "Measurement and analysis of angular response of bare and encapsulated silicon solar cells," *Solar Energy Materials and Solar Cells,* vol. 86, no. 1, pp. 53-83, 2005.

[4] F. Plag, I. Kröger, T. Fey, F. Witt and S. Winter, "Angular-dependent spectral responsivity—Traceable measurements on optical losses in PV devices," *Progress in Photovoltaics: Research and Applications,* vol. 26, no. 8, pp. 565-578, 2018.

[5] N. Martín and J. M. Ruiz, "Annual angular reflection losses in PV modules," *Progress in Photovoltaics: Research and Applications,* vol. 13, no. 1, pp. 75-84, 2005.

[6] Y. S. Khoo, J. P. Singh, T. M. Walsh and A. G. Aberle, "Comparison of angular reflectance losses between PV modules with planar and textured glass under singapore outdoor conditions," *IEEE Journal of Photovoltaics,* vol. 4, no. 1, pp. 362-367, 2014.

[7] IEC 61853-2, "Photovoltaic (PV) module performance testing and energy rating – Part 2," 2016.

[8] B. Mihaylov, J. Bowers, T. Betts, R. Gottschalg, T. Krametz, R. Leidl, K. Berger, S. Zamini, N. Dekker, G. Graditi, F. Roca, M. Pellegrino, G. Flaminio, P. Pugliatti, A. Di Stefano, F. Aleo, G. Gigliucci, W. Ferrara, G. Razongles, J. Merten, A. Pozza, A. Santamaria Lancia, S. Hoffman, M. Koehl, A. Gerber, J. Noll, F. Paletta, G. Friesen and S. Dittmann, "Results of the Sophia module intercomparison part-1: stc, low irradiance conditions and temperature coefficients measurements of C-Si technologies," in *29th European Photovoltaic Solar Energy Conference and Exhibition*, Amsterdam, 2014.

[9] E. Salis, D. Pavanello, M. Field, U. Kräling, F. Neuberger, K. Kiefer, C. Osterwald, S. Rummel, D. Levi, Y. Hishikawa, K. Yamagoe, H. Ohshima, M. Yoshita and H. Müllejans, "Improvements in world-wide intercomparison of PV module calibration," *Solar Energy,* vol. 155, pp. 1451-1461, 2017.

[10] D. Dirnberger, U. Kräling, H. Müllejans, E. Salis, K. Emery, Y. Hishikawa and K. Kiefer, "Progress in photovoltaic module calibration: Results of a worldwide intercomparison between four reference laboratories," *Measurement Science and Technology,* vol. 25, no. 10, 2014.

[11] J. H. Fatehi, C. Kedir, C. Tumengko, N. Riedel and J. L. R. Watts, "Results From Flash Testing At Multiple Irradiances and Temperatures Across Five PV Test Labs," *2014 PV Performance Modeling Workshop,* 2014.

[12] C. Monokroussos, S. Dittmann, T. Herbrecht, H. Müllejans, E. Salis, D. Etienne, G. Friesen, J. Stang, V. Fakhfouri, N. Rebeaud and D. Pavanello, "Electrical characterization intercomparison of high-efficiency c-Si modules within Asian and European laboratories," vol. 27, pp. 603-622, 2019.

[13] B. H. King, D. Riley, C. D. Robinson and L. Pratt, "Recent advancements in outdoor measurement techniques for angle of incidence effects," *2015 IEEE 42nd Photovoltaic Specialist Conference, PVSC 2015,* 2015.

[14] S. Boppana, K. Passow, J. Sorensen, B. H. King and C. Robinson, "Impact of Uncertainty in IAM Measurement on Energy Predictions," *2018 IEEE 7th World Conference on Photovoltaic Energy Conversion, WCPEC 2018 - A Joint Conference of 45th IEEE PVSC, 28th PVSEC and 34th EU PVSEC,* pp. 2276-2281, 2018.

[15] J. Meydbray, I. Suez and J. Webber, "Measurements Matter (White Paper)," PV Evolution Labs, Berkeley, CA, 2019.

[16] N. Riedel, A. A. S. Lancia, M. Amdemeskel, S. Thorsteinsson, P. B. Poulsen, I. Kröger, L. H. Slooff, M. J. Jansen, A. J. Carr, P. Manshanden, M. Bliss, T. Betts, I. P. Jauregui, M. E. Mayo, J. L. Balenzategui, R. Roldan, U. Kräling, G. Baarah, B. Iandolo, R. S. Davidsen, A. Thorseth, C. Dam-hansen, A. Gisele and R. Benatto, "Interlaboratory Comparison of Methodologies for Measuring the Angle of," *35th European Photovoltaic Solar Energy Conference and Exhibition,* no. i, pp. 1034-1039, 2018.

[17] H. Holst, M. Winter, M. R. Vogt, K. Bothe, M. Kontges, R. Brendel and P. Altermatt, "Application of a New Ray Tracing Framework to the Analysis of Extended Regions in Si Solar Cell Modules," *Energy Procedia,* vol. 38, pp. 86-93, 2013.

[18] C. Schinke, M. R. Vogt and K. Bothe, "Optical Modeling of Photovoltaic Modules with Ray Tracing Simulations," in *Photovoltaic Modeling Handbook*, Wiley, 2018.

[19] W. De Soto, S. A. Klein and W. A. Beckman, "Improvement and validation of a model for photovoltaic array performance," *Solar Energy,* vol. 80, no. 1, pp. 78-88, 2006.

[20] D. J. Wright, "Closed-Form, Analytic Solution for Diffuse Irradiance on a Tilted, Photovoltaic Collector," *IEEE Journal of Photovoltaics,* vol. 9, no. 2, pp. 391-396, 2019.

[21] H. Al Husna, "Characterisation of Spectral and Angular Effects on Photovoltaic Modules for Energy Rating," 2018.

[22] B. Knisely, S. V. Janakeeraman, J. Kuitche and G. Tamizhmani, "Validation of IEC 61853-2 standard (Draft): Angle of incidence effect on photovoltaic modules," *Conference Record of the IEEE Photovoltaic Specialists Conference,* pp. 675-680, 2013.

[23] J. John, V. Rajasekar, S. Boppana, S. Tatapudi and G. Tamizhmani, "Angle of incidence effects on soiled PV modules," *Reliability of Photovoltaic Cells, Modules, Components, and Systems VII,* vol. 9179, no. October 2014, p. 91790D, 2014.

[24] D. Zirzow, "Improvements in CFV's Outdoor IAM Measurement Method," in *Sandia PV Systems Symposium*, Albuquerque, 2018.

[25] W. Herrmann and L. Rimmelspacher, "Angular Response of thin-film PV Modules," in *TÜV Rheinland PV Module Forum*, Cologne, 2019.

[26] W. Hermmann, M. Schweiger and L. Rimmelspacher, "Solar Simulator Measurement Proceedures for Determination of the Angular Characteristics of PV Modules," in *29th European Photovoltaic Solar Energy Conference and Exhibition*, 2014.

[27] J. J. Michalsky, L. C. Harrison and W. E. Berkheiser, "Cosine response characteristics of some radiometric and photometric sensors," *Solar Energy,* vol. 54, no. 6, pp. 397-402, 1995.

[28] R. S. Davidsen, H. Li, A. To, X. Wang, A. Han, J. An, J. Colwell, C. Chan, A. Wenham, M. S. Schmidt, A. Boisen, O. Hansen, S. Wenham and A. Barnett, "Black silicon laser-doped selective emitter solar cell with 18.1% efficiency," *Solar Energy Materials and Solar Cells,* vol. 144, pp. 740-747, 2016.

[29] B. Kafle, T. Freunda, A. Mannana, L. Clochard, E. Duffy, S. Wernera, P. Saint-Casta, M. Hofmanna, J. Rentscha and R. Preua, "Plasma-free Dry-chemical Texturing Process for High-efficiency Multicrystalline Silicon Solar Cells," *Energy Procedia,* vol. 92, pp. 359-368, 2016.

[30] I. Geisemeyer, N. Tucher, B. Muller, H. Steinkemper, J. Hohl-Ebinger, M. Schubert and W. Warta, "Angle Dependence of Solar Cells and Modules: The Role of Cell Texturization," *IEEE Journal of Photovoltaics,* vol. 7, no. 1, pp. 19-24, 2017.

[31] ISO 17043, "Conformity assessment – General requirements for proficiency testing," 2010.

[32] T. H. Fung, T. P. D. Veeken, B. Veettil, A. Polman and M. Abbott, "Application and validity of the effective medium approximation to the optical properties of nano-textured silicon coated with a dielectric layer," *Optics Express,* vol. 27, no. 26, pp. 38645-38660, 2019.

[33] H. Holst, H. Schulte-Huxel, M. Winter, S. Blankemeyer, R. Witteck, M. R. Vogt, T. Booz, F. Distelrath, M. Köntges, K. Bothe and R. Brendel, "Increased Light Harvesting by Structured Cell Interconnection Ribbons: An Optical Ray Tracing Study Using a Realistic Daylight Model," *Energy Procedia,* vol. 92, pp. 505-514, 2016.

[34] M. R. Vogt, R. Witteck, T. Gewohn, H. Schulte-Huxel, C. Schinke, M. Köntges, K. Bothe and R. Brendel, "Boosting PV Module Efficiency Beyond the Efficiency of Its Solar Cells – A Raytracing Study with Daidalos Now Available to the Scientific Community," in *36th EU PVSEC*, Marseille, 2019.

[35] ISFH, "Daidalos Cloud," [Online]. Available: https://www.daidalos-cloud.de/. [Accessed 1 May 2020].

[36] M. R. Vogt, "Development of physical models for the simulation of optical properties of solar cell modules, doctoral thesis," Gottfried Wilhelm Leibniz Universität , Hannover, Germany, 2015.

[37] D. L. King, J. A. Kratochvil and W. E. Boyson, "Measuring solar spectral and angle-of-incidence effects on photovoltaic modules and solar irradiance sensors," *Conference Record of the IEEE Photovoltaic Specialists Conference,* pp. 1113-1116, 1997.

[38] N. Martín and J. M. Ruiz, "A new model for PV modules angular losses under field conditions," *International Journal of Solar Energy,* vol. 22, no. 1, pp. 19-31, 2002.

[39] A. F. Souka and H. H. Safwat, "Determination of the optimum orientations for the double-exposure, flat-plate collector and its reflectors," *Solar Energy,* vol. 10, no. 4, pp. 170-174, 1966.

[40] IEC 61853-3, "Photovoltaic (PV) module performance testing and energy rating – Part 3," 2018.

[41] J. H. Fatehi and K. J. Sauer, "Modeling the incidence angle dependence of photovoltaic modules in PVsyst," *2014 IEEE 40th Photovoltaic Specialist Conference, PVSC 2014,* pp. 1335-1338, 2014.

[42] W. F. Holmgren, C. W. Hansen and M. A. Mikofski, "Pvlib Python: a Python Package for Modeling Solar Energy Systems," *Journal of Open Source Software,* vol. 3, no. 29, p. 884, 2018.

[43] IEC 61853-4, "Standard reference climatic profiles," 2018.

[44] T. Huld, E. Salis, A. Pozza, W. Herrmann and H. Müllejans, "Photovoltaic energy rating data sets for Europe," *Solar Energy,* vol. 133, pp. 349-362, 2016.

[45] D. Faiman, "Assessing the outdoor operating temperature of photovoltaic modules," *Progress in Photovoltaics: Research and Applications,* vol. 16, no. 4, pp. 1062-7995, 2008.

[46] M. Vogt, S. Riechelmann, A. Gracia-Amillo, A. Driesse, A. Kokka, K. Maham, P. Kärhä, R. Kenny, C. Schinke, K. Bothe, J. Blakesley, E. Music, F. Plag, G. Friesen, G. Corbellini, N. Riedel-Lyngskær, R. Valckenborg, M. Schweiger and W. Herrmann, "Interlaboratory Comparison of the PV Module Energy Rating Standard IEC 61853-3," in *37th European Photovoltaic Solar Energy Conference and Exhibition*, 2020.

[47] M. J. Brandemuehl and W. A. Beckman, "Transmission of diffuse radiation through CPC and flat plate collector glazings," *Solar Energy,* vol. 24, no. 5, pp. 511-513, 1980.

[48] F. Plag, I. Kröger, S. Riechelmann and S. Winter, "Multidimensional model to correct PV device performance measurements taken under diffuse irradiation to reference conditions," *Solar Energy,* no. 174, pp. 431-444, 2018.

[49] B. Marion, "Numerical method for angle-of-incidence correction factors for diffuse radiation incident photovoltaic modules," *Solar Energy,* vol. 147, pp. 344-348, 2017.

[50] PVsyst, "How to Determine the IAM Profile," [Online]. Available: https://forum.pvsyst.com/viewtopic.php?t=2690. [Accessed 24 March 2020].

[51] D. Dirnberger, B. Muller and C. Reise, "PV module energy rating: opportunities and limitations," *Progress in Photovoltaics,* vol. 23, pp. 1754-1770, 2015.

Appendix I

Table 5: Participating laboratories and details of their measurement systems used for measuring the angle of incidence response in the intercomparison.

Lab	Institution description	Rotation stage AOI range and control	Additional details regarding the measurement system and the methodology used
CENER	National lab with ISO 17025 accreditation. Not accredited to do IEC 61853-2 Incident Angle Test.	2-axis, 0° to 90°, Automated	Outdoors in natural sunlight on dual axis tracker. Plane of array diffuse calculated from global and beam measurements. Reported values are not the result of averaged measurements. All I_{SC} measurements are corrected to a common temperature using measurements from a thermocouple attached to the back of the DUT.
CFV Labs	Commercial test lab with ISO 17025 Accredited. Is accredited to do Incident Angle Test (IEC 61853-2).	2-axis, 0° to 90°, Automated	Outdoors in natural sunlight on dual axis tracker. Plane of array diffuse calculated from global and beam measurements. Global pyranometer measurements use individual AOI calibration coefficients. DUTs are kept in the open-circuit state between ISC measurements. Reference modules used for spectral corrections. Tracker dwells for 3 minutes at each AOI to allow DUTs and irradiance sensors to stabilize. Reported values are based on the average of at least 5 I_{SC} measurements at each AOI.
CIEMAT	Public R&D company. Not ISO 17025 accredited.	1-axis, -90° to 90°, Automated	Pasan flasher with broadband Xe arc lamp (class AAA). Lamp distance to DUT = 4.5 m. Flash tunnel with large windows acting as optical diaphragms. Maximum full-area DUT size for AOI measurements = 0.5 x 0.5 m (mounting plane area). Reported values are based on the average of 9 I_{SC} measurements. All I_{SC} measurements are corrected to 25°C. Irradiance stability correction applied to I_{SC} based on reference cell measurements at normal incidence.
CREST	University with ISO 17025 accreditation. Not accredited to do IEC 61853-2 Incident Angle Test.	1-axis, -90° to +90°, Automated	Pasan 3b flasher with broadband Xe arc lamp (class AAA). Lamp distance to DUT = 7.5 m. To measure the negative direction the module was mounted the other way around and then measured again. This method reduces the stray light the DUT is exposed to. No temperature correction applied as it was considered a minor contribution to overall uncertainty. Irradiance stability correction applied to I_{SC} based on reference cell measurements at normal incidence. Maximum full-area DUT size for AOI measurements = 1.7 m x 1.1 m (i.e. mounting table area). When the DUT is a PV module, the non-destructive partial shade method described in [26] is used to examine a subpart of the DUT.
DTU	University. Not ISO 17025 accredited.	1-axis, -90° to +90°, Automated	Energetiq (EQ-99FCX) broadband laser driven light source collimated using an off axis parabolic mirror. Active area of test samples partially illuminated. All I_{SC} measurements are corrected to 25°C. Reported values at each AOI result from the

			average of 5 I_{SC} measurements and the average of 3 AOI *(Θ)* measurements.
Fraunhofer ISE	Research institute with ISO 17025 accreditation. Not accredited to do IEC 61853-2 Incident Angle Test.	1-axis, -90° to +90°, Manual	Pasan 3b flasher with broadband Xe arc lamp (class AAA). Lamp distance to DUT = 8.0 m. Measurements made in 10° steps between 0° and 50°, and in 5° steps between 50° and 85°. Values reported are based on single I_{SC} measurements except at 0° (3 I_{SC} measurements averaged) and 70° (2 I_{SC} measurements averaged) to establish repeatability. All I_{SC} measurements acquired with DUT at 25°C ± 1.0°C and normal incidence irradiance 1000 W/m^2 ± 2 W/m^2. All I_{SC} measurements are corrected to 25°C. Irradiance stability correction applied to I_{SC} based on WPVS reference cell measurements at normal incidence. Geometrical factor correction for the 6 mm out-of-axis rotation in test set-up. No spectral mismatch corrections applied.
PVEL	Commercial lab with ISO 17025 accreditation. Not accredited to do IEC 61853-2 Incident Angle Test.	0° to 90°, Automated	Collimated pulsed LED light source with steady-state bias light. The distance between the light source and the DUT is approximately 18 meters. Lock-in amplifiers used to isolate signal from collimated light. I_{SC} at each AOI is measured at 512 samples/second for 30 seconds. Thus, reported values at each AOI are the average of nearly 15,000 data points. Irradiance stability correction applied to I_{SC} based on irradiance measurements at normal incidence.
PTB	National lab with ISO 17025 accreditation. Not accredited to do IEC 61853-2 Incident Angle Test.	2-axis, -90° to +90°, Automated, Azimuthal rotation of DUT possible.	Angular-dependent measurement of the differential spectral responsivity using a tuneable laser system with broadband bias lamps. Diffuse light from the ambience has no impact since Lock-In technique is applied. Reported values at each AOI are the average of 25 measurements. Divergence of the light source is < 5° (uncertainty related to divergence is considered).
RETC	Commercial lab with ISO 17025 accreditation. Accredited to do IEC 61853-2 Incident Angle Test.	1-axis, -90° to +90°, Manual	Pasan 3b with broadband Xe arc lamp (class AAA). No methodological details provided.
Sandia Labs	Test lab. Not ISO 17025 accredited.	0° to 90°, Automated	Outdoors in natural sunlight on dual axis tracker. Plane of array diffuse directly measured using the tracker's ability to maintain constant azimuth with the sun's position. Values reported were based on 3 days of clear sky measurements. Thus, reported values at each AOI are the average of approximately 100 measurements. All I_{SC} measurements are corrected to a common temperature using measurements from a resistance temperature detector (RTD) attached to the back of the DUT.

SUPSI	Commercial lab with ISO 17025 accreditation. Not accredited to do IEC 61853-2 Incident Angle Test.	1-axis, -90° to +90°, Manual	Pasan flasher with broadband Xe arc lamp (class AAA). Distance between the lamp and center of the rotational axis of DUT = 7.2 m. All I_{SC} measurements acquired with DUT at 25°C ± 0.5°C and normal incidence irradiance 1000 W/m^2 ± 20 W/m^2, thus no additional corrections were applied. Reported values at each AOI result from the average of 3 I_{SC} measurements.
TNO	R&D lab. Not ISO 17025 accredited.	1-axis, -90° to +90°, Manual	Pasan flasher with broadband Xe arc lamp (class AAA). Flash tunnel length = 8 m. Suppression of stray light with diaphragms, black paint, and black coverings. Maximum DUT size for AOI test = 160 x 160 mm. All I_{SC} measurements are corrected to 25°C. Irradiance stability correction applied to ISC based on measurements at normal incidence.

Appendix II: Supplemental Data

The relative transmittance data reported by the laboratories can be found in DTU's open access repository **https://doi.org/10.11583/DTU.12613325.v1**. This data set can assist researchers in developing and validating new models that describe the angular-dependent behavior of encapsulated PV devices.

Publication VIII. Measuring irradiance with bifacial reference panels

Authors:

Nicholas Riedel-Lyngskær, Martin Bartholomäus, Jan Vedde, Peter Poulsen, and Sergiu Spataru

Published in:

IEEE Journal of Photovoltaics 2022 (early access)

Measuring Irradiance With Bifacial Reference Panels

Riedel-Lyngskar, Nicholas; Bartholomaus, Martin; Vedde, Jan; Poulsen, Peter Behrensdorff; Spataru, Sergiu

Published in:
IEEE Journal of Photovoltaics

Link to article, DOI:
10.1109/JPHOTOV.2022.3201468

Publication date:
2022

Document Version
Peer reviewed version

This article has been accepted for publication in IEEE Journal of Photovoltaics. This is the author's version which has not been fully edited and content may change prior to final publication. Citation information: DOI 10.1109/JPHOTOV.2022.3201468

Measuring Irradiance with Bifacial Reference Panels

Nicholas Riedel-Lyngskær[1], Martin Bartholomäus[1], Jan Vedde[2], Peter B. Poulsen[1] and Sergiu Spataru[1]

[1]Technical University of Denmark, Department of Photonics Engineering, 4000 Roskilde, Denmark

[2]European Energy A/S, 2680 Søborg, Denmark

***Abstract*—The heterogenous nature and spectral distribution of rear plane-of-array irradiance R_{POA} presents challenges when measured by small-area sensors such as pyranometers. Bifacial reference modules serving as large-area sensors can simplify irradiance monitoring because their electrical response follows that of the power generating modules in an array. This article compares R_{POA} and effective irradiance G_E measured by calibrated reference modules against three commonly used small-area sensors including pyranometers, reference cells, and photodiodes. A technology-matched monofacial module is mounted side-by-side with the bifacial reference to decouple effective irradiance measurements into front and backside contributions. The results show that R_{POA} and G_E measurements made with reference panels have the best correlation to reference cells. The mean absolute errors between the two measurement approaches are 9% relative, 4 W/m^2 absolute for R_{POA} and 4% relative, 7 W/m^2 absolute for G_E. When G_E measurements from the four sensor types are used to predict string-level power, the reference panel measurements show a 3.4% prediction error, which is comparable to that achieved when using G_E measurements from pyranometers (3.0%) and reference cells (2.9%) thereby suggesting that reference modules can be used to accurately measure R_{POA} and G_E in bifacial systems.**

***Index Terms*—Bifacial PV, IEC 60904, rear irradiance, performance ratio, measurement.**

I. Introduction

The commercial rise of bifacial photovoltaic (PV) modules and the growing capacity of bifacial systems [1] has forced the PV community to update several international standards that were initially written for single sided PV devices [2] – [5]. Of interest in this work are the bifacial I-V measurement procedures defined in IEC TS 60904-1-2. Our aim is to assess whether the single-side illumination method described in [2] can be used to calibrate bifacial reference modules that are deployed in large-scale bifacial PV parks to measure effective irradiance.

Accurate bifacial PV modeling can only be achieved when the rear, and ultimately total (i.e., combined front and rear) irradiance is understood, but the PV community is still developing its best-practice guidance on the type, quantity, and placement of sensors for the assessment of rear plane-of-array irradiance (R_{POA}). The many challenges that frustrate accurate R_{POA} measurements are discussed systematically in [6]. Rear-side edge brightening [7], non-uniform irradiance patterns that change with conditions [8] [9], structural shading effects [10] [11], and in some cases self-shading from a module's frame and/or its conductors make it hardly possible for PV system designers to identify a single small-area location that is representative of the rear array. Ray-trace simulations can be used to determine a suitable small-area sensor location [10], but such methods are prohibitive due to computational intensity, steep learning-curve, and because the results are unique to a given PV substructure design and park layout. Meanwhile, spectral albedo effects [12] – [14] make sensor type selection non-trivial (e.g., pyranometer, reference cell, or Si photodiode).

The literature contains comparisons of small-area irradiance sensors for R_{POA} measurements [15] – [18], works that used monofacial reference modules for frontside plane-of-array irradiance (G_{POA}) measurements [19] [20], and recently, an investigation of bifacial reference panels for effective irradiance monitoring [21].

In this work, we evaluate the potential of bifacial reference panels, calibrated indoors per IEC TS 60904-1-2, to measure rear and effective irradiance. In section III.A, the rear and effective irradiance measurements from reference modules are evaluated against measurements from an array of small-area sensors that includes pyranometers, reference cells and Si-photodiodes. We supplement the analysis in III.A by showing how effective irradiance derived from string-level I-V measurements of a 24-module array compares to the module-level approach. In section III.B, the measurement differences due to spectral albedo effects are estimated using an in-plane spectrometer. The open-circuit voltage (V_{OC}) data from the I-V curves allowed us to calculate the equivalent cell temperature, the results of which are reported on in section III.C. In section III.D, we demonstrate how R_{POA} sensor type and position lead to uncertainty of the bifacial performance ratio (PR_{BIFI}). Finally, section III.E provides comparisons of yield predictions with effective irradiance data from the various sensors against string-level power of an operational system.

II. Methods

A. Outdoor Measurement Platform

The testbed shown in Fig. 1(a) is located near Roskilde, Denmark (55.6°N, 12.1°E) within the Technical University of Denmark's (DTU) outdoor PV test facility [18] [22]. The 25° fixed-tilt 14.2 kWp grid-tied array contains 24 large-area bifacial PERC (passivated emitter and rear cell) modules that became commercially available in 2021. Each bifacial PERC module contains 120 half-cut G12 (210 mm) wafers. The modules are framed glass/glass, have a 595 W frontside rating at standard test conditions (STC, 1000 W/m^2, 25 °C, AM1.5G),

This article has been accepted for publication in IEEE Journal of Photovoltaics. This is the author's version which has not been fully edited and content may change prior to final publication. Citation information: DOI 10.1109/JPHOTOV.2022.3201468

and a mean measured P_{MAX} bifaciality coefficient of 0.67 (±0.02). The market share of such high-power modules based on large-format wafers has grown in the last two years because they have lower production costs per watt and potentially lower balance of system costs [23]. The 2022 ITRPV report states that M10 (182 mm) and G12 (210 mm) wafer sizes will have majority market share from 2022 onward [24].

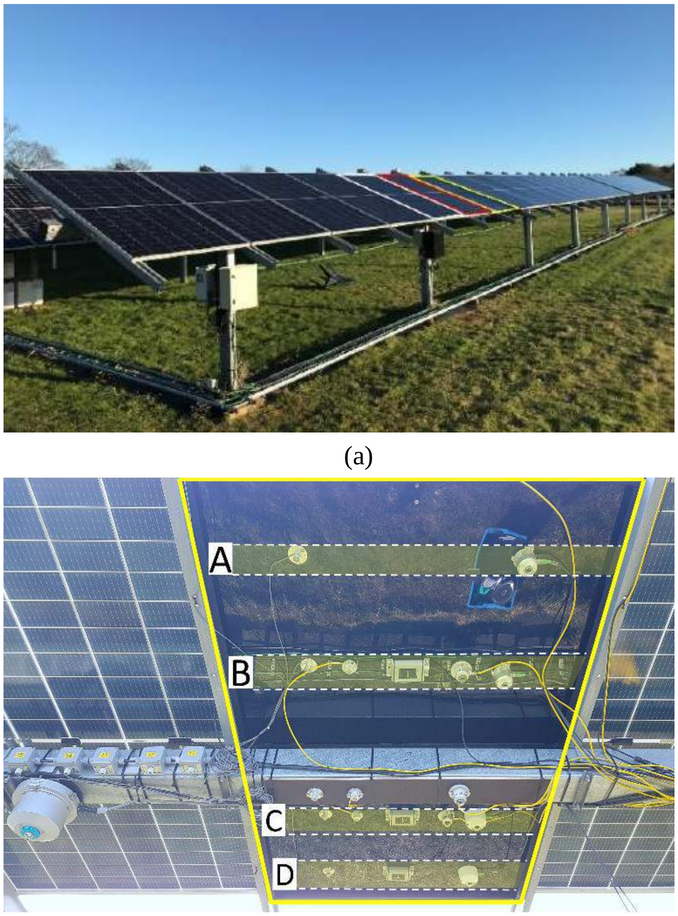

(a) (b)

Fig. 1. (a) The 14.2 kWp bifacial PERC testbed. The monofacial reference panel is highlighted in white, the bifacial reference panel in red, and the rear-side POA sensor plate in yellow. Panels that are not highlighted are connected in series to a grid-tied inverter. (b) Image of the rear POA sensor plate showing spectroradiometer, Si-photodiodes, Si reference cells, and pyranometers. The annotations A through D indicate the sensor locations.

Two reference modules are mounted within the 24-module string and are highlighted with white and red polygons in Fig. 1(a). The reference module highlighted in white was made monofacial by applying several spray-on layers of air-dry Plasti Dip® rubber to the back glass. The reference module highlighted in red was not modified and has the same properties as the other bifacial modules in the string. The monofacial and bifacial reference panels are electrically isolated from the grid-tied string. An EKO PV-Blocks system measures I-V curves of the reference panels every five minutes and holds them at P_{MAX} between I-V scans.

The grid-tied inverter can measure string-level I-V curves. Although most PV inverters have such a hardware capability, this inherent feature is often not used because of software limitations [25]. We perform continuous inverter-level I-V scans on three select days to estimate the effective irradiance received by the 24-module string, eight of which were calibrated using the IEC TS 60904-1-2 single-side illumination method.

The R_{POA} sensor plate shown in Fig. 1(b) is mounted roughly eight meters from the nearest array edge. We performed ray-trace simulations of the structure in *bifacial_radiance* [26] version 0.3.4 [27] and determined that this location avoids edge brightening. The naming convention we use for the highest to lowest sensor is A to D. The distances between the center beam, where the spectrometer is mounted, and the sensor locations A to D are as follows: A is 77 cm (70%) above, B is 33 cm (30%) above, C is 33 cm (−30%) below, and D is 77 cm (−70%) below. Table 1 summarizes the sensor types that are used in this work for R_{POA} measurements. The pyranometers and photodiodes are ISO 9060 Class C instruments, while the reference cells meet the Class B requirements defined in IEC 61724-1.

Because IEC 61724-1 states that an optical model can be used to estimate R_{POA} as an alternative to direct R_{POA} measurement, we also present results from a 2D view factor model [28] at array locations A to D. The view factor model takes as input onsite albedo, direct normal (DNI), and diffuse horizontal irradiance (DHI) measurements.

TABLE 1. REAR PLANE-OF-ARRAY SENSORS USED

Instrument	#	Make	Model
Spectrometer	1	EKO	MS-711
Si Photodiode	4	EKO	ML-01
Reference cell	3	IMT	Si-I-420TC-T
Pyranometer	4	EKO	MS-40M

B. Indoor Calibration of Bifacial Reference Panels

The reference panels are of the same make, model, and batch as the 595 W panels within the 24 panel (14.2 kWp) string. Before deployment, a random sample of 10 panels from the batch was selected for flash testing at DTU according to the single-side illumination method described in IEC TS 60904-1-2. The DTU flash solar simulator is a large-area Endeas QuickSun 540XLi (class AAA), which easily accommodates such large (i.e., 1300 mm x 2170 mm) panels. A summary of the flash test results is shown in Table 2. The expanded measurement uncertainty in Table 2 was derived with the methodology proposed by [29]. The uncertainty of backside I-V measurements is higher than frontside because of the increased distance between the reference cell and the cells inside the test module. This effect is caused by the module frame's thickness.

The flasher and measurement method were recently evaluated in a round robin campaign [30] wherein bifacial PV module measurements per IEC TS 60904-1-2 were compared among several accredited European labs. The results showed that DTU's bifacial PERC measurements agreed to the group median within uncertainty for all parameters, which gives us confidence in the reference panel calibration.

Two calibration factors, CF_{Rear} and CF_{Ge}, were derived from the single-side illumination measurements performed indoors. These calibration factors are used to translate the outdoor short-circuit current (I_{SC}) measurements to rear irradiance (R_{POA}) or effective irradiance (G_E), respectively. CF_{Rear} is the linear slope (in $A/W{\cdot}m^{-2}$) extracted from the plot of I_{SC} measured at multiple R_{POA} irradiances, with offset forced to the frontside I_{SC}

This article has been accepted for publication in IEEE Journal of Photovoltaics. This is the author's version which has not been fully edited and content may change prior to final publication. Citation information: DOI 10.1109/JPHOTOV.2022.3201468

measured at STC. Similarly, the calibration factor CF_{Ge} is calculated as the linear slope of I_{SC} as a function of single-side equivalent irradiances G_E, with offset forced to zero (see Fig. 4 in IEC TS 60904-1-2 [2]).

TABLE 2. SUMMARY OF I-V MEASUREMENTS MADE ON A SAMPLE OF TEN MODULES (N=10) AT STANDARD TEST CONDITIONS. THE TABLE SHOWS THE MEAN, STANDARD DEVIATION AND EXPANDED MEASUREMENT UNCERTAINTY.

I-V Measurement		Mean	Standard Deviation	Uncertainty (%)
I_{SC} (A)	Front	17.84	0.03	2.2
	Back	11.92	0.09	4.6
V_{OC} (V)	Front	41.05	0.05	0.8
	Back	40.61	0.07	0.9
P_{MAX} (W)	Front	585.91	1.61	3.5
	Back	389.99	3.31	5.5
Fill Factor (%)	Front	80.02	0.19	-
	Back	80.53	0.73	-

C. *Irradiance Measurements from Reference Modules and Small-Area Sensors*

When analyzing the field measurements, the rear POA irradiance from the reference modules ($R_{POA,Module}$) is determined using (1).

$$R_{POA,Module} = (I_{SC,Bifi} - I_{ISC,Mofi})/CF_{Rear} \tag{1}$$

Where CF_{Rear} ($A/W{\cdot}m^{-2}$) is the calibration factor for rear irradiance, $I_{SC,Bifi}$ (A) is the I_{SC} of the bifacial reference panel, and $I_{SC,Mofi}$ (A) is the I_{SC} of the monofacial reference panel. $I_{SC,Bifi}$ and $I_{SC,Mofi}$ are corrected to 25°C with the datasheet I_{SC} temperature coefficient and back-of-module temperature measurements. The back-of-module temperature sensors are class A PT1000s encased in aluminum housing and attached to the center of the module's back glass with adhesive.

The bifacial reference panel measurements provide a direct estimate of effective irradiance with (2).

$$G_{E,Module} = I_{SC,Bifi}/CF_{Ge} \tag{2}$$

Where $G_{E,Module}$ (W/m^2) is the effective irradiance measured by a single reference module, or string of modules, CF_{Ge} ($A/W{\cdot}m^{-2}$) is the calibration factor for total effective irradiance, and $I_{SC,Bifi}$ is the I_{SC} of the bifacial reference panel, or string. G_E comparisons between the large-area modules and small-area sensors are possible with (3).

$$G_{E,Sensor} = G_{POA} + \varphi \cdot R_{POA} \tag{3}$$

In (3) G_{POA} (W/m^2) is the frontside POA irradiance, φ is the I_{SC} bifaciality coefficient at STC (0.67 ±0.02), and R_{POA} (W/m^2) is the average rear-side POA irradiance at locations A to D measured by a given small-area sensor type. G_E calculated with (3) uses a consistent sensor type for G_{POA} and R_{POA}. For example, when using (3) to calculate G_E with reference cells, the G_{POA} data comes from a reference cell mounted on the frontside POA that is of the same make and model of those used to measure R_{POA}. In the case of G_E with pyranometers, we use measurements from a class A pyranometer for G_{POA} in (3).

III. RESULTS

The data presented here were recorded from January 4th to May 17th, 2022. Neither the sensors nor the modules were cleaned regularly, but frequent rainfall in Denmark's humid continental climate leads to minimal soiling ratios throughout the year. This assumption was verified with soiling ratio (SR) measurements from a DustIQ optical sensor [31]. The mean SR during the test period was 0.997, with a minimum of 0.992.

We apply two data filters in the analysis. First, data are removed when the angle of incidence (AOI) between the array and the Sun's beam component is greater than 80°. Secondly, an irradiance stability filter removes data when global horizontal irradiance (GHI) measurements sampled at 1 Hz vary by more than 15 W/m^2 within a ±15 second period around each R_{POA} measurement.

A. *Rear and Effective Irradiance (R_{POA} and G_E)*

Fig. 2 shows exemplary R_{POA} and G_E measurements on three mostly sunny days. The diurnal profiles in Fig. 2 were selected to demonstrate results under different solar zenith

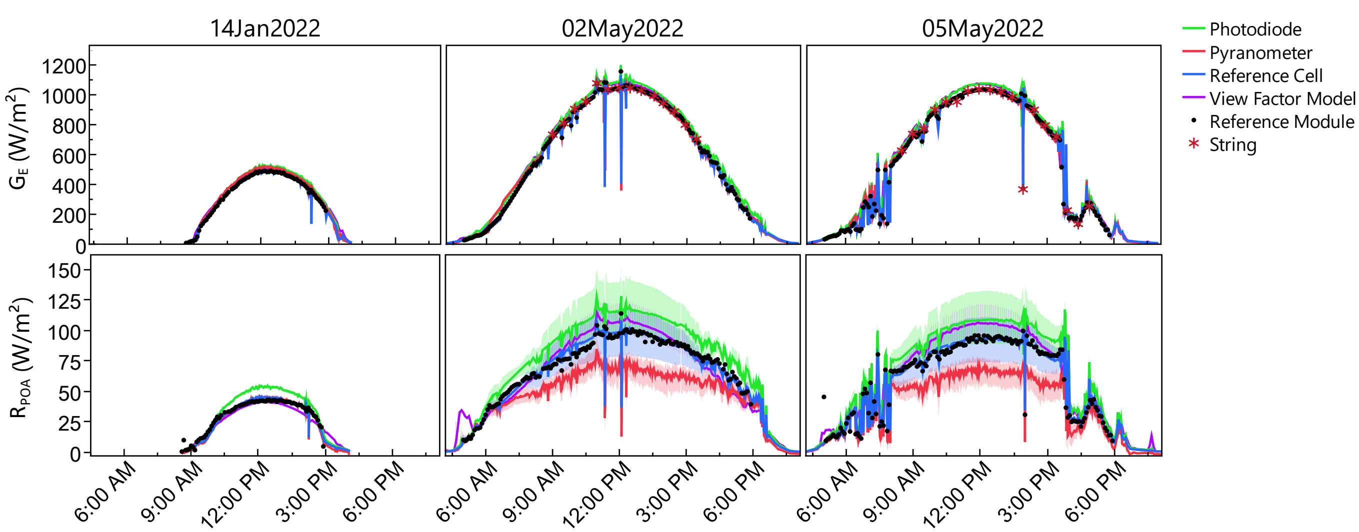

Fig. 2. Timeseries of effective irradiance (G_E) and rear irradiance (R_{POA}) on three mostly sunny days. The semi-transparent bands around R_{POA} timeseries represent the range of values measured at the sensor positions shown in Fig. 1(b). The reference cells, pyranometers, and photodiodes are sampled every minute. The reference modules are sampled every five minutes. The string I-V is performed every 30 minutes on the selected days.

This article has been accepted for publication in IEEE Journal of Photovoltaics. This is the author's version which has not been fully edited and content may change prior to final publication. Citation information: DOI 10.1109/JPHOTOV.2022.3201468

angles, and to show two days when string-level measurements were performed for G_E estimation (May 2nd and May 5th). The solar elevation peaked at 13° on January 14th and at 51° on May 5th, which explains why light intensity in May is about double what it is in January. The semi-transparent bands around the R_{POA} timeseries represent the range of values measured at the 3–4 locations shown in Fig. 1(b).

The photodiode measurements show a positive bias relative to other R_{POA} and G_E methods. In Section III.B, we quantify that up to 10% of the bias in R_{POA} measurement is due to spectral albedo effects. There are other reasons for the differences in R_{POA} measurement that we have not quantified including the different calibration sources and the nonlinearity of signal-to-irradiance relationships. The different directional responsivities of the sensors are not likely causing significant R_{POA} measurement discrepancies because the sensors on the rear-side receive only diffuse light for practically the whole test period. The reference cells have embedded temperature sensors, which are used to translate their output to 25°. The readings from these embedded sensors were between −6 °C and 26 °C. Such a temperature range could change the pyranometer readings up to 3% while causing minimal change to the photodiode outputs, according to the instruments' datasheets.

Fig. 3 shows the differences between R_{POA} measured with the various small-area sensors and R_{POA} measured with the large-area reference modules. Modeled R_{POA} at locations A to D using the view factor approach are shown for reference. The differences between methods are shown as cumulative distribution functions (CDFs). CDF curves with steeper slopes indicate distributions with lower variances. The reference cell group shows the steepest slope of all groups with 80% of the measurements agreeing to the reference module measurements within ±5 W/m^2. The reference cell group also shows the lowest median bias (0.7 W/m^2) of all small-area methods tested. The pyranometer, view factor and photodiode methods show median biases of −2.4 W/m^2, 5.5 W/m^2, and 7.5 W/m^2 relative to the reference module, respectively. The good agreement of the reference cell and reference module approaches is not surprising given that the two device types share similar—but not identical—spectral, directional, thermal, and temporal responsivities.

The R_{POA} sensor plate in Fig. 1(b) lacks a reference cell at location A. Our ray-trace simulations showed that light intensity on the top half of the system (i.e., locations A and B) is more homogenous than the bottom half (i.e., locations C and D). Therefore, a reference cell placed at location A would likely have yielded R_{POA} results comparable to that of location B.

Fig. 4 shows how the reference module G_E measurements compare to three small-area G_E measurement approaches and to G_E simulated with the view factor model. Only four curves are displayed in Fig. 4 since R_{POA} in Equation (3) is the average of the 3–4 small-area locations. The reference cell measurements again show the best agreement to the module-based measurements, with 83% of the measurements within ±10 W/m^2. Although the pyranometer and reference cell measurements show median biases near zero (i.e., −1.1 W/m^2 and −0.4 W/m^2), the pyranometers show about twice the dispersion, with 77% of measurements within ±20 W/m^2 of the reference module G_E measurements.

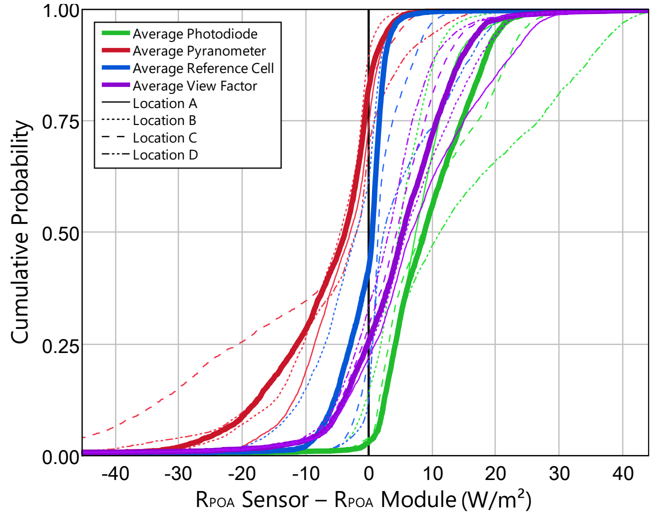

Fig. 3. Cumulative distribution functions of the R_{POA} differences between four small-area measurement\simulation methods and the reference modules. The thick solid lines show the average of 3–4 locations within a given method.

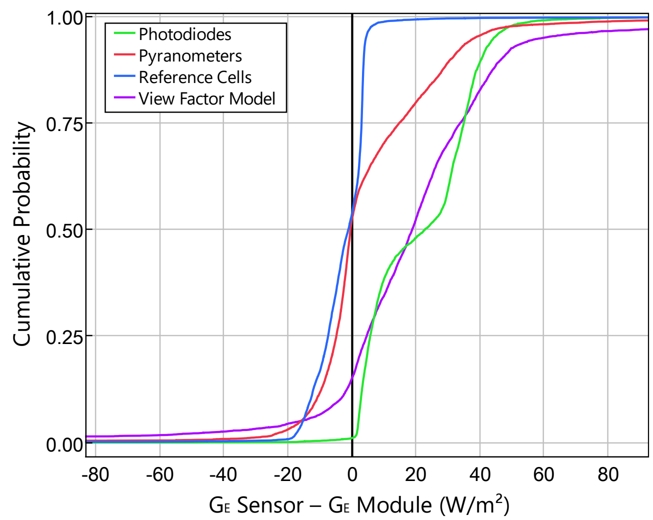

Fig. 4. Cumulative distribution functions of G_E differences between small-area measurement\simulation methods and the reference module.

Fig. 5 summarizes the differences between the small-area methods and the reference module measurements in terms of mean bias error (MBE), mean absolute error (MAE), and mean absolute percentage error (MAPE). The MBE values are comparable to the 50% values of the CDFs in Fig. 3 and Fig. 4, but there are small deviations because the distributions are non-normal.

Fig. 5 shows that the reference cell approach nearly always gives the lowest MBE, MAE and MAPE of all methods, regardless of the reference cell's rear-side location. The lowest MAE and MAPE are achieved when the reference cell is placed at location B (+30% from center) or location C (−30% from center). This suggests that a reference cell placed at one, or both, locations could serve as a representative location of the effective rear-side irradiance – so long as the fixed-tilt substructures are geometrically similar to those used here. This result differs from [10] where ray-trace simulations suggested that, for single-axis trackers, placing irradiance sensors at 20% from the array edges yields the closest value to the average.

This article has been accepted for publication in IEEE Journal of Photovoltaics. This is the author's version which has not been fully edited and content may change prior to final publication. Citation information: DOI 10.1109/JPHOTOV.2022.3201468

However, the result in this work is consistent with [32] where ray-trace simulations suggested that, for four-in-landscape fixed tilt systems, placing rear-side sensors 68% from the lower edge is representative of the average irradiance. Location B in Fig. 1(b) is 65% from the lower edge.

A comparison of bifacial modules and pyranometers for G_E measurements on trackers was recently performed by [21]. Their results showed pyranometer G_E was on average 3.6% higher than reference module G_E. The results in Fig. 5 show a 6.6% MAPE for pyranometer versus reference module G_E. Adjustments for AOI and spectral dependencies were made to the pyranometer G_E in [21], but were not done here, which may be the cause of discrepancy between the two works.

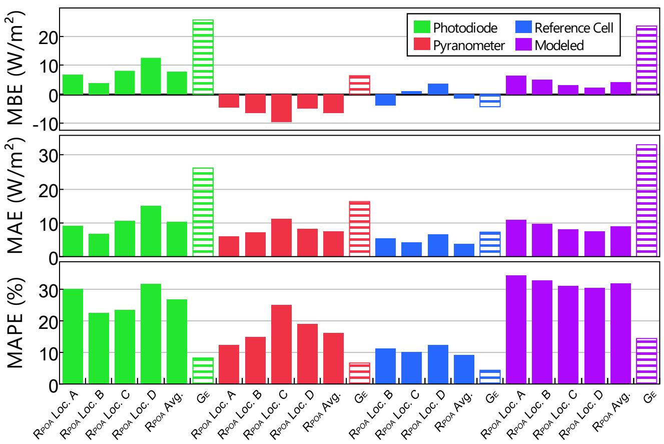

Fig. 5. Error summaries for R_{POA} and G_E measurements using various methods. The mean bias error (MBE), mean absolute error (MAE), and mean absolute percentage error (MAPE) for each method and location are relative to the reference module results. The solid bars show R_{POA} and hatched bars show G_E.

Having established that the reference cell and reference module measurements show the strongest correlation for R_{POA} and G_E, we now provide a deeper look at their relationships. Fig. 6 shows the difference between R_{POA} measured by the reference module pair and R_{POA} measured by the reference cells (average of locations B and C). The color scale in Fig. 6 reveals that the R_{POA} residuals have a dependence on the ratio of DHI to GHI, also known as the diffuse fraction (F_D).

Fig. 7 shows the difference between G_E measured by the bifacial reference module and G_E from the monofacial reference cell measurements calculated with (3). The difference between reference module and reference cell G_E measurements is less than 1% when AOI is less than 30° and the irradiance is between 900 and 1100 W/m^2. The reference panels have an antireflective coating (ARC) on the front glass whereas the reference cells do not. This means that the I_{SC} of the two devices may not follow the same AOI dependency.

The green asterisks in Fig.7 show G_E results using string-level I_{SC} measurements on three days. The trend of the string-level measurements mostly follows that of the module-level measurements. However, larger differences sometimes occur, which may be attributed to differences in I_{SC} between modules within the string, edge brightening effects, and\or time synchronization between measurements.

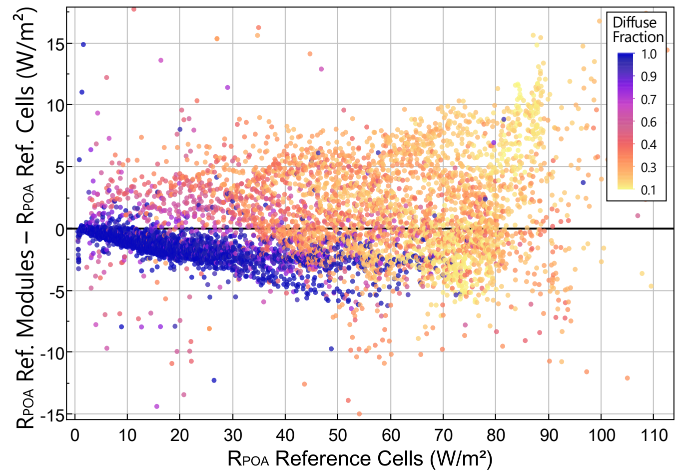

Fig. 6. Difference between R_{POA} as measured by the large-area reference module pair and R_{POA} measured with small-area reference cells. The x-axis shows the average of reference cell R_{POA} measurements at locations B and C. The color scale shows the fraction of diffuse light in the sky hemisphere.

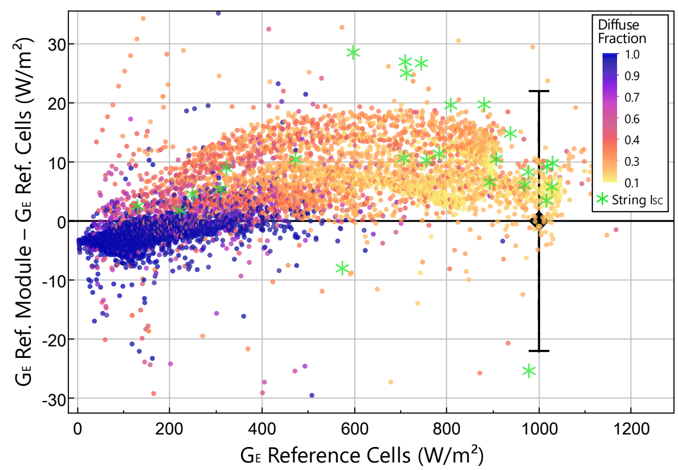

Fig. 7. Difference between G_E as measured by the large-area bifacial reference module and G_E measured with small-area reference cells. The asterisk symbols indicate G_E calculated from string-level I_{SC} measurements on select days. The x-axis shows G_E from the reference cell measurements. The error bars at 1000 W/m^2 represent the ±2.2% uncertainty of the laboratory measurement of I_{SC} at STC. The color scale shows the fraction of diffuse light in the sky hemisphere.

B. *Spectral Implications*

Here we show how spectral effects can influence the sensor outputs. Fig. 8(a) shows typical R_{POA} spectra recorded during green vegetation—the predominant albedo during the measurement campaign—and a condition with partial snow coverage. Consistent with [12] – [14], the green grass R_{POA} spectrum displays a heavy redshift relative to the AM1.5G reference spectrum. Snow spectra such as that shown in Fig. 8(a) were observed on three days during the test period. Such spectra demonstrate how significantly the redshift is reduced during snow conditions. Fig. 8(b) shows the spectral responsivities (SR) of the various devices used in this work. The PERC cell's backside SR is taken from the PERC measurements performed in [14], the photodiode and pyranometer SR files were provided by the manufacturer, and the reference cell SR was digitized from the datasheet.

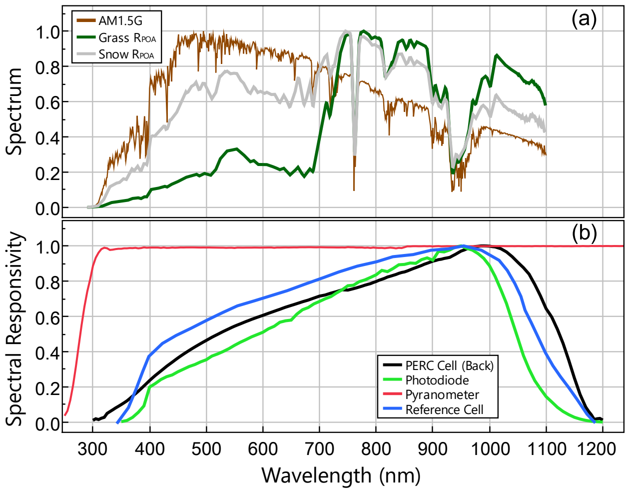

Fig. 8. (a) normalized rear-side spectral irradiance measured at midday on clear days with green grass albedo and when the ground is partially covered in snow. The AM1.5G calibration spectrum is shown to illustrate the spectral shifts observed in the field. (b) normalized spectral responsivity of a PERC cell's backside, photodiodes, pyranometers and reference cells used in this work.

With the continuous in-plane spectral measurements and equation 7 of IEC 60904-7 [33], we derive spectral mismatch (SMM) for the rear-side POA.

$$Rear\ SMM = \frac{G_{Ref} \cdot \int_a^b SR(\lambda) \cdot R_{POA}(\lambda) d\lambda}{R_{POA} \cdot \int_a^b SR(\lambda) \cdot G_{Ref}(\lambda) d\lambda} \qquad (4)$$

SR(λ) is the normalized device spectral responsivity, $R_{POA}(\lambda)$ is the normalized rear-side spectral measurement recorded every five minutes, and $G_{Ref}(\lambda)$ is the normalized AM1.5G reference spectrum [34]. The 300 nm to 1100 nm integration limits are determined by the sensitive range of the spectroradiometer. In (4), R_{POA} is calculated as the integral of $R_{POA}(\lambda)$ and G_{Ref} is calculated as the integral of $G_{Ref}(\lambda)$ over the same integration limits. SMM values greater than 1 indicate spectrally induced gains in photocurrent relative to AM1.5G, and SMM values less than 1 indicate spectrally induced losses. If SMM is ignored, the fractional measurement error due to spectral shift is 1 – SMM.

Fig. 9 shows the relationships between the rear-side SMM factors of each device type shown in Fig. 8(b). Each data point in Fig. 9 is calculated with a single rear-side spectral measurement. Fig. 9 therefore contains 2,655 rear-side SMM factors, for each device, that collectively represent the actual spectral conditions recorded during the four-month test period. The contours around regression lines in Fig. 9 highlight 90% of the SMM values. When snow conditions were present, the rear-side SMM of the Silicon-based sensors is less than 1.10.

The photodiode shows the highest SMM due to its narrow SR and weak response in the visible spectrum (400–700 nm). Some commercially available photodiode models have a lower visible light SR than that shown in Fig. 8(b) [35]. For such devices, we calculated SMM as high as 1.5 with our R_{POA} spectra above green grass. The reference cell SMM is 8% to 11% lower than that of the photodiode. When the reference cell and photodiode measurements are adjusted by a factor of 1/SMM, then the R_{POA} differences shown in Fig. 2 are reduced in half. The remaining differences may be due to different calibration sources.

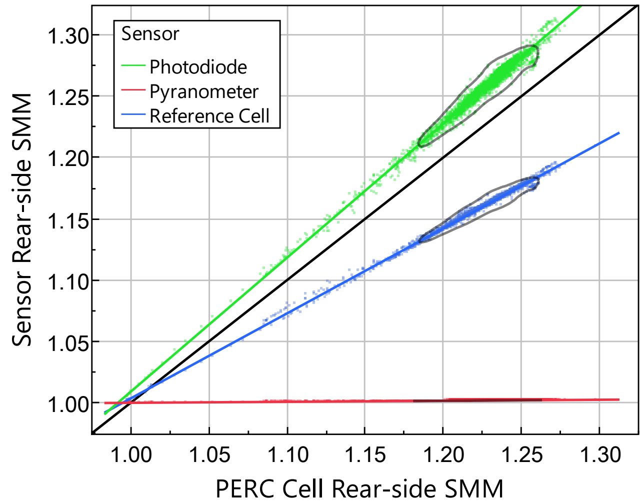

Fig. 9. Bivariate of spectral mismatch (SMM) calculated with the rear-side spectral measurements during the 4-month test period. The regression shows rear-side SMM of the photodiode, pyranometer, and reference cell versus the rear-side SMM of a PERC cell. The black 45° line indicates a spectral match to the PERC cell's rear side. The contour around each regression line indicates where 90% of the SMM values are located.

Fig. 9 shows that the reference cell SMM is 5% to 7% lower than PERC cell backside. In other words, the two are not spectrally matched and 5% to 7% of the measured differences are attributable to spectral effects. Although this result runs counter to the common perception that silicon reference devices are similar enough to silicon power-generating devices such that no spectral corrections are needed [36], R_{POA} is typically an order of magnitude less than G_{POA}. Therefore, spectral errors in R_{POA} measurements are likely to impact yield predictions of bifacial PV systems by less than 1%.

Equation (4) assumes that the reference device is spectrally flat. Apart from some absorption of UV light, the pyranometer used in this work has a spectrally flat response and therefore its rear-side SMM is always near 1, wherein 90% of values are between 1.001 and 1.002. The spectroradiometer's 300 – 1100 nm sensitive range presents limitations because the pyranometer has a 280 – 3000 nm spectral range. However, rear-side SMM calculated over the full 280 – 3000 nm range was comparable (1.002) when using AM1.5G multiplied by the green grass spectral albedo from SMARTS as $R_{POA}(\lambda)$ [37].

C. *Equivalent Cell Temperature (ECT) Results*

Back-of-module temperature (T_{MOD}) measurements performed on bifacial modules will inevitably partially-shade some active area. The shading induced by a single T_{MOD} sensor is not likely to create local hotspots when albedo is low (i.e., < 0.3). However, bifacial T_{MOD} measurements during high albedo conditions such as snow, or during periods when the sun is behind the PV structure, may put the partially shaded cell into reverse bias. The V_{OC} data from the reference panels and string offer an opportunity to avoid rear-side sensor shading by calculating T_{MOD} with the equivalent cell temperature (ECT) approach [38]. Here we describe our experience applying the ECT procedures to the outdoor V_{OC} measurements of a single bifacial module, and to a string of 24 bifacial modules with (5).

This article has been accepted for publication in IEEE Journal of Photovoltaics. This is the author's version which has not been fully edited and content may change prior to final publication. Citation information: DOI 10.1109/JPHOTOV.2022.3201468

$$ECT = T_{STC} + \frac{1}{\beta}\left[\frac{V_{OC}}{V_{OC,STC}} - 1 - a \cdot \ln\left(\frac{G}{G_{STC}}\right)\right] \quad (5)$$

According to [38], ECT in (5) represents the average temperature (°C) at the p-n junctions within a module or array, V_{OC} is the outdoor measured open-circuit voltage (V), β is the temperature coefficient of V_{OC} (1/°C), T_{STC} is 25 °C, $V_{OC,STC}$ is the open-circuit voltage measured at STC in the lab (V), G_{STC} is 1000 W/m^2, G is the irradiance (W/m^2), and *a* is a dimensionless parameter that depends on the module's voltage-irradiance response. The value for the *a* coefficient was determined from our laboratory measurements at 200 W/m^2 and 800 W/m^2. We applied a self-referencing approach by substituting G with the field measured I_{SC}, and G_{STC} with the lab measured $I_{SC,STC}$. We looked to recent literature [39] to find a representative β value for PERC (−0.31%/°C) as the DTU lab is not equipped to measure β of the large-area 595 Wp modules.

For single panel ECT measurements, the error (ECT − T_{MOD}) is calculated with a single PT1000 sensor on the bifacial reference panel, while for string-level ECT measurements, the error is with the average of four PT1000 measurements across the string (Fig. 1a). We adjust the back-of-module surface temperature T_{MOD} to cell temperature using the King model [40] for glass-glass modules, which adds an offset of 3 °C · (G_E/1000 W/m^2) to the measured T_{MOD}. A recent field trial [41] showed that this simplistic approximation of cell temperature is reasonably accurate.

Fig. 10 shows the difference between ECT and T_{MOD} when $G_E \geq 200$ W/m^2. In this irradiance range, the MAE is 2.5°C and 2.1°C for the module and string measurements, respectively. The MBE is similar at 2.4°C and 2.1°C, respectively. The error has a positive correlation with irradiance.

There are several uncertainty contributions that must be considered when evaluating the error, including the ECT model parameter values, the temperature non-uniformity of cells within a module, the difference between back-of-module surface and p-n junction temperature, the PT1000 sensor accuracy, and the thermal contact between PT1000 sensor and module surface.

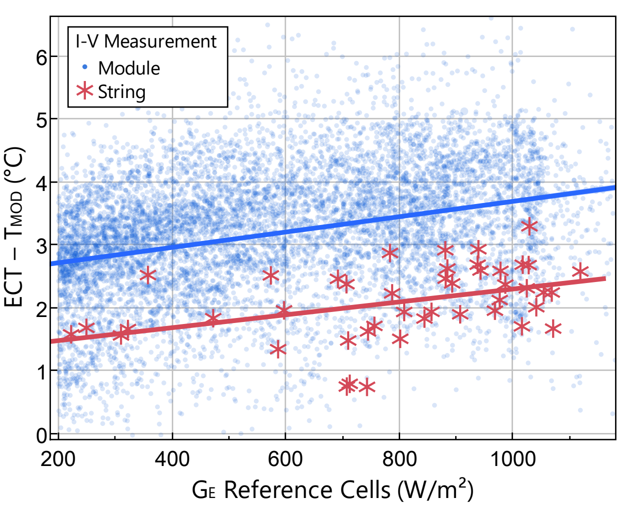

Fig. 10. Errors between the equivalent cell temperature (ECT) method and back of module temperature (T_{MOD}) measurements applied to a bifacial module and a bifacial string. The x-axis shows effective irradiance (G_E) calculated with reference cell measurements. The data shown here includes four months of module measurements and three days of string-level measurements.

We found that the ECT model is most sensitive to the value of the $V_{OC,STC}$ and β. For example, the expanded uncertainty of the $V_{OC,STC}$ measurements is ±0.8% (i.e., ±0.3 V for a single module). Varying $V_{OC,STC}$ within uncertainty results in a ±2.4° change in ECT. Meanwhile, the stated accuracy of the class A PT1000 sensors used to compare to the ECT method is ±1°C. Given, the many uncertainties, our results suggest that the ECT method via V_{OC} measurements is a practical approach for monitoring bifacial module temperature. Previous works have proposed that the ECT method is more accurate than direct T_{MOD} measurements of monofacial modules [42], largely because of the challenges and uncertainties associated with direct T_{MOD} measurements [43].

D. Bifacial Performance Ratio (PR_{BIFI})

IEC 61724-1 [3] states that the classic performance ratio (PR) formula [44] can be transformed to bifacial PR (PR_{BIFI}) if an adjustment is made for the rear irradiance. This is done in practice by multiplying G_{POA} by a factor of either BIF_{sensor} or BIF_{module}. When small-area sensors such as reference cells are used to measure R_{POA}, (6) is used to calculate BIF_{sensor}.

$$BIF_{sensor} = (1 + \varphi_{pmax} \cdot \rho_i) \quad (6)$$

Where bifaciality φ_{pmax} is the ratio of rear to frontside P_{MAX} at STC and the optical gain ρ_i is the ratio of R_{POA} to G_{POA}. When the reference modules are used to derive PR_{BIFI}, BIF_{module} is calculated with (7).

$$BIF_{module} = \frac{I_{SC,Bifi}}{I_{SC,Mofi}} \quad (7)$$

Where $I_{SC,Bifi}$ and $I_{SC.Mofi}$ are the I_{SC} measurements of the bifacial and monofacial panels, respectively. Since R_{POA} from small-area sensors is used to calculate PR_{BIFI} with (6), the question arises: which R_{POA} location to use and from which sensor type?

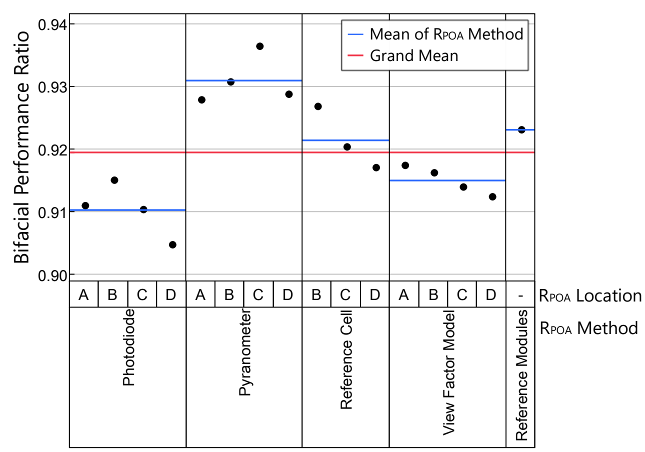

Fig. 11. Variability of the bifacial performance ratio PR_{BIFI} calculated according to the IEC 61724-1 using three small-area sensor types, an optical model, and a reference module pair. All sensors are eight meters from the nearest array edge. See Fig. 1(b) for illustration of R_{POA} sensor locations A to D.

Fig. 11 shows the 14.2 kWp system's PR_{BIFI} calculated with the five methods and four rear-side locations used in this work. Frontside G_{POA} from the same Class A pyranometer is used in all calculations, which means that all variation of PR_{BIFI} in Fig. 11

This article has been accepted for publication in IEEE Journal of Photovoltaics. This is the author's version which has not been fully edited and content may change prior to final publication. Citation information: DOI 10.1109/JPHOTOV.2022.3201468

is caused by the R_{POA} measurement used. Fig. 11 shows that PR_{BIFI} differs up to 3% with the R_{POA} methods considered here. The 14.2 kWp system used for study has a 1.7 m ground clearance, which is higher than typical utility-scale fixed tilt systems. The spread of possible PR_{BIFI} values is likely to increase with lower ground clearance because nonuniformity of R_{POA} will be higher [8] [32].

E. Comparisons of Measured and Modeled DC Power

Here we compare the measured DC power of the 14.2 kWp string to modeled DC power using the various G_E measurement methods. We model DC power using the PVWatts model [45], which calculates DC power with (8).

$$P_{DC} = \frac{G_E}{1000\ W/m^2} \cdot P_{STC}[1 + \gamma \cdot (T_{Mod} - 25\ °C)] \tag{8}$$

Where P_{DC} (W) is the modeled string-level DC power, G_E (W/m^2) is the effective irradiance from either the bifacial reference module, reference cells, pyranometers, or photodiodes, P_{STC} (W) is the average module power measured at STC (Table 2) multiplied by the number of modules in the string, γ (%/°C) is the temperature coefficient for power, and T_{MOD} (°C) is the module temperature measured at four locations on the back of the array.

Equation (8) does not account for angular-dependent reflection losses, spectral shifts, or low-irradiance performance. Therefore, the results shown in Fig. 12 only contain data where AOI < 45°, optical air mass (AM) is between 1 and 2, and G_{POA} > 700 W/m^2. Recall that G_E calculations for pyranometers use frontside G_{POA} from a class A device and use the average of class C devices for R_{POA}.

Table 3 shows the error summary when the various G_E data sources are used to predict string-level power. The mean absolute error (MAE) and mean bias error (MBE) are normalized to the 14.2 kWp rating of the modeled array. The results show that photodiodes yield the highest MAE, MBE and MAPE, which is consistent with the comparisons shown in Fig. 2 through Fig. 5. The normalized MAE and MAPE are all within about 0.5% when the pyranometers, reference cells and reference modules are used for G_E in the modeling. However, the reference cell data provides the lowest bias relative to the field measurements.

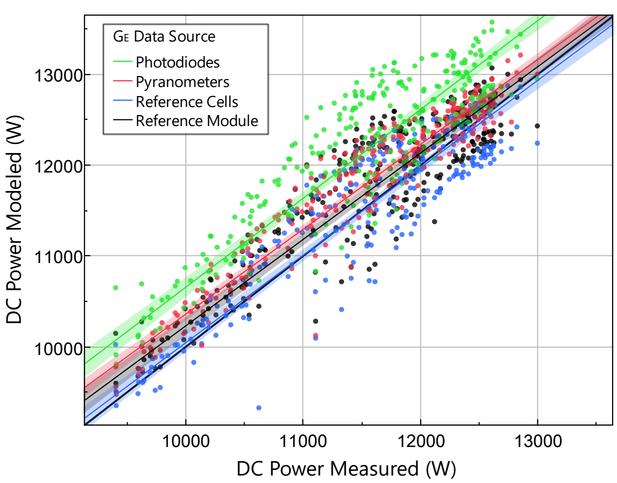

Fig. 12. Bivariate regressions of modeled DC power using four different sources for effective irradiance versus measured DC power.

TABLE 3. ERROR SUMMARY RESULTING FROM USE OF DIFFERENT GE DATA SOURCES WHEN MODELING DC POWER. THE MEAN BIAS ERROR AND MEAN ABSOLUTE ERROR ARE NORMALIZED TO THE 14.2KW RATING OF THE ARRAY.

G_E Data Source	MBE (W/kWp)	MAE (W/kWp)	MAPE (%)
Photodiodes	46.4	49.1	6.1
Pyranometers	19.0	23.6	3.0
Reference cells	1.2	23.3	2.9
Reference module	13.2	27.0	3.4

IV. DISCUSSION

We have compared rear plane-of-array (R_{POA}) and effective irradiance (G_E) measurements made with calibrated reference modules against measurements from small-area sensors that included photodiodes, pyranometers and reference cells. The results showed that the reference cell R_{POA} and G_E measurements had the strongest correlation to R_{POA} and G_E measured with reference modules. The average agreement between the two approaches was 9% relative, 4 W/m^2 absolute for R_{POA} and 4% relative, 7 W/m^2 absolute for G_E. We found that reference cells located at ±30% from the center of the fixed-tilt array had the best agreement to the reference module R_{POA} measurements. Thus, a single small-area rear facing reference cell can provide comparable results to the large-area reference module approach.

The G_E derived from I_{SC} measurements of a 24-module string agreed to module-level G_E measurements within 2.5% or better when G_E was near one-sun. Although the string-level I-V measurements were limited to three clear days, the results are encouraging that continuous string-level I-V scans (e.g., made by inverters) can be used to estimate G_E of healthy bifacial PV arrays. We leave deeper investigations of effective irradiance modeling via string-level I-V for future work.

We examined spectral effects in R_{POA} measurements. Although the spectral distribution of R_{POA} differed significantly from the AM1.5G reference, the overall impact of rear spectral mismatch is less than 1% when considering that the dominant contribution to bifacial performance is frontside irradiance.

We also evaluated the potential of bifacial reference panels to measure cell temperature with V_{OC} measurements. We found mean absolute errors of 2.5°C and 2.1°C when performing this method with module and string-level bifacial measurements, respectively. This level of error translates to approximately 1% uncertainty in power measurements of modern Silicon modules. Thus, the V_{OC} data can add value to continuous I-V measurements by offering a method that avoids the rear-side shading created by conventional module temperature sensors.

It was shown that bifacial performance ratios can vary by 3% based on the placement and type of small-area sensor used for R_{POA} measurements. Using bifacial reference panels for performance ratio calculations can reduce this variation because they circumvent the need to identify representative small-area sensor locations.

Finally, we used the G_E data to predict string-level power. G_E data from pyranometers, reference cells and reference modules resulted in 2.9–3.4% average errors relative to measured power. The comparable prediction errors between traceable small-area irradiance sensors and calibrated modules suggests that reference modules are a suitable and accurate approach for measuring irradiance in bifacial systems.

This article has been accepted for publication in IEEE Journal of Photovoltaics. This is the author's version which has not been fully edited and content may change prior to final publication. Citation information: DOI 10.1109/JPHOTOV.2022.3201468

V. Conclusion

This work investigated the capability of bifacial modules, calibrated per the single-side equivalent irradiance method of IEC TS 60904-1-2, to be used as large-area sensors that measure R_{POA} and G_E. A supplemental monofacial reference module was used in the field to decouple the rear irradiance R_{POA} from the effective irradiance G_E. We compared the reference module measurements to three types of commonly used small-area sensors, all with traceable calibrations.

Out of all the small-area sensors tested, we found that reference cell measurements of R_{POA} and G_E had the best agreement to those made by reference modules. The array of 3–4 rear facing sensors showed that a single small-area R_{POA} sensor location can agree to large-area reference module R_{POA} measurements by 4 W/m^2 absolute, 9% relative. PVWatts yield predictions that used G_E data from pyranometers, reference cells, and modules were within 2.9%–3.4% of measured string-level power, thereby demonstrating the absolute accuracy of the bifacial reference module approach.

We found that the choice of small-area sensor type and mounting location adds at least ±1.5% uncertainty to bifacial performance ratio calculations. Calibrated reference modules can be used to reduce said variation in bifacial performance ratio calculations, while at the same time simplifying the monitoring system design and offering the ability to estimate cell temperature through the V_{OC} of the I-V curve.

Acknowledgements

This work was funded by the Danish Energy Technology Development and Demonstration Program (EUDP) under contract 64021-2082. We thank Dr. Christos Monokroussos of TUV for discussions on ECT measurements and Dr. Mário Pó of EKO Instruments for providing spectral response data.

VI. References

[1] J. Stein et al., "Bifacial Photovoltaic Modules and Systems: Experience and Results from International Research and Pilot Applications," IEA PVPS Task 13, 2021.

[2] IEC TS 60904-1-2 "Measurement of current-voltage characteristics of bifacial photovoltaic (PV) devices", 2019.

[3] IEC 61724-1 Edition 2 "Photovoltaic system performance - Part 1: Monitoring", 2021.

[4] M. Waters et al., "Suggested Modifications for Bifacial Capacity Testing," in *46th IEEE PVSC*, Chicago, IL, 2019.

[5] A. Gracia-Amillo et al., "Extension of energy rating to bifacial modules – proposals from the PV-enerate project," JRC Technical Report, 2020.

[6] M. Gostein et al., "Measuring Irradiance for Bifacial PV Systems," in *IEEE 48th PVSC*, 2021.

[7] S. A. Pelaez et al., "Model and Validation of Single-Axis Tracking with Bifacial PV," *IEEE JPV*, vol. 9, no. 3, pp. 715-721, 2019.

[8] C. Deline et al., "Estimating and parameterizing mismatch power loss in bifacial photovoltaic systems," *PiP*, vol. 28, no. 7, 2020.

[9] G. Janssen et al., "Impact of inhomogenous irradiance at the rear of bifacial panels on modelled energy yield," in *33rd EUPVSEC*, 2017.

[10] S. Pelaez et al., "Effect of torque-tube parameters on rear-irradiance for bifacial PV on trackers," in *46th IEEE PVSC*, Chicago, 2019.

[11] C. Zhao et al., "Accurate shading factor and mismatch loss analysis of bifacial HSAT systems through ray-tracing modeling," *Solar Energy Advances*, vol. 1, 2021.

[12] J. C. Blakesley et al., "Effective spectral albedo from satellite data for bifacial gain calculations of PV systems," in *36th EUPVSEC*, 2020.

[13] M. Gostein, B. Marion and B. Stueve, "Spectral Effects in Albedo and Rearside Irradiance Measurement for Bifacial Performance," in *47th IEEE PVSC*, 2020.

[14] N. Riedel-Lyngskær et al., "The effect of spectral albedo in bifacial performance," *Sol. Energy*, vol. 231, no. 1, pp. 921-935, 2022.

[15] A. Asgharzadeh et al., "A Benchmark and Validation of Bifacial PV Irradiance Models," 46th *IEEE PVSC*, 2019.

[16] S. Peleaz et al., "Field-Array Benchmark of Commercial Bifacial PV Technologies with Publicly Available Data," in *47th IEEE PVSC*, Calgary, 2020.

[17] P. Babal et al., "Uncertainties in irradiance measurements of sensors to POA-rear of bifacial solar panels," in *47th IEEE PVSC*, Calgary, 2020 .

[18] N. Riedel-Lyngskær et al., "Validation of Bifacial Photovoltaic Simulation Software against Monitoring Data from Systems in Denmark," *Applied Sciences*, vol. 10, no. 23, pp. 1-29, 2020.

[19] J. Polo, W. Fernandez-Neira and M. Alonso-Garcia, "On the use of reference modules as irradiance sensor for monitoring and modelling rooftop PV systems," *Renewable Energy*, vol. 106, pp. 186-191, 2017.

[20] Y. Hishikawa et al., "Improved precision of the outdoor performance measurements of photovoltaic modules by using the photovoltaic irradiance sensor," *Sol. Energy*, vol. 211, pp. 85-89, 2020.

[21] J. Braid et al., "Effective Irradiance Monitoring Using Reference Modules," in 49th *IEEE PVSC*, Philadelphia, 2022.

[22] N. Riedel-Lyngskær et al., "Value of bifacial photovoltaics used with highly reflective ground materials on single- axis trackers and fixed-tilt systems: a Danish case study," *IET RPG*, vol. 14, pp. 3946-3953, 2021.

[23] S. Chunduri and M. Schmela, "Very High-Power Solar Modules," TaiyangNews, 2021.

[24] VDMA, "International Technology Roadmap for Photovoltaics (ITRPV): 2021 Results," 2022.

[25] S. Spataru et al., "Monitoring and Fault Detection in PV Systems Based On Inverter Measured I-V Curves," in *31st EUPVSEC*, Hamburg, 2015.

[26] C. Deline and S. Pelaez, "bifacial_radiance: a python package for modeling bifacial solar photovoltaic systems.," *Journal of Open Source Software*, vol. 5, no. 50, 17 Dec 2020.

[27] S. Pelaez, C. Deline, J. Alderman, M. Mikofski and C. Stark, "bifacial_radiance: a python package for modeling bifacial solar photovoltaic systems," 27 May 2020. [Online].

[28] M. Anoma et al., "View Factor Model and Validation for Bifacial PV on Single-Axis Trackers," in *44th IEEE PVSC*, Washington D.C., 2017.

[29] D. Dirnberger and U. Kräling, "Uncertainty in PV Module Measurement—Part I: Calibration of Crystalline and Thin-Film Modules," *IEEE JPV*, vol. 3, no. 3, pp. 1016-1026, 2013.

[30] G. Koutsourakis et al., "Results of the Bifacial PV Cells and PV Modules Power Measurement Round Robin Activity of the PV-Enerate Project," in *37th EUPVSEC*, 2021.

[31] M. Korevaar et al., "Novel Soiling Detection System for Solar Panels," in *33rd EUPVSEC*, Amsterdam, 2017.

[32] M. Korevaar et al., "Simulation and Validation of Bifacial Irradiance Sensor Mounting Position," in *37th EUPVSEC*, Lisbon, 2020.

[33] IEC 60904-7 Ed. 4.0, 2019.

[34] IEC 60904-3 Ed. 4.0, 2019.

[35] A. Driesse and W. Zaaiman, "Characterization of Global Irradiance Sensors for use with PV Systems," in *42nd IEEE PVSC*, 2015.

[36] L. Dunn, M. Gostein and K. Emery, "Comparison of Pyranometers vs. PV Reference Cells for Evaluation of PV Array Performance," in *39th IEEE PVSC*, 2012.

[37] D. Myers and C. Gueymard, "Description and availability of the SMARTS spectral model for photovoltaic applications," in *Proceedings of SPIE - The International Society for Optical Engineering*, 2004.

[38] IEC 60904-5 Ed. 2.0, 2011.

[39] S. Zhang et al., "Illumination-dependent temperature coefficients of the electrical parameters of modern silicon solar cell architectures," *Nano Energy*, vol. 98, 2022.

[40] D. King, B. Boyson and J. Kratochvill, "Photovoltaic Array Performance Model," Sandia Report (SAND2004-3535), 2004.

[41] M. Chowdhury et al., "Sensitivity analysis of the state of the art PV temperature estimation methods," in *IEEE 48th PVSC*, Miami, 2021.

[42] S. Krauter and A. Preiss, "Comparison of module temperature measurement methods," in *34th IEEE PVSC*, Philadelphia, 2009.

[43] R. Smith, "Improving Long-Term Back-of-Module Temperature Measurements," SolarPro Magazine, May/June 2015.

[44] N. Reich et al., "Performance ratio revisited: is PR > 90% realistic?," *PiP*, vol. 20, pp. 717-726, 2012.

[45] A. Dobos, "PVWatts Version 5 Manual," National Renewable Energy Laboratory, 2014.

Publication IX. Value of bifacial photovoltaics used with highly reflective ground materials on single-axis trackers and fixed-tilt systems: a Danish case study

Authors:

Nicholas Riedel-Lyngskær, Per Nørgaard, Peter Poulsen, Michael Linde Jakobsen, and Jan Vedde

Published in:

Renewable Energy Power Generation EIT 2020, 14(6), 3946-3953

DTU Library

Value of bifacial photovoltaics used with highly reflective ground materials on singleaxis trackers and fixed-tilt systems: a Danish case study

Riedel-Lyngskær, Nicholas Chistopher; Poulsen, Peter Behrensdorff; Jakobsen, Michael Linde; Nørgård, Per Bromand; Vedde, Jan

Published in:
IET Renewable Power Generation

Link to article, DOI:
10.1049/iet-rpg.2020.0580

Publication date:
2021

Document Version
Publisher's PDF, also known as Version of record

IET Renewable Power Generation

Research Article

Value of bifacial photovoltaics used with highly reflective ground materials on single-axis trackers and fixed-tilt systems: a Danish case study

ISSN 1752-1416
Received on 11th May 2020
Revised 22nd December 2020
Accepted on 14th January 2021
doi: 10.1049/iet-rpg.2020.0580
www.ietdl.org

Nicholas Riedel-Lyngskær[1] ✉, Peter Behrensdorff Poulsen[1], Michael Linde Jakobsen[1], Per Nørgaard[2], Jan Vedde[3]

[1]*Department of Photonics Engineering, Technical University of Denmark, Roskilde, Denmark*
[2]*Center for Electric Power & Energy, Technical University of Denmark, Roskilde, Denmark*
[3]*European Energy, Søborg, Denmark*
✉ *E-mail: nrie@fotonik.dtu.dk*

Abstract: The energy produced by bifacial photovoltaic (PV) arrays can be augmented via albedo enhancements. However, the value of the additional energy must outweigh the costs for such modifications to be economically viable. In this work, the electrical performance and economic value of six 13 kWp crystalline-silicon (c-Si) PV arrays with distinct configurations are evaluated. The system designs include horizontal single axis trackers (HSAT) and 25° fixed-tilt structures, monofacial and bifacial PV panels, and low and high ground albedo. The value of the system designs is assessed using onsite electrical measurements and spot prices from the Nord Pool electricity market. We find that HSAT systems increase the annual value factor (*VF*) by 4% and decrease levelized cost of energy (*LCOE*) by 3.5 EUR/MWh relative to fixed-tilt systems. The use of bifacial panels can increase the *VF* by 1% and decrease *LCOE* by 4.0 EUR/MWh. However, a negligible VF increase and modest *LCOE* decrease was found in systems with bifacial panels and ground albedo enhancements. Although our results show that albedo enhancements result in lower LCOE than designs without, the uncertainty in upfront and ongoing costs of altering the ground in utility-scale PV parks makes the solution presently unadvisable.

1 Introduction

Recent years have shown a steady increase in bifacial photovoltaic (PV) installations because the light that impinges on the backside of a bifacial PV array can be converted into useable photocurrent. Historically, PV cells based on crystalline silicon (c-Si) have featured a rear side electrical contact fully covered in aluminium, which inhibits rear side light absorption. In contrast, the rear side of bifacial PV cells is only partially covered with metallisation [1]. When such bifacial cells are assembled into a module with a transparent rear cover (such as glass or a transparent back sheet) there is potential for considerable energy gains compared to monofacial (single-sided) modules that are deployed in the same conditions. The growth of bifacial PV implementation in large-scale systems is driven by the continuous reductions in PV module prices [2, 3] to the extent that the ITRPV forecasts that bifacial PV cells will account for 70% of the market share by 2030 [4].

The increased energy produced by a bifacial PV system over a monofacial PV system with equivalent front side power operating in the same conditions is known as the bifacial energy gain (*BEG*). The *BEG* is attributed to light reaching the backside of a PV system, which typically consists of diffuse (scattered) light from the ground, sky, or neighbouring PV rows, but the contributions of direct beam light are possible when the sun is behind a fixed-tilt system. In utility-scale PV parks, *BEG* is typically between 5 and 12%, depending on the configuration and the ground albedo [5–8]. Bifacial PV has potential to reach the lowest levelised cost of energy (*LCOE*) of any commercially available PV technology because such bifacial energy gains are achievable using the same land area that is used for monofacial PV designs while maintaining comparable upfront costs [9, 10]. A study by Rodriguez-Gallegos *et al.* [11] assessed the economics of different PV designs and found that bifacial PV on single-axis trackers achieves the lowest *LCOE* for >90% of the world's land area.

In 2018 (the time of this work's inception) the state-of-the-art bifacial PV simulation software lacked wide-scale validation [12], but according to a 2020 PV technology roadmap, bifacial PV model validation remains an urgent task [13]. Recent efforts have been made by the authors in [14–17] to close this gap. Still, bifacial PV installations do not have the decades of field experience that conventional monofacial PV technology has [18, 19]. The uncertainty surrounding bifacial PV performance results in perceived risk by investors, and consequently, an increase in project soft costs such as interest rates and cost of capital. Therefore, in 2018 the Danish-based renewable energy developer European Energy A/S constructed a 420 kWp pilot project to test bifacial PV technology against monofacial counterparts on large-scale fixed tilt (FT) structures and horizontal single-axis trackers (HSAT) [20]. The site was constructed to observe real-world bifacial gains under different conditions, to benchmark those gains against estimates made by reduced-order bifacial PV performance tools such as PVsyst and SAM, and ultimately to determine the economic value of bifacial PV on trackers within the Danish context.

The literature contains several studies that experimentally demonstrate the annual energy production gain of real HSAT systems versus equator facing FT systems. For example, a three-year study performed by Kinsey *et al.* [21] showed that the utility-scale HSAT systems in Andhra Pradesh, India produced a 14% higher yield than the latitude tilted static systems collocated at the same site. Another field study performed in Boca Raton, Florida showed that a 7.5 kWp HSAT system produced about 15% more energy on an annual basis than a latitude tilted static reference system [22]. Meanwhile, simulations indicate that the advantage of HSAT over static systems with optimally aligned fixed-tilt structures is between 10 and 25% depending on the ground cover ratio (GCR) and site latitude [23, 24]. It has been demonstrated that the *BEG* is mostly additive to the tracker gain [25].

Although PV power plants are commonly designed to maximise annual generation, when the business model is based on power markets the interesting parameter is not the total production or even the average cost of the energy, but the market value of the electricity PV generated relative to the capital and ongoing costs within the investment horizon, which is typically 10 years. As shown in Fig. 1, the hourly power prices of the Nordic Nord Pool spot market [26] (also known as the 'day-ahead' market) are dynamic on hourly, daily, seasonal and yearly timescales. This price variability is driven considerably by the intermittent nature of renewable resources (e.g. hydro, wind and solar). Such price variability occurs not only in Scandinavia but in all Northern Europe [27, 28].

The profiles in Fig. 1 consistently show a midday drop in pricing due to high supply and low demand. This is consequentially the same time that equator facing fixed-tilt PV systems have their peak production on clear sky days. Bifacial PV and HSAT technologies – whether used individually or together – offer the possibility to shift peak production to match times of peak demand. Investigations to this end have been conducted for vertically mounted east-west facing bifacial systems (VBPV), and their potential to match supply and demand profiles, stabilise the grid and increase self-consumption [29–31]. Simulations performed by Van Aken [32] have shown that bifacial on HSATs can generate more revenue per watt peak than VBPV in climates with both low and high fractions of diffuse irradiance.

We presented a preliminary version of this work in [33], but expand on it here by presenting nearly 1 year of energy production from six different systems installed at the test site. The six systems include bifacial and monofacial PV arrays mounted on a south-facing 25° tilt static structures and HSATs wherein the bifacial systems are above either natural grass or a highly reflective white

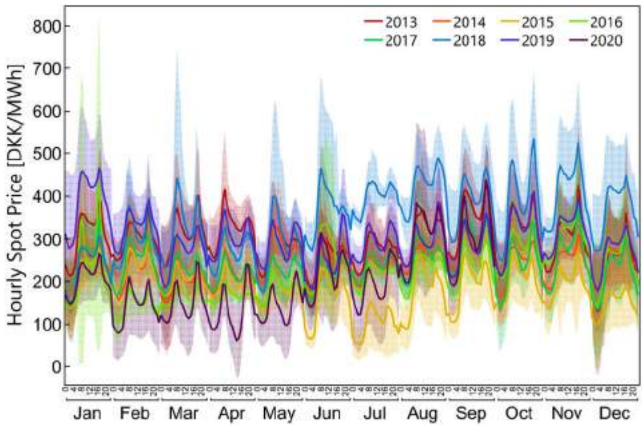

Fig. 1 *Variation of hourly Danish spot price from 2013 to 2020. The lines represent the mean hourly price within each month. The error bands show one standard deviation of the mean. Prices are in Danish Kroner (DKK)*

tarp. The use of reflective materials to enhance bifacial gain has been studied by several authors [34–37], but the validation in these studies has only been made on small systems consisting of an individual bifacial cell or panel. Furthermore, according to a recent bifacial PV review paper [38], there is still an open question as to whether the cost of increasing the albedo is worth the additional energy yield. The present study investigates the extent to which largescale bifacial PV on HSATs above highly reflective ground can optimise not only the annual generation but also the value of generation compared to monofacial static tilt designs. Additionally, the paper explores the potential for bifacial PV systems over highly reflective materials to create value-driven PV designs, wherein the bifacial boost may be exploited to load shift towards periods of high grid demand. This is achieved with measurements and simulations of large-scale bifacial PV systems that have structural dimensions analogous to those found in utility-scale installations.

2 Methods

2.1 Bifacial test site

Fig. 2 shows an aerial view of the test site and highlights the six systems investigated in this work. The balance of system (BoS) is identical in all systems investigated with the exception of the following differences: the orientation of the PV panels (static or tracked), the cell type (monofacial or bifacial), and the ground albedo (low or high). A description of the systems is given in Table 1. The natural grass vegetation is used to represent a low albedo (reflectance) scenario and a white polymeric tarp is used to represent a high albedo scenario. Ground view images of the FT and the HSAT systems above the white tarp are shown in Fig. 3.

Fig. 4 summarises the measured albedo of the two ground surfaces during a nine-month measurement campaign. Both surfaces exhibit a slight reduction in reflectance during winter, which is likely due to low sun angles but could also be attributed to an increase in the dew and moisture on the ground during that period. Also notable is that the white tarp's reflectance gradually degrades over time – about 0.07 (0.7%) per month. This degradation is expected, and the material's integrity is not expected to last longer than five years. Please note that the white tarps underneath the PV structures in Fig. 3 only extend about ± 2.0 m from the torque tube axis and, therefore, are not representative of uniform ground coverage.

We have used view factor calculations to estimate the effective reflectance along the vertical chord of the backside array for the white tarp scenarios. In the case of the FT structure, the percentage of reflected light originating from the white tarp out of the total ground reflected light is 65% for the bottom cells in the array. In other words, 35% of the ground reflected light received by bottom

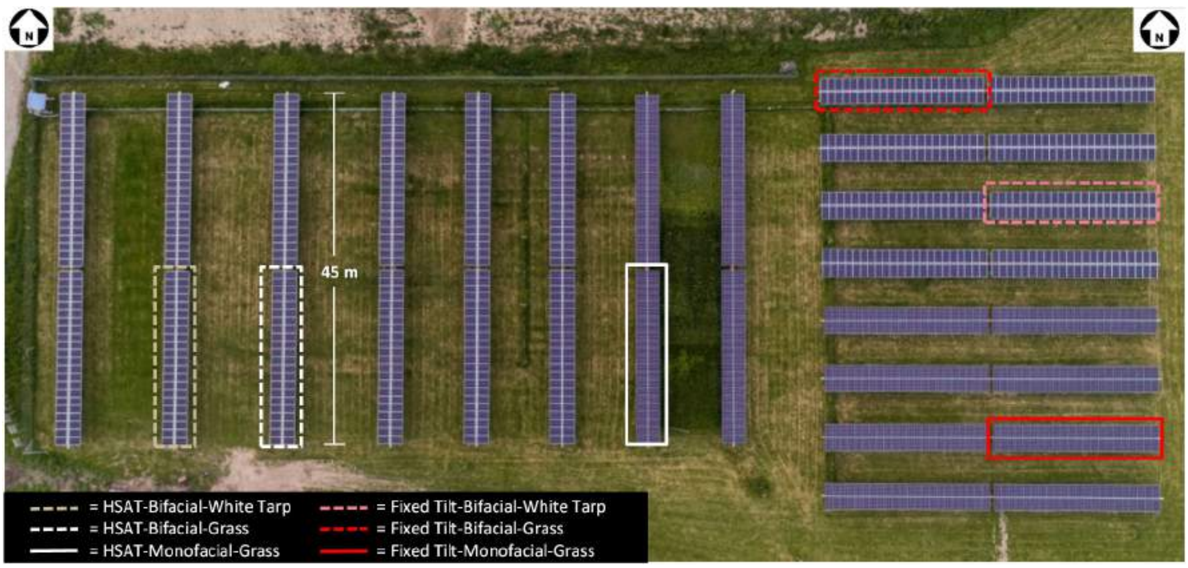

Fig. 2 *Aerial view of the 420 kWp test site. There are eight HSATs on the western side of the park and eight south-facing FT rows on the eastern side. The six systems studied here are highlighted according to the legend. The peak capacity of each system studied here is about 13 kWp*

Table 1 Technical descriptions of the six PV systems studied in this work. Note that ground clearance for tracker (HSAT) systems refers to the torque tube height while for FT systems it refers to the height from the lowest module edge to the ground

System description (structure-PV array-ground)	PV Array	Average ground Albedo	Row-to-row pitch, m	GCR	Ground clearance, m
FT-monofacial-grass	44× 305 W_P p-PERC (13.4 kW_P)	0.22	7.6	0.40	1.56
FT-bifacial-grass	44× 295 W_P p-PERC (13.0 kW_P)	0.22	7.6	0.40	1.56
FT-bifacial-white tarp	44× 295 W_P p-PERC (13.0 kW_P)	0.6	7.6	0.40	1.56
HSAT-monofacial-grass	44× 305 W_P p-PERC (13.4 kW_P)	0.22	12	0.28	2.10
HSAT-bifacial-grass	44× 295 W_P p-PERC (13.0 kW_P)	0.22	15	0.22	2.10
HSAT-bifacial-white tarp	44× 295 W_P p-PERC (13.0 kW_P)	0.6	15	0.22	2.10

Fig. 3 *Ground level views of the test site*
(a) South facing FT rows with bifacial PV and white tarp, ***(b)*** HSAT with a bifacial and white tarp. The white tarp coverage in both systems is ∼±2 m from the torque tube

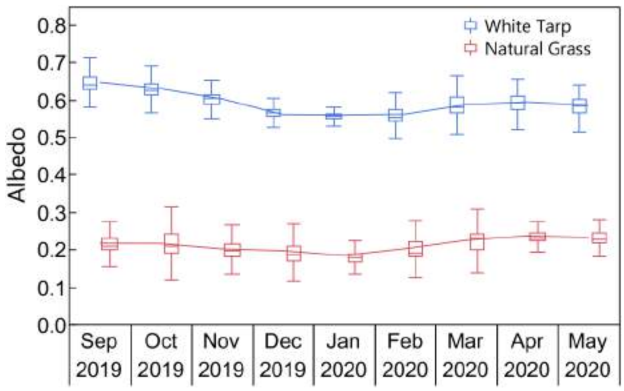

Fig. 4 *Box plots of monthly albedo measured onsite during a nine-month campaign. The connecting lines show the monthly means. The white tarp measurements are made with upward and downward facing EKO ML-02 sensors. The grass measurements are made with upward and downward facing Kipp & Zonen CMP10 sensors. Both measurements are made in unshaded areas of the park*

cells comes from surfaces other than the white tarp. The percentage is lower for cells at the top of the FT array: ∼43% of the total ground reflected light received by these cells originates from the white tarp. In the case of the HSAT, the calculation is dynamic. At the extreme angle of 60° we find that for cells at the bottom, ∼96% of the ground reflected light received originates from the white tarp, with a reduction to just 35% for cells at the top of the array. We demonstrated in [39] that the electrical mismatch losses induced by such gradients amount to <1%. Finally, ray-trace simulations performed by Rhazi *et al.* [40] have shown that increases in the coverage area (m^2) of highly reflective materials below bifacial systems do not correspond with linear increases in bifacial energy gain. This indicates that adding additional white material is not likely to improve project economics beyond what is achievable with the modest amount of white material shown here.

The FT arrays are adjustable but are oriented with a 25° tilt angle during the period studied here. This tilt angle was chosen to reduce the mechanical stress on the structure compared to a more optimal tilt angle of 45°, which in an unshaded installation, could increase the annual generation by about 3% according to our PVsyst simulation. The horizontal single-axis tracker (HSAT) is mounted on a north–south oriented axis, where the rotation is varied from −60° in the morning (facing east) to +60° in the evening (facing west) by an algorithm that uses astronomical equations to track the sun in azimuth. The angular position is monitored by inclinometer sensors mounted on the back of the trackers. These data are within 2° of the tracker algorithm described by Marion and Dobos [41] for 50% of timestamps, and within 8° for 95% of the timestamps presented here when backtracking is not active.

Production data are recorded every minute from all installations on the DC and AC sides independently of their respective inverters. However, in some cases, there are systems with unique configurations (e.g. natural grass and white tarp) connected to the same inverter. Although such systems are connected to dedicated maximum power point trackers (MPPTs), it is not possible to distinguish between their performance on the AC side. Therefore, only maximum power (P_{MAX}) measurements from the DC side are used in this work and the partial load efficiency curve from the inverter manufacturer is used to model AC power. The monofacial and bifacial system have the same cell type (p-PERC) and are from the same manufacturer, but the front side rating of the bifacial modules is 10 W lower than the monofacial ones. Therefore, the AC power is normalised by the ratio of two front side power ratings to make their performance comparable. The analysis presented here is limited to the period where the polymeric white tarps were installed underneath the HSAT and FT systems, which spans from August 2019 to June 2020 (11 months). Unfortunately, the inverter connected to the bifacial FT system above the white tarp experienced a failure during Denmark's COVID-19 lockdown, which resulted in three months of lost data. Therefore, the results from this system are excluded from the analysis in some cases.

2.2 Economic analysis

The real-time hourly spot price of electricity at the back-feed location is used to determine the economic value generated by the six systems. However, as explained by Hirth [42] it is often more meaningful to study the *relative*, rather than the absolute market value. Therefore, the value of the energy generated by the six systems is not estimated and compared solely based on hourly Nord Pool Spot power market prices and income. We additionally use the value factor (*VF*) as used in [31, 43], which is the ratio of the income generated by a specific PV system relative to the average spot price during the period analysed the following equation:

$$\mathrm{VF} = \frac{\bar{P}_{\mathrm{PV}}}{\bar{P}} \tag{1}$$

Derivations of the *VF* numerator and denominator are shown in (2) and (3), respectively. In (2), $\bar{P}_{\mathrm{PV}}$ is the calculated hourly spot price (P_t) weighted according to the hourly electricity (E_t) generated by a given PV system. And in (3), $\bar{P}$ is the base price calculated simply as the arithmetic mean of all spot prices during the period T. Our *VF* calculations only consider times when PV generation is greater than zero (i.e. night data is excluded).

$$\bar{P}_{\mathrm{PV}} = \frac{\sum_{t=1}^{T} E_t \cdot P_t}{\sum_{t=1}^{T} E_t} \tag{2}$$

$$\bar{P} = \frac{1}{T} \sum_{t=1}^{T} P_t \tag{3}$$

The *VF* would equal one if a PV system generated a flat (i.e. time-invariant) production curve during the analysed period. A *VF* of less than one means that the value of electricity produced is less than what a constant production profile would earn. When comparing the production curves of two or more generating technologies, increasing *VF* simply indicates that the power production curve is better aligned with high spot prices.

Additionally, we use the *LCOE* to compare the different system types in terms of their upfront and ongoing (i.e. lifecycle) costs and the electricity generated during a 30-year project period. The full *LCOE* model we use here is described in Annex 2 of [44], but the basic form of the *LCOE* calculation is shown in the following equation:

$$\mathrm{LCOE} = \sum_{t=1}^{N} \frac{C_t/(1+d)^t}{E_t/(1+d)^t} \tag{4}$$

where C_t is the total expenditures (capital, operation and maintenance, debt and equity service etc.) in year t and E_t is the energy generated in year t. All cashflows are discounted by the discount rate d. Many input values within the LCOE equation are highly project-specific (e.g. cost of capital and debt, land costs, local taxes etc.) and as such, the absolute *LCOE* values published here will vary for PV projects in different regions. However, the *LCOE* remains a practical and intuitive tool for assessing the costs and economic benefits of different energy generation technologies relative to each other.

2.3 Simulation

Since the specific installation conditions of this test site are not likely to yield the optimum annual generation, revenue, or value factor achievable with bifacial PV, we have performed simulations where the installation parameters known to affect bifacial PV performance were varied (e.g. row spacing, module height, tilt angle etc.). These simulations have been performed on an hourly basis using the System Advisor Model (SAM), free software from the US National Renewable Energy Laboratory [45]. The model parameters, coefficients and settings have been estimated in a parallel work [17], and are also used here. The site-specific meteorological data have been measured at DTU Fotonik's Solar Radiation Station located ∼400 m from the PV test field.

3 Results

3.1 Electrical performance and economics

Fig. 5 shows specific yields of the six PV systems and a statistical display of daily spot prices at the test site location. The average production profiles are illustrated for each month. Compared to the FT systems, the performance of HSAT systems generally have longer generation periods over the day, especially in summer months when the sun's path is higher in the sky and spans a wider range of azimuth angles. The HSAT systems show higher generation in the morning/evening, but lower generation during midday when the tracker is oriented horizontally, and the sun's angle of incidence is higher relative to the HSAT plane than it is to the FT plane. Nevertheless, the HSAT production profile corresponds well to the typical variation of the power market prices over the day – wherein relatively high prices are observed in the morning/evening and relatively low prices observed during midday. Little difference is observed in FT versus HSAT production on cloudy days when 100% of the solar irradiance comes from diffuse light. Under such conditions, similar income is expected among all PV systems. The income from each system is calculated by simply multiplying the energy generation (MWh) by the spot price (DKK/MWh) at the time the energy was generated. The Danish Kroner is part of the European Exchange Rate Mechanism, and as such, it is tied to the Euro within ± 2.25%.

As expected, the income from each system shows a strong correlation with the energy generated ($R^2 = 0.995$). Fig. 6 shows the total income plotted as a function of the total energy generated during the entire 11-month test period. The data on the x-axis and the y-axis are normalised to the maximum energy and income, which in both cases is the bifacial HSAT system above the high reflectance white tarp.

Fig. 6 provides a convenient way to compare relative gains among the systems due to their different configurations. For example, the tracker gain can be inferred as the difference in normalised energy between the HSAT and FT systems that use the same module type. In the case of the monofacial arrays, the tracker gain is 12.8% and for the bifacial arrays, the tracker gain is 16.0%. The tracker gain for the bifacial arrays is larger because bifacial HSAT and monofacial HSAT have a different row to row pitches. The bifacial HSAT has a 15 m pitch while the monofacial HSAT has a 12 m pitch; the wider pitch of the bifacial HSAT leads to fewer hours backtracking from the ideal roll angle.

Similar to the tracker gain, the bifacial gain can be inferred as the difference between bifacial and monofacial systems mounted on the same structure type. For example, the bifacial gain on the FT system is 7.2% and for the HSAT the bifacial gain is 10.5%. Indoor *I–V* measurements of the p-PERC panels at DTU have shown that the rear side is about 67% efficient as the front side. The bifacial gains above grass therefore are reasonable considering the albedo of the grass is on average 22%. The reason the bifacial gain is higher for the HSAT system is most likely because rows within the FT field are more densely packed than in the HSAT field. The distance between HSATs is twice as far as the distance between FT rows. The shorter pitch (i.e. higher GCR) leads to greater mutual shading by adjacent PV structures, thereby permitting less light to reach the backside of the array [46, 47]. The difference in bifacial gains observed between the systems with differing GCR is consistent with the simulations performed by [7], which showed about a 3% reduction in bifacial gain when GCR is increased from 0.25 to 0.5.

The bifacial boost due to use of the high reflectance white tarp can be inferred from Fig. 6 by the difference between two bifacial systems on the same structure. In this case, the only comparison on the HSAT is possible because the FT bifacial system above the white tarp experienced 3 months of downtime. The bifacial boost from the white tarp below the HSAT is 2.8%, which is on top of the bifacial gain on grass (10.5%), and the monofacial tracker gain (12.8%), resulting in a total energy gain of 26.1% relative to the monofacial FT system.

The relative income delivered by the different PV systems mostly corresponds to the relative energy gains previously mentioned. However, there are deviations from a linear trend. These differences can be inferred from Fig. 6 by the difference between that 45° black unity line and the symbols representing the various systems. The largest differences from unity are on the order of 4%, which occur for both FT system types. This suggests that the additional economic value is mostly due to the single-axis

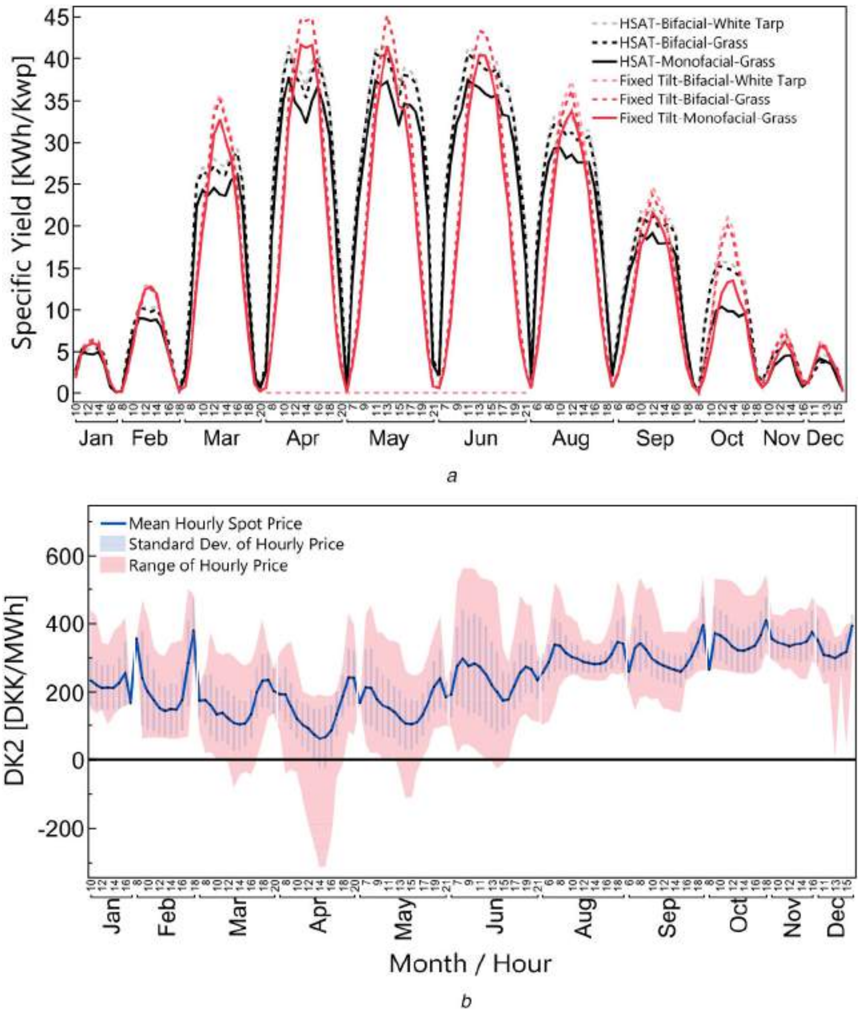

Fig. 5 *Measured energy production and corresponding electricity spot prices*
(a) Specific yield (kWh/kWp) generated by the six different PV systems during each hour of the test period. These plots can be interpreted as the average daily profiles within a given month. Note that the FT-bifacial-white tarp system was non-operational from April to June 2020, ***(b)*** Hourly Nord Pool spot prices within each month where the solid line shows the mean, blue bars show one standard deviation, and red bands show the range of hourly prices within a given month

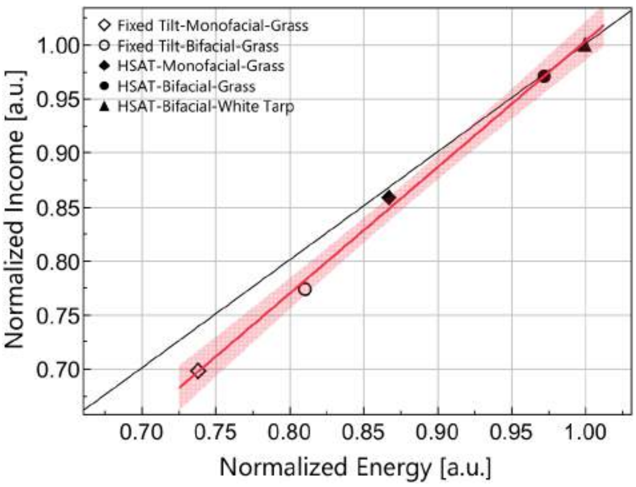

Fig. 6 *Total income as a function of total energy normalised to the maximum. Data points shown are from August 2019–June 2020, which excludes the FT bifacial system above white tarp. The 45° black line shows a 1:1 ratio between income and energy. The shaded areas around the red regression line show the 95% confidence interval of the regression line*

tracking gain rather than due to the bifacial gains. This will be discussed further in the *Value Factor Analysis* section.

Fig. 7 gives insight into the electrical generation and cumulative income on two select days. In the first case, (Fig. 7*a*) a clear sky day near the equinox is shown. This day shows the classic price profile with morning/afternoon prices that are higher than midday prices. The measured electrical performance of six PV systems is shown in the middle of the figure. The benefit of the HSAT's twin-peak profile is captured in the cumulative income plot shown in the bottom frame.

Fig. 7*b* depicts a day with high cloud variability and negative pricing for most of the day. When the spot price goes below zero, power producers are charged for electricity they put onto the grid. On a day such as the one shown here, PV operators would be penalised most heavily for the production of the bifacial systems. This is a scenario where bifaciality can indeed harm project financials unless actions like placing the PV systems in the open-circuit state are taken. The lowest (i.e. most negative) prices are observed in the middle of the day and therefore penalise the bifacial FT systems greatest of all.

3.2 Value factor analysis

Fig. 8 shows value factors (*VFs*) calculated according to (1). Recall that systems with a higher *VF* have a generation profile that is better aligned with high hourly spot prices than systems with lower *VFs*. The historic variability in *VF* is calculated using the electrical data measured during the period studied (Fig. 5*a*) and scaled according to the solar radiation and temperature measured onsite between 2015 and 2019. Each box plot is constructed using the historic hourly Nord Pool prices (Fig. 1) within each respective period to demonstrate the interannual variability in VF. There is a downward trend in the last five years, which makes sense because the market value of electricity from renewables drops with increasing grid penetration rates [42]. As Denmark's capacity of

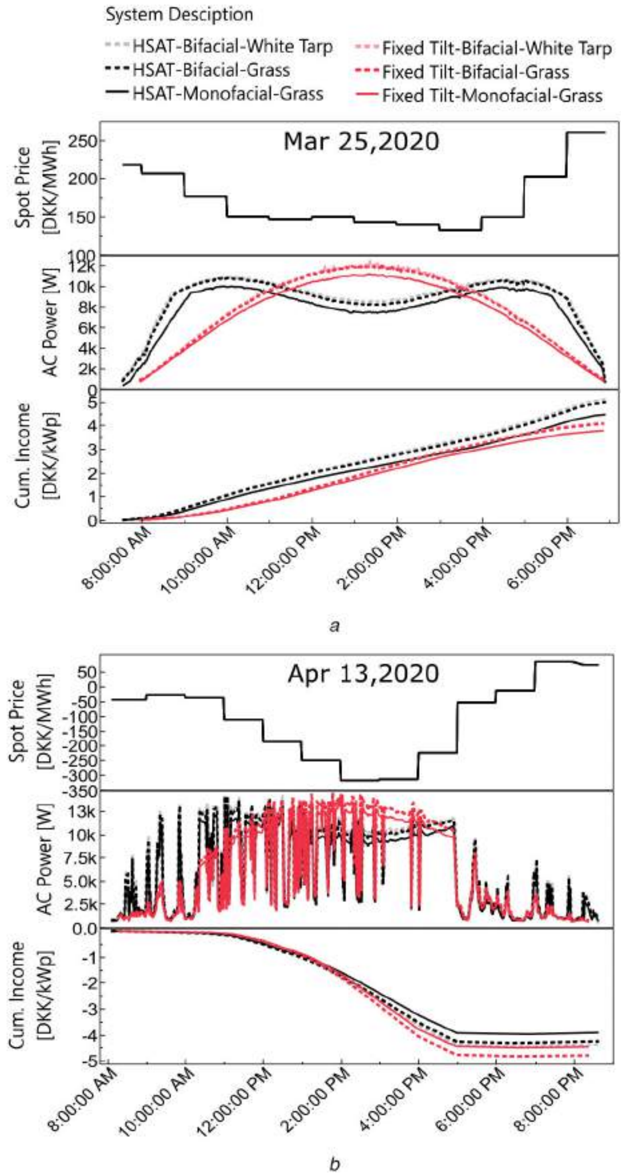

Fig. 7 *Profiles of hourly spot price, measured PV power generation, and cumulative income on two select days*
(a) Clear sky day with typical price profile (25 Mar 2020), ***(b)*** Variably cloudy day with negative pricing (13 Apr 2020)

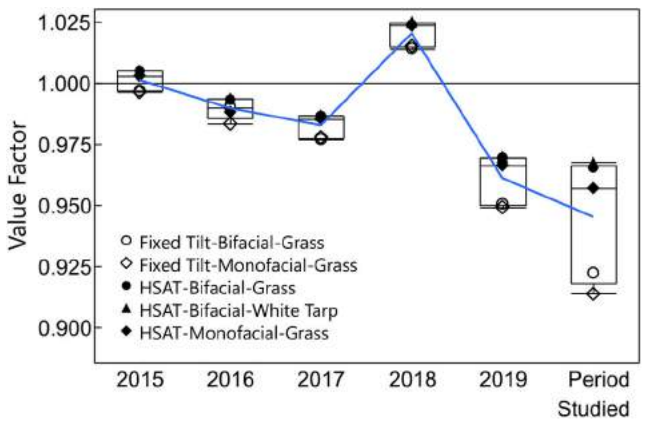

Fig. 8 *Value factors calculated for five PV systems according to (1). The electrical performance measured during the period studied is scaled according to solar radiation and temperature measured from 2015 to 2019. The hourly Nord Pool Spot prices from the respective periods are used to generate the value factors within each box plot. The solid blue line connects the average value factor within periods*

solar-generated electricity increased from 2% in 2015 to 4% at the end of 2020 [48], the historical VFs show a corresponding reduction. In most years, the HSAT systems yield about a 1–2% higher *VF* than the FT systems. Interestingly, the largest spread in VF occurs in the 11-month period of data collection performed in this work (Aug 2019–Jun 2020). During this period there is about a 4% difference in *VF* between HSAT and FT systems, wherein about an additional 1% in *VF* is observed for bifacial over monofacial systems. The notable differences in *VF* during the period studied here (Aug 2019 – Jun 2020) are likely due to the occasional – but sometimes significant – negative pricing observed midday during March to June 2020. Negative midday pricing will always penalise the economics of the 25° FT system more severely than HSAT systems due to the higher midday electrical production at this latitude.

Fig. 9 shows the internal rate of return (*IRR*) plotted as a function of *LCOE*. The *IRR* is shown in conjunction with *LCOE* because the *IRR* is oftentimes a more meaningful metric for investors while the LCOE is mostly used by technical experts to compare different technologies. A clear negative correlation is observed, wherein the *IRR* decreases as the *LCOE* increases. Notably, whether the *VF* or *LCOE* is used as a figure of merit, the relative ranking of the six system types is largely the same.

In Fig. 9, the missing energy production data from the FT bifacial white tarp system have been imputed from months with a similar solar resource (e.g. missing April data is filled in with measured August data). Cost assumptions for all cases are based on discussions with suppliers. We have multiplied the expected capital cost of the white tarp by a factor of four to account for installation costs, which makes the white tarp ∼15% of the total hard capital costs. This capital cost of the white tarp recurs every five years to account for replacement. Additional assumptions in the model include a 20-year mortgage with 0.5% interest that covers 80% of the total (i.e. soft and hard) capital expenditures, spot prices from 2018 as a baseline with inflation of 1.3%/year, linear depreciation over 30 years, a tax rate of 22%, system degradation of 0.5%/year and unavailability of 0.5%/year.

The results show that there are similar decreases in *LCOE* (and thus increases in *IRR*) between FT and HSAT systems and between monofacial and bifacial systems (3.5–4.0 EUR/MWh). There is a small, but a notable decrease in *LCOE* between bifacial above grass and bifacial above white tarp cases. In the FT bifacial grass versus FT bifacial white tarp case, there is a 0.6 EUR/MWh *LCOE* decrease and a 0.4% *IRR* increase. While the comparison of the HSAT bifacial grass and HSAT bifacial white tarp systems shows a smaller difference: a 0.1 EUR/MWh decrease in *LCOE* and a 0.1% increase in *IRR*. The larger *LCOE* and *IRR* differences in the FT case could be due to the use of data imputation.

For both the bifacial FT and bifacial HSAT system, the extra cost of the white tarp does appear to be compensated by the additional energy production. The *LCOE* and *IRR* differences between bifacial grass and bifacial white tarp are, however, small. Therefore, the uncertainty in the capital expenditure and O&M parameters leads to the prudent conclusion that the white tarp is not advisable until O&M and/or CAPEX of such an albedo enhancement solution comes down. For example, an O&M increase of just 10% in the bifacial white tarp cases increases the *LCOE* and decreases *IRR* to levels less favourable than bifacial cases without ground albedo enhancement.

3.3 Simulations with varying GCR

It is worth repeating that the measurements and simulations of the FT and HSAT systems presented here have been made for one specific set of installation conditions (i.e. GCR of the FT = 0.4, and GCR of the HSAT = 0.28). In practice, the net benefit of HSAT over FT systems is highly dependent on the GCR [49]. The net increase both in the energy yield and revenue achieved by HSAT systems will be higher for low GCR sites (i.e. wide PV row spacing) than for low GCR sites. This is large because in low GCR sites, HSAT systems can spend more hours in the early morning and late evenings oriented at an ideal angle without shading

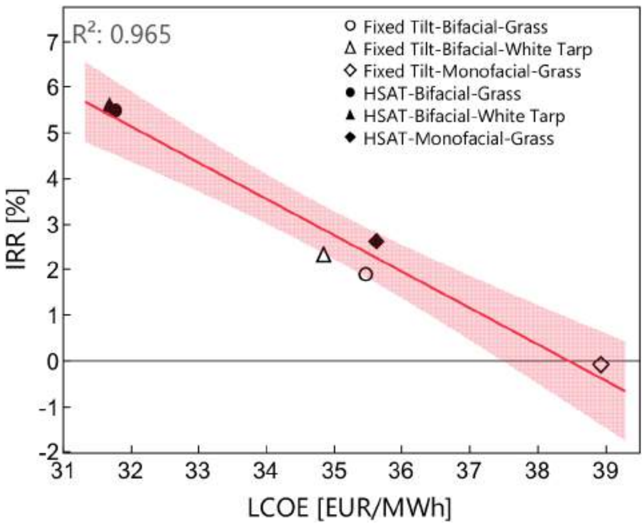

Fig. 9 *Internal rate of return versus LCOE calculated for a 30-year period in Denmark. The shaded areas around the red regression line show the 95% confidence interval of the regression line*

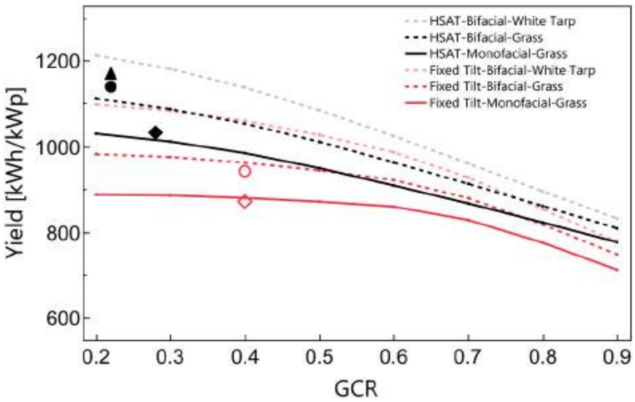

Fig. 10 *Specific yield as a function of GCR. The simulated values are shown as lines and the measured values are shown as markers with symbols that represent five different PV systems*

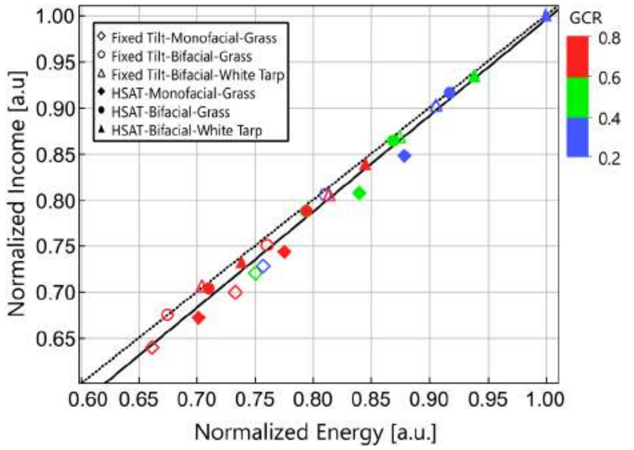

Fig. 11 *Results from simulations using the System Advisor Model for energy generation and Nord Pool for income. The plot shows total income as a function of total energy normalised to the maximum for six different PV system types and four GCRs. All data are normalised to the results of the HSAT-bifacial-White Tarp system at a GCR of 0.2. The dashed 45° black line shows a 1:1 ratio between income and energy*

neighbouring rows. In other words, the trackers must backtrack less at low GCR sites.

Fig. 10 shows the specific yield (kWh/kWp) results from simulations where the GCR is varied. The measured yields are shown as individual markers. The measured and modelled electrical data have been filtered (i.e. removed) during periods when maintenance was performed on either the tracker, inverter, or PV array, or when the data acquisition system was interrupted. The number of filtered (i.e. removed) simulated and measured data points due to these instances amounts to 3.5% of the total data set.

The model predicts the specific yield of the fielded HSAT, FT systems above grass within 30 kWh/kWp, or better (about 3% of full scale). Simulation error of the white tarp system is higher (40 kWh/kWp), which is likely because the reduced-order rear plane of array irradiance model does not account for the fact that the white tarp only covers a limited area. We have analysed the residual error as a function of all the meteorological input variables and as a function of sun height. This error analysis showed that the error is not due to any systematic pattern in meteorological variables. The largest deviations occur in the winter months when there is a significant amount of self-shading from adjacent rows. Modelling the power loss in such scenarios is complex and thus inaccuracies in the shading model or any modest misrepresentation of the physical system geometry in the model are suspected to cause the larger errors in these months.

Fig. 11 shows the theoretical income of four GCR cases (0.2, 0.4, 0.6 and 0.8) using the Nord Pool market prices from Aug 2019 – Jun 2020. All data points are normalised to the results for the 'HSAT-Bifacial-White Tarp' system at 0.2 GCR (i.e. the system that generates the highest income and energy). These results are like those shown in Fig. 6 in that income is correlated with energy for all system types. The deviations from an entirely linear trend are shown by the difference between the dashed 45° black line and the symbols that represent the various systems. The largest differences from unity are on the order of 4%. In all such cases, it is the FT monofacial systems that show a relative income about 4% lower than what would be achieved in a 1:1 situation of energy to income. Since this 4% delta is consistent with findings from the fielded systems shown in Fig. 6, these results indicate that modifying the GCR would not change the relative *Value Factor* results shown in Fig. 8.

The largest difference in energy gains is observed for the 0.2 GCR case. In this case, there is a 24% energy gain of the 'HSAT-Bifacial-White Tarp' system compared to the 'Fixed Tilt-Monofacial-Grass'. As for the 0.8 GCR case, there is only an 8% energy gain between the same two system types, which suggests that modifying the ground with high reflectance material has the greatest benefit for PV installations with a wide row-to-row pitch.

4 Conclusions

We have assessed the relative energy gains and prospective economic advantages of six different PV array designs installed in Denmark. The design variations tested were FT versus single-axis tracker designs, monofacial versus bifacial PV array designs, and designs that have low versus high ground reflectance. Nearly one year of measurements showed that the relative energy gains between the different PV systems are as high as 26.1%. Specifically, it was found that the tracker gain using monofacial panels is 12.8%, the bifacial energy gain on grass is 10.5% using trackers and is 7.2% using FT systems, and finally, the bifacial boost from using a polymeric white tarp below the tracker is 2.8%.

We have assessed the economic advantage of each system by analysing *VF* and *LCOE* values of the system designs. For the system designs studied here, we found that the largest economic advantage due to daily energy generation profiles is obtained with single-axis tracking designs. Specifically, single-axis tracker designs can improve the *VF* by as much as 4% relative to FT designs. Although the bifacial designs studied did show higher *VF* relative to their monofacial counterparts, the increase was lower than the relative economic benefit achieved by single-axis trackers, on the order of 1%. We found a negligible increase in *VF* when a highly reflective white tarp was mounted below the bifacial PV arrays. The *VF* results dovetail with the *LCOE* findings. The *LCOE* of bifacial systems with the white tarp is between 0.1 and 0.4 EUR/MWh lower than bifacial systems without it. However, we found that small variations in the capital and/or O&M cost of the white tarp could easily reverse the financial allure of this albedo augmentation solution. Therefore, it is our prudent recommendation to not recommend such ground albedo enhancements until definite cost reductions are achieved.

5 Acknowledgment

The work presented in this paper was supported by the Danish Energy Technology Development and Demonstration Program (EUDP) under project contract 64018-0624 which is gratefully acknowledged. Thanks to European Energy A/S for sharing the data presented in this paper. Thanks also to Jørn Rosager from SolTec for providing the polymeric white tarps. An acknowledgment is also given to Martynas Ribaconka (DTU) and Michael Graversen (MG Solar) for their work affixing the white tarps to the ground.

6 References

[1] Romijn, I., Janssen, G., Dullweber, T., *et al.*: 'Bifacial cells', In: '*Bifacial Photovoltaics: Technology, Applications and Economics, Herts*' (The Institution of Engineering and Technology, Golden, CO, USA, 2018), pp. 17–40

[2] Fu, R., Feldmnan, D., Margolis, R.: 'U.S. Solar Photovoltaic System Cost Benchmark: Q1 2018'. National Renewable Energy Laboratory Report (NREL/TP-6A20-72399), 2018

[3] Woodhouse, M., Smith, B., Ramdas, A., *et al.*: 'Crystalline Silicon Photovoltaic Module Manufacturing Costs and Sustainable Pricing'. National Renewable Energy Laboratory Report (NREL/TP-6A20-72134), 2020

[4] 'International Technology Roadmap for Photovoltaics: 2019 Results', ITRPV, 2020

[5] Deline, C., Palaez, S., Marion, B., *et al.*: 'Bifacial PV system performance: separating fact from fiction'. 46th IEEE Photovoltaic Specialists Conf., Chicago, IL, 2019

[6] Beardsworth, G., Asgharzadeh, A.: 'Quantifying your bifacial gains', NextTracker White Paper, 2020

[7] Berrian, D., Libal, J., Klenk, M., *et al.*: 'Performance of bifacial PV arrays with fixed tilt and horizontal single-axis tracking: comparison of simulated and measured data', *IEEE J. Photovoltaics*, 2019, **9**, (6), pp. 1583–1589

[8] Janssen, G., Van Aken, B., Carr, A., *et al.*: 'Outdoor performance of bifacial modules by measurements and modelling', *Energy Procedia*, 2015, **77**, pp. 364–373

[9] Kopecek, R., Veschetti, Y., Gerritsen, E., *et al.*: 'Bifaciality: one small step for technology, one giant leap for kWh cost reduction', *Photovoltaics Int.*, 2015, **26**, pp. 32–45

[10] Tillman, P., Jager, K., Becker, C.: 'Minimising the levelised cost of electricity for bifacial solar panel arrays using Bayesian optimisation', *Sustain. Energy Fuels*, 2020, **4**, (1), pp. 254–264

[11] Rodriguez-Gallegos, C., Liu, H., Gandhi, O., *et al.*: 'Global techno-economic performance of bifacial and tracking photovoltaic systems', *Joule*, 2020, **4**, pp. 1514–1541

[12] Kopecek, R., Libal, J.: 'Towards large-scale deployment of bifacial photovoltaics', *Nat. Energy*, 2018, **3**, (6), pp. 443–446

[13] Wilson, G., Al-Jassim, M., Metzger, W.K., *et al.*: 'The 2020 photovoltaic technologies roadmap', *J. Phys, D: Appl, Phys.*, 2020, **53**, pp. 1–47

[14] Pelaez, S.A., Deline, C., MacAlpine, S., *et al.*: 'Comparison of bifacial solar irradiance model predictions with field validation', *IEEE J. Photovoltaics*, 2019, **9**, (1), pp. 82–88

[15] Asgharzadeh, A., Anoma, M., Hoffman, A., *et al.*: 'A benchmark and validation of bifacial PV irradiance models'. 46th IEEE Photovoltaic Specialists Conf., Chicago, IL, 2019

[16] Nussbaumer, H., Janssen, G., Berrian, D., *et al.*: 'Accuracy of simulated data for bifacial systems with varying tilt angles and share of diffuse radiation', *Sol. Energy*, 2020, **197**, pp. 6–21

[17] Riedel-Lyngskaer, N., Berrian, D., Alvarez, D., *et al.*: 'Validation of bifacial photovoltaic simulation software against monitoring data from large-scale single axis trackers and fixed tilt systems in Denmark', *Appl. Sci.*, 2020, **10**, (23), pp. 1–29

[18] Virtuani, A., Caccivio, M., Annigoni, E., *et al.*: '35 years of photovoltaics: analysis of the TISO-10 kW solar plant, lessons learnt in safety and performance – part 1', *Prog. Photovolt.*, 2019, **27**, (4), pp. 328–339

[19] Jordan, D., Marion, B., Deline, C., *et al.*: 'PV field reliability status – analysis of 100 000 solar systems', *Prog. Photovolt.*, 2020, **28**, (8), pp. 739–754

[20] Riedel, N., Protti, A.A., Jakobsen, M.L., *et al.*: 'The outdoor bifacial PV testing facility at technical university of Denmark'. BifiPV Workshop, Amsterdam, 2019

[21] Kinsey, G.S., Partani, M., Kulkarni, M., *et al.*: 'Performance comparison of co-located fixed-tilt and single-axis tracker arrays'. Conf. Record of the 46th IEEE Photovoltaic Specialists Conf., Chicago, IL, 2019

[22] Moradi, H., Abtahi, A., Messenger, R.: 'Annual performance comparison between tracking and fixed photovoltaic arrays'. Conf. Record of the 44th IEEE Photovoltaic Specialists Conf., Washington D.C., 2017

[23] Weinstock, D., Appelbaum, J.: 'Optimization of solar photovoltaic fields', *J. Sol. Energy Eng.*, 2009, **131**, (3), pp. 0310031–0310039

[24] Vanicek, P., Stein, S.: 'Simulation of the impact of diffuse shading On the yields of large single axis tracked PV-plants'. 24th European Photovoltaic Solar Energy Conf., Hamburg, Germany, 2009

[25] Janssen, G., Burgers, A.B.A., Carr, A., *et al.*: 'How to maximize the kWh/kWp ratio: simulations of single-axis tracking in bifacial systems'. 35th European Photovoltaic Solar Energy Conf. and Exhibition, Brussels, 2018

[26] 'Nord Pool', Available at: https://www.nordpoolgroup.com/historical-market-data/

[27] Paraschiv, F., Erni, D., Pietsch, R.: 'The impact of renewable energies on EEX day-ahead electricity prices', *Energy. Policy*, 2014, p. pp. 196–210

[28] Gürtler, M., Paulsen, T.: 'The effect of wind and solar power forecasts on day-ahead and intraday electricity prices in Germany', *Energy Econ.*, 2018, (75), pp. 150–162

[29] Ranta, S., Stein, J., Huerta, H., *et al.*: 'Self-consumption rate achieved by the bifacial east-west vertical PV system compared to the conventional south facing system in Nordic conditions'. 36th European Photovoltaic Solar Energy Conf. and Exhibition, Marseille, 2019

[30] Ganilha, S.C.: 'Potential of bifacial PV installation and its integration with storage solutions'. Dissertation, Universidade de Lisboa, 2017

[31] Chudinzow, D., Nagel, S., Gusewell, J., *et al.*: 'Vertical bifacial photovoltaics – a complementary technology for the European electricity supply?', *Appl. Energy*, 2020, **264**, p. 114782

[32] Van Aken, B.: 'Generated kWh value as a function of system design and daily price profile: towards value driven PV designs'. 37th European Photovoltaic Solar Energy Conf. and Exhibition (EUPVSEC), Lisbon, Portugal, 2020

[33] Nørgaard, P., Poulsen, P., Riedel, N., *et al.*: 'The value of a new east-west facing single axis PV tracker setup'. 9th Solar & Storage Integration Workshop, Dublin, 2019

[34] Ooshaksaraei, P., Sopian, K., Zulkfli, R., *et al.*: 'Characterization of a bifacial photovoltaic panel integrated with external diffuse and semimirror type reflectors'. Hindawi, 2013

[35] Lim, Y.S., Lo, K.C., Kee, S.Y., *et al.*: 'Design and evaluation of passive concentrator and reflector systems for bifacial solar panel on a highly cloudy region – a case study in Malaysia', *Renew. Energy*, 2014, **63**, pp. 415–425

[36] Jakobsen, M.L., Thorsteinsson, S., Poulsen, P., *et al.*: 'Bifacial PV cell with reflector for stand-alone mast for sensor powering purposes'. 13TH Int. Conf. on Concentrator Photovoltaic Systems (CPV-13), Ottawa, Canada, 2017

[37] Bowersox, D., GovindaSami, T.: 'Design and construction of controlled back reflectors for bifacial photovoltaic modules'. 7th World Conf. on Photovoltaic Energy Conversion (WCPEC), Waikoloa, HI, 2018

[38] Urrejola, E., Valencia, F., Fuentealba, E., *et al.*: 'bifiPV2020 bifacial workshop: a technology overview'. National Renewable Energy Laboratory, NREL/TP-5K00-77817., Golden, CO, 2020

[39] Riedel-Lyngskaer, N., Petit, M., Berrian, D., *et al.*: 'A spatial irradiance map measured on the rear Side of a utility-scale horizontal single axis tracker with validation using open source tools'. 47th IEEE Photovoltaic Specialists Conf., Ottawa, Canada, 2020

[40] Rhazi, O., Chiodetti, M., Dupuis, J., *et al.*: 'Optimising the utilisation of reflective materials for bifacial plants'. 37th European Photovoltaic Solar Energy Conf. and Exhibition, Lisbon, Portugal, 2020

[41] Marion, B., Dobos, A.: 'Rotation angle for the optimum tracking of one-axis trackers', National Renewable Energy Laboratory Report (NREL/TP-6A20-58891), 2013

[42] Hirth, L.: 'The market value of Variable renewables', European University Institute (EUI), Working Paper RSCAS 2013/36, 2013

[43] Hirth, L.: 'The benefits of flexibility: the value of wind energy with hydropower', *Appl. Energy*, 2016, **181**, pp. 210–223

[44] Moser, D., Lindig, S., Richter, M., *et al.*: 'Uncertainty in yield assessments and PV LCOE (IEA-PVPS T13-18:2020)', International Energy Agency (IEA), 2020

[45] Gilman, P., Dobos, A., DiOrio, N., *et al.*: 'SAM photovoltaic model technical reference update (NREL/TP-6A20-67399)', National Renewable Energy Laboratory, 2018

[46] Janssen, G., Gali, R., deGroot, K., *et al.*: 'Impact of inhomogenous irradiance at the rear of bifacial panels on modelled energy yield'. 33rd European Photovoltaic Solar Energy Conf. and Exhibition, Amsterdam, 2017

[47] Deline, C., Pelaez, S.A., MacAlpine, S., *et al.*: 'Estimating and parameterizing mismatch power loss in bifacial photovoltaic systems', *Prog. Photovolt.*, 2020, **28**, (7), pp. 691–703

[48] Dansk Energistyrelsen, 'Annual and Monthly Statistics,' [Online]. Available: https://ens.dk/en/our-services/statistics-data-key-figures-and-energy-maps/annual-and-monthly-statistics. [Accessed 7 January 2021]

[49] Chudinzow, D., Klenk, M., Eltrop, L.: 'Impact of field design and location on the techno-economic performance of fixed-tilt and single-axis tracked bifacial photovoltaic power plants', *Sol. Energy*, 2020, **207**, pp. 564–578